ISSN 0289-260X
UDC 06.055.8

SP-29

航空宇宙技術研究所特別資料

SPECIAL PUBLICATION OF NATIONAL AEROSPACE LABORATORY

SP-29

第13回航空機計算空気力学シンポジウム論文集

特別企画
高エンタルピー流れ企画セッション及びワークショップ

航空機計算空気力学シンポジウム運営委員会
特別企画実行ワーキンググループ

1996年1月

航 空 宇 宙 技 術 研 究 所
NATIONAL AEROSPACE LABORATORY

第１３回航空機計算空気力学シンポジウム論文集

特別企画

高エンタルピー流れ

企画セッション及びワークショップ

Proceedings of the 13th NAL Symposium on Aircraft Computational Aerodynamics

High Enthalpy Flow Organized Session and Workshop

開催期日　　平成７年６月８日

開催場所　　航空宇宙技術研究所

8 June ,1995

National Aerospace Laboratory

Tokyo

航空宇宙技術研究所

航空機計算空気力学シンポジウム運営委員会

特別企画実行ワーキンググループ

特別企画

高エンタルピー流れ
企画セッション及びワークショップ

諸　言

第１２回の極超音速流CFDワークショップにひきつづき、特別企画として高エンタルピー流れの企画セッション及びワークショップを開催し、おかげさまで参加者の皆様の御協力を得て、実りのある企画となりました。今回はオランダにあるヨーロッパ宇宙機構(ESA)のESTEC研究所から、特別講演者としてJ. Muylaert氏を招待し、ワークショップの課題の一部が、ESAから提案された課題を採用するなど、国際化にも、わずかですが、貢献できたと考えております。

今日、我が国においては、無人有翼宇宙往還実験機HOPE-Xの実現に向けてNAL-NASDA間で共同研究チームが組織され、OREX, HYFLEX等の実飛行実験、また高エンタルピー衝撃風洞設備の整備等を進めており、高エンタルピー流れの解明が、非常に重要な課題となっております。このような状況下、計算空気力学を活用し、CFDを高エンタルピー流れ解明の主要手段の一つとして確立するため、本特別企画が開催できたことは、大変有意義なことであったと思っております。本企画を行うにあたり、御協力いただいた関係各位に深く感謝申し上げます。

第１３回航空機計算空気力学シンポジウム
運営委員会委員長
曽我　国男

特別企画；高エンタルピー流れ

企画セッション　及び
ワークショップ実行ワーキンググループ

コーディネーター	山本　行光（空気力学部）
委員	廣瀬　直喜（数理解析部）
	小川　哲　（数理解析部）
	岩宮　敏幸（数理解析部）
	中道　二郎（構造力学部）

第１３回航空機計算空気力学シンポジウム運営委員会委員

委員長	曽我国男	（空気力学部）
委　員	◎山本稀義	（空気力学部）
	山本行光	（空気力学部）
	中道二郎	（構造力学部）
	○江尻　宏	（構造力学部）
	牧田光正	（熱流体力学部）
	小川　哲	（数理解析部）
	福田正大	（数理解析部）
	野村聡幸	（空力性能部）
	山本　武	（原動機部）
	斎藤　茂	（飛行実験部）
	○末松俊二	（新型航空機研究ｸﾞﾙｰﾌﾟ）
	舞田正孝	（宇宙研究ｸﾞﾙｰﾌﾟ）
	石垣　博	（ロケット推進研究部）
	伊藤勝宏	（ラムジェット推進研究部）

［◎印：研究幹事、○印：事務局］

目　　次

I　高エンタルピー流れ

企画セッション

1-1

高温衝撃風洞の駆動気体汚染に関する数値計算

ランディ チュー　　伊藤勝宏
航技研 角田研究センター

A Computational Study of Driver Gas Contamination in a High Enthalpy Shock Tunnel

by

Randy S. M. CHUE and Katsuhiro ITOH
National Aerospace Laboratory, Kakuda Research Center
1 Kimigaya, Koganesawa, Kakuda
Miyagi, JAPAN 981-15

Abstract

A computational study has been carried out to examine driver gas contamination in a high-enthalpy reflected shock tunnel. The investigation focused on the nonsteady events as the reflected shock interacts with the wall boundary layer and the contact interface and their contribution to driver gas contamination. Both tailored and off-tailored tunnel operating conditions and the effects of a choked nozzle are discussed in the present paper.

1. Introduction

In reflected-shock tunnel facilities, the reflection of the incident shock at the end of the shock tunnel generates a reservoir of high enthalpy gas which, upon flowing through a nozzle, provides a source of high Mach number flow that can be utilized for aerodyamic testing. The ideal testing time of the facility is governed by the duration for the test gas slug to be exhausted through the nozzle. If, however, the driver gas arrives prematurely at the nozzle, the testing time of the facility would be decreased. The contamination of the test gas by driver gas is an important problem in shock tunnel testing and particularly in high enthalpy impulse facilities where the the useful test time would severely be limited.

The interaction of the reflected shock with viscous boundary layers has been recognized as one of the major candidates to cause driver gas contamination. The theoretical treatment first developed by Mark[1] has established the framework for understanding the resulting bifurcated shock structure and the transport of boundary layer fluid by wall jetting towards the end of the shock tube. Based on this mechanism, analytical models have been developed to estimate the premature arrival of the driver gas at the shock tube end-plate (e.g., Davies & Wilson[2], Stalker & Crane[3]). More recently numerical simulations have provided more detailed information about the contamination process (e.g. Wilson et al.[4]), which has become a great concern in the current interest in high enthalpy impulse facilities. Wilson examined the bifurcated shock structure and the transport of driver gas along the wall to the end-plate for an over-tailored case with laminar boundary layer.

However, the mechanism that is responsible for the premature arrival of driver gas remains unclear and therefore it is still difficult to predict driver gas contamination in reflected-shock tunnels. Furthermore, many experimental works done to understand the phenomena are carried out under relatively low incident shock Mach numbers (of less than 6) and are therefore not sufficient for high enthalpy studies. Also, because the main interest has been the phenomenon of reflected shock/boundary layer interaction itself, most of the experimental and computational works tended to be done for strongly over-tailored conditions where the interaction is more significant and easily observable. The tailored operating condition, which is of greater relevance to high enthalpy testing, has not been clearly examined.

Stalker and his colleagues have been carrying out experimental measurements and analytical predictions of driver gas contamination based on the interaction of reflected shock and wall boundary layers in their high-enthalpy free-piston shock tunnel and have found that the tunnel testing time was signifi-

cantly reduced at high enthalpies (see for example, Skinner[5]). The experiments and analyses have been carried out for fixed driver condition with variable shock tube initial conditions. Thus far, their analytical predictions of the arrival of driver gas at the test section has not shown reasonable agreement with the experimental results. Moreover, the experimental detection of driver gas remains a difficult problem and it is not easy to vary the tunnel operating conditions in actual experiments. Computational study is thus expected to be an important tool for examining driver gas contamination.

The objective of the present work is twofold—to analyze computationally the reflected shock/boundary layer interaction in order to determine its role in causing driver gas contamination and the lost of testing time, and to conduct numerical experiments to evaluate the influence of different tunnel operating conditions on driver gas leakage.

2. The Computational Model

Time-dependent viscous calculations were carried out for a reflected-shock tunnel with circular cross-section. The shock tube investigated is assumed to have dimensions: internal diameter 30 mm, length 4 m, shock-tube-to-driver-tube area ratio 0.09. The computational domain covered only the region near the end of the shock tube with the upstream inflow condition and the tube-wall temperature assumed to be fixed. Because the emphasis is on the events after the incident shock has reflected from the end-plate of the shock tube, the initial condition of the computation was taken at the moment just before shock reflection, with the initial flow field behind the shock estimated from the turbulent boundary layer theory of Mirels[6].

The present study focuses on high shock Mach numbers ($M_s \simeq 10$) typically encountered in high enthalpy impulse facilities. The driver and driven gases are helium and air, respectively, which are assumed to be perfect gases. The driver gas has specific heat ratio of 5/3 and molecular mass of 4.003 kg/kmol. The test gas is assumed to be high temperature air having specific heat ratio of 1.25, molecular mass of 25.9 kg/kmol. The viscous boundary layer along the tube wall is assumed to be turbulent and the Baldwin-Lomax[7] algebraic eddy viscosity model is used in the present preliminary analysis. To single out the effect of reflected shock/boundary layer interaction, the contact region between the driver and driven gases is initially assumed to be a plane discontinuous surface and no attempt is made to consider the effects of non-ideal diaphragm rupture and mixing.

The computational code used in the analysis is developed by Takahashi et al.[8] using a second order KRC scheme, which is a pointwise nonoscillatory shock capturing method developed by Itoh et al.[9] Time integration was done using the second order Runge-Kutta method. The computational mesh covers 26 cm of the end portion of the shock tube with a 433×121 grid with clustering in the boundary layer and the end-plate regions. A more detailed account of the numerical method used and its validation can be found in Takahashi et al.[8]

3. Results and Discussions

Two sets of computations have been carried out—one for a closed-end shock tube and another for a shock tunnel with a choked nozzle. The shock Mach number (M_s) is fixed at 10 with initial shock tube pressure (p_1) at 10 kPa. The total enthalpy behind the reflected shock is 13 MJ/kg.

3.1 Wall Jetting

Figure 1 presents the sequence of contour plots of temperature and driver gas mass fraction as the reflected shock interacts with the turbulent boundary layer for times up to 100 μsec after shock reflection at the end-plate. In this calculation, the "tailored" interface condition, where the ratio of transmitted shock pressure to the reflected shock pressure (p_7/p_5) equals 1.0, is enforced. Particular attention is directed towards the bifurcated shock structure produced as the reflected shock propagates into the boundary layer flow. The formation of the bifurcated shock and the resulting mechanism of wall jetting of the "cold" boundary layer fluid towards the end-plate which generates a vortex at the corner region of the end-plate is clearly illustrated in Fig. 1a. The distortion of the contact surface and the leakage of driver gas into the test gas through the bifurcated shock foot can be seen in Fig. 1b. The interaction immediately results in a stream of driver gas, near the edge of the boundary layer and the triple point of the bifurcated shock, being driven towards the wall boundary layer and is then partially transported towards the end-plate (at 50 μsec). This phenomenon agrees well with the previous analytical model proposed (Mark[1], Davies & Wilson[2]). However, the vortical structure generated at the contact surface has a counter-clockwise direction which serves to retard further transport of driver gas towards the end-plate. Moreover, the bifurcated shock structure weakens drastically as the reflected shock transmits through the contact surface and wall jetting is less apparent as the shock propagates into the driver gas region. It is also noted that the contact surface shape remains rather

planar as would be predicted by inviscid theory, except near the boundary layer region. The driver gas transported by wall jetting arrives at the end-plate at about 95 μsec after shock reflection.

3.2 Off-tailored Interface Conditions

The effects of off-tailored tunnel conditions are compared in Fig. 2. Figures 2a and 2c show the temperature and driver gas mass fraction distributions at 100 μsec for off-tailored conditions while keeping the primary shock Mach number to be 10. The values of p_7/p_5 are respectively 0.8 and 1.1 for the under- and over-tailored conditions. The tailored case is redisplayed in Fig. 2b for comparison. The effect of wall jetting is most severe for the over-tailored condition as driver gas arrives at the end-plate the earliest, but the overall shape of the contact surface remains largely undistorted. On the other hand, the effect of reflected shock/boundary layer interaction appears to be least severe for the under-tailored case where wall jetting is too weak to transport the driver gas towards the end-plate. However, the vortex-generated flow strongly distorts the contact surface near the center-line and builds up a large protruded region of driver gas that flows towards the end-plate.

The present results therefore indicate that reflected shock/boundary layer interaction does not necessarily play the major role in the driver gas contamination process as the driver gas may be transported towards the end-plate by other means. The nature of the vortex dynamics produced also appeared not to favor driver gas leakage by purely the mechanism of wall jetting alone. This points out the need to examine other mechanisms, such as instabilities and mixing in the contact region, in causing driver gas contamination in experiments where the lost of testing time had been observed to be more severe.

Besides the contamination by "cold" wall fluid and driver gas, Fig. 3 shows that the pressure at the center of the shock-tube end plate becomes quite nonsteady with a large pressure peak occurring near 80 μsec for both the tailored and off-tailored cases. The quality of the freestream flow would then be affected if the gas is allowed to discharge through a nozzle at the end of the shock tunnel.

3.3 Effect of Nozzle Flow

As an initial effort to include the effect of nozzle flow at the end of the shock tube, a calculation is performed assuming the nozzle to be an effective "sink" with choked flow. The nozzle throat diameter is taken to be 10 mm. The exhaust flow takes effect as soon as the shock has arrived at the end-plate and is assumed to be choked based on the condition in the center-line immediately upstream of the end-plate. Although the present analysis may be overly crude for describing the actual shock/nozzle flow interaction, it should provide a qualitative picture of how the driver gas may exhaust into the nozzle. Figure 4 shows the sequence of contour plots of temperature and driver gas mass fraction for the tailored condition as the driver gas is transported towards the nozzle. The early events of reflected shock/boundary layer interaction is quite similar to the case without the nozzle, although the vortex at the corner of the end-plate appears to be larger with nozzle flow (c.f. Fig. 1). From 80 μsec, the volume of driver gas leakage at the end-plate appears to be entrained into a vortex closed to the end-plate, with a stagnation point dividing the vortex and the exhaust flow slightly upstream of the nozzle on the center-line. Because of this, only part of leakage gas is exhausted into the nozzle with the rest being recirculated in the shock tube (100 μsec). The time of arrival of driver gas at the nozzle is at 90 μsec and is not significantly different from the closed-end case. A set of off-tailored conditions has also been recalculated with the nozzle flow, and the results are again quite close to those for the closed-end conditions presented in Fig. 2.

3.4 Loss of Test Time

The arrival time of the driver gas at the end plate is summarized in Table 1 for the tailored condition. Also included in the table are the values calculated using the analytical approximation of Davis & Wilson[2], based on the mechanism of wall jetting, and the "ideal" drainage time for reference. The drainage time is the time required to drain the test gas with consideration of mass loss due to boundary layer effects prior to shock reflection. The approximation of Davies obtained a value on the conversative side and can be a useful tool for predicting test time in actual tunnel operations if the effect of wall jetting is dominant. However, as wall jetting may not always be the cause of driver-gas contamination, as illustrated earlier in the under-tailored condition, the formulation may not always be adequate. In any case, the premature arrival of the driver gas can significantly reduce test time. For the shock tunnel considered in the present study, the arrival time of driver gas is less than 50% of the drainage time.

4. Concluding Remarks

The interaction of reflected shock with a turbulent boundary layer has been analyzed numerically to assess its contribution to driver gas contamina-

tion. The results illustrated that the contamination of test gas can be manifested in at least two ways—the transport of low-temperature boundary layer fluid as well as driver gas leakage. While the results demonstrated that wall jetting is an important mechanism to cause contamination of the test gas, it may not necessarily be the dominating one. In particular, the mechanism for contamination is quite dependent on the tunnel operating condition with under-tailoring appeared to be affected more by the distortion of the contact surface rather than by wall jetting. It is thus necessary to consider other mechanisms, such as contact surface instabilities and mixing subsequent to diaphragm rupture, before a more precise understanding of driver gas contamination can be achieved.

Acknowledgement

Special thanks are due to M. Takahashi for his help and discussions, and to G. Eitelberg of DLR-Göttingen for suggesting the calculation with nozzle flow. R.S.M. Chue is supported by the STA Fellowship program of Japan.

References

[1]Mark, H., "The Interaction of a Reflected Shock Wave with the Boundary Layer in a Shock Tube," NACA TM 1418, 1958.

[2]Davies, L. and Wilson, J. L., "Influence of Reflected Shock and Boundary-Layer Interaction on Shock-Tube Flows," *The Phys. of Fluids Supplement I*, pp. I-37–I-43, 1969.

[3]Stalker, R. J. and Crane, K. C. A., "Driver Gas Contamination in a High-Enthalpy Reflected Shock Tunnel," *AIAA Journal*, Vol. 16, pp. 277-279, 1978.

[4]Wilson, G. J., Sharma, S. P., and Gillespie, W. D., "Time-Dependent Simulations of Reflected-Shock/Boundary Layer Interaction," AIAA Paper 93-0480, 1993.

[5]Skinner, K. A., "Mass Spectrometry in Shock Tunnel Experiments of Hypersonic Combustion," Ph.D thesis, Department of Mechanical Engineering, The University of Queensland, March 1994.

[6]Mirels, H., "Shock Tube Test Time Limitation Due to Turbulent-Wall Boundary Layer," *AIAA Journal*, Vol. 2, pp. 38-54, 1964.

[7]Baldwin, B. S., and Lomax, H., "Thin Layer Approximation and Algebraic Model for Separated Turbulent Flows," AIAA Paper no. 78-257, 1978.

[8]Takahashi, M., Itoh, K., Tani, K., and Tanno, H., "Numerical Analysis of the Driver Gas Contamination in a Reflected Shock Tunnel," In: *Proc. of Symp. on SHOCK WAVES, JAPAN '94* (in Japanese), pp 211-214, 1994.

[9]Itoh, K., Takahashi, M., and Hiraiwa, T., "Pointwise Non-Oscillatory Shock Capturing Scheme," In: *Proc. of 6th Symp. on Computational Fluid Dynamics* (in Japanese), pp 535-538, 1992.

Table 1: Time of arrival of driver gas at the end wall.

	Time after shock reflection (μsec)
Closed-off end wall	95
With nozzle	90
Analytical approx. by Davies	62
"Ideal" drainage time [a]	226

[a] $t_{drainage} = \frac{4M}{A^*}\frac{1}{\rho_5 a_5}\left(\frac{\gamma+1}{2}\right)^{\frac{\gamma+1}{2(\gamma-1)}}$, M = mass of test slug, a = sound speed, and A^* = nozzle throat area. Subscript 5 denotes the condition behind the reflected shock.

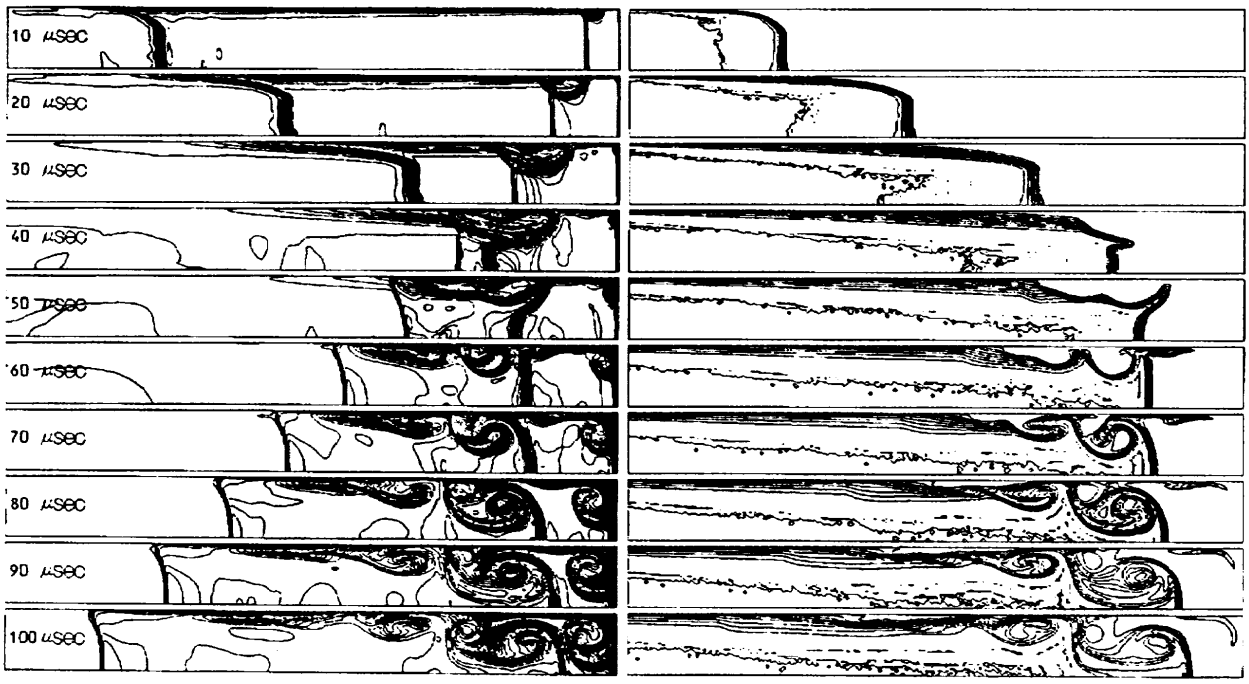

(a) Temperature (b) Driver gas mass fraction

Figure 1: Temperature and driver-gas contours after shock reflection.

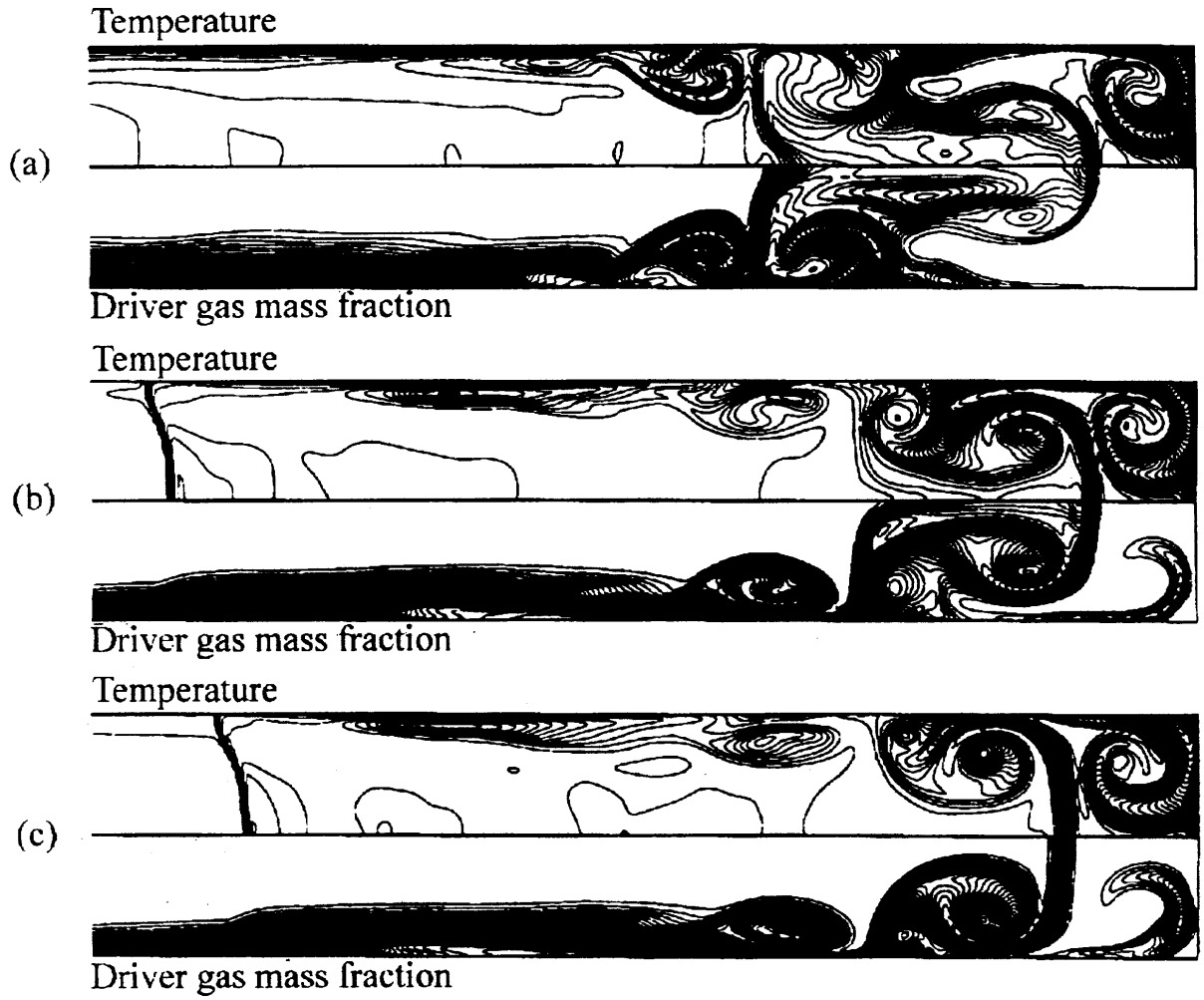

Figure 2: Effect of tunnel operating condition on driver gas contamination at $t = 100$ μsec: (a) Under-tailored. (b) tailored. and (c) over-tailored condition.

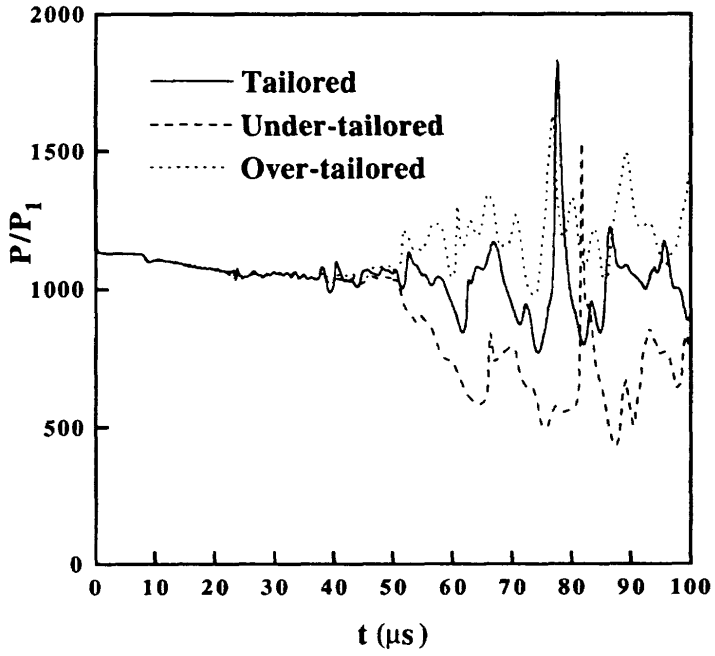

Figure 3: Pressure (p/p_1) history at the center of the shock-tube end plate.

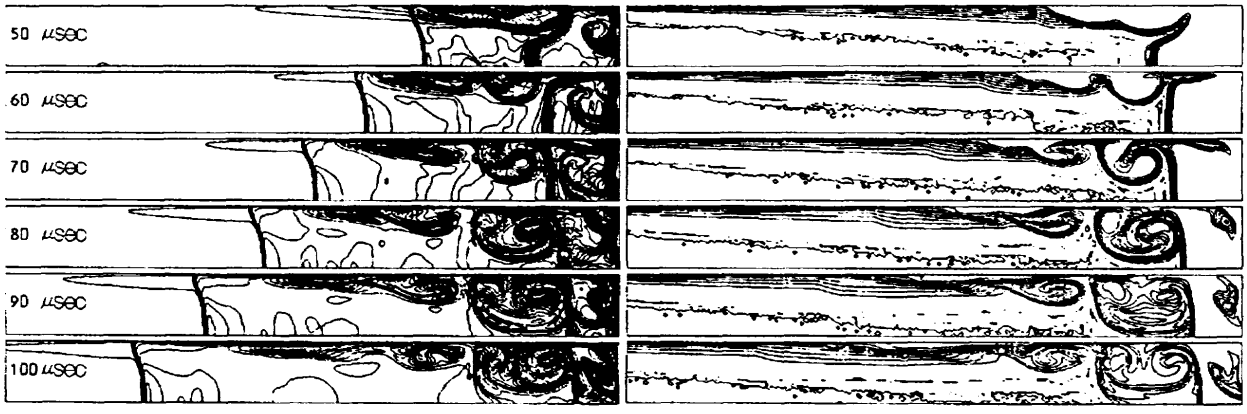

(a) Temperature (b) Driver gas mass fraction

Figure 4: Effect of nozzle flow on driver gas transport. $M_s = 10$, tailored interface condition.

1-2

HIGH ENTHALPY FLOW COMPUTATION AND EXPERIMENT AROUND THE SIMPLE BODIES

A.HANAMITSU T.KISHIMOTO
Kawasaki Heavy Industries, Ltd.

and

H.BITO
National Space Development Agency of Japan

Abstract

High enthalpy shock tunnel test was performed at HEG (High Enthalpy Shock Tunnel in Göttingen) to examine the real gas effect on shock interference heating. Heat transfer distributions were measured along the sphere model and the leading edge of simple wing-body model, whose sweep-back angle on the starboad side is 55° and on the port side is 60° . Flow visualization was also made for simple wing-body model by LIF (Laser Induced Fluorescence) method. CFD analysis has been performed about the heat transfer distribution along the sphere model both in the conditions of frozen flow and equilibrium air flow. Good agreement with experiment was achived in the condition of equilibrium air flow.

This test program was performed under contract with National Space Depelopment Agency of Japan, NASDA, and is a part of wind tunnel test programs for HOPE (H-II Orbiting Plane) development.

Introduction

HOPE developement program has been proceeding by NAL and NASDA. Aerothermodynamic design of HOPE is one of the main problem in the design of HOPE config-uration. It is much more severe than that of Space Shuttle Orbiter, because the scale is about one third of Space Shuttle Orbiter. It is required to accurately predict the aerothermodynamic environment during reentry, especially in high temperature hypersonic flight regime, where maximum heat transfer occurs.

To measure heat transfer in high temperature hypersonic flight regime, there are two flight experiment program in Japan. One was the Orbital Reentry Experiment (OREX) project, which was a Japanese first entry experiment from orbit and successfully flied on February 4, 1994. Another is the Hypersonic Flight Experimet(HYFLEX) project, which is planned to be launched by J- I Rocket on February, 1996. These flight experimental resuts will give us much information about the aerothermodynamic environ-ment during reentry. But this information is not enough to design HOPE Orbiter. Because OREX and HYFLEX configurations are much different from HOPE; OREX is a capsule type Orbiter and HYFLEX has only fins on the body for lateral stability control, but HOPE is a winged Orbiter with tipfins. This difference means that the problem of local high heating rate caused by the nose bow-shock and leading edge-shock interference still remains. Because the basic configuration of HOPE is a double delta type, a shock interference heating will be an inevitable problem, especially in high temperature hypersonic flight regime, where nose bow-shock is close to the body because of the real gas effect.

To investigate the real gas effect, some high enthalpy shock tunnels were built. But They are not matured yet and they can not simulate completely the real condition. CFD technique, which is not also matured on high enthalpy flows, is required to supplememt the wind tunnel test data.

High enthalpy shock tunnel test was performed at HEG to investigate the real gas effect on heat transfer distribution along the sphere and on shock interference heating for a simple wing-body model, whose sweep-back angle on the starboad side is 55° and on the port side is 60° . The results of the heat transfer measurements are shown and the comparisons of CFD result on heat transfer distribution about the sphere model with experiment are made in this paper.

Test Facility

The HEG[1] is a so called free-piston driven shock tunnel capable of producing high enthalpy and high density test gas flow (figure 1). It is the largest free-piston shock tunnel in the world (60m total length). To create the high pressure of up to 100 MPa in the compression tube, a heavy piston (up to 800 kg and 500 mm in diameter) is used. The nozzle is the hypersonic contoured

nozzle. It has an exit diameter of 880 mm, which results in a core flow of about 500 mm.

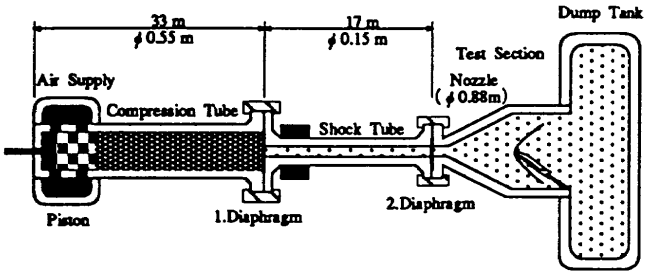

Fig.1 High Enthalpy Shock Tunnel in Göttingen (HEG)

The LIF Method as Applied to HEG

The beams of the two ArF eximer lasers, tuned to different rovibronic transitions of NO, are focused to sheets and introduced to the test section. Since the lasers are fired sequentially in time by some microseconds, the induced fluorescence of each laser is captured only by its corresponding imaging system. These systems consist of an intensified gated CCD-camera combined with a Nikkor uv objective[(2)].

The plane-convex cylindrical lenses to focus the beams to sheets are mounted in the configuration of a Newton-telescope inside the macrobenches, which also contain the mirrors and beam splitter modules. These modules deflect again only a small percentage of both beams to beam profile CCD-cameras. This enables the recording of each laser sheet before and after its passage through the test section to correct the fluorescence images with respect to laser intensity and profile fluctuations. (Laser intensity and profile change along their path.)

Not only to tune the lasers prior to the wind tunnel run, but also to make quantitative measurement of the detuning (i.e. wavelength drift) for each laser shot during the wind tunnel run, a small percentage of both beams is deflected via the beam splitter module to the heated calibration cell containing NO. An intensified CCD-camera (possibly used with a spectrograph) monitors the induced NO fluorescence of both, spatially separated laser beams.

NO was exicited at around 193 nm. All tests were carried out with three transition lines:

- $R_{21}(17.5)$
- $R_{22}(27.5)$
- a mixed line made up of $Q_{11}(32.5)$, $Q_{21}(26.5)$, $R_{11}(26.5)$ and $R_{21}(21.5)$ as the major components.

The first two single lines were used to obtain LIF images which could be used for temperature determination, while the last mixed line, which was the strongest line available in the laser tuning range, was used only for flow visualization.

Test Models

The models tested are sphere model and simple wing-body model, which are shown in figure 2. 4 Cu-Ni thin film gages, which were formed on the cylindrical pirex glasses, and 5 chromel-constantan coaxial thermocouples are installed in the sphere model. Cu-Ni thin filem gages were coated with Si02, which makes the surfaces of the gages noncatalytic. Unfortunately they were broken at first shot because of high temperature gas and contamination from the shock tube. (Shock tube inner wall is protected by cupper liner from high stagnation tempature.) Coaxial thermocouples were coverd with epoxy regin for thermal and electrical insulation from the model wall.

The wing-body model has different sweep-back angel to get sweep back angle effect on shock interference heating, 55° on starboad side and 60° on port side. 16 and 18 coaxial thermocouples are installed on the leading edge of the starboad and port side wing, respectively.

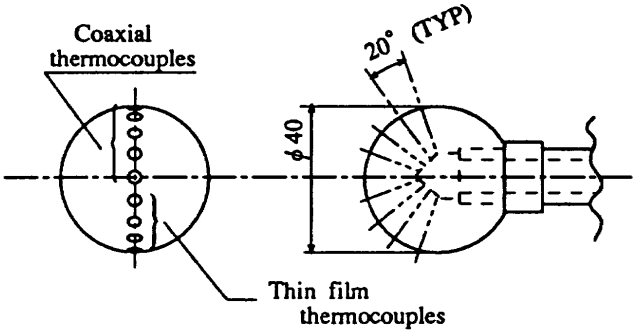

※ Model-sting adapter is provided to rotate the sphere model of ±20°

(a) Sphere Model

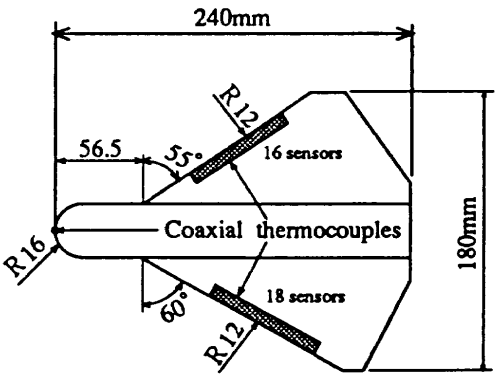

(b) Wing-Body Model

Fig.2 Test Models

Test Conditions

Figure 3 shows three test conditions selected for this test program together with HOPE reentry trajectry and HEG operating envelop. Horizontal axis is total enthalpy and vertical axis is $\rho_\infty L$ termed " binary scal-ing parameter". L is the reference length. Body length (0.24m) was taken as the reference length L in figure 3. These two parameters are very important in high enthalpy flow, because they are similarity parameters for dissociation reactions. Nominal test conditions are also tablated in table 1.

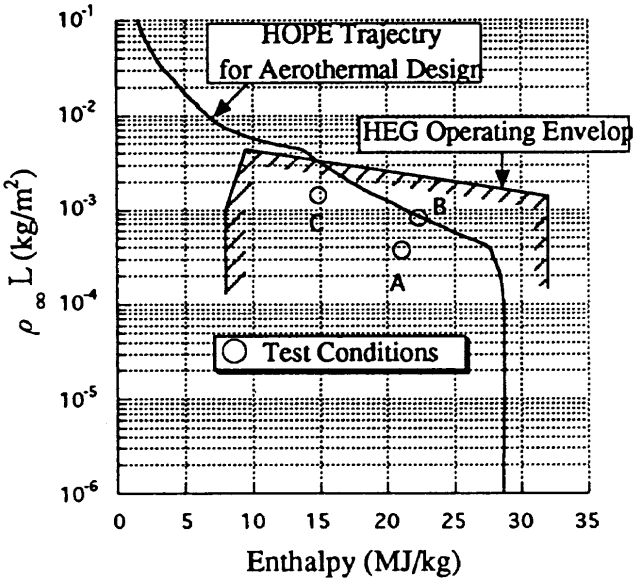

Fig3. Test Conditons and HOPE Reentry Trajectory

Table.1 Nominal Test Conditions

	Conditions		
	A	B	C
Po(MPa)	38.63	90.85	111.1
To(K)	9055	9727	8113
Ho(MJ/kg)	21.06	22.30	14.84
U (m/s)	5939	6180	5151.
$\rho_\infty L$ ($\times 10^{-4}$ kg/m^2)	3.74	8.16	14.09

※ L:Body length=0.24 m

CFD Analysis

Basic equations are Thin-layer Navier-Stokes equations . Flow solver adopted in the present calculations is finite volume TVD upwind scheme[3] based on a AUSMDV[4] scheme Implicit time integration using Gauss Seidel Relaxation method is adopted Computations are performed on the sphere model both in the conditions of frozen gas flow and chemical equilibrium air flow. Curve fitting method[5,6] is used for equilibrium air flow computations.

Grid system is a single domain structured multi-block grid system. Computational grid is shown in figure 4.

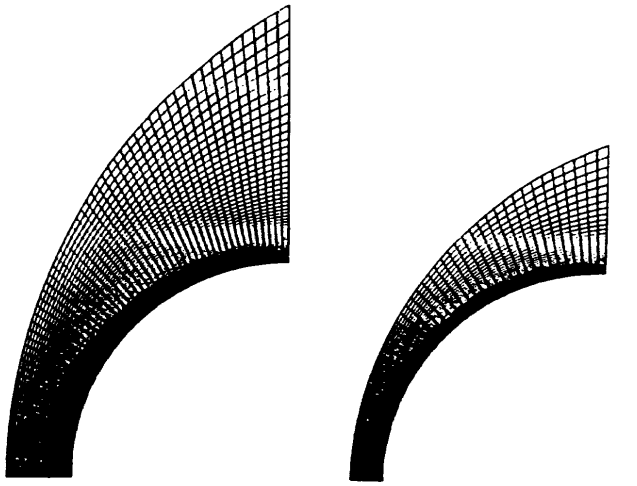

For Perfect Gas Flow (61×81) For Equilibrium Air Flow (61×81)

Fig.4 Computational Grid for Sphere Model

Heat Transfer Distribution along the Sphere Model

HEG permanent probe (its diameter is 20mm) and sphere model (its diameter is 40mm) were always installed in the test section with other models. Figure 5 shows stagnation point Stanton number vs. Reynolds number based on nose radius. Data from reference (7) are also shown in this figure. Stanton number and Reynolds number were calculated from the flow conditions behind the shock. 1-D nonequilibrium nozzle flow analysis code was used for the computation of free stream conditon and equilibrium code was used for the computation of the condition behind the normal shock.

From this figure, the following relation can be obtained.

$$S_t \propto \left(R_{e,2r}\right)^{-0.5} \propto 1/\sqrt{R_N}$$

This means that the stagntion heat transfer is proportional to square root Reynolds number even in high enthalpy flow condi-tions. Since the stagnation heat transfer is given by

$$\dot{q}_S = S_t R_{e,2r} P_r \cdot \kappa_e (T_{aw} - T_w)$$

However, the level of St is 20~30% higher than estimated data from reference (7), which were taken in

the low enthalpy conditons. The cause of this higher level of St may be the catalitic wall effect in HEG conditions. The sensors used were chromel-constantan coaxial thermo-couples, which had metal surfaces, so that the surfaces of the sensors could be considered as fully catalitic wall.

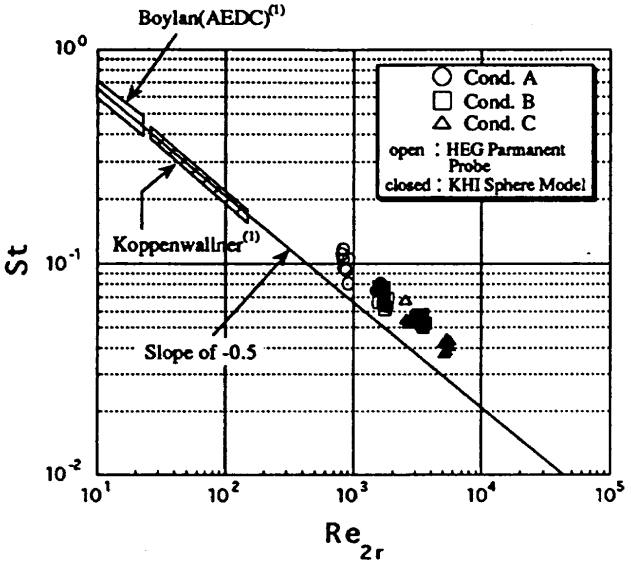

Fig.5 Stagnation Point Stanton Number versus Reynolds Number Based on Nose Radius

Heat transfer distribution along the sphere model in test condition B is shown in figure 6(a). Heat transfer values are normalized by the measured stagnation heat transfer value at $\theta=0^{\circ}$. The local values vary approximately as $\cos^{1.5}\theta$, but the value at $\theta=20^{\circ}$ is slightly higher than the stagnation value. Same result was obtained when the sphere model was rotated 20° (see figure 5(b)). In other conditions A and C, same trend was observed. This higher value at $\theta=20^{\circ}$ may be caused by a transition from laminar to turbulent flow, though the Reynolds numbers were too low (see figure 5). It is possible that the sensor can be a trigger of the transision. The sensor was surrounded with epoxy regin, and it slightly melted because of high temperature air and small gap around the sensor was observed. Another possibility is a ununiformity of free stream. (Small disturbance can cause the transition.)

Comparisons of experiments with CFD results were made for three typical test cases of condtion A, B and C. Computations were performed both for the perfect gas (γ=const.) and equilibrium air. The comparison in condition A is shown in figure 7. The result for equi-librium air flow shows good agreement with the experi-ment, but the result for perfect gas flow is about 20% lower in stagnation heat transfer than experiment or equilibrium air result.

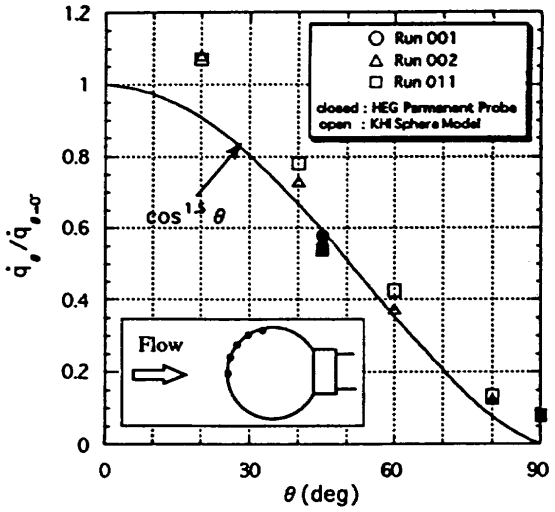

(a) Angle of Attack 0°

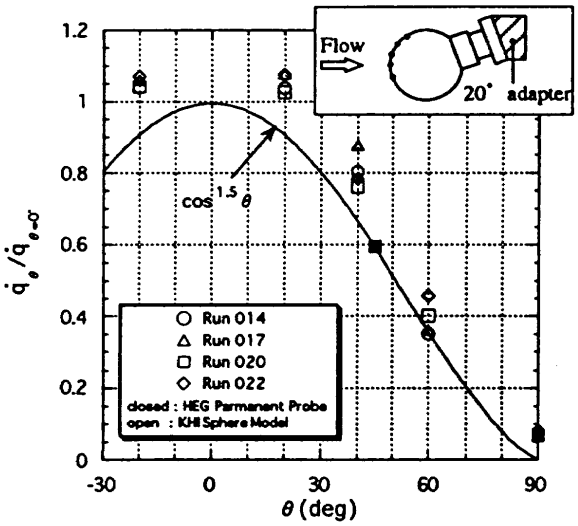

(b) Angle of Attack 20°

Fig.6 Heat Transfer Distribution along the Sphere Model in Condition B

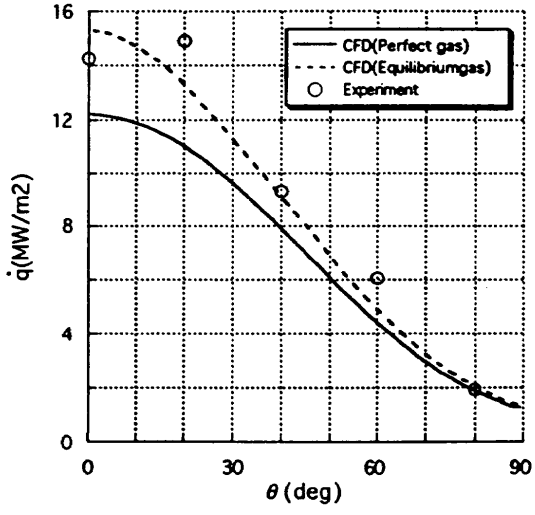

Fig.7 Comparison of Experiment with CFD in Condition A

Heat Transfer Distribution along the Leading Edge of Simple Wing-Body Model

For the delta-wing configuration with highly swept leading edges, the interaction between the bow-generated shock and the wing-generated shock wave exhibit the characteristics of a TYPE VI shock interaction pattern[8]. The sketch of the TYPE VI shock interaction pattern is shown in figure 8.

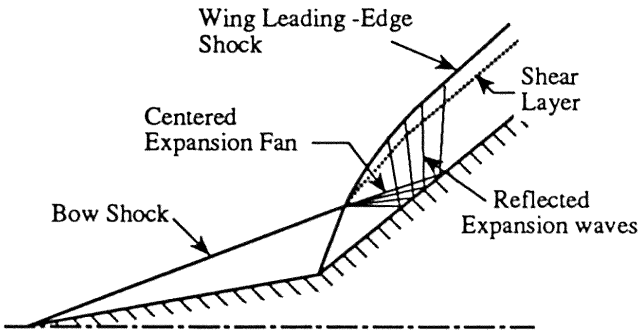

Fig.8 The Sketch of the TYPE VI Shock Interaction Pattern

As has been discussed, the shock interaction for the simple wing-body model will exhibit the characteristics of a TYPE VI shock interaction pattern. Figure 9 is the heat transfer distribution along the leading edge on the starboad side wing; sweep-back angle $\Lambda=55^\circ$. In all tests, Angle of attack is 0° . Data are normalized by the nose stagnation heat transfer and η_w is the distance from the wing-root normalized by exposed semi-span.

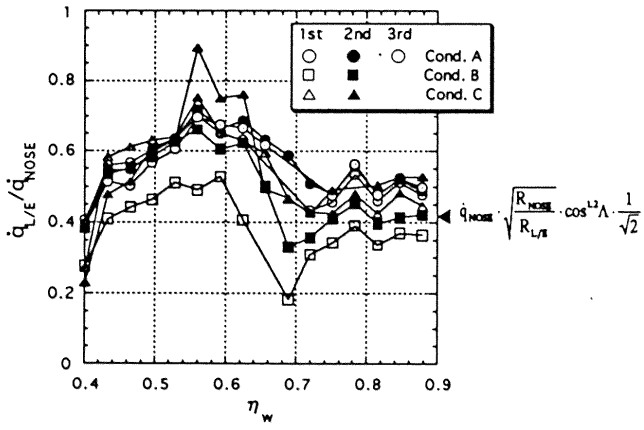

Fig.9 Heat Transfer Distribution Along the Leading Edge with Sweep-Back Angle 55°

Heat transfer near the wing-tip are almost constant so that this region can be considered outside of the shock interference region. The theoretical value without shock interference for oblique cylinder is given by ;

$$\dot{q}_{L/E}=\dot{q}_{NOSE}\cdot\sqrt{\frac{R_{NOSE}}{R_{L/E}}}\cdot\cos^{1.2}\Lambda\cdot\frac{1}{\sqrt{2}}$$

In this equation, sweep-back angle effect is estimated by $\cos^{1.2}\Lambda$, which was derived from the flight data of Space Shattle Orbiter[9]. The constant values near the wing-tip agrees well with this theoretical value. But for perfect gas, $\cos^{1.5}\Lambda$ is reported in some papers as the sweep-back angle effect. This means that real gas effect can decrease the sweep-back angle effect on wing leading edge heating.

The LIF images both for $\Lambda=55^\circ$ and 60° taken at condition B are shown in figure 10. These images show the raw intensity of fluorescence of NO and are not corrected with regard to the laser intensity and profile fluctuations. But the colors of the LIF image are almost proportional to the temperature and density of NO molecule. The shock impingement point on the wing of $\Lambda=55^\circ$ could be read to about $\eta_w=0.6$ from this figure. The maximum heating occurs just inside this point, and is about 1.5 times as large as the values without shock interference.

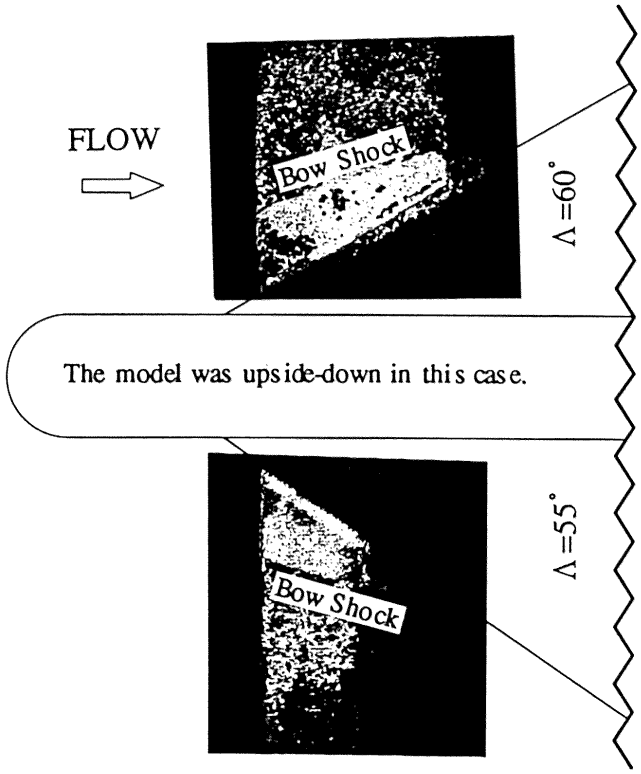

Fig.10 LIF images in Condition C

For a basic TYPE VI shock interaction pattern, the heating increases uniformly in the portion of the leading edge subjected to the flow within the bow shock and there are no localized increases in heating[10]. However a localized increase can be seen clearly in figure 9. One of this reason may be like this; the bow shock is generated by the spherical nose so that the total pressure within the bow shock along each stream line is different, i.e. the total pressure loss along the stream line which pass though the bow shock near the nose is larger than that pass though

pressure loss along the stream line which pass though the bow shock near the nose is larger than that pass though the oblique bow shock.. These gives the nonuniform heating within the bow shock.

The higher heat transfer within the bow shock than that without shock interference is partly caused by the difference of the flow properties between inside and outside of the bow shock. The flow coming to the portion of the leading edge within the bow shock passes through two weak oblique shock waves; the bow shock and leading edge shock. On the other hand, the flow coming to the portion of the leading edge outside of the bow shock passes through only one shock wave; the leading edge shock. The total pressure loss of the former flow is lower than that of the latter flow. However, the the flow direction is deflected through the bow shock, which results in the increase of the effective sweep-back angle of the leading edge with respect to the flow. This cancels some part of the increase in heating caused by the smaller total pressure loss. Further investigations should be made to understand the reasons for the increase in heating within the bow shock.

Figure 11 shows the heat transfer distribution for $\Lambda=60^\circ$. From figure 10, shock impingement point is about $\eta_w=0.7$. Heat transfer data are very scattered, but trend and the ratio of maximum heat transfer to outer wing value are almost same as that for $\Lambda=55^\circ$. The heat transfer distribution within the bow shock is relatively uniform for $\Lambda=60^\circ$, which will be cuased by the difference of the sweep-back angle effect. Sweep-back angle effect for $\Lambda=60^\circ$ is larger than that for $\Lambda=55^\circ$ so that the heat transfer distribution within the bow shock will be smoothed.

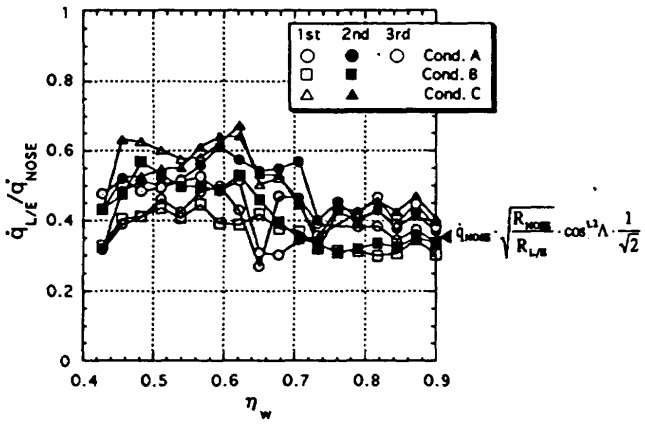

Fig.11 Heat Transfer Distribution Along the Leading Edge with Sweep-Back Angle 60°

The decrease in heating caused by the expansion fan generated from the intersection of the bow shock and wing shock can be seen just outside of the bow shock in some cases for $\Lambda=55^\circ$. But there are no distinct decrease in heating for $\Lambda=60^\circ$. It is possible that three-dimesional effect, i.e. cross flow, is dominant near the leading edge so that the influence of the expansion fan can not be seen as clear as in the two-dimensional case.

Conclusions

High enthalpy shock tunnel test was performed at HEG under contract with NASDA for sphere model and simple wing-body model. Comparison of measured heat transfer distribution along the sphere model with CFD both for the perfect gas flow and equilibrium air flow has been made. Based on the experimental result and present computations, the following conclusions are made.

1) The slope of the stagnation Stanton number with regard to the stagnation Reynolds number showed good agreement between high and low enthalpy flow. However, Stagnation heat transfer of the spherical nose in high enthalpy flow showed a 20～30% higher value than that in low enthalpy flow (perfect gas flow).
2) Measured heat transfer at $\theta=20^\circ$ of the sphere model showed the higher value than the stagnation value in all test conditons. CFD analysis for laminar flow didn't give such a result so that this would be caused by a transition from laminar to turbulent flow.
3) Good agreement of CFD results for an equilibrium air flow with experiment in heat transfer distribution along the sphere has been obtained. But perfect gas computations gave the lower value than the values for an equilibrium air flow or experiment. This is consistent with the statement 1).
4) Though the shock interference pattern for the simple wing-body model had been considered as a TYPE VI and there would be no localized increase in heating, a localized peak heating just inside the bow shock was observed in this experiment. This will be cuased that the degree of the total pressure loss of the flow within the bow shock varies along the leading edge.
5) The maximum heating on the leading edge of the simple wing-body model occured just inside the bow shock,which value is about 1.5 times as large as the value without the shock interference. The heat transfer outside of the shock interference region agrees well with the theoretical value.

References

(1)G.Eitelberg, T.J.McIntyre, and W.H.Beck, "The High Enthalpy Shock Tunnel in Göttingen," AIAA 92-3942, 1992.
(2)W.H.Beck, C.Dankert, G.Eitelberg, and G.Gundlach, "Preliminary Laser Induced Fluorescence Measurements in Several Facilities in Preparation for Application to Studies in the High Enthalpy Shock Tunnel Gottingen (HEG)," AIAA 92-0143, 1992.
(3)Sawada,K., and Takanashi,S., "A Numerical Investigation on Wing/Nacelle Interferences of USB Configuration," AIAA 87-0455, 1987.
(4)Wada, Y., and Liou,M., "A Flux Splitting Scheme with High-Resolution and Rubustness for Disontinuities," AIAA 94-0083, 1994.
(5)Srinivasan,S., Tannehill,J.C., and Weilmuenster,K. J., "Simplified Curve Fits for the Thermodynamic Properties of Equilibrium Air," ISU-ERI-Ames-86401, ERI Project 1626, CFD 15, 1986.
(6)Srinivasan,S., and Tannehill,J.C., "Simplified Curve Fits for the Transport Properties of Equilibrium Air," NASA-CR-178411, 1987.
(7)J.D.Anderson, Jr., "Hypersonic and High Temperature Gas Dynamics," McGraw-Hill Series in Aeronautical and Aerospace Engineering, 1989, p.257, quoted from Koppenwallner,G., "Fundamentals of Hypersonics :Aerodynamics and Heat Transfer," in the Short Course Notes entitled Hypersonic Aerothermodynamics, presented at the von Karman Institute for Fluid Dynamics, Rhose Saint Genese, Belgium, 1984.
(8)J.J.Bertin, S.J.Mosso, and D.W.Barnette, " Engineering Flowfields and Heating Rates for Highly Swept Leading Edges," Journal of Spacecraft and Rockets, Vol.13, No.9, 1976, pp.540-546.
(9)J.A.Cunningham, and J.W.Haney, Jr., "Space Shuttle Wing Leading Edge Heating Environment Prediction Derived from Development Flight Data", NASA -CP-2283 Part II, " Shuttle Performance: Lessons Learned", 1983.
(10)J.J.Bertin, and B.W.Graumann, "Hypersonic Shock-Interaction Phenomina Applicable to Space Shuttle Configurations," NASA-CR-128586, 1972.

1-3

THE RESULT OF AN ANALYSIS OF AERODYNAMICS OF OREX

軌道再突入実験の空力及び空力加熱解析結果

Takayuki Shimoda ; National Space Development Agency of Japan
Takashi Matsuzaki ; National Aerospace Laboratory
下田孝幸（宇宙開発事業団）
松崎貴至（航空宇宙技術研究所）

ABSTRACT

We are going to perform three experiments preceding to the development of HOPE. We performed OREX taking the opportunity of H- II TF#1 on Feb.4,1994. We report a result of one of the main purpose of OREX, acquisition of fundamental data of aerothermo- and aerodynamics during re-entry.
As to aerothermodynamics, we evaluated comparison between wind tunnel test data and values estimated from Fay&Riddell method before a flight experiment. After the experiment, we estimated heating rate induced from flight orbit using Fay&Riddell method validated before. And we calculated a temperature at the stagnation point using thermal-analysis model, then we compared the value with flight data.
As to aerodynamics, we compared flight pressure data with estimated value.

Analysis of aerothermodynamics

Analysis before flight-*hypersonic wind tunnel test*

We conducted a hypersonic wind tunnel test of OREX June 1991. At this time, we used phase-change paint to measure aerodynamic heating rate. We calculated the heating rate using the phase-change speed. We estimated aerodynamic heating rate using Fay&Riddell equation assuming perfect gas, while conducting wind tunnel.

The comparison between this estimation and wind tunnel test result is shown in Fig.1. This shows that the value of wind tunnel test is 30% larger than the Fay&Riddell estimation. Then, to compare these data more correctly we chose the value that we directly measured instead of catalogue value as maerial property of wind tunnel model. Measured values are shown in Table 1. And comparison using measured values is also shown in Fig.1.

Finally we get the result as follows. The aerodynamic heating rate obtained in wind tunnel test is 10% larger than the estimation by Fay&Riddell equation. So, we took an 10% value of Fay&Riddell estimation as an error for designing OREX vehicle. But actually we took a large margin taking 3σ distribution because this is the first re-entry experiment .

The result of flight experiment

estimation of thermal conductivity

Thermal contact resistance at thermocouple is an important factor to estimate aerodynamic heating rate from the result of flight. So we performed thermal analysis to estimate thermal contact resistance between C/C material and thermocouple.

First, we performed heating test of a test piece similar to the part of C/C Nose Cap where the thermocouple is attached. The test piece is made with the same condition with C/C Nose Cap, using the same material, being treated under the same condition and the same thickness and so on. The outline of the test piece is shown in Fig.2. Using this test piece, we performed heating test in a vacuumed chamber. The outline of the heating test is shown in Fig.3. The result of the heating tests are shown in Table 2-3. Table 2 shows the relation between heating rate and measured temperature, and Table 3 shows the temperatures at various points of the test piece.

Next, we estimated thermal contact resistance between C/C material and thermocouple using the data of heating test of test pieces. At this analysis, we used an analysis model shown in Fig.4. We considered thermal conductivity between C/C material and thermocouple, and emissivity and thermal conductivity from the surface. We analyzed three cases. Table 4 shows thermal property we used, and Table 5 shows the cases of analysis. The way of analysis is that we varied the value of thermal contact resistance as a parameter and identified when the analyzed temperature at the thermocoupple agreed with the measured temperature in the heating test. The result of identification of thermal contact resistance is also shown in Table 5.

Estimation of aerodynamic heating rate by analysis model of C/C Nose Cap

We estimated the temperature at the thermocouple of C/C Nose Cap using the thermal contact resistance in Table 5 and the aerodynamic heating rate induced by the best estimated real flight path and Fay&Riddell equation. And we compared the value with the data gained from

flight experiment.

The analysis model is shown in Fig.6. It is a 3-D and 1/36 peel part model of full C/C Nose Cap. We considered thermal conductivity between C/C material and thermocouple, and emissivity and thermal conductivity from the surface. Analysis conditions are as follows:

Heating condition :

We use heating rate distribution obtained by Lees equation. And we use the value obtained by Fay&Riddell equation along the best estimated real flight path as the value of heating rate at the stagnation point, and we deal this value as Q.

Side temp. of test piece :

adiabatic considering symmetry.

Emission inside :

We took the temperature of inside insulation as that of emission inside.

Emission of Nose cap :

Emission outside is ε_c, and inside is ε_i. Measured values on the ground are both 0.84.

Thermal contact resistance :

We used Table 5, and represented by R.

Initial condition : Initial temperature is 20 degree.

Material property : We used Table 4.

Analysis time : 7284-7540 sec. after lift-off.

On these conditions we analyzed in several cases. The cases we analyzed are shown in Table 6. The analysis result of each case is shown in Fig.7-13.

Case1:(Fig.7)

This is a nominal case, using the gained data directly. Emission is the value measured on the ground test, but it may not be an absolutely real data, because the way of measuring is not established yet. This may be why analyzed value is lower than the measured value at the top of temperature. Analyzed value increases around 7420 sec. This may be why the thermal contact resistance is too large at low temperature. At higher temperature, we use the value induced from a paper as thermal contact resistance, so both values are close. The peaks of both temperature almost agree.

Case2:(Fig.8)

We analyzed the effect of variation of emission. Emission may vary at high temperature, so we analyzed taking 0.7 instead of 0.84 as emission. The result is that the peak temperatures of analyzed and measured value almost agree.

Case3:(Fig.9)

We noticed a large inclination at lower temperature at case 1, 2. So assuming that the thermal contact resistance at lower temperature we gained on the ground test before is too large, we analyzed taking 1/2 value of thermal contact resistance gained on the ground test. The result is that the analyzed value comes close to the measured value.

Case4:(Fig.10)

Furthermore, we analyzed taking 1/10 value of thermal contact resistance. The result is that the analyzed value almost agreed with measured one. From this result, we can estimate thermal contact resistance to be 1/10 of the one gained on the ground test. This is also reinforced by the value reported on the paper.

Case5:(Fig.11)

In this flight we could not get the whole temperature data at the thermocouple on the insulation. We got only half a data at this point, so we have some doubt about reliability of this data. For this reason, we assumed emission inside C/C Nose Cap is zero to get the data of heat conduction into insulation. The result is that trend of temperature variation is the same as that of case 1, but the peak of temperature is higher because heat doesn't run away.

Case6:(Fig.12)

Because of the doubt of the reliability of the data at thermocouple on the insulation, we analyzed taking the temperature data below the insulation instead of that on the insulation. In this time we also took insulation into consideration as analysis model. And we took 1/10 value of thermal contact resistance. The result is that the trend of curving of both value almost agree, and the peak of analyzed temperature is a little higher.

Case7:(Fig.13)

On the base of Case 6, we analyzed taking the 88% value of aerodynamic heating rate estimated by Fay&Riddell equation to conform the peak temperature of analyzed value to that of measured one. The result is that analyzed value and measured value almost agree.

From these result of analysis of Orbital Re-entry Experiment, we could get the following conclusions.

1.We can estimate the aerodynamic heating rate of OREX to be 88% of the value obtained from Fay&Riddell equation.

2.It appeared that error of emission and estimation error of heat movement inside C/C Nose Cap effected the estimation of aerodynamic heating rate very much.

3.We can estimate the value of thermal contact resistance to be 1/10 of that induced on the ground test.

But the value of thermal contact resistance is effected greatly by the way of attachment of thermocouple, and some papers reported that it varied in the range of 10^3. Then this value is so important that we should accumulate a lot of test data to estimate aerodynamic heating rate correctly.

Evaluation of estimation method of heating rate

Evaluation of time history of heating rate

We evaluate time history of the estimated heating rate by various estimation methods along the best estimated flight path and that of heating rate identified from flight data. We evaluated such methods as:

1.Fay&Riddell equation : assuming perfect gas (being used in the chapter before)

2.Fay&Riddell equation : assuming equilibrium flow

3.Detra, Kemp & Riddell equation

The comparison between heating rate by each method and that from flight data is shown in Fig.14. It shows nominal value and we should evaluate considering estimation error. All the same, we can understand the value by Fay&Riddell equation assuming equilibrium flow is the closest to flight data. This may be because Fay&Riddell equation is defined assuming equilibrium gas. In this case, we use the standard atmosphere as the data of density, so we should also consider the effect of using real atmosphere data.

Evaluation of distribution of aerodynamic heating rate

We adopted Lees distribution as aerodynamic heating rate distribution of OREX for designing. Fig.15 shows heating rate distribution estimated by Lees distribution used for designing the vehicle, the result of CFD assuming perfect gas and non-equilibrium, and flight data at some points. We can see such trend in Lees distribution as decrease of heating rate at the edge of nose cap and re-increase at the first line of tiles. We have also obtained this trend by CFD, so designing using Lees distribution can be valid. And we should consider such factors to estimate heating rate below the first line of tiles as:

1.production of non-equilibrium flow below the stagnation point

2.difference of material property of ceramic tiles based on the deference of tile maker.

3.error of measurement and identification

Analysis of aerodynamics

The outline of pressure sensor

We compared the flight results of two pressure sensors (sensor for middle altitude and one for high altitude) on the OREX with the estimation by various ways. Fig.16 shows the outline of pressure sensors and installation. Middle altitude sensor can measure the altitude 40km-85km, and measurement error is 1114.3Pa. High pressure sensor is used for measuring faint pressure at over 75 km altitude.

Flight result of middle altitude pressure

Analysis condition

We analyzed along the best estimated real flight path, and used 1976U.S.Standard Atmosphere Model. We show this model in Table 7.

Estimation of pressure value

We calculated pressure value at the height of 40, 51.1, 60, 65, 70km with the condition of Table 7 and by such ways as below;

1.Newton method

2.VSL equation;

Assumig non-catalysis and emission of 0.8, we analyzed the cases of ideal gas and non-equilibrium gas.

3.CFD by NS-equation;

Assuming ideal gas at 51.1km altitude

Comparison between flight data and estimated value

We compared flight data of middle altitude pressure sensor with some values estimated by each method above. Fig.17 shows the comparison between flight data and estimated values. We can say each estimated value is almost the same value, but flight data is about 800Pa higher than estimation. This can be within the error of sensor which is 1114Pa, and this may be because of the error of standard atmosphere. The data of high altitude sensor is also shown in the figure and it is connected with the data of middle altitude smoothly.

As reference, fig.18 shows comparison between flight data and estimated value which used the atmospheric data 1km below the flight data. In this case, flight data and estimation agree very well. Fig.19 shows surface pressure distribution at the height of 51.1 and 70km, and Fig.20 used the data 1km below the flight data for estimation.

Conclusion

For aerothermodynamics, heating rate of 88% value estimated by Fay&Riddell agreed with the flight data very well. But we used 1/10 value of thermal contact resistance obtained on the ground test, so it is very important to get a correct value of such value as thermal contact resistance, material property and so on.

For aerodynamics, estimation of several method almost agreed with flight data. But it is important to use real atmospheric data to get a precise estimation.

Table 1. Comparison of Material Property

	Cataloge ①	Measurement ②	② ÷ ①
ρ (g/cm^3)	2.1	2.3	1.095
Cp (cal/g·K)	0.3	0.261	0.870
κ (cal/cm·s·K)	3.3×10^{-3}	2.72×10^{-3}	0.824

Table 2. Measurement of heating rate

Voltage(V)	Temp.(℃)	heating rate(W/cm^2)
30	338.2	0.27
50	479.3	1.88
115	721.1	7.66

Table 3. Measure d temperature s

heating rate / points	0.27(W/cm^2)	1.82(W/cm^2)	7.38(W/cm^2)
#1	331.7	475.3	720.1
#2	339.6	480.6	723.2
#3	336.8	478.0	718.9
#4	332.3	474.5	719.4
#5	321.7	461.2	700.6
#6	325.4	465.9	708.0
#7	272.5	399.6	623.7
#8	72.7	106.7	173.9

Table 4. Thermal Property

	Representative Temp.	Density (g/cm^3)	Specific Heat(cal/g℃)	Termal Conductivity(cal/cm·s·℃)	Emissivity
C/C composit (longitudinal)	RT	1.50	0.159	0.2187	0.84
	500		0.371	0.3645	
	1000		0.434	0.3749	
	1500		0.544	0.4680	
C/C composit (transverse)	RT	1.50	0.159	0.0486	
	500		0.371	0.0810	
	1000		0.434	0.0833	
	1500		0.544	0.1040	
Temp.sensor	RT	13.31	0.11	0.0922	-
Adhesive	RT	3.5	0.1169	0.00251	-
Insulation	330	-	-	-	0.74
	470				0.73
	700				0.70

Table 5. Cae of Analysis

case	Measured Surface Temp.(℃)	Thermal Contact Resistance (m^2·hr·℃/kcal)
case1	340	0.0842
case2	481	0.0751
case3	723	0.0370

Table 6. Analysis cases about aerothermodynamics

Case No.	Heating Rate	ε c	ε i	thermal contact resistanc	Inside temp.
①	Q	0.84	0.84	R	Outside
②	Q	0.7	0.7	R	Outside
③	Q	0.84	0.84	R × 0.5	Outside
④	Q	0.84	0.84	R × 0.1	Outside
⑤	Q	0.84	0	R	Outside
⑥	Q	0.84	0.84	R × 0.1	Inside
⑦	Q × 0.88	0.84	0.84	R × 0.1	Inside

Table 7. 1976 U.S.Standard Atmosphere Model

Time after Lift Off(s)	Height (km)	M number	Temp. (K)	Pressure (Pa)	Density (kg/m^3)
7445.875	70	23.31	219.585	5.221	8.283×10^{-5}
7457.875	65	20.98	233.292	1.093×10^{1}	1.632×10^{-4}
7470.675	60	17.84	247.02	2.196×10^{1}	3.097×10^{-4}
7493.875	51.1	11.10	270.65	7.046×10^{1}	9.069×10^{-4}
7526.675	40	4.11	250.35	2.871×10^{2}	4.000×10^{-3}

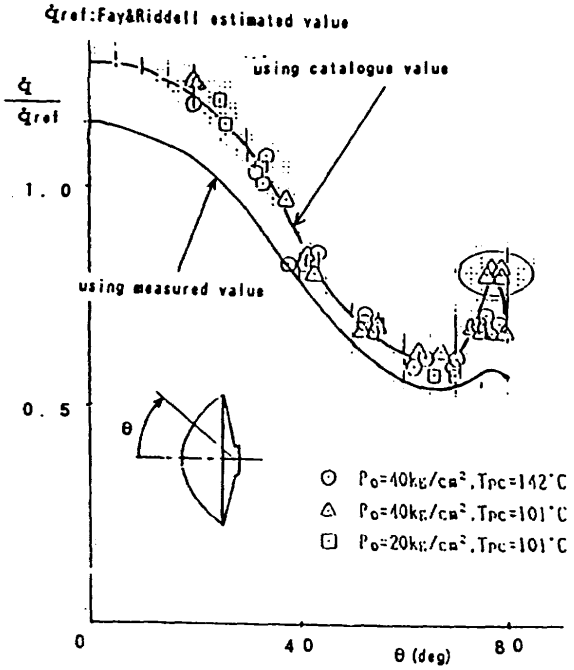

Fig.1 Comparison between tunnel test result and Fay&Riddell estimation

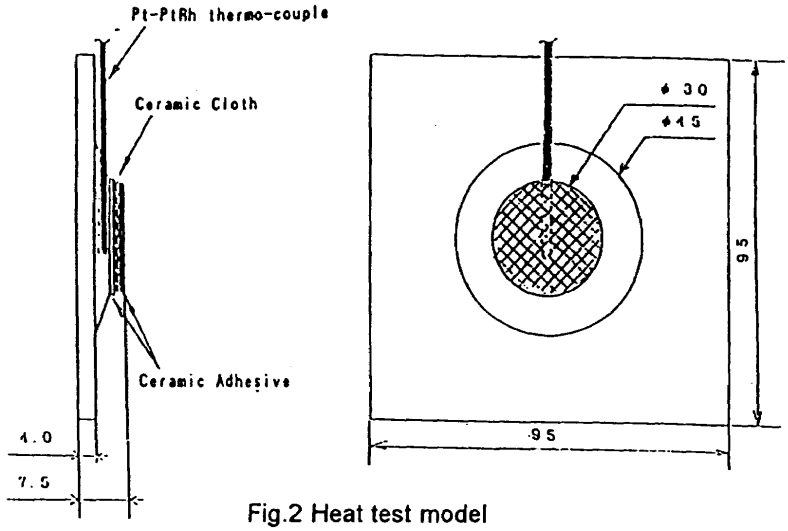

Fig.2 Heat test model

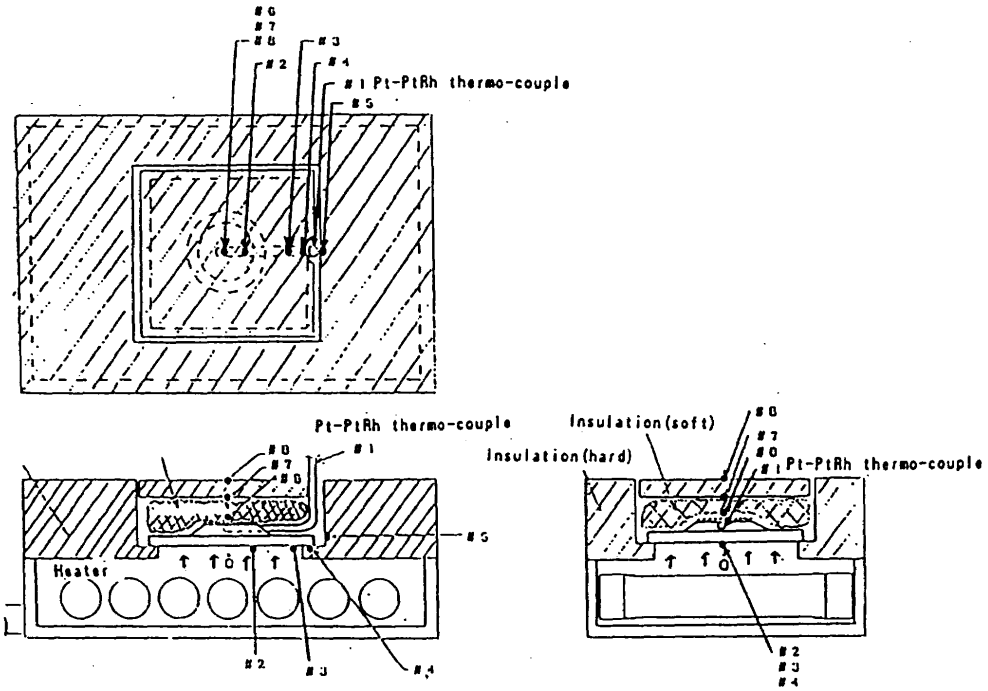

Fig.3 Outline of heat test

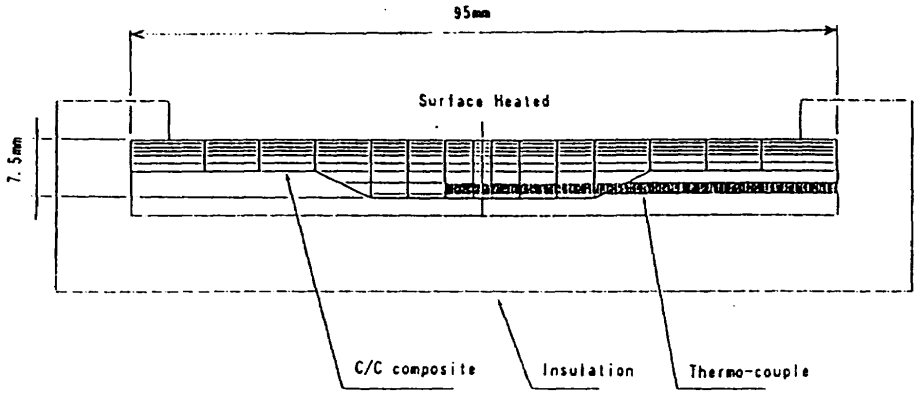

Fig.4 Analysis model for heat test

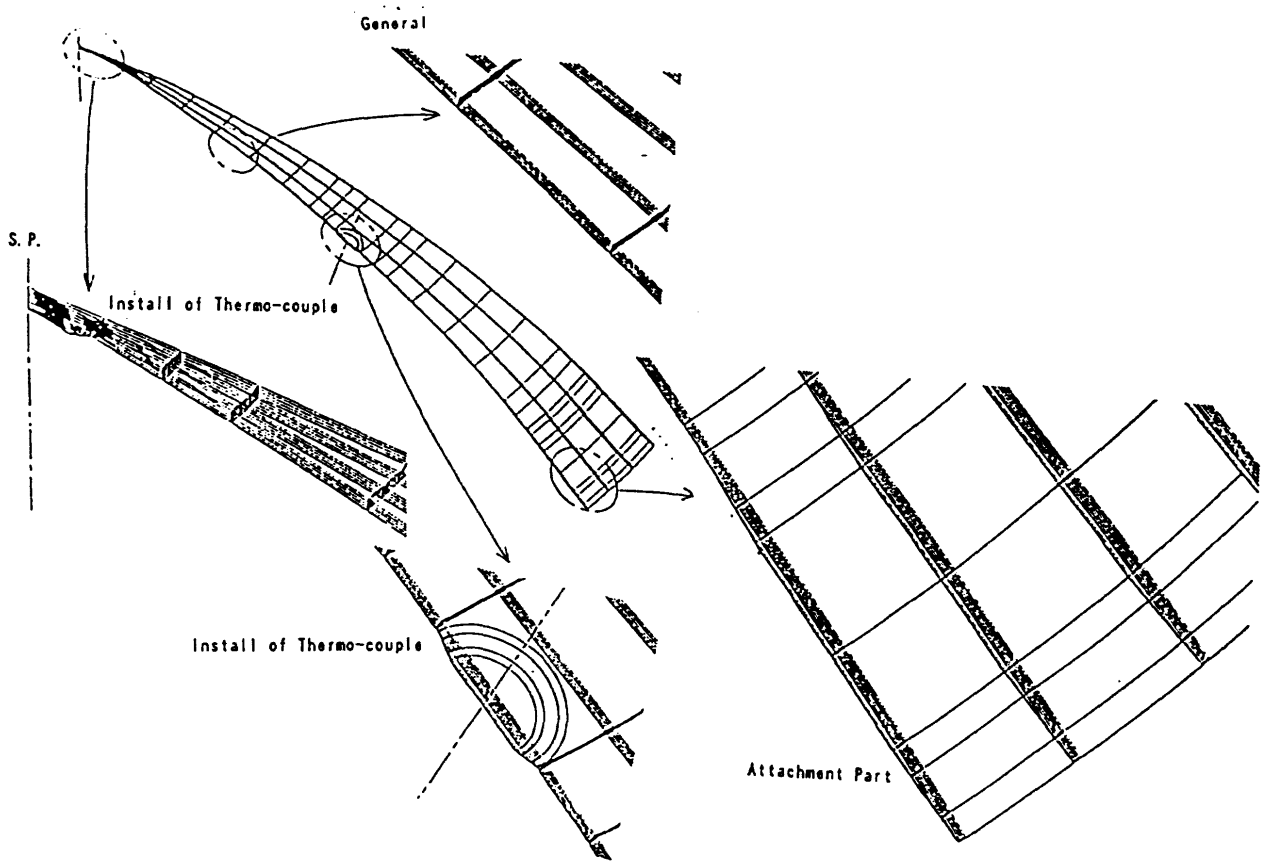

Fig.5 ANALYSIS MODEL OF C/C NOSE CAP

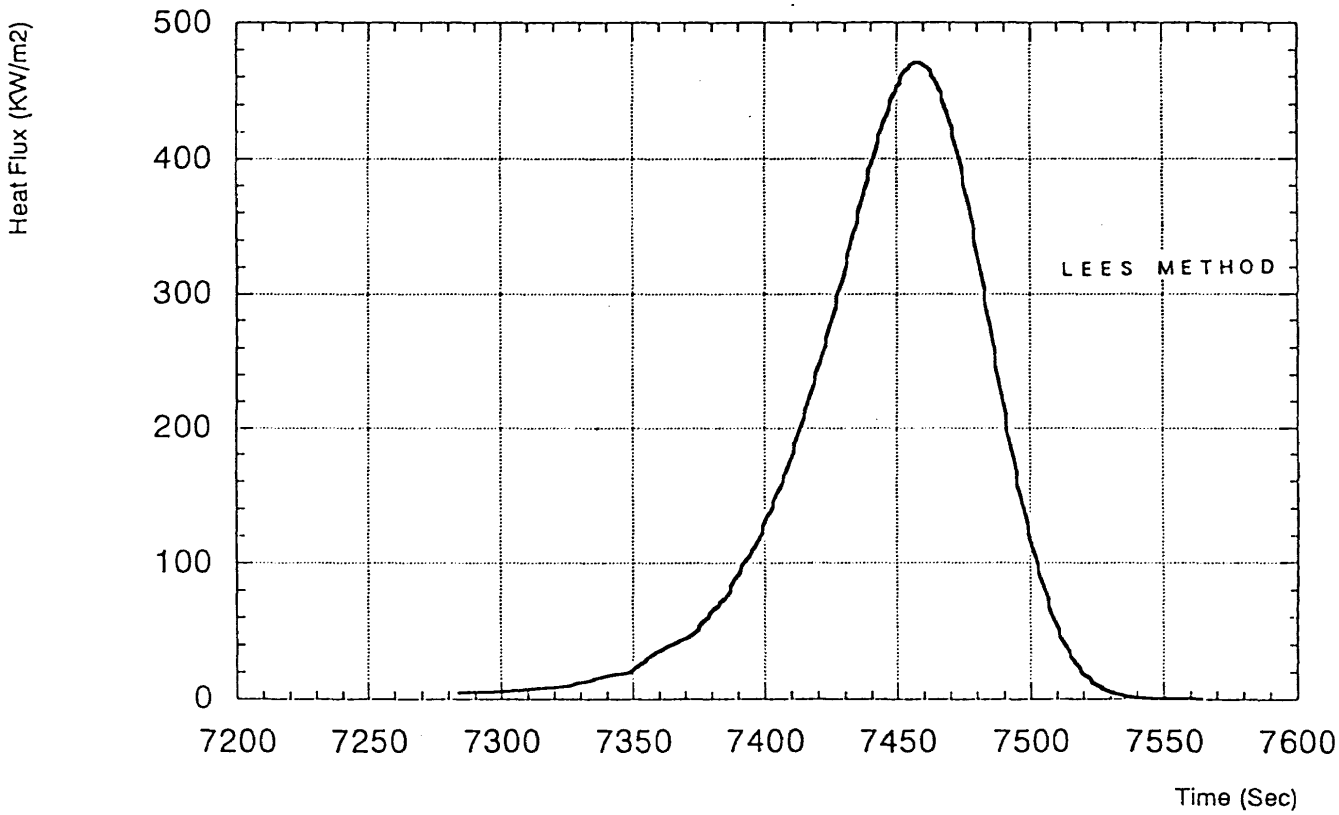

Fig.6 Heating rate estimated by Fay&Riddell

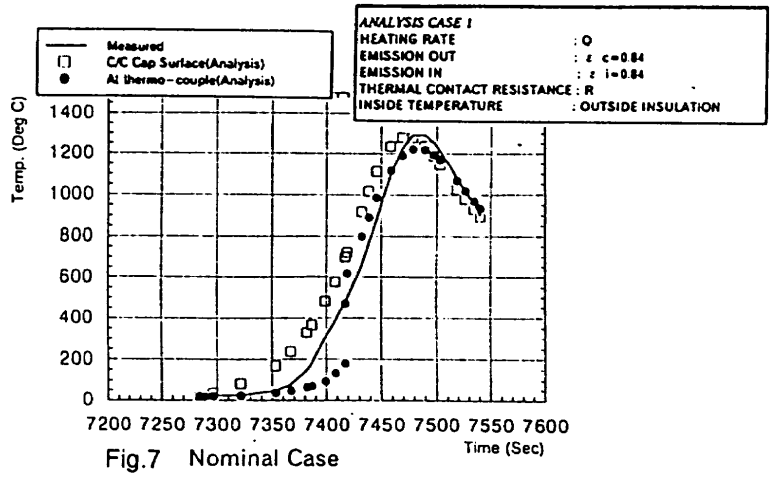

Fig.7 Nominal Case

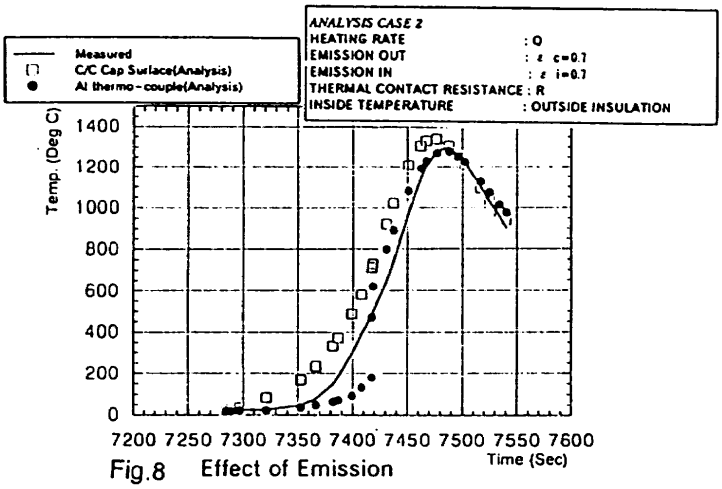

Fig.8 Effect of Emission

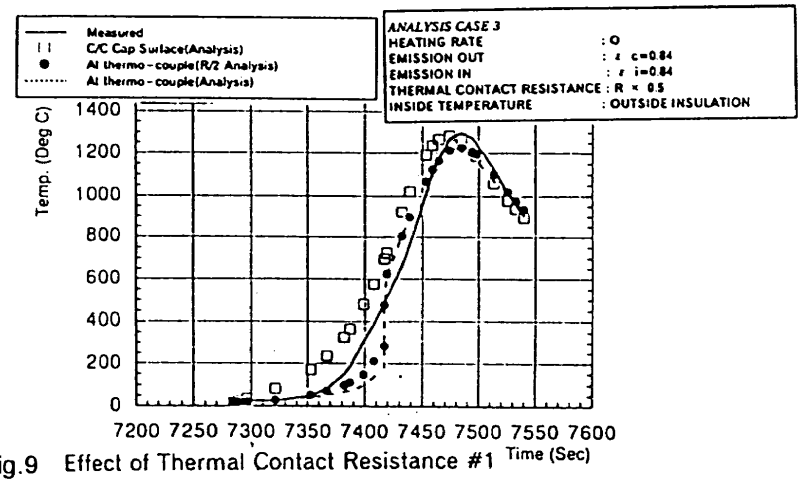

Fig.9 Effect of Thermal Contact Resistance #1

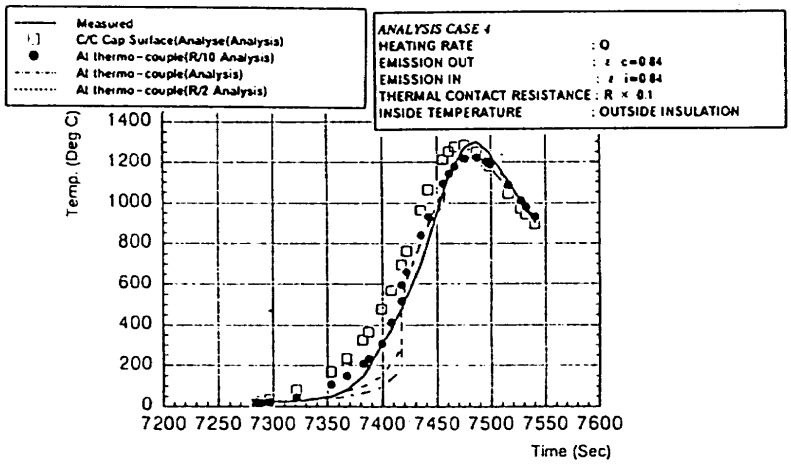

Fig.10 Effect of Thermal Contact Resistance #2

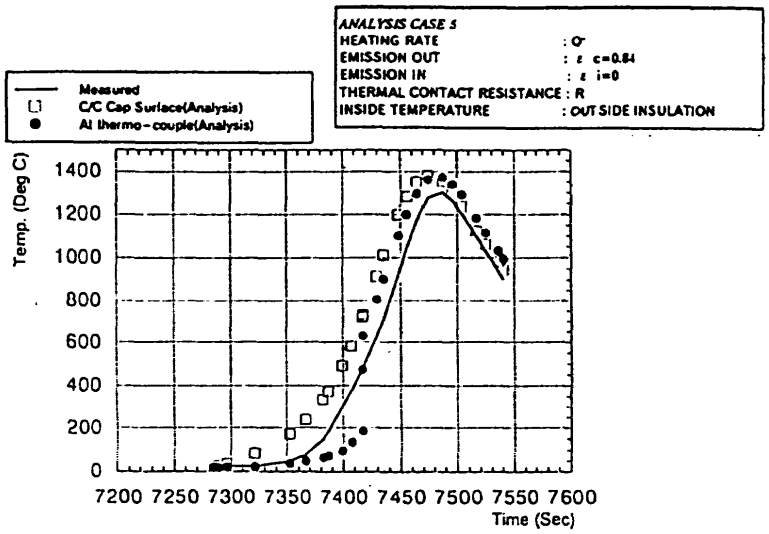

Fig.11 Effect of Emission inside C/C Nose Cap

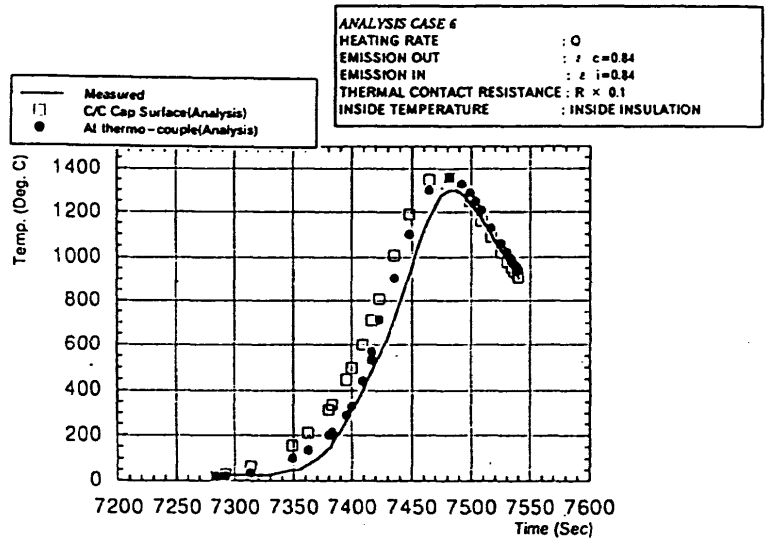

Fig.12 Analysis using Temp. data inside Insulation

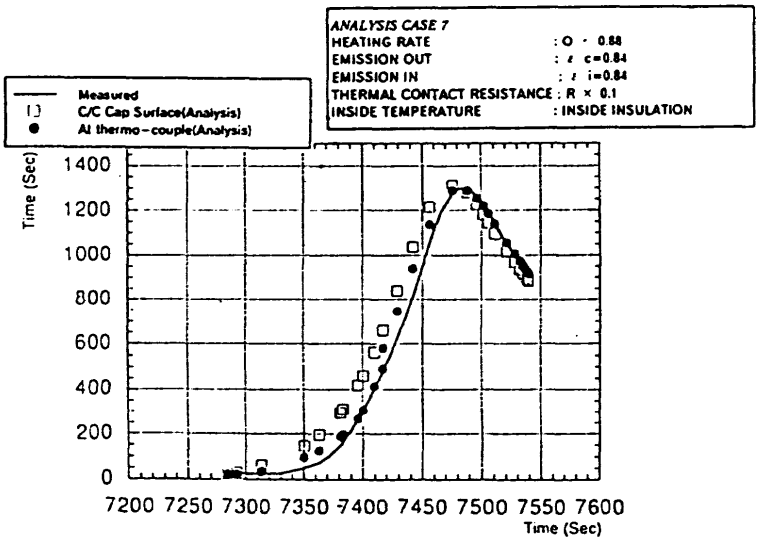

Fig.13 Analysis taking heating rate 12% OFF

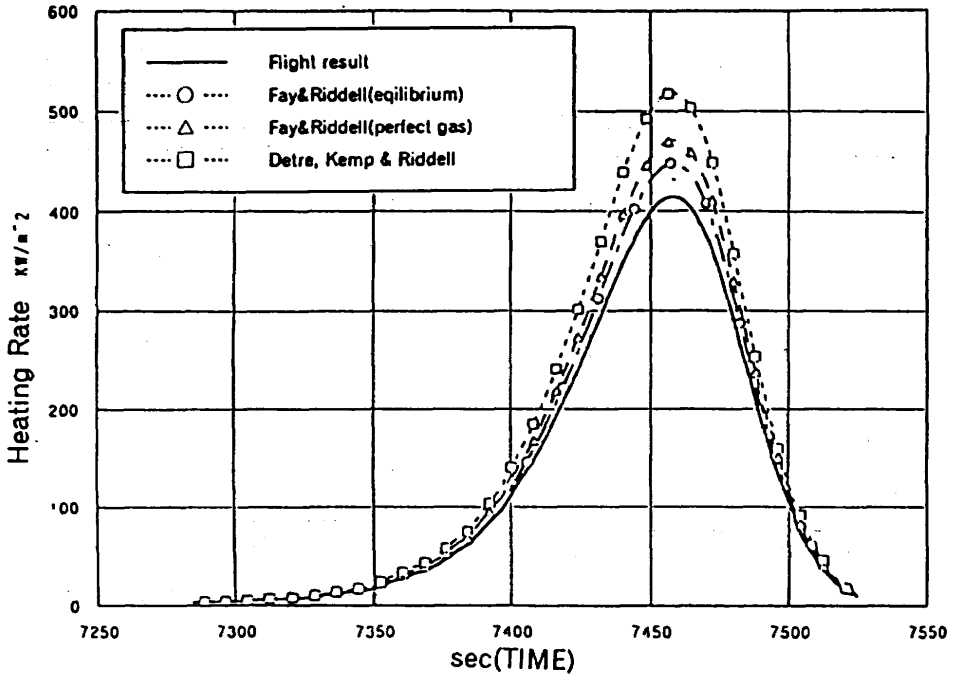

Fig.14 Comparison between Flight data and Estimation Method

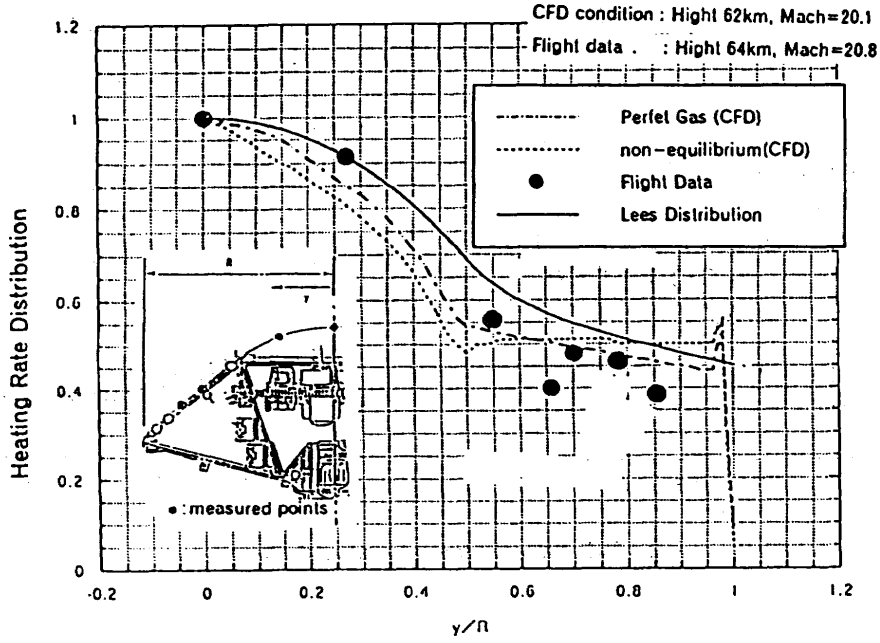

Fig.15 Comparison of heating rate distribution

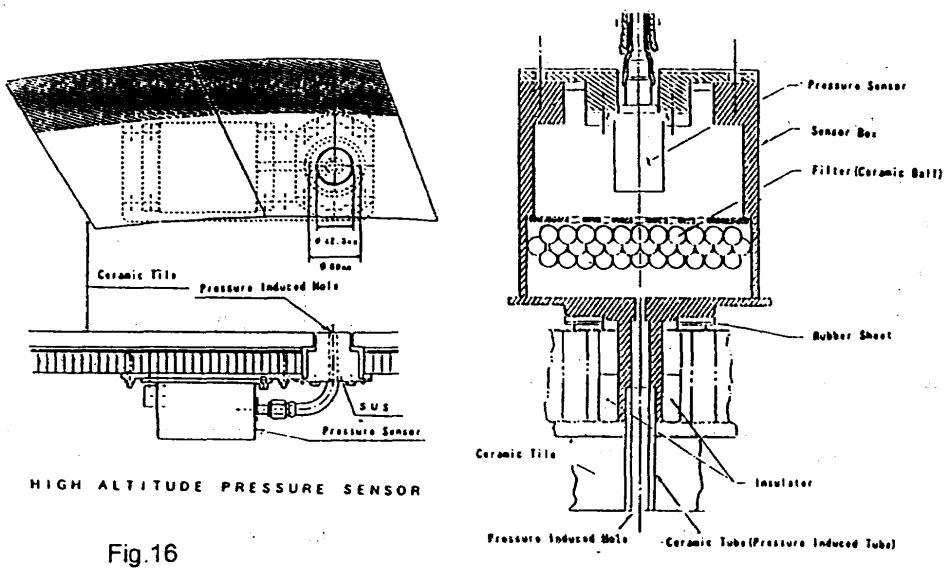

Fig.16

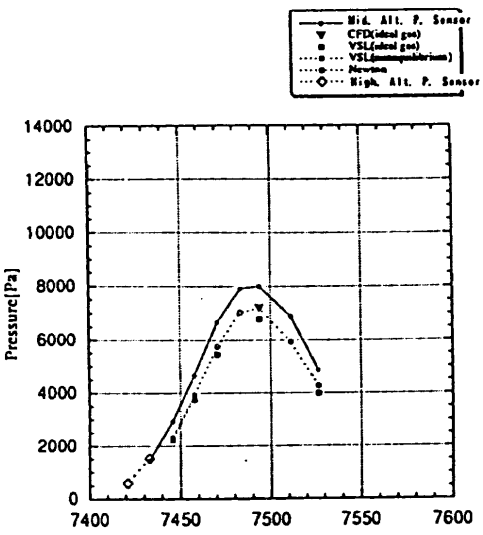

Fig.17 The result of Pressure data

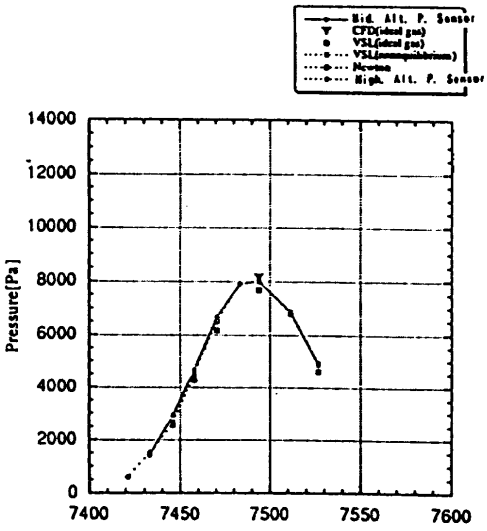

Fig.18 The result of Pressure data (1km shift)

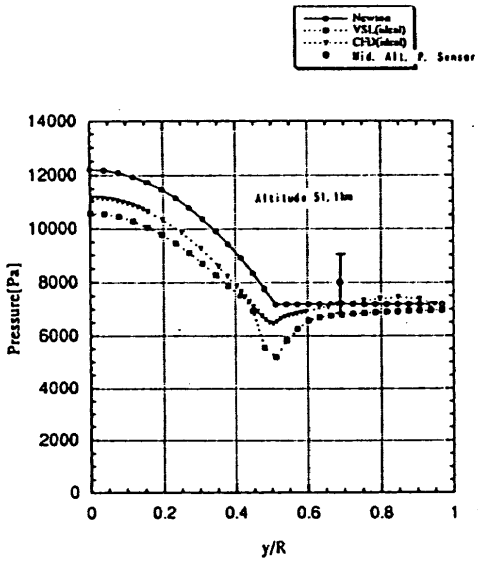

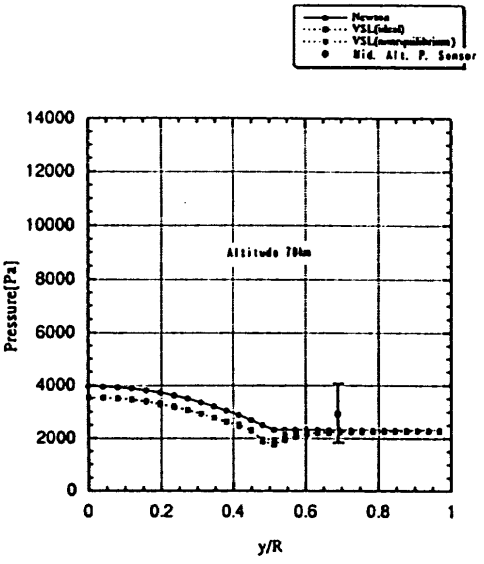

Fig.19 Surface Pressure distribution

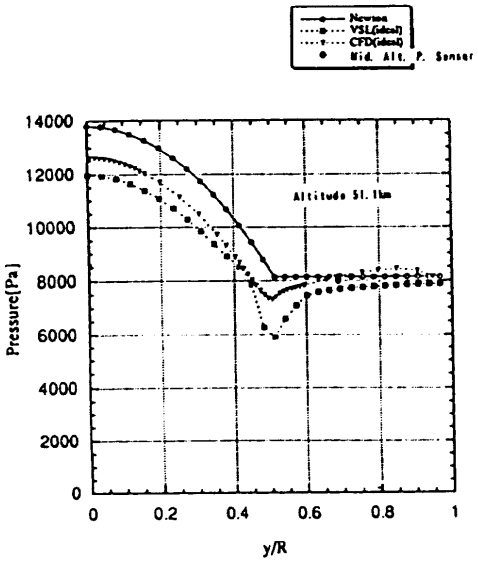

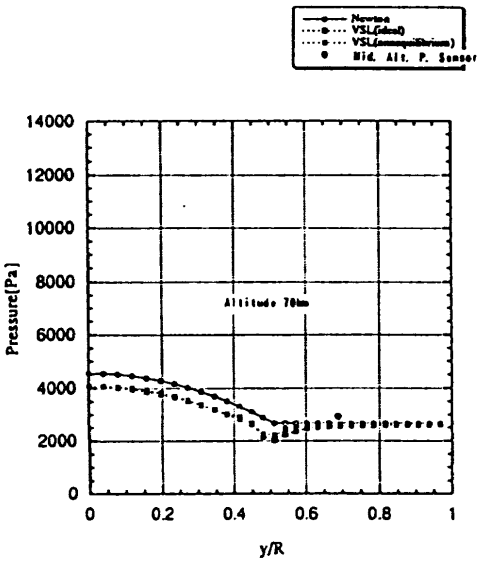

Fig.20 Surface Pressure distribution (1km shift)

1-4

Recent Comparisons of Aerothermodynamic Results by CFD and FEM Coupling Analysis with OREX Flight Experiments

by

Yukimitsu Yamamoto
National Aerospace Laboratory,Japan

ABSTRACT

Accuracy of CFD is investigated by comparing numerical results with the measured flight temperature data on the TPS material of OREX. Flow is caluculated by the non-equilibrium Navier-Stokes code and internal thermal response is computed by FEM. Coupling CFD and FEM along the OREX flight trajectry, temperature increase of the TPS during re-entry is favorably predicted. In FEM analysis, the effects of temperature and directional dependence of heat conduction coefficient and radiation effects of TPS material are evaluated. These works have been done as the joint research of NAL and NASDA

1. Introduction

For the development of space transportation vehicles, it is required to predict accurately their aerothermodynamic environments during re-entry, espeacially in high temperature hypersonic flight regime. OREX (Orbital Reentry Experiments) is the first flight experiments planned as a part of the HOPE (H-II Orbiting Plane) projects. OREX was launched by the H-II rocket on February 4, 1994, from Tanegashima Space Center of Japan. The flight experiments were succssfully conducted as almost planned and various kinds of flight data, concerning to aerothermal environment, were aquired[1]. On these experiments, one of the most important purposes is the evaluation of aerothermodynamic heating, which has a large effects on TPS design of re-entry vehicles.

However, in the hypersonic re-entry flight condition, dessociations and ionization of the air are caused due to high temperature environments and real gas effects must be considered in the analysis of aerothermodynamic heating. On the other hands, advanced CFD (Computational Fluid Dinamics) has now potential to simulate such real flow and become a powerful tool for the aerothmal predictions.[2] In our study, based on the OREX flight trajectry data, temperature response of OREX TPS material are analyzed by the non-equilibrium Navier-Stokes CFD code and internal thermal response is computed by FEM.

Data exchange of surface temperature and heat transfer is made alternatively, every 10 seconds along the OREX flight trajectory. Caluculated temperature increase is compared with the mearured flight temperature on the TPS material, such as C/C nose, C/C TPS and ceramic tiles. The purpose of our study are 1) to analyze OREX TPS flight temperature hisory, 2) to well understand the aerothemodynamic environment and the coupled flow thermal-structural interactions, and 3) to investigate the applicability the real gas CFD code as the tool for the evaluation aerothermodynamic heating.

2. Numerical Algorithm

Basic equations used in the present analysis, are Navier-Stokes equations with thin layer assumption. The differencing is based on the upwind TVD flux-split method.[2] Real gas effects are evalueted by using 7 species chemically non-equilibrium one temperature model. In the present, preliminaly analysis, uncertainty of the real gas modeling must be eliminated, and the heat transfer dose not change between one (chemically non-equilibrium) and two (thermo-chemically non-equilibrium) temperature models. So, the aerothermal analysis are made by one temperature real gas CFD code. Detailed description of numerical algorithm is presented in Ref.2. As the boundary conditions, non-catalytic wall surface is assumed and wall temperature is given by FEM analysis at each trajectory points.

In the present study, internal temperature increase is calculated by FEM, using heat transfer distributions on the surface. In FEM analysis, the effects of temperature and differential directional dependence of heat conduction coefficients of each TPS materials are considered and radiation effects of each TPS materials are also evaluated.

3. Numerical Results

OREX geometry is shown in Fig.1 with the detailed dimensions. The forebody shape is composed of a spherical nose, cone and a circular shoulder. OREX weight is 760 kg just befor the re-entry. Table 1 indicates OREX re-entry flight trajectory focused on the present study. This table shows the flow data and C/C nose cap stagnation point temperature history at evey ten seconds. The altitude changes from 105Km to 48Km and Mach number from 27.0 to 9.1. At each trajectory points in the table, flow is computed by using the chemicalhy non-eguilibrium Navier-Stokes code. Computational mesh consists of 41 points distributed streamwise along the body and 60 points between the body and outside of the bow shock wave.

Figure 2 shows thermo-couple locations for temperature measurements, where comparison with numerical predictions are made. Fig 2(a) indicates the measurement points just behind C/C nose cap. Temperature are measured at the center of C/C nose cap (Termocouple No. TH1) and at the $\theta = 20$ deg points (TH2, TH3, TH4) from the axis. At the right hand side of the figure, outline of OREX structure system is drawn. It is noticed that heat shield plate is set behind the C/C nose cap in order to protect thermal radiation from the internal nose. For the C/C TPS panels, circumferentially different three measurement points (TH7, TH8, TH9) are set, as shown in Fig.2(b). In the left of the fingure, temperature history of three thermo-couples are plotted. On the ceramic tile, three point (TH22, TH23, TH24) data in Fig 2(c) are used for comparisons. In this case, thermo-couples are embedded in the ceramic tile surface. The depth of measurement center from the surface is about 1.5 mm. Also, in the left side of Fig 2(c), temperature history is plotted. It is known that maximum temperature reachs about 1000°C.

In Fig.3, a series of temperature contours are shown at trajectory points listed in Table 1. We use chemically non-equilibrium one temperature code for flow analysis. So, translational and rotational temperature are plotted in the figure. About the altitude of 90 km, it is noticed that the rarefaction effects are conspicuous and shock stand off distance becomes large with the increase of the altitude. Maximum temperature reaches more than 20000 K in high altitudes flight, where high temperature region beyond 12000 K is also large. With the decrease of the altitude, this high temperature area disappears and maximum temperature in the shock layer drops gradually.

In Fig.4, FEM grids of TPS material are shown. Grids are drawn in a enlarged form to the inner direction. OREX TPS are composed of 4mm thick C/C nose cap, 1.5mm thick C/C TPS and 20mm thick ceramic tiles. Thermal properties of each TPS are presented in Table 2. In the present FEM analysis, the effects of temperature and differential directional dependence of heat conduction coefficient of TPS materials are considered. Also, radiation effects (emissivity of 0.84 on the OREX C/C materials and 0.8 on the ceramic tile)are evaluated. Intenal radiation is assumed to be zero for the C/C nose cap region, because heat sheald after the nose cap protects the inner radiation. For the other TPS material surface, emissivity of internal radiation is assumed to be 0.7.

CFD-FEM coupling analysis are made along the OREX trajectory every 10 seconds. Computational procedure are as follows.

(1) At the flight time of 7361.0sec and an altitude of 105Km, flowfield is calcutated using free stream conditions of Table 1. Wall temperature distribution is given by the constant value of temperature of 332 K on the whole surface. This assumption is considered to be valid, because on the C/C nose cap temperatures at TH1,2,3 and 4 is almost the same level at 332 K and, on the other area, temperature is almost constant at 302 K. On the ceramic tiles, temperature increases in short time and reach to radiation equilibrium state, so, initial temperature difference on ceramic tiles may be ignored.

(2) From the flow calculations, heat transfer distributions are determined and surface temperature after 10 seconds is computed by FEM analysis.

(3) Based on the freestream conditions after the 10 seconds and the wall temperature distributions obtained by step(2), flow fields are calculated by CFD code and heat transfer distributions are computed at the new altitude.

These procedures are done alternatively and temperatude increase of TPS materials is evaluated at each altitude in order.

In Fig.5, temperature increase of OREX TPS material is depicted at each OREX trajectory points. Temperature increase is rapid on the ceramic tile surface due to low conductivity coefficient. However, maximum temperature is caused at an altitude of 56 km on the C/C nose cap stagnation point. At the innner point of C/C nose cap temperature is about 3 deg below than the outer surface. On the inner ceramic surface, remarkable increase of temperature are not observed.

Figure 6 shows the change of heat transfer distributions along the OREX trajectory. It is shown that maximum heating is produced at an altitude of 60 km, where stagnation point heating reaches to 0.383 MW/m^2. Also in the figure, local peak heating is generated at the shoulder due to the local flow acceleration. Figure 7 is the surface temperature distributions at OREX trajectory points. In the early stage of OREX re-entry, temperature on the ceramic tile increases rapidly and may reach to local radiation equilibrium state. Maximum tolerable temperature of C/C and ceramic TPS are 2000°C and 1400°C, respectively.

Fig.8 shows the comparison between measured temperature history and CFD-FEM coupling results at C/C nose cap stagnation point. Measured maxinum temperature reaches about 1570 K, whereas numerical prediction represents almost the same temperature. In our analysis, emissivity of 0.84 and non catalytic surface conditions are assumed. In Fig.9, similar comparison of temperature history are shown at $\theta = 20$ deg point of C/C nose cap. Numerical maxinum temperature is about the same as the measurements.

In flight analysis, aerothermodynamic heating is alternatively estimated by decoupling the flow analysis. In this method, only FEM is used by assuming more complete thermo structual models. The result of stagnation point heating about 1.2 times higher than the CFD-FEM coupling results. The difference may originate in the surface catalycity of C/C nose cap.

Comparison of the C/C TPS temperature is pre-

sented in Fig.10. Measured temperature becomes maxinum about 1000°C for all three mesurement points. In this case, numerical reults predict almost the same value as the experiments.

Figure 11 shows the comparison of ceramic tile surface temperature. Measured temperature has the maxinum peak of about 1000°C at the TH23 point and temperature at TH22, and TH24 points follows. In this case, comparison is made at 1.5 mm lower points than surface, corresponding to the thermo-couple center locations. Numerical prediction shows almost similar temperature. However, in the numerical analysis, the maximum temperature appears at slightly lower altitude.

Finaly, comparison of stagnation point heating on the C/C nose cap are shown in Fig.12, where the maximum heating by CFD-FEM coupling analysis are slightly lower than the flight data analysis[1)] and the location of peak heating are shifted to lower altitude. Also, in the figure, prediction by Fay and Riddell's theory and Detra, Kemp and Riddell's calculations are plotted. It is noticed that analytical predictions overestimate the stagnation point heating.

Conclusions

OREX TPS temperature history is analyzed by CFD-FEM coupling analysis. In our study, the approach by one-temperature chemically nonequilibrium flow model is adopted. In this preliminary studies, the applicability of one-temperature real gas CFD code are investigated in detail and its accuracy is evaluated. Numerical results favorably predict the behaivior of temperature increase of each TPS material during OREX re-entry. On the C/C nose cap, calculated maximum temperature at each measurement points coincide with the flight experiment. However, maximum stagnation point heating predicted by flight analysis[1)] differs from the value obtained by CFD-FEM coupling mathods. This may be due to the different treatments of internal thermal structure analysis and the surface catalycity. In the real enviroments, heat sheald effects after the nose cap, etc, have to be introduced in our CFD-FEM analysis. On the other C/C TPS and ceramic tiles, good agreements are also obtained in maximum temperature predictions, although slight time difference of peak appearence exists. In OREX flight experiment, atomospheric data is not gathered, so, the accuracy of standard atomosphere model used in the present CFD computations must be also investigated by using the other available flight experimental data such as pressure coefficients. In addition, the study of the sensitivity of thermal properties and catalytic surface effects must be made.

References

1) NAL/NASDA Joint Research Report. [OREX] March, 1995 (in Japanese)

2) Yamamoto,Y,"Numerical simulation of Hypersonic Viscous Flow for the design of H-II Orbiting Plane (HOPE), Part II" AIAA Paper 91-1390, June 1991

3) Yamamoto,Y, Wada,Y, and Yoshioka,M, "HYFLEX Computational Fluid Dynamic Analysis ; Part II. " AIAA Paper 95-2274, June, 1995

4) Yamamoto,Y, Wada,Y, and Yoshioka,M, "Hypersonic CFD Analysis for the Aerothermodynamic Design of HOPE " AIAA Paper 95-1770, June, 1995

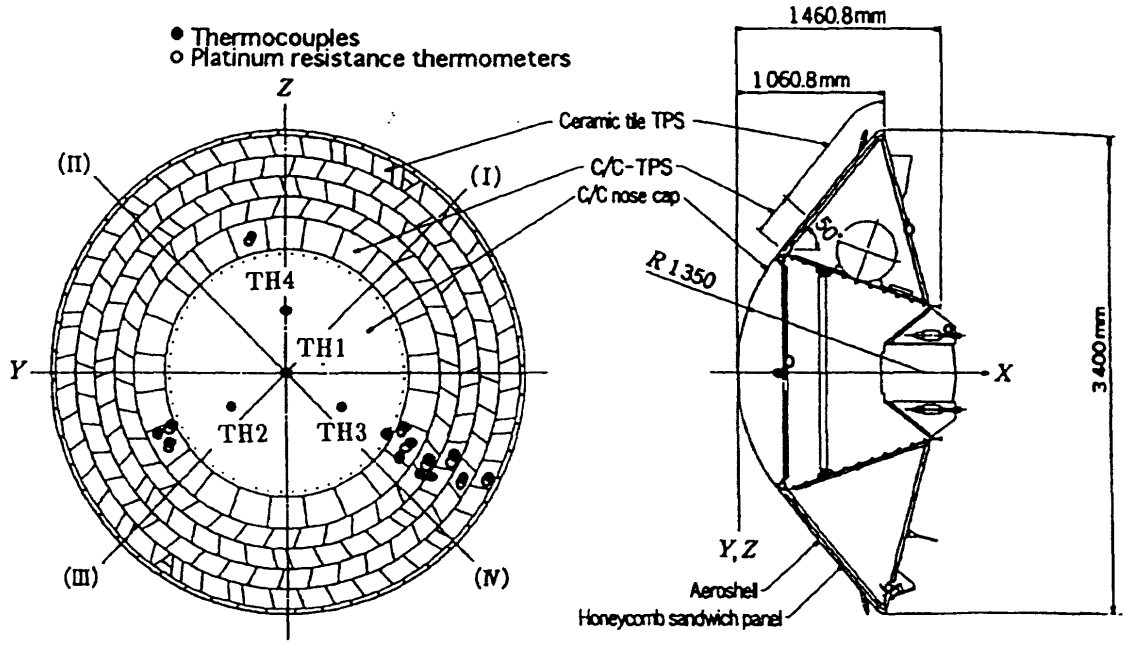

a) C/C nose cap sensor Locations and Structure systems.

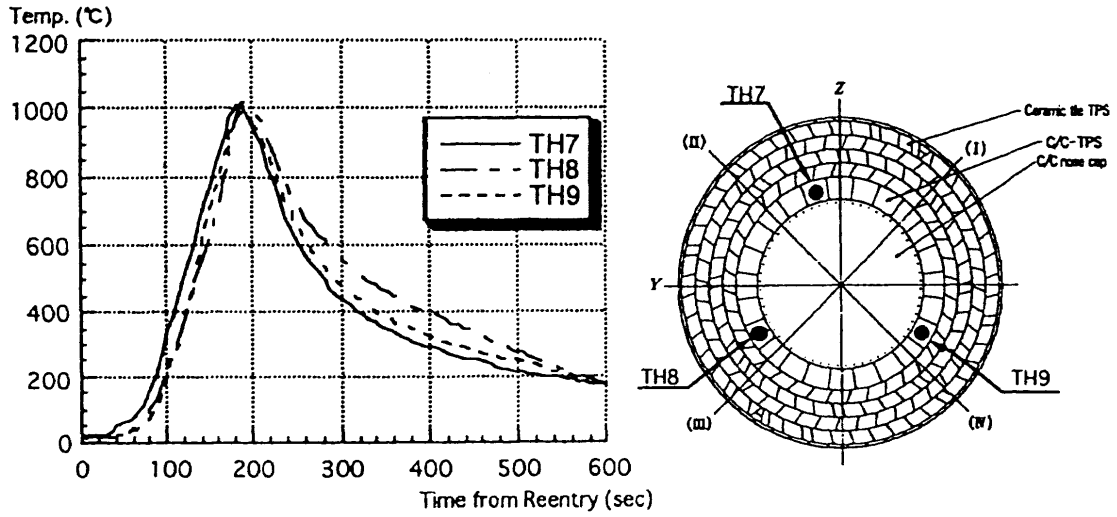

b) CC-TPS Sensor Locations and Temperature Histroy

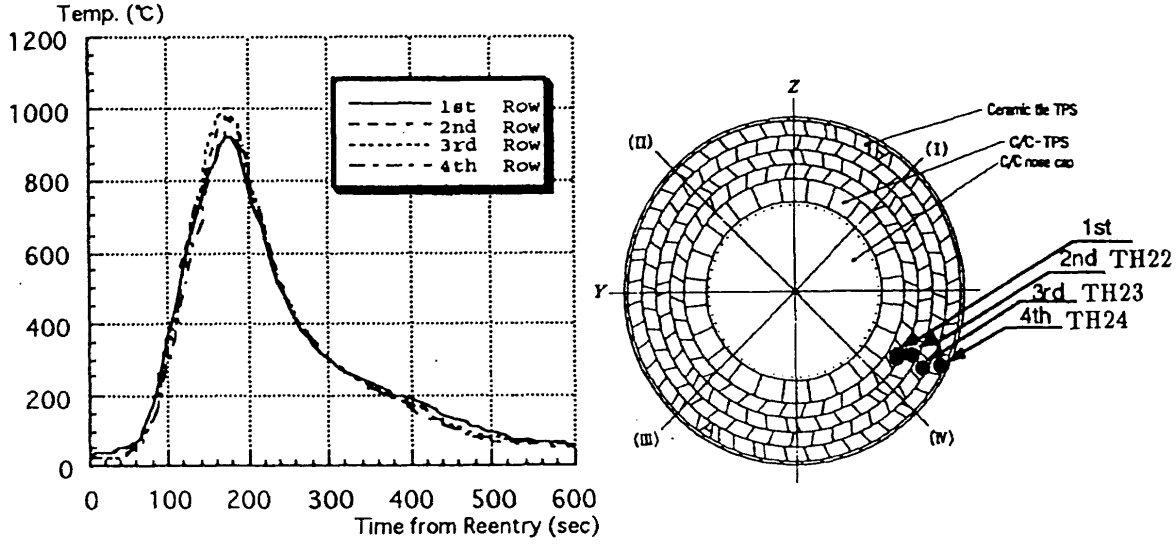

c) Ceramic Tile Sensor Locations and Temperature History

Fig.2 OREX Temperature measurement Location

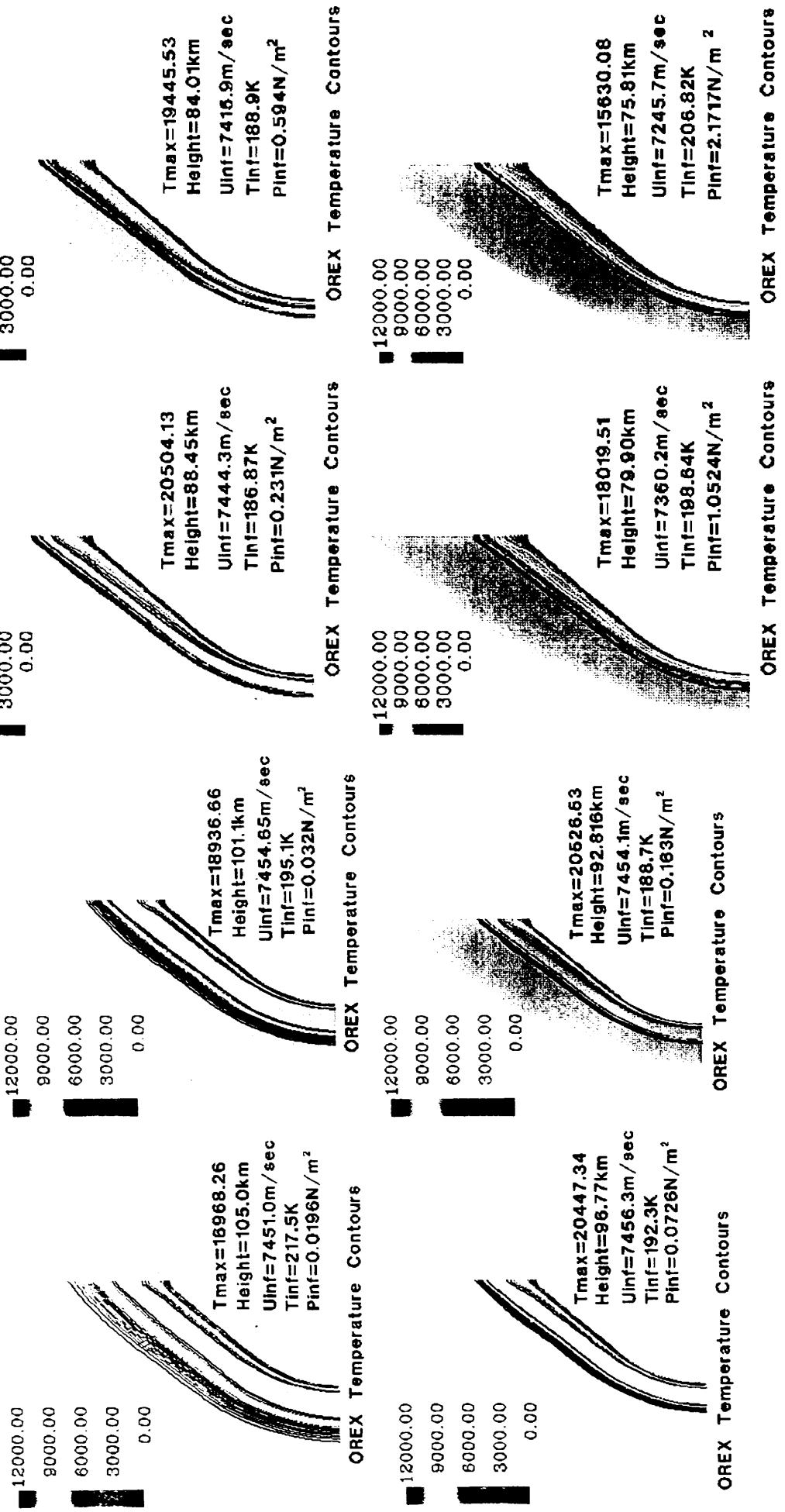

Fig 3. OREX Flow Temperature Contours along at Each Flight Trajectory Points in Table 1

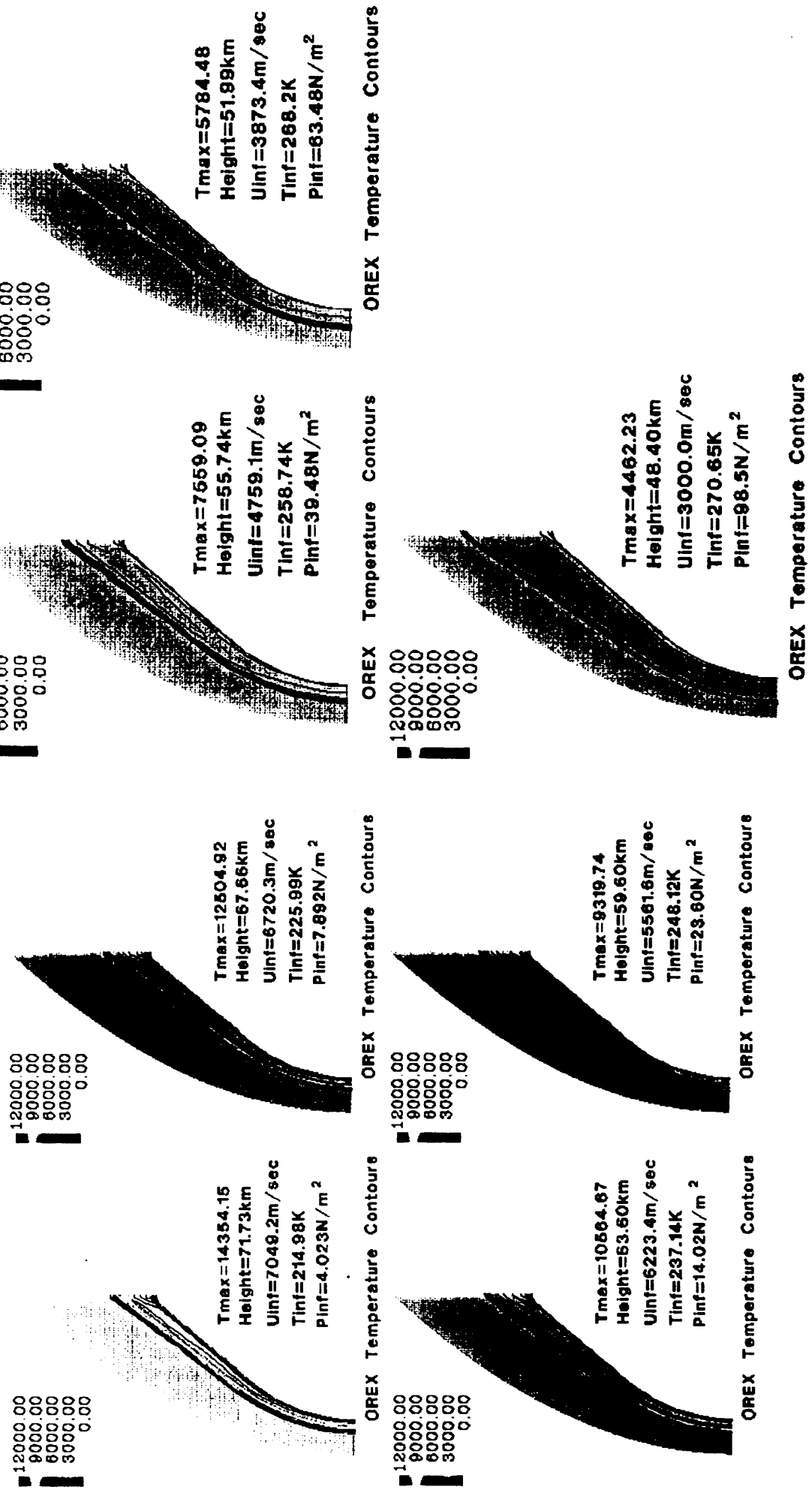

Fig 3. OREX Flow Temperature Contours along at Each Flight Trajectory Points in Table 1

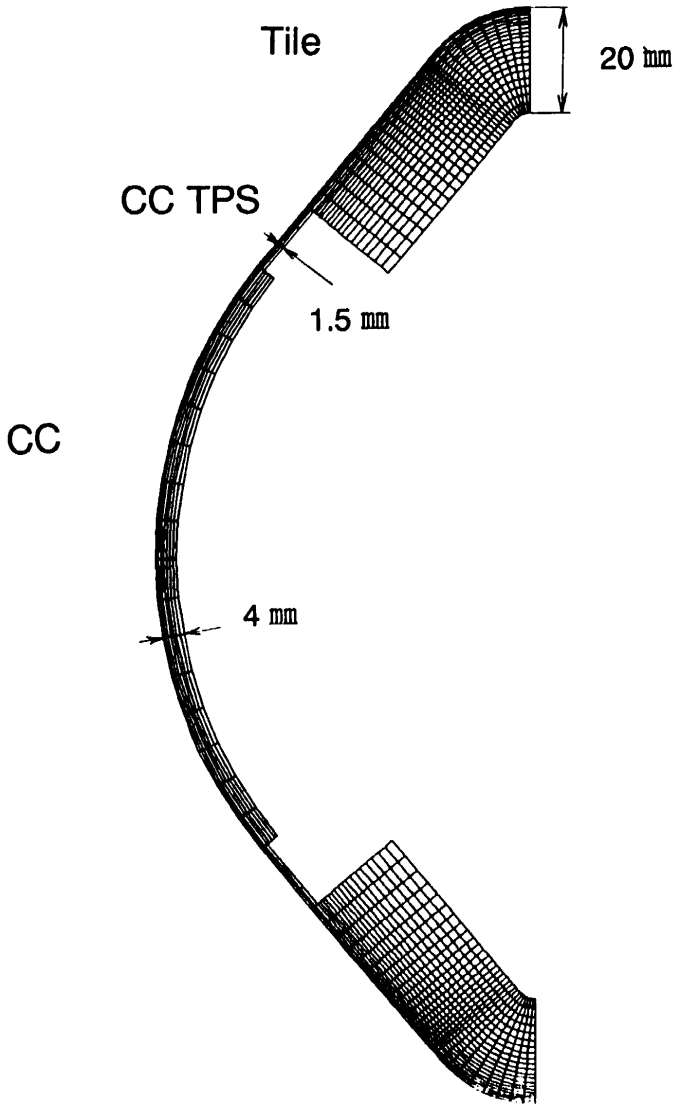

Fig.4 OREX TPS Grids for FEM Analysis Thermal

OREX Thermal Properties of TPS Materials

Material	Density	Temp	Specific Heat	Thermal Conductivity	Emissivity
C/C Nose Cap	(g/ cm³)	(℃)	(kcal/ kg ℃)	(cal/cm•S• ℃)	
C/C Parallel Direction	1.50	RT	0.159	78.732	0.84
		500	0.371	131.22	
		1000	0.434	134.96	
		1500	0.544	168.48	
C/C Normal Direction		RT		17.50	
		500		29.16	
		1000		29.99	
		1500		37.44	

Material	Density	Temp	Specific Heat	Thermal Conductivity (W/mk)		Emissivity
	(kg/ m³)	(℃)	(J/kg K)	Normal	parallel	
C/C TPS (MHI)	1890	25	615	0 ℃	206.1	0.84
		500	1476	300 ℃	166.6	
		1000	1714	600 ℃	119.0	
		1300	1838	900 ℃	110.2	
		1500	1970	1200 ℃	117.1	

Material	Density	Specific Heat		Thermal Conductivity		Emissivity
	(g/c m³)	(kcal/ kg ℃)		(kcal/mhr ℃)		
Ceramic Tile	0.216	0 ℃	0.151	0 ℃	0.040	0.8
		500 ℃	0.212	300 ℃	0.050	
		1000 ℃	0.232	600 ℃	0.065	
		1400 ℃	0.243	900 ℃	0.104	
				1200 ℃	0.153	

Table2 Thermal Properties of TPS Materials

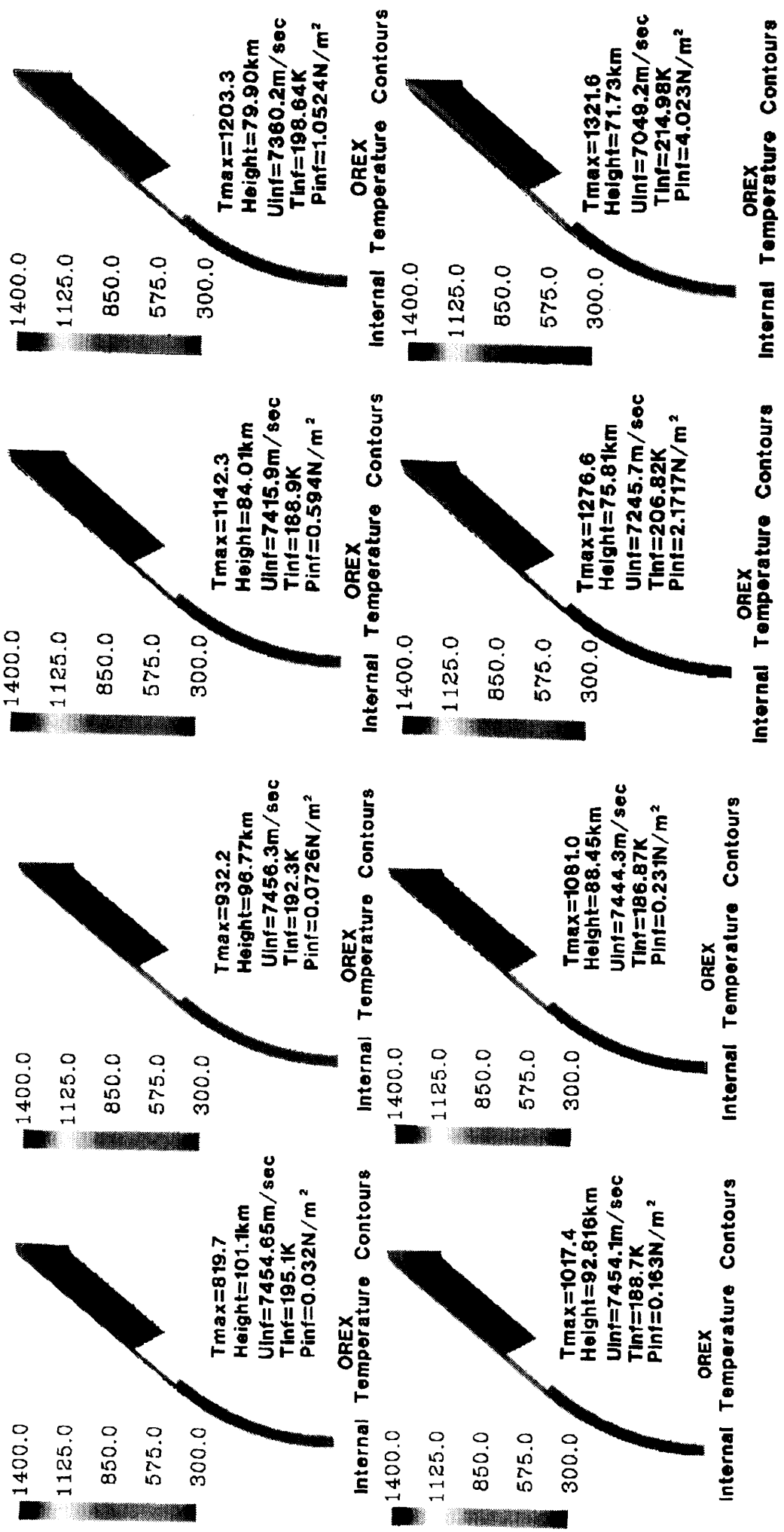

Fig 5. Internal Temperature Contours of OREX TPS at Each Flight Trajectory Points in Table 1

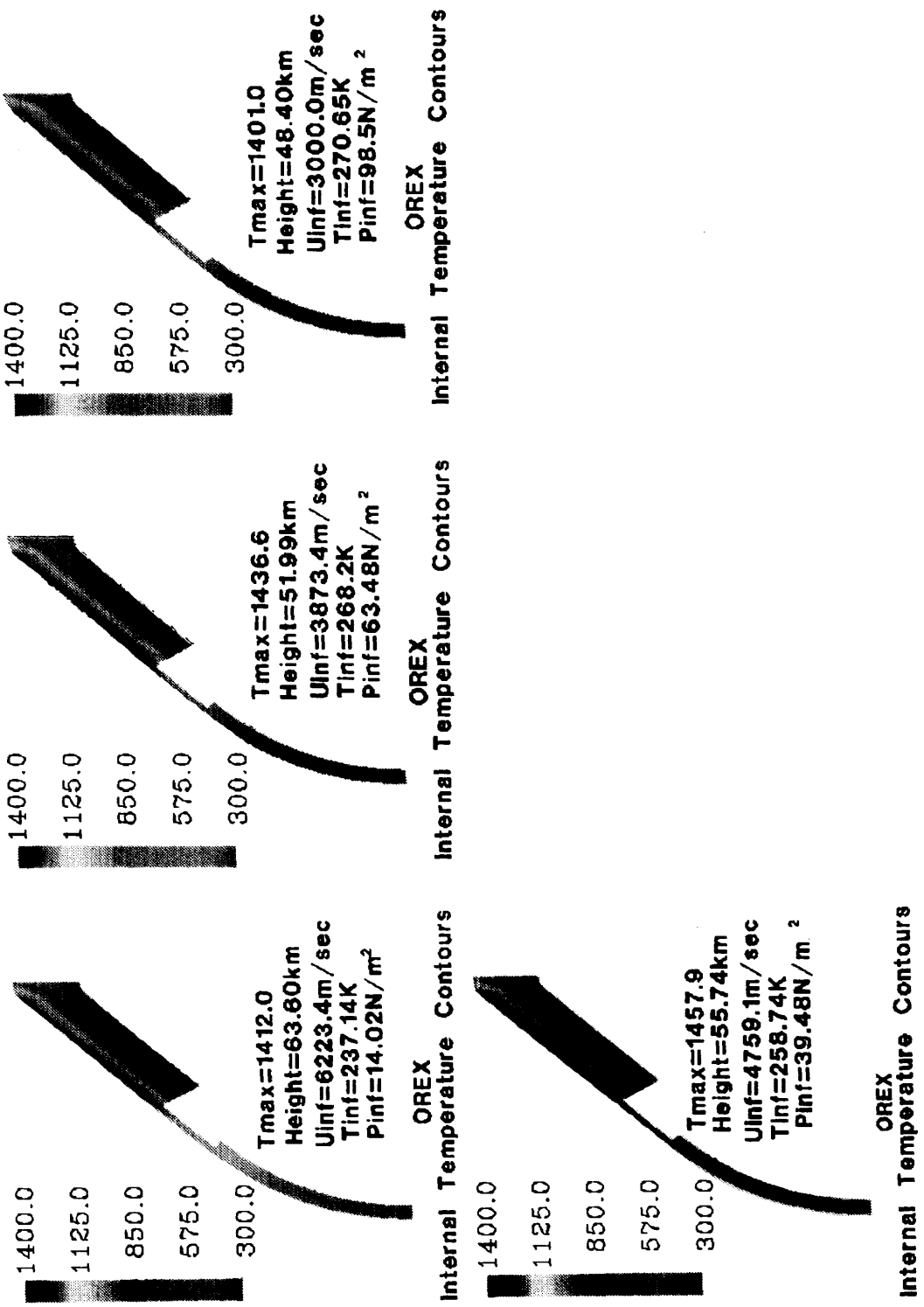

Fig 5. Internal Temperature Contours of OREX TPS at Each Flight Trajectory Points in Table 1

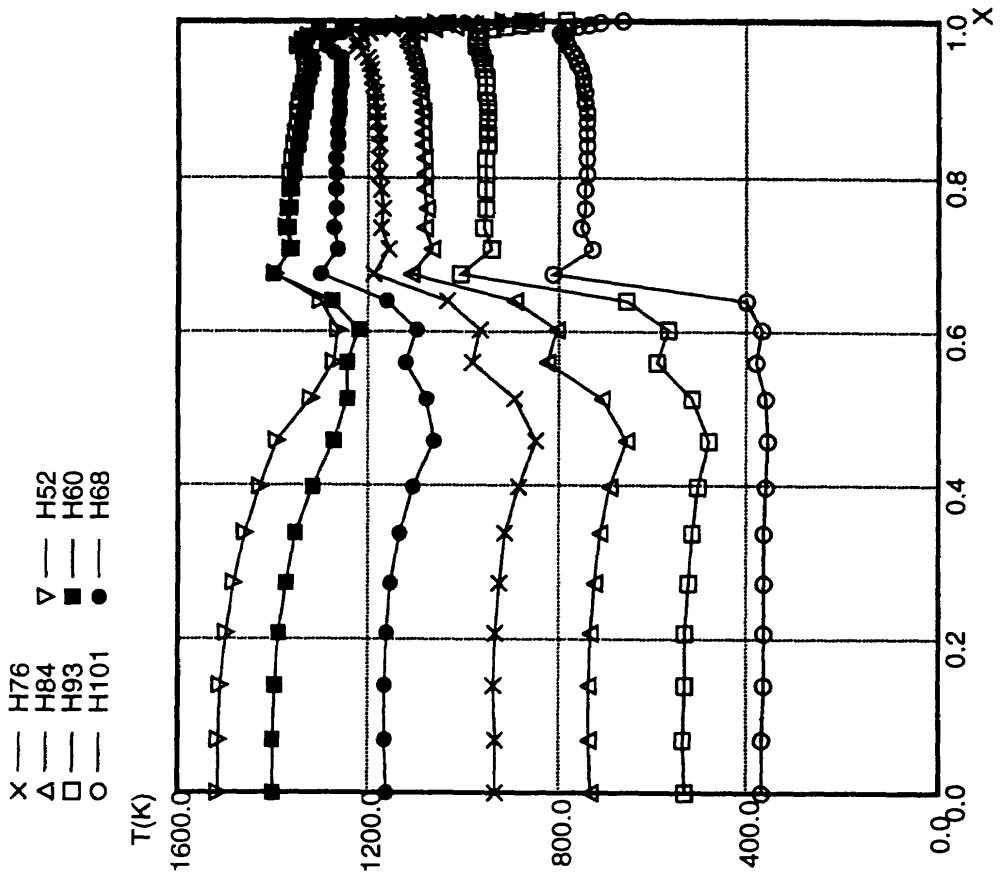

Fig.7 Surface Temperature Distributions along the Vertical Coodinate of OREX at Several Flight Trajectry Points Trajectory Points

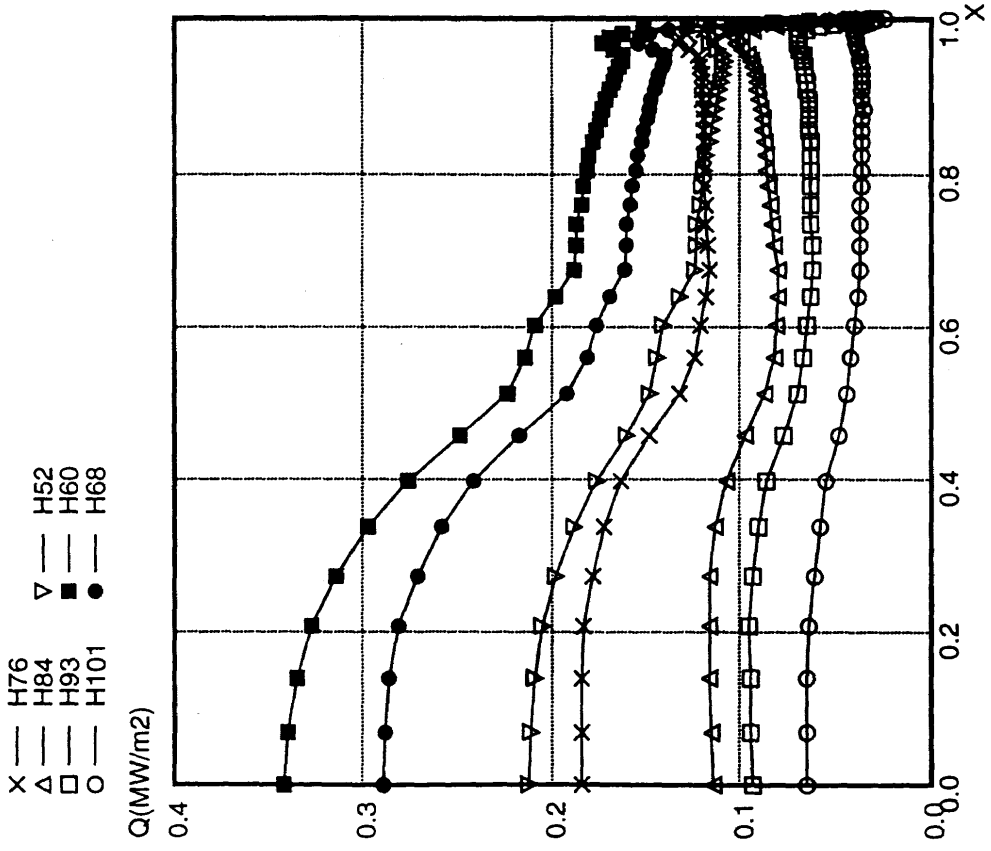

Fig.6 Heat Transfer Distributions along the Vertical Coordinate of OREX at Several Flight Trajectory Points

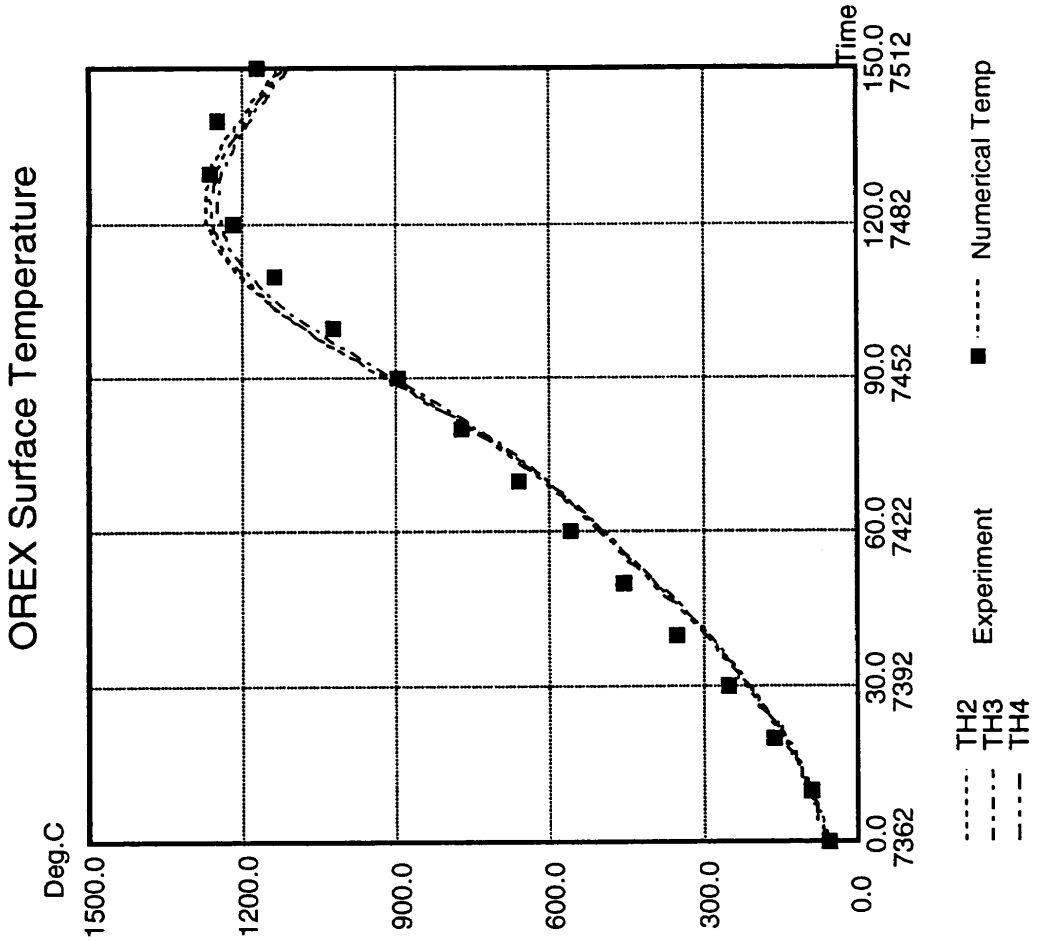

Fig.9 Comparison of C/C Nose Cap Temperature History at θ=20deg

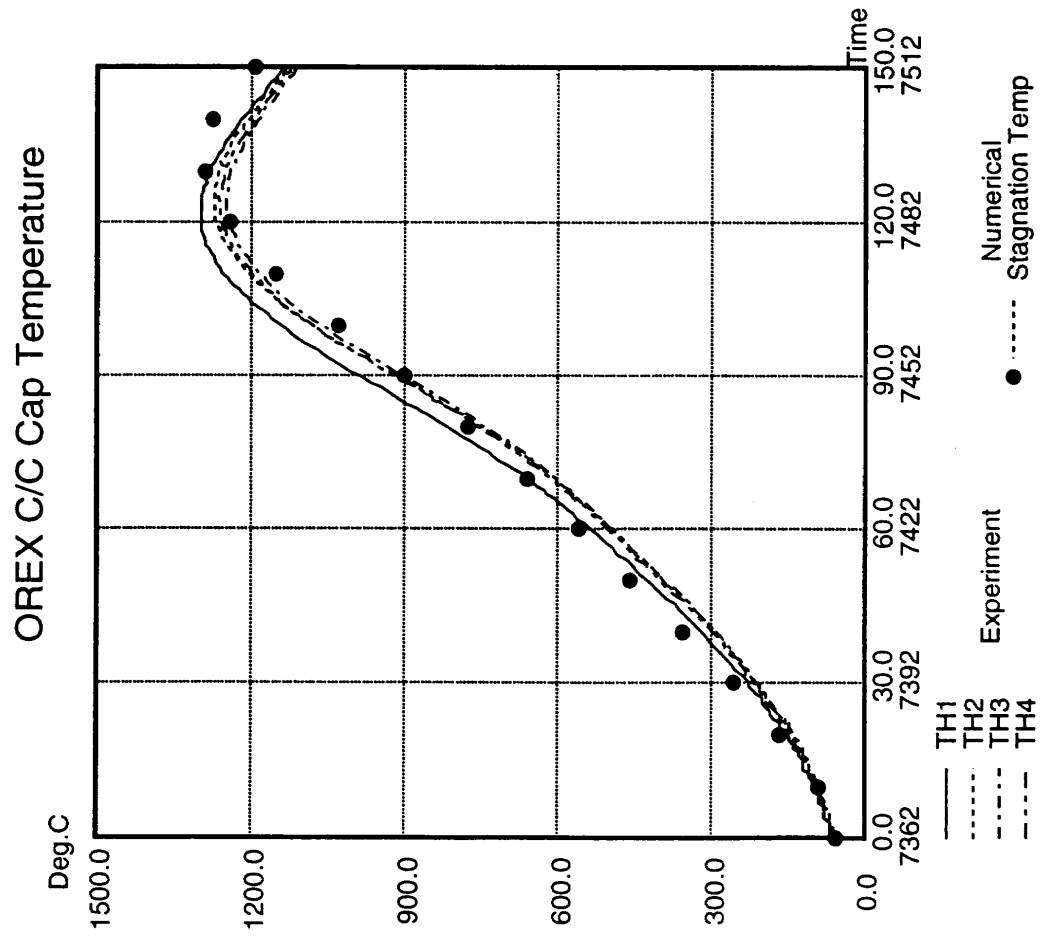

Fig.8 Comparison of C/C Nose Cap Stagnation Point Temperature History

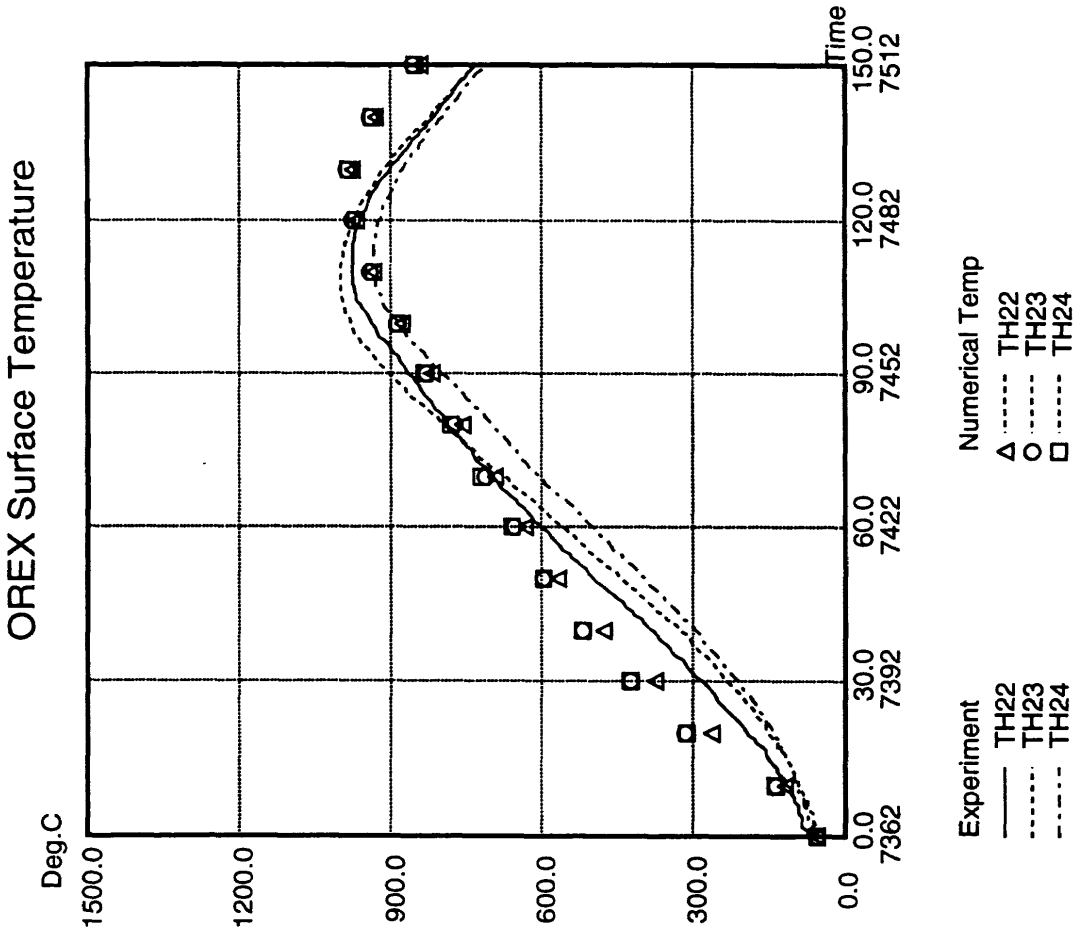

Fig.11 Comparison of Ceramic Tile temperature History

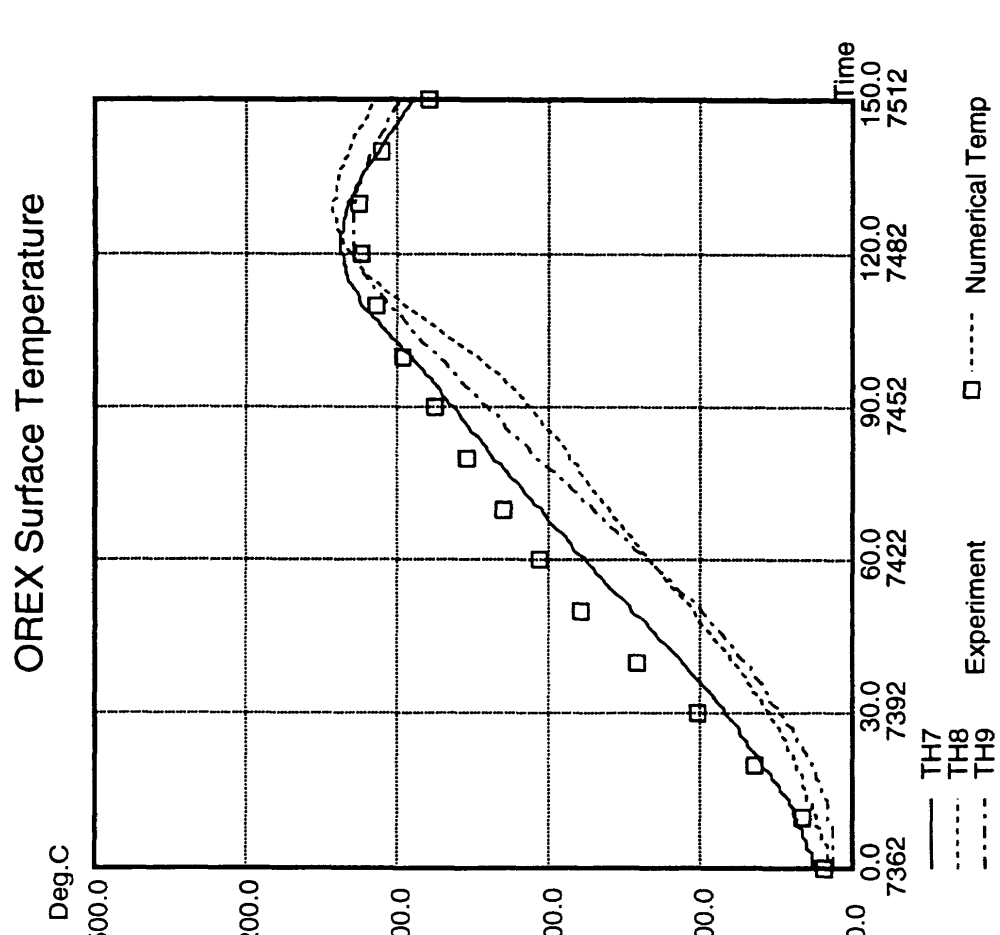

Fig.10 Comparison of C/C TPS Panel Temperature History

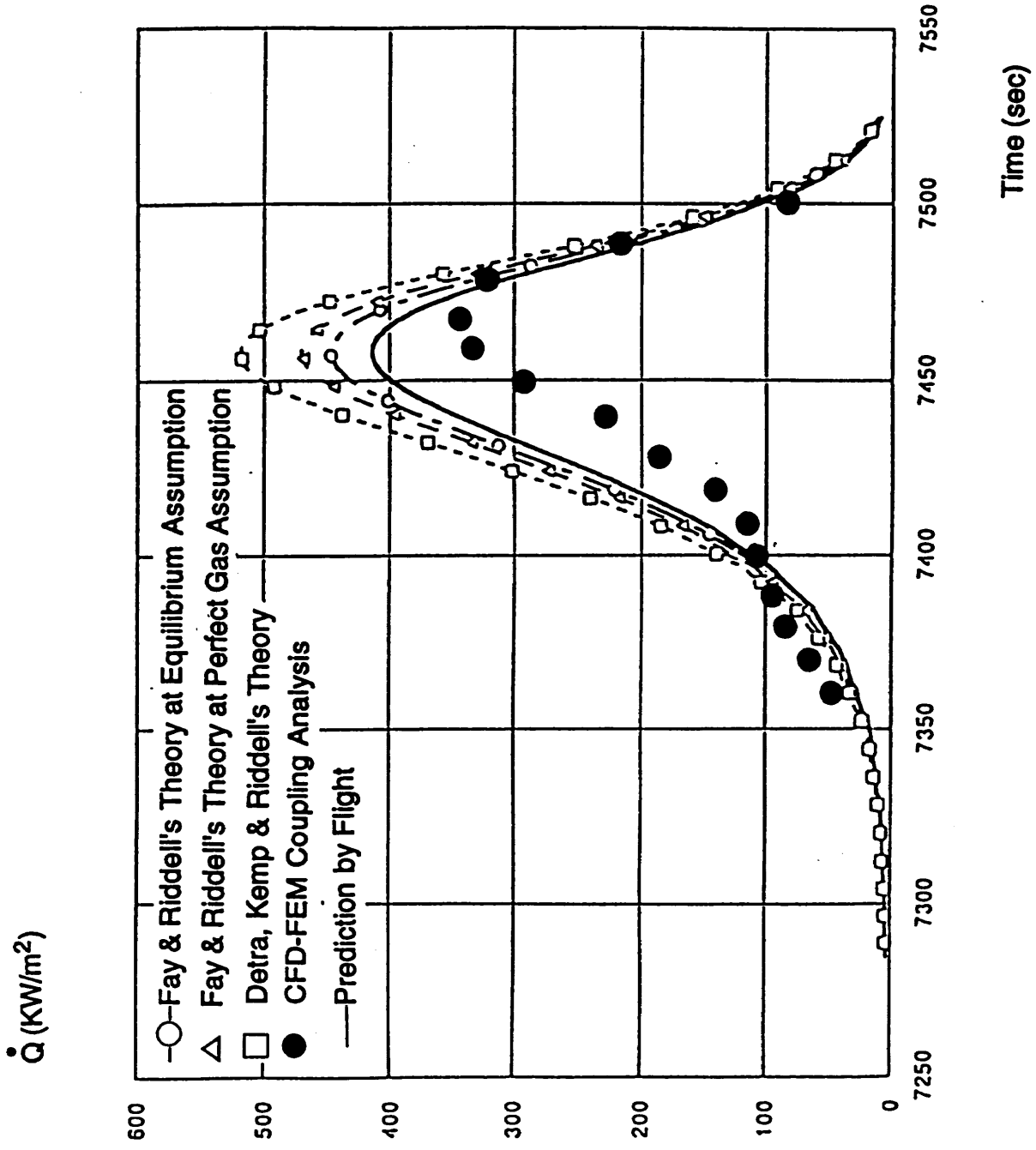

Fig.12 Comparison of Stagnation Point Heat Transfer

1-5

Numerical Simulations of Shock Wave Induced Unsteady Aerodynamic Heating Phenomena with Chemical Nonequilibrium

Shigeru ASO, Toshiteru MITOMO
Department of Aeronautics and Astronautics., Kyushu University
Hakozaki 6-10-1,Higasiku, Fukuoka 812, JAPAN
tel:81-92-641-1101 fax:81-92-651-5863 e-mail:aso@aero.kyushu-u.ac.jp

Toshi FUJIWARA
Department of Aeronautics, Nagoya University, Nagoya, JAPAN

Masanori HAYASHI
Department of Mechanical Engineering, Nishinippon Institute of Technology, Fukuoka, JAPAN

Abstract

In the present study the full two-dimensional Navier-Stokes equations are solved in order to investigate unsteady aerodynamic heating phenomena induced by the shock impingement on a ramp surface. The effects of chemical reactions to aerodynamic heating are investigated. The results show the effects of chemical reactions to shock induced aerodynamic heating phenomena are quite significant at high temperature.

1. Introduction

Recently high speed winged vehicles have been studied. One of the most important problems for designs of such vehicles is the severe aerodynamic heating and pressure rise caused by the impingement of shock waves on the surfaces. Especially the unsteady aerodynamic heating caused by shock wave reflections at a higher shock Mach number has been investigated and the peak heating due to a Mach stem and the second peak heating due to a slip layer have been observed by the present authors[1,2].

In the present study the full two-dimensional Navier-Stokes equations are solved in order to investigate unsteady aerodynamic heating phenomena induced by the shock impingement on a ramp surface. When the shock is much strong, nonequilibrium chemical reactions are occurred in the flows. The effects of chemical reactions to aerodynamic heating are investigated and the results are compared with experiments and calculated results without reactions.

2. Numerical Methods

In the numerical caluculations nonequilibrium chemically reacting flows are considered. The governing equations are two-dimensional full Navier-Stokes equations. Two-dimensional full Navier-Stokes equations in conservation form is as follows:

$$\frac{\partial \boldsymbol{U}}{\partial t} + \frac{\partial \boldsymbol{E}}{\partial x} + \frac{\partial \boldsymbol{F}}{\partial y} = \boldsymbol{J}$$

where each vector is expressed as follows:

$$\boldsymbol{U} = \begin{bmatrix} \rho \\ \rho u \\ \rho v \\ \rho(E + \frac{V^2}{2}) \\ \rho c_i \end{bmatrix}, \boldsymbol{E} = \begin{bmatrix} \rho u \\ \rho u^2 + p - \tau_{xx} \\ \rho uv - \tau_{xy} \\ \rho(E + \frac{V^2}{2})u + pu - q_x - u\tau_{x_{xy}} \\ \rho c_i u - \rho D_{im} \frac{\partial c_i}{\partial x} \end{bmatrix}$$

$$F = \begin{bmatrix} \rho v \\ \rho uv - \tau_{yx} \\ \rho v^2 + p - \tau_{yy} \\ \rho(E + \frac{V^2}{2})v + pv - q_y - u\tau_{yx} - v\tau_{yy} \\ \rho c_i v - \rho D_{im}\frac{\partial c_i}{\partial y} \end{bmatrix}, J = \begin{bmatrix} 0 \\ 0 \\ 0 \\ 0 \\ \dot{w}_i \end{bmatrix}$$

Heat conductionterms are expressed as follows:

$$q_x = k\frac{\partial T}{\partial x} + \sum_i \rho D_{im}\frac{\partial c_i}{\partial x}h_i, \quad q_y = k\frac{\partial T}{\partial y} + \sum_i \rho D_{im}\frac{\partial c_i}{\partial y}h_i$$

For chemical reactions of oxygen gas the 6 elementary reactions are assumed.

Forward rate constant, k_f, and backward rate constant, k_b, are obtained from Arrhenius equation as follows:

$$k_f = A_f T^{B_f} e^{-\frac{C_f}{T}}, \quad k_b = A_b T^{B_b} e^{-\frac{C_b}{T}}$$

For convective terms a Harten and Yee's upwind TVD scheme is used and for viscous terms a conventional central difference is used. For boundary conditions non-slip conditions are applied for the ramp surface and zero derivatives along freestream are assumed at incoming and downstream boundaries. Since in the flows with nonequilibrium chemical reactions the density, temperature and chemical compositions behind shock are changed along the distance from shock front, one-dimensional steady Euler equations for nonequilibrium chemically reacting flows are solved at first in order to obtain the initial conditions for incident shock wave. Also zero physical derivatives normal to incoming flow are imposed for the upper boundary in order to keep the incident shock wave normal. For the energy equation a constant wall temperature condition is assumed. Both fully catalytic wall case and non catalytic wall case are considered. Thermally equilibrium is assumed.

3. Numerical Results and Discussions

Calculated results of shock reflection processes in air at M_s=10.37, θ=10^0, p_∞=50 Torr and T_∞=299.0 K is shown in Fig.1 (a) and (b) with experiments[3]. At this testing conditions O_2 is fully dissociated and N_2 gas is slightly dissociated. The calculated results assuming chemically frozen gas and chemically non-equilibrium gas also show quite good agreements with experiments. In this flow conditions oxygen gas is fully dissociated and nitrogen is slightly dissociated. Since oxygen gas is only 20 % of total gas, total dissociation rate is quite small and almost no change is observed in the shock patterns and heat flux distribution as shown in Fig.1(b).

4. Conclusions

In the present study the full two-dimensional Navier-Stokes equations are solved in order to investigate unsteady aerodynamic heating phenomena induced by the shock impingement on a ramp surface. When the shock is much strong, chemically and thermally nonequilibrium reactions are occurred in the flows. The effects of chemical reactions to aerodynamic heating are investigated. The results show the effects of chemical reactions to shock induced aerodynamic heating phenomena are quite significant at high temperature.

References

[1] S. Aso et. al.: Proc. of 17th ISSWST, 1989, pp.777-782.
[2] K. Ohyama, S. Aso and M. Hayashi: Proc. of 19th ISSW, 1993.(to be published)
[3] R.R. Weynabts: UTIAS TN No.126 (1968).

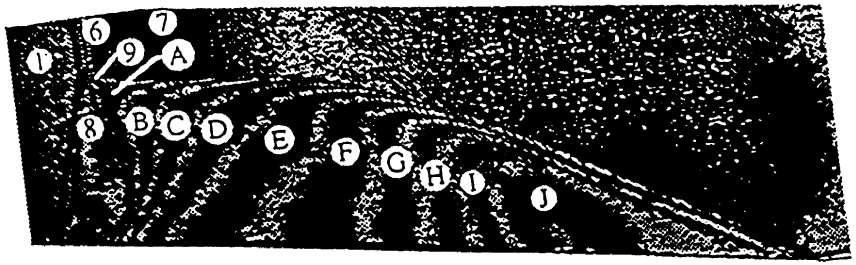

Experiment by R. L. Deschambault and I. I. Glass
Air , θ=10,Ms=10.37,P_0=50(torr),T_0=299.0(K)

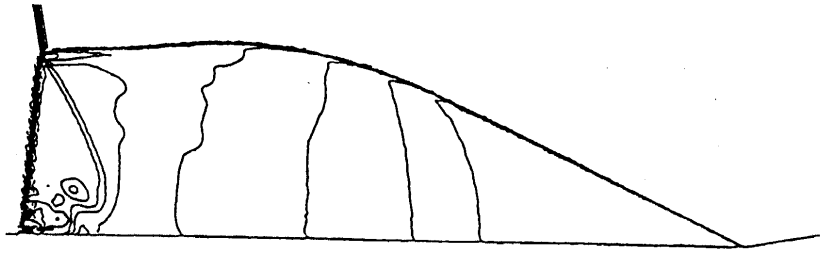

Computational result (Chemically frozen flow)

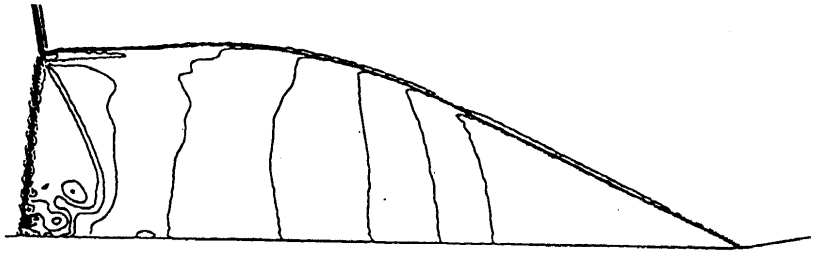

Computational result (Fully catalytic wall)

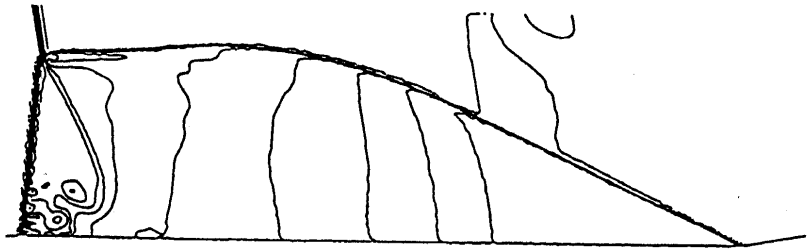

Computational result (Non catalytic wall)

(a) Shock wave patterns

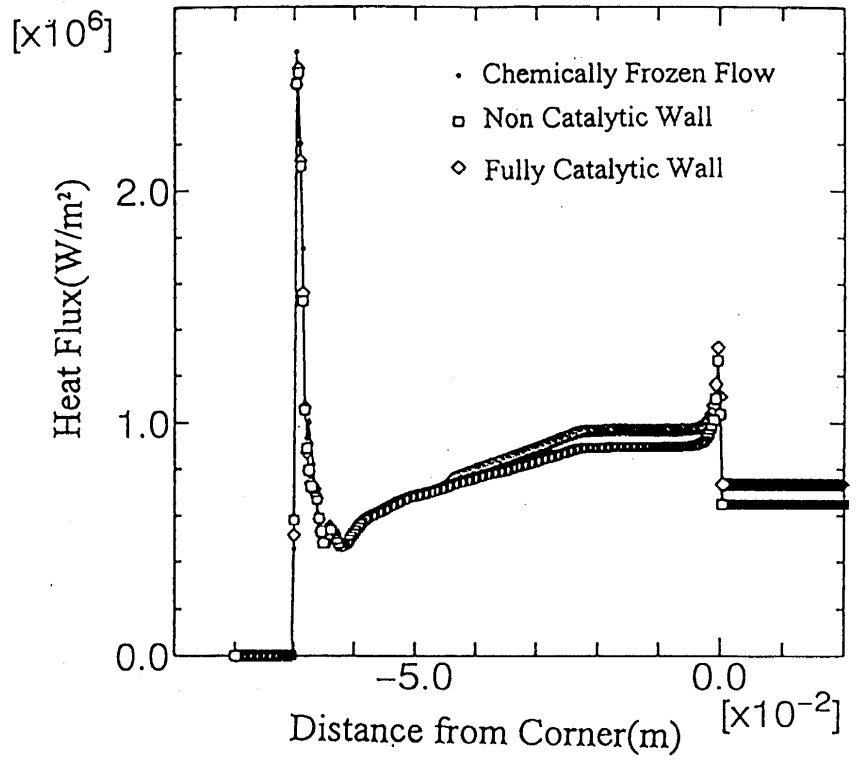

(b) Surface heat flux distributions

Fig.1 Comparison of calculated results with experiments
(*Air*, M_s=10.37, θ=10^0, p_∞=50 Torr and T_∞=299.0 K)

Ⅱ　特別講演

On the Interaction between CFD and Hypersonic Testing

J.Muylaert
ESA, ESTEC, Noordwijk, The Netherlands

Abstract

The paper presents the achievements and challenges in aerothermodynamics in Europe in the period May 1991 to November 1994, which corresponds to the time interval between the First and Second European Symposia on Aerothermodynamics for Space Vehicles. During this period, the lifting reentry vehicle Hermes, which had set the targets for European aerothermodynamic developments, was cancelled and replaced by a programme focused on ballistic re-entry vehicles: the Atmospheric Reentry Demonstrator (ARD), the Crew Transfer Vehicle (CTV) and an ambitious technology programme to support these vehicles. Additionally, Europe made a major investment in ground testing facilities with the approval for the construction of the Scirocco high enthalpy facility in Italy and a large induction-heated plasmatron facility in Belgium. Europe also initiated the Future European Space Transportation Investigation Programme (FESTIP) in October 1994. This programme has set major aerothermodynamic challenges: the reentry and descent problems will benefit from the extensive knowledge base already achieved from the Hermes programme; the ascent problems will set new challenges for Europe. Finally, the paper addresses the aerothermodynamic challenges posed by planetary entry vehicles for ESA's scientific satellite programme.

Introduction

In 1987 ESA embarked on a major extension of its space activities by the adoption of several challenging reentry vehicles. These were:

- the Hermes spaceplane: a reusable, lifting body, reentry vehicle;
- the Huygens spacecraft: an aerodynamically controlled entry vehicle into the Titan atmosphere;
- the Rosetta spacecraft: an aerodynamically controlled Earth reentry vehicle, returning from a comet rendez-vous and landing mission.

These programmes necessitated the setting up in August 1988 of a specialist capability in modern aerothermodynamics in the ESA Technical Directorate located at ESTEC in Noordwijk, The Netherlands. This new group at ESTEC rapidly established itself as a focal point for space vehicle aerothermodynamics in Europe: to coordinate European technical activities; to prepare and implement a technology research programme: to stimulate activities in space vehicle aerothermodynamics. The progress made by this group, stimulated by the aerothermodynamic challenges posed by the new ESA reentry programmes, permitted the convening of the First European Symposium on Aerothermodynamics for Space Vehicles, which was held at ESTEC in May 1991. Since then, the Huygens programme is nearing its completion, with the launch of the spacecraft scheduled for 1996. The Rosetta mission has been reduced in scope to delete its challenging Earth reentry requirement. The Hermes programme has evolved into a major programme focussed on ballistic reentry vehicles.

Current ESA activities in Aerothermodynamics

Within the manned space flight and microgravity programmes the following activities have been initiated:

- an Atmospheric Reentry Demonstrator vehicle (ARD), which is guided reentry vehicle of the Apollo type;
- a crew rescue vehicle (CRV), which is also a guided vehicle, utilizing the experience to be gained from the ARD;
- an automatic transfer vehicle (ATV), which is a logistics vehicle for the transport of equipment and propellant for the International Space Station A (ISSA).
- a technology programme for basic research and developments in aerothermodynamics, with emphasis on ground based facilities, capsule critical issues, industrial numerical tool improvements including validation within workshops, parafoil technology combined with the creation of an engineering data base.
- the design and construction of an induction heated plasma facility (plasmatron), at the VKI Belgium, for the study of gas surface interactions such as catalycity and ablation in a contaminant free environment.

- the approval for the construction of the 70 MW SCIROCCO arc heated plasma facility at CIRA in Capua, Italy.

Additionally, ESA has engaged in a Future European Space Transportation Investigation Programme (FESTIP), to investigate potential fully reusable future launchers for Europe and to engage in technology developments for such vehicles.

Thus, despite the changes that have been made to the original ESA programme of reentry vehicles, the programme that has evolved since 1991, is now greater in scope and offers more challenges in aerothermodynamics. This has motivated the convening of the Second European Symposium on Aerothermodynamics for Space Vehicles, which was held at ESTEC in November 1994. This paper presents the achievements and challenges in aerothermodynamics in Europe since the first symposium held in May 1991.

Challenges in Aerothermodynamics

Hypersonic testing and use for design

The decision to build 2 new hypersonic facilities in Europe i.e. the ONERA hot shot F4 and the DLR Stalker Tube HEG was made during the Hermes programme. At that time the major driver for the construction of these high enthalpy facilities was the real gas and viscous interaction effects experienced by the Shuttle Orbiter during its maiden reentry flight. Apart from the under prediction of the pitch-up moment as shown in Figure 1, local hot spots were detected on the fuselage side walls due to vortex scrubbing, on the windward side due to transition and on the wing- and vertical stabilizer leading edges due to shock /shock interactions. Today, ESA is focusing on low L/D capsule configurations and as also shown in Figure 1, important unpredicted real gas effects have occurred during the Apollo reentry. The figure shows the trim pitching moment error; preflight prediction compared to flight data for the Apollo and the Orbiter Shuttle. A ground testing technology programme was started by ESA to assess flow quality of the major European hypersonic facilities, to enlarge their operational envelop, and to improve their operational utilization:

- the construction of a pilot Stalker tube at the University of Marseille called the TCM2, for the study of nozzle-wall boundary layer development including transition, for the analysis of different types of stagnation heat flux probes (Fay and Riddell) including influence of wall catalycity, and to perform a detailed study of the nozzle flow quality where also the the species concentrations as well as their vibrational temperatures are to be measured;

- the development of non intrusive measurement techniques for F4 and HEG in order to characterize their free stream conditions, in addition to the classical pitot and heat flux measurements using classical probes;

- the design and construction of a new static and high enthalpy probe,

- the testing of a standard model called ELECTRE, and simple axisymmetric configurations such as the hyperboloid flare to ease the computational rebuilding;

- the development of nonequilibrium Navier Stokes codes at several national research establishments and industries for analysis of experimental data and extrapolation to flight, whereby the experimental and numerical data are to be compared in a workshop type environment.

The layout of the F4 facility and of the HEG facility are shown respectively in Figure 2 and 3. Apart from the activities related to the high enthalpy facilities, an important effort has been made to improve flow quality of the classical hypersonic facilities and in particular the so called R and D facilities which play a major role in the CFD validation process. Finally it should be mentioned that an activity was initiated to investigate the influence of variable gamma effects in the VKI Longshot facility with the aim to qualitatively simulate real gas effects.

Extrapolation to Flight.

The issue of the extrapolation of ground test results to flight conditions must be seen in the light of a general aerodynamic and aerothermodynamic strategy of progressive building up of confidence in the design of a space vehicle. This general strategy consists of a development phase and a qualification phase. We will not elaborate on the qualification phase but we will outline possible approaches which will allow the designer to verify his ability to rebuild critical points in windtunnels and in flight. Some elements in critical points follow the well known physical laws so that scaling effects are well identified but others are not at all evident and require detailed analysis using advanced numerical tools. For a feasibility demonstration of a spaceplane design not only the mean probable aerothermodynamic values are important but more critically the minimum and maximum values associated with realistic uncertainties. Margins needed to cover uncertainties decrease with the increase of knowledge and the quantification of the phenomena. This is to be done with good experimental tools including instrumentation, good modeling of the physics and good numerical analysis for the computation of the solution of the equations around vehicles in windtunnels and in flight. The conventional approach for the evaluation of the margins used in the past i.e. adding all errors as evaluated from experiments and computations leads to

excessive requirements for the margins and is therefore not realistic. The approach to be taken is a progressive computational / experimental improvement of the physical modeling leading to a better understanding and use of existing facilities. Designing the windtunnel models using CFD such that in windtunnel conditions one approaches the flight phenomenon of interest, is part of this modern approach. Because of the impossibility of duplicating flight conditions in ground based facilities, a computational modeling approach is required. Indeed Mach numbers in shock tunnels or hot shot facilities are far from those in flight. Due to nozzle expansion processes the distribution of the energy is different compared to flight. Free flight models accelerated in ballistic ranges avoid errors in redistribution of energy on the forebody when the Reynolds number is matched. However chemical processes at the base or leeside are not simulated because in those regions recombination reactions are dominant. The time required for the recombination reactions to occur are inversely proportional to the square of the density whereas for the dissociation reactions it is inversely proportional to the density. It means that if a test is set to scale with the forebody dissociation reactions it results in simulating a leeside flow or a base flow which is closer to equilibrium that in flight. All this means that corrections are always required for flight extrapolation. Figure 4 shows the approach to validate an extrapolation to flight methodology. The right branch shows the classical testing in cold windtunnels where Mach Reynolds simulation is possible and where using generic forms, code validation for perfect gas phenomena is feasible. Examples are the hyperboloid flare for the study of the boundary layer separation and reattachment and associated shock boundary layer interaction, the capsule-like blunt cone in rarefied flow for the study of the wake, the delta wing for the study of vortex flow fields and the Electre blunt cone for the detailed study of the nozzle flow quality and which serves as a standard model. On the left branch of the Figure are the similar generic models for the study of real gas effects. CFD validation includes here facility simulation because of the necessity to take into account the nozzle free stream species concentrations and vibrational temperatures. In order to study the extrapolation to flight it is necessary to test flight configurations in the so called cold as well as high enthalpy facilities. Computations in windtunnel as well as in flight conditions are to be performed. The Orbiter/Halis was selected as the configuration for the study of the extrapolation to flight. Figure 5 shows a computational rebuilding of the Halis configuration in the S4 facility. It is through a computational windtunnel rebuilding including nozzle expansion processes that a study of the uncertainties associated with the extrapolation to flight can be performed. This computational rebuilding will provide a better understanding of the facility and measurement techniques used as well as for a better use for design, in particular for the high enthalpy facilities. Obviously this implies the availability of 3D nonequilibrium Navier Stokes codes or Euler codes coupled with boundary layer codes. Because of the large computing power required to perform 3D nonequilibrium computations and because most of the existing 3D codes still require detailed validation especially the validation of the physical models, a framework for real gas high enthalpy validation is needed.

Real Gas Validation Methodology

The proposed real gas validation methodology is shown in Figure 6. The thermodynamic coefficients, transport properties , radiation properties and chemical kinetics need to be reassessed using modern shock tubes combined with the latest nonintrusive measurement techniques. Because most of the existing data derive from older shock tube experiments where the relaxation processes behind a moving normal shock was measured; it is believed that new shock tube experiments combined with the latest nonintrusive measurement techniques are required to reasses these reaction rates and thermodynamic properties. Moreover the validation of the above coefficients need also to be done for expanding flow fields. There is an urgent need to standardize the chemical and vibrational reaction rates for air and other gases such as CO_2 for specific classes of high enthalpy flows e.g. flows encountered in shock tubes or hot shot facilities which do not necessarily require the modelization of ions. Standardization of reaction rates will also take away a source of discrepancies when performing code to code comparisons.

In addition there is an urgent need to improve our understanding of the reaction mechanisms associated with gas surface interactions such as catalysis and ablation. These fundamental experiments could be performed in arc jet facilities or clean environments such as solar furnaces or induction heated facilities (plasmatrons).

Flap Efficiency and Heating

The assessment of flap efficiency and heating has always been a critical point in the design of space vehicles. This problem has been extensively analyzed in the context of the industrial technology conservation studies and will be briefly discussed using a generic axisymmetric configuration. This configuration is the hyperboloid flare. We will discuss here a computational analysis performed on this model in high enthalpy conditions corresponding to the HEG reservoir conditions of 500 bar and 9500 K. The nozzle exit conditions are computed with a 1 D chemical and vibrational multi temperature nonequilibrium Euler code. The Edenfield boundary layer correction is included in this code. Figure 7 shows the centerline

evolution of static and vibrational temperatures and the growth of the boundary layer. Note the rapid freezing of the vibrational temperatures and the velocity which quickly reaches constant values. All the important chemical kinetic effects occur at and just downstream of the throat.

This 1 D code provides the required input parameters to start subsequently a 2 D axisymmetric nonequilibrium Navier Stokes code.

Obviously, the way to study the extrapolation to flight is to perform computations in wind tunnels and in flight conditions following some scaling law. The scaling law used is, as discussed above, the binary scaling ρL which simulates the dissociation reactions combined with the speed to simulate the kinetic energy. The scale factor for this case was 120.

Figures 8 and 9 show respectively the computed Cp and the Stanton distribution for the nonequilibrium HEG wind tunnel condition, for the nonequilibrium flight and the equilibrium flight condition. Some important conclusions can be drawn: an increase in pressure recovery on the flare for flight of approximately 15% relative to the wind tunnel case is noted and another increase for flight in equilibrium of approximately 25% relative to the flight nonequilibrium case can be seen. Similarly, from Figure 9 one can see that an increase in Stanton on the flare for flight of 30% relative to the wind tunnel and another increase of approximately 50% for equilibrium flight relative to nonequilibrium flight is obtained. Clearly the assumption of chemical and vibrational equilibrium leads to a significant over estimation of the peak pressure and peak heat flux on the flare. Going from wind tunnel to flight, a reduction is seen in separation length combined with a forward shift of the pressure peak giving rise to an increase in flap efficiency.

Parachute Deployment

Not all the problems are in the hypersonic domain; in fact in the hypersonic domain the margins can be taken large enough to cope with the uncertainty. Often the real problem occurs in subsonic flow when a heat shield needs to be released and parachutes need to be deployed. Figure 10 shows the Huygens entry into Titan and its descent scenario. Here a large amount of engineering expertize is required to achieve a design for safe flight until landing. Issues like static and dynamic stability during the parachute deployment phase are crucial and require expert skills.

Future Perspectives

In the future it is clear that CFD will play a more dominant role; however not to the expense of experimental testing. The role of the windtunnels will change: the R and D facilities will be used more for the validation of the physical modeling whereas the industrial windtunnels, especially the transonic facilities, will be used for static and dynamic data base generation.

The use of CFD will be progressively and continuously increased:

- in the design of experiments, the definition of the test environment, the development, application and interpretation of diagnostics and in the analysis of the results. The test data will then form a basis for validating this process including CFD tools.
- for the extrapolation from windtunnel to flight. The flight data will then be used to qualify the whole process.

Improvement for the following physical models are required:

- Transition, in particular transition due to roughness and that induced by cross flow instability.
- Turbulence, with emphasis on turbulence within shock boundary layer interactions.
- Gas - surface interactions ; catalycity and ablation
- Transport properties and physical /chemical transformations such as V-V or V-T couplings.

Finally the efficiency of the numerical tools needs to be improved by:

- automatic or semi-automatic grid generation,
- improvement of algorithms,
- further exploitation of parallel computing.

Concluding Remarks

Aerothermodynamics is a specialized and challenging technology which requires continuing and dedicated research at the highest scientific and engineering level, using new scientific knowledge as it is gained for the development of computational codes and their experimental validation. It has important multidisciplinary interactions with vehicle materials, structures, thermal protection, propulsion and guidance and control systems

In addition to the validation of physical models, an effort is still required to improve grid generation tools and to enhance the efficiency of the codes by using parallel platforms. Finally ESA's objectives to set up a coherent programme between its research activities and future projects requirements have been achieved, allowing for the conservation and continuous improving of the European aerothermodynamic capabilities by setting up collaborations between agencies, research establishments and industries.

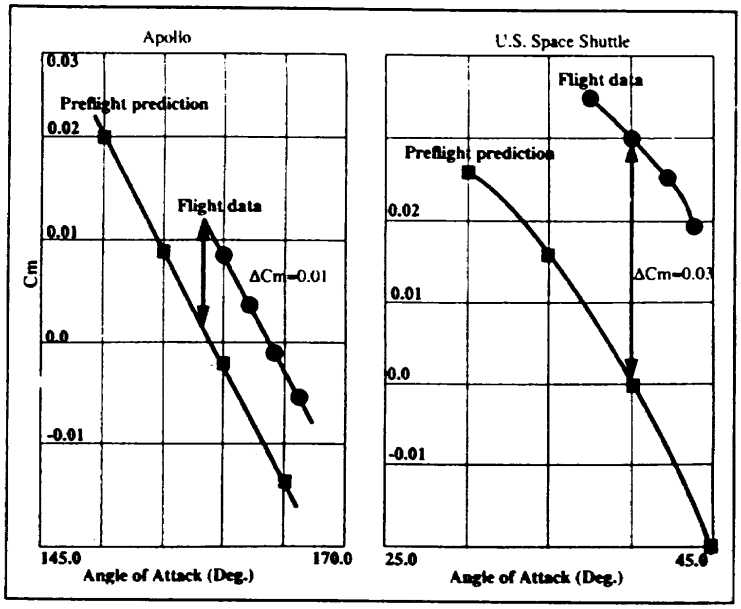

Figure 1: Trim Cm Error in Past Experience

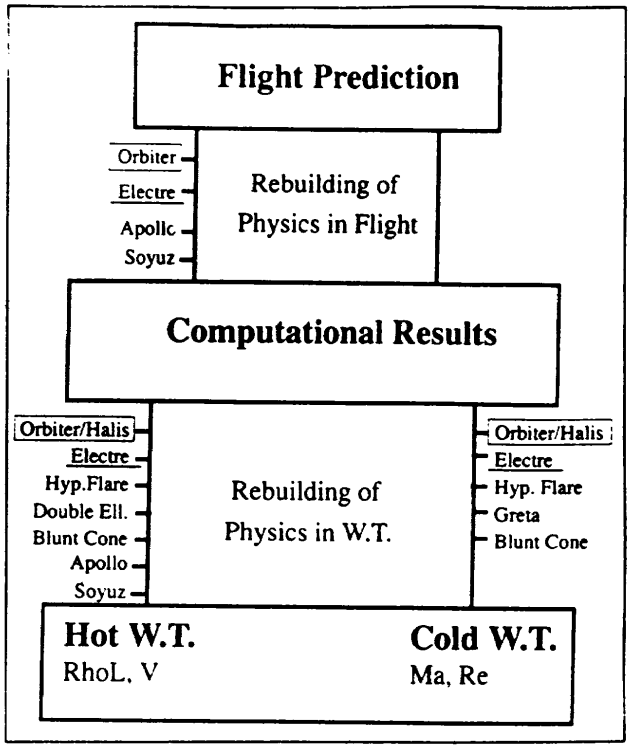

Figure 4: Extrapolation to flight Approach

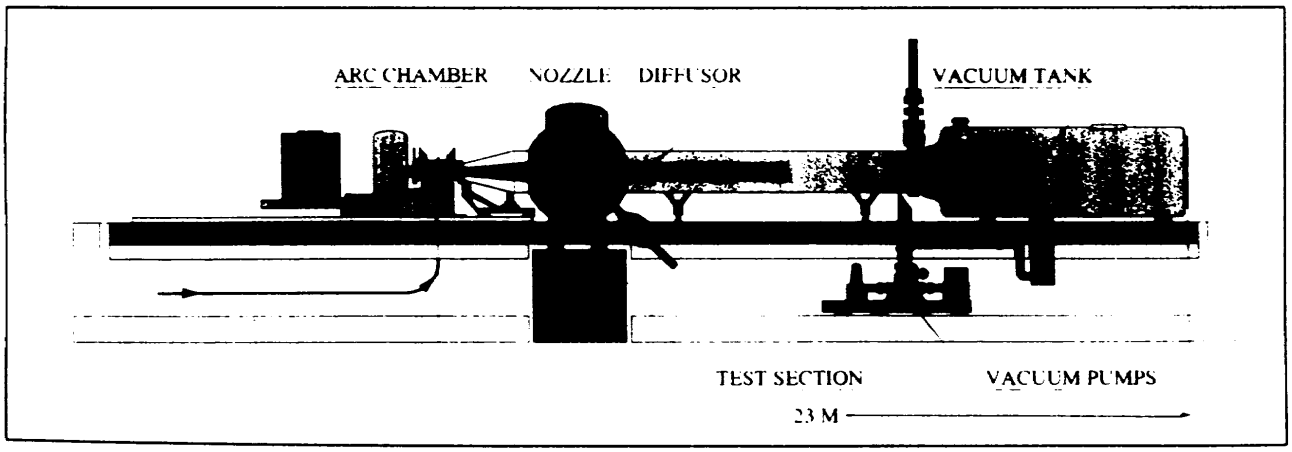

Figure 2: The F4 facility at ONERA Le Fauge

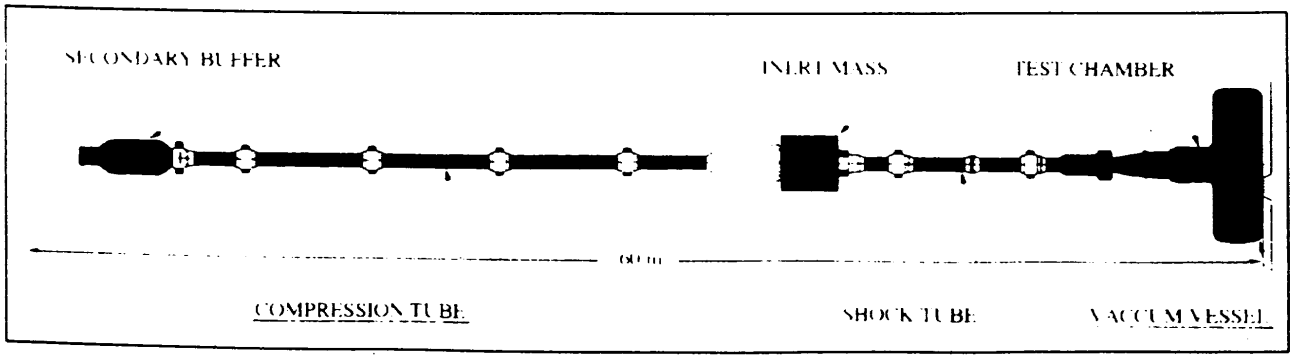

Figure 3: The HEG facility at DLR Goettingen

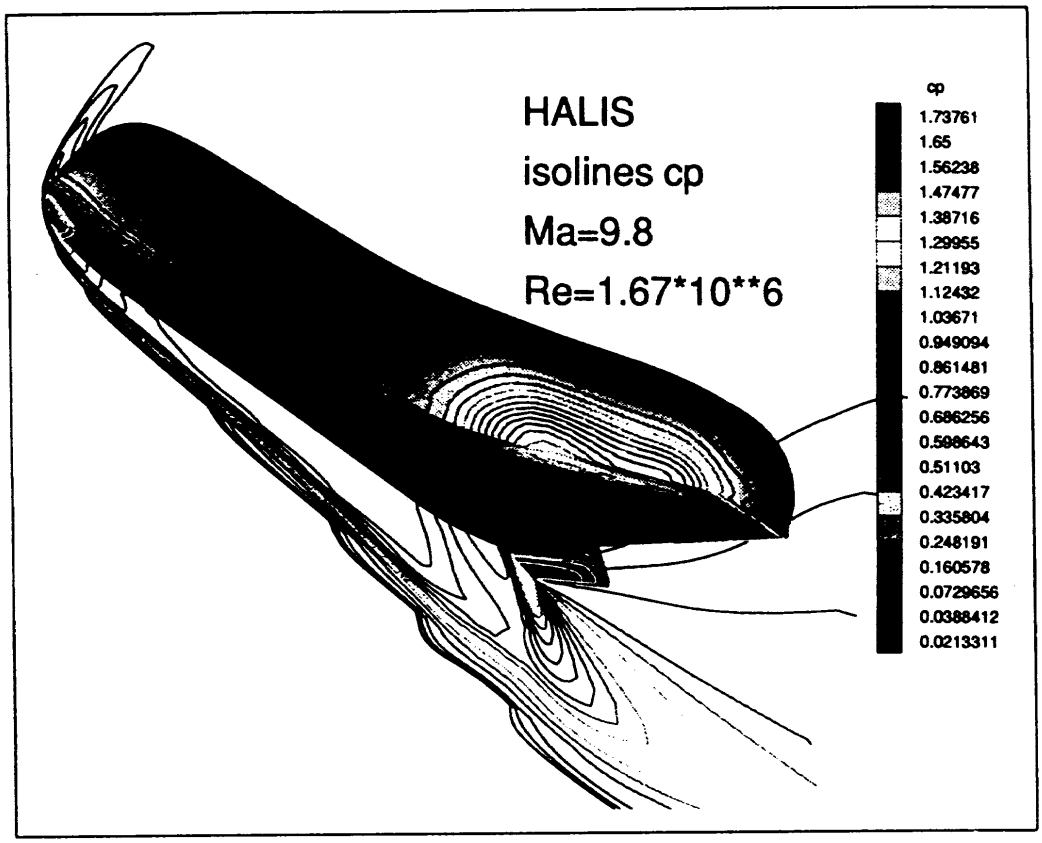

Figure 5: Halis in S4 Modane

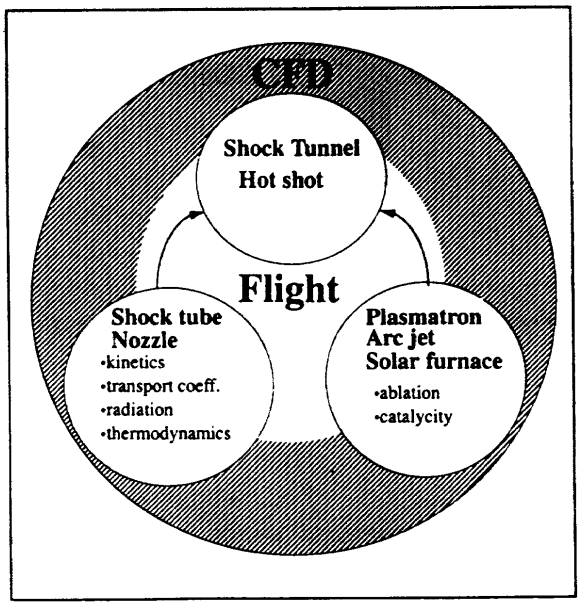

Figure 6: Real gas validation methodology

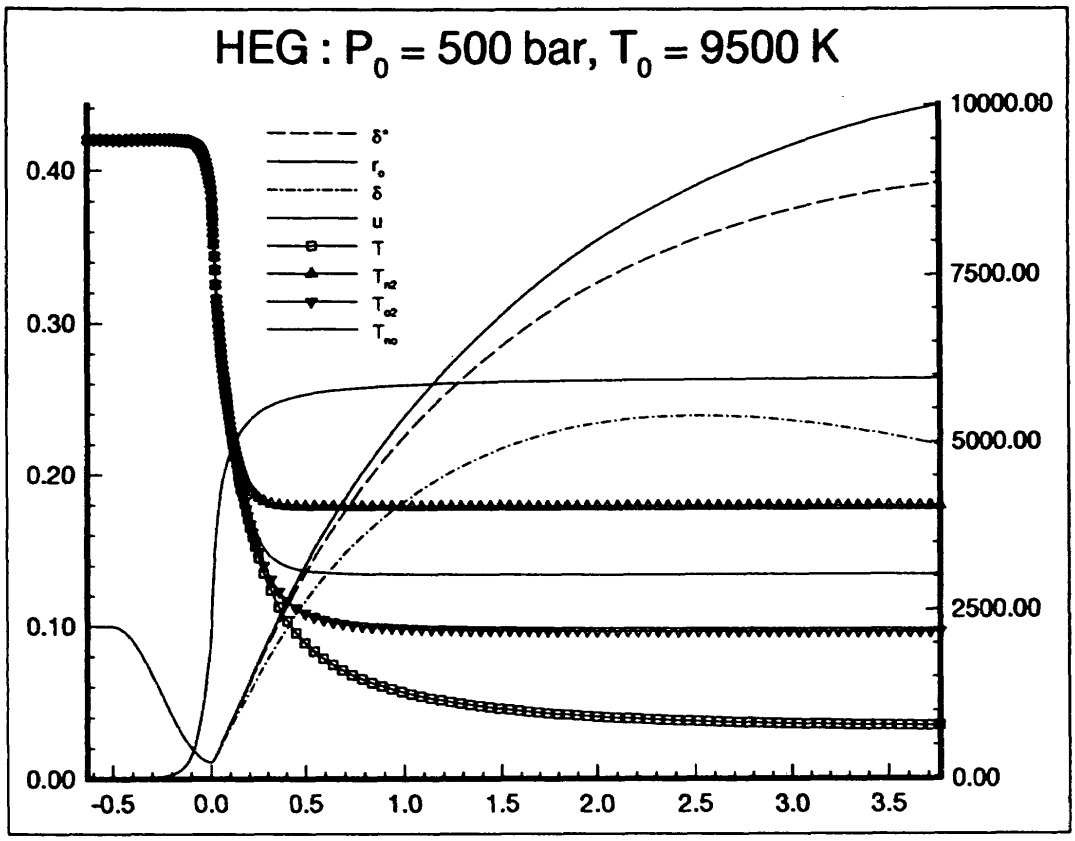

Figure 7: HEG wall boundary layer and center line temperatures as computed with LORE1D

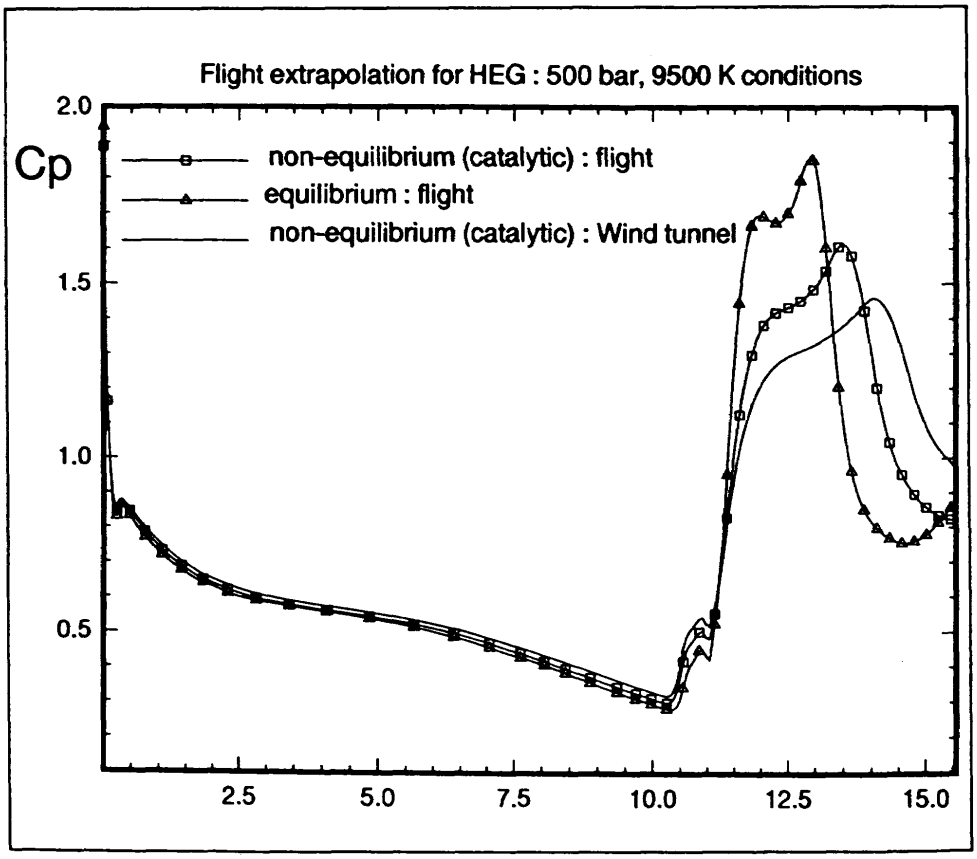

Figure 8: Cp distribution on hyperbolid flare: comparison between wind tunnel and flight

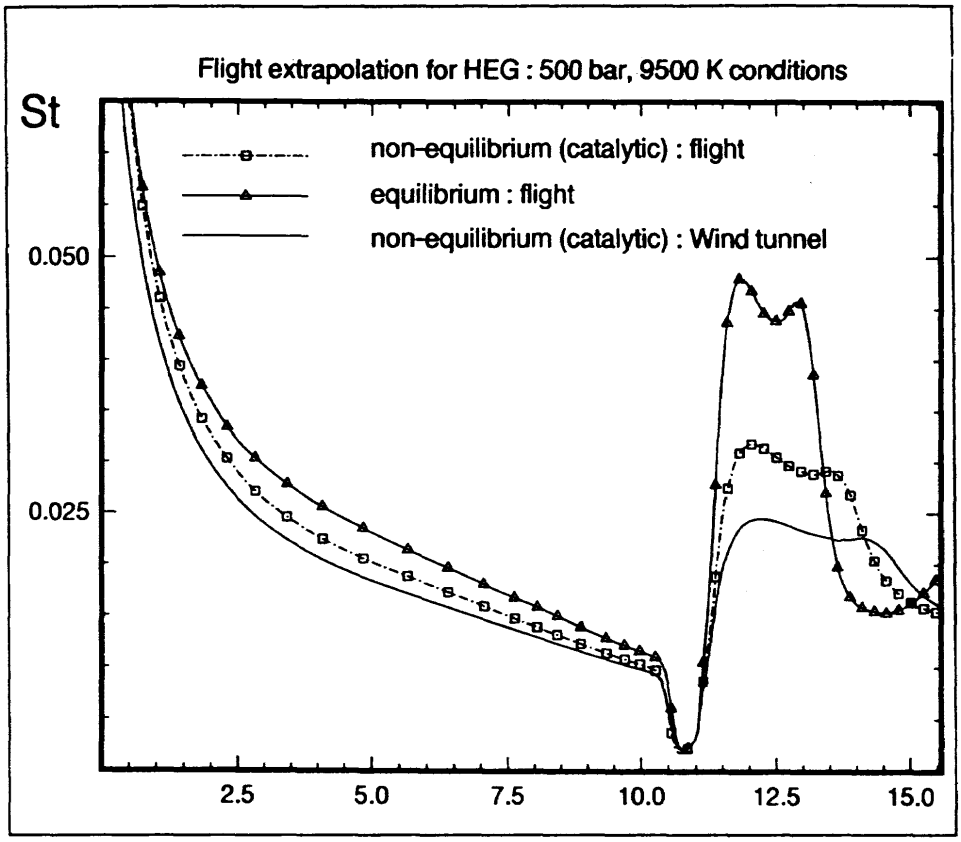

Figure 9: St distribution on hyperbolid flare: comparison between wind tunnel and flight

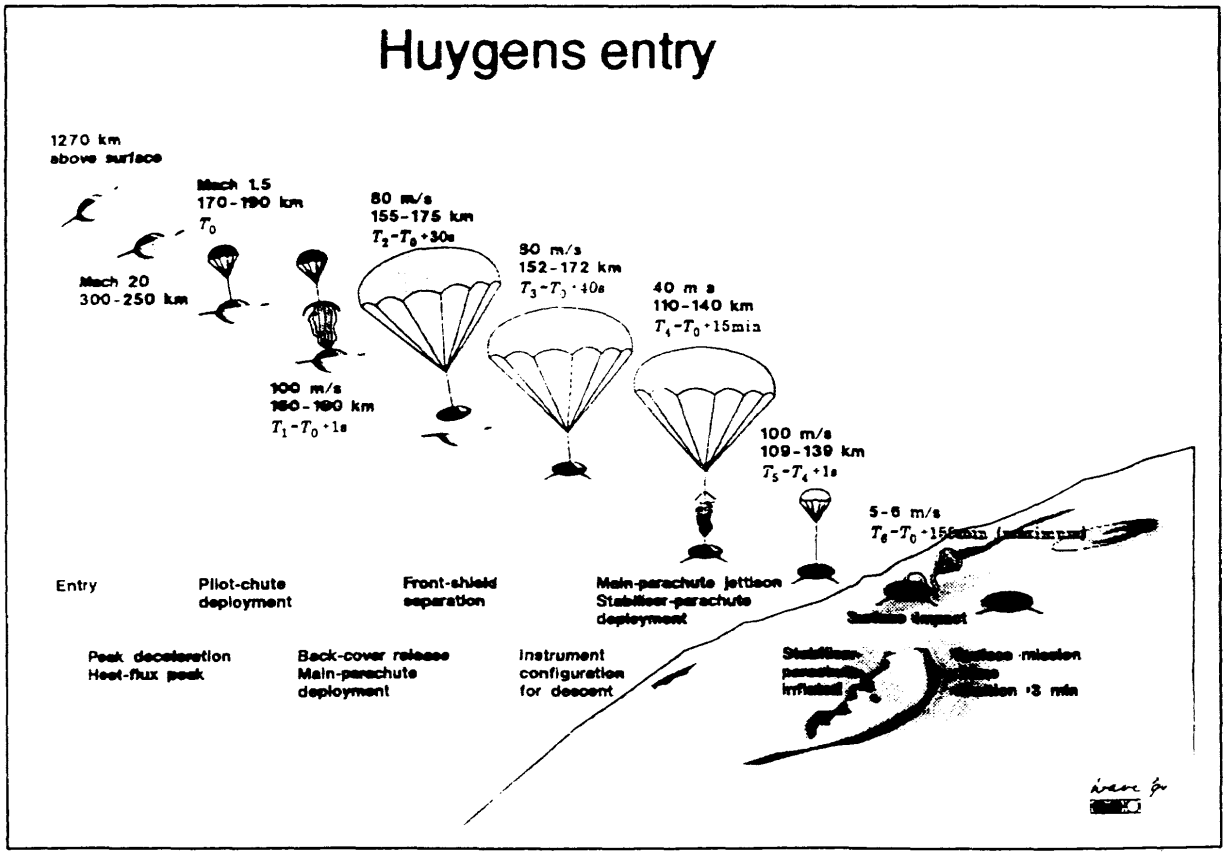

Figure 10: Huygens entry descent scenario

Ⅱ－2　特別講演資料

esa

EQUIPE ESA / CNES M S T P TEAM

Hypersonic Flow Phenomena

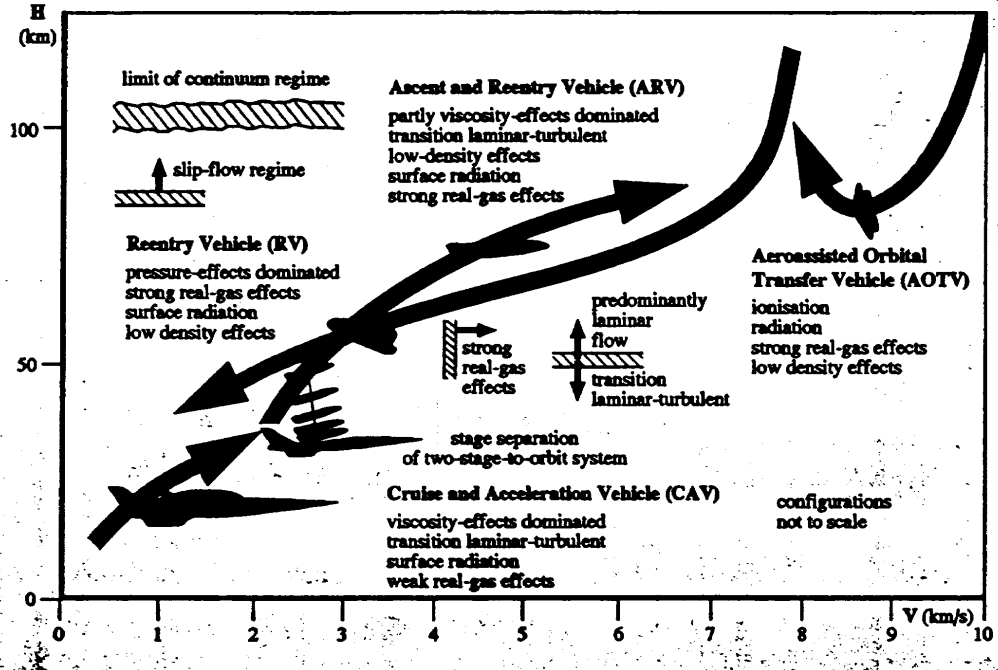

Directorate of Manned Spaceflight and Microgravity

October 6, 1994

Space Shuttle Orbiter

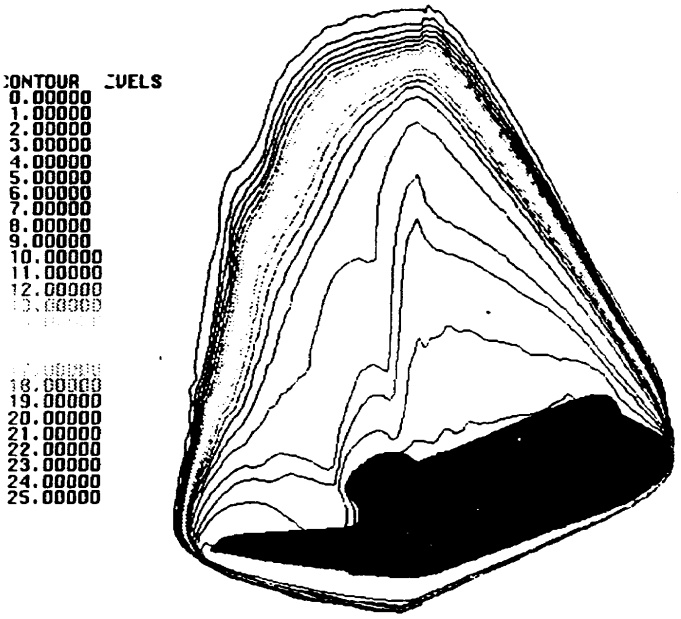

STS1 pitching moment discrepancy

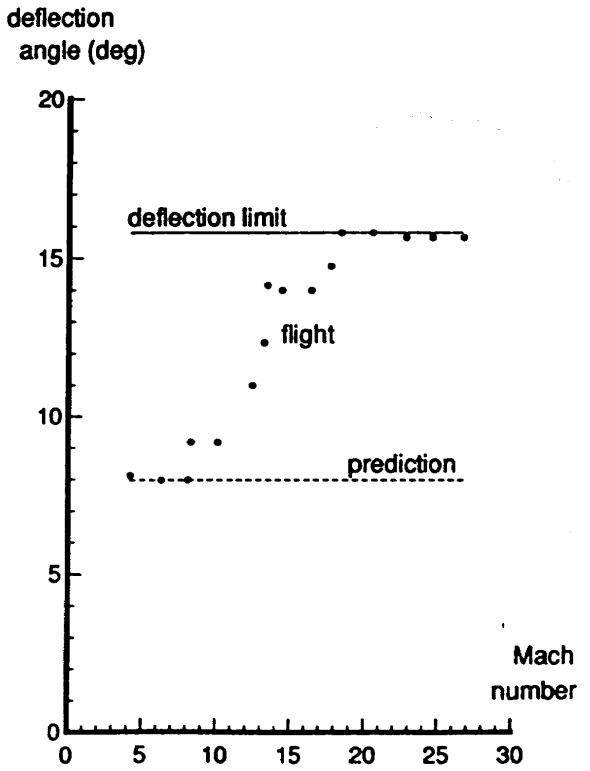

CIS BURAN

trim deflection angle discrepancy

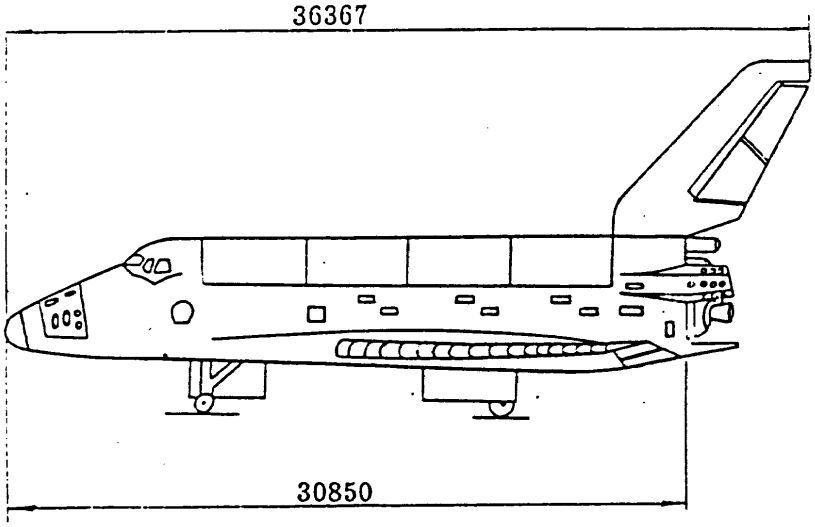

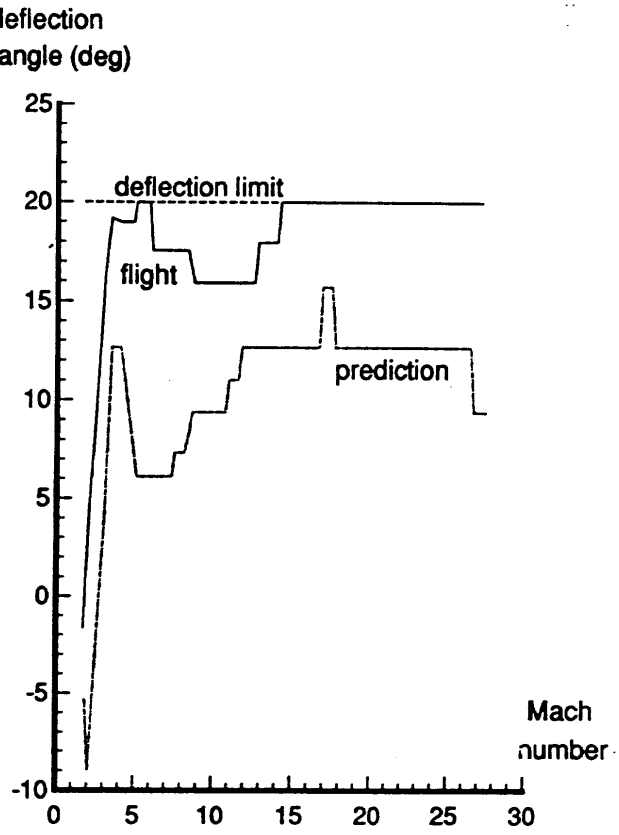

esa european space agency agence spatiale européenne

EQUIPE ESA / CNES M S T P TEAM

Hypersonic test facility caracteristics

BLOW-DOWN FACILITY S4	ONERA	FRANCE	AIR	6, 10, 12	0.7, 1.0	15	1100 (1500)	30 - 100
LONGSHOT FACILITY	VKI	BELGIUM	N2, (CO2)	14, 20	0.43, 0.60	400	2500	0.005 - 0.01
SHOCK TUNNEL TH2	RWTH AACHEN	GERMANY	AIR, N2	7, 6 - 12	0.6, 1.1, 2.0	63	4700	0.002 - 0.009
HIGH ENTHALPY FACILITY HEG	DLR	GERMANY	AIR, N2	7	0.8	180	10000	0.001
HOT SHOT FACILITY F4	ONERA	FRANCE	AIR, N2	9 -18	0.43, 0.67, 0.93	200	5500	0.02 - 0.1

Trim Cm Error in Past Experience

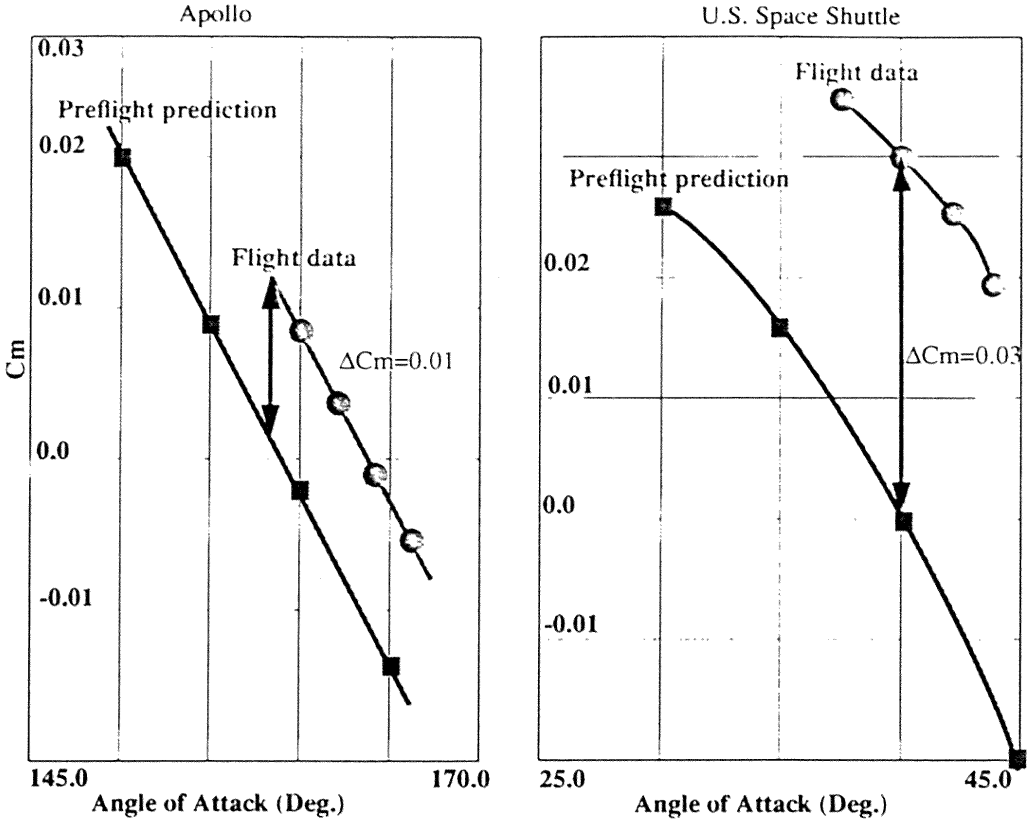

ESA/ESTEC

Ref.: NASA-S-85-02304

Propulsion and Aerothermodynamics Division

Second European Symposium on Aerothyermodynics for Space Vehicles

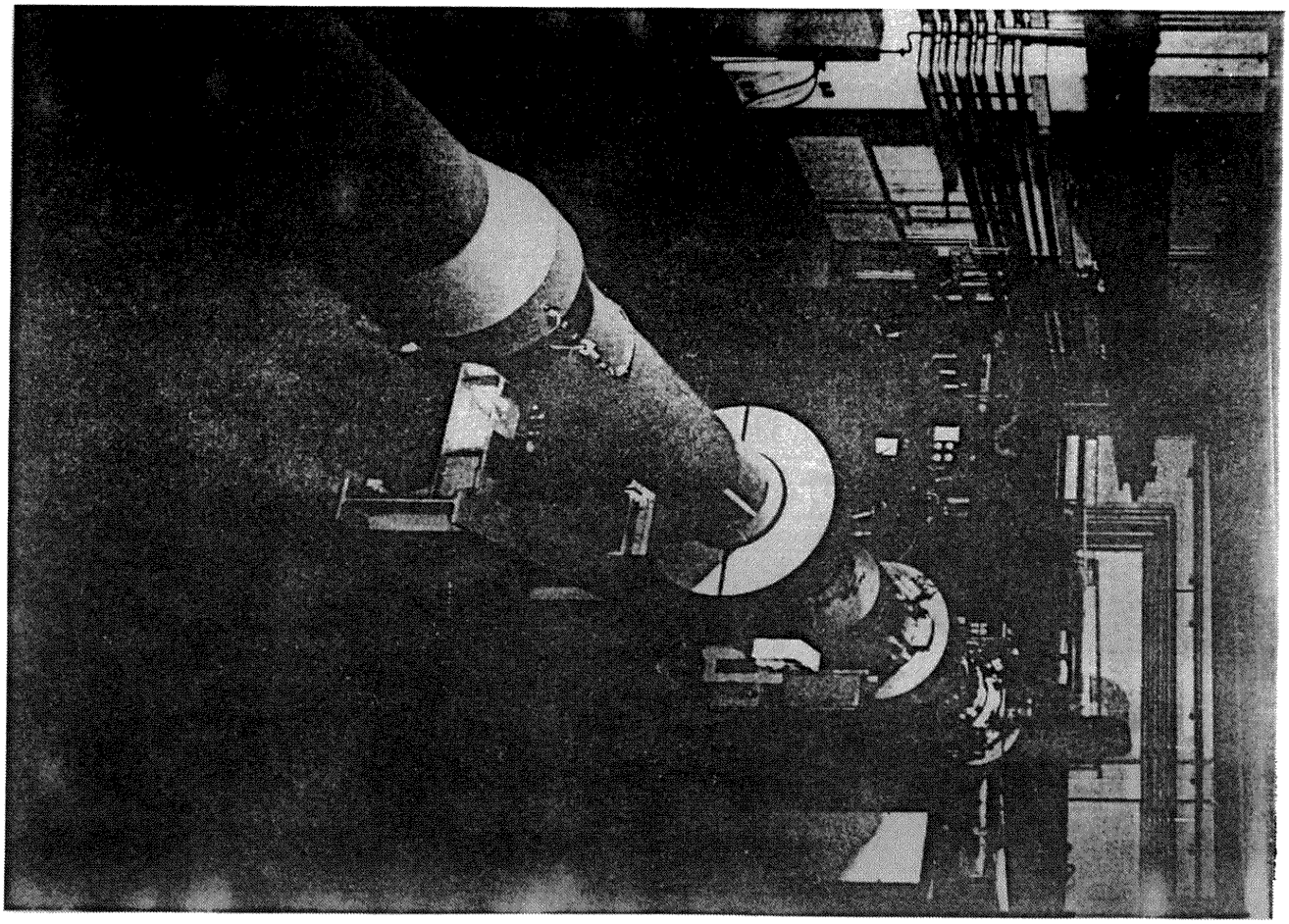

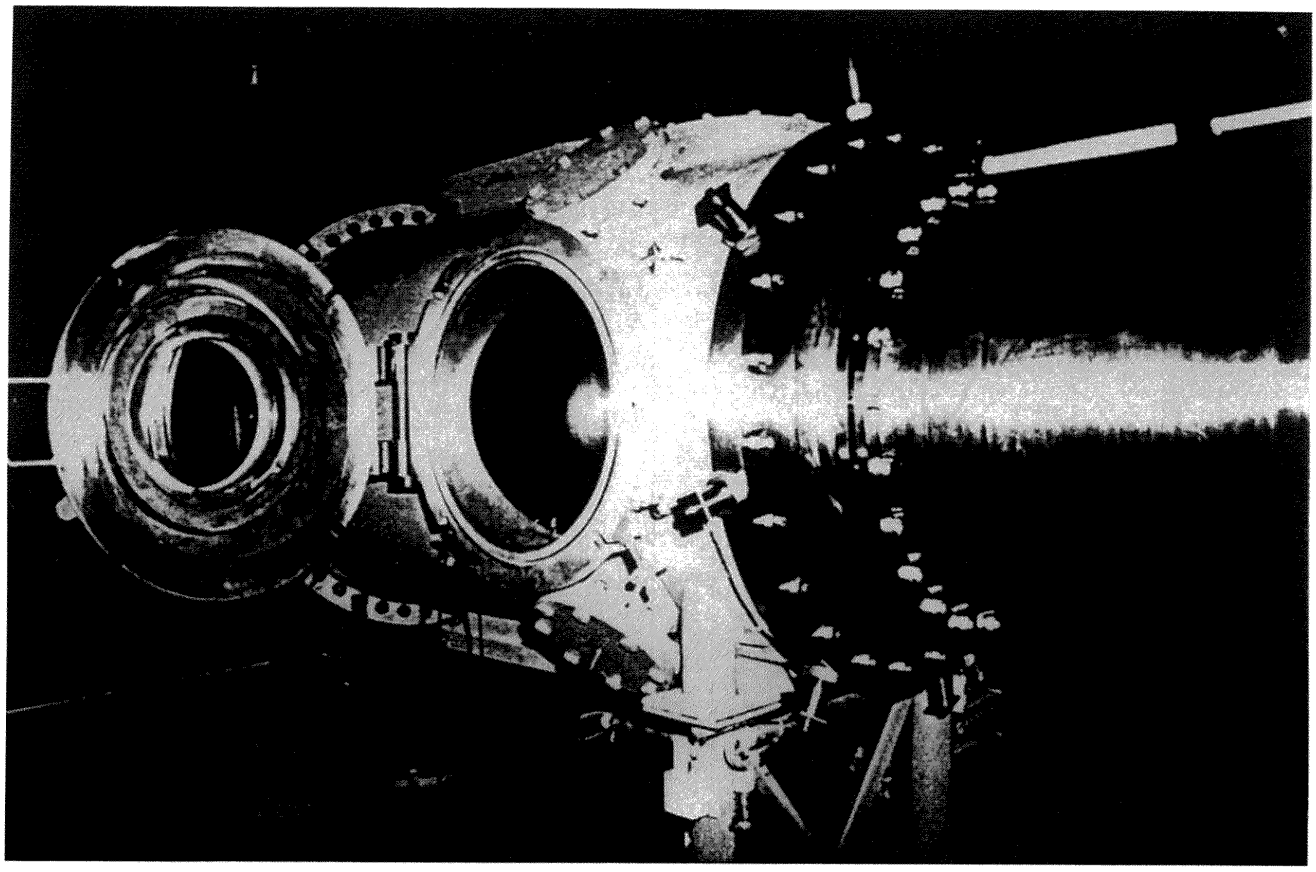

esa european space agency agence spatiale europeenne

EQUIPE ESA / CNES M S T P TEAM

Hot Shot Facility F4

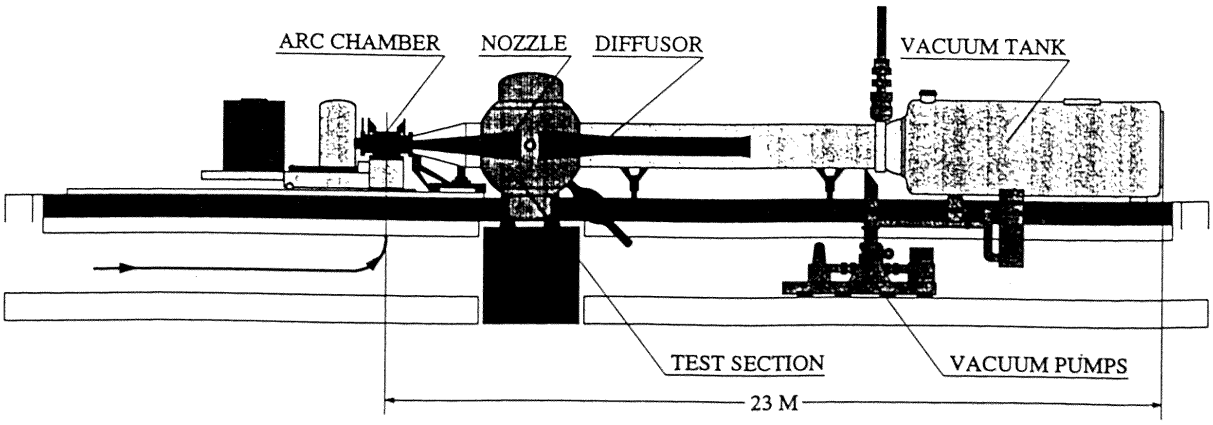

Directorate of Manned Spaceflight and Microgravity

October 6, 1994

esa european space agency agence spatiale europeenne

EQUIPE ESA / CNES M S T P TEAM

Binary Scaling performance

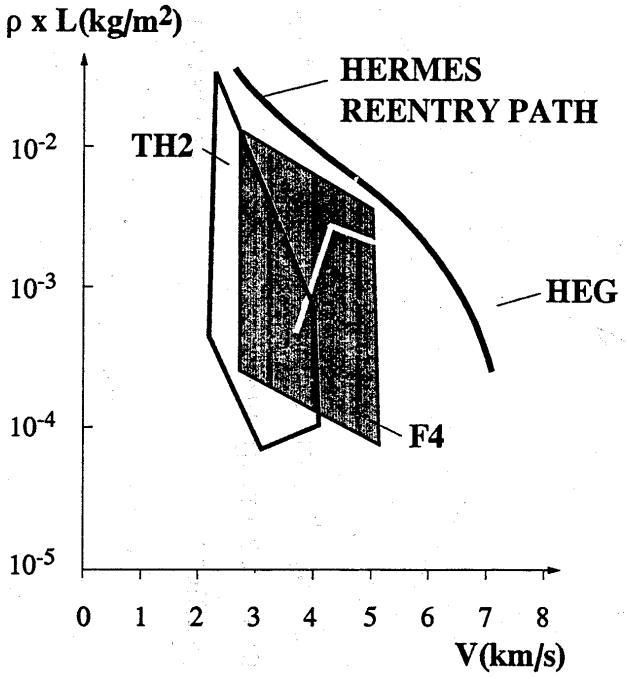

Directorate of Manned Spaceflight and Microgravity

October 6, 1994

esa european space agency agence spatiale europeenne

EQUIPE ESA / CNES M S T P TEAM

Performances Envelopes

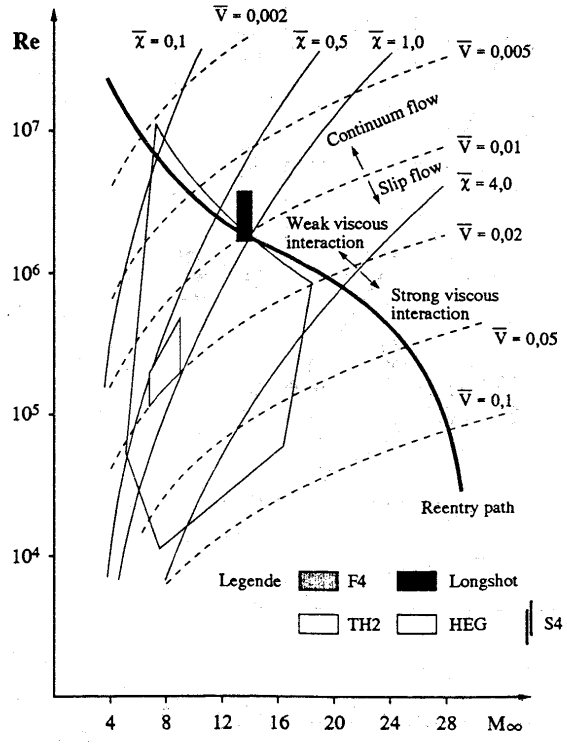

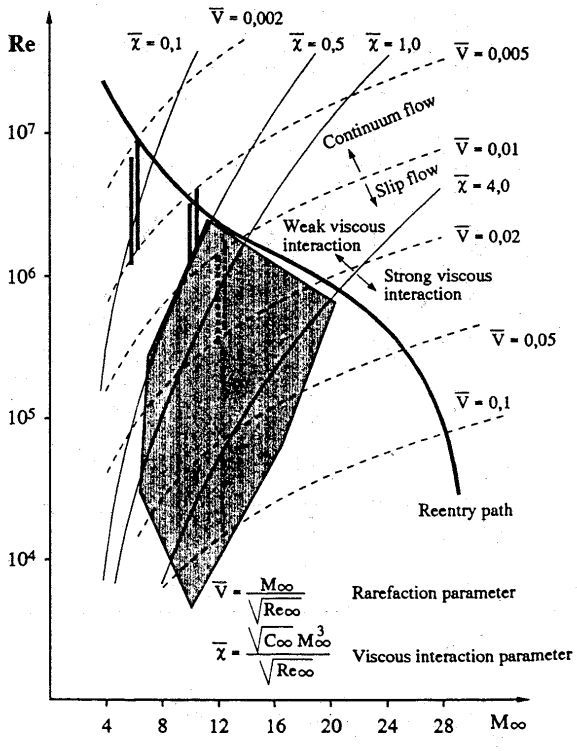

Directorate of Manned Spaceflight and Microgravity

October 6, 1994

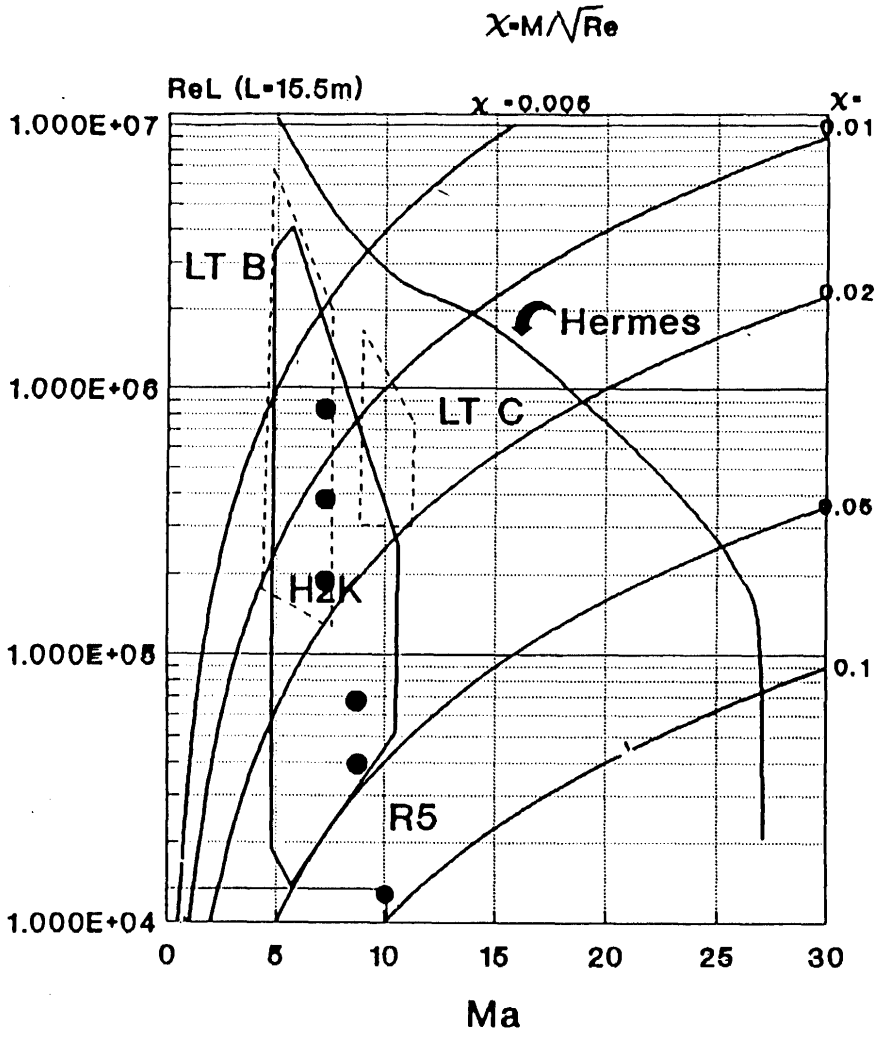

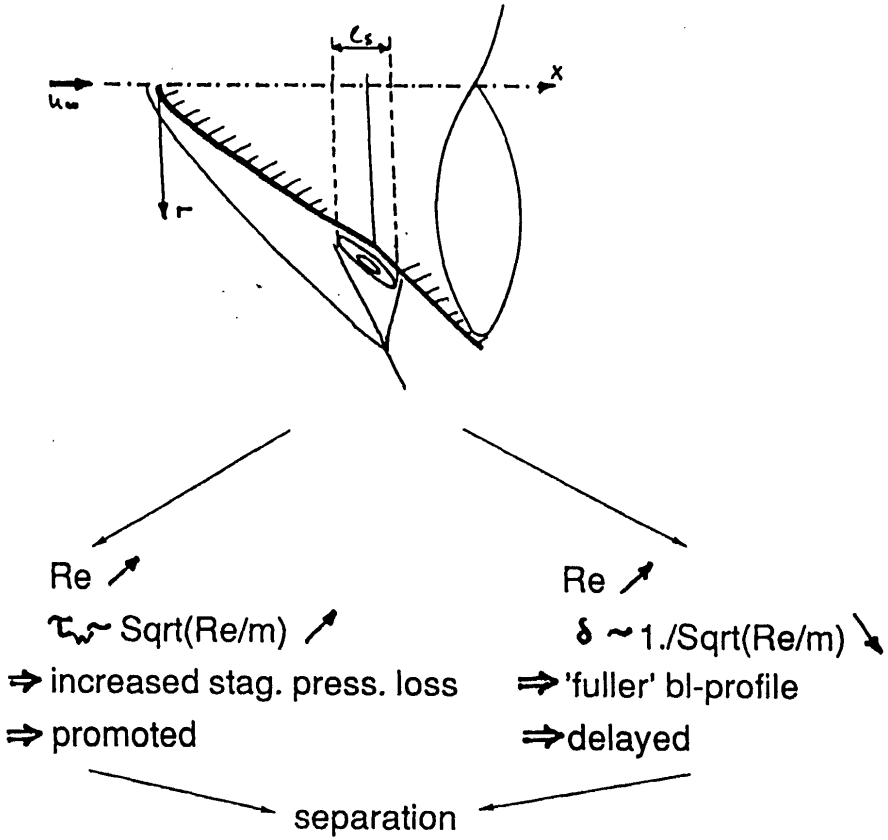

Influence of the viscous interaction parameter on the separation length:

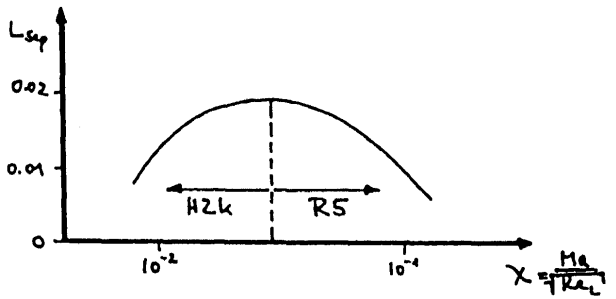

Hyperboloid-flare: Experiments & Computations

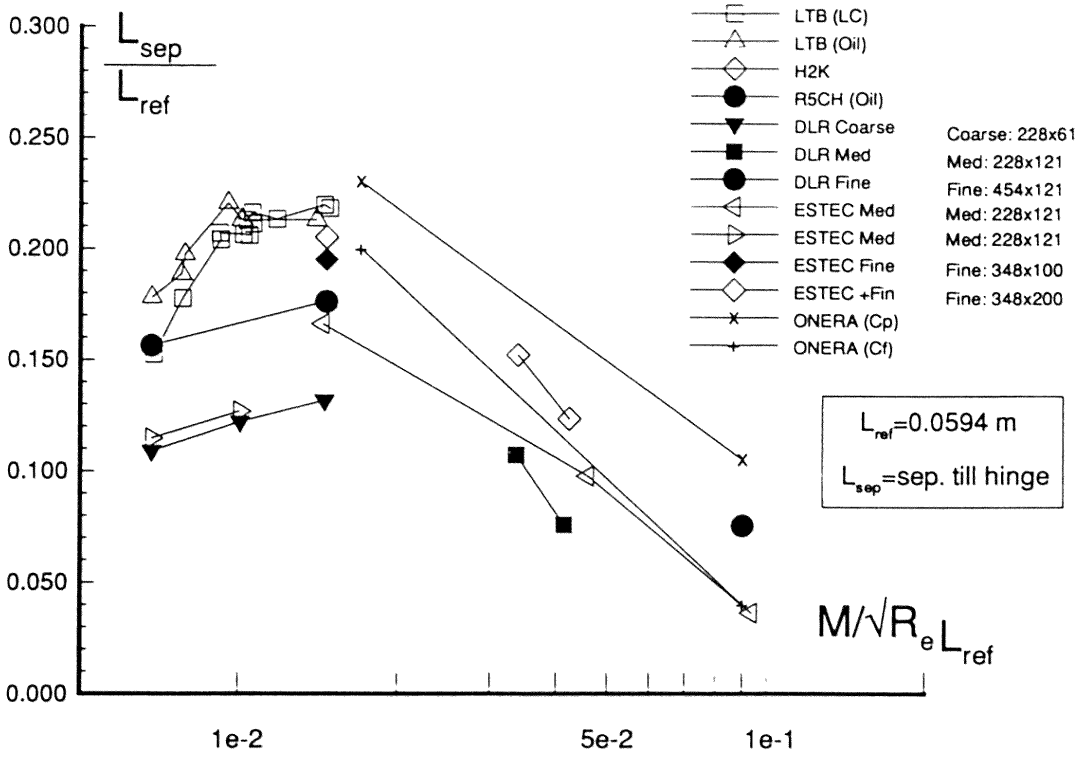

Representative Flow Models

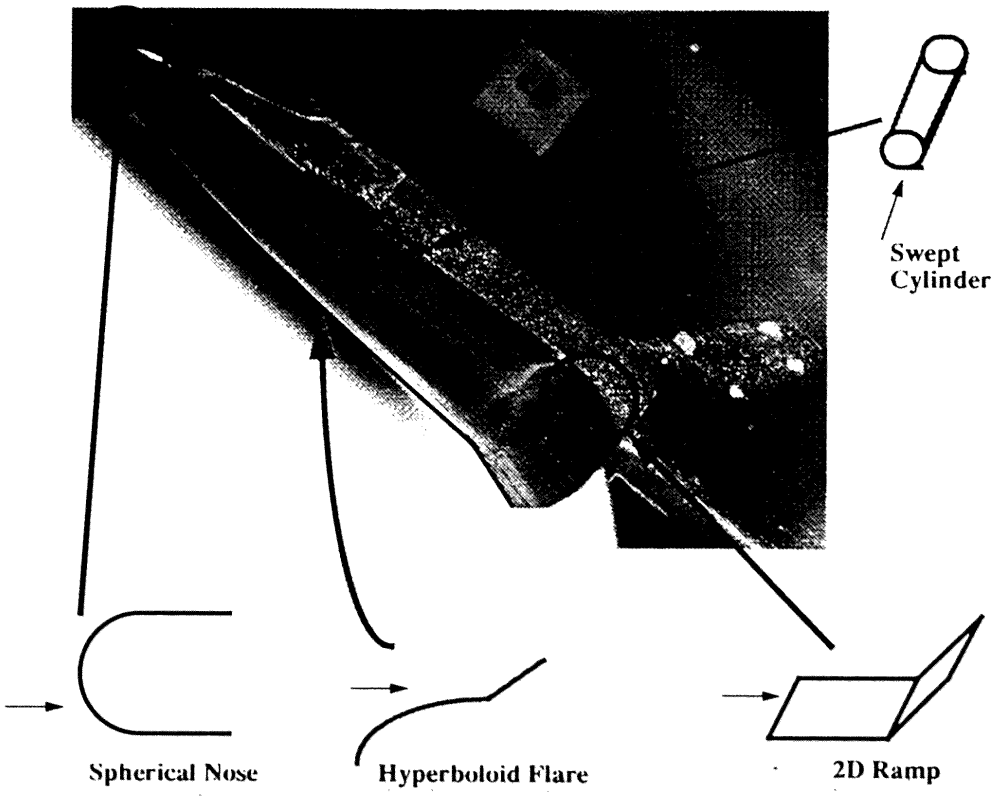

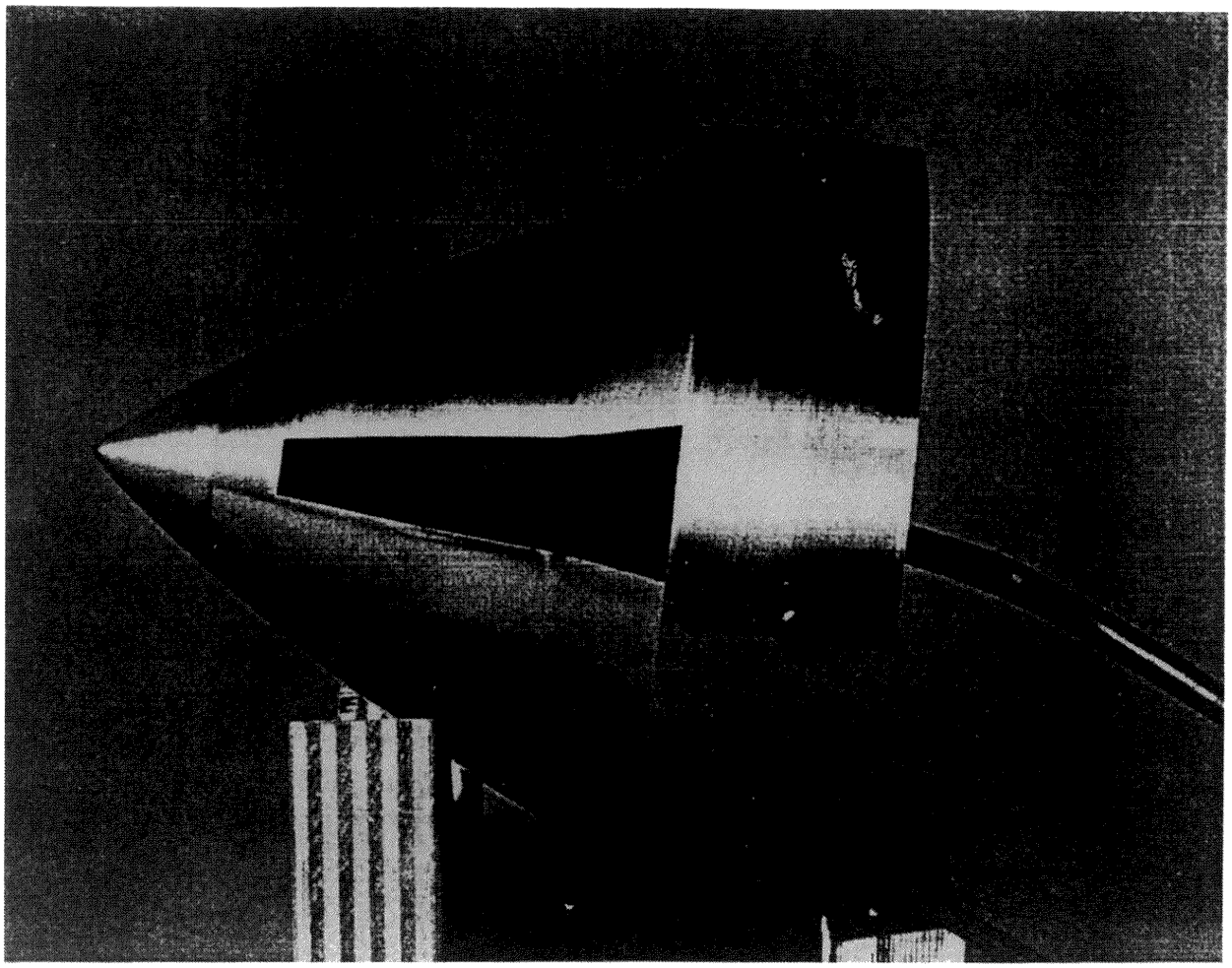

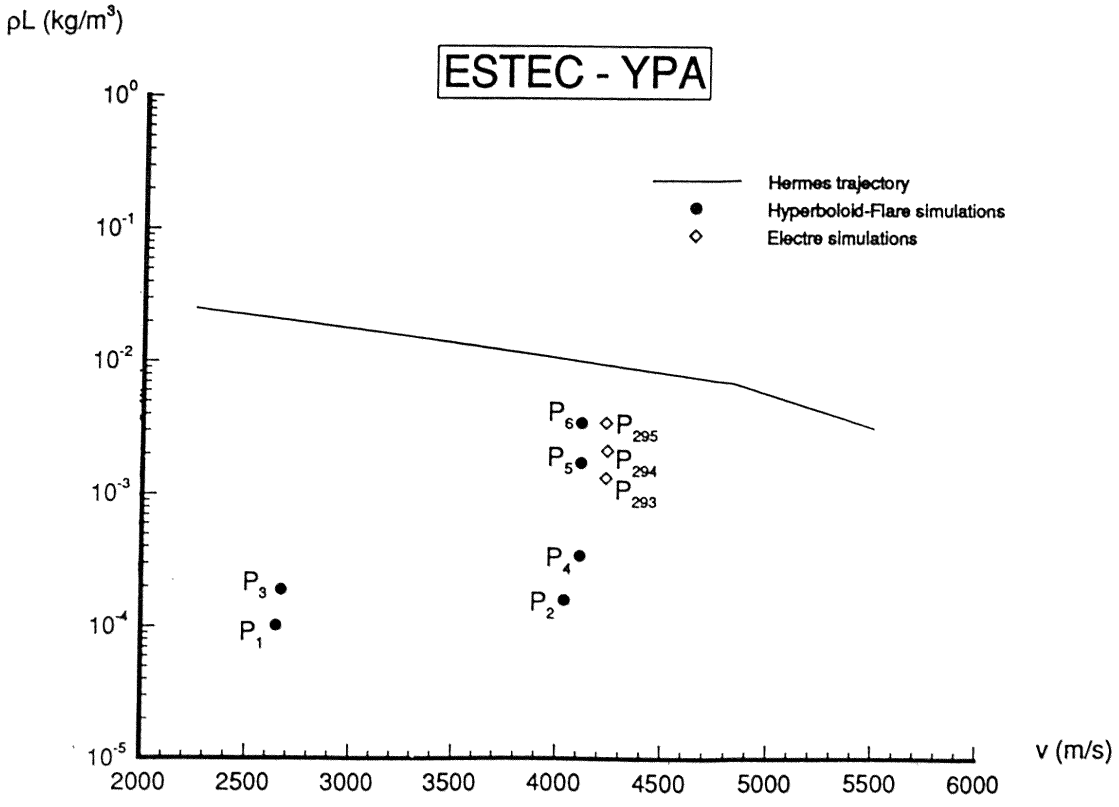

fig 4.17

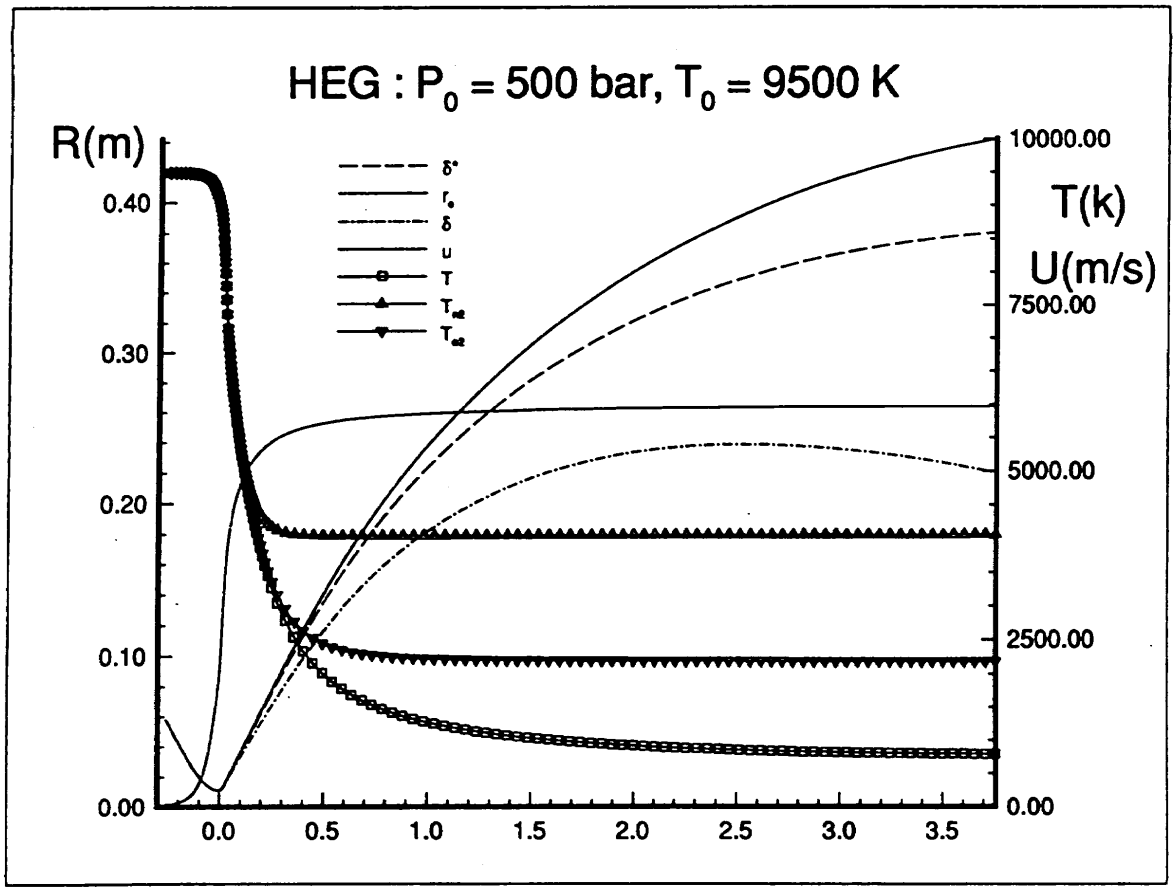

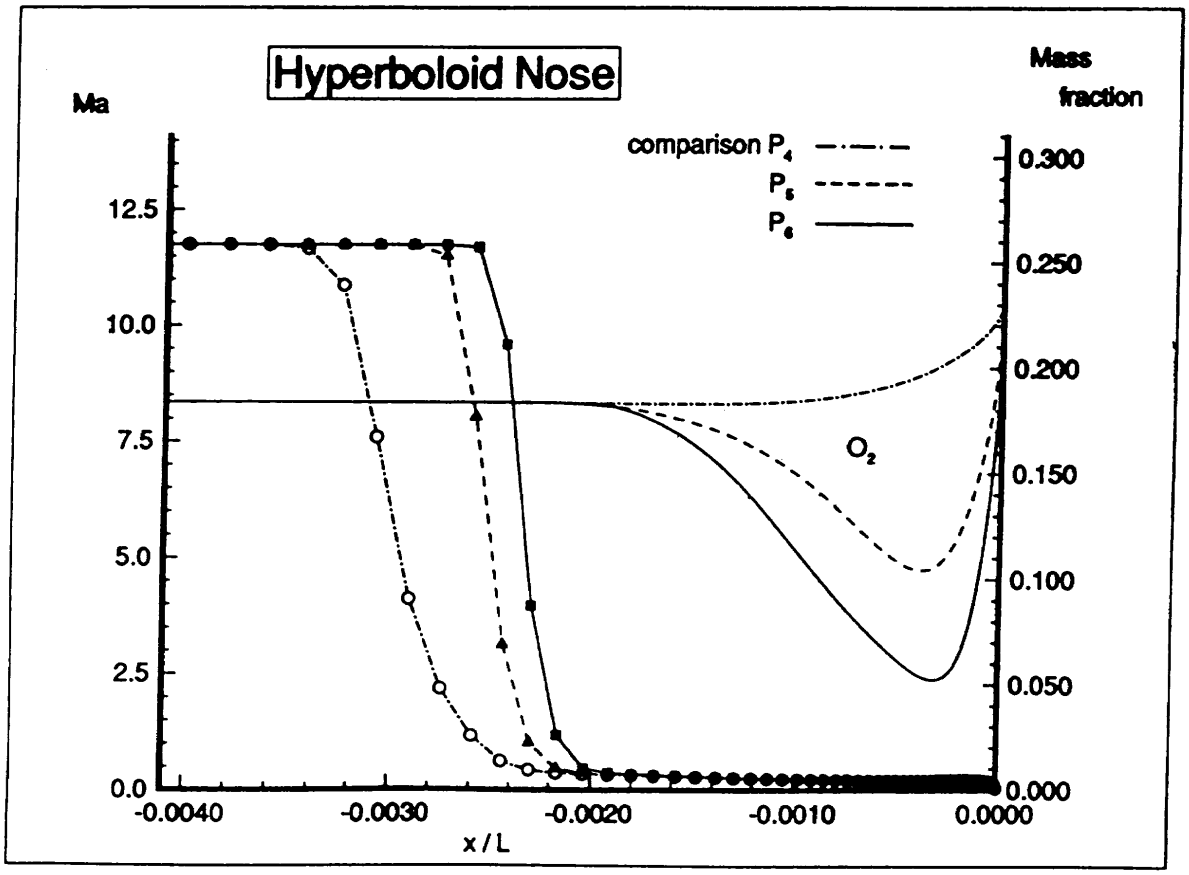

fig 4.20

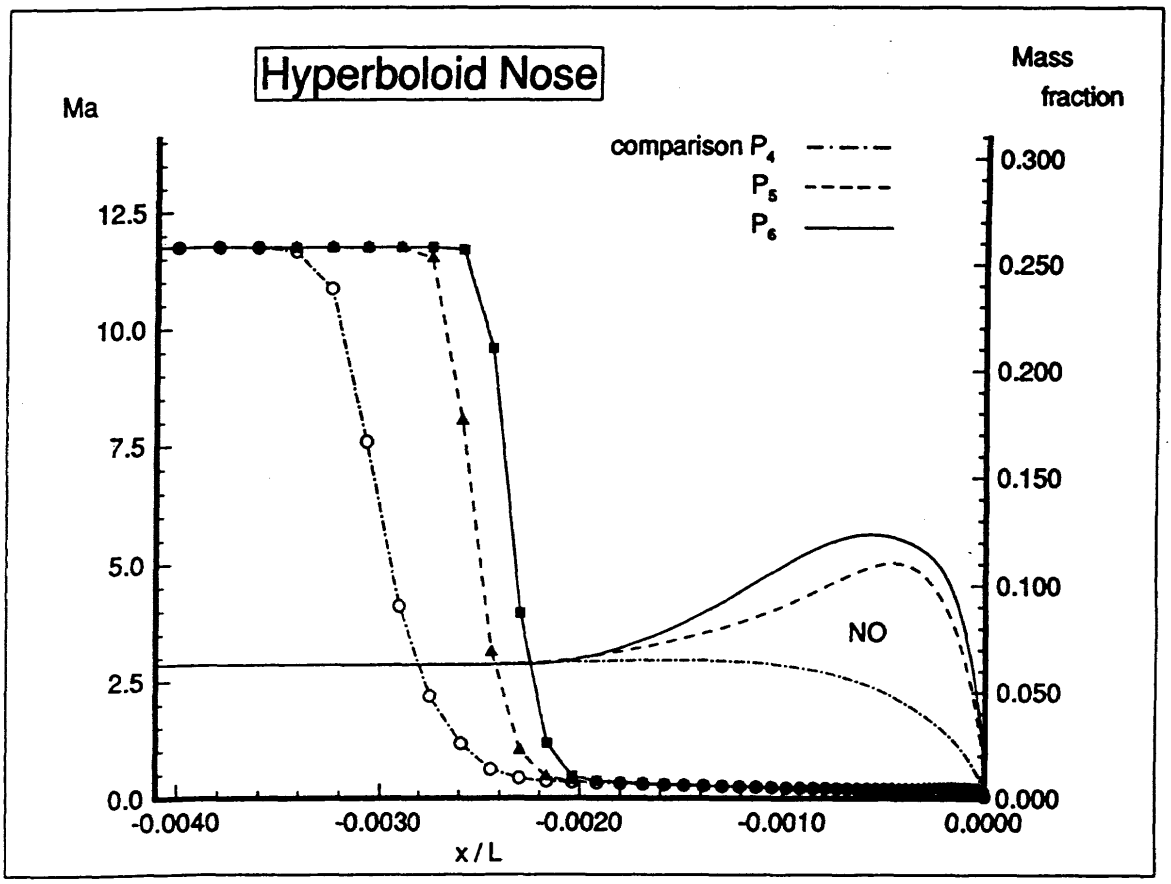

fig 4.22

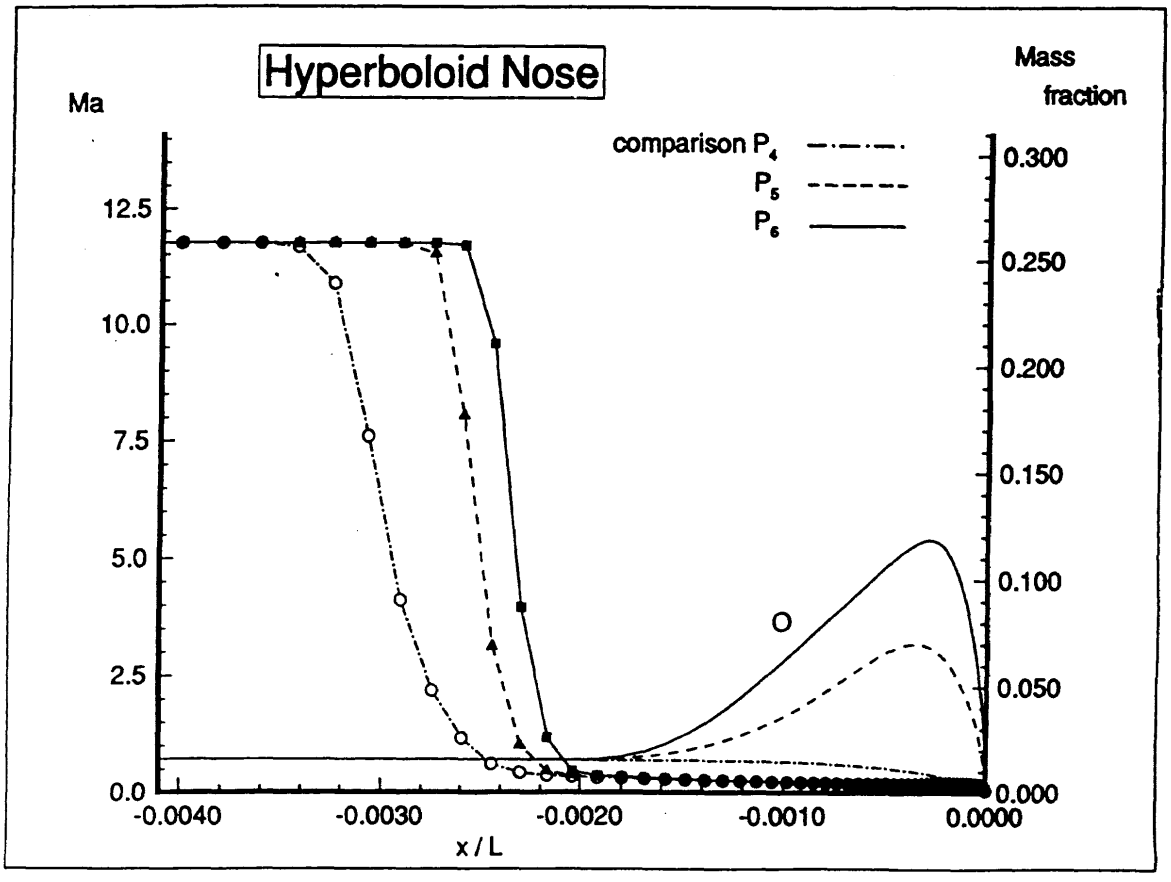

fig 4.21

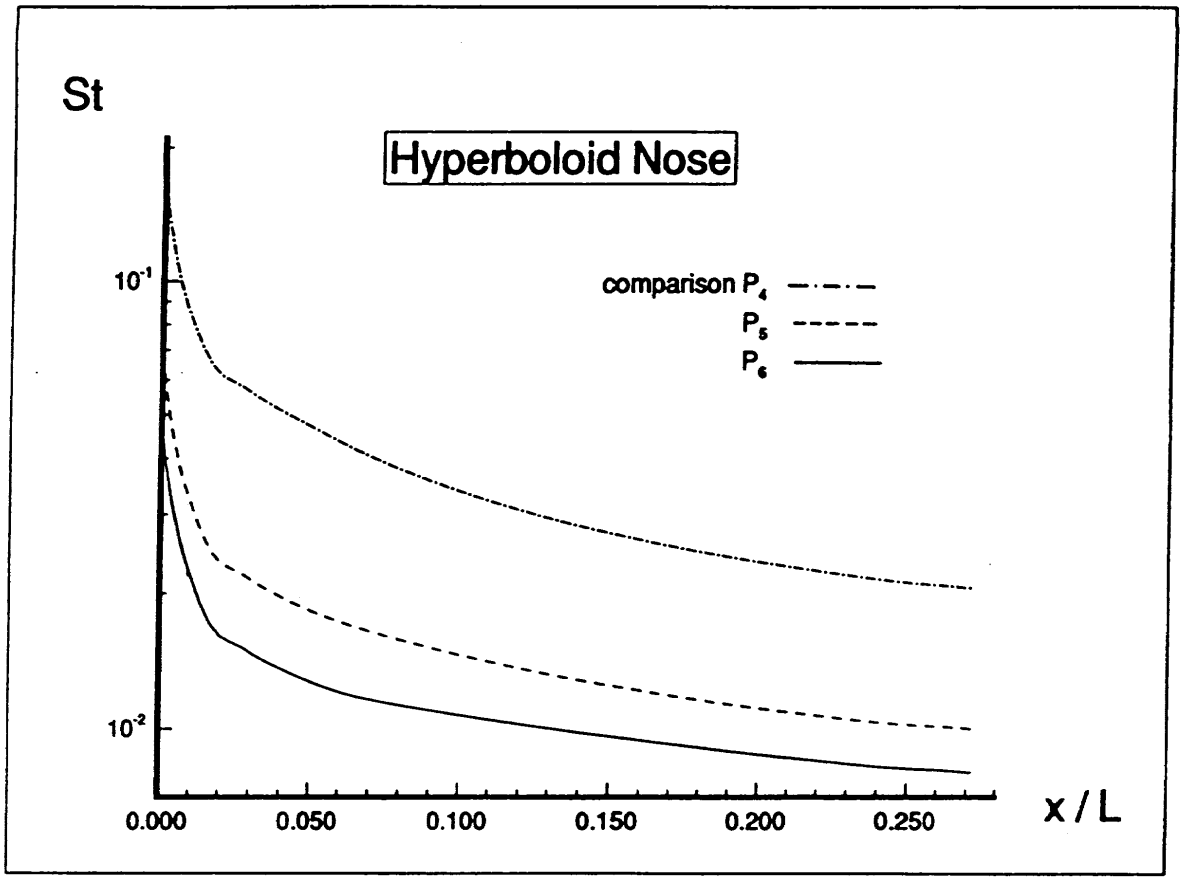

fig 4.23

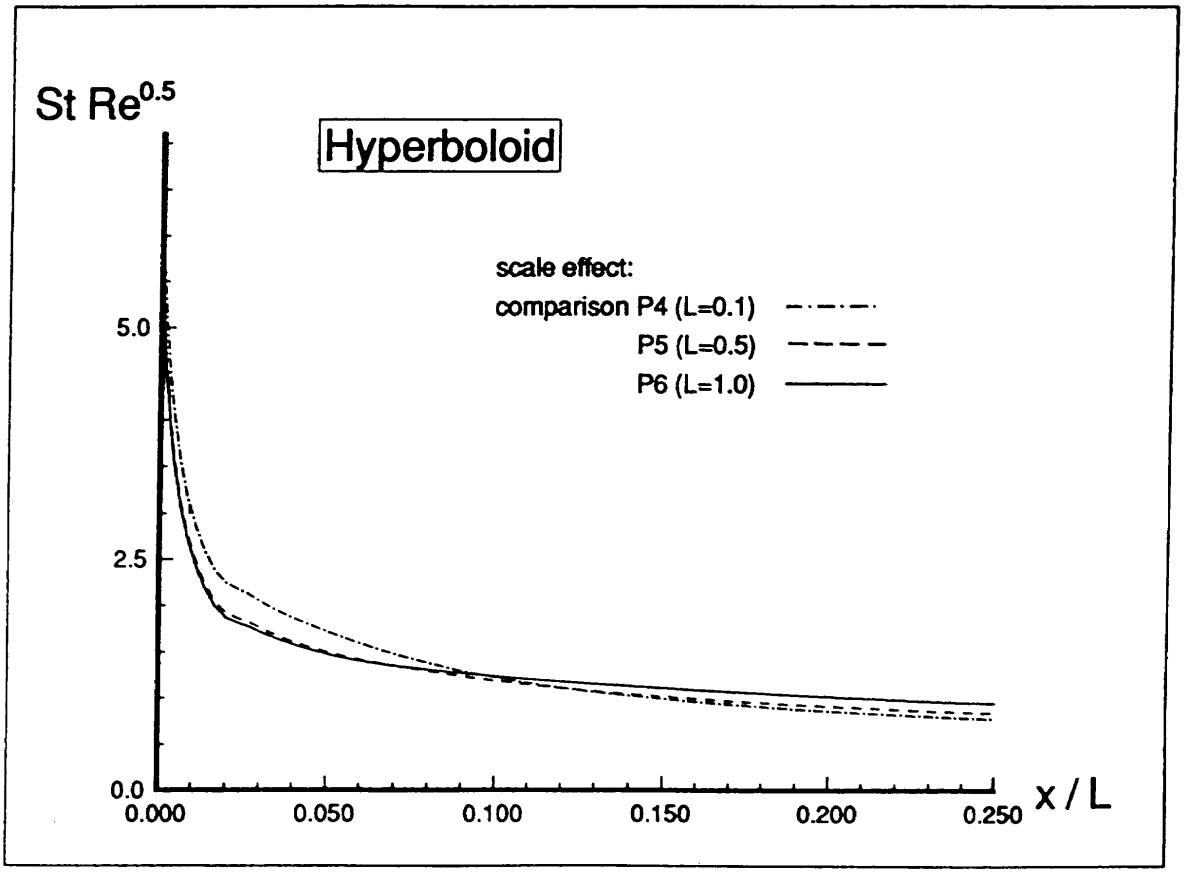

fig 4.24

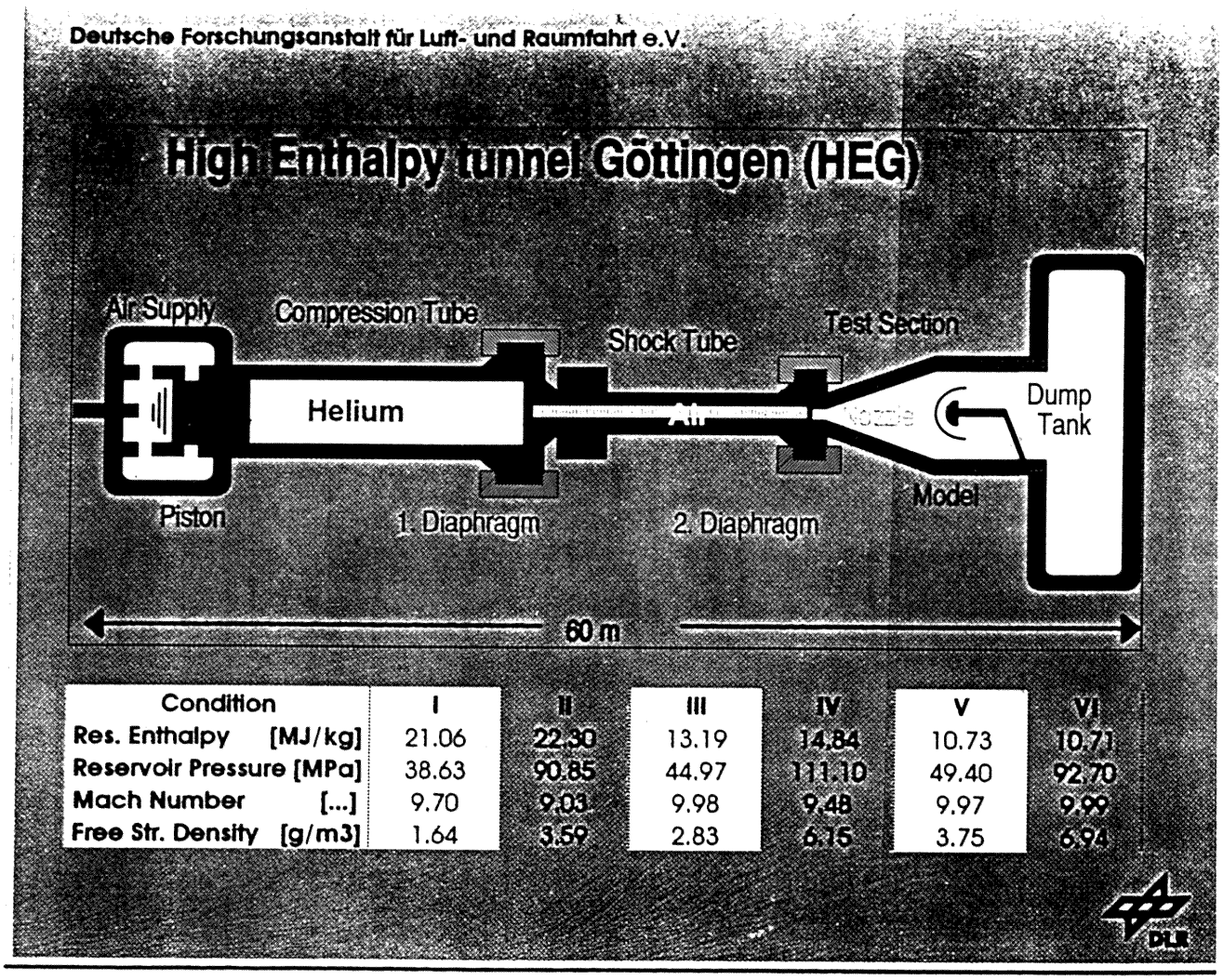

HEG exit conditions thermal/chemical nonequilibrium

		CONDITION 1		CONDITION 4
			thermal equil.	
$P_0(bar)$	=	386.3		1111.0
$H_{tot}(\frac{MJ}{kg})$	=	21.		14.8
U (m/s)	=	5576.7	5682.37	4879.21
T_∞ (K)	=	510.00	747.0	485.86
Tv_∞ (K)	=	5401.29	747.0	3924.02
$\rho\ (kg/m^3)$	=	2.036e-3	1.929e-3	6.846e-3
C_{N_2}	=	.76108	0.76143	.73244
C_N	=	.00015	.00027	.00000
C_{O_2}	=	.00722	.005935	.10860
C_O	=	.21885	.220657	.08450
C_{NO}	=	.01270	.011708	.07446
T_w (K)	=	300.	300.	300

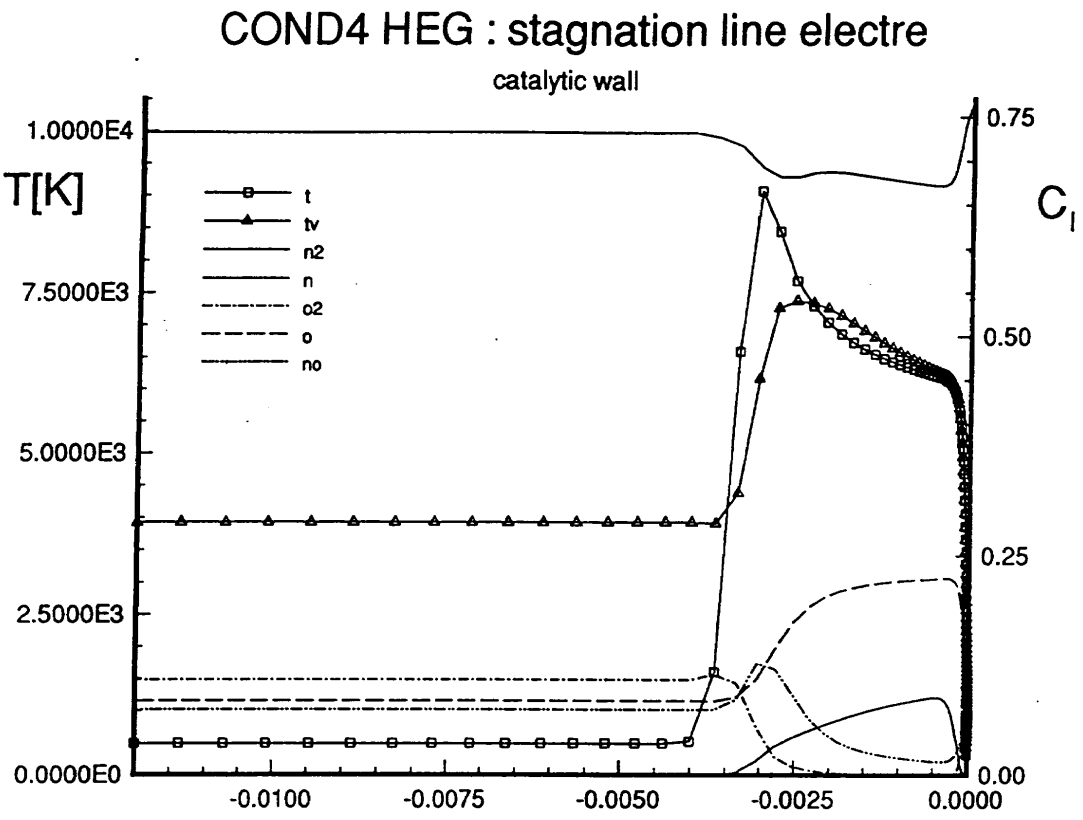

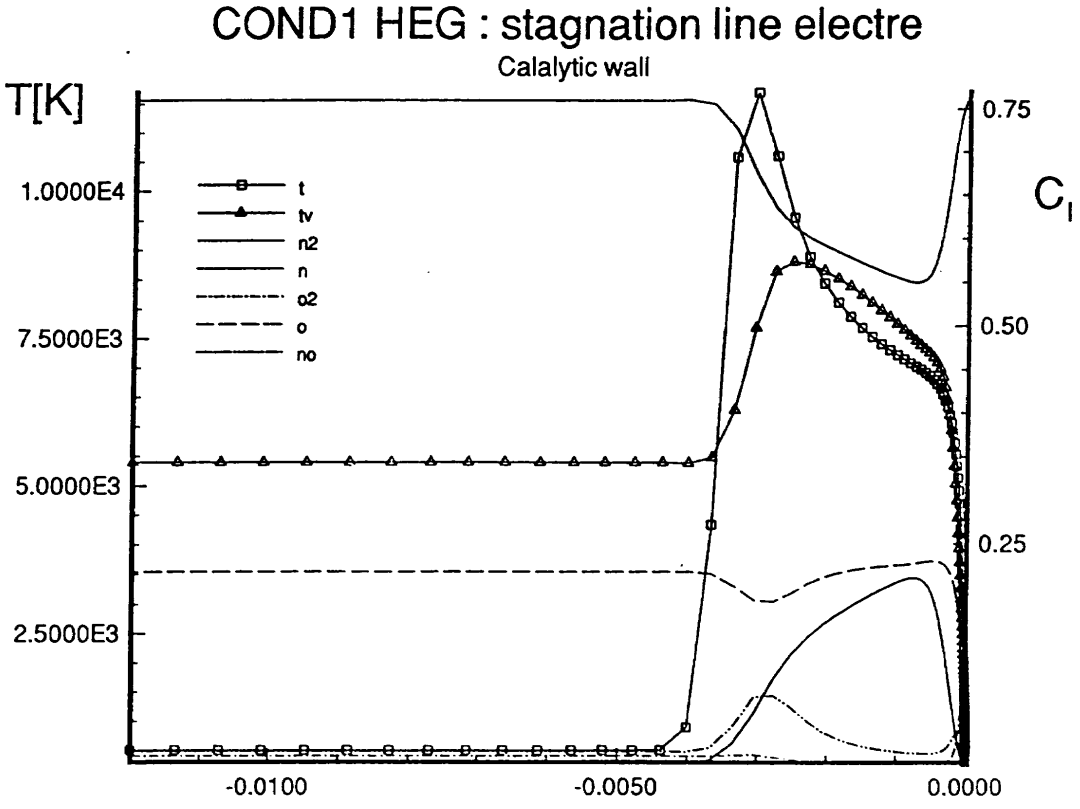

Deutsche Forschungsanstalt für Luft- und Raumfahrt e.V.

General Flow Features around a Blunt Body during Re-Entry

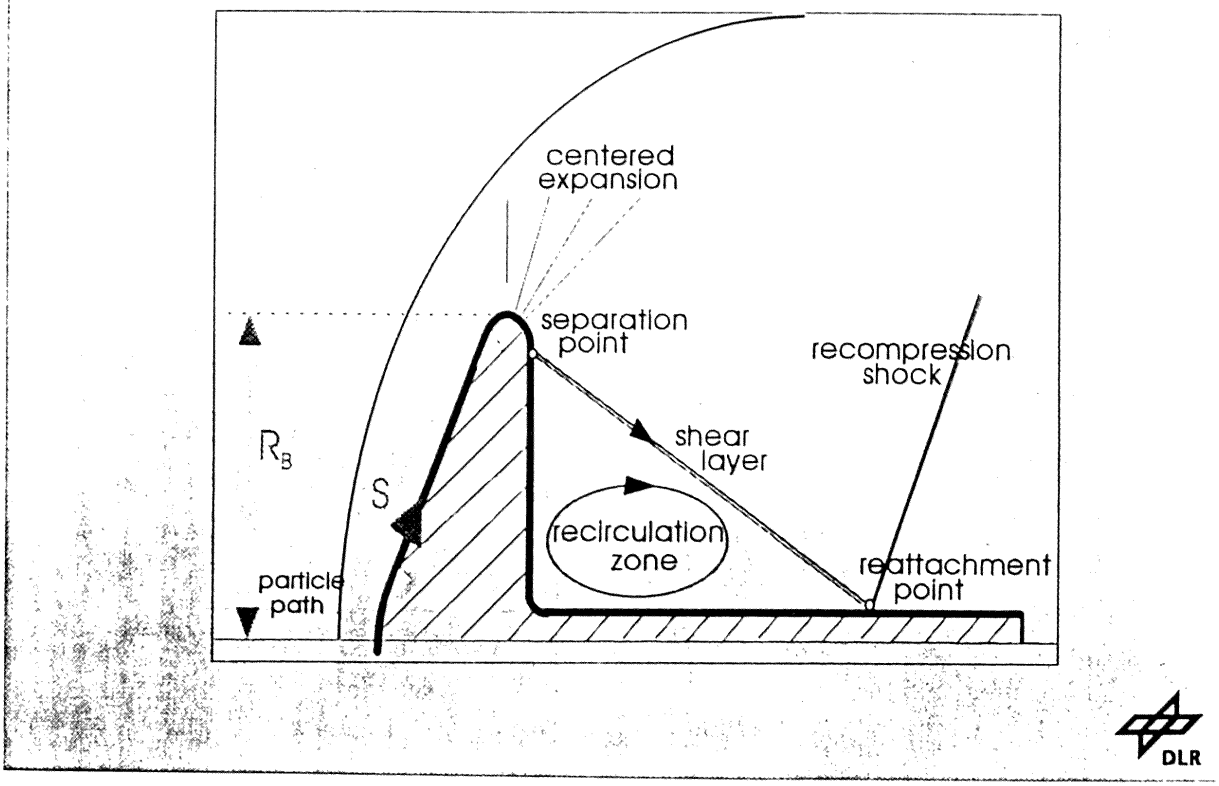

Deutsche Forschungsanstalt für Luft- und Raumfahrt e.V.

Flight Path of MESUR and OREX with HEG test points

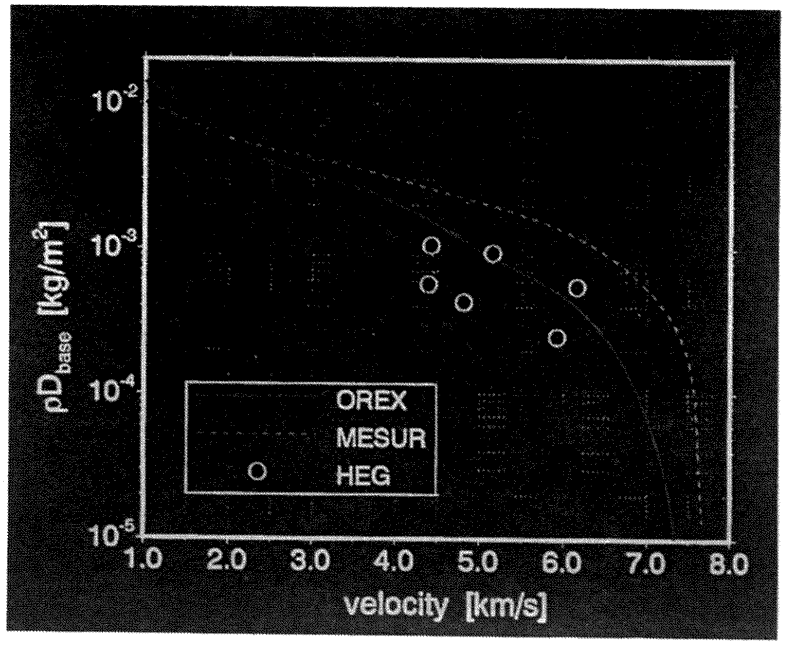

DLR

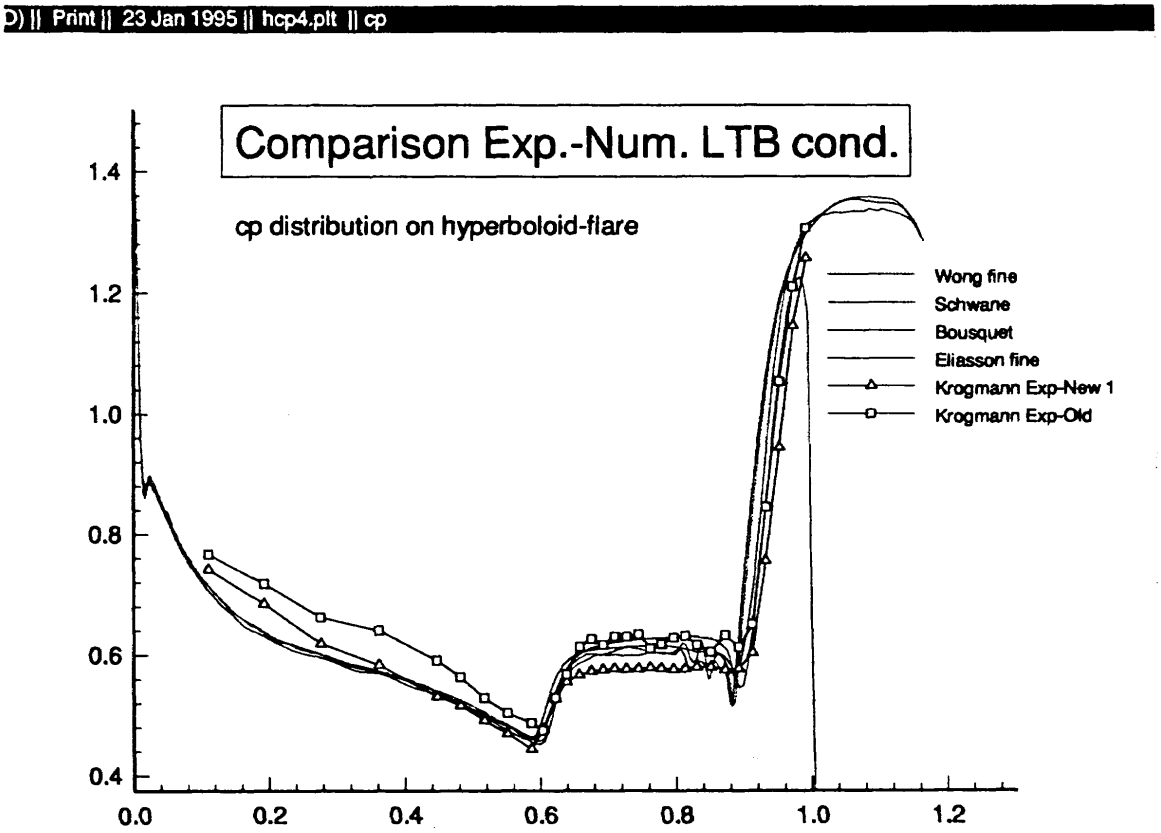

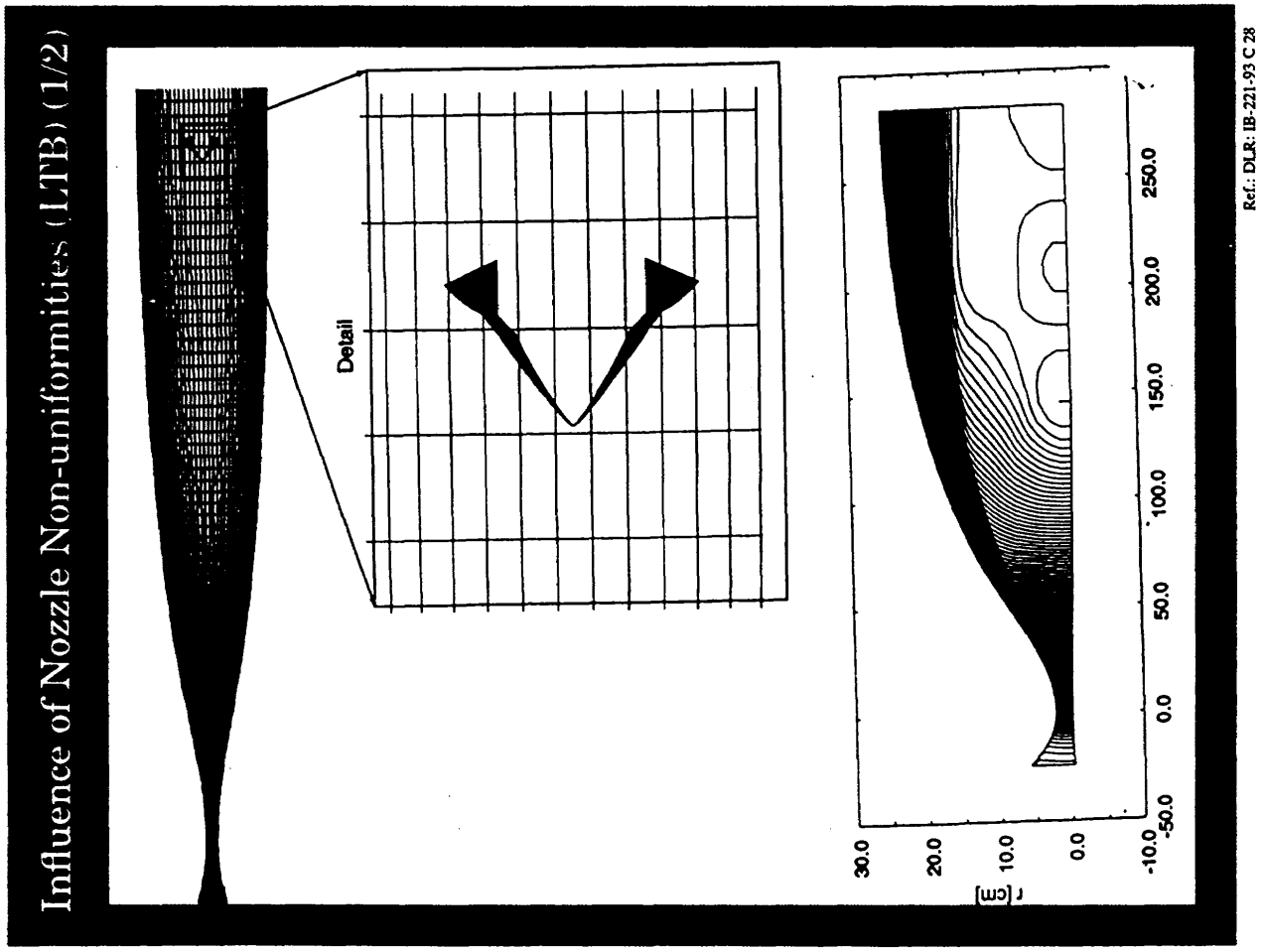

Influence of Nozzle Non-uniformities (LTB) (2/2)

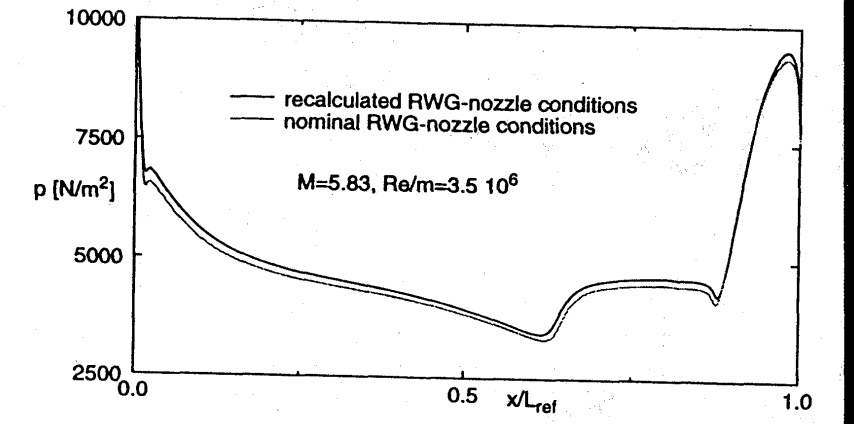

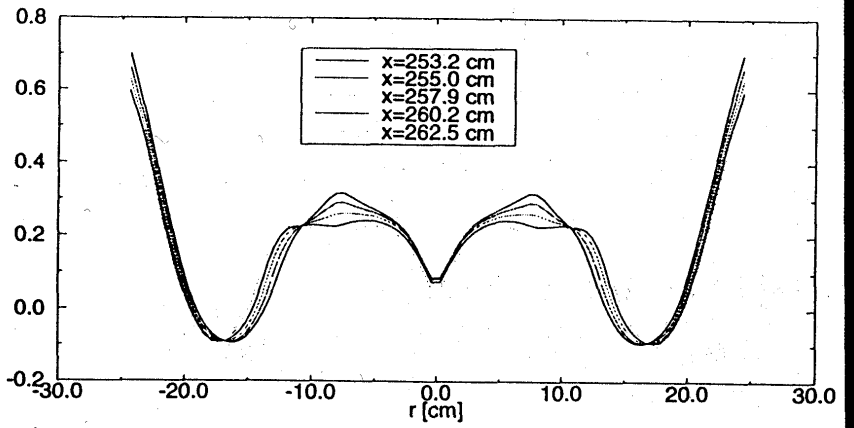

Ref.: DLR: IB-221-93 C 28

DASSAULT AVIATION

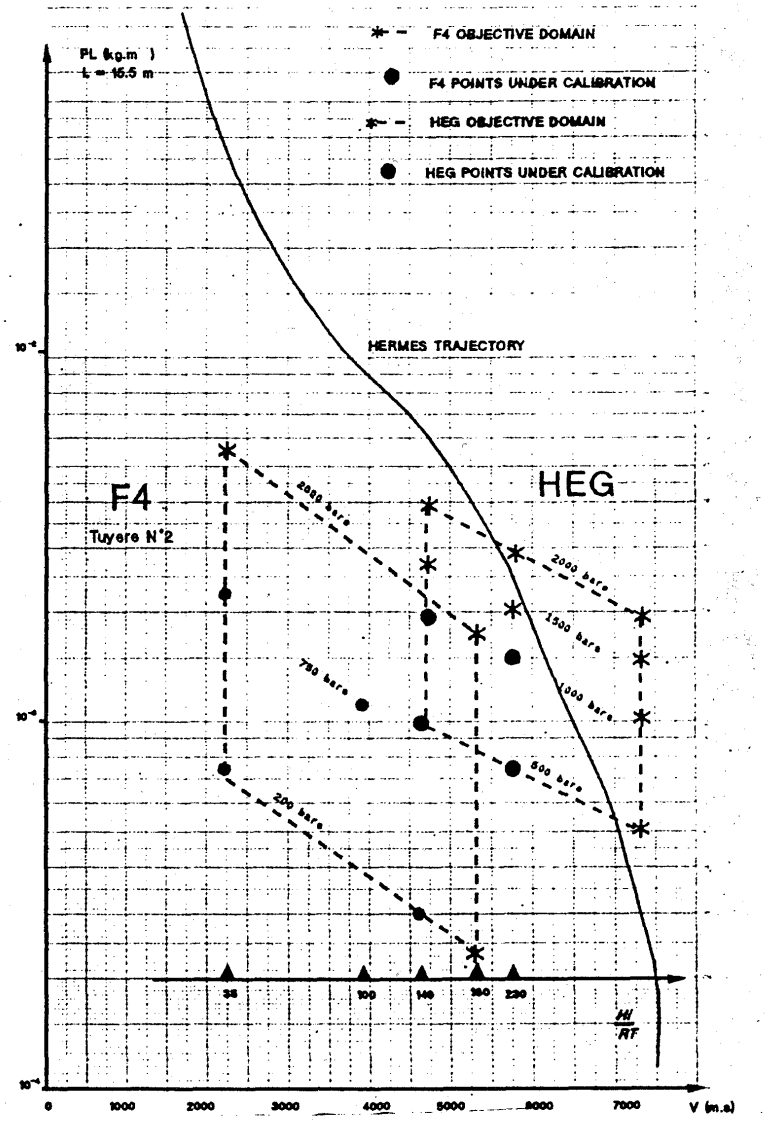

State of Calibration Work for F4 and HEG

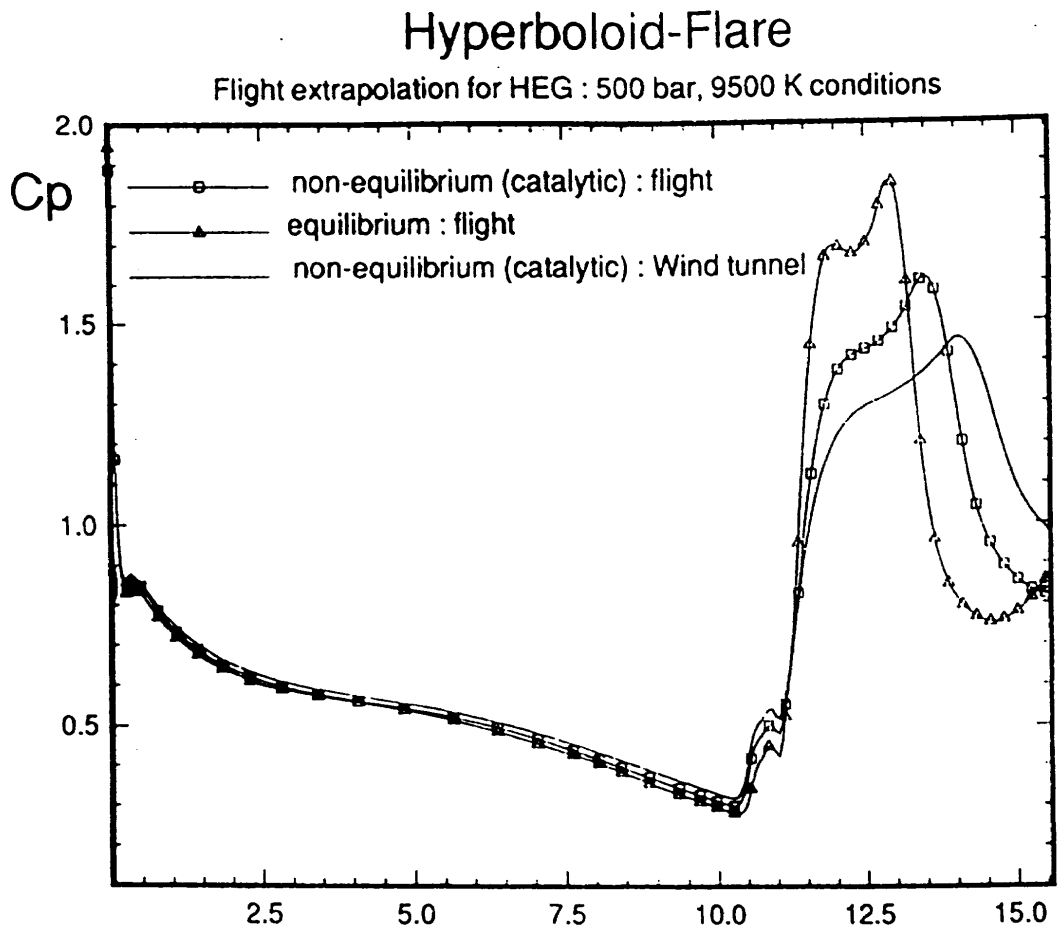

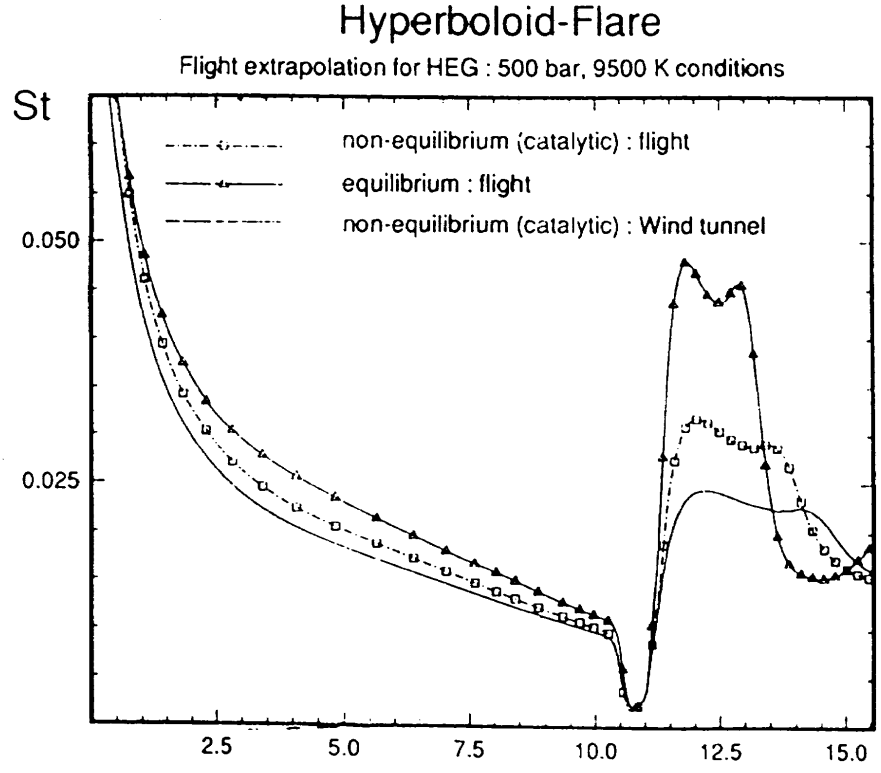

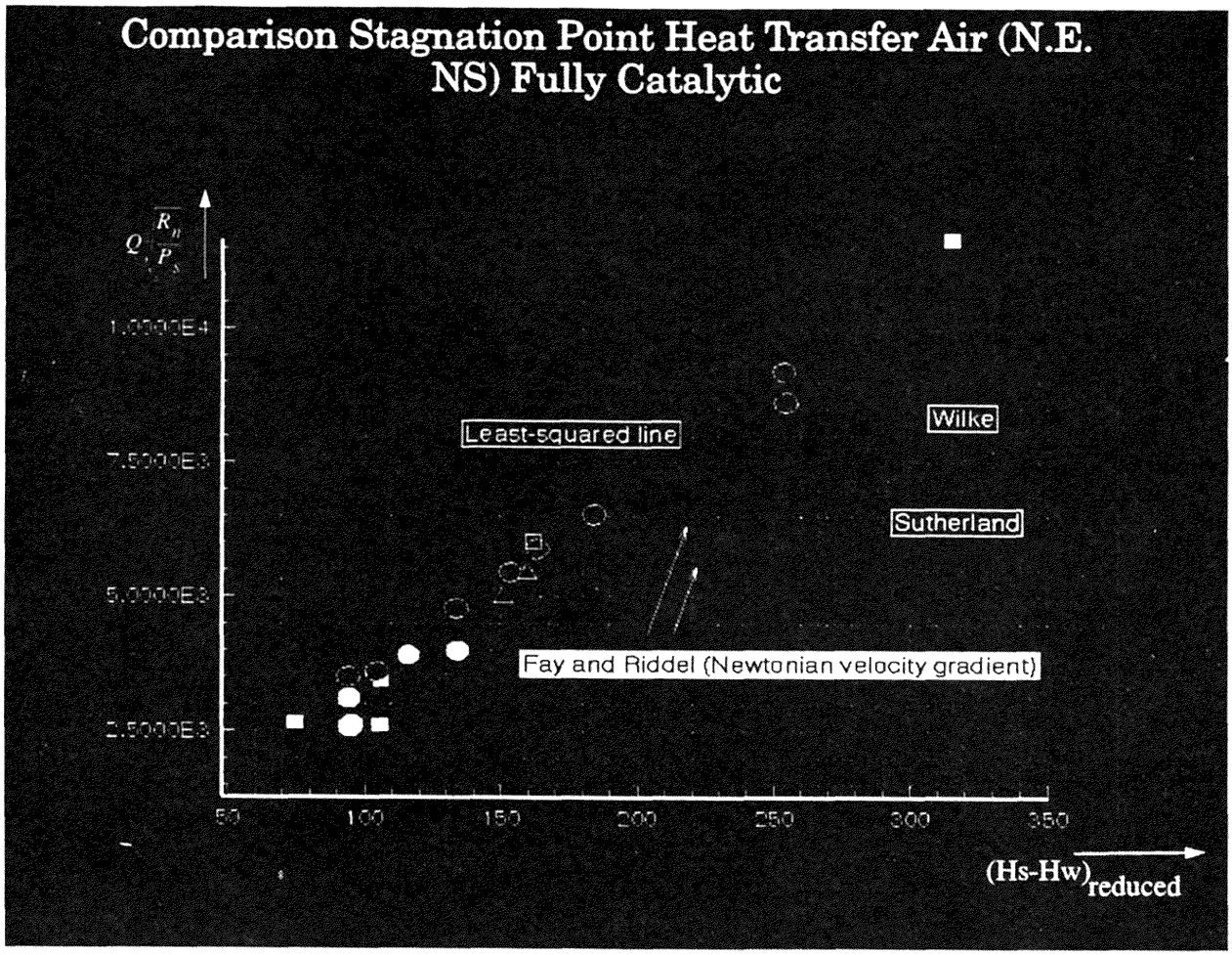

Ref: HT-Tn-E-1-201-ONER

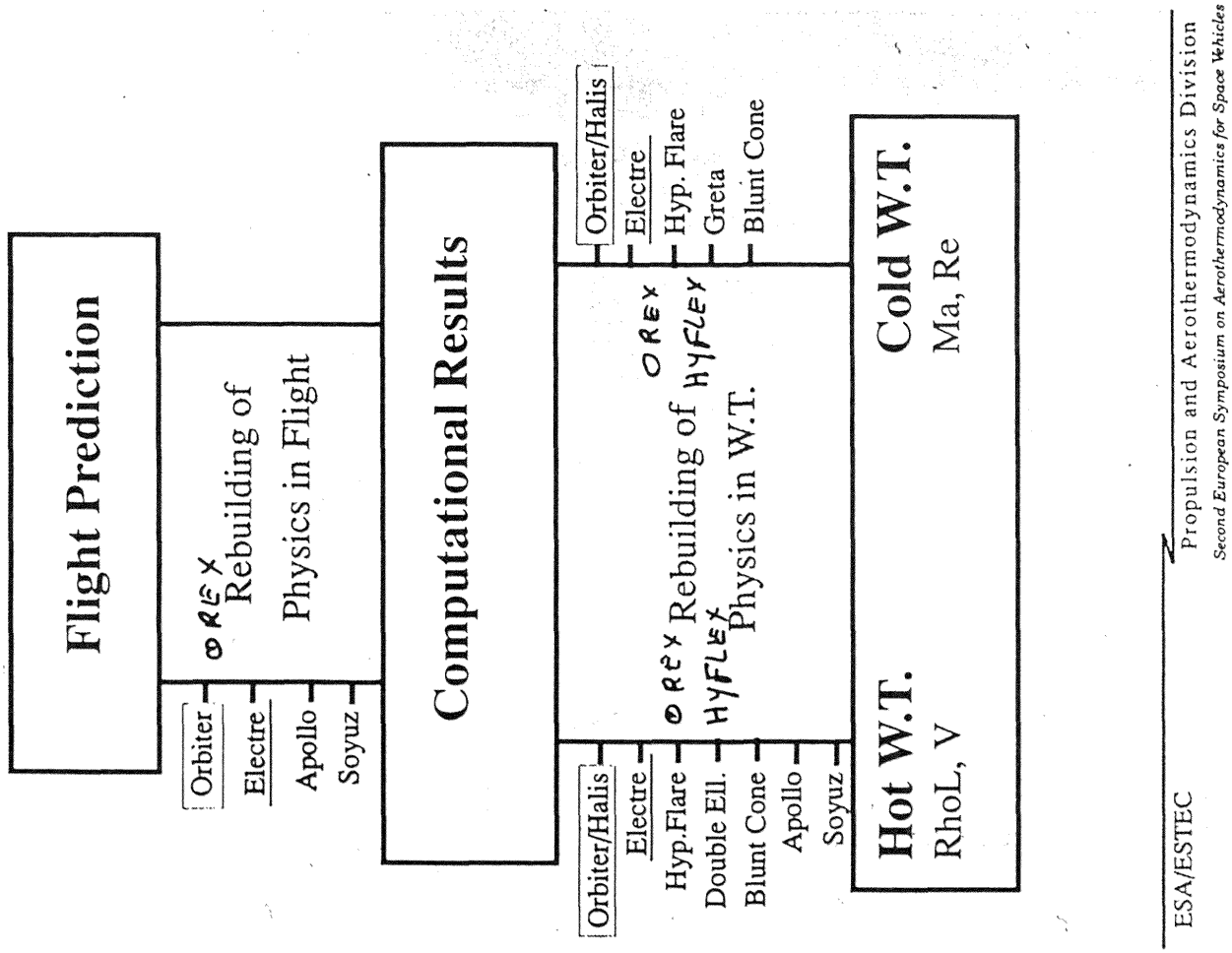

Qualification methodology

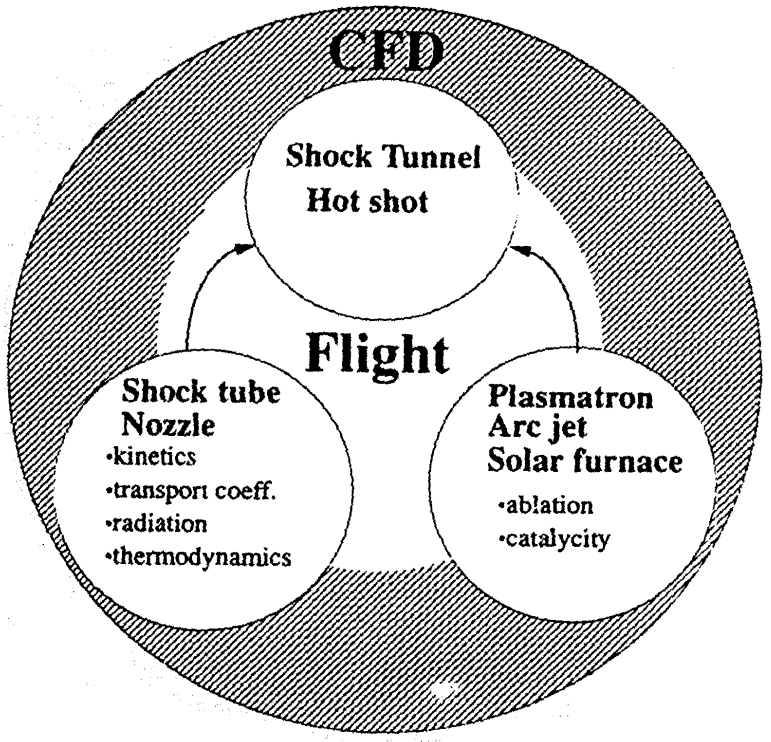

Ⅲ　高エンタルピーの流れのワークショップ

Ⅲ－１　課題募集要項

課題　課題はすべて軸対称流れとし、層流を仮定します。

テーマは大きく４つに分けます。

課題Ｉ　Sphere　DLR HEG 風洞条件による高エンタルピ流れ空力加熱解析

課題II　OREX　OREX(Orbital Re-Entry Experiment) 実験機形状

実飛行条件解析

課題III Hyperboloid Flare

ゲッチンゲン ルードヴィックチューブ及び

ONERA F4 トンネル条件による剥離を伴う流れの

極超音速流解析

課題IV　Spherically Blunted-Cone

カルスパンＬＥＮＳ、ＤＬＲ．ＨＥＧ等の高エンタルピー

風洞条件によるベース・フローを含む解析

課題Ｉ　Sphere　背景

ＤＬＲ、ＨＥＧ高エンタルピー風洞を用いた球の周りの空力加熱試験が宇宙開発事業団によりＨＯＰＥ研究開発の一環として実施される。本課題の目的は上記高エンタルピー試験の基本的な特性の解明と壁の触媒性が空力加熱に与える影響を調べることにある。空力加熱分布がデータとして提出される予定である。

課題II　OREX 背景

OREX は宇宙開発事業団により１９９４年２月に打ち上げが行われ、航空宇宙技術研究所と共同して、実飛行時の圧力、耐熱材の温度、電子密度等が計測された。これらの貴重なデータとＣＦＤによる実在気体計算結果を比較することにより、実験及びＣＦＤ相互のアプローチから、極超音速流における実在気体現象を解明することを目的とする。本課題は第１２回の極超音速流のＣＦＤワークショップの課題にも取り上げられ、その後の飛行条件の変更、及び計算手法の向上をうけて、再度、完全気体、平衡流、及び非平衡流について、ＣＦＤ解析手法間の相互比較を行う。

課題 III　Hyperboloid Flare 背景

高迎角における空力舵面を模擬した形状として、剥離・再付着を伴う流れの解明を目的とする。実験はゲッチンゲンのルードヴィックチューブ(Cold Case)及び ONERA F4 ハイエンタルピ風洞を用いて、圧力、空力加熱分布、剥離点の位置、及び衝撃波形状が計測された。実験データはＥＳＡ（ヨーロッパ宇宙機構）から提出される。

課題 IV　Spherically Blunted-Cone 背景

ベースフローの解明を目的としてカルスパン ＬＥＮＳ、ＤＬＲ ＨＥＧ、及びＮＡＳＡ Ａｍｅｓの３つの風洞により、同一の一様流条件で実験を行う予定で、ベース及び後部シリンダー上で得られた圧力、及び空力加熱分布の比較を主眼とする。本課題は各風洞間の特性の違いを見るとともに、計算の極めて困難なベース・フローの問題に取り組み、ＣＦＤの計算シミュレーションの精度をみることも目的の一つである。実験データはＥＳＡ（ヨーロッパ宇宙機構）から提出される予定となっている。

記

応募方法	応募申込書および資料をお送りします。 応募申込書の受付を以って応募したものとします
応募締切り	平成７年１月２７日
計算結果提出期限	平成７年５月３１日必着
開催日	平成７年６月８日（予定）
開催場所	航空宇宙技術研究所
応募資料請求先と問い合わせ先	山本行光 〒182　東京都調布市深大寺東町７-４４-１ TEL　(0422)-47-5911　Ext.2302 Fax　(0422)-47-4927 e-mail　Yukimitu@nal.go.jp

なお、今回はProblem III (Hyperboloid Flare) 及び Problem IV(Spherically Blunted Cone) については基本となる格子を３．５インチフロッピー(MS-DOSフォーマット)にて配布する予定です。希望者は上記連絡先までご連絡下さい。なお、Problem III-1の Hyperboloid Flare の Cold Case については、少なくとも流れ方向４００点以上の格子を用いないと正しい剥離点が得られない可能性があります。

第１３回　（平成７年度）　航空機計算空気力学シンポジウム
特別企画ワークショップ応募申込書

応募者は下記の欄に記入の上、下記宛に送って下さい。重複して２つ以上の部門に申し込む場合は本紙をコピーして、別々に申し込んで下さい。

応募締切　平成７年１月２７日
送り先　航空宇宙技術研究所　空気力学部
山本　行光
〒１８２　東京都調布市深大寺東町７－４４－１
Ｔｅｌ　０４２２－４７－５６１１　ｅｘ．２３０２
Ｆａｘ　０４２２－４７－４９２７

１．受付番号　Sphere　OREX　Hyperboloid Flare　Blunted Cone

２．応募部門　（どれかの部門を○で囲む。具体的な計算条件が決まっている場合には課題番号にも○を付ける。）

Problem Ⅰ	Problem Ⅱ	Problem Ⅲ	Problem Ⅳ
Sphere部門	OREX部門	Hyperboloid Flare部門	Spherically Blunted Cone部門
Ⅰ－１	Ⅱ－１	Ⅲ－１	Ⅳ－１
Ⅰ－２	Ⅱ－２	Ⅲ－２	Ⅳ－２
Ⅰ－３	Ⅱ－３	Ⅲ－３	
Ⅰ－４	Ⅱ－４		
Ⅰ－５	Ⅱ－５		
Ⅰ－６			

３．応募者氏名

４．所属

５．連絡先　住所　：
Ｔｅｌ：
Ｆａｘ：

６．使用する解法の概要（空欄内に収まる範囲で簡単に記入）

（１）計算モデル　（非平衡流、平衡流、ＶＳＬ、Euler＋境界層方程式）

（２）解法　（ＦＤＭ，ＦＥＭ等）

（３）化学反応モデル等

（４）格子形成法

第１３回［平成７年度］
航空機計算空気力学シンポジウム

高エンタルピー流れ
ワークショップ応募資料

航空宇宙技術研究所

航空機計算空気力学シンポジウム
ワークショップ実行委員会

Description of the Test Case Problems

Thirteenth Aircraft Computational Fluid Dynamics Symposium

High Enthalpy Flow Workshop

June 8, 1995

National Aerospace Laboratory

Workshop Working Group

1 Problem I Sphere

Axisymmetric laminar flow is assumed and it is not necessary to calculate the base region. Experimental data at DLR HEG flow conditions will be provided for the heat transfer distributions.

1.1.1 Geometry

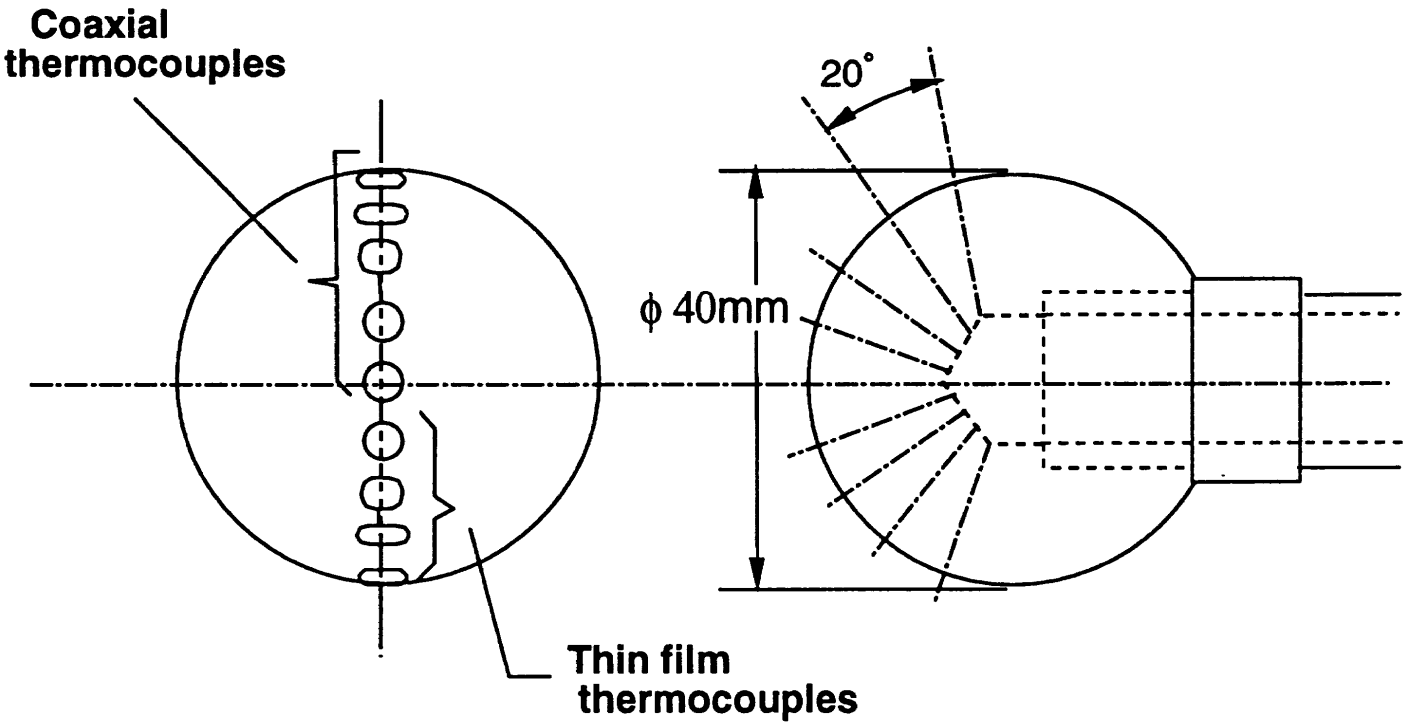

Sphere model

1.1.2 Test Cases

Case	V ∞	T ∞	ρ ∞ (kg /m ^{3})	Twall	Modelization	Level
I-1	5939m/s	705K	0.00156	300K	Lam, Non-eq, Non-cat	***
I-2	〃	〃	〃	〃	〃 Full-cat	***
I-3	6180m/s	934K	0.0034	300K	Lam, Non-eq, Non-cat	***
I-4	〃	〃	〃	〃	〃 Full-cat	***
I-5	5151m/s	708K	0.0058	300K	Lam, Non-eq, Non-cat	***
I-6	〃	〃	〃	〃	〃 Full-cat	***

(Non-cat =Non catalytic, Full-cat =Full catalytic surface condition)

(Non-eq =Non-equilibrium, Lam =Laminar)

Mass fractions of free stream air are as follows.

Case	N_2	O_2	NO	N	O
I-1, 2	0.762	0.0348	0.0317	0.0	0.1708
I-3, 4	0.744	0.0659	0.0429	0.0	0.1468
I-5, 6	0.733	0.1578	0.0688	0.0	0.0406

2 Problem II OREX

2.1 Description of problem II

Axisymmetric laminar flow is assumed and it is not necessary to calculate base flow.

2.1.1 Geometry

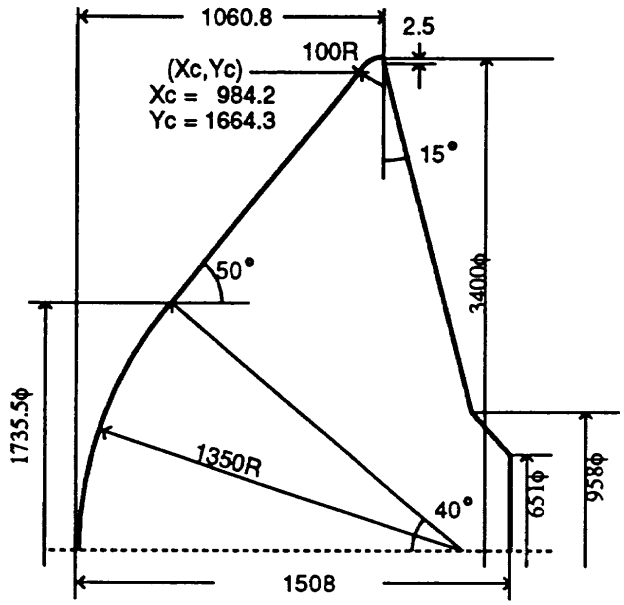

OREX Configuration(Unit:mm)

2.1.2 Test cases

	U_∞	T_∞	P_∞	T_{wall}	Modelization	Level
II.1	$7450m/s$	$186.9K$	$0.169N/m^2$	$540K$	Lam.Non-equilibrium,Non-cat	***
II.2	$5562m/s$	$248.1K$	$23.60N/m^2$	$1519K$	Lam.Non-equilibrium,Non-cat	***
II.3	//	//	//	//	Lam.Non-equilibrium,Full-cat	***
II.4	//	//	//	//	Lam.Equilibrium,	**
II.5	//	//	//	//	Lam. n.react	*

(Non-cat = Non catalytic Full-cat = Full catalytic surface condition)

Flight Experiment results are available for Test cases II.1,2

(Wada and Yamamoto and Inouye , Japan)

3 Problem III Hyperboloid Flare

Axisymmetric laminar flow is assumed and it is necessary to calculate cylinder part. Experimental data obtained by Geottingen Ludwig Tube (Cold Case) and ONERA F4 (Hot Case) are available for the surface pressure and Stanton number distributions. Also, separation point is determined by oil flow test (Cold Case). Shock wave patterns are also available.

3.1.1 Geometry

The contour of hyperboloid flare forebody is defined by fourth order polynomials. The angle between flare and body axis is 43.6 degrees. The length of the straight flare part is 20% of the length of the forebody. It is continued by cylinder from X=1.0 to X=1.25. Definition of polynomials of the forebody part is described in 3.2.

Total Geometry and basic grid (521X31) data are available by 3.5 inch floppy disk. Please, contact to the workshop organizer.

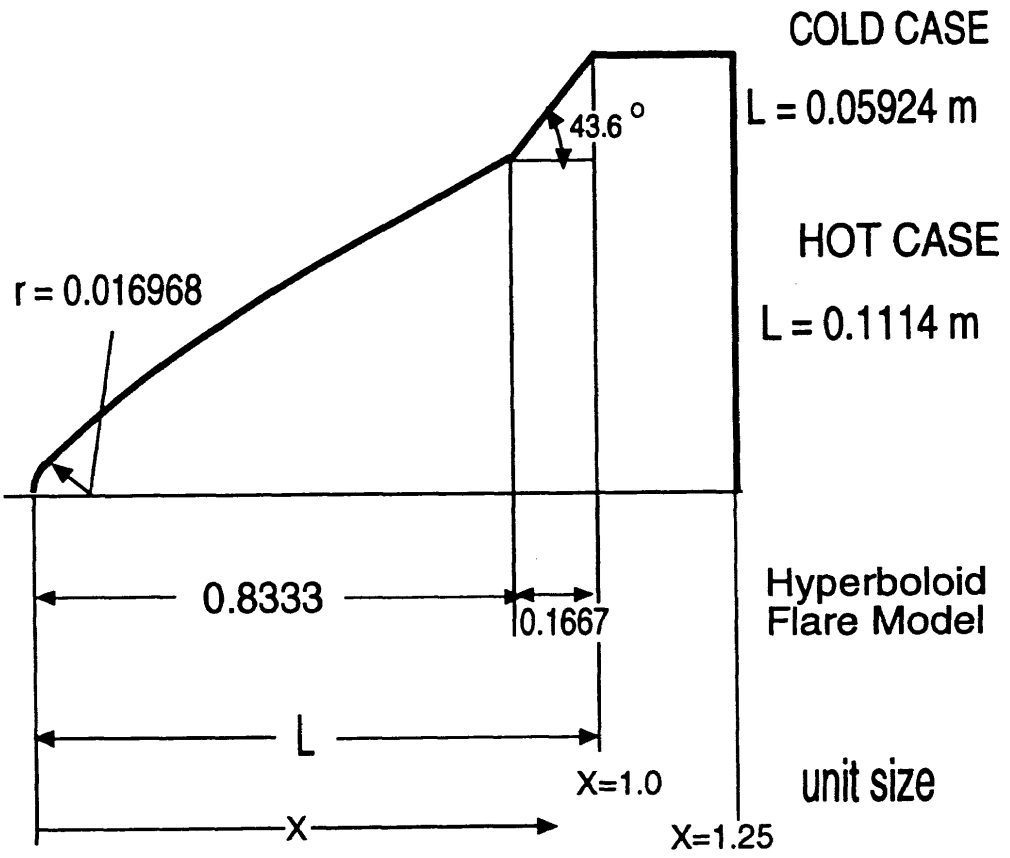

3.1.2 Test Cases

LTB (Cold Case)

	M ∞	T ∞	Re∞ /m	Twall	Modelization	Level
III-1	6.83	67.765K	$7.0X10^{6}$	310K	Perfect Gas	****

ONERA F4 (Hot Case)

	V ∞	T ∞	Tv	ρ ∞	Twall	Modelization 1	Level
III.2	3934m/s	188.3K	3200K	$1.557X10^{-3}$	300K	Lam,Non-eq,Non-cat	****
III.3	〃	〃	〃	〃	〃	Lam,Non-eq,Full-cat	****

(Non-cat =Non catalytic, Full-cat =Full catalytic surface condition)

(Non-eq =Non-equilibrium, Lam =Laminar)

Mass Fraction of the free stream

N_2	N	O_2	O	NO
0.7254	0.0	0.1354	0.0497	0.0895

One temperature model can be used by equating free stream vibrational temperature Tv to transrational and rotational temperature T ∞ .

3.2 Geometry Difinition of Hyperboloid Flare Forebody.

The contour of the hyperboloid flare is defined by matched fourth order polynomials for the axial coordinate x as a function of the surface abscissa y.

Please note:

Since the x and y coordinates are dimensionless with the body-length including a flap of 20% of the contour, the following relations are only valid for:

$$\begin{aligned} 0 &\leq x \leq \frac{5}{6} \\ -.514683 &\leq y \leq 0. \end{aligned}$$

The general form of the polynomials is :

$$xp_1(y) = a_{11} + a_{21} * (-y) + a_{31} * (-y)^2 + a_{41} * (-y)^3 + a_{51} * (-y)^4$$

with:

$$\begin{aligned} a_{11} &= 0.000000000000 \\ a_{21} &= 0.000000000000 \\ a_{31} &= 29.467034497212 \\ a_{41} &= 0.000000000000 \\ a_{51} &= -5645.240573904950 \end{aligned}$$

and:

$$xp_2(y) = a_{12} + a_{22} * (-y) + a_{32} * (-y)^2 + a_{42} * (-y)^3 + a_{52} * (-y)^4$$

with:

$$\begin{aligned} a_{12} &= -0.009250713659 \\ a_{22} &= 0.948176696531 \\ a_{32} &= 3.004115746723 \\ a_{42} &= -6.927993520959 \\ a_{52} &= 7.173047861368 \end{aligned}$$

The contour from the nose to the contour-flap intersection is given by:

$$xgs(y) = xp_1(y) \ \ for \ \ y > y_1$$

$$\begin{aligned} xgs(y) &= fakt * xp_1(y) + (1 - fakt) * xp_2(y) \\ with: \ fakt &= (cos((y - y_1)/(y_2 - y_1) * pi) + 1.)/2. \\ &\quad . \quad for \ \ y1 \geq y > y2 \end{aligned}$$

and

$$xgs(y) = xp_2(y) \ \ for \ \ y_2 \geq y$$

$$\begin{aligned} y_1 &= -1.74418427 * 10^{-2} \\ y_2 &= -3.42209451 * 10^{-2} \end{aligned}$$

4 Problem IV Spherically Blunted Cone

4.1 Description of Probrem IV

Three experimental data obtained by Calspan LENS facility, DLR, HEG and NASA Ames, are available at the same freestream flow condition. Axisymmetric laminar flow is assumed and Base flow must be calculated .

4.2.1 Geometry

Basic grid will be provided by 3.5*inch* floppy disk. Please, contact to the workshop organizer.

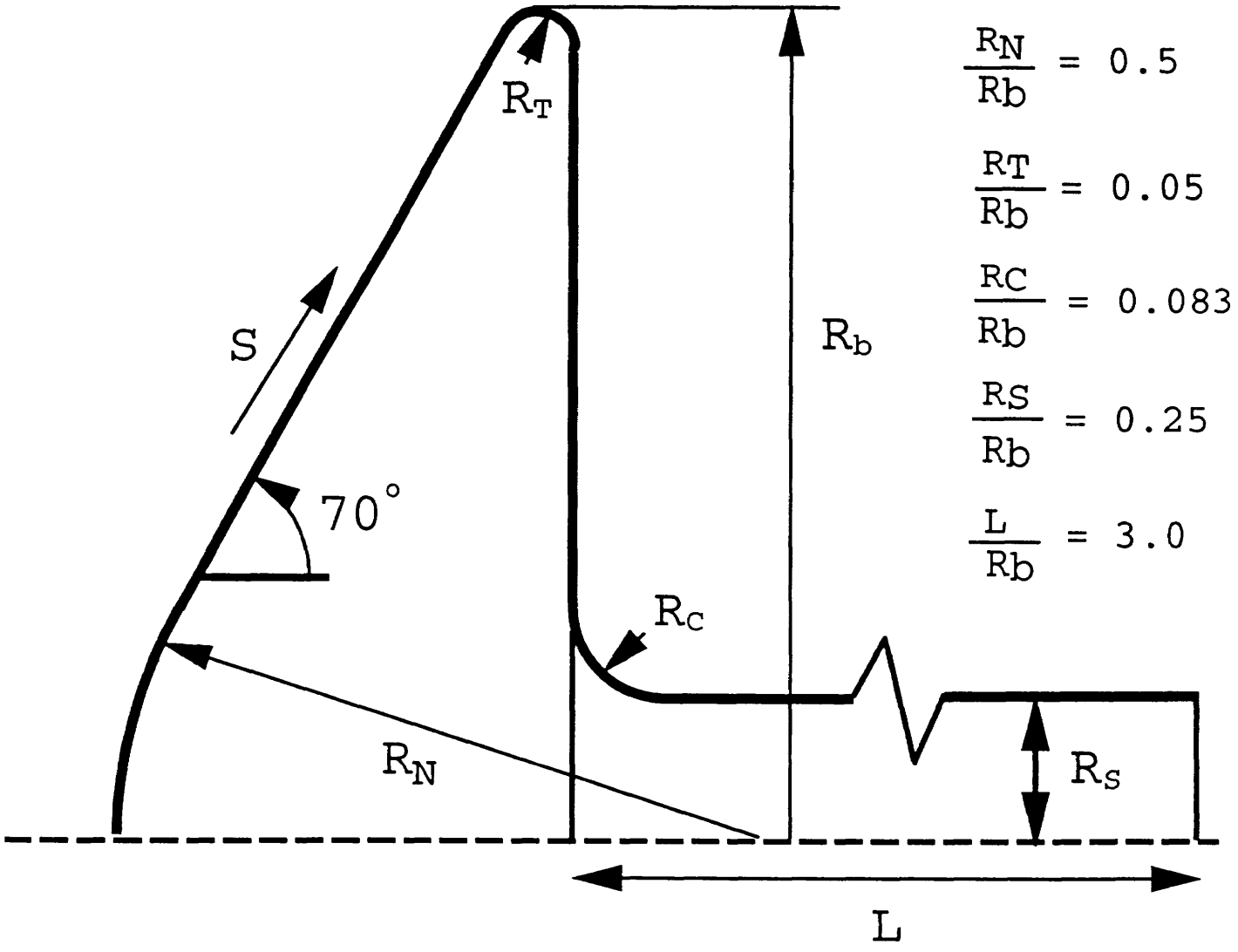

Axisymmetric Spherically Blunted Cone

The base radius of model, R_B is 76.2mm

4.2.2 Test Cases

Air is assumed.

	M_∞	T_∞	ρ_∞ (kg /m ^{3})	T_{wall}	Modelization	Level
IV.1	10.31	489.9*K*	4.085 × 10 $^{-3}$	295*K*	Lam,Non-equilibrium,Non-cat	*****
IV.2	//	//	//	//	Lam,Non-equilibrium,Full-cat	*****

(Non-cat =Non catalytic, Full-cat =Full catalytic surface condition)

(Non-eq =Non-equilibrium, Lam =Laminar)

The mole fractions of the freestream air are as follows.

	N_2	O_2	O	NO	N
Mole fraction	0.7350	0.1490	0.0483	0.0677	0.0

付録　　格子データ配布資料

御応募いただいた方々のうち Problem Ⅲ Hyperboloid Flare 及び Problem Ⅳ Spherically Blunted Cone にエントリーまたは興味のお持ちの方々には３．５インチフロッピーディスク、及び説明書を同封し、基本格子及び計算格子のデータをお渡しいたします。何卒、よろしくお願い申しあげます。なお上記課題については以下の点にご注意下さい。

Problem Ⅲ Hyperboloid Flare

格子は、流れ方向５２１点、物体面と垂直方向１０１点です。計算格子は物体表面における格子巾のあらい計算格子 HYPERBLD.CM1 及び細かい計算格子 HYPERBLD.CM2 の２つを用意しました。

Problem Ⅳ Sphericaly Plunted Cone

基本格子は流れ方向１６１点、物体面に垂直方向１３１点です。これに対して計算格子は流れ方向格子数はおなじで、物体面に垂直方向は２４１点となっております。また、各Ｘ，Ｚの座標値を３８倍すると課題に設定された寸法になります。

データの読み込み方法

1. データはすべて圧縮してあります。
   使う前に LHAコマンド（フロッピー内にあります）で解凍してから使ってください。

① LHA X CONE.LZH
このコマンドで、 CONE.ORG … CONE基本格子
CONE.DAT … CONE計算格子 が解凍されます。

② LHA X HYPB_ORG.LZH
このコマンドで、 HYPERBLD.ORG … HYPERBOLOID 基本格子 が解凍されます。

② LHA X HYPB_CMP.LZH
このコマンドで、 HYPERBLD.CM1 … HYPERBOLOID 計算格子（粗い格子）
HYPERBLD.CM2 … HYPERBOLOID 計算格子（細かい格子）が解凍されます。

なお、解凍すると、約7MBになるので、ハードディスクなどにコピーしてから、
解凍してください。

2. データ形式

① CONE.ORG（CONE.DATも同じデータ形式）

```
      PARAMETER ( L = 161,  N = NN )
      DIMENSION  XC(L,N), ZC(L,N)

      WRITE(10,100)  L, N
      WRITE(10,101)  (( XC(K,I), K=1,L), I=1,N)
      WRITE(10,101)  (( ZC(K,I), K=1,L), I=1,N)

  100 FORMAT ( 2I5 )
  101 FORMAT ( 5E16.8 )
```

〔注意〕CONE.ORG …… NN = 131
CONE.CMP …… NN = 241

② HYPERBLD.ORG （HYPERBLD.CM1, HYPERBLD.CM2 も同じデータ形式）

```
      PARAMETER ( L = 521,  N = 101 )
      DIMENSION  XC(L,N), ZC(L,N)

      WRITE(10,100)  L, N
      WRITE(10,101)  (( XC(K,I), K=1,L), I=1,N)
      WRITE(10,101)  (( ZC(K,I), K=1,L), I=1,N)

  100 FORMAT ( 2I5 )
  101 FORMAT ( 5E16.8 )
```

Ⅲ－2　応募論文

2−1

High Enthalpy Air Flow Computations with a Sphere and a Blunted Cone Models

Igor MEN'SHOV and Yoshiaki NAKAMURA

Dep. of Aerospace Engineering, Nagoya University

ABSTRACT

A computational fluid dynamics (CFD) technique is employed to study hypersonic high enthalpy air flow around blunt bodies at a range of enthalpies relevant to suborbital flight speeds of aeroassisted orbital transfer vehicles (ASTVs). The method uses the two-temperature model of Park for the description of thermo-chemical nonequilibrium processes in high temperature air and solves the full Navier-Stokes equations for multicomponent reacting gas mixture in finite volume formulation on a grid of arbitrary structure. The calculations performed in this work simulate in detail the experiments carried out recently at the KHI (Japan), and at the DLR (Germany), where heat flux distribution over a sphere and a capsule-like blunt cone model was measured at several freestream conditions related to the range of enthalpies mentioned above. The main emphasis in this paper is given to comparison between numerical and experimental results in order to verify adequacy of data in terms of heat flux distributions predicted by the CFD technique for suborbital ASTV flight range.

1. Introduction

The assessment of heating load during re-entry has always been one of key points in the design of ASTVs. This problem has been extensively investigated initially by both experimental and analytical methods for the purpose of estimating the convective heat transfer rates at the stagnation point (e.g. Refs.1, and 2). However, all these experiments and theoretical considerations were performed at the range too far from flight situations that may be encountered by ASTVs, and where nonequilibrium phenomena are not essential and the flow can be considered on the assumption of thermo-chemical equilibrium.

The development of experimental base makes now possible to realize high enthalpy flow experiments through a range of enthalpies: 2.5 MJ/kg to 45 MJ/kg, equivalent to velocities: 2 km/s to 10 km/s, which covers re-entry flight speeds of the ASTV (e.g. Refs.3, and 4), and where nonequilibrium effects should play a considerable role. The results derived from these experiments are of crucial importance for the justification of existing CFD's models for flows in chemical and thermal nonequilibrium mainly in the question that to what extent these models can predict close to real values such basic thermo- and aerodynamic characteristics as forces, moments, and heat flux rates.

The two-temperature model of Park (Ref.5) seems at present to be a most widely used model in the CFD for the simulation of high enthalpy nonequilibrium air flows. In this model, two assumptions are made to describe species' energy distributions. The first is that the translational mode is in equilibrium with the rotational mode and the distribution of energies in these two modes are described by one translational-rotational temperature for all heavy particle species. In the second one, another temperature (vibrational-electronic) is introduced to characterize the vibrational energy of molecules, translational energy of electrons, and electronic excitation energy of atoms and molecules.

Supported by many experimental data, a justification for the two-temperature model is based on the facts that (a) the energy transfer between the translational and rotational modes, and between the translational mode of free electrons and the vibrational mode of molecular nitrogen are very fast, and (b) the low-level electronic states of heavy particles become equilibrium very quickly with the ground electronic state at the electronic temperature.

In Ref. 6, the effects of thermochemical nonequilibrium on forces and moments at hypersonic flight speeds were studied by using Park's model, and a 10% change in lift and drag and a 20% change in pitching moment for the airfoil caused by the nonequilibrium phenomena were numerically predicted. In this paper, we make an attempt to apply the two-temperature model in the prediction of heat characteristics by numerically simulating the experiments carried recently out at the DLR, Germany (Ref.3), and at the KHI, Japan (Ref. 4), where convective heat flux distribution over model' surface was measured at different freestream conditions with enthalpies ranging from 20 MJ/kg to 40 MJ/kg.

Towards this end, a numerical code for obtaining steady-state solutions to the equations of 2D fluid motion coupled with the finite-rate chemistry in thermal and chemical nonequilibrium air has been developed in the Fluid Dynamics Laboratory, Department of Aerospace Engineering, Nagoya University. The code basically described in Ref.7 solves the Euler or Navier-Stokes equations for multicomponent reacting gas flow in finite-volume formulation on a grid of arbitrary structure. Inviscid convective terms are discretized with a modification of the Advection Upstream Splitting Method (AUSM) (Ref. 8). Viscous fluxes are approximated with a standard centered scheme. Time integration is performed in two-step implicit manner, and an approximate linearization is made for inviscid and viscous fluxes and exact that is used for the thermo-chemical sources. The approximate linearization of the

inviscid fluxes is performed based on the method proposed in Ref. 9, which leads to an implicit operator in diagonal form after applying the Lower Upper Symmetric Gauss-Siedel (LU-SGS) factorization (Ref. 9) in the case of strucured grid. We proved that this remarkable property is conserved if the LU-SGS factorization is applied to unstructured grid, and hence independently on the grid considered, in order to invert the implicit operator in this way only the Jacobian matrix of the thermochemical source needs to be inverted in each computational cell.

2. Physical model and governing equations

With the exception of ionization phenomena that are neglected in this paper, we closely follow the two-temperature model of Park (Ref.10). The five neutral species: N, O, NO, N_2, O_2 are considered and 17 most important chemical reactions among these species are employed. The reaction rate coefficients are controlled by the temperature (rate-controlling temperature), which is a geometrically averaged temperature between the translational-rotational and vibrational-electronic temperatures. The rate parameters are cited from Ref. 11.

Transport coefficients are evaluated by extending Yos's formula based on the first Chapman-Enskog approximation to multitemperature gas mixture (Ref.12). To simplify evaluation of the collision integrals in Yos's formula, the formulas of Chapman and Cowling for species viscosity and binary-diffusion coefficient along with the semiempirical formula of Wilke for mixture viscosity (Ref.13) are invoked. Comparing these formulas with the corresponding Yos's ones, compact and easily computed expressions can be obtained for the collision integrals by which the transport coefficients are expressed.

The relaxation of vibrational-electronic excitation energy due to collisions with heavy particles is modeled according to the theory of Landau and Teller (Ref.14). The relaxation time employed in this theory is computed as the sum of the empirical correlations of Millikan and White and high temperature correction proposed by Park (Ref. 15).

The system of governing equations with the physical model described above can be expressed as follows:

$$\partial_t \mathbf{q} + \partial_k \mathbf{f}_k = \partial_k \mathbf{g}_k + \mathbf{H} \qquad (1)$$

where $\mathbf{q}$ is the solution vector, the components of which are the species densities, 3 momentum components, the vibrational-electronic excitation energy, and the total energy, respectively. The vectors $\mathbf{f}_k$ and $\mathbf{g}_k$ $(k = 1,2,3)$ are inviscid and viscous flux vectors, respectively, and $\mathbf{H}$ is the thermochemical source. The summation on repeating index is assumed in eq.(1) and hereafter.

3. Numerical algorithm

We use the finite volume method with two-step implicit time integration to obtain spatial and time discretizations of the governing equations (1) . Having been given a spatial decomposition, which is structured or unstructered, of the computational domain by a set of control volumes (CV), the resulting system of discrete equations can be written as:

$$\omega_i \Delta \mathbf{q}_i + \Delta t \sum_\sigma s_\sigma \mathbf{f}_\sigma^{n+1} = \Delta t \sum_\sigma s_\sigma \mathbf{g}_\sigma^{n+1} + \omega_i \Delta t \mathbf{H}_i^{n+1}, \qquad (2)$$

$$\mathbf{f}_\sigma = \mathbf{f}_{k,\sigma} n_k, \quad \mathbf{g}_\sigma = \mathbf{g}_{k,\sigma} n_k, \quad i = 1,\ldots,N$$

where $\mathbf{q}_i$ is the solution vector averaged on the CV, ω_i is the CV volume, s_σ is the area of the CV interface, $\mathbf{n} = (n_1, n_2, n_3)$ is the exterior normal to the CV interface. Here the superscript denotes the time level, σ denotes the CV interface, and Δ denotes the increment in time. The summation in eq. (2) is performed for all faces bordering the CV under consideration.

The inviscid numerical flux $\mathbf{f}_\sigma$ at the interface σ is expressed in terms of the local one-dimensional flux $\mathbf{F}$ as follows:

$$\mathbf{f}_\sigma = \mathbf{T}_\sigma^{-1} \mathbf{F}, \quad \mathbf{F} = \mathbf{f}_1(\mathbf{Q}), \quad \mathbf{Q} = \mathbf{T}_\sigma \mathbf{q} \qquad (3)$$

where $\mathbf{T}_\sigma$ is the transforming matrix defined by the coordinates of the unit vectors of the local orthonormal basis at the interface (Ref.16).

To solve the system of discrete equations (2) we linearize the thermochemical source vector and approximate the inviscid local flux and the viscous flux in the following way (Refs.7, and 17):

$$\mathbf{F}^{n+1} = \mathbf{F}^n + \mathbf{A}_i^+ \Delta \mathbf{Q}_i + \mathbf{A}_{\sigma(i)}^- \Delta \mathbf{Q}_{\sigma(i)} \qquad (4)$$

$$\mathbf{g}_\sigma^{n+1} = \mathbf{g}_\sigma^n + \mathbf{D}_\sigma (\Delta \mathbf{q}_{\sigma(i)} - \Delta \mathbf{q}_i)$$

Here, $\mathbf{A}^+$ is a positive matrix, and $\mathbf{A}^-$ is a negative matrix such that their sum equals to the Jacobian matrix of the flux $\mathbf{F}$ with respect to the vector $\mathbf{Q}$:

$$\mathbf{A}^+ + \mathbf{A}^- = \mathbf{A} = \partial \mathbf{F} / \partial \mathbf{Q} \qquad (5)$$

The coefficient D_σ in eq. (4) is taken in the form:

$$D_\sigma = \rho_{dis} / h_\sigma \qquad (6)$$

$$\rho_{dis} = \max(d_1, \ldots, d_5, \nu, \alpha, \alpha_v)$$

where d_k $(k = 1$ to $5)$ are diffusion coefficients, ν is the viscous diffusivity, α, α_v are the thermal diffusivity for translational-rotational and vibrational-electronic mode, respectively, and h_σ is the distance between i- and $\sigma(i)$-node points projected on the normal to the interface, $h_\sigma = |\mathbf{n} \bullet (\mathbf{x}_i - \mathbf{x}_{\sigma(i)})|$.

By substituting eq. (4) in eq. (2), we obtain the system of linear equations with respect to the increment of the solution vector:

$$(\mathbf{I} + \sum_\sigma \mu_i^+ - \Delta t \mathbf{S}_i) \Delta \mathbf{q}_i + \sum_\sigma \mu_{\sigma(i)}^- \Delta \mathbf{q}_{\sigma(i)} = \mathbf{R}_i \qquad (7)$$

where $\mathbf{S}_i$ is the Jacobian matrix of the thermochemical source vector $\mathbf{H}_i$. $\mathbf{R}_i$ is the residual defined as

$$\mathbf{R}_i = \Delta t \mathbf{H}_i^n + \frac{\Delta t}{\omega_i} \sum_\sigma s_\sigma (\mathbf{g}_\sigma^n - \mathbf{f}_\sigma^n) \qquad (8)$$

and the matrices $\mu^\pm$ are defined at each CV interface as follows:

$$\mu^\pm = \frac{\Delta t}{\omega_i} s_\sigma (\mathbf{T}_\sigma^{-1} \mathbf{A}^\pm \mathbf{T}_\sigma \pm D_\sigma \mathbf{I}) \qquad (9)$$

The system of equations (7) has a large block band matrix, which requires many operations for its

inversion. To reduce the computational cost, which is usually encountered in direct solvers, the matrix in the left hand side of eq. (7) is often approximately factorized as product of a number of easily invertible factors. One of such factorizations referred to as the Lower-Upper Symmetric Gauss-Siedel (LU-SGS) method was proposed in Ref. 9 for strucured spatial discretizations. We employ this method and extend it to unstructured grids to solve eq. (7).

The generalization of the LU-SGS to unstructured grids is obtained in the following way (see Ref.16). First, the second term in the left hand side of eq. (7) is represented by the sum of two terms:

$$\sum_{\sigma} \mu^{-}_{\sigma(i)} \Delta \mathbf{q}_{\sigma(i)} = \Sigma_L(\Delta \mathbf{q}) + \Sigma_U(\Delta \mathbf{q}) \qquad (10)$$

where

$$\Sigma_L(\Delta \mathbf{q}) = \sum_{\sigma:\sigma(i)<i} \mu^{-}_{\sigma(i)} \Delta \mathbf{q}_{\sigma(i)} \qquad (11)$$

$$\Sigma_U(\Delta \mathbf{q}) = \sum_{\sigma:\sigma(i)>i} \mu^{-}_{\sigma(i)} \Delta \mathbf{q}_{\sigma(i)}$$

Then, the equation (7) is replaced by the two coupled equations

$$(I + \sum_{\sigma} \mu^{+}_{i} - \Delta t S_i) \Delta \mathbf{q}^{*}_{i} = -\Sigma_L(\Delta \mathbf{q}^{*}) + \mathbf{R}_i \qquad (12.1)$$

$$(I + \sum_{\sigma} \mu^{+}_{i}) \Delta \mathbf{q}_{i} = -\Sigma_U(\Delta \mathbf{q}) + (I + \sum_{\sigma} \mu^{+}_{i}) \Delta \mathbf{q}^{*}_{i} \qquad (12.2)$$

which are used for calculating intermediate values of the increment, $\Delta \mathbf{q}^{*}_{i}$, and its final values, $\Delta \mathbf{q}_{i}$, respectively.

The system (12.1) has a lower triangular matrix, while that of (12.2) is a upper triangular with elements of block (Nsp+5)×(Nsp+5) matrices, where Nsp is the number of species. It allows us to efficiently solve eqs. (12.1) and (12.2) by implementing forward (i=1,...,N) and backward (i=N,...,1) relaxation sweeps, which involve the inversion of the block (Nsp+5)×(Nsp+5) matrices on the diagonal only. Thus, the final increment $\Delta \mathbf{q}_i$ can be obtained, which then used to update the solution vector $\mathbf{q}_i$.

The method described above needs to be comleted by setting up the formulas for the approximation of inviscid and viscous fluxes at the lower time level, and by defining concretely the Jacobian matrix splitted in eq. (5).

The discretization of the viscous terms requires an approximation to the derivatives of the solution vector at each face of the CV. In order to evaluate the derivatives we employ the following two-step procedure. First, the solution vector is interpolated from cell centers to cell vertices. Then, the derivatives are calculated by applying the Gauss formula to a dual cell coupled with the face.

To approximate the inviscid flux, a modification to the Advection Upstream Splitting Method (AUSM) proposed in Ref. 8 is used. A key issue of the AUSM is to divide the flux vector **F** into two terms: convective and pressure terms, and approximate them separately. The main achievement of this approach is that a stationary contact discontinuity can be captured without excess numerical dissipation, and consequently, shear layers can be calculated quite accurately even with a first order approximation.

Introducing the vector Φ with the components

$$\Phi_k = Q_k, \quad k \neq Nsp+5 \qquad (13)$$

$$\Phi_{Nsp+5} = Q_{Nsp+5} + p$$

the flux vector **F** can be expressed as

$$\mathbf{F} = u\Phi + \mathbf{P} \qquad (14)$$

where u is the projection of the velocity vector onto the exterior normal to the interface, and the pressure term **P** has the following components

$$P_k = 0, \quad k \neq Nsp+1 \qquad (15)$$

$$P_{Nsp+1} = p$$

Here p denotes the pressure.

The first term on the right hand side of eq. (14) can be treated as a passive advection of the vector Φ with the velocity u, and approximated in upwind fashion according to a suitable defined velocity u_σ. Approximation of the pressure term is in fact to define an appropriate value for the pressure at the interface p_σ. In this way, giving values to interface pressure and velocity, one can obtain a two-parametric approximation to the inviscid flux **F**, which can be written in the following form:

$$\mathbf{F} = 0.5\left[u_\sigma(\Phi_i + \Phi_{\sigma(i)}) - |u_\sigma|(\Phi_{\sigma(i)} - \Phi_i)\right] + \mathbf{P}_\sigma \qquad (16)$$

Hence, a specific approximation to the flux **F** is uniquely defined by an appropriate interface velocity u_σ and an interface pressure p_σ. In the AUSM scheme, these values are defined with Van Leer's splitting procedure (Ref.18) as

$$u_\sigma = u^{+}_{i} + u^{-}_{\sigma(i)} \qquad (17)$$

$$p_\sigma = p^{+}_{i} + p^{-}_{\sigma(i)}$$

where

$$u^{\pm} = \begin{cases} \pm 0.25a(M \pm 1)^2, & \text{if } |M| \le 1 \\ 0.5a(M \pm |M|), & \text{otherwise} \end{cases} \qquad (18)$$

$$p^{\pm} = \begin{cases} 0.25p(M \pm 1)^2(2 \mp M), & \text{if } |M| \le 1 \\ 0.5p(M \pm |M|)/M, & \text{otherwise} \end{cases}$$

Here a is the sound velocity, and M=u/a is the Mach number.

The definition of the inviscid flux as eqs. (16) to (18) is computationaly very simple, and requires *O*(Nsp+5) operations per grid point. At the same time, numerous numerical experiments show that it provides just the same accuracy in capturing discontinuities as Godunov's type schemes based on the solution of the local Riemann problem. In addition to these positive properties, the method has the disadvantage that it may produce slight numerical overshoots just behind shock waves, essentialy precluding the possibility of an accurate high-order extension in the vicinity of shock waves.

In Ref.19, the reason of these overshoots is supposed to be due to the fact that the mass flux in (16) does not directly take into account of the density behind the shock wave. Several attempts have been performed to eliminate these overshoots (Refs.19, and 20), based

mostly on the adding of blending elements of more diffusive schemes into the AUSM formulation. In this paper, we propose a very simple modification to the AUSM, which alleviates the monotonicity problems.

In authors' opinion, the nonmonotonicity at shocks might be caused by the definition of the interface velocity in the form of Van Leer's splitting. In fact, because the first term in eq. (16) is treated as a passive advection of the vector Φ, the propagation of disturbances in this process is defined by one eigenvalue of the Jacobian matrix A, which is equal to the normal velocity u, while the pressure disturbance propagation is in accordance with two acoustic eigenvalues. Therefore, the evaluation of p_σ in a splitting manner is justified, but as for u_σ , an interpolation between u_i and $u_{\sigma(i)}$ seems to be a more plausible approach.

To this end, we substitute the splitting form definition of u_σ in (17), and (18) by the symmetric averaging:

$$u_\sigma = 0.5(u_i + u_{\sigma(i)}) \tag{19}$$

It was observed in numerous numerical experiments that due to this modification the overshoots can be eliminated, and the method produce monotonic solution behind shock waves. As an example, Figure 1 illustrates the density contours for hypersonic flow around a cylinder at the freestream Mach number of 20 computed assuming non-reacting inviscid perfect gas by the AUSM with formulas (17), and (18) (Fig.1a), and (19) (Fig.1b) for the interface velocity u_σ on a coarse grid of 15x40 meshes.

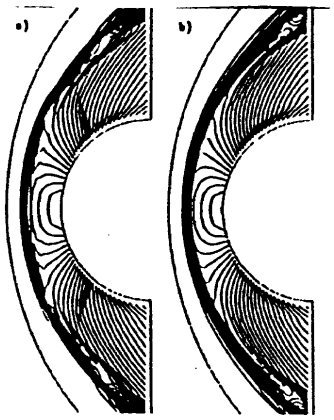

Fig.1 Density contours: a) splitting, b) averaging velocity

The system of discrete equations (12.1), and (12.2) can be written in the standart LU operator form as follows:

$$LD^{-1}U\Delta q = R \tag{21}$$

where

$$L = D + \Sigma_L - \Delta t S, \quad U = D + \Sigma_U \tag{22}$$

$$D = \tilde{D} + (1 + \frac{\Delta t}{\omega}\sum_\sigma D_\sigma)I, \quad \tilde{D} = \frac{\Delta t}{\omega}\sum_\sigma s_\sigma T_\sigma^{-1} A^+ T_\sigma$$

If the thermochemical noneqilibrium process are not considered (S=0), then the solution to eq. (21) requires inversion of the operator D only. A merit of the LU-SGS approximate factorization is found when it is used coupled with the Jacobian matrix splitting proposed in Ref. 22:

$$A^\pm = 0.5(A \pm \rho_A) \tag{23}$$

If a structured grid is used and a transformation to curvilinear coordinates followed by the LU-SGS factorization with the splitting (23) is performed, the operator D in eq. (21) is reduced to a diagonal form, and any matrix inversion is excluded from the algorithm (Ref.9).

It appears that this remarkable property is kept even in a general approach described above. This fact comes from the following property of the Jacobian matrix A, which is formulated for simliticity for a non-reacting one-component gas model in the following

Lemma. Let S be a closed surface in R^3, $\mathbf{n}=(n_1,n_2,n_3)$, $\mathbf{k}=(k_1,k_2,k_3)$, $\mathbf{l}=(l_1,l_2,l_3)$ are unit vectors of the orthonormal basis at S, where $\mathbf{n}$ is the exterior normal, and $\mathbf{k}$, $\mathbf{l}$ are tangential unit vectors to S. T_s is the transforming matrix associated with the basis:

$$T_s = \begin{vmatrix} 1 & 0 & 0 & 0 & 0 \\ 0 & n_1 & n_2 & n_3 & 0 \\ 0 & k_1 & k_2 & k_3 & 0 \\ 0 & l_1 & l_2 & l_3 & 0 \\ 0 & 0 & 0 & 0 & 1 \end{vmatrix} \tag{24}$$

$\mathbf{q}$ is the conservative solution vector, $\mathbf{Q}=T_s\mathbf{q}$, and $\mathbf{F}=\mathbf{F}(\mathbf{Q})$ is the local one-dimensinal inviscid flux associated with the basis.

Then, for any constant vector $\mathbf{q}$ the Jacobian matrix $A=\partial F/\partial Q$ satisfies the following identity:

$$\int_s T_s^{-1} A T_s ds \equiv 0 \tag{25}$$

Proof. The identity (25) comes from the conservative property of the inviscid flux:

$$\int_s f_m n_m ds \equiv 0 \tag{26}$$

From eq. (3) we can rewrite this as

$$\int_s T_s^{-1} F ds \equiv 0 \tag{27}$$

As $\mathbf{F}$ is the homogeneous function of degree one in $\mathbf{Q}$, one can substitute $\mathbf{F} = AQ = AT_s\mathbf{q}$ and obtain

$$\int_s T_s^{-1} A T_s \mathbf{q} ds \equiv 0 \tag{28}$$

from which (25) follows immediately.

It follows from the lemma that the matrix $\tilde{D}$ in (22) with the splitting (23) reduces to the diagonal matrix

$$\tilde{D} = 0.5\frac{\Delta t}{\omega}\sum_\sigma \rho_A I \tag{29}$$

for an arbitrary unstructured spatial discretization, and any matrix inversion is not required to solve the discrete equation (21) if S=0. For reacting gas flow, the Jacobian matrix of thermochemical source, S, needs to be inverted at each computational cell only.

3. Sphere model calculations

Calculations are performed for the flow around a sphere to simulate the experiments carried out at the K.H.I. (Ref.4). The radius of the sphere r_{sp} is 2cm. In these experiments, the heat transfer rate along the

sphere surface was measured for three cases of freestream conditions listed in Table I.

Table I

Case	A	B	C
V_∞, km/s	5.939	6.180	5.151
ρ_∞, kg/m^3	0.00156	0.0034	0.0058
T_∞, K	705	934	708
m.frac., N	0	0	0
m.frac., O	0.1708	0.1468	0.0406
m.frac., NO	0.0317	0.0429	0.0688
m.frac., N_2	0.762	0.744	0.733
m.frac., O_2	0.0348	0.0659	0.1578
M_∞	10.19	9.33	9.43
Re_∞	33535.6	64148.3	120641

A nonuniform grid consisting of 60 cells in the radial direction and 30 (60 in the case C) cells in the direction along the sphere surface is clustered in the boundary layer and characterized by a minimum cell size at the sphere wall, h_{min}, which is taken such that the cell Reynolds number at the wall varies from 1 to 3 depending on the calculations.

The total heat flux q_h is calculated by the summation of 3 contribution parts: translational temperature mode flux, vibrational temperature mode flux, and diffusion mode flux:

$$q_h = k\frac{\partial T}{\partial n} + k_v\frac{\partial T_v}{\partial n} + \rho\sum_{s=1}^{5} h_s D_s \frac{\partial Y_s}{\partial n} \qquad (30)$$

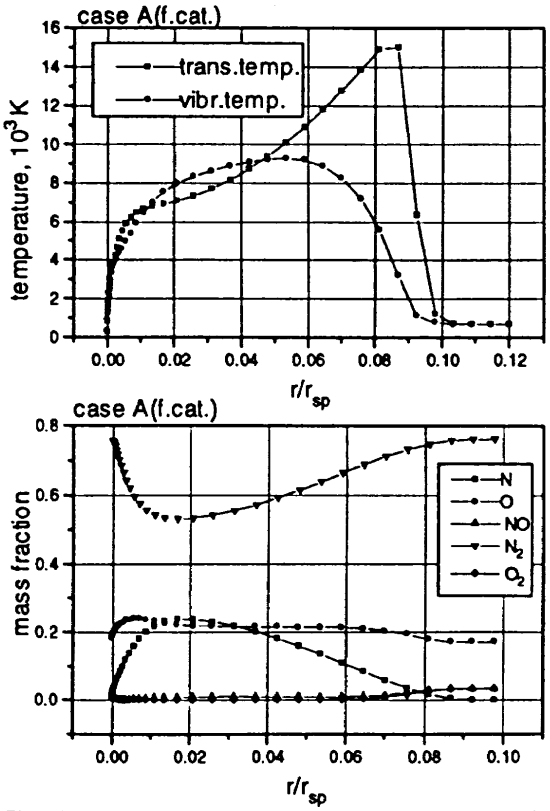

Fig.2 Case A: mass fraction and temperature along stagnation line

Both fully catalytic and non-catalytic boundary conditions are imposed at the wall, the temperature of which is assumed to be 300K for all cases.

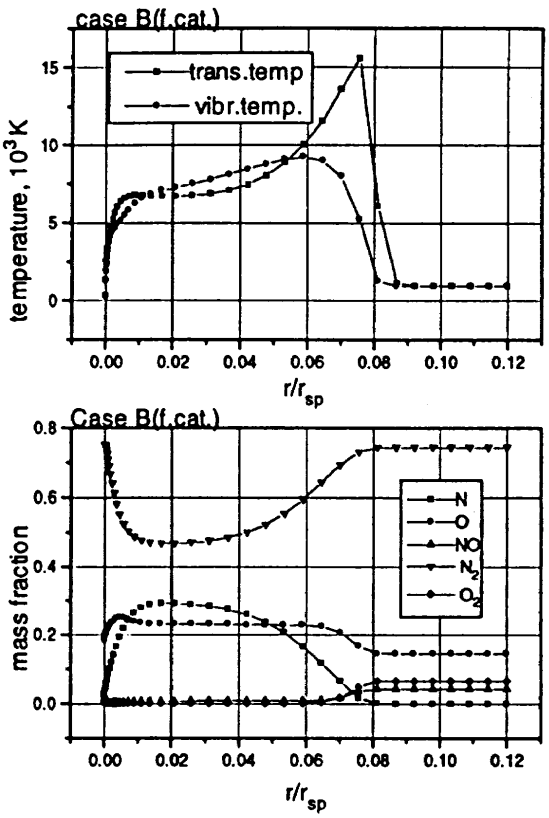

Fig.3 Case B: mass fraction and temperature along stagnation line

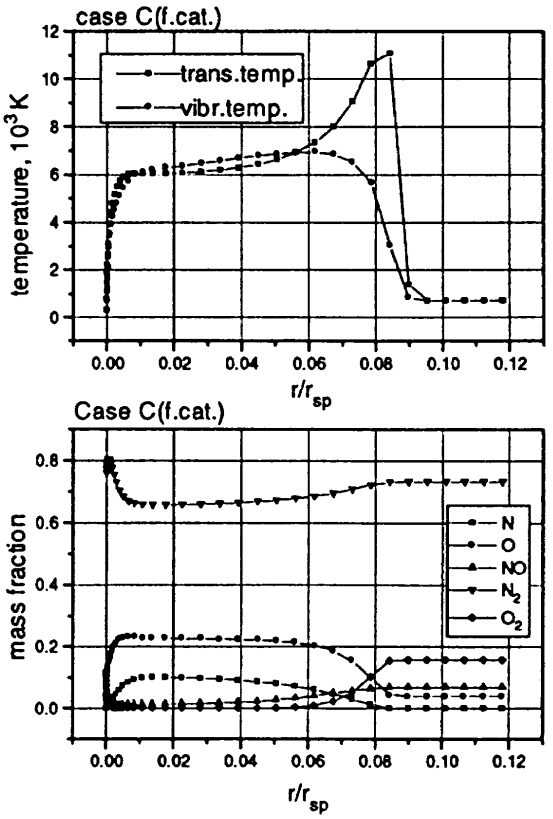

Fig.4 Case C: temperatura and mass fraction along stagnation line

Figures 2, 3, and 4 illustrate distributions of the translational/rotational and vibrational/electronic temperatures, and mass fractions of species along the stagnation streamline for the case A, B, and C, respectively, computed under the assumption that the wall surface is fully catalytic to chemical reactions. The

distance is calculated from the stagnation point and normalized with the radius of the sphere.

The translational/rotational temperature grows up abruptly at the shock wave, reaching a maximum value of approximately 15000K for the case A, 15600K for the case B, and 11100K for the case C. The vibrational/electronic mode does not change across the shock. As a result, a stretched zone is formed behind the shock where translational/rotational and vibrational/electronic modes are in non-equilibrium. Due to the relaxation process between these modes the vibrational/electronic temperature increases gradually, achieving its maximum value at the end of the relaxation process. This value is about 9200K for the cases A and B, and 7000K for the case C.

High temperature behind the shock wave initiates dissociation processes, which dissociate diatomic species (N_2, O_2, NO) and produce atomic species (N, O). This can be seen in mass fraction distributions of species (Figs.2, 3, and 4). Comparison of computed mass fractions with equilibrium composition of air under conditions obtained in the calculations show that the flow in the shock layer is mostly nonequilibrium. The equilibrium state is achieved near the wall only, where the species mass fractions tend to their freestream values due to fully catalytic boundary conditions.

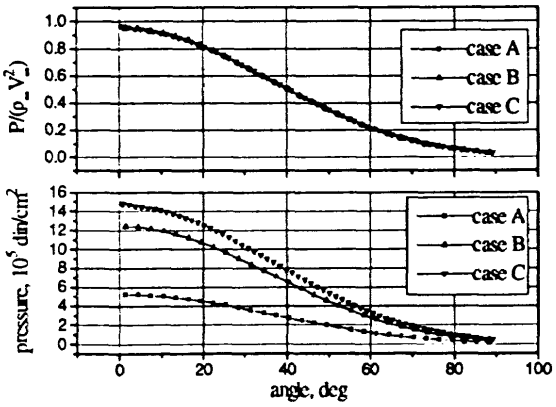

Fig.5 Pressure over sphere, f.cat. wall

The pressure distribution over the sphere surface is shown in Fig.5 for absolute values (lower graph) and normalized values (upper graph) for the case of fully catalytic case. One can see that the pressure normalized with the freestream density and velocity are in fact described by a unique curve for all cases. That is, this means a good correlation with the Newton-Busemann asymptotic theory.

The calculations with non-catalytic boundary conditions on the wall show no essential distinctions in comparison with fully catalytic wall cases in all flow parameters except for species mass fractions. Their distributions along the stagnation streamline are presented in Fig.6 for the cases A, B, and C.

The heat flux at the sphere surface with its contribution parts in translational/rotational, vibrational/electronic, and diffusion modes are shown in Figs. 7, 8, and 9 for the cases A, B, and C, respectively, for both fully catalytic and non-catalytic wall calculations. Here, we also give the experimental data obtained by the KHI (Ref.4).

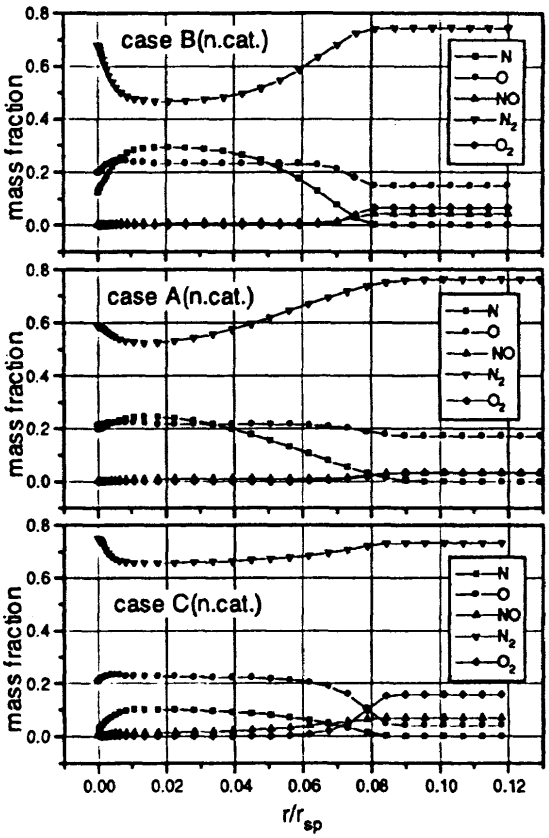

Fig.6 Non-catalytic wall: species mass fractions along the stagnation streamline

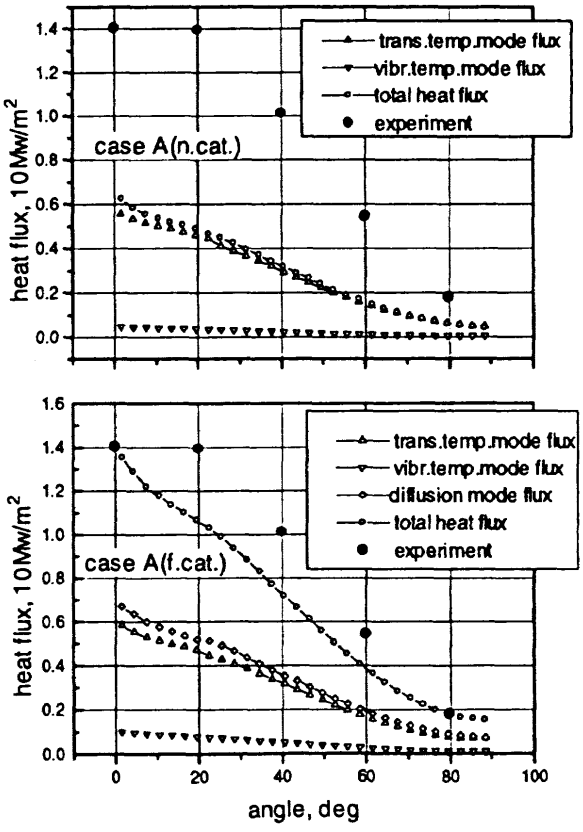

Fig.7 Case A: heat transfer rate at the wall

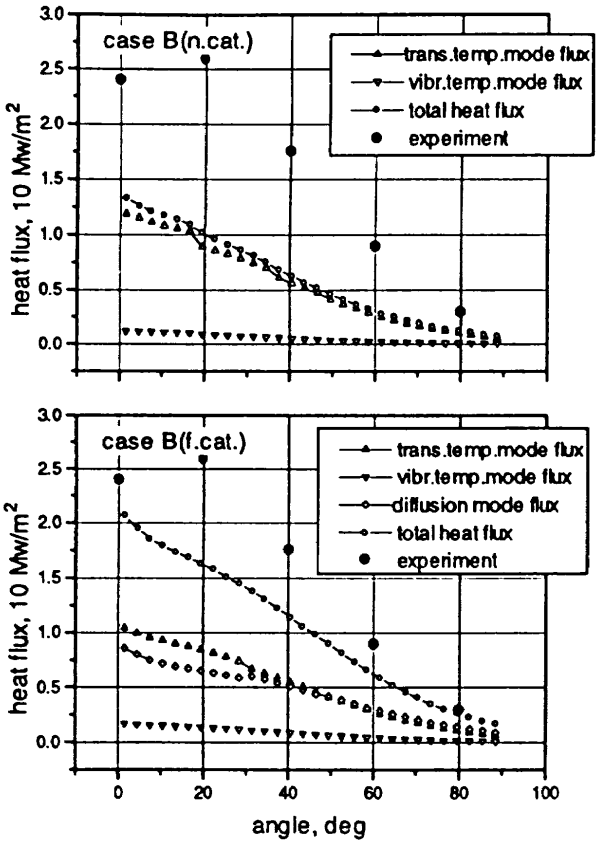

Fig.8 Case B: heat transfer rate at the wall

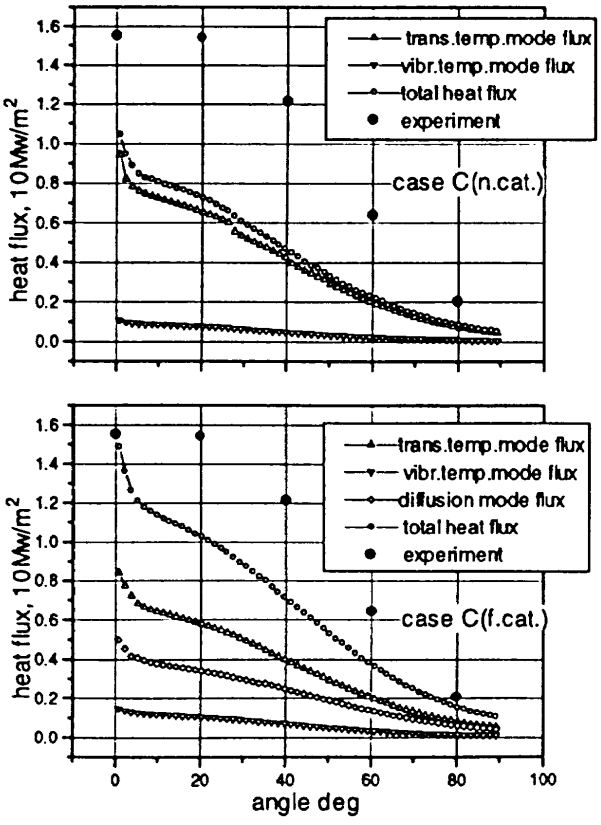

Fig.9 Case C: heat transfer rate at the wall

Main conclusions, which can be derived from the analysis of heat flux data, are made in the following. The contribution due to the convective flux in the vibrational/electronic mode is found to be considerably less that that in the translational/rotational and diffusion mode, and hence, the estimation of the corresponding dissipative coefficients seems to be of crucial importance in the prediction of heating characteristics. The heat fluxes obtained in calculations under non-catalytic wall boundary conditions are much deviated from the experimental data than those with fully catalytic wall surfaces. The latter differs from the experimental data within 20% for the cases A, and C and 40% for the case B. Especially for the case B, where even a non-monotonic profile of the heat flux over the sphere surface was observed (Fig.8), the maximum distinction in numerical and experimental data lies in a middle region, which corresponds to the angle between 20 and 40 degree. The reason for this is not clear now, but a hypothesis can be put forward that the transition to turbulent flow might happen in the boundary layer around here, leading to an increase of heat flux.

4. Blunt cone model calculations

A 140° blunt cone model with a cylindrical afterbody part (sting) utilized in many high enthalpy tunnel experiments (Refs.3, 21) is employed in the calculations described herein. The model consists of a) the forebody part I-II (Fig.10) in the form of a 140° spherically blunted cone with a base radius R_b of 7.62cm, and a nose radius R_n of 3.81cm, b) the back side of the forebody (the afterbody) II-III , and c) the cylindrical support (the sting) III-IV with a length L = 22.1cm and a diameter D = 1.91cm.

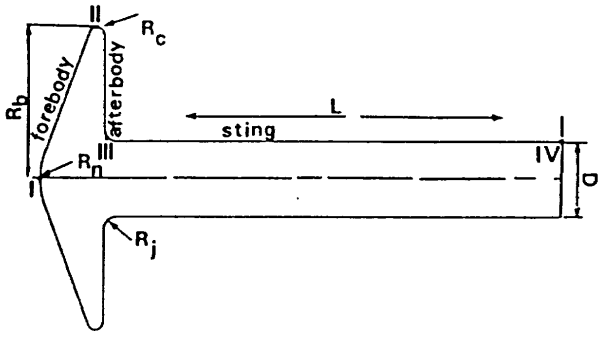

Fig.10 Geometry of blunt cone model

The forebody and the afterbody are smoothly joined by a circumference with a radius R_c of 0.382cm. The sting is connected with the afterbody through a junction radius R_j of 0.635cm.

The calculations have been performed for the freestream conditions listed below:

pressure:	$p_\infty = 5785.2 \mathrm{dyn/cm^2}$
density:	$\rho_\infty = 4.085*10^{-6} \mathrm{g/cm^3}$
velocity:	$v_\infty = 4.5395*10^5 \mathrm{cm/s}$
temperature:	$T_\infty = 489.89 \mathrm{K}$
Mach number:	$M_\infty = 10.19$
Reynolds number:	$Re_\infty = 3.79*10^5$

where the Reynolds number is based on the base diameter $2R_b$.

These parameters correspond to the test No132 in a series of high enthalpy flow experiments recently carried out at the HEG of the DLR (Ref.2), where the heat transfer rate along the blunt cone model was measured with fast response surface thermocouples on the forebody and sensitive thin film heat transfer gauges on the sting. The test No132 was implemented with a special system designed by NASA for high spatial resolution of the heat transfer on the model surface, where the model was instrumented with 113 sensors mostly located on the sting.

Air in the freestream is considered to consist of oxygen and nitrogen with the molar concentrations of 0.21 and 0.79, respectively.

The calculations are carried out with a non-uniform grid greatly clustered in the boundary layer. The grid consists of 65 cells in the direction away from the body and 160 cells in the direction along the model surface. The wall cell Reynolds number defined as $Re_{cell} = Re\,\Delta h_w / R_b$, where Δh_w is the normal spacing at the wall, is equal to 2.37 . It is expected that this is sufficient to achieve grid convergence at least in terms of heat flux distribution (Ref. 17).

At the wall surface, the vibrational/electronic temperature is assumed to be equal to the given wall temperature of 295K. The wall surface is assumed to be fully catalytic to chemical reactions.

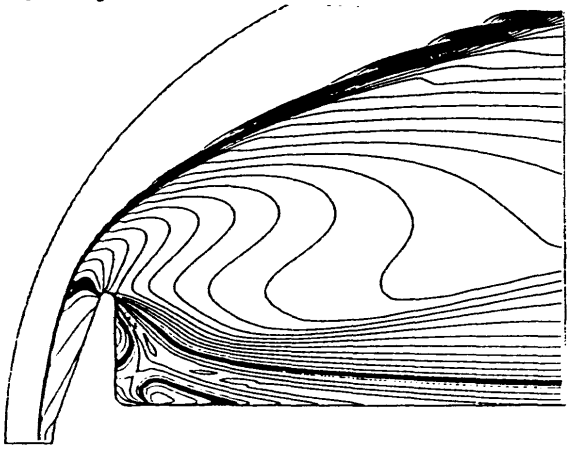

Fig.11 Mach number contours

The Mach number contours are shown in Fig.11 with a contour line increment of 0.2, where sonic lines are singled out by bold lines. It can be seen that the flow accelerates at the edge, turning toward the sting, and then separates from the wall near the edge on the afterbody. It leads to formation of a recompression shock and a zone with strong recirculation flow. The recompression shock has a small angle of about 20° with the centerline. It does not have a good resolution due to a coarse grid used in this part of the wake. Nevertheless the reattachment point and the position of the shock can be identified. The recirculation zone has a complicated structure characterized by two closed supersonic zones located on the sting and on the afterbody near the separation point.

The flow in this zone is characterized by an extensive vortex, the center of which is strongly shifted toward the separation point as shown in Fig.12 where vorticity contours are presented.

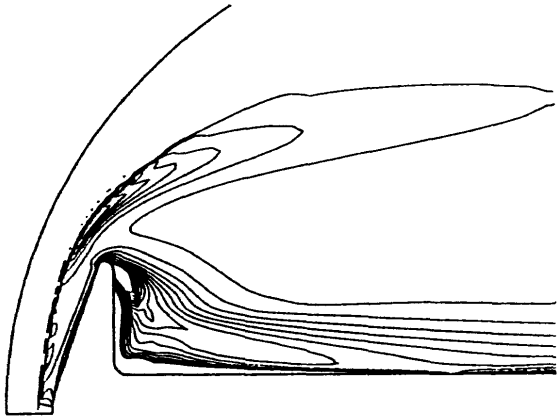

Fig.12 Vorticity contours

The following discriptions are associated with the heat transfer q_w and the pressure p_w on the model surface. The total heat transfer is calculated by the summation of 3 contribution parts: the translational temperature mode flux, the vibrational temperature mode flux, and the diffusion mode heat flux.

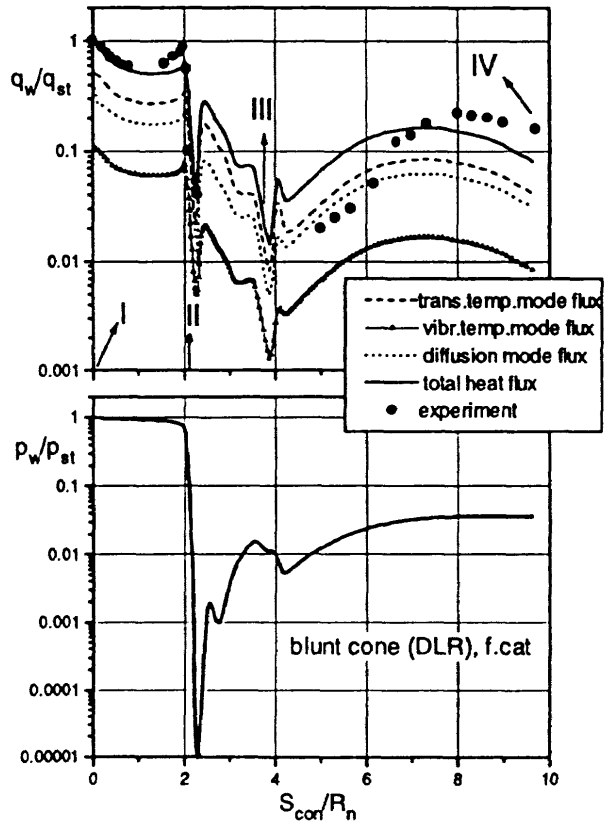

Fig.13 Normalized heat flux and pressure along the body contours

Figure 13 illustrates normalized heat flux with each contribution part and pressure along the model surface. Here, the solid symbols were obtained from the test No132 in the set of experiments performed at the HEG of the DLR (Ref.3).

The data are normalized by the stagnation point heat flux and pressure, which were found to be $q_{st} = 3.64 MW/m^2$ and $p_{st} = 8.08*10^5 din/cm^2$, respectively. The horizontal axis is the distance along the model contour S_{con} (measured from the stagnation point) normalized by the base radius R_b.

It can be seen that the numerical data are in good agreement with the experimental data except for the values near the edge of the forebody. The experiment data show a rise of heat flux at the edge up to 90% of the stagnation point value, while it is 64% in the calculations. The heat flux on the afterbody (II-III, Fig.13) abruptly drops at the edge, and suddenly rises on the upper part of the afterbody reaching the value of about 30% of the stagnation point value. This unexpected effect might be caused by the presence of a supersonic zone close to upper afterbody (Fig.11), where gas tends to come to the wall, forming a high intensity vortex around the separation point (Fig.12).

The numerical model predicts a local heat load peak on the sting (III-IV, Fig.13) caused by the compression of the flow in the shear layer with a formation of a recompression shock in the near wake. However, in comparison with the experimental data it turns out to be about 20% less, slightly shifted towards the afterbody, and spatially stretched. This might be due to a coarse grid used in this region of the wake, leading to insufficient accuracy in resolution for the recompression shock with a reattachment point.

As in the sphere calculations described above, the contribution due to the convective flux in the vibrational-electronic temperature mode is found to be considerably less than that in the translational-rotational temperature mode and the diffusion mode, which confirms that estimations of the corresponding dissipative coefficients seems to be very important in heat transfer rate predictions.

5. Summary

A numerical model for the calculation of thermochemical nonequilibrium air flows has been applied to simulate the experiments with a sphere model and a blunted cone model carried out by the KHI and the DLR, respectively. For the calculations with the blunted cone model, main features as separation of the flow, recompression shock with a reattachment point, and a recirculation zone were obtained. It was found that the recirculation zone is characterized by a vortex shifted strongly towards the separation point with two supersonic zones.

Despite good qualitative agreement with experimental data, the heat transfer obtained with the numerical model turned out to be underpredicted in comparison with the experimental data at the middle part of the sphere (20%-40%) in the sphere model calculations, and at the edge of the forebody (30% less) and in the peak value on the sting (20% less) in the blunted cone model calculations. It was also found that an abrupt heating rise on the upper part of the afterbody (blunted cone case) reaches 30% of the stagnation point value.

Acknowledgment. This work was supported in part by Grants N8Q300 and JBR100 from the ISF.

References

[1]Fay J.A., Riddel, F.R., Theory of stagnation point heat transfer in dissociated air, J. Aero. Sci., V.25, No2, 1958, pp.73-85.

[2] Anderson L.A., Effect of surface catalytic activity on stagnation heat transfer rates, AIAA J., V.11, 1973, pp.649-656.

[3]Kastell, D., Horvath, T.J., Eitelberg, G., Nonequilibrium flow expansion experiment around a blunted cone, 1995 (some conference proceeding).

[4]Kishimoto T., Hanamitsu A., Bitoh H., High enthalpy flow computation and experiment around the simple bodies, presented at High Enthalpy Flow Workshop, June 1995, NAL (Japan).

[5]Park, C., Assessment of Two-Temperature Kinetic Model for Ionizing Air, AIAA-87-1574, June 1987.

[6]Park, C., and Yoon, S., Fully Coupled Implicit Method for Thermochemical Nonequilibrium Air at Suborbital Flight Speeds, Jour. of Spacecraft, 1991, v.28, No1, pp.31-39

[7]Men'shov I.S., and Nakamura Y., An Implicit Advection Upwind Splitting Scheme for Hypersonic Air Flows in Thermochemical Nonequilibrium, in: A Collection of Technical Papers of 6th Int.Symp.on CFD, Lake Tahoe, Nevada, 1995, v.II, pp.815-821.

[8]Liou, M.-S., Steffen, C.J., A New Flux Splitting Scheme, J. Comp. Phys., 107, 1993, pp.23-39.

[9]Yoon S., Jameson A., Lower-Upper Symmetric-Gauss-Seidel Method for the Euler and Navier-Stokes Equations, AIAA Journal, 1988, v.26, No9, 1025-1026.

[10]Gnoffo, P.A., Gupta, R.N., Shinn, J.L., Conservation Equations and Physical Models for Hypersonic Air Flows in Thermal and Chemical Nonequilibrium, NASA Tech. Pap., 2867, 1989.

[11]Park, C., Nonequilibrium Hypersonic Aerothermodynamics, 1989.

[12]Lee, J.-H., Basic Governing Equations for the Flight Regimes of Aeroassisted Orbital Transfer Vehicles, Prog. Astr. Aeron., 96, 1984, pp.3-54.

[13]White, F.M., Viscous Fluid Flow, McGraw-Hill Book Comp., 1974, pp.27-36.

[14]Vincenti, W.G., Kruger, C.H., Introduction to Physical Gas Dynamics, Krieger Publ.Comp., 1993, pp.197-245.

[15]Park, C., Convergence of Computation of Chemical Reacting Flows, Prog. Astr. Aeron., 103, 1986, pp.478-513.

[16]Men'shov, I.S., Nakamura Y., Numerical Study of an Implicit AUSM with Application to Hypersonic Flows, Proc.8th Int. Conf. on CFD, Tokyo, Dec.1994, pp13-16.

[17]Men'shov, I.S., Nakamura Y., Numerical Simulation of Nonequilibrium Air Flow over Spheres, in: Proc.27th Fluid Dynamics Conf., Gifu, Japan, 1995, 169-172.

[18]Liou, M.-S., B.v Leer, Shuen, J.S., Splitting of Inviscid Fluxes for Real Gases, J.Comp.Phys., 1990, v.87, pp.1-24.

[19]Wada , Y., and Liou, M.-S., A Flux Splitting Scheme with High-Resolution and Robustnees for Discontinuities, AIAA Paper 94-0083, Jan.1994.

[20]Liou, M.-S., Progress Towards an Improved CFD Method:AUSM, AIAA Paper 95-1701, Jun.1995.

[21]Stewart, D.A., Chen, Y.K., Convective heat transfer rate distributions over a 140^0 blunt cone at hypersonic speeds in different gas environments, 1993, AIAA paper No 93-2787.

[22]Jameson, A., Yoon, S., Lower-Upper Implicit Schemes with Multiple Grids for the Euler Equations, AIAA J., 25, 7, 1987, pp.929-935.

2-2

High Enthalpy Flow Workshop

Problem II-1 OREX Configuration

Ichiro NAKAMORI* and Yoshiaki NAKAMURA†

Dept. of Aerospace Engineering, Nagoya University

In this computation, an upwind method with MUSCL type extrapolation was applied to nonequilibrium chemical reacting hypersonic flow around an orbital re-entry experimental (OREX) configuration. The flow solver employed in this computation is based on Steger and Warming's[1] flux-vector splitting (FVS), and classified as a variation of the advection upstream splitting method (AUSM)[4]. It has been confirmed that the present scheme has many good characteristics in the ideal gas flow such as monotonicity for shock wave, robustness for expansion wave, and high resolution for contact discontinuity and shear layer. In order to extend the present scheme to a chemical reacting flow, we used Park's two temperature model for 5 neutral species(N, O, NO, O_2, N_2) with 17 chemical reaction, and the finite volume formulation was employed to discretize the axisymmetric Navier-Stokes equations.

Nomenclature

c	= speed of sound
e	= internal energy per unit volume
E	= total energy per unit volume
e_v	= vibrational energy per unit volume
F	= inviscid flux vector
G	= viscous flux vector
H	= thermochemical source
H	= total enthalpy
p	= pressure
q	= solution vector
u, v, w	= Cartesian velocity components
x, y, z	= Cartesian coordinates
λ	= eigenvalue
ρ	= density
Superscript	
$\pm$	= positive and negative flux contributions
Subscript	
L	= left hand side of the cell interface
R	= right hand side of the cell interface
s	= species

Introduction

We computed a hypersonic flow around OREX configuration under the following assumptions:

free stream velocity: 7450m/s
free stream pressure: 0.169N/m^2
free stream temperature: 186.9K;
the mass fraction of species in free stream:
N_2-79%, O_2-21%.

Moreover, we assumed the flow is laminar and chemically and thermally nonequilibrium. The wall temperature was fixed at 540K. In order to take the thermal nonequilibrium into account, we employed Park's two temperature model, where the translational-rotational modes have the translational temperature, while the vibrational mode has the vibrational temperature. In this study, a 5-species and 17-chemical reaction model is used:

$$O_2 + M \leftrightarrow O + O + M, \quad M = N, NO, O, N_2, O_2$$
$$N_2 + M \leftrightarrow N + N + M, \quad M = N, NO, O, N_2, O_2$$
$$NO + M \leftrightarrow N + O + M, \quad M = N, NO, O, N_2, O_2$$
$$O + NO \leftrightarrow N + O_2,$$
$$O + N_2 \leftrightarrow N + NO.$$

The numerical method is based upon the modified Flux-Vector Splitting to estimate the cell-interface inviscid fluxes, and the Lower-Upper Symmetric Gauss-Siedel (LU-SGS) factorization[6,7] was utilized for the time integration to efficiently solve the system equations in Δ-form.

Governing Equations

A nonequilibrium chemical reacting flow has the system of governing equations with the physical model, which is expressed in the following form:

*Graduate student
†Professor, Aerospace Engineering

$$\frac{\partial \mathbf{q}}{\partial t}+\frac{\partial \mathbf{F}_i}{\partial x_i}=\frac{\partial \mathbf{G}_i}{\partial x_i}+\mathbf{H} \tag{1}$$

where

$$\mathbf{q}=\begin{bmatrix}\rho\\ \rho u\\ \rho v\\ \rho w\\ E\\ \rho_1\\ \vdots\\ \rho_n\\ e_v\end{bmatrix},\ \mathbf{F}_i=\begin{bmatrix}\rho u_i\\ \rho u_1u_i+\delta_{1,i}p\\ \rho u_2u_i+\delta_{2,i}p\\ \rho u_3u_i+\delta_{3,i}p\\ (E+p)u_i\\ \rho_1u_i\\ \vdots\\ \rho_nu_i\\ e_vu_i\end{bmatrix},\ \mathbf{G}_i=\begin{bmatrix}0\\ \tau_{i,1}\\ \tau_{i,2}\\ \tau_{i,3}\\ \tau_{e,i}\\ \rho D_1\frac{\partial \chi_1}{\partial x_i}\\ \vdots\\ \rho D_n\frac{\partial \chi_n}{\partial x_i}\\ \tau_{v,i}\end{bmatrix},\ \mathbf{H}=\begin{bmatrix}0\\ 0\\ 0\\ 0\\ 0\\ H_1\\ \vdots\\ H_n\\ H_v\end{bmatrix}$$

$$E=e+\frac{1}{2}\rho\left(u_1^2+u_2^2+u_2^2\right),$$

and

$$p=p(\rho,e,\rho_1,\ldots,\rho_n,) \tag{2}$$

the solution vector **q** consists of the total density ρ, the momentum components in x, y, and z directions:ρu, ρv, ρw, the total energy E, the species density ρ_s, and the vibrational energy e_v. D_s, X_s, and H_s denote the diffusion coefficients, the mole fraction, and source terms, respectively. These equations include the internal energy e, which can be expressed as the sum of translational-rotational energy e_T and vibrational energy e_v, which are given as

$$e_T=\sum_s \rho_s e_{T_s} \tag{3}$$

$$e_v=\sum_s \rho_s e_{v_s} \tag{4}$$

Numerical Method

Inviscid flux evaluation

The inviscid flux vector in the x direction of the Cartesian coordinates is written as

$$\mathbf{F}=\left[\rho u,\ \rho u^2+p,\ \rho uv,\ \rho uw,\ \rho uH,\ \rho_1 u,\ \cdots,\ \rho_n u,\ e_v u\right]^t \tag{5}$$

where H is the total enthalpy:

$$H=(e+p)/\rho \tag{6}$$

We first describe the cell-interface mass flux formula[8,9], because other fluxes are constructed based upon it. We define the cell-interface mass flux following the FVS formulas for the ideal gas flow, which is given as

$$(\rho u)_{i+1/2}=\left(\rho_L\tilde{\lambda}_1^+ +\rho_R\tilde{\lambda}_1^-\right)+\frac{p_L}{\tilde{c}_L^2}\left(-2\tilde{\lambda}_1^+ +\tilde{\lambda}_2^+ +\tilde{\lambda}_3^+\right)_L +\frac{p_R}{\tilde{c}_R^2}\left(-2\tilde{\lambda}_1^- +\tilde{\lambda}_2^- +\tilde{\lambda}_3^-\right)_R \tag{7}$$

It has been pointed out that FVS schemes[1,2,3] generally produce excessive numerical dissipation for contact discontinuity and shear layer. In order to eliminate such dissipation, we separated pressure contributions from the cell-interface mass flux, because there is no difference of pressure across the contact discontinuity. Then, we introduced the virtual speed of sound instead of the local speed of sound, which is expressed as

$$\begin{aligned}\tilde{c}_L&=c_mK+c_L(1-K)\\ \tilde{c}_R&=c_mK+c_R(1-K)\end{aligned} \tag{8}$$

where

$$c_m=\frac{c_L+c_R}{2} \tag{9}$$

and

$$K=min(p_L,p_R)/max(p_L,p_R) \tag{10}$$

Moreover, the eigenvalues employed in this formula are defined as the polynomials of Mach number, which is redefined by using the virtual speed of sound $\tilde{c}$.

$$\tilde{\lambda}_1^{\pm}=\frac{1}{2}\tilde{c}\left(\tilde{M}\pm\left|\tilde{M}\right|\right) \tag{11a}$$

$$\tilde{\lambda}_2^{\pm}=\begin{cases}\tilde{c}\left[\alpha^{\pm}+\beta^{\pm}\right] & if\ \left|\tilde{M}\right|\le 1\\ \frac{1}{2}\tilde{c}\left(\tilde{M}+1+\left|\tilde{M}+1\right|\right) & othewise\end{cases} \tag{11b}$$

$$\tilde{\lambda}_3^{\pm}=\begin{cases}\tilde{c}\left[\alpha^{\pm}-\beta^{\pm}\right] & if\ \left|\tilde{M}\right|\le 1\\ \frac{1}{2}\tilde{c}\left(\tilde{M}-1+\left|\tilde{M}-1\right|\right) & othewise\end{cases} \tag{11c}$$

where

$$\tilde{M}=\frac{u}{\tilde{c}} \tag{12}$$

and

$$\alpha^{\pm}=\pm\frac{1}{8}\left(\tilde{M}\pm 1\right)^2\left(\tilde{M}^2\mp 2\tilde{M}+3\right) \tag{13}$$

$$\beta^{\pm}=\frac{1}{4}\left(\tilde{M}\pm 1\right)^2\left(2\mp\tilde{M}\right) \tag{14}$$

$\alpha^{\pm}$ and $\beta^{\pm}$ are defined so as to satisfy the restriction of the compatible conditions, which are given as

$$\alpha^+ +\alpha^- =\tilde{M} \tag{15}$$

and

$$\beta^+ +\beta^- =1 \tag{16}$$

These expressions can be extended to nonequilibrium gas flow on the assumption that a speed of sound c is calculated from the eigenvalues included in the Jacobian matrices. As a result, th speed of sound employed in this solver is equivalent to an appropriate frozen speed of sound.

Then, the interface momentum flux can be also expressed by the FVS formula, which is given as

$$\left(\rho u^2+p\right)_{i+1/2}=\tilde{F}_{1,L}^+u_L+\tilde{F}_{1,R}^-u_R +\frac{1}{2}\left[\left(\tilde{\lambda}_2^+ -\tilde{\lambda}_3^+\right)\frac{p_L}{\tilde{c}_L}+\left(\tilde{\lambda}_2^- -\tilde{\lambda}_3^-\right)\frac{p_R}{\tilde{c}_R}\right] \tag{17}$$

where

$$\tilde{F}_1^{\pm} = \rho\,\tilde{\lambda}_1^{+} + \frac{p}{\tilde{c}^2}\left(-2\tilde{\lambda}_1^{\pm} + \tilde{\lambda}_2^{\pm} + \tilde{\lambda}_3^{\pm}\right) \tag{18}$$

To prevent the scheme from having some difficulties at the stagnation point, $\tilde{\lambda}_1$ would be redefined as

$$\tilde{\lambda}_1^{\pm} = \begin{cases} \frac{1}{2}\tilde{c}\left(\tilde{M} \pm \left|\tilde{M}\right|\right) & \text{if } \left|\tilde{M}\right| \geq \varepsilon \\ \frac{1}{2\varepsilon}\tilde{c}\left(\tilde{M} \pm \varepsilon\right)^2 & \text{otherwise} \end{cases} \tag{19}$$

where

$$\varepsilon = 0.2\frac{min(p_L, p_R)}{max(p_L, p_R)} \tag{20}$$

ε is a small empirical value depending on the pressure gradient. However, this modification results in dissipative solution for the stationary contact discontinuity. Then, for the practical use, density was calculated with the upstream values as follows:

$$\begin{aligned} &\tilde{\rho}_L = \rho_L,\ \tilde{\rho}_R = \rho_L && \text{if } \left|\tilde{M}\right| \leq \varepsilon \text{ and } u_{i+1/2} \geq 0 \\ &\tilde{\rho}_L = \rho_R,\ \tilde{\rho}_R = \rho_R && \text{if } \left|\tilde{M}\right| \leq \varepsilon \text{ and } u_{i+1/2} < 0 \\ &\tilde{\rho}_L = \rho_L,\ \tilde{\rho}_R = \rho_R && \text{otherwise} \end{aligned} \tag{21}$$

Then, we utilized the advection upstream splitting method(AUSM)[4,5] for tangential momentum fluxes, energy flux, species mass flux, and vibrational energy flux, which are expressed according to the sign of the cell-interface mass flux previously obtained. The fluxes are written as

$$(\rho uv)_{i+1/2} = \frac{1}{2}(\rho u)_{i+1/2}(v_L + v_R) - \frac{1}{2}\left|(\rho u)_{i+1/2}\right|(v_R - v_L) \tag{22}$$

$$(\rho uw)_{i+1/2} = \frac{1}{2}(\rho u)_{i+1/2}(w_L + w_R) - \frac{1}{2}\left|(\rho u)_{i+1/2}\right|(w_R - w_L) \tag{23}$$

$$(\rho uv)_{i+1/2} = \frac{1}{2}(\rho u)_{i+1/2}(H_L + H_R) - \frac{1}{2}\left|(\rho u)_{i+1/2}\right|(H_R - H_L) \tag{24}$$

$$(\rho uv)_{i+1/2} = \frac{1}{2}(\rho u)_{i+1/2}(e_{v_L} + e_{v_R}) - \frac{1}{2}\left|(\rho u)_{i+1/2}\right|(e_{v_R} - e_{v_L}) \tag{22}$$

A piecewise linear interpolation was used with a minimum-modulus (minmod) TVD limiter in such a way that these inviscid fluxes have the second-order accuracy in space.

Transport Coefficients

In order to evaluate the transport coefficients, we use Yos's formulas based upon Chapman-Enskog's first approximation. To simplify the estimation of the collision integral in Yos's formulas, we invoke Chapman-Cowling's formulas for viscosity and diffusion coefficients with Wilke's empirical formulas. Comparing these formulas with Yos's one, a compact expression is available for the collision integral, leading to the easily computed expression for the transport coefficients.

Translational Vibrational Energy Relaxation

In this study, the relaxation model introduced by Landau and Teller for the vibrational-electronic excitation energy was employed, where the relaxation time can be calculated in Millikan-White's[14] empirical correlation with Park's[10] correction at high temperature.

Numerical Results

To verify the calculation method mentioned above, we computed the flow field around OREX configuration, whose diameter is 6.8m. Figure 1 shows the grid system of 32×64, where the minimum value of $\Delta\eta$ is 1×10^{-4} near the wall. The OREX configuration has the following flight conditions :

free stream velocity: 7450m/s;
free stream temperature: 186.9K;
free stream pressure: 0.169N/m^2;
mass fraction of species in free stream:
N_2-79%, O_2-21%.

These data were employed at the High Enthalpy Flow Workshop. In addition, the body surface temperature was fixed at 540K along with the assumption of a non-catalytic wall. Steady solutions were calculated with the residual reduced by three order of magnitude from the initial one. Figures 2-6 show pressure, translational-rotational temperature, and vibrational temperature contours along with the mole fraction of species, translational-rotational temperature and vibrational temperature profiles along the stagnation stream line. The present scheme can capture a strong shock wave with no oscillation in the fields of pressure, translational-rotational temperature, vibrational temperature, and mole fraction of species. It should be noted that the present scheme does not need the special procedure to protect the numerical oscillation of the bow shock wave near the stagnation stream line, called the carbuncle phenomenon[4].

Figures 7 and 8 show pressure and heat flux distributions along the body surface. The heat flux at the stagnation was 41.6kW/m^2. These value must be verified by comparing with the experimental data, because it is difficult to estimate the heat flux distribution on the body surface.

Conclusion

In the present study, an improved Flux-Vector Splitting method was applied to a nonequilibrium chemical reacting hypersonic flow around OREX configuration selected at the High Enthalpy Flow Workshop. The results show the validity of the numerical method in shock capturing, monotonicity, and robustness. Further comparison between numerical solution and experimental data is required.

Acknowledgment

We would like to acknowledge to Dr. I. S. Men'shov for his help to compute a chemical reacting flow.

References

(1) Steger, J. L. and Warming, R. F., "Flux Vector Splitting of the Inviscid Gasdynamic Equations with Application to Finite Difference Methods," *J. Comput. Phys.*, Vol. 40, 1981, pp. 263-293.

(2) Van Leer, B., "Flux–Vector Splittings for the Euler Equations," Lecture Notes in Physics, Vol. 170, 1982, pp. 507–512.

(3) Hänel, D. and Schwance, "An Implicit Flux–Vector Splitting Scheme for the Computation of Viscous Hypersonic Flow," AIAA Paper 89–0274, 1989.

(4) Liou, M. S. and Steffen, C. J., "A New Flux Splitting Scheme," *J. Comput. Phys.* Vol. 107, 1993, pp. 23-39.

(5) Wada, Y. and Liou, M. S., "A Flux Splitting Scheme With High–Resolution and Robustness for Dis-continuities," NASA TM 106452, 1994.

(6) Jameson, A. and Yoon, S., "Lower-Upper Implicit Schemes with Multiple Grids for the Euler Equations," *AIAA Journal*, Vol. 25, 1987, pp. 929-935.

(7) Jameson, A. and Turkel, E., "Implicit Schemes and LU Decompositions," *Math. of Comput.* 37, pp. 385-397, 1981.

(8) Nakamori, I. and Nakamura, Y., "An Upwind Scheme Based on the Flux-Vector Splitting," AIAA Paper 95-0471, 1995.

(9) Nakamori, I. and Nakamura, Y., "An Upwind Scheme for the Inviscid and Viscous Hypersonic Flow," AIAA Paper 95-1732, 1995.

(10) Park, C., "Assessment of Two-Temperature Kinetic Model for Ionizing Air," AIAA Paper 87-1574, 1987

(11) Gnoffo, P. A., Gupta, R. N., and Shinn, J. L., "Conservation Equations and Physical Models for Hypersonic Air Flows in Thermal and Chemical Nonequilibrium," NASA TP 2867, 1989.

(12) Hornung, H. G. and Wen C.-Y.,"Nonequilibrium Dissociating Flow over Spheres," AIAA Paper 95-0091, 1995.

(13) Rock, S. G. and Tramel, R. W., "A Three-Dimensional Thermo-Chemical Nonequilibrium Chimera Flow Solver for Moving Grids, Part I:Steady State," AIAA Paper 95-0151, 1995.

(14) Millikan, R. C. and White, D. R.,"Systematics of Vibrational Relaxation," *J. Chem. Phys.*, 39, pp. 3209-3213, 1963.

(15) White, F. M., "Viscous Fluid Flow," McGraw-Hill Book Company, pp. 27-36, 1974.

(16) Vincenti, W. G. and Kruger, C. H.,"Introduction to Physical Gas Dynamics," Krieger Pub. Company, pp. 197-245, 1993.

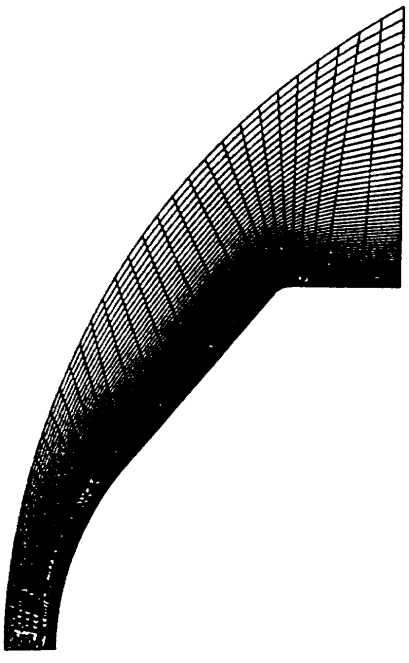

Figure 1 Grid configuration: 32×64

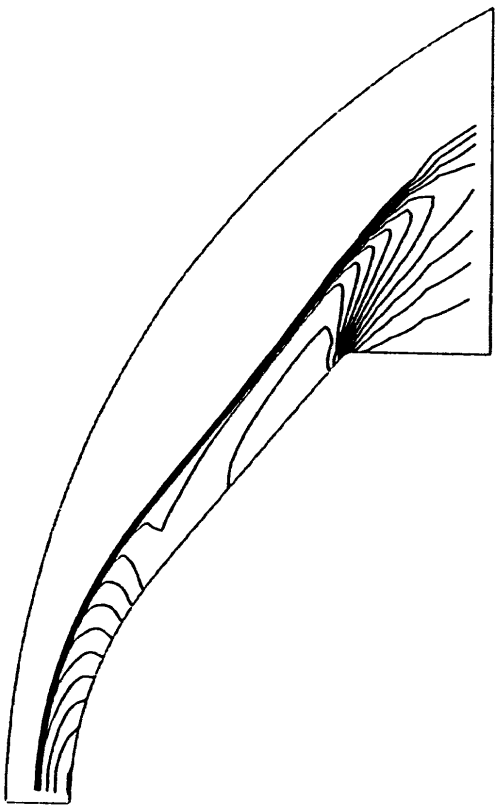

Figure 2 Pressure contours.

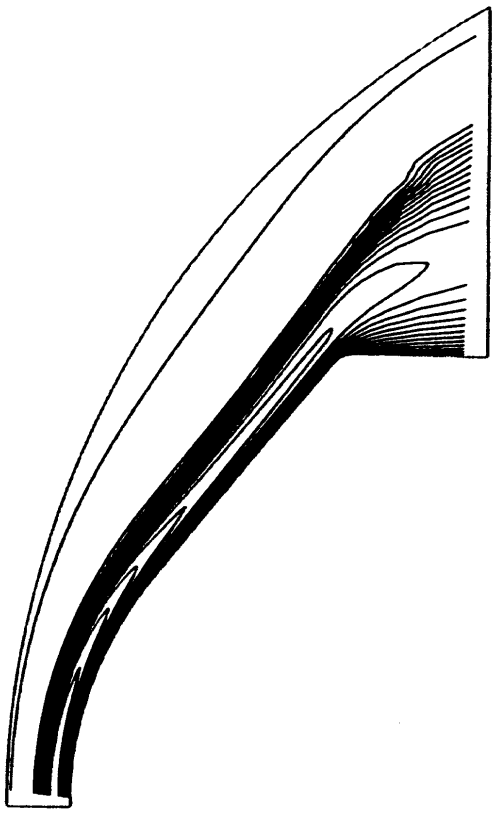

Figure 4 Vibrational temperature contours.

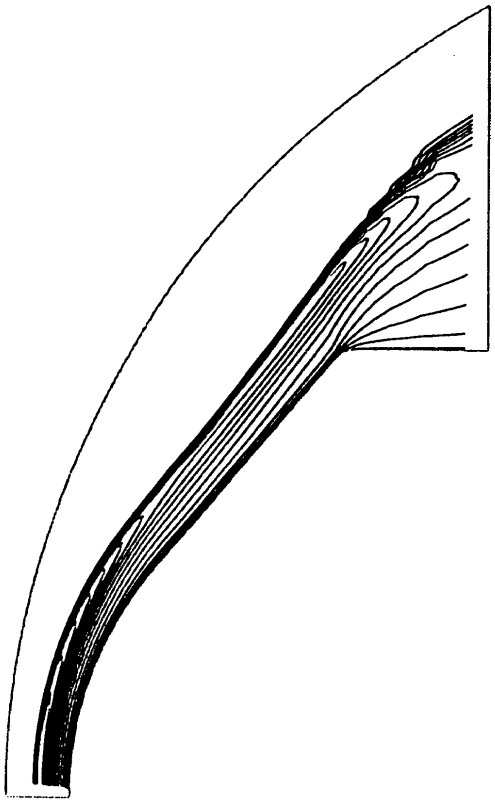

Figure 3 Translational temperature contours.

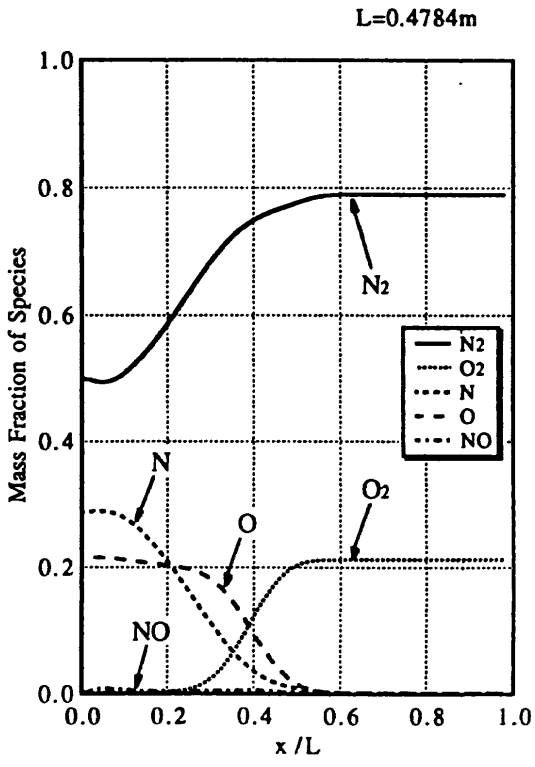

Figure 5 Mass fraction of species distributions along the stagnation stream line.

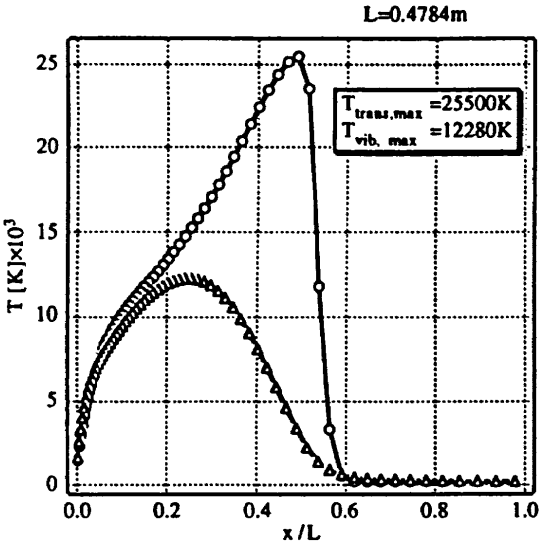

Figure 6 Translational and vibrational temperature distributions along the stagnation stream line.

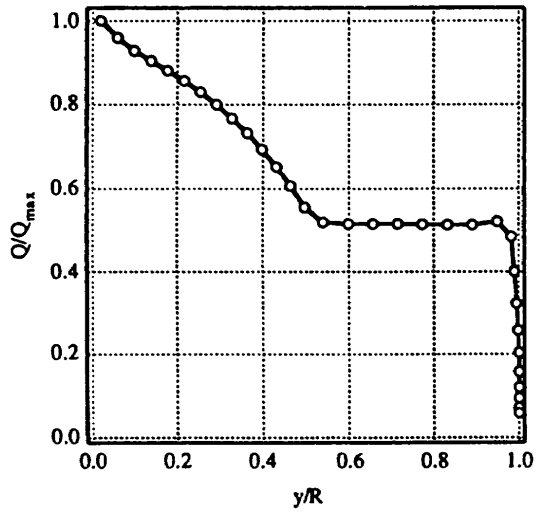

Figure 7 Heat flux distributions along the body surface.

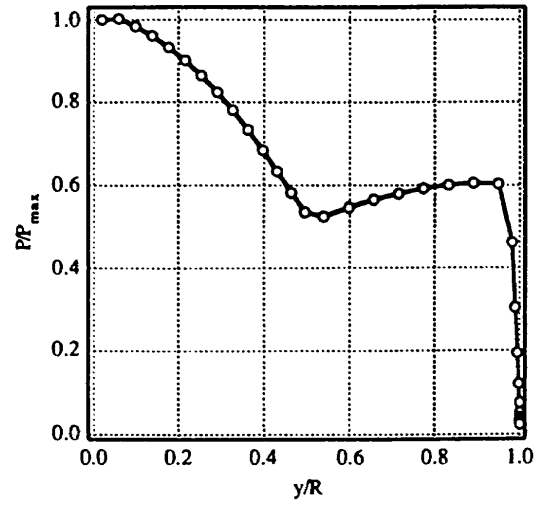

Figure 8 Pressure distributions along the body surface.

2-3

Numerical Analysis of Thermochemical Nonequilibrium Hypersonic Flow around Blunt Body

Takuji KUROTAKI
Kamakura Works, Mitsubishi Electric Corporation, Kamakura, Japan

Abstract

Numerical analyses of chemically and thermally nonequilibrium hypersonic flow around a blunt body are carried out. Several types of flow; Problem I (Sphere cases), Problem II. 1-3 (Orex cases) and Problem IV. 1-2 (Spherically Blunted Cone cases) specified in the "High Enthalpy Flow Workshop" are investigated.

Axisymmetric full Navier-Stokes equations which have chemically and thermally nonequilibrium effects are considered by using Park's two-temperature model and the vibrational relaxation model from the SSH theory. For the time integration, an efficient numerical algorithm of an implicit finite difference method is used, which consists of the combination of LU-SGS scheme and the implicit diagonal method for a source Jacobian matrix. For convective terms, AUSMDV scheme generalized into the nonequilibrium flow case is applied.

Some numerical results of each flow cases are presented and discussed. All cases indicate that the flow inside the shock layer is in strong nonequilibrium and very complex real gas effects are observed. It is shown that fairly reasonable results can be obtained with both numerical methods and physical models applied here. However, numerical results of some cases indicate that more careful analyses and comparison with experimental results are necessary in order to clarify the more complex flow structures in the back flow region.

1. Introduction

When designing reentry vehicles such as capsules or space shuttle-type space planes, it is important to predict the very severe aerodynamic heating around the body at an high altitude. However, it is almost impossible now to get all the solutions from only wind tunnel experiments since their flight is at high Mach number and the temperature inside the shock layer usually becomes very high. Therefore, numerical analysis is a hopeful approach and it is now becoming a main tool to get information of the flow at real flight conditions.

Because the flow contains the strong shock wave, the numerical scheme should be the one with high resolution and robustness for discontinuities. Furthermore, the presence of real gas effects such as dissociation or ionization etc. in these flight regime complicates the flow characteristics drastically and even the influence of chemical and thermal nonequilibrium should be sometimes considered. Therefore, careful validation of both the numerical scheme and the physical models are necessary.

In this paper, the numerical methods and physical models applied in the analyses of the problem specified in the "High Enthalpy Flow Workshop" are mentioned and several numerical examples of the results are presented and discussed. The flow cases analyzed in this study are Problem I (Sphere cases), Problem II. 1-3 (Orex cases) and Problem IV. 1-2 (Spherically Blunted Cone cases).

2. Governing Equations and Numerical Methods

We consider axisymmetric full Navier-Stokes equations as governing equations. Air is assumed to have 7 species (O_2, N_2, O, N, NO, NO^+, e^-) and steady and laminar flow is considered for all cases.

In order to include thermal-chemical nonequilibrium effects in numerical analyses, Park's two-temperature model is used [1]. In this model, an assumption that the translational and rotational energy modes are in equilibrium at the translational temperature T, while the vibrational, electronic and electron-translational modes are in equilibrium at the vibrational temperature Tv, is employed.

The governing equations under these assumptions in the Cartesian coordinate system are

$$\frac{\partial Q}{\partial t} + \frac{\partial}{\partial x}(E - E_v) + \frac{\partial}{\partial y}(F - F_v) + \alpha H = S + \alpha H_v , \quad (1)$$

where

$$\alpha = \begin{cases} 0 & \text{for a two-dimensional flow} \\ 1 & \text{for an axisymmetric flow} \end{cases} , \quad (2)$$

$$Q = \begin{bmatrix} \rho u \\ \rho v \\ E_t \\ E_{vib}+E_e \\ \rho_s \end{bmatrix}, E = \begin{bmatrix} \rho u^2 + p \\ \rho uv \\ u(E_t + p) \\ u(E_{vib}+E_e) \\ \rho_s u \end{bmatrix}, F = \begin{bmatrix} \rho uv \\ \rho v^2 + p \\ v(E_t + p) \\ v(E_{vib}+E_e) \\ \rho_s v \end{bmatrix} \quad (3)$$

and the vector E_v and F_v are a set of elements of viscous

terms in the ξ and η-direction respectively. The vector S is a set of elements of source terms. H and H_v are a set of elements of convective and viscous terms respectively added only when the flow is axisymmetric. In eq. (3), the quantities ρ, p, E_t, E_{vib} and E_e denote density, pressure, the total energy per unit volume, the vibrational energy per unit volume and the electronic energy per unit volume respectively. The quantities u and v are velocity components. The subscript "s" denotes a species of air.

For chemical reaction rates, the model proposed by Park is used, and the forward reaction rate is assumed to be the function of $\sqrt{T\,T_v}$ and the following twenty-four chemical reactions are assumed,

(1) $O_2+M \rightleftarrows O+O+M$, $M = O_2, N_2, O, N, NO, NO^+, e^-$

(2) $N_2+M \rightleftarrows N+N+M$, $M = O_2, N_2, O, N, NO, NO^+, e^-$

(3) $NO+M \rightleftarrows N+O+M$, $M = O_2, N_2, O, N, NO, NO^+, e^-$

(4) $O+NO \rightleftarrows N+O_2$

(5) $O+N_2 \rightleftarrows N+NO$

(6) $O+N \rightleftarrows NO^+ + e^-$.

Transport properties such as viscosity, thermal conductivity and diffusion coefficients are calculated from the kinetic theory described in [1], [2].

The governing equations (1) is solved by a finite difference method after non-dimensionalized and transformed into the general coordinate system. In this study, the implicit formulation is used and Lower-upper symmetric Gauss-Seidel (LU-SGS) scheme [3] is applied for the time integration of the system. In this scheme, no matrices need not be inverted and, especially for the use of a parallel computer, very high efficiency can be achieved since it can be completely vectorizable. Some difficulties arise, however, when LU-SGS scheme is directly applied to the flow with finite-rate chemistry because coefficient matrices include a Jacobian matrix of source vector S which is dense. In order to avoid these difficulties, the diagonal implicit method [4] is applied in which the Jacobian matrix of S is approximated to a diagonal matrix whose elements are the function of characteristic time for chemical reactions [4, 5].

Since the hypersonic flow, in general, contains very strong shock wave systems, the numerical scheme with high resolution and robustness should be used for the evaluation of convective terms . Most of such high resolution schemes are categorized as Flux Difference Splitting (FDS) or Finite Vector Splitting (FVS). Roe scheme is one of the most popular one among FDS schemes, however it has a serious problem, so-called "carbuncle phenomenon", in capturing a strong shock around a stagnation region. FVS schemes are more robust in multi-dimensional calculations but they are too dissipative in shear layers such as boundary layers to apply for Navier-Stokes flow analyses.

Recently, some new approaches to develop less dissipative upwind schemes are reported, in which the large dissipation of FVS is reduced by introducing the flavor of FDS into FVS schemes. One of examples of them is Advection Upstream Splitting Method (AUSM) and some variations of it are reported [6].

In this study, AUSMDV proposed by Wada and Liou [6] is applied after being generalized into nonequilibrium flow cases. This scheme is mixture of AUSMD-type (flux-difference-splitting-biased) schemes and AUSMV-type (flux-vector-splitting-biased) ones and is recognized as an improved AUSM scheme because numerical overshoot immediately behind the shock is removed. In order to remove the carbuncle phenomenon in calculating the flow which contains a very strong shock in front of the stagnation region, their approach is also applied, in which Hänel's FVS scheme is used only immediately after the shock wave.

3. Physical Models for Vibrational Relaxation Time

In order to include thermal nonequilibrium effects in the numerical analyses, the following vibrational relaxation term which appears in the vibrational-electronic energy equation plays an important role,

$$\frac{\overline{E_{vib,s}} - E_{vib,s}}{\tau_{s,q}} \qquad (4)$$

where $E_{vib,s}$ is the vibrational energy of molecule s per unit volume, $\tau_{s,q}$ is a vibrational relaxation time of molecule s colliding with a chemical species q and " $\bar{}$ " denotes that the quantity is in thermal equilibrium.

Usually a semi empirical law proposed by Millikan and White based on the the Landau-Teller theory is used in order to calculate $\tau_{s,q}$,

$$p\tau_{s,q} = \exp\left[1.16\times10^{-3}\mu_{s,q}^{1/2}\theta_{v,s}^{4/3}\left(T^{-1/3} - 0.015\mu_{s,q}^{1/4}\right) - 18.42\right] \qquad (5)$$

where p is pressure in atmospheres, $m_{s,q}$ is reduced mass in grams and $\theta_{v,s}$ is vibrational characteristic temperature of molecule s. However, it is well known that this model underestimates $\tau_{s,q}$ when translational temperature is more than about 8,000 K since this model neglects the collision frequency and $\tau_{s,q}$ loses even physical meaning at a certain temperature as it becomes smaller than the collision time.

In this study, the another model from the SSH theory proposed by Schwartz, Slawsky and Herzfeld [7, 8] in 1950's is applied to evaluate $\tau_{s,q}$. Under the assumptions that the molecule is a harmonic oscillator and only monoquantum transition of vibrational energy modes is allowed, $\tau_{s,q}$ is expressed as,

$$1/\tau_{s,q} = Z_{col}^{sq} P_{10}(A_s, A_q)\left[1 - \exp\left(-\theta_{v,s}/T\right)\right] \qquad (6)$$

where Z^{sq}_{coll} is collision frequency of molecule s with a chemical species q, $P_{10}(A_s, A_q)$ is transition probability in which vibrational energy level changes from 1 to 0. Furthermore, transition probability $P_{10}(A_s, A_q)$ in the SSH theory has the following form,

$$P_{10}(A_s, A_q) = A / (Z^s_0 \; Z^s_v \; Z^{sq}_T \; Z^{sq}_+) \qquad (7)$$

where A is a collision cross-reference factor, Z^s_0 is a steric factor, Z^s_v is a vibrational factor, Z^{sq}_T is a translational factor and Z^{sq}_+ is a factor from the attractive force.

Figure 1 and 2 show τ_{O_2,O_2} for O_2-O_2 collision and τ_{N_2,N_2} for N_2-N_2 collision respectively from both the Landau-Teller type model and the model from the SSH theory. There is clearly a difference between these models at very high translational temperature more than about 10,000K. Although the model from the SSH theory can reasonably predict a vibrational relaxation time at high temperature for molecule-molecule collision, it is reported that there is often disagreement between the result from this model and experimental data for molecule-atom collision such as O_2-O or N_2-O collision [8]. For these cases, the following semi empirical equations are used under the assumption that the relaxation times have the same temperature dependency as that in eq. (6),

$$p\,\tau_{O_2,O} = T^{2/3} \exp(33.4\,T^{-1/3} - 24.98)$$

$$p\,\tau_{N_2,O} = T^{2/3} \exp(49.7\,T^{-1/3} - 22.55).$$

Figure 3 shows $\tau_{O_2,O}$ and $\tau_{N_2,N}$ for both the Landau-Teller type model and the model from the SSH theory. For other relaxation times, we made the following assumptions,

$$p\,\tau_{NO,NO} = T^{2/3} \exp(75.6\,T^{-1/3} - 27.63)$$

$$p\,\tau_{O_2,N} = p\,\tau_{O_2,O}\;,\; p\,\tau_{N_2,N} = p\,\tau_{N_2,O} \qquad (9)$$

$$p\,\tau_{NO,s} = p\,\tau_{NO,NO} \quad (s = O_2, N_2, O, N, NO^+).$$

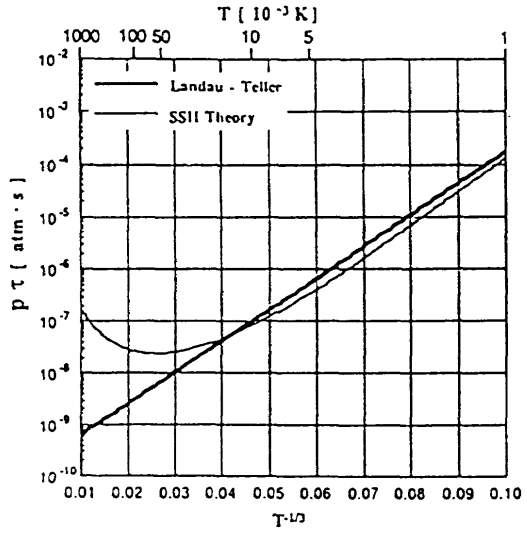

Fig.1 Relaxation time τ_{O_2,O_2} for O_2-O_2 collision

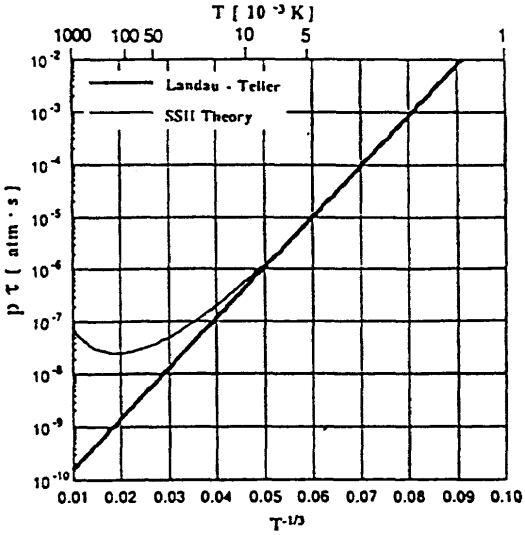

Fig.2 Relaxation time τ_{N_2,N_2} for N_2-N_2 collision

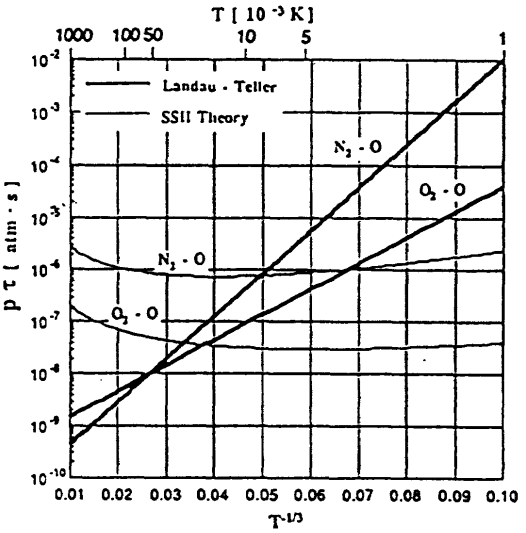

Fig.3 Relaxation time $\tau_{O_2,O}$ for O_2-O collision and $\tau_{N_2,N}$ for N_2-N collision

4. Wall Boundary Conditions

In this study, the gradient of pressure perpendicular to the wall is assumed to be zero, and for velocities and translational temperature, no slip boundary condition is applied along the wall. The wall vibrational temperature T_{v_w} is assumed to be the same as the translational temperature T_w at the wall which is specified in each flow cases.

The treatment of densities of each chemical species depends on whether the wall is catalytic or non-catalytic. When the wall is non-catalytic, the gradient of mass fraction of each species s perpendicular to the wall is assumed to be zero;

$$\frac{\partial c_s}{\partial \eta} = 0 \qquad (10)$$

where c_s is a mass fraction of a chemical species s, and η is coordinates perpendicular to the wall.

When the wall is catalytic, all O and N atoms colliding with the wall are assumed to become O_2 and N_2 molecules respectively through the recombination process at the wall, while for other species such as NO, NO^+, e^-, the wall is assumed to be non-catalytic and eq. (10) is applied. At so-called "p-plane" which is one mean-free path away from the wall, the mass flux of N atoms, for example, is expressed as using the Fick's law,

$$-k_N\rho_N = -\rho D_N\frac{\partial c_N}{\partial \eta}, \quad +k_N\rho_N = -\rho D_{N_2}\frac{\partial c_{N_2}}{\partial \eta} \qquad (11)$$

where k_s is catalytic velocity ($= \gamma\sqrt{kT_w/(2\pi m_s)}$), γ is catalytic efficiency, k is Boltzmann constant, m_s is a mass of one particle of a species s and D is a diffusion coefficient. By discretizing eq. (11) and under the assumption that $\rho_N = 0$ at the wall, we can get the expression of density of N_2 molecules at the wall in the following form,

$$\rho_{N_2,w} = \left(\rho_{N_2,j=2} + \frac{D_N}{D_{N_2}}\rho_{N,j=2}\right)\frac{\rho_w}{\rho_{j=2}} \qquad (12)$$

where the subscript "j = 2" denotes that the property is at the grid point next to the wall.

5. Numerical Results and Discussions

Figure 4. (a) - (d) show grid systems used in this study. The number of grid points is 81 in ξ-direction (along the body) and 81 in η-direction (perpendicular to the body) for Problem I and II and 161×131 for Problem IV. An algebraic method is applied to generate all grid systems.

So-called "Cell Reynolds number" at the wall around the stagnation region for each cases are determined after preliminary analyses and the quantity 0.2 for Problem I and II.1, 2.0 for Problem II.2 and II.3 and 1.0 for Problem IV are used. These preliminary calculations show that we should be very careful to determine a grid interval in η-direction at the wall especially for the case in which the wall temperature is low since this interval has a great influence on the heat flux at the wall even for such a sophisticated scheme as AUSMDV applied in this study.

Figure 5. (a) - (c) show the temperature distribution for Problem I.1, I.3 and I.5 respectively. These translational temperature distribution shown on the upper side are almost the same, while the vibrational temperature distribution shown on the under side depends on the free stream density condition. For the case in which the free stream density is relatively high such as Problem I.5, the vibrational temperature distribution become to resemble the translational one since the flow in the shock layer approaches the thermal equilibrium.

The heat flux Q along the wall for all cases of Problem I are shown in Figure 6, 7 and 8. The maximum heat flux at the stagnation point of a catalytic wall case is about 1.5 times higher than that of a non-catalytic case.

Figure 9 and 10 show the examples of results for Problem II.1 whose free stream conditions are corresponding to a flight at a very high altitude. The pressure distribution in Figure 9 and the translational and the vibrational temperature distribution along the stagnation streamline in Figure 10 indicate that the shock wave is thick and the flow inside the shock layer is in strong nonequilibrium.

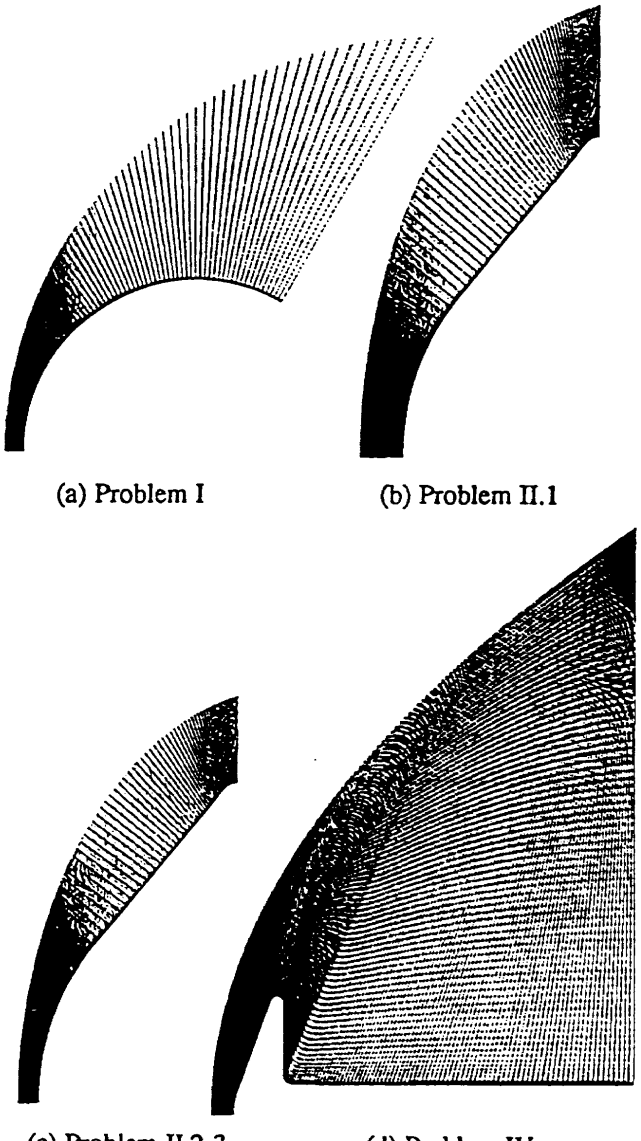

(a) Problem I (b) Problem II.1

(c) Problem II.2-3 (d) Problem IV

Fig.4 Mesh system

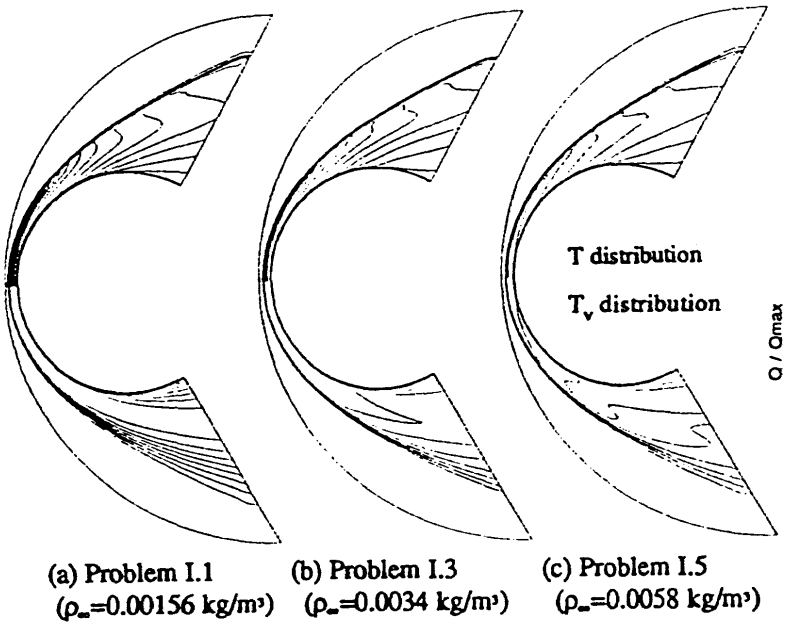

Fig. 5 Temperature distribution for Problem I

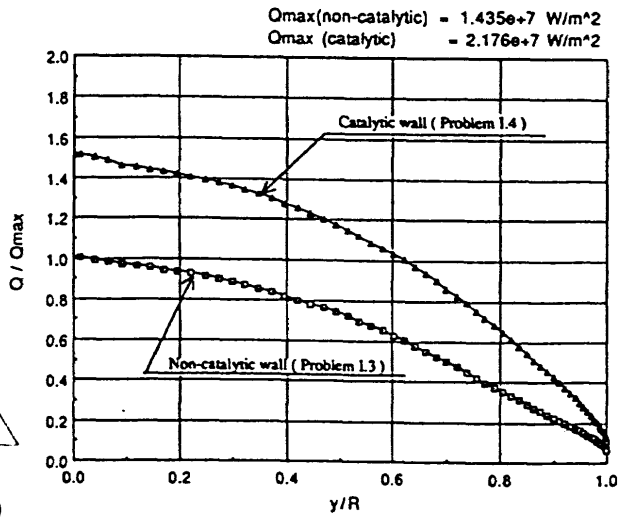

Fig. 7 Heat flux distribution for Problem I.3 and 4

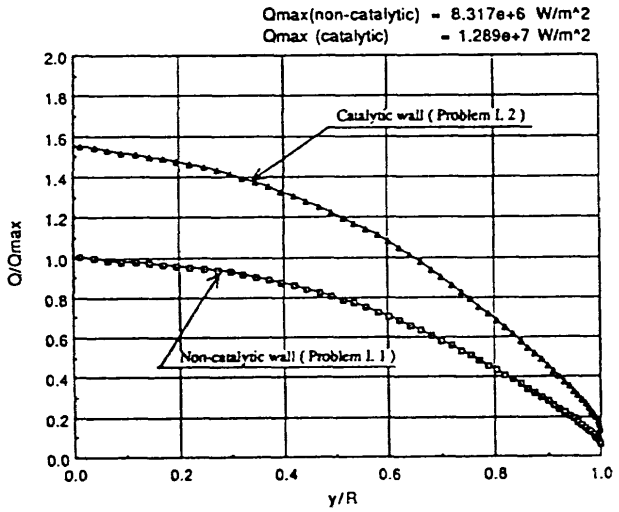

Fig. 6 Heat flux distribution for Problem I.1 and 2

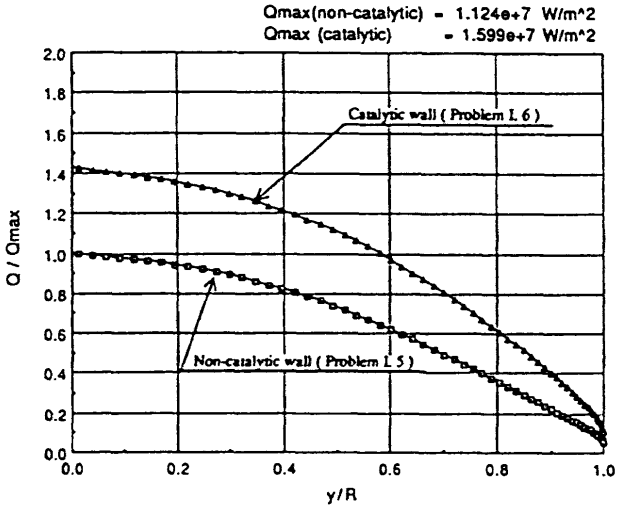

Fig. 8 Heat flux distribution for Problem I.5 and 6

Figure 11 shows the translational temperature distribution for Problem II.2. Since the altitude corresponding to the free stream conditions for this problem is lower than the one for Problem II.1 and the free stream density and pressure are relatively high, very sharp shock wave is captured. A comparison of the heat flux distribution along the wall for the non-catalytic (Problem II.2) and the catalytic (Problem II.3) case in Figure 12 shows that the stagnation heat flux of a catalytic wall case is about 1.8 times higher than that of a non-catalytic wall

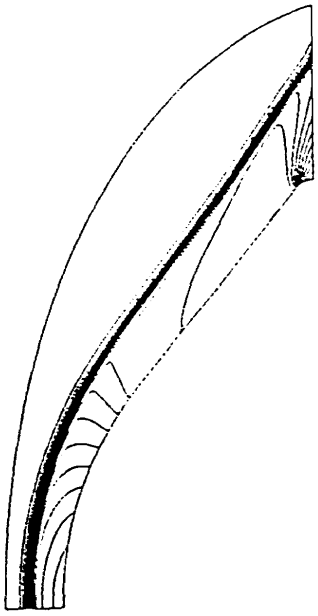

Fig. 9 Pressure distribution for Problem II.1

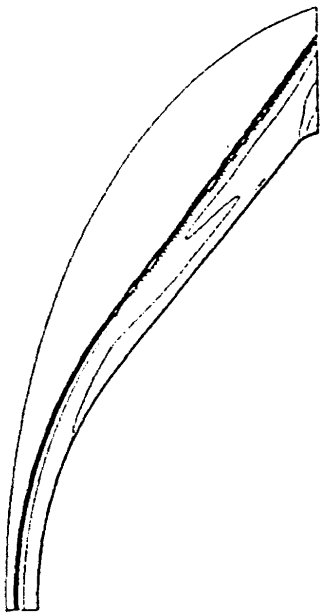

Fig. 11 Translational temperature distribution for Problem II.2 (T_{max} = 1.32 ×10^4 K)

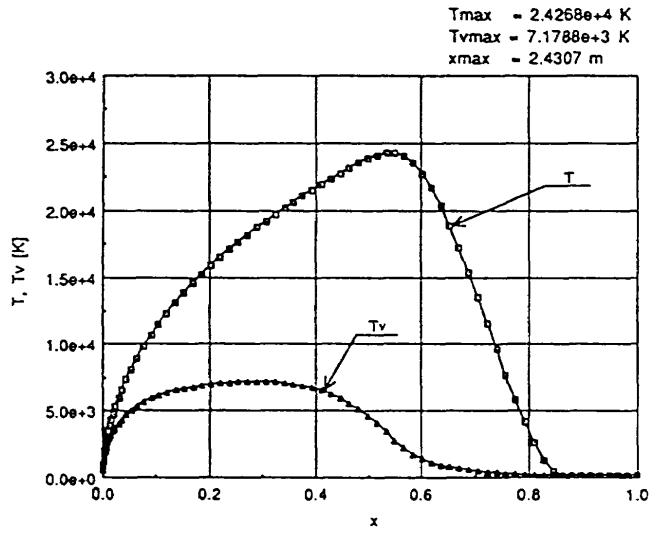

Fig.10 Translational and vibrational temperature distribution along the stagnation streamline for Problem II.1

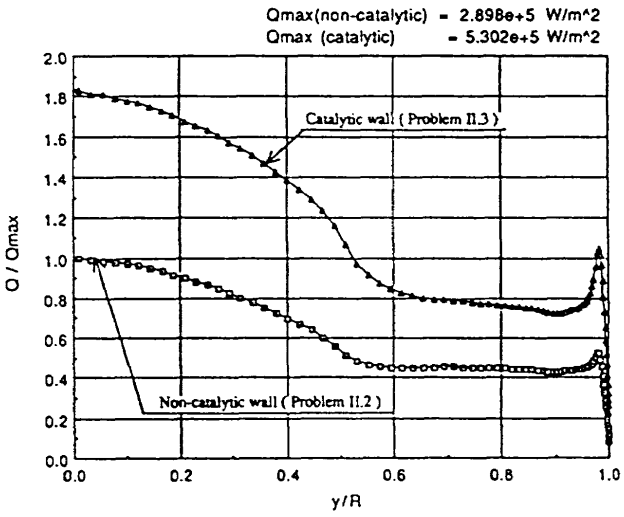

Fig. 12 Heat flux distribution for Problem II.2

case.

Problem IV is a very challenging case for a numerical analysis since both the very strong non-equilibrium shock layer around the forebody and the very complicated flow structures around the afterbody must be captured. Especially, the latter include the rapid expansion at the shoulder, the separation of the flow on the backside of the body, the shear layer and the recompression shock in the back flow region, which are now becoming to be main subjects of research in hypersonic aerodynamics.

Figure 13 and 14 are the translational and vibrational temperature distribution for Problem IV.1 respectively. They clearly show these flow characteristics mentioned above. More careful observation of the numerical results indicates that the flow in the recirculation zone becomes supersonic of about Mach 2, therefore, the shock appears at the corner just after the body.

Figure 15 and 16 show the heat flux distribution along the wall for the non-catalytic (Problem IV.1) and catalytic wall case (Problem IV.2) respectively. The small disturbance of the heat flux just after the body observed in both cases also indicates the existence of the shock in the recirculation zone. However, the increase of the heat flux after the reattachment point (where x / L is about 0.6) is not so high as expected. More careful analyses and comparison with experimental results are necessary in order to determine whether this is real physical phenomenon or caused by some numerical errors such as mesh intervals or physical models applied here.

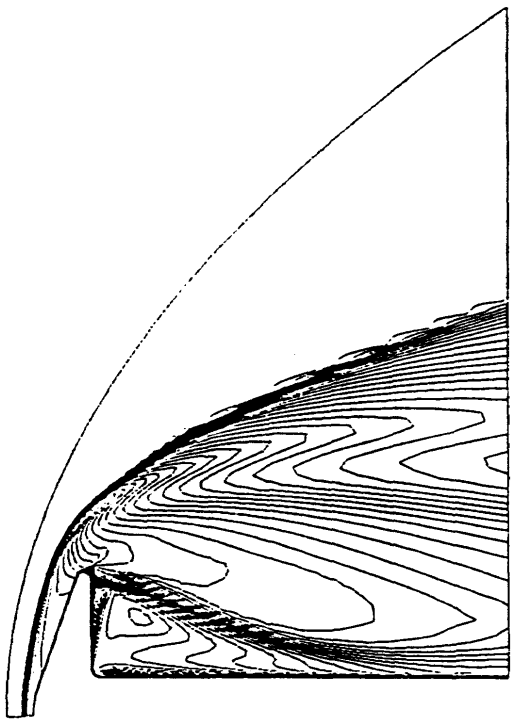

Fig.14 Vibrational temperature distribution for Problem IV.1 (T_{vmax} = 6.26 ×10^3 K)

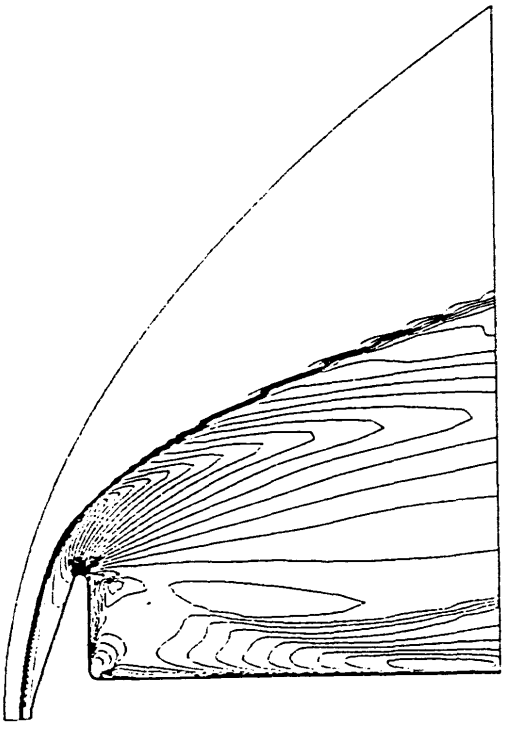

Fig. 13 Translational temperature distribution for Problem IV.1 (T_{max} = 9.20 ×10^3 K)

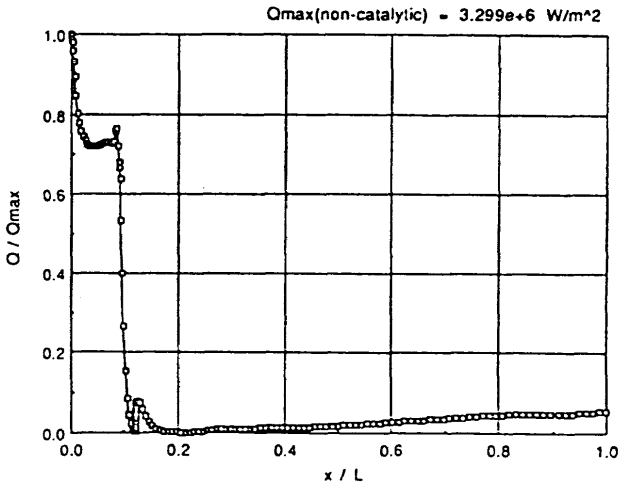

Fig 15 Heat flux distribution for Problem IV.1 (Non-catalytic wall case)

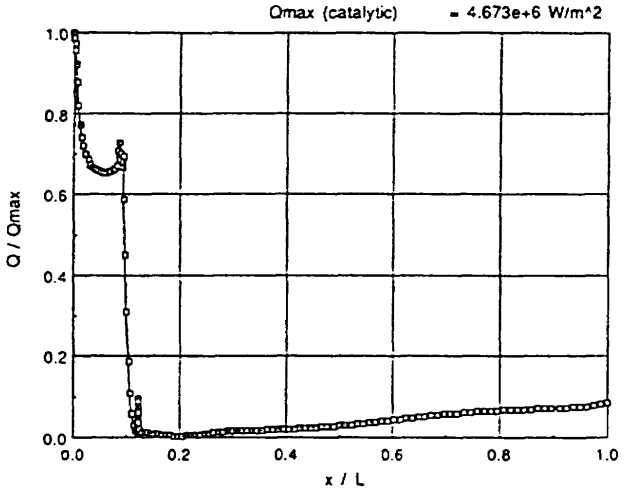

Fig 16 Heat flux distribution for Problem IV.2
(Catalytic wall case)

6. Conclusion

In this paper, brief outlines of physical assumptions and numerical methods applied to calculate several non-equilibrium hypersonic flows are mentioned and some numerical results of them are presented and discussed.

Axisymmetric full Navier-Stokes equations which have chemically and thermally nonequilibrium effects are considered by using Park's two-temperature model and the vibrational relaxation model from the SSH theory. For the time integration, an efficient numerical algorithm of an implicit finite difference method is used, which consists of the combination of LU-SGS scheme and the implicit diagonal method for a source Jacobian matrix. For convective terms, AUSMDV scheme generalized into the nonequilibrium flow case is applied.

Several types of flow cases are investigated; Problem I (Sphere cases), Problem II.1-3 (Orex cases) and Problem IV. 1-2 (Spherically Blunted Cone cases). All cases indicate that the flow inside the shock layer is in strong nonequilibrium and very complex real gas effects are observed. The comparison of heat fluxes between the catalytic and non-catalytic walls shows that the stagnation heat flux for catalytic wall cases are about 1.5-1.8 times higher than those for non-catalytic cases.

It is shown that fairly reasonable results can be obtained with both numerical methods and physical models applied here. However, numerical results of some cases indicate that more careful analyses and comparison with experimental results are necessary in order to clarify the more complex flow structures in the back flow region, for example, of Problem IV in this study.

References

[1] Park,C., Nonequilibrium Hypersonic Aerothermodynamics, John Wiley & Sons, Inc., 1990.

[2] Gnoffo, P.A., Gupta, R.N. and Shinn , J.L., "Conservation Equations and Physical Models for Hypersonic Air Flows in Thermal and Chemical Nonequilibrium", NASA TP-2867, 1989.

[3] Yoon,S. and Kwak,D., "Implicit Methods for the Navier-Stokes Equations", Computational Technology for Flight Vehicles, Vol. I, pp.535-547, 1990.

[4] Eberhardt, S. and Imaly, S., "A Diagonal Implicit Scheme for Computing Flows with Finite-Rate Chemistry", AIAA Paper 90-1577, 1990.

[5] Kurotaki, T., "Numerical Analysis of Two Dimensional / Axisymmetric Non-equilibrium Hypersonic Flow", NAL SP-19, pp.93-98, 1992.

[6] Wada, Y. and Liou, M.-S., "A Flux Splitting Scheme with High-Resolution and Robustness for Discontinuities", AIAA Paper 94-0083, 1994.

[7] Schwartz, R.N., Slawsky, Z.I. and Herzfeld, R.N., "Calculation of Vibrational Relaxation Times in Gases", J. Chem. Phys., 20, PP. 1591-1599, 1954 .

[8] Thivet, F., Perrin, M.Y. and Candel, S., "A Unified Nonequilibrium Model for Hypersonic Flows", Phys. Fluids, A3, pp. 2799-2812, 1991.

2−4

NUMERICAL SIMULATIONS OF THE HYPERSONIC FLOWFIELDS AROUND OREX

Masahiro NAKAO
Mitsubishi Heavy Industries, Ltd.

The hypersonic flowfields around the OREX have been simulated by the MHI hypersonic Navier-Stokes code CHRIS(Computer code for Hypersonic Reentry Information Synthesis). This code is based on the upwind, implicit, finite-difference method using Roe's Riemann solver with MUSCL(Monotonic Upstream Schemes for Conservation Laws) type higher-order accurate formulation of the convective terms. The real gas effects are taken into consideration using a VEG(Variable Equivalent Gamma) method with simplified curve fit of equilibrium air properties. Computations for the OREX are done under the assumption of equilibrium gas and perfect gas. Comparisons between the results obtained for real gas and perfect gas calculations are discussed.

1. INTRODUCTION

Recent progress of computing power has enabled us to simulate complex and high speed flowfields numerically around complex configurations of aircraft. The flowfields around a reentry vehicles are complex and provide one of the most challenging problems in the application of the computational fluid dynamics. One of the problems of the development of the hypersonic CFD code is the lack of the test data for code validation. Because existing wind tunnel facilities may not realize such a high stagnation enthalpy flow.

The OREX(Orbital Re-Entry Experiment) flight test was done in 1994. The one of objectives of the test is to get hypersonic flow data for CFD code validation. The heat transfer, wall pressure, and electron density data were acquired in the flight tests. In 1995, the high enthalpy workshop was held in NAL(National Aerospace Laboratory) and simulation of the flowfield around OREX is included as one of the problems.

In this paper, the flowfield around the OREX was simulated using our hypersonic real gas Navier-Stokes code. Computations were done under the assumption of an equilibrium gas and a perfect gas.

2. GOVERNING EQUATIONS

Compressible, Reynolds-averaged Navier-Stokes equations are formulated in the body fixed frame.

$$\hat{Q}_\tau + \hat{F}_\xi + \hat{G}_\eta + \hat{H}_\zeta = Re^{-1}\hat{S}_\zeta$$

where

$$\hat{Q} = \frac{1}{J}\begin{pmatrix} \rho \\ \rho u \\ \rho v \\ \rho w \\ e \end{pmatrix} \qquad \hat{F} = \frac{1}{J}\begin{pmatrix} \rho U \\ \rho uU + \xi_x P \\ \rho vU + \xi_y P \\ \rho wU + \xi_z P \\ (e+P)U - \xi_t P \end{pmatrix}$$

$$\hat{G} = \frac{1}{J}\begin{pmatrix} \rho V \\ \rho uV + \eta_x P \\ \rho vV + \eta_y P \\ \rho wV + \eta_z P \\ (e+P)V - \eta_t P \end{pmatrix} \qquad \hat{H} = \frac{1}{J}\begin{pmatrix} \rho W \\ \rho uW + \zeta_x P \\ \rho vW + \zeta_y P \\ \rho wW + \zeta_z P \\ (e+P)W - \zeta_t P \end{pmatrix} \qquad (1)$$

and F, G, H are the convective flux vectors and S is the viscous flux under the thin layer approximation. J is the Jacobian of transformation and the sign^ indicates that the quantity is normalized by the Jacobian. Re is the Reynolds number. The primitive variables of Q are the density r, the three mass fluxes ru, rv, and rw in the three coordinate directions x, y, and z, respectively and the energy per unit volume e. All these variables are normalized by freestream reference values. The velocities are normalized by the free stream speed of sound. The real gas effects are taken into account using the VEG(Variable Equivalent Gamma) method [1)-2)] under the assumption of chemical and thermal equilibrium state.

In the general expression the equation of state is written in the following form:

$$P = P(\rho, \rho ei) \qquad (2)$$

where ei is specific internal energy.

Unlike the perfect-gas case, explicit expression for the pressure as a function of density and internal energy is not available. The VEG method assumes that pressure is written in the same form as perfect gas:

$$P=\rho ei(\hat{\gamma} - 1) \tag{3}$$

where gamma $\hat{\gamma}$ is not constant but the function of density and internal energy:

$$\hat{\gamma} = \hat{\gamma}(\rho, ei) \tag{4}$$

This $\hat{\gamma}$ is called equivalent gamma and is calculated from the efficient simplified curve fits developed by S. Srinivasan and C. Tannehill[3]. These curve fits have the save range of validity of NASA RGAS data, namely, temperatures up to 2500 K and densities from 10^{-7} to 10^{3} amagats (ρ/ρ_0, ρ_0 : density at reference condition at 1 atm and 273.15 K). Utilization of this equation of pressure requires no essential change in the expression of Roe's approximate Riemann solver, time integration scheme and boundary conditions for the perfect gas[4]. The gamma and pressure are calculated using the curve fits at each time step. In the real gas Navier-Stokes code, the viscosity and thermal conductivity should also be calculated in the equilibrium air. These coefficients are obtained from curve fits which have been developed again by Srinivasan et. al[5]. A modified version of LU-ADI time integration algorithm[6] is used in the present code.

3. NUMERICAL ALGORITHM

Generalized Riemann Solver

In this code generalized Roe's Riemann solver is adopted to calculate inviscid flux. The essence of Roe's scheme is the solution of local Riemann problems stemming from the consideration of piecewise uniform states between cell interfaces on an initial data line. For simplicity, non-conservative form of the equation in one-dimensional case is considered;

$$Q_t+AQ_x= 0 \tag{5}$$

where A is a (locally constant) Jacobian matrix for each pair of initial data(Q_R,Q_L), where the subscripts R and L denote the right and the left side values of the cell face. The requirements for the matrix A are described in Ref.4 and the major property is

$$\Delta F = \bar{A}\Delta Q \tag{6}$$

where $\Delta Q = Q_R - Q_L$ and $\Delta F = F_R - F_L$ is obtained using

$$\bar{A} = \bar{A}(\bar{Q}) \tag{7}$$

The above expression is known as a Roe-averaged state and was derived by Roe for a perfect gas[4]. The components of the average state of $\bar{A}(\hat{\gamma})$ are obtained as follows

$$\begin{aligned} \bar{\rho} &= \sqrt{\rho_R\rho_L} \\ \bar{u} &= \alpha u_L + (1-\alpha)u_R \\ \bar{H} &= \alpha H_L + (1-\alpha)H_R \end{aligned} \tag{8}$$

where

$$\alpha = \frac{\sqrt{\rho_L}}{(\sqrt{\rho_L}+\sqrt{\rho_R})} \tag{9}$$

An important quantity in the approximate Riemann solver is the column vector $R^{-1}\Delta Q$. Its components are the jumps in the characteristic variables. It can be expressed simply in terms of ΔP, $\Delta\rho$ and Δu as

$$R^{-1}\Delta Q = \begin{bmatrix} \Delta\rho - \Delta P/a^2 \\ \frac{1}{2}(\Delta\rho/a^2 + \Delta u/a) \\ \frac{1}{2}(\Delta\rho/a^2 - \Delta u/a) \end{bmatrix} \tag{10}$$

This has the same form as for perfect gas. In the real-gas case, pressure derivative ΔP is given as

$$\Delta P = \chi\Delta\rho + \kappa\Delta\varepsilon \tag{11}$$

where $\varepsilon = \rho e_i$ and the derivatives are denoted by

$$\chi = \left(\frac{\partial P}{\partial \rho}\right)_{\varepsilon} \quad \kappa = \left(\frac{\partial P}{\partial \varepsilon}\right)_{\rho} \tag{12}$$

Here the subscript ε (ρ) denotes the partial derivative of p with respect to ρ (ε) by holding ε (ρ) constant.

Using Eqs. (3) and (12) Eq.(11) can be expressed as follows:

$$\Delta P = \varepsilon \frac{\partial \hat{\gamma}}{\partial \rho} \Delta \rho + \left\{ \left(\hat{\gamma} - 1 \right) + \frac{\partial \hat{\gamma}}{\partial \varepsilon} \right\} \Delta \varepsilon \tag{13}$$

In Eq (13), gamma varies more slowly than the other thermodynamic variables since gamma remains between 1 and 5/3, for any combination of ρ and ε that may vary several order of magnitude . and will be very small and can be assumed to be zero. Then Eq.13 may be approximated as

$$\Delta P = \left(\hat{\gamma} - 1 \right) \Delta \varepsilon \tag{14}$$

This is the form of pressure derivative which corresponds to that of Grossman et al. [7].

Chemical Component Calculation

Chemical components of the equilibrium air are calculated by the method of Ref.9. Eleven chemically reacting species-O_2, N_2, O, NO, N, NO^+, e^-, N^+, O^+, Ar, and Ar^+ - are included. The method involves the algebraic combination of the equilibrium, elemental mass-balance, and charge-neutrality equations and solves the resulting equation by an iterative method.

Numerical Grid

Figure 1 shows the OREX configuration. This configuration simulates the nose shape of the HOPE.

In the hypersonic flow calculations, the grid adaptation technique is effective for capturing strong shock waves. In this calculation the out boundary of the grid is fitted to the bow shock by estimating pressure derivatives. Figure 2 shows the initial grid. Figure 3 shows the boundary fitted grid.

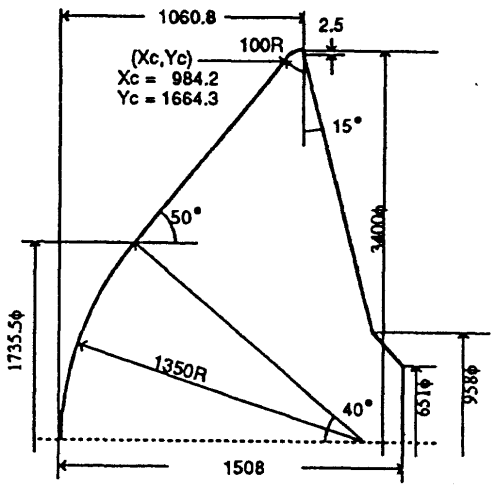

Fig. 1 OREX Configuration

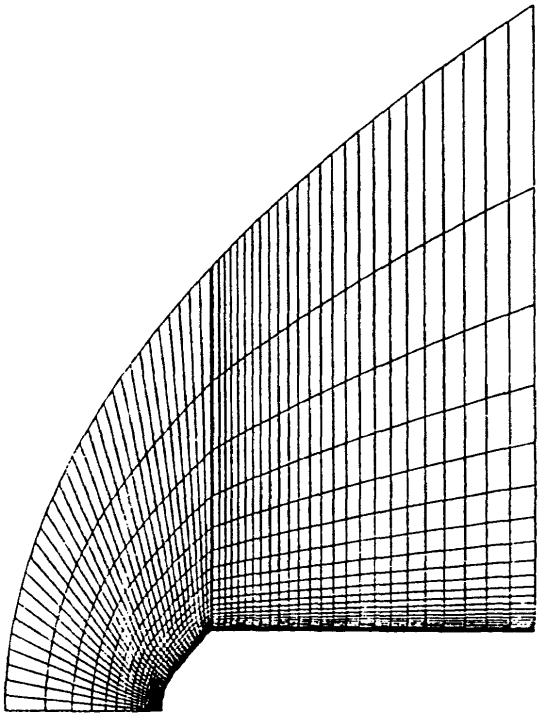

Fig. 2 Initial Grid for OREX

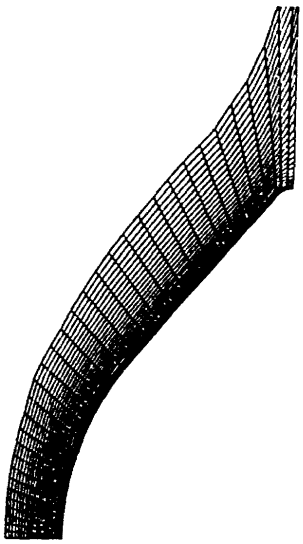

Fig. 3 (a) Grid for perfect gas case

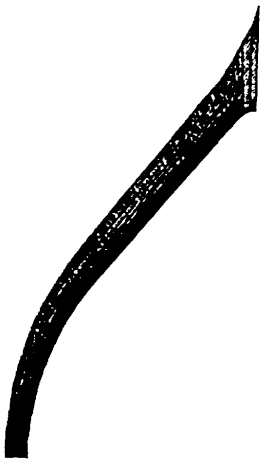

Fig. 3 (b) Grid for real gas case

4. RESULTS

The flow condition is the free stream velocity of 5562m/s, free stream temperature of 248.1 K, free stream pressure of 23.6 N/m^2 and wall temperature of 1519 K. The calculations were done under the assumption of real gas and perfect gas.

Figure 3(a) shows the numerical grid of the perfect gas case and figure 3(b) shows that of the real gas case. The number of the grid points of these two cases is the same and is 40x8x50 totaling up to about 16,000. The difference of the out boundary of the grid between the real gas and perfect gas is due to the difference of the shock stand-off distances. Figure 4 shows the comparison of computed pressure distribution between perfect gas and real gas. The shock stand-off distance of the real gas case is significantly shorter than that of the real gas case.

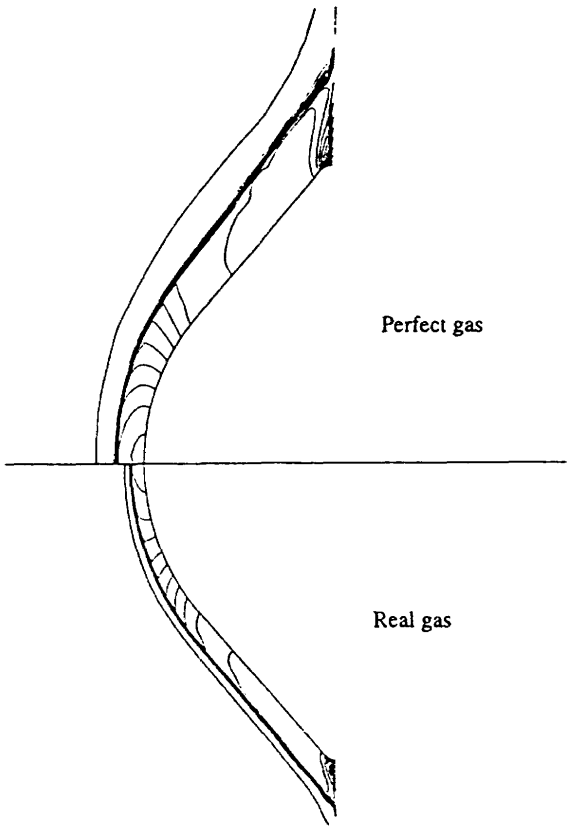

Fig. 4 Pressure Contour Plots

Figure 5 shows the comparison of computed temperature contour plots. Figure 6 shows pressure distributions along the body surface. The y/r=0 point is the stagnation point. The pressure distribution of the real gas case is similar to that of the perfect gas case. Figure 7 shows temperature distribution along the stagnation line. The peak temperature of the perfect gas case is three times higher than that of the real gas case.

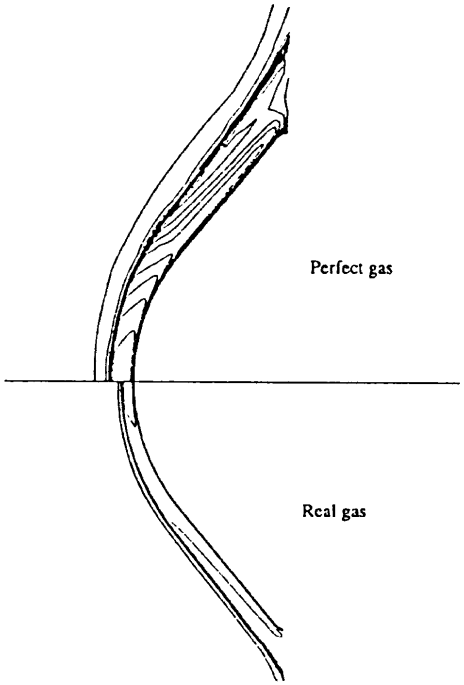

Fig. 5 Temperature contour plots

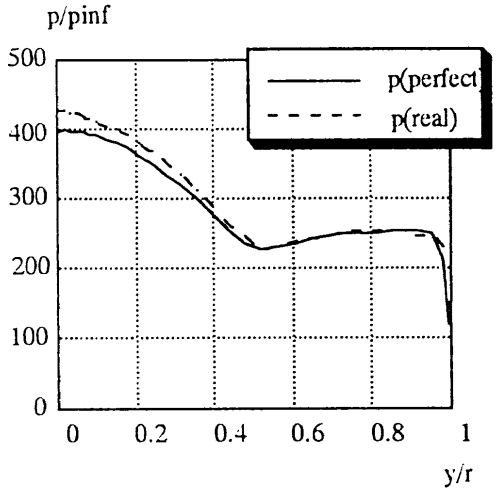

Fig. 6 Pressure Distribution along the body surface

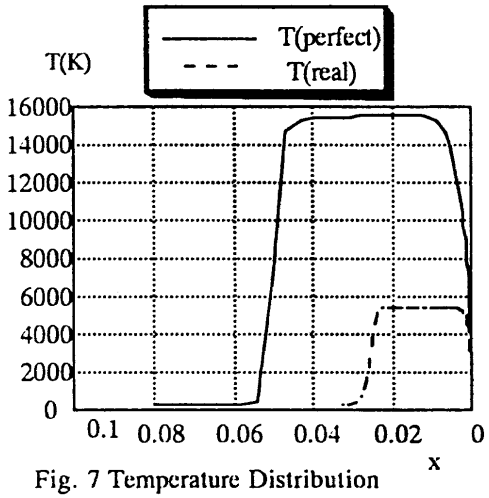

Fig. 7 Temperature Distribution along the stagnation line

Figure 8 shows the heat transfer distributions along the body surface. The maximum heat transfer of the perfect gas case is slightly higher than that of the real gas case.

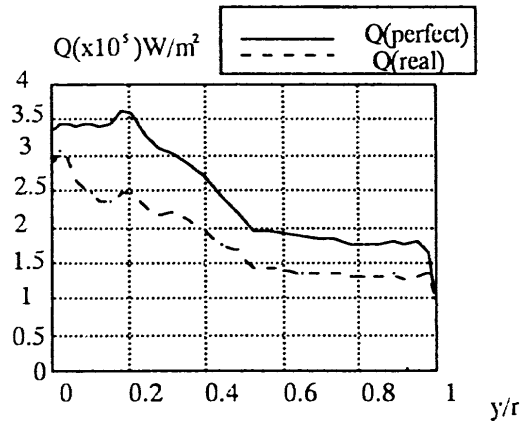

Fig.8 Heat Transfer Distribution along the body surface

The fluctuating characteristic near the stagnation point is thought to be caused by the artificial dissipation that added to cure the

carbuncle phenomena. The carbuncle phenomenon is one of the numerical instabilities in capturing a strong shock wave. The Roe scheme has this problem. The dissipative scheme, however, cannot catch the strong shock sharply and cannot simulate the heat transfer ratio accurately.

Figure 9 shows the air component distribution along the stagnation line. N2 and O2 are dissociated and NO and O appear in the region between the bow shock and the body. This dissociation absorbs the internal energy of the air.

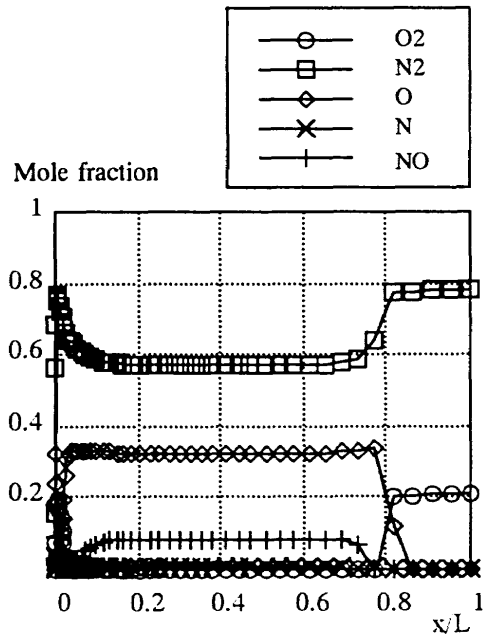

Fig.9 Chemical Component along the stagnation line

5. CONCLUSIONS

The flowfields around OREX is calculated by the MHI Navier-Stokes code(CHRIS). The real gas and perfect gas case are calculated. Results show the significant differences between the two cases in the shock stand-off distance and the temperature distribution. Some glitch due to the artificial dissipation is observed at the heat transfer distribution. The adaptation of a more robust and less dissipative scheme is now under the study.

REFERENCES

(1) Ota, D. K., Chakravarthy, S.R. and Darlin, J.C. , 'An Equilibrium Air Navier-Stokes Code for Hypersonic Flows," AIAA -88-0419.
(2) Prabhu, R.K., Stewart, J.R. and Thareja, R. R., 'A Navier-Stokes Solver for High Speed Equilibrium Flows and Application to Blunt Bodies,' AIAA-89-0668, 1989.
(3) Srinivasan, S., Tanehill, J.C. and Weilmuenster, K.J., 'Simplified Curve Fits for the Thermodynamic Properties of Equilibrium Air', NASA RP-1181, 1987.
(4) Roe, P. L., 'Characteristic-Based Schemes for the Euler Equations,' Fluid Mech. 1986. 18:337-365.
(5) Srinivasan, S., and Tanehill, J. C., 'Simplified Curve Fits for the Transport Properties of Equilibrium Air', NASA CR-178411, 1987.
(6)Fujii, K.,and Obayashi, S., 'High-Resolution Upwind Scheme for Vortical Flow Simulations,' Journal of Aircraft, Vol.226, No.12, December 1989, pp.1123-1129.
(7) Grossman, B. and Walters, R. W., 'An Analysis of Flux Split Algorithms for Euler Equations with Real Gases,' AIAA 87-1117.
(8) Prabhu, R.K., and Erickson, W. D., 'A Rapid Method for the Computation of Equilibrium Chemical Composition of Air of 15,000 K,' NASA TP-2797, 1988.

2-5

HIGH ENTHALPY WORKSHOP PROBLEM II OREX

K. Murakami* and T. Fujiwara**
Nagoya University
Furou-cho Chikusa-ku Nagoya-shi 464-01, Japan
and
S. Nakano†
Hitachi Ltd.
3-1-1, Saiwai-cho, Hitachi-shi, Ibaraki-ken 317, Japan

Abstract

We have developed a CFD code to calculate a hypersonic flow around a reentry body including the base flow region. In order to inspect our CFD code we calculate Problem II OREX II-1, 2, 3 and 5 in this workshop. The problems II-1, 2 and 3 are laminar nonequilibrium gas flow. The result of Problem II-5 is used for the initial value of the reacting flow calculations of Problem II-2 and 3. For the thermally and chemically nonequilibrium flow calculations, 11-species air is considered, along with the Park's two-temperature model. For the calculation of flowfield, the governing equations are full Navier-Stokes ones and are solved using a non-MUSCL-type second-order explicit upwind-TVD scheme by Harten-Yee. For the problem II.1, 2 and 3, a semi-implicit method is applied to all species-mass-conservation-equations because of stiff source terms.

Introduction

Japanese first purely-national rocket, launched successfully 1994 February 4, carried an experimental reentry vehicle named OREX to orbit. The vehicle traveled at a hypersonic velocity in high altitudes where the air density is low. In this case, the flowfield behind the bow shock formed over the vehicle tends to be nonequilibrium chemically and thermally; the molecules N_2 and O_2 internally excite, dissociate and ionize in the shock layer and entailing downstream. Thus, we must consider internal excitation, dissociation and ionization. In other words, thermally- and chemically-nonequilibrium 11 species (O_2, N_2, O, N, NO, O_2^+, N_2^+, O^+, N^+, NO^+ and e^-) must generally be considered, using a model consisting of 17 chemical reactions and two temperatures, for example.

We have developed a CFD code to estimate the heat transfer on the surface of the reentry body like OREX because of its importance. In order to inspect our CFD code we participate High Enthalpy Flow Workshop and we calculate the Problem II OREX II-1, 2, 3 and 5. The flight conditions of OREX of these problems are shown in Table 1.

Mathematical Description of Hypersonic Flow

A system of governing equations that describe a three-dimensional, axisymmetric viscous flow of multi-component reacting air is given in terms of the cylindrical coordinate[1], after setting the angle of attack equal to zero; i.e. the equations are reduced to spacially two-dimensional system (r, z). We assume (a) the flow is in thermally non-equilibrium, (b) the radiation pressure and body forces are of negligible order, and (c) the molecular diffusion is binary only. These equations are then transformed into a general body-oriented curvilinear coordinate system (ξ, η), and then rearranged into a non-dimensional strong-conservation-form as follows:

$$\frac{\partial \hat{q}}{\partial \tau} + \frac{\partial \hat{E}}{\partial \xi} + \frac{\partial \hat{F}}{\partial \eta} = \frac{1}{Re}\left[\frac{\partial \hat{E}_v}{\partial \xi} + \frac{\partial \hat{F}_v}{\partial \eta}\right] + \hat{H} + \hat{H}_1, \quad (1)$$

where $\hat{H}$ and $\hat{H}_1$ are the mass production and cylindrical coordinate terms, respectively. When we are calculating 11-species flowfields using the Park 2-temperature model, we need one more equation, which is the vibrational energy conservation

$$\frac{\partial}{\partial t}(J^{-1}e_{ev}) + \frac{\partial}{\partial \xi}(J^{-1}e_{ev}U) + \frac{\partial}{\partial \eta}(J^{-1}e_{ev}V)$$

*Graduate Student, Department of Aerospace Engineering, Nagoya University.

**Professor, Department of Aerospace Engineering, Nagoya University.

†Researcher, 5th Department of Mechanical Engineering Research Laboratory, Hitachi Ltd.

$$= \frac{1}{Re}\left[\frac{\partial}{\partial\xi}J^{-1}\left(\xi_z Re\lambda\frac{\partial T_v}{\partial z}+\xi_r Re\lambda\frac{\partial T_v}{\partial r}\right)\right.$$
$$\left.+\frac{\partial}{\partial\eta}J^{-1}\left(\eta_z Re\lambda\frac{\partial T_v}{\partial z}+\eta_r Re\lambda\frac{\partial T_v}{\partial r}\right)\right]$$
$$-\frac{J^{-1}}{r}\left[(P_e+e_{ev})v-\lambda\frac{\partial T_v}{\partial r}\right]$$
$$+J^{-1}\left(3\gamma_e\sum_{i=1}^{6}\frac{m_e}{m_i}\theta_i+\frac{\gamma_m}{\tau}\right)\rho(T-T_v)$$
$$-P_e\left[\frac{\partial}{\partial\xi}\left(J^{-1}U\right)+\frac{\partial}{\partial\eta}\left(J^{-1}V\right)\right]. \qquad (2)$$

See the results of Park[2] for further information.

In order to consider a thermally- and chemically-nonequilibrium gas, a two-temperature model is used here: T indicates the translational and rotational temperature, while T_v the vibrational and electron temperature. When 11 chemical species (N_2, O_2, N, O, NO, N_2^+, O_2^+, N^+, O^+, NO^+ and e) are considered in the analysis, we utilize 17 chemical reactions shown in Table 2.

The forward k_f and backward k_b reaction rates of j-th reaction are given by the modified Arrhenius law as a function of T_a, which is defined in the two columns of Table 2:

$$k_f = CT_a{}^n exp(-E_1/kT_a), \quad k_b = k_f/K_c(T_a), \quad (3)$$

where the equilibrium constant Kc is given by the curve-fitting formula

$$K_c = exp(A_1 + A_2 \ln Z + A_3 Z + A_4 Z^2 + A_5 Z^3). \quad (4)$$

Here $Z = 10000/T_a$.

When the present two-temperature model is applied, the viscosity and thermal conductivity are calculated from the Yos formulation which is based on molecular collision cross section. Using the formulation, the following three thermal conductivities are introduced; (a) translational mode including the rotational energy, (b) vibrational mode, and (c) electron translational mode. The first is the function of the translational temperature T, while the others are of the vibrational temperature T_v. We can treat the thermal conduction of each mode separately. For more explanations, see Lee[3].

Calculation of Flowfield

For the calculation of flowfield, the governing equations (1) and (2) are solved using a non-MUSCL-type second-order explicit upwind-TVD scheme by Harten-Yee[4] and generalized Roe's average by Liu and Vinokur[5]. For the problem II.1, 2 and 3, a semi-implicit method is applied to all species-mass-conservation-equations because of stiff source terms.

Figure 1 is a typical example of body-oriented grid system. The grid system is generated by solving a hyperbolic equation. The minimum value of $\Delta\eta$ is 50 μm and the interval ratio between adjacent grids is limited below 1.04, therefore 150 points are needed for η direction. The innermost surface η=0 agrees with the body surface. The axis of symmetry is located in the center of two adjacent grid points. At the beginning of calculation the most outer boundary of calculation domain is set artificially. When the location of bow shock is almost fixed, the outer boundary and inner grid system are adjusted along the η direction. After that the flowfield calculation is continued. For each problem, this re-griding is done.

Results and Discussions

At first we calculate the perfect gas flow cases of Problem II-1 and 5 using the same CFD code for the perfect gas which is made up by ourselves. After we get converged solution of perfect gas, the nonequilibrium calculations are started from these solution as the initial inputs. The CFD code witch is used for the thermally and chemically nonequilibrium gas flow calculations is same for Problem II-1, 2 and 3 except for the initial input and free stream and wall conditions.

Figure 2 shows the dimensionless pressure contours. Since Problem II-1 is the low density and high speed case, the bow shock is spread in comparison with other cases. That effect of low density is seen from the dimensionless translational temperature contours Fig.3 and vibrational one Fig.4. We can see that in detail from Fig.7 which is the temperature distributions along the stagnation stream line.

The results of the heat transfer distributions along the body surface are shown in Fig.5. The wall heat transfers are calculated by following equation,

$$Q = -\left(\lambda\frac{\partial T}{\partial n}\right)_{wall} - \left(X_m\lambda_v\frac{\partial Tv}{\partial n}\right)_{wall}$$
$$-\left(X_e\lambda_e\frac{\partial Tv}{\partial n}\right)_{wall} - \sum_{i=1}^{Ns}\left(\rho_i h_i\frac{D_i}{Y_i}\frac{\partial Y_i}{\partial n}\right)_{wall} \quad (5)$$

The value of thermal conductivities of translational, vibrational and electronic excitation mode are listed in Table 3. Heat conduction by translational mode over body is calculated by Yos's formula and Wassilewas' formula for two-temperature model and non-reacting flow, respectively. In Eq.(??) n is normal vector to wall, then

$$\frac{\partial f}{\partial n} = \frac{(\eta_x\xi_x+\eta_y\xi_y)f_\xi+(\eta_x^2+\eta_y^2)f_\eta}{\sqrt{\eta_x^2+\eta_y^2}}. \quad (6)$$

where f is some physical value, f_ξ and f_η are calculated on wall by central-difference and foward-difference, respectively.

The maximum value of heat transfer along the body surface, however, becomes lower in all results of calculations. That lower estimate of heat transfer comes from the entropy fix of Harten-Yee type upwind-TVD scheme. The entropy fix is calculated by following equations.

$$\Psi(z) = \begin{cases} |z| & |z| \geq \delta \\ (z^2 + \delta^2)/2\delta & |z| < \delta \end{cases} \quad (7)$$

$$\delta = \delta_1(|\xi_r u + \xi_z v| + a\sqrt{\xi_r^2 + \xi_z^2}) \quad (8)$$

At the start point of calculation we set δ_1 equal to 1.0, and decrease to 0.1 finally. The constant δ_1 is used to all of the calculation domain. According to Eq.(8) the narrow the grid interval is, the smaller δ namely numerical viscosity becomes. Because of the sufficient numerical viscosity the temperature gradient near the body is made smaller. The effect of the numerical viscosity will be appeared in the distributions of mass fractions (Fig.6) near the surface. In order to estimate the heat transfer on the reentry body surface correctly we have to introduce some high-resolution method for boundary layer to our CFD code.

The vibrational temperature distributions along the stagnation stream line are shown in Fig.7. As seen from Fig.7 II-2, the vibrational temperature distribution has a sharp peak behind the shock front similar to translational one. It will come from that the electron pressure is ignored for simplicity when TVD scheme is applied to the system of governing equations which include the vibrational energy conservation. Therefore, we must re-examin the method for solving the vibrational energy conservation equation.

In the pressure and temperature contour Fig.2 and 3, there is something the matter with contour line around the axisymmetric line. According to our recent study, however, that is reduced by using the fractional step method for the calculations of two dimensional flow.

Conclusions

In this workshop, we can find several points that we must improve our CFD code to simulate a hypersonic thermally and chemically nonequilibrium gas flow around a reentry body like OREX. First, more higher resolution of boundary layer witch effect on the heat transfer along the body surface is need to estimate the heat transfer correctly. Second, when we consider the ionization and two temperature model we must re-examin the method for solving the vibrational energy conservation equation.

Further comparison between the results of numerical calculation and the experimental data is desirable after improvement of our CFD code in order to inspect its validity.

References

1) Kuo K.K. 1986, Principles of Combustion, John Wiley & Sons, pp.161-227.

2) Park C. 1985, Problems of rate chemistry in the flight regimes of aeroassisted orbital transfer vehicles, thermal design of aeroassisted orbital transfer vehicles, ed. H.F. Nelson, Progr. Astronaut. Aeronaut. 96, pp.511-537.

3) Lee J.H. 1985, Governing equations for the flight regimes of aeroassisted orbital transfer vehicles, thermal design of aeroassisted orbital transfer vehicles, ed. H.F. Nelson, Progr. Astronaut. Aeronaut. 96, pp.5-53.

4) Yee H.C. 1989, A class of high resolution explicit and implicit shock capturing methods, NASA TM 101088.

5) Liu Y. and Vinokur M. 1989, Upwind Algorithms for General Thermo-Chemical Nonequilibrium Flows, AIAA-89-0201.

Table 1: Flight conditions of OREX

	U_∞ [m/s]	T_∞ [K]	P_∞ [N/m^2]	T_{wall} [K]
II-1	7450	186.9	0.1629	540
II-2				
II-3	5562	248.1	23.60	1519
II-5				

Table 2: Elementary chemical reactions and temperature Ta contributing to each reaction rate

	k_f Ta	k_b Ta
$O_2 + M \rightleftarrows O + O + M$	$T^{1/2}T_v^{1/2}$	$T^{1/2}T_v^{1/2}$
$N_2 + M \rightleftarrows N + N + M$		
$NO + M \rightleftarrows N + O + M$		
$N_2 + O \rightleftarrows NO + N$	$T^{1/2}T_v^{1/2}$	$T^{1/2}T_v^{1/2}$
$NO + O \rightleftarrows N + O_2$		
$O + O_2^+ \rightleftarrows O_2 + O^+$	$T^{1/3}T_v{}^{2/3}$	$T^{1/3}T_v{}^{2/3}$
$N^+ + N_2 \rightleftarrows N_2^+ + N$		
$O + NO^+ \rightleftarrows NO + O^+$		
$N_2 + O^+ \rightleftarrows O + N_2^+$		
$N + NO^+ \rightleftarrows NO + N^+$		
$O_2 + NO^+ \rightleftarrows NO + O_2^+$		
$NO^+ + N \rightleftarrows N_2^+ + O$		
$O + N \rightleftarrows NO^+ + e^-$	$T^{1/2}T_v{}^{1/2}$	T_v
$O + O \rightleftarrows O_2^+ + e^-$		
$N + N \rightleftarrows N_2^+ + e^-$		
$O + e^- \rightleftarrows O^+ + e^- + e^-$	T_v	T_v
$N + e^- \rightleftarrows N^+ + e^- + e^-$		

Table 3: Value of thermal conductivities of translational, vibrational and electronic excitation mode

Problem	II-1	II-2
T_{wall} [K]	540	1519
λ [W/m/K]	3.942×10^{-2}	7.652×10^{-2}
$X_m\lambda_m$ [W/m/K]	2.537×10^{-3}	7.554×10^{-3}
$X_e\lambda_e$ [W/m/K]	7.650×10^{-7}	1.565×10^{-11}
Problem	**II-3**	**II-5**
T_{wall} [K]	1519	1519
λ [W/m/K]	7.663×10^{-2}	8.042×10^{-2}
$X_m\lambda_m$ [W/m/K]	1.860×10^{-2}	-
$X_e\lambda_e$ [W/m/K]	0.0	-

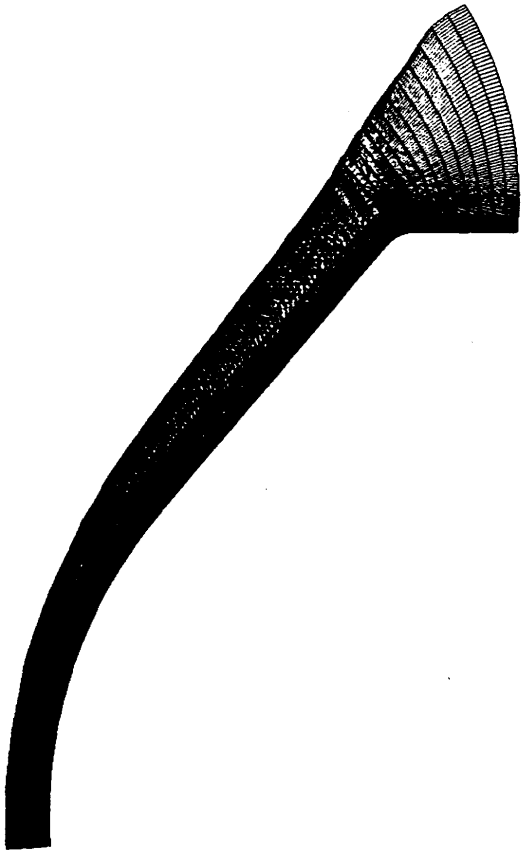

Figure 1: An example of body-oriented grid system. $\xi \times \eta = 51 \times 150$

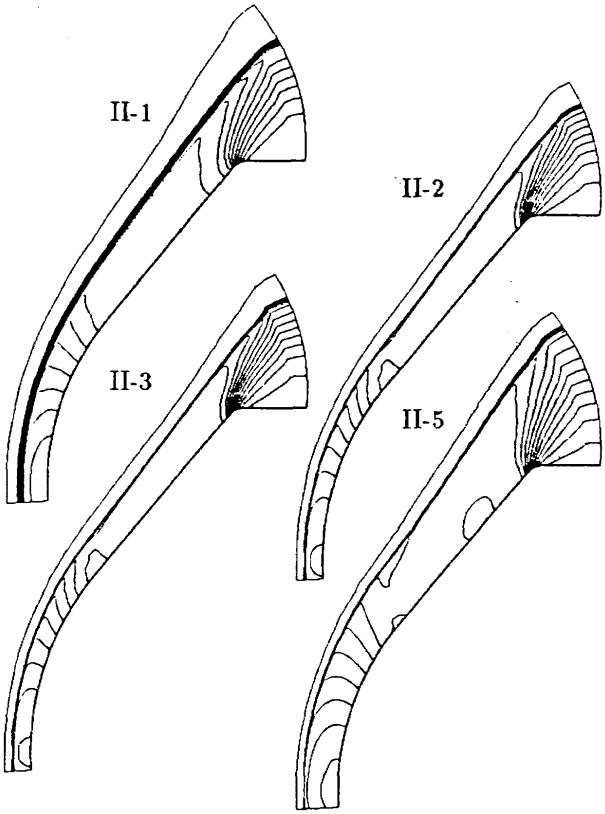

Figure 2: Dimensionless Pressure Contours

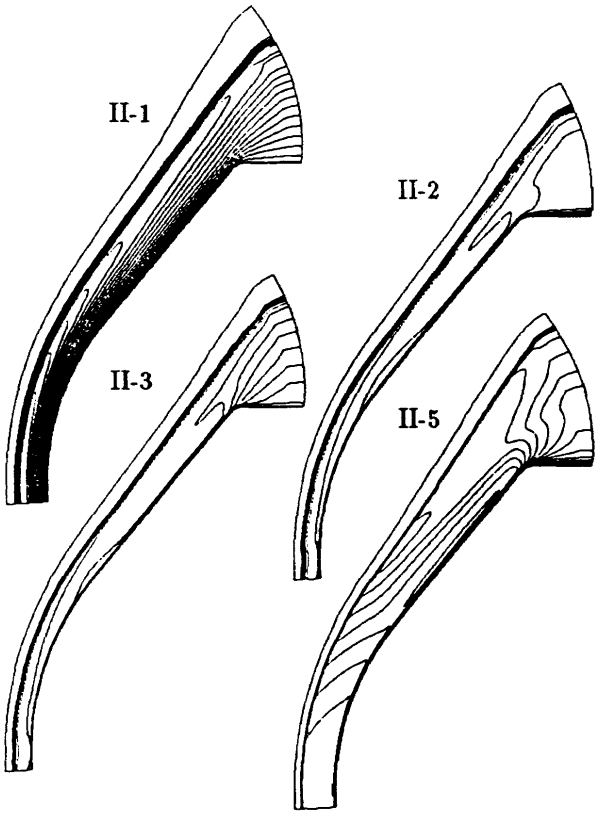

Figure 3: Dimensionless Translational Temperature Contours

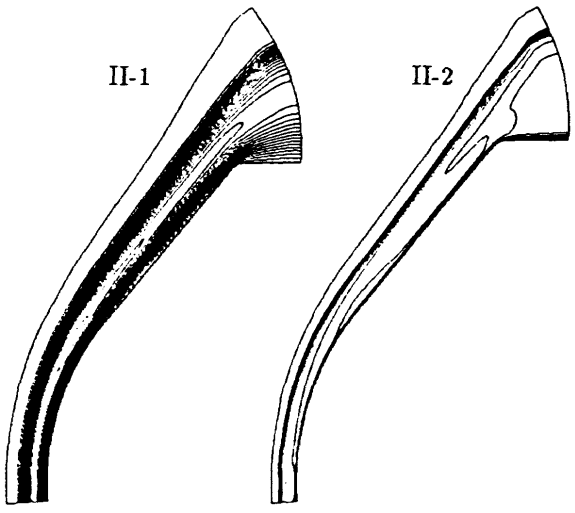

Figure 4: Dimensionless Vibrational Temperature Contours

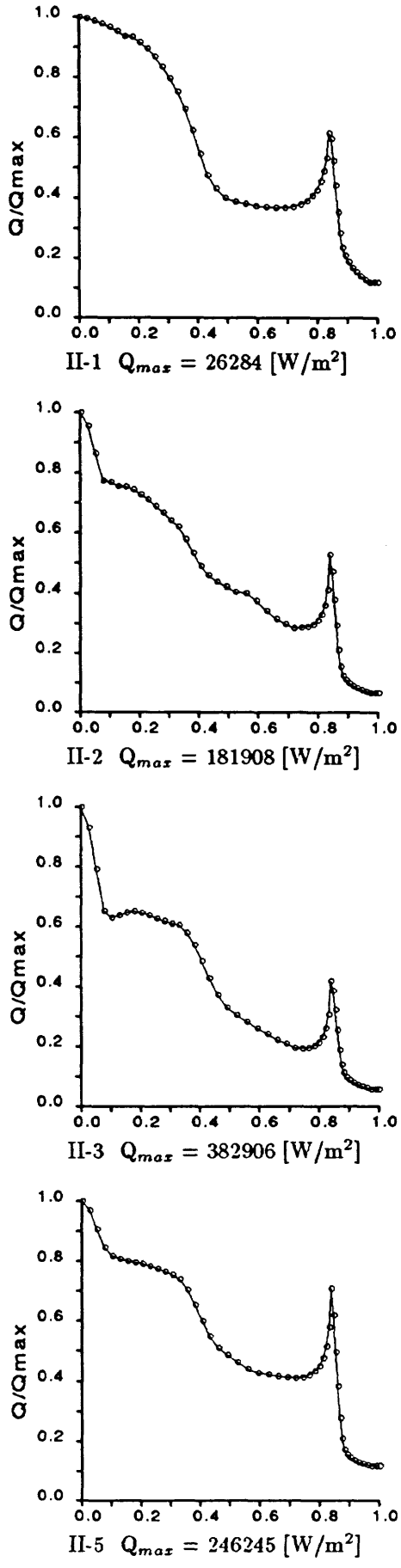

Figure 5: Heat Transfer Distribution along Body Surface

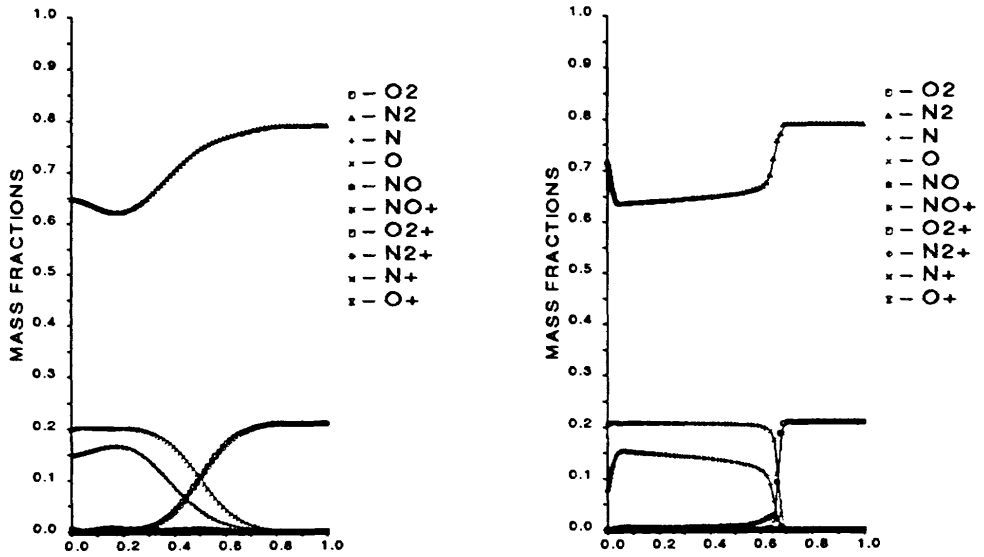

II-1 II-2

Figure 6: Mass Fraction Distribution along Stagnation Stream Line

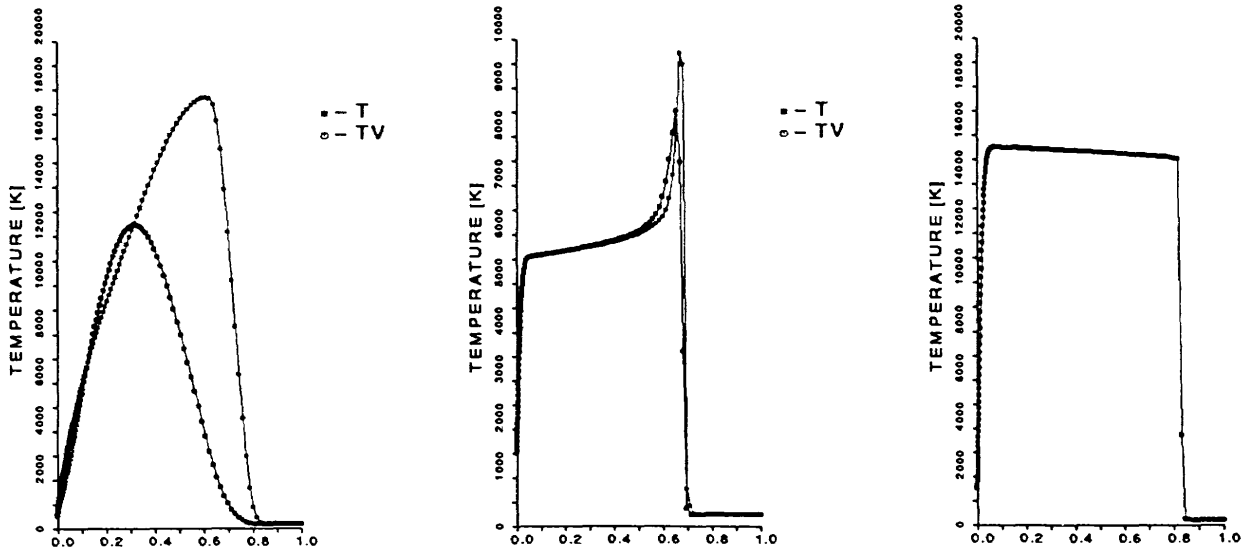

II-1 T_{max} = 17713 [K] TV_{max} = 12488 [K]

II-2 T_{max} = 9719 [K] TV_{max} = 8529 [K]

II-5 T_{max} = 15541 [K]

Figure 7: Temperature Distribution along Stagnation Stream Line

2-6

Hypersonic Flow Analysys around OREX and Hyperboloid Flare

Takuji Kishimoto
Gifu Technical Institute,
Kawasaki Heavy Industries, LTD.

Shinichi Kaneko
Aerospace Engineering Division,
Kawasaki Heavy Industries, LTD.

ABSTRACT

We have carried out hypersonic flow analysis around OREX(Orbiter Reentry Experiment) and hyperboloid flare by solving axi-symmetric Navier-Stokes Equations. Our flow solver is based on a finite volume implicit TVD upwind scheme. Convective fluxes are evaluated by AUSMDV scheme in order to remove "carbuncle phenomena", that are unphysical solution often appeared on hypersonic flow analysis around a blunt body. We also adopted a curve fitting to estimate thermodynamic and transport properties of an equilibrium air.

Flow condition for OREX is correspond to a flight condition at altitude 56.9km, where real gas effect should not be ignored. Therefore, we assumed this flow not only to be a perfect gas, but to be an equilibrium air.

In the case of hyperboloid flare, flow condition is correspond to experiment by Gottingen Ludwig Tube used cold gas. Numerical result of this problem suggests us that the flow unsteadiness must be taken into account, in order to predict accurately the aerodynamic and aerothermodynamic characteristics of a hypersonic flow including seperations induced by the interaction between a shock wave and a boundary layer.

1. Introduction

In Japan, HOPE(H-II Orbiting Plane) development program has been proceeding by NAL(National Aerospace Laboratory) and NASDA(National Space Development Agency of Japan). In a design of such a winged reentry vehicle, aerodynamic heating in a hypersonic flight regime is one of some critical points over a wide range of flight speed.

In order to investigate the characteristics of aerodynamic heating in a hypersonic flow with "real gas effects", we have carried out some wind tunnel tests using a high enthalpy shock tunnel in recent years[1]. But we cannot depend only on high enthalpy shock tunnel tests to get all aerodynamic heating data that we need, because the technique of high enthalpy shock tunnel testing are not matured yet, especially in the decision of free stream conditions and the reproducibility of test data.

Therefore, CFD is required to supplement the wind tunnel test data. In order that CFD fill this role, it is indispensable that the validation for the wind tunnel test data or the flight data have been carried out sufficiently, because CFD technique also are not matured yet, especially in numerical physical/chemical models.

Simultaneously with the validation of our hypersonic flow analysis system, we have participated in this "High Enthalpy Flow Workshop" and carried out hypersonic flow analysis around OREX(Orbital Reentry Experiment) and a hyperboloid flare with/without real gas effects. We will show the outline of our numerical results as follows .

2. Numerical Approaches[2,3]

Our flow solver for a perfect gas and an equilibrium air is based on finite volume TVD upwind scheme for thin layer Navier-Stokes equations as basic equation.

MUSCL type TVD scheme is adopted for descretization in space. This scheme limits the variation of characteristic variables by MINMOD function in each cell. Our flow solver has a second order accuracy in space by using this method.

Convective fluxes are evaluated by AUSMDV scheme[4]. This method is one of AUSM type splitting schemes[5] , and has equal simplicity and robustness to flux vector splitting schemes and equal resolution to flux difference splitting schemes. By using AUSMDV scheme, carbuncle phenomena, that are unphysical solution often appeared on a hypersonic flow analysis around a blunt body, can be suppressed to some extent.

Time Integration is implicitly executed by planar Gauss-Seidel relaxatiom method.

In the case of an equilibrium air, thermodynamic and transport properties are calculated by a curve fitting method proposed by Dr.Srinivasan et al[6,7].

3. Numerical Results

Our numerical results as follows assume a laminar flow for either OREX or a hyperboloid flare.

(1) OREX

Our numerical results for OREX are solutions to Problem Ⅱ.4(chemical equilibrium) and Ⅱ.5(perfect gas) of this workshop, respectively.

Sizes of computational grids as we used are 71×81 for a perfect gas case, and 66×41 for an equilibrium air case(Fig.1).

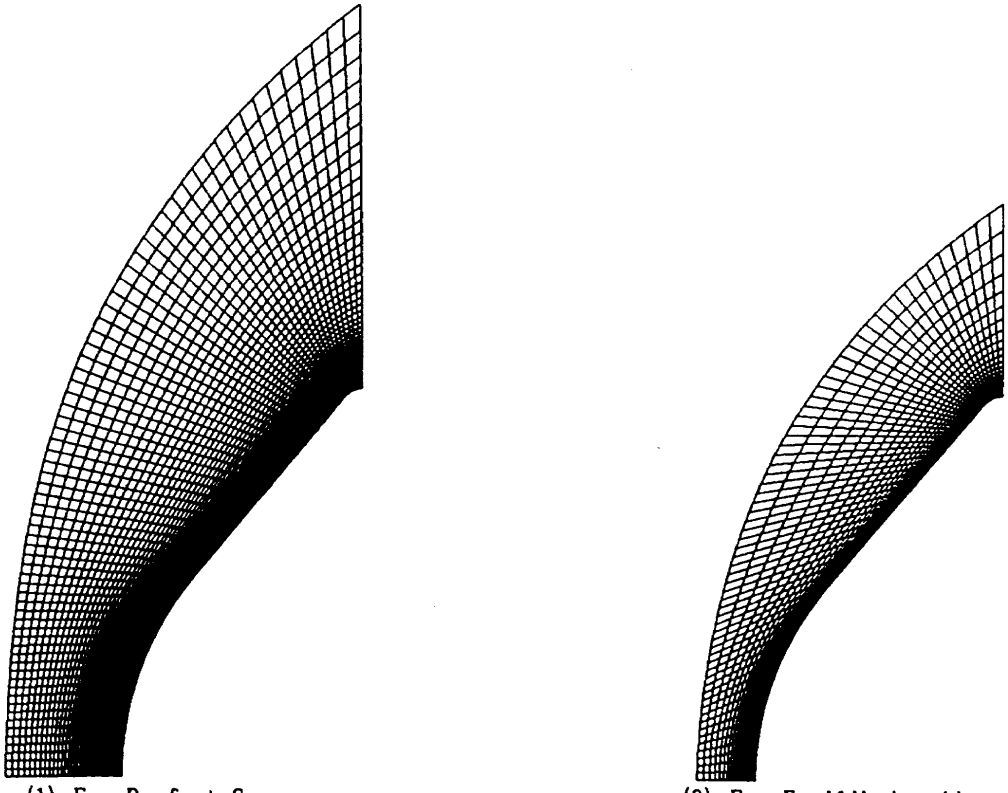

(1) For Perfect Gas (2) For Equilibrium Air

Fig.1 Computational Grids around OREX

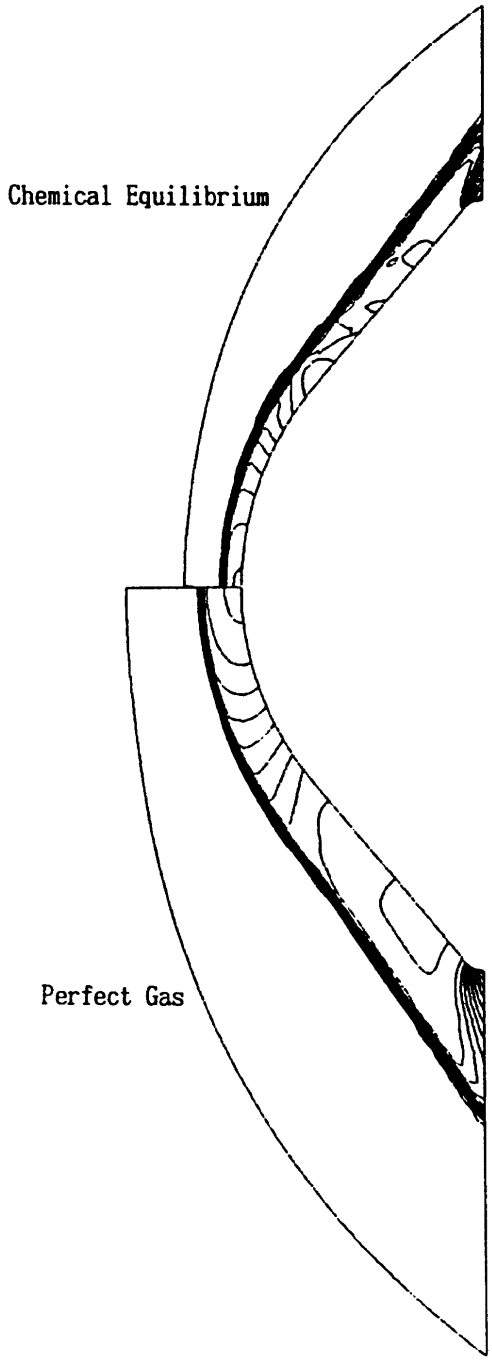

Fig.2 Pressure Contours around OREX

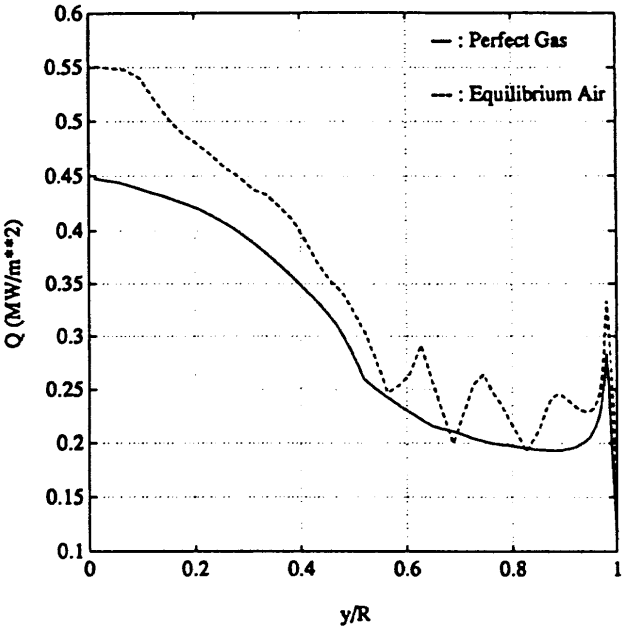

Fig.3 Heat Flux Distribution on OREX

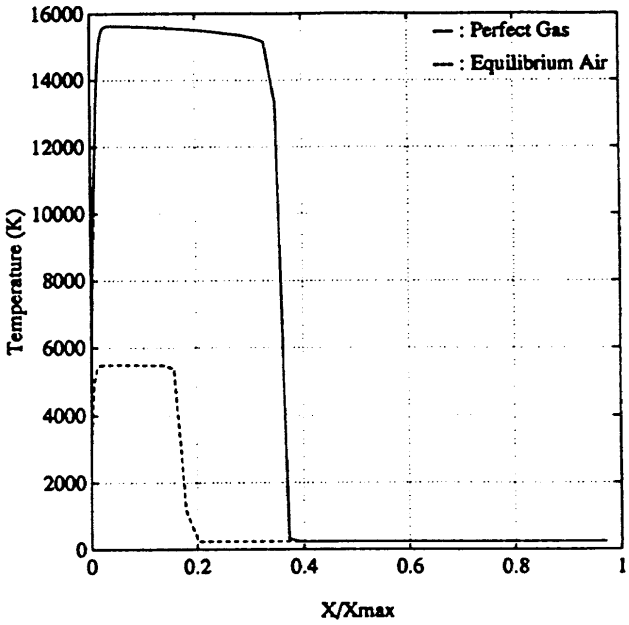

Fig.4 Temperature Distribution on Stagnation Stream Line of OREX

Flow condition, which is correspond to flight condition at altitude 56.9km in a Japanese first successful reentry experiment from orbit, are as follows.

Velocity : 5562 m/s
Temperature : 248.1 K
Pressure : 23.60 Pa
Wall Temperature : 1519 K

In these results, the characteristic difference between a perfect gas and an equilibrium air is that surface heat flux of an equilibrium air is higher than of a perfect gas(Fig.3), though a temperature behind a bow shock of an equilibrium air is about 10,000K lower than of a perfect gas(Fig.4). This difference of heat flux is led by recombination, in which reaction heat is released, near solid surface in an equilibrium air, which is regarded as a fully catalytic wall in our numerical

simulation.

With respect to the bow shock location, the result of an equilibrium air case is about a half distance from a body of a perfect gas case(Fig.4). In the view of this aspect, these numerical results show that our hypersonic flow analysis system can definitely capture the real gas effects in chemical equilibrium.

But heat flux distribution on surface shows unexpected oscillation in an equilibrium air case(Fig.3). Therefore, our next goal of hypersonic flow analysis is that such unphysical oscillation in an equilibrium air flow should be removed.

(2) Hyperboloid Flare

Our numerical result for a hyperboloid flare is solution to Problem Ⅲ-1 of this workshop, that is only a perfect gas case. This problem is correspond to an experiment by Gottingen Ludwig Tube used cold gas.

Computational grid as we used is generated by Dr.Y.Yamamoto(NAL), and a size of this grid is 521×101(Fig.5).

Flow conditions are as follows.

Mach Number	:	6.83
Temperature	:	67.765 K
Reynolds Number	:	7.0×10^{6} /m
Wall Temperature	:	300 K

In a heat flux distribution on a surface (Fig.7), negative values appear from x/L=0.8 to 1.0, where is just before and behind a peak value at a reattached region. This may be because we do not take account of the unsteadiness owing to a seperation induced by the interaction between an oblique shock wave and a boundary layer in this calculation which is used local time stepping to get a steady solution.

Such influences of the lack of the flow unsteadiness in numerical simulation also appears as a small oscillation in temperature contours(Fig.6) and a pressure distribution on a surface (Fig.8).

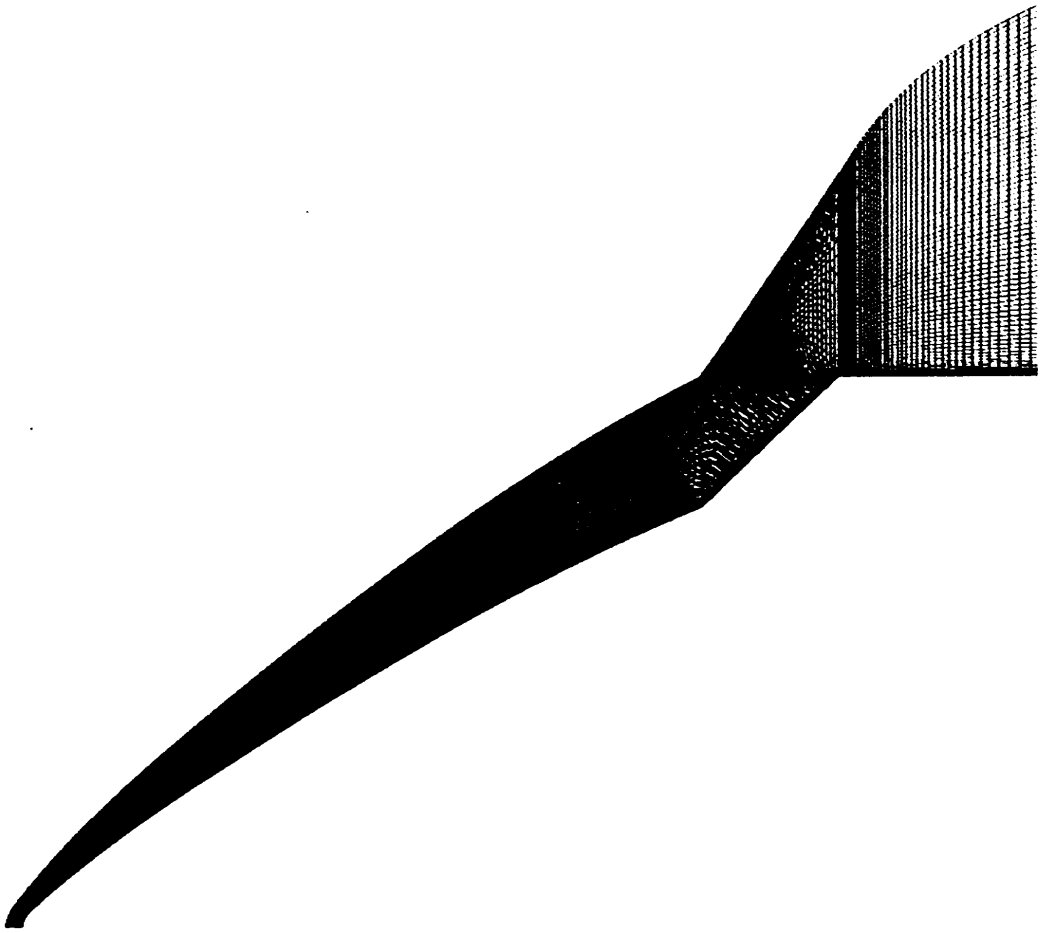

Fig.5 Computational Grid around Hyperboloid Flare

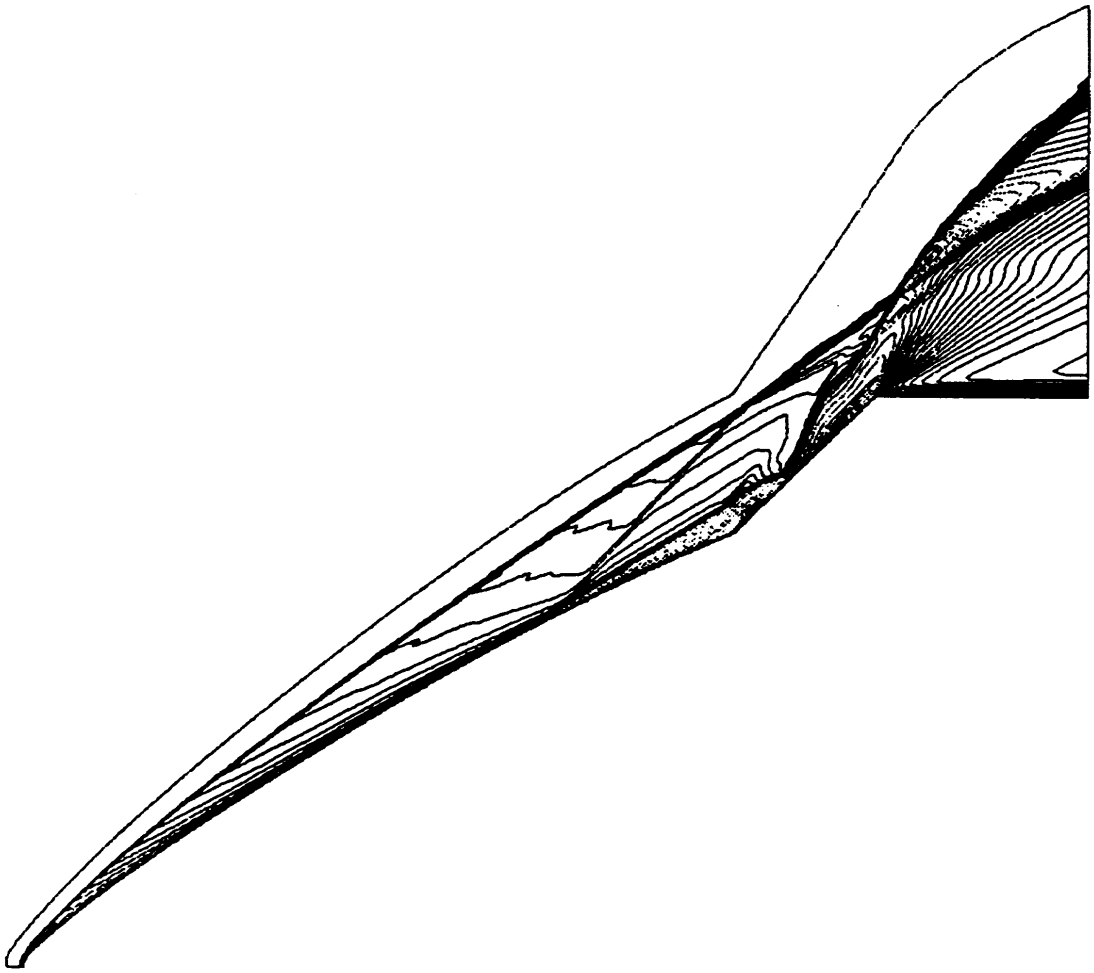

Fig.6 Temperature Contures around Hyperboloid Flare

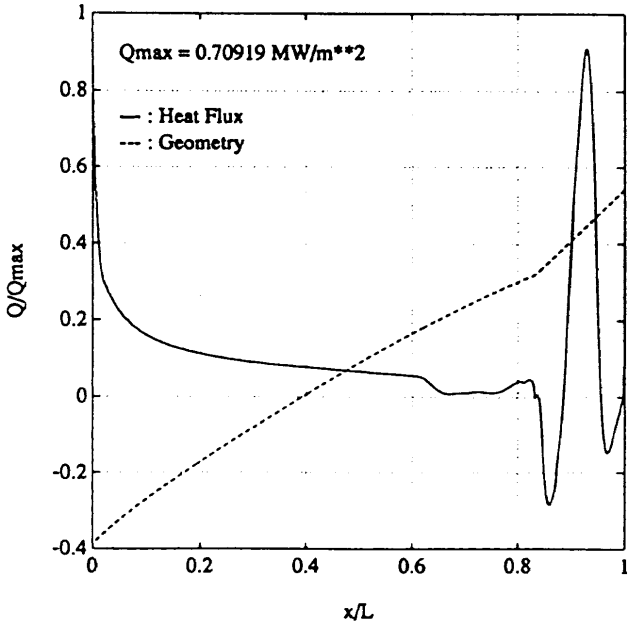

Fig.7 Heat Flux Distribution on Hyperboloid Flare

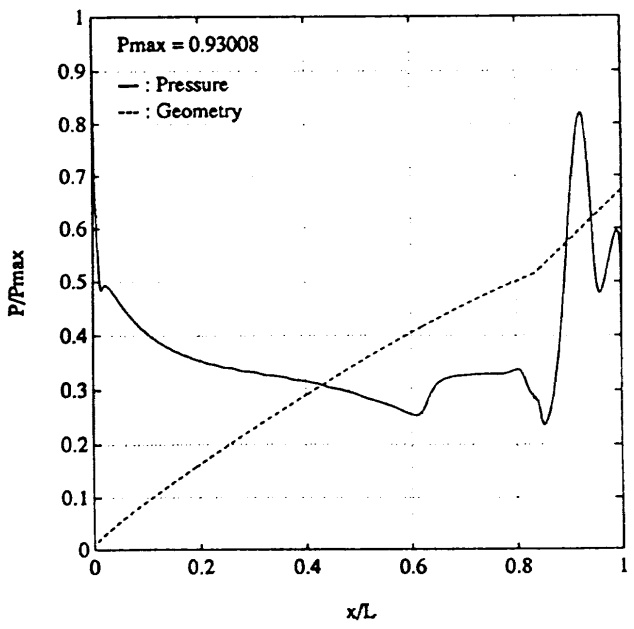

Fig.8 Pressure Distribution on Hyperboloid Flare

4. Conclusions

We introduced our numerical results of hypersonic flow analysis around OREX and hyperboloid flare with/without real gas effects.

Numerical results of OREX suggest us that our flow analysis system for a hypersonic flow is not completed yet, especially for an equilbrium air flow. The result of a hyperboloid flare also shows that the flow unstediness must be taken into account, in order to predict more accurately the aerodynamic and aerothermodynamic characteristics of a hypersonic flow including seperations induced by the interaction between a shock wave and a boundary layer.

Therefore, we intend to make our system more accurate and usable, and our final goal is that our flow analysis system can be used as one of aerodynamic and aerothermodynamic design tools for the development of reentry vehicles.

References

(1) Hanamitsu,A., Kishimoto,T., and Bito,H., "High Enthalpy Flow Computation and Experiment around the Simple Bodies", Proceedings of the 13th NAL Symposium on Aircraft Computational Aerodynamics, to be appeared.

(2) Sawada,K., and Takanashi,S.,"A Numerical Investigation on Wing/Nacelle Interferences of USB Configuration", AIAA Paper 87-0455, 1987.

(3) Kishimoto,T., and Kaneko,S.,"Hypersonic Flow Analysis around OREX", Proceedings of the 12th NAL Symposium on Aircraft Computational Aerodynamics, CFD Workshop on Hypersonic Flow, NAL SP-26, pp.56-60, 1994. In Japanese.

(4) Wada,Y., and Liou,M.-S.,"A Flux Splitting Scheme with High-Resolution and Robustness for Discontinuities", AIAA Paper 94-0083, 1994.

(5) Shima,E., and Jounouchi,T.,"Role of Computational Fluid Dynamics in Aeronautical Engineering(No.12) -Formulation and Verification of Uni-Particle Upwind Schemes for the Euler Eqations-", Proceedings of the 12th NAL Symposium on Aircraft Computational Aerodynamics, NAL SP-27, pp.255-260, 1994. In Japanese.

(6) Srinivasan,S., Tannehill,J.C., and Weilmuenstar,K.J.,"Simplified Curve Fits for the Thermodynamic Properties of Equilibrium Air", ISU-ERI-Ames-86401, ERI Project 1626, CFD 15, 1986.

(7) Srinivasan,S., and Tannehill,J.C., "Simplified Curve Fits for the Transport Properties of Equilibrium Air", NASA CR-178411, 1987.

2−7

Numerical Simulation of Hypersonic Flow around Hyperboloid Flare Body

by

Hirotaka OHTSU

Department of Aeronautics and Astronautics, Graduate school of Engineering, University of Tokyo

Kojiro SUZUKI

Department of Aeronautics and Astronautics, Graduate school of Engineering, University of Tokyo

Takashi ABE

The Institute of Space and Astronautical Science (ISAS)

Abstract

A numerical simulation of the flow around the Hyperbolid Flare Body has been performed in a Mach 6.83 air stream by solving axisymmetric laminar Navier-Stokes equations. The result shows that shock-shock interactions occurs.

Introduction

During reentry flight of a space craft from an earth orbit, the freestream Mach number varies very widely from the hypersonic regime at high altitude flight to the low subsonic regime at landing. For the system design of such space craft, it is very important to predict the aerodynamic characteristics of the space craft over the whole range of flight Mach numbers. Especially, in the hypersonic range, the real gas effect of air affects the aerodynamic characteristics of the vehicle. And in such a region the tests on the ground are very difficult. So numerical simulations of the hypersonic flow are very important. But the validity of the code must be checked very carefully. The purpose of this paper is to calculate the flow properties and to check results precisely.

Numerical Analysis

Governing equations

In this study, the flow is assumed to be an laminar and axisymmetric. So we used the axisymmetric compressible laminar Navier-Stokes equation in the generalized coordinate.

$$\frac{\partial Q}{\partial t}+\frac{\partial F}{\partial \xi}+\frac{\partial G}{\partial \eta}+H=\frac{\partial Fv}{\partial \xi}+\frac{\partial Gv}{\partial \eta}+Hv$$

where

$$Q=\frac{1}{J}\begin{bmatrix}\rho\\ \rho u\\ \rho v\\ Et\end{bmatrix}$$

$$F=\frac{1}{J}\begin{bmatrix}\rho U\\ P\xi_x+\rho uU\\ P\xi_r+\rho vU\\ (Et+P)U\end{bmatrix},\quad G=\frac{1}{J}\begin{bmatrix}\rho V\\ P\eta_x+\rho uV\\ P\eta_r+\rho vV\\ (Et+P)V\end{bmatrix}$$

$$Fv=\frac{1}{J}\begin{bmatrix}0\\ \tau_{xx}\xi_x+\tau_{rx}\xi_r\\ \tau_{rx}\xi_x+\tau_{rr}\xi_r\\ (\tau_{xx}\xi_x+\tau_{rx}\xi_r)u+(\tau_{rx}\xi_x+\tau_{rr}\xi_r)v+q_x\xi_x+q_r\xi_r\end{bmatrix}$$

$$H=\frac{1}{J}\begin{bmatrix}\rho v/r\\ \rho uv/r\\ \rho v^2/r\\ (Et+P)v/r\end{bmatrix},$$

$$Hv=\frac{1}{J}\begin{bmatrix}0\\ \tau_{rx}/r\\ 2\mu(\partial v/\partial r-v/r)/r\\ (\tau_{rr}v+\tau_{rx}u+q_r)/r\end{bmatrix}$$

and

$$U=u\xi_x+v\xi_r,\quad V=u\eta_x+v\eta_r$$

$$\tau_{rr}=\lambda\left(\frac{\partial u}{\partial x}+\frac{\partial v}{\partial r}+\frac{v}{r}\right)+2\mu\frac{\partial v}{\partial r}$$

$$\tau_{xx}=\lambda\left(\frac{\partial u}{\partial x}+\frac{\partial v}{\partial r}+\frac{v}{r}\right)+2\mu\frac{\partial u}{\partial x}$$

$$\tau_{rx}=\mu\left(\frac{\partial u}{\partial r}+\frac{\partial v}{\partial x}\right)$$

$$q_x=-k\frac{\partial T}{\partial x},\quad q_r=-k\frac{\partial T}{\partial r}$$

where k is a thermal conductivity and J is a Jacobian. We selected a Sutherland's law for viscous coefficient.

$$\mu=C_1\frac{T^{3/2}}{T+C_2}$$

where, $C_1=1.458\times10^{-6}$. $C_2=110.4$. This equation is valid for low temperature. And ξ is a coordinate along to the body surface, and η is a coordinate normal to the body surface. Q is avector of conserved variables. F and G are vectors of fluxes. H is a term including 1/r. The subscript v indicates viscous terms.

Scheme

Viscous terms and Jacobian are evaluated by central difference. As for convective terms, we selected explicit symmetric TVD scheme.[1] The numerical fluxes can be expressed in this form,

$$\tilde{F}_{j+1/2}=\frac{1}{2}\left(F_j+F_{j+1}+\phi_{j+1}\right)$$

$$\phi_{j+1}=-\left[\lambda(a_{j+1/2})^2\hat{Q}_{j+1/2}+\psi(a_{j+1/2})(\alpha_{j+1/2}-\hat{Q}_{j+1/2})\right]$$

where $\hat{Q}_{j+1/2}$ is a limiter function and $\alpha_{j+1/2}$ is the difference of the characteristic variables in the local ξ or η direction and $\psi(x)$ is a function for entropy correction. In most cases, the function can be expressed ,

$$\psi(x)=\begin{cases}|x|, & (|x|>\delta)\\ (x^2+\delta^2)/2\delta, & (|x|<\delta)\end{cases}$$

where δ is chosen for enhancement of stability of the scheme in this form [2],

$$\delta_{j+1/2}=\delta\left(|U|+|V|+c\sqrt{\xi_x^{\,2}+\xi_r^{\,2}+\eta_x^{\,2}+\eta_r^{\,2}}\right)$$

where, U and V are contravariant velocity components and c is a sonic. The value $\bar{\delta}$ is chosen in the range $0.05 < \bar{\delta} < 0.25$. In this calculation $\bar{\delta}$ is set to 0.2. We used Yee's minmod function as a limiter function, which is expressed

$$\hat{Q}_{j+1/2} = \text{minmod}\left[2\alpha_{j-1/2}, 2\alpha_{j+1/2}, 2\alpha_{j+3/2}, \frac{1}{2}(\alpha_{j-1/2} + \alpha_{j+1/2})\right]$$

For Riemann solver, we used Roe's approximate solution. And the time integration is performed by 2 step Runge-Kutta method.

Mesh

We have used for this problem the body-fitted computational grid as shown in Figure 1. The grid points are 177 points along the body surface (ξ direction) and 34 points normal to the body surface (η direction). We reduced the grid points for ξ direction from 521 points to 174 points and for η direction from 101 points to 34 points for saving the calculation time. The original computational grid was distributed by National Aerospace Laboratory (NAL).

Flow condition and boundary condition

Flow condition is showed in Table 1. As for boundary condition, on body surface, the velocity components are 0 and pressure gradient normal to the body surface is 0 and the temperature on the body surface is fixed at 310K. That is,

$$u = v = 0$$

$$\frac{\partial P}{\partial \eta} = 0$$

$$T = T_w$$

table 1 Flow condition

M_∞	T_∞	Re	T_{wall}
6.83	67.765	7.0×10^6	310

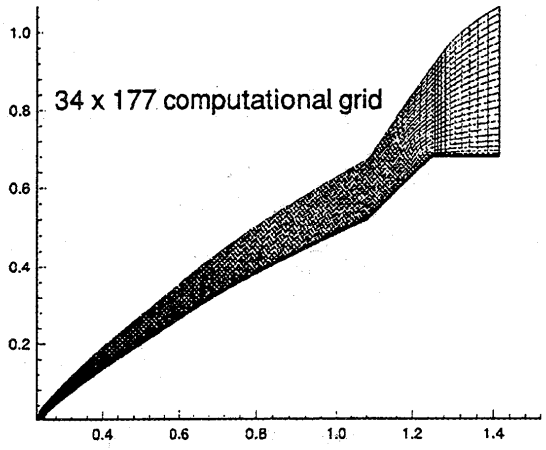

Fig. 1 Computational grid

Results and Discussions

Convergence history

The convergence history is shown in Figure 2. This shows that the convergence rate of symmetric TVD scheme is relatively good for this case.

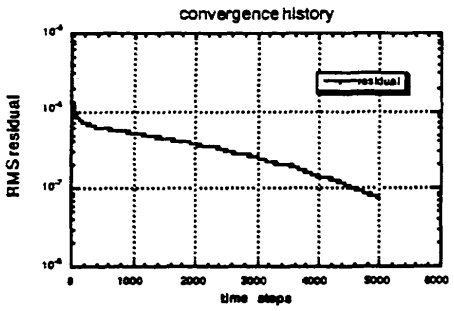

Fig. 2 Convergence history

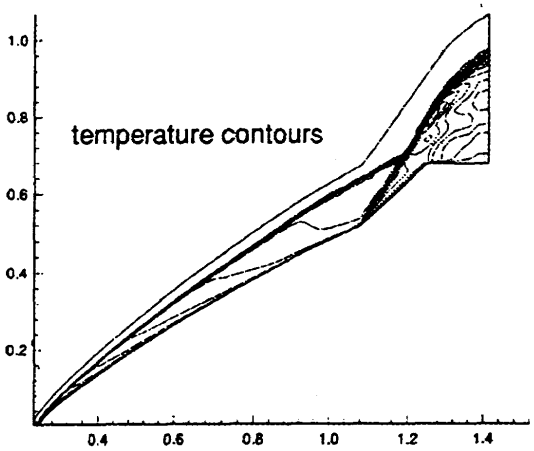

Fig. 4 Temperature contours

Pressure contours

In Figure 3, we can see clearly the interaction of the two shock lines, which are from the stagnation region and from the flare. And the expansion from the corner is also captured clearly.

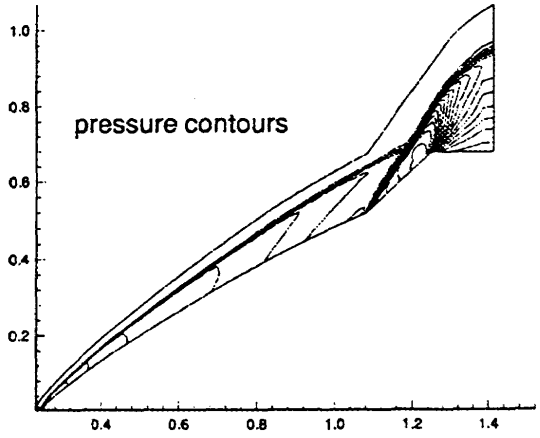

Fig. 3 Pressure contours

Temperature contours

Figure 4 shows the temperature contours. In this plot, we can see the boundary layer of temperature because of the fixed temperature at wall. And we can see also the shock-shock interactions clealy.

Pressure distribution along the body surface

The pressure distribution along the body surface is shown in Figure 5. In this plot, we can see the pressure increases rapidly around the stagnation region and the flare. But we can't capture the flow separation in front of the flare. One of the reasons may be that we don't set sufficient grid points along the body surface and in the boundary layer.

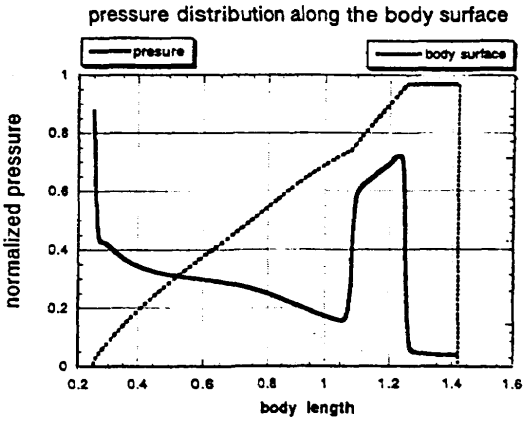

Fig. 5 Pressure distribution along the body surface

Heat flux distribution along the body surface

Figure 6 and 7 show the heat flux distribution along the body surface. Figure 6 shows the heat flux distribution along the whole body surface and Figure 7 shows the distribution around the flare precisely. In Figure 6, the maximum value is on the stagnation point and the value is much higher than other region. This shows that the temperature around the stagnation point is very high and the phenomina is captured clearly.

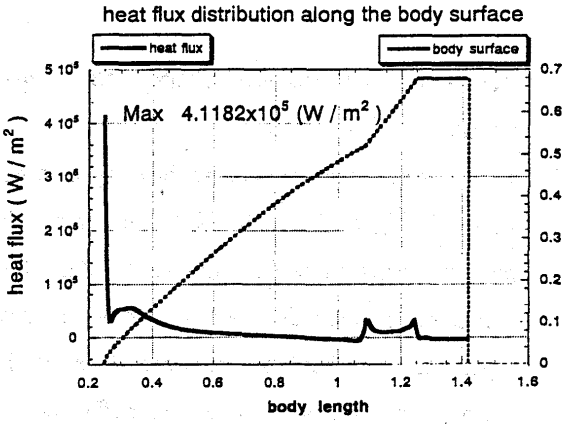

Fig. 6 Heat flux distribution along the body surface

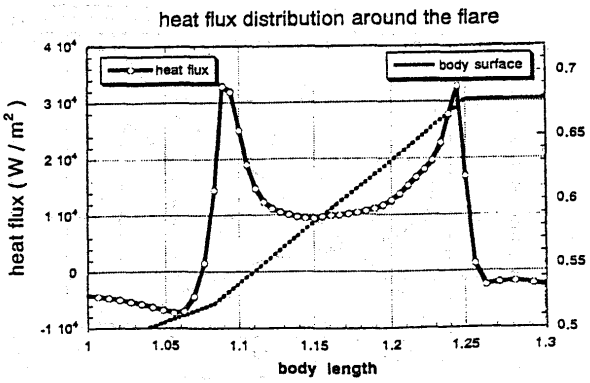

Fig. 7 Heat flux distribution around the flare

As shown in Figure 6 and 7, two peaks can be seen around the flare. The left one is made by shock from the flare and the other is made by expansion from the corner.

Summary and Conclusion

In this study, we calculated the flow around the hyperboloid flare body in the region of hypersonic speed. The results are summarized as follows,

1. Pressure contours show clearly the shock waves and their interactions. And the expansion also can be seen clearly.
2. Temperature contours show clearly the temperature boundary layer and shock-shock interactions.
3. According to the pressure distribution along the body surface, we couldn't capture the flow separation in the flare. In order to capture the flow separation, it seems to be necessary to set sufficient grid points around the flare and in the boundary layer.
4. The maximum value of heat flux is on the stagnation point. And two peaks, which are made by shock and expansion, can be captured clearly.

Based on these results and this symmposium, we would like to cure the above problems.

References

[1]H. C. Yee "Construction of Explicit and Implicit Symmetric TVD Schemes and Their Applications," *Journal of Computational Physics*, No 68, 1987, pp. 151-179

[2]H. C. Yee, "A Class of High-Resolution Explicit and Implicit Shock-Capturing Methods" NASA TM 101088

2-8

Computational Analysis of High Enthalpy Flow around Blunt Body

by

Yukimitsu Yamamoto
National Aerospace Laboratory Chofu, Tokyo, Japan

ABSTRACT

Flux-split upwind Navier-Stokes CFD code are applied to high entalpy flow around several blunt bodies. In this paper, sphere problems in DLR HEG experiments, OREX (Orbital Re-entry Experiments) flight flowfield, hyperboloid flare flows in ONER F4 experiments and 70 deg blunt body flows including base flow regions are investigated. Real gas effects are analyzed by using the one temperature chemically non-equilibrium Navier-Stokes code, which is developed by combining finite-rate chemical reactions to the current perfect gas flux splitting code. A fully implicit ADI scheme is used to avoid the stiffness problem of the time integrations. Numerical results are discussed for each flow problems and fairly good agreements are quantitatively obtained for heat transfer distributions.

Introduction

For developing and designing space transportation re-entry vehicles, accurate prediction and evaluation of hypersonic aerodynamic and aerothermodynamic characteristics are greatly important, because severe aerodynamic heating occurs and they are important research subjects for the design of thermal protection systems. For these high enthalpy re-entry flows, ground based test facilities can not simulate and reproduce realistic flight enviroments. Therefore, CFD becomes to play an important role for evaluating the aerodynamic and aerothermodynamic characteristics. However, real gas effects must be explored carefully and corresponding CFD code has to be validated by comparisons with high enthalpy wind tunnel tests and flight experiments. In our numerical code, 7 species, one temperature models are used to account for real gas effects due to dissociation and ionization, because current study is focused on the atomospheric re-entry, where thermally equilibrium state may be dominant. In addition, the difference of heat flux computed two and one temperature models may be ignored. Species mass conservation equations with source terms are combined to the present three-dimensional flux splitting Navier-Stokes equations. New algorithms for flux-splitting schemes are developed by several authors in order to decrease their dissipative features. However, in the present, these schemes may not be sufficiently established for the aerodynamic design use.

In the present study, conventional flux splitting scheme is used and the accuracy and applicability of our numerical approach are investigated . In order to avoid stiffness problems, associated with chemical reactions, fully implicit ADI method is applied.

Numerical Algorithm

Basic Equations

The three-dimensional chemically non-equilibrium Navier-Stokes equations including species continuity equations with thin-layer assumption are expressed as ;

$$\frac{\partial \overline{Q}}{\partial t}+\frac{\partial \overline{F}}{\partial \xi}+\frac{\partial \overline{H}}{\partial \eta}+\frac{\partial\left(\overline{H}-\overline{H}_{v}\right)}{\partial \zeta}=\overline{S} \qquad (1)$$

$$\overline{Q}=\begin{bmatrix}\rho_1\\ \rho_2\\ \vdots\\ \rho_n\\ \rho u\\ \rho v\\ \rho w\\ E\end{bmatrix} \qquad (2)$$

$$\overline{F}=\frac{|\nabla \xi|}{J}\begin{bmatrix}\rho_1 U\\ \rho_2 U\\ \vdots\\ \rho_n U\\ \rho u U+\tilde{\xi}_x P\\ \rho v U+\tilde{\xi}_y P\\ \rho w U+\tilde{\xi}_z P\\ (E+P)\cdot U\end{bmatrix} \qquad (3)$$

$$\overline{G}=\frac{|\nabla \eta|}{J}\begin{bmatrix}\rho_1 V\\ \rho_2 V\\ \vdots\\ \rho_n V\\ \rho u V+\tilde{\eta}_x P\\ \rho v V+\tilde{\eta}_y P\\ \rho w V+\tilde{\eta}_z P\\ (E+P)\cdot V\end{bmatrix} \qquad (4)$$

$$\overline{\boldsymbol{H}} = \frac{|\nabla\zeta|}{J}\begin{bmatrix} \rho_1 W \\ \rho_2 W \\ \vdots \\ \rho_n W \\ \rho u W + \tilde{\zeta}_x P \\ \rho v W + \tilde{\zeta}_y P \\ \rho w W + \tilde{\zeta}_z P \\ (E+P)\cdot W \end{bmatrix} \tag{5}$$

$$\overline{\boldsymbol{H}}_v = \frac{|\nabla\zeta|}{J}\begin{bmatrix} -\rho_1\left(\tilde{\zeta}_x u_{s1} + \tilde{\zeta}_y v_{s1} + \tilde{\zeta}_z w_{s1}\right) \\ -\rho_2\left(\tilde{\zeta}_x u_{s2} + \tilde{\zeta}_y v_{s2} + \tilde{\zeta}_z w_{s2}\right) \\ \vdots \\ -\rho_n\left(\tilde{\zeta}_x u_{sn} + \tilde{\zeta}_y v_{sn} + \tilde{\zeta}_z w_{sn}\right) \\ \mu\cdot|\nabla\zeta|\cdot\left(u_\zeta + W_\zeta\cdot\tilde{\zeta}_x/3\right) \\ \mu\cdot|\nabla\zeta|\cdot\left(u_\zeta + W_\zeta\cdot\tilde{\zeta}_y/3\right) \\ \mu\cdot|\nabla\zeta|\cdot\left(u_\zeta + W_\zeta\cdot\tilde{\zeta}_z/3\right) \\ |\nabla\zeta|\cdot\Theta \end{bmatrix} \tag{6}$$

$$\begin{aligned} U &= \tilde{\xi}_x u + \tilde{\xi}_y v + \tilde{\xi}_z w \\ V &= \tilde{\eta}_x u + \tilde{\eta}_y v + \tilde{\eta}_z w \\ W &= \tilde{\zeta}_x u + \tilde{\zeta}_y v + \tilde{\zeta}_z w \end{aligned} \tag{7}$$

$$\tilde{\zeta}_x = \zeta_x / \sqrt{\zeta_x^2 + \zeta_y^2 + \zeta_z^2} \;\; etc. \tag{8}$$

$$\Theta = \frac{\mu}{2}(u^2+v^2+w^2)_\zeta + k\cdot T_\zeta + \rho\sum_{i=1}^{n} h_i D_i Y_{i\zeta} + \frac{u\cdot W\cdot W_\zeta}{3} \tag{9}$$

$$\rho = \rho_1 + \rho_2 + \rho_3 + \cdots + \rho_n \tag{10}$$

$$Y_i = \rho_i / \rho \tag{11}$$

where ζ is the coodinate normal to the body surface. The vector Q consists of species density, momentum and total energy. P and ρ are the pressure and total density, respectively. μ and k are mixture viscosity and thermal conductivity. The chemical source term $\bar{s}$ has non-zero components corresponding to species conservation equations. It is written as ;

$$\overline{\boldsymbol{S}} = \frac{1}{J}\begin{bmatrix} w_1 \\ w_2 \\ \vdots \\ w_n \\ 0 \\ 0 \\ 0 \\ 0 \end{bmatrix} \tag{12}$$

where ω_i is the mass production rate of species i.

The differencing used in the present algorithm is conventional flux vector splitting. Details of this methed is described in Ref.1.

In the present analysis, the effects of multicomponent diffusion are neglected and the binary Lewis numbers for all the species are assumed to be the same, then a simple expression for the mixture's diffusion coefficients $\tilde{D}$ results

$$\tilde{D} = \frac{\tilde{\kappa}\, Le}{\tilde{\rho}\,\tilde{C}p} \tag{13}$$

where tildes denote dimensional quantities and the following nondimensionalization has been employed.

$$C_{pf} = \frac{\widetilde{C_{pf}}\,\widetilde{T^\infty}}{U^{\infty 2}} \qquad D = \frac{\tilde{D}}{\widetilde{D^\infty}} \tag{14}$$

The equations of state for mixture is written as

$$P = \frac{\beta_1\,\rho\, T}{M} \qquad M = \frac{\widetilde{M}}{\widetilde{M^\infty}} \tag{15}$$

where the mixture molecular weight is determined by

$$M = \left(\sum_{i=1}^{n}\frac{Y_i}{M_i}\right)^{-1} \tag{16}$$

Here,Y_i is the species mass fraction and defined as ρ_i/ρ. The expression for total enthalpy is

$$H = \frac{E+P}{\rho} = h + \frac{1}{2}\left(u^2+v^2+w^2\right) \tag{17}$$

The enthalppy of the mixture is determined by summing the individual contributions of each species.

$$\tilde{h} = \sum_{i=1}^{h} Y_i\,\tilde{h}_i \tag{18}$$

$$\tilde{h}_i = \widetilde{h_{i0}} + \int_0^{\tilde{T}} \widetilde{C_{pi}}\, d\tilde{T} \tag{19}$$

The dimensional enthalpies and specific heat of each species are determined by using equations of Ref.23.

Transport Properties

The viscosity of a species, s, is calaculated using the following curve fit.

$$\tilde{\mu}_s = 0.1 exp\left[\left(A_s log_e\tilde{T} + B_s\right) log_e\tilde{T} + C_s\right] \tag{20}$$

where A_s, B_s,and C_s are constants for each species.

Eucken's formula is used to compute thermal conductivity.

$$\tilde{\kappa}_s = \frac{\tilde{\mu}_s \tilde{R}}{\widetilde{M}_s}\left(\tilde{C}_{p,s}\frac{\widetilde{M}_s}{\tilde{R}} + \frac{5}{4}\right) \tag{21}$$

Wilke's mixing rule is used to compute the mixture viscosity and thermal conductivity from those of the individual species.

$$\tilde{\mu} = \sum_{s=1}^{n} \frac{X_s \tilde{\mu}_s}{\phi_s} \qquad \tilde{\kappa} = \sum_{s=1}^{n} \frac{X_s \tilde{\kappa}_s}{\phi_s} \tag{22}$$

where

$$\begin{aligned} \phi_s &= \sum_{\gamma=1}^{n} X_\gamma \left[1 + \sqrt{\frac{\tilde{\mu}_s}{\tilde{\mu}_\gamma}}\left(\frac{M_s}{M_\gamma}\right)^{\frac{1}{4}}\right]^2 \left[\sqrt{8}\sqrt{1+\frac{\widetilde{M}_s}{\widetilde{M}_\gamma}}\right]^{-1} \\ X_s &= \frac{Y_s \widetilde{M}}{\widetilde{M}_s} \end{aligned} \tag{23}$$

Chemical Model

The chemistry model is air and 7 chemical species are taken into account ;

(1) molecular oxygen	O_2
(2) atomic oxygen	O
(3) molecular nitrogen	N_2
(4) atomic nitrogen	N
(5) nitric oxide	NO
(6) nitric oxide ion	NO^+
(7) ion	e^-

An assumption employed in this model is that the gas possesses a zero net local charge. This allows the conservation of electron mass equation to be eliminated from the set of governing equations. The reactions that are considered are ;

$$\begin{aligned} O_2 + M &= O + O + M \quad (R1) \\ N_2 + M &= N + N + M \quad (R2) \\ NO + M &= N + O + M \quad (R3) \\ NO + O &= N + O_2 \quad (R4) \\ O + N_2 &= N + NO \quad (R5) \\ O + N &= NO^+ + e^- \quad (R6) \end{aligned}$$

where impacting body M can be any one of the species. The forward and backward reaction ratets are of the form.

$$kf(T) = CfT^{nf}e^{-\theta d/T} \qquad kb(T) = \frac{kf(T)}{K_{eq}(T)} \tag{24}$$

where K_{eq} is the equilibrium constants and a function of temperature.

$$\begin{aligned} K_{eq}(T) &= exp(A1 + A2z + A3z^2 + A4z^3 + A5z^4) \\ z &= \frac{10000}{T} \end{aligned} \tag{25}$$

All the constants appearing in the reaction rate equation are given by Park.

Then, the production of species from each reaction can be expressed as ;

$$\begin{aligned} R1 &= \sum_M [-kf_{1M}[N_2][M] + kb_{1M}[N][N][M]] \\ R2 &= \sum_M [-kf_{2M}[O_2][M] + kb_{2M}[O][O][M]] \\ R3 &= \sum_M [-kf_{3M}[NO][M] + kb_{3M}[N][O][M]] \\ R4 &= -kf_4[NO][O] + kb_4[N][O_2] \\ R5 &= -kf_5[O][N_2] + kb_5[N][NO] \\ R6 &= -kf_6[N][O] + kb_6[NO^+][e^-] \end{aligned} \tag{26}$$

The souce tetrms are given by

$$\begin{aligned} w_N &= M_N(-2R1 - R3 - R4 - R5 - R6) \\ w_{N_2} &= M_{N_2}(R1 + R5) \\ w_O &= M_O(-2R2 - R3 + R4 + R5 + R6) \\ w_{O_2} &= M_{O_2}(R2 - R4) \\ w_{NO} &= M_{NO}(R3 + R4 - R5) \\ w_{NO+} &= M_{NO+}(-R6) \\ w_{e-} &= M_{e-}(-R6) \end{aligned} \tag{27}$$

Numerical Results

Numerical calculations were performed for high enthalpy flow around four type of blunt bodies. In the present study, non-equilibrium flow analysis were made for sphere (Problem I-1~6), OREX (Problem II-1,2) and hyperboloid flare (Problem III-2). Non-react perfect gas flow analysis were also made for OREX (Problem II-5) and 70 deg blunt cone. Final computational test case is not listed in the workshop problems. However, preliminaly investigation was made to find the real gas effects through comparisons of experiental data.

Sphere

Figure 1 shows pressure contours around sphere for Problem I-1 (high enthalpy, low density case),Problem I-3 (high enthalpy, high density case). Similar results can be observed for these pressure contours. However, mass fraction distributions along the stagnation stream line indicate different characteristics in each flow cases. As for the N_2 (Nitrogen molecule) mass fraction distributions of Fig.2, strong dissociation occurs in high enthalpy, high density case (Problem I-3). In the low enthalpy case (Problem I-5), significant dessociation of N_2 dose not occur compared to the other high enthalpy cases (Problem I-1 and I-3). Heat transfer distributions along the sphere surface are shown in Fig.3. In the figure, non-catalytic and full catalytic heat transfer in are plotted for the same free stream condition case. Solid line represents the sphere geometry. Dot-dash line indicates the full catalytic heat transfer distributions and dotted line shows non catalytic ones. It is remarked that full catalytic heat transfer is about two times larger than the non-catalytic one for all three flow conditions. In addition, maximum peak of heat transfer distributions appears away from the stagnation point. These flow phenomena may be caused by very low Reynolds number effects. Experimental results shows the similar tendency, however, further investigation must be done. Quantitative comparisons of full catalytic heat transfer distributions are made and presented in Fig.4. Open symbols shows experimental data and closed ones are numerical results. Relatively good agreements are obtained, especially in high enthalpy, high density flow case. However, the difference between numerical and experimental results exists in low enthalpy flow case. Detailed investigation of may be needed in this case.

OREX

In OREX flow fields calculations, 41 grid points are distributed surface and 60 points normal to be body. Temperature contours are plotted in Fig.5. From this figure, it is noticed that shock wave is smeared in high altitude case (Problem II-1) and shock also it is clearly observed that layer thickness of the reacting flow case (problem II-2) is smaller than that of corresponding perfect gas case (Problem II-5). Heat transfer distributions are plotted in Fig.6. The value of maximum stagnation point heat transfer is increased as the altitude becomes lower and 0.344 MW/m^2 at an altitude of 60 km. These values may be considered reasonable compared to the other numerical results and flight data estimations. Temperature and mass fraction distributions along the stagnation stream line are plotted in Fig.7 and 8 for the reacting flow cases of Problem II-1 and II-2.

It is remarked that shock wave region is smeared at high altitude due to the rarefaction effects. Maximum temperature in high altitude case is about two times larger than that of the low alttitude one and it reaches to more than 20,000 K. Dissociation of nitrogen molecule N_2 in high altitude is enhanced by the these high temperature effects.

Hyperboloid Flare

For this analysis, 262 (streamwise) × 51 (normal to the body) grid points are used. Pressure and temperature contours are shown in Fig.9 and Fig.10. Recompression shock wave is generated above the flare part. Pressure and heat transfer distributions are plotted in Fig.11 and Fig.12. High pressure comparable to the nose stagnation point value is caused on the flare part and small recirculation region appears ahead of the juncture point of foreward body and flare. Heat transfer is also increased, corresponding to this pressure rise. However, the peak value is about 40 percent of stagnation point one. Detailed comparison are underway and will be presented in near future. This time rough calculation is made for the preliminaly estimation. More precise and large scale computation will be done.

Blunt Cone

In this case, omly perfect gas calculations were conducted. Computational grid consists of 161 (streamwise) × 121 (normal to the body) points. In Fig.13 and Fig.14, pressure and temperature contours are depictetd, where recompression shock wave is generated from the mid region of the afterword cylinder surface. As shown in Fig.15, surface pressure and heat transfer becomes high there. The value of local peak is about 0.2, nondimensionalized by the stagnation point heating. These results are similar to the LaRC low enthalpy hypersonic wind tunnel experiments [2]. More detailed comparisons will be made in near future.

Conclusions

By using the flux-split upwind Navier-Stokes code, several blunt body problems, proposed in NAL high enthalpy flow workshop, are analyzed. Our approach is one temperature, chemically non-equilibrium computational method for reacting flow problems. This is not sufficient for the exact analysis of high enthalpy flow phenomena. However, in practical purposes, it is useful in evaluating aerothermodynamic characteristics, because the siginificant difference of heat transfer is not observed between one-temperature and two-temperature models. Therefore, we try first the simple one temperature modeling for high enthalpy flow analysis and the limitations of this modeling is investigated.

In the present preliminary studies, numerical results favorably predict heat transfer distributions of four type of blunt bodies. However, these problems contain difficult phenomena to analyze, such as surface catalycity, the effects of the flow separation and reattachment, base flow problems etc. So, more precise study and exact validation of the CFD code will be needed.

References

1) Y.Yamamoto, "Numerical Simulation of Hypersonic Viscous Flow for Design of H-II Orbiting Plane (HOPE), Part II." AIAA Paper 91-1390, June, 1991

2) D.Kastel, T.J.Harvath, and G.Eitelberg "Non-equilibrium Flow Expansion Experiment around a Blunted Cone." Proc. of Second European Symp. on Aerothermodynamics for Space Vehicles. ESTEC, Noordwijk, The Netherlands, 21-25 Nov. 1994, ESASP-367, pp 383-389

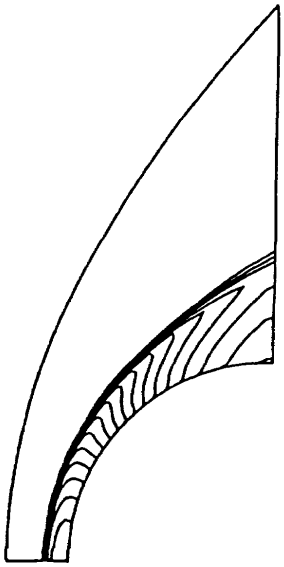

(a)

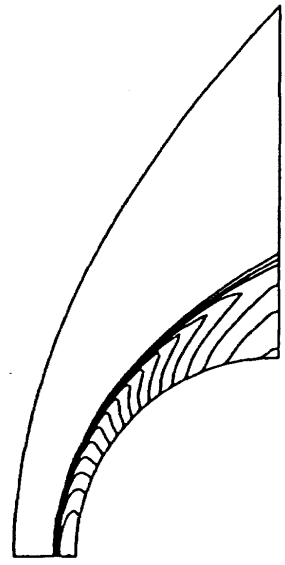

(b)

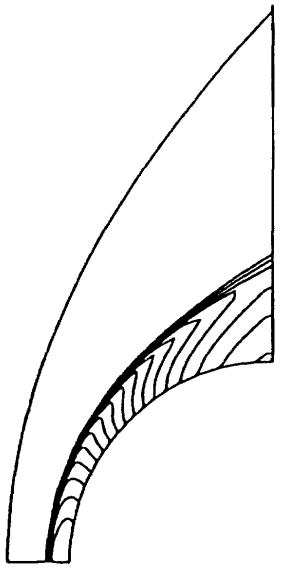

(c)

Fig.1 Pressure Contour around Sphere

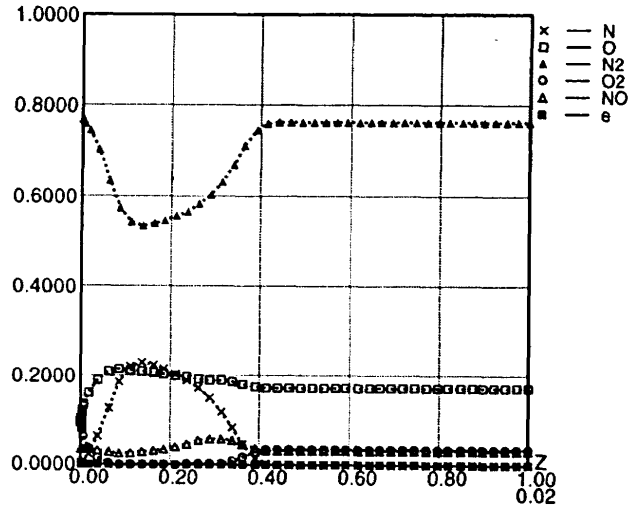

(a) Problem I - 1 Sphere Non Catalytic

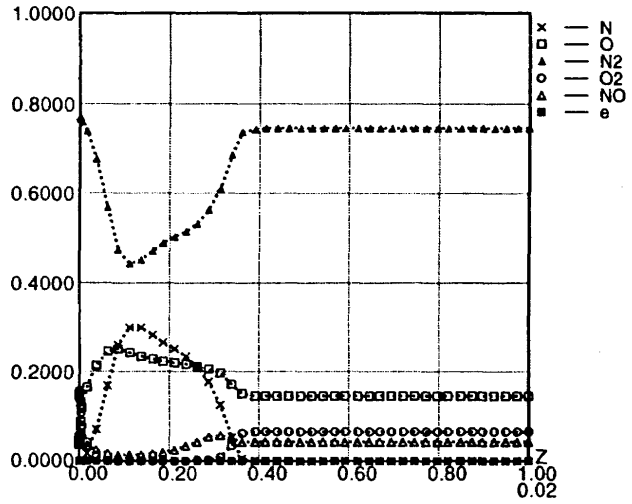

(b) Problem I - 3 Sphere Non Catalytic

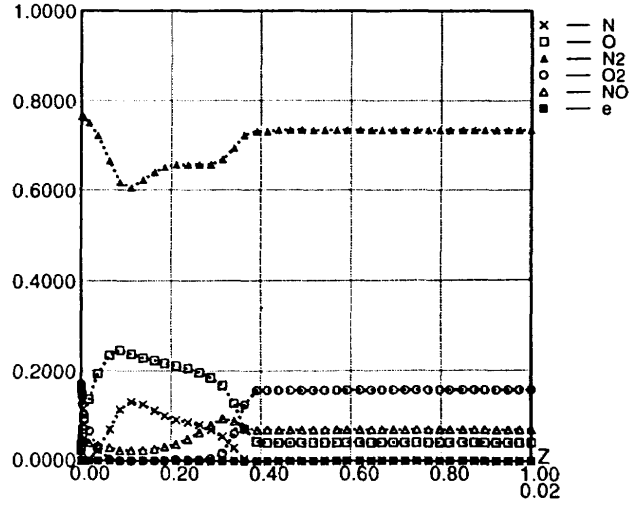

(c) Problem I - 5 Sphere Non Catalytic

Mass Fraction along the Stagnation Stream Line

Fig.2

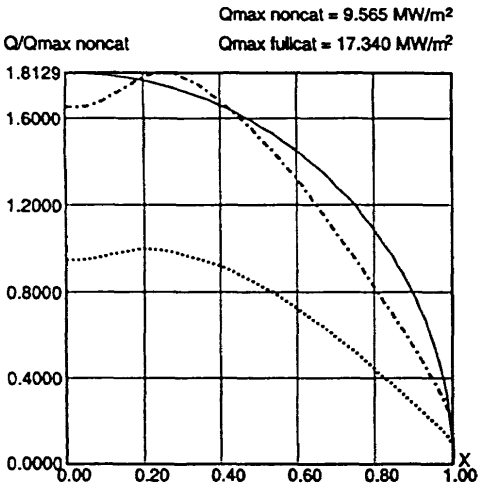

(a) Problem I - 1,2 Sphere Heat Transfer Distribution

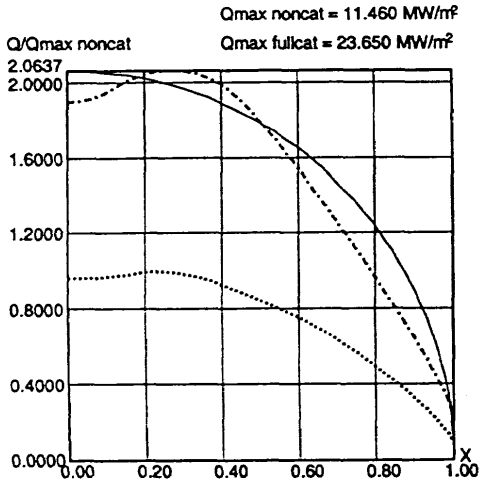

(b) Problem I - 3,4 Sphere Heat Transfer Distribution

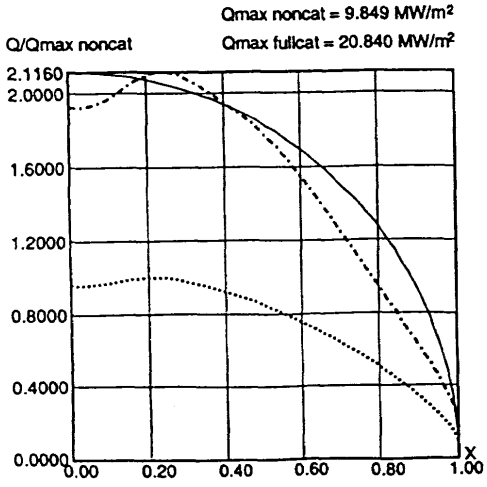

(c) Problem I - 4,5 Sphere Heat Transfer Distribution

Fig.3

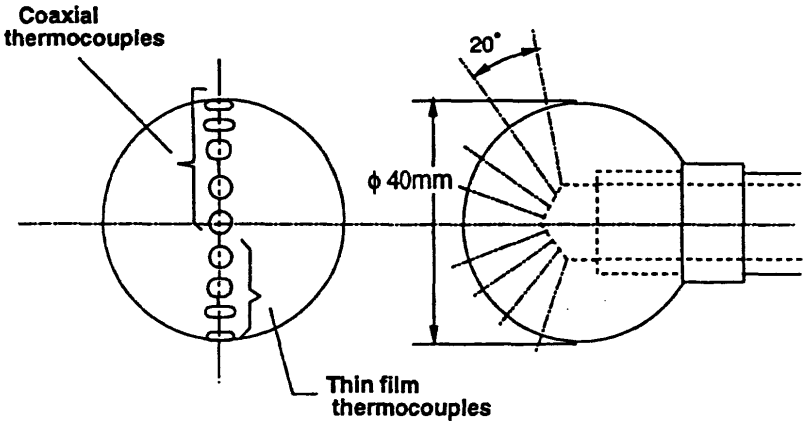

Sphere model

1.1.2 Test Cases

Case	V ∞	T ∞	ρ ∞ (kg /m ³)	Twall	Modelization	Level
I-1	5939m/s	705K	0.00156	300K	Lam, Non-eq, Non-cat	•••
I-2	〃	〃	〃	〃	〃 Full-cat	•••
I-3	6180m/s	934K	0.0034	300K	Lam, Non-eq, Non-cat	•••
I-4	〃	〃	〃	〃	〃 Full-cat	•••
I-5	5151m/s	708K	0.0058	300K	Lam, Non-eq, Non-cat	•••
I-6	〃	〃	〃	〃	〃 Full-cat	•••

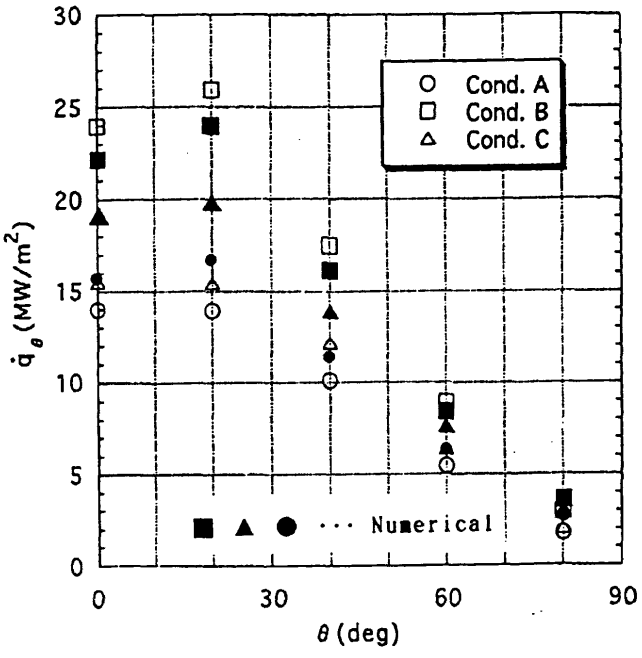

Fig.4 Comparison of Heat Transfer with HEG Experiments

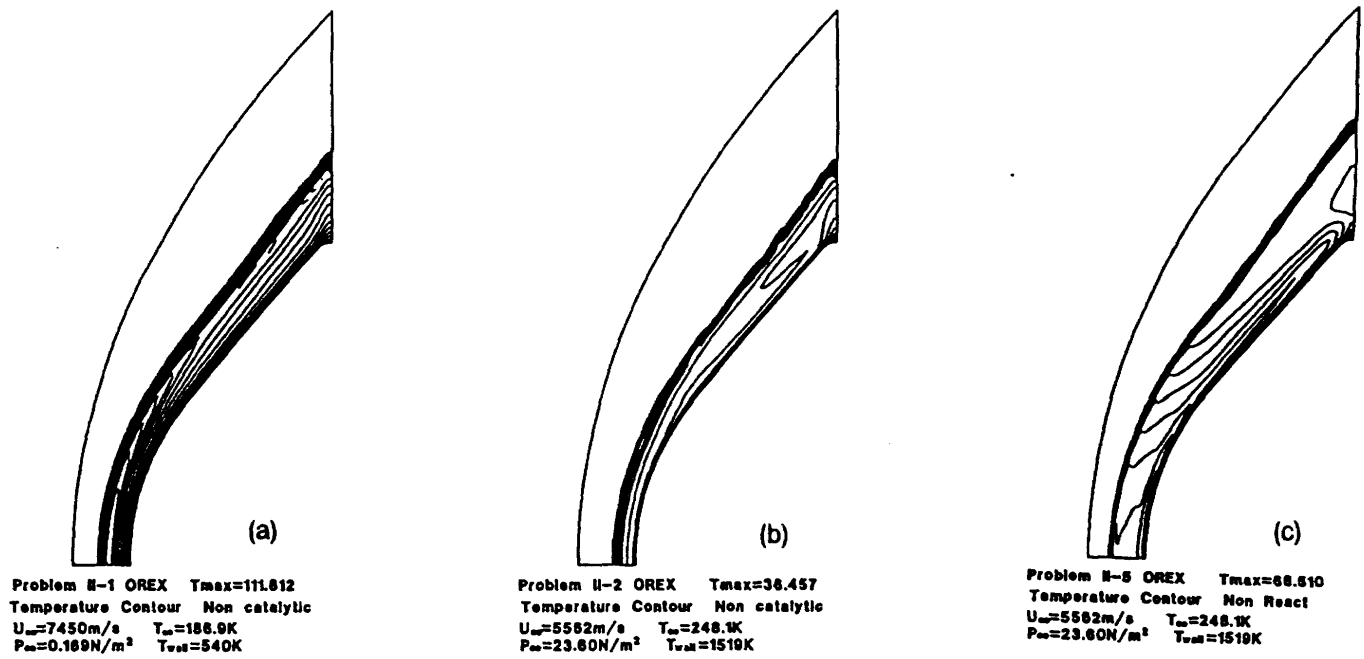

Fig.5 Temperature Contour around OREX

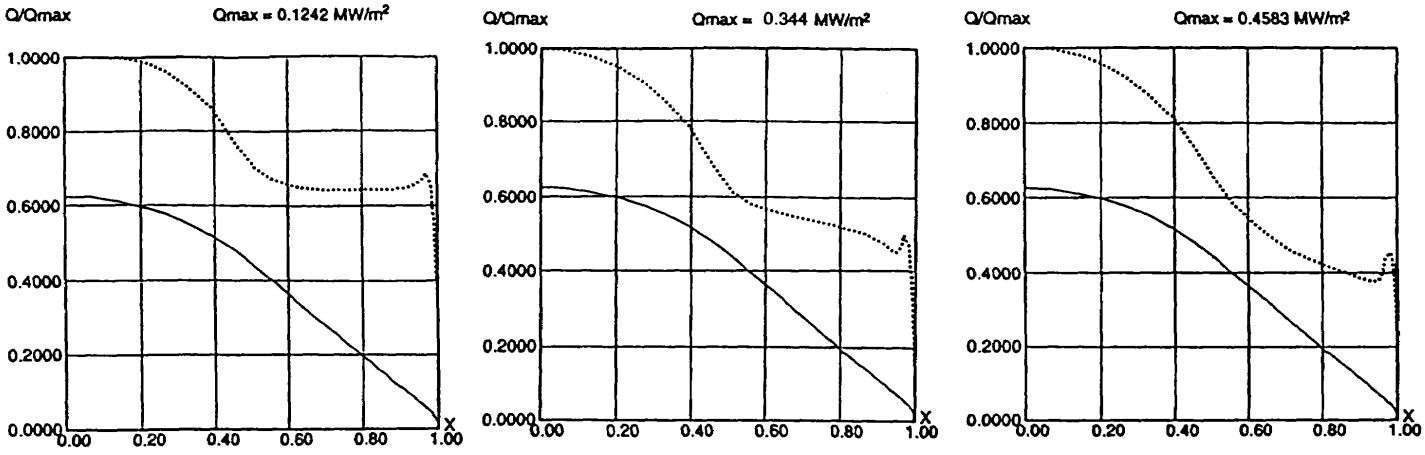

(a) Problem II - 1 OREX (b) Problem II - 2 OREX (c) Problem II - 5 OREX

Fig.6 Heat Transfer Distribution

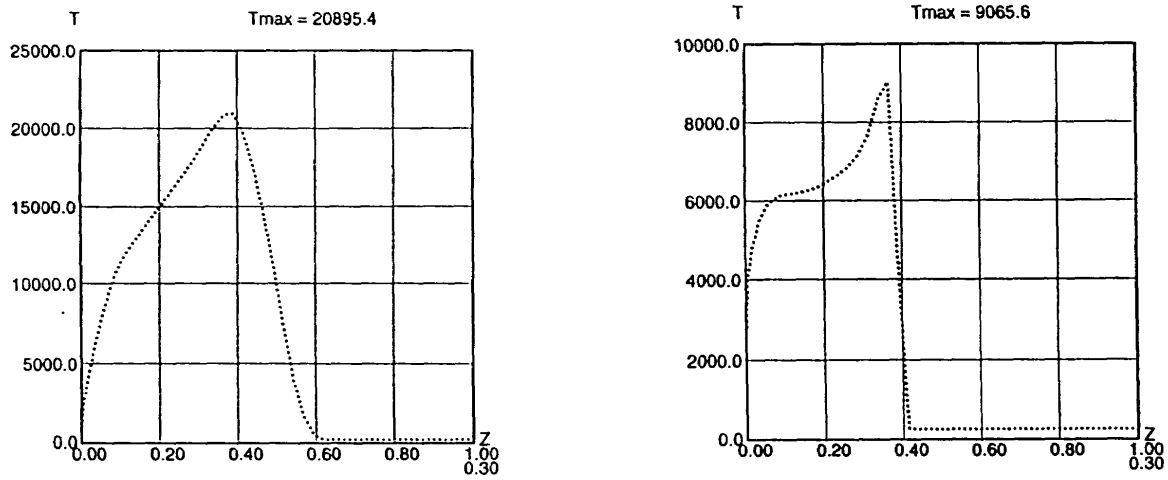

Problem II - 1 -⑥ OREX
Non Catalytic Case
Stagnation Line Temperature Distribution

Problem II - 2 -⑥ OREX
Non Catalytic Case
Stagnation Line Temperature Distribution

Fig.7

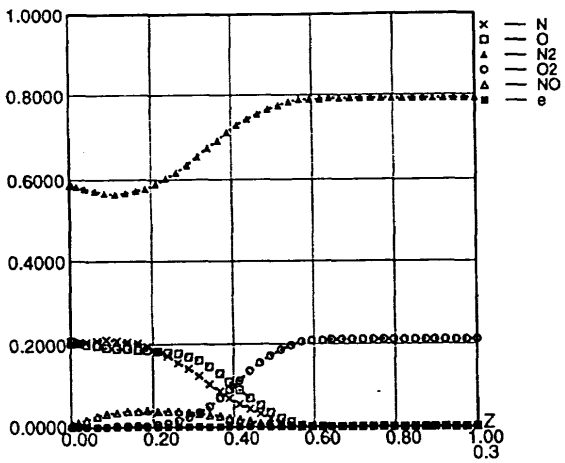

Problem II - 1 OREX Non Catalytic

Mass Fraction along the Stagnation Stream Line

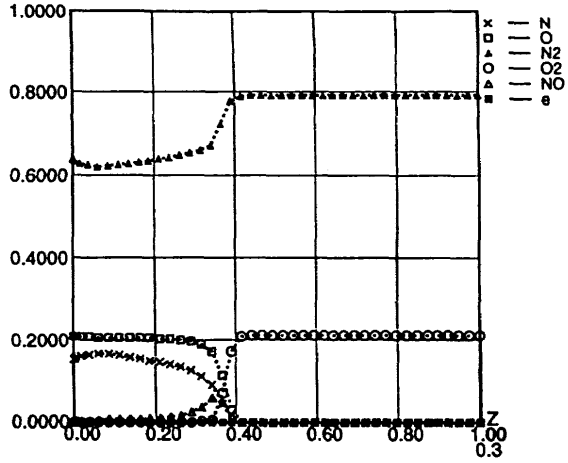

Problem II - 2 OREX Non Catalytic

Mass Fraction along the Stagnation Streem Line

Fig.8

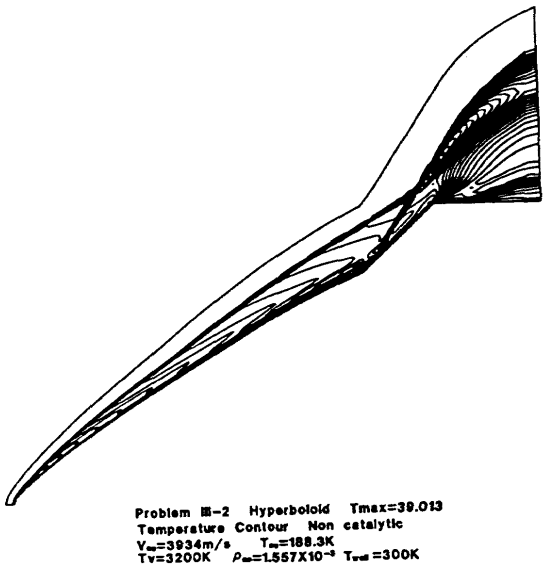

Fig.9

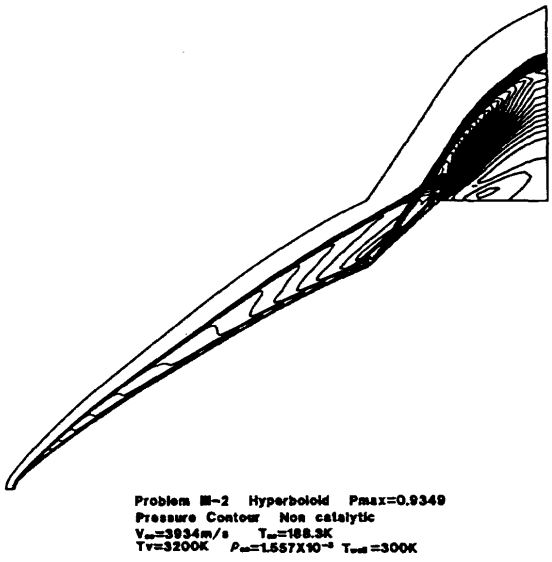

Fig.10

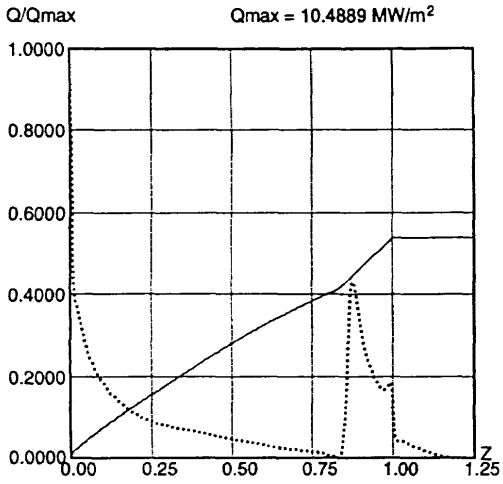

Problem III - 2 Hyperboloid Flare

Heat Transfer Distribution

Fig.11

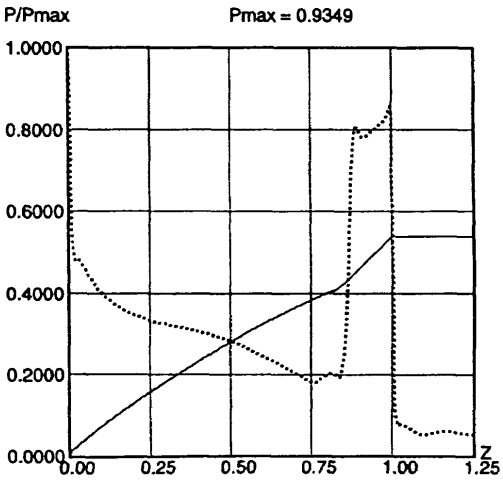

Problem III - 2 Hyperboloid Flare

Pressure Distribution

Fig.12

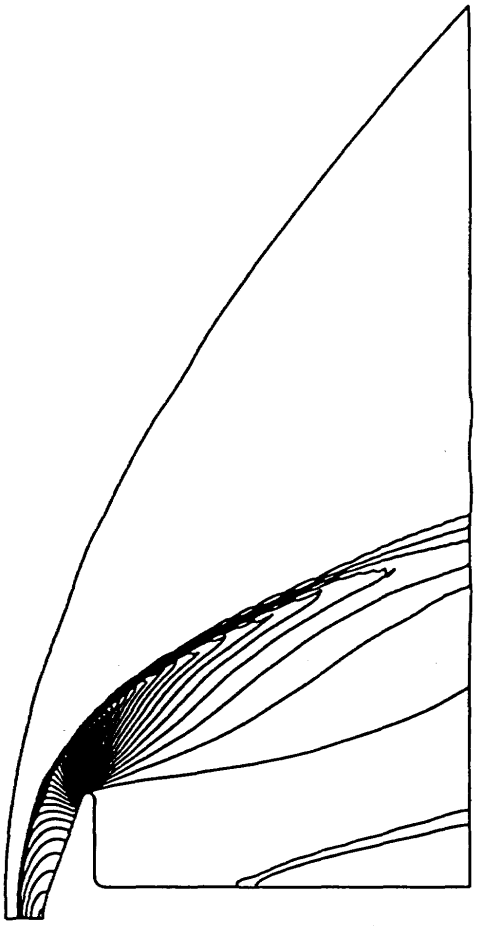

Fig.13

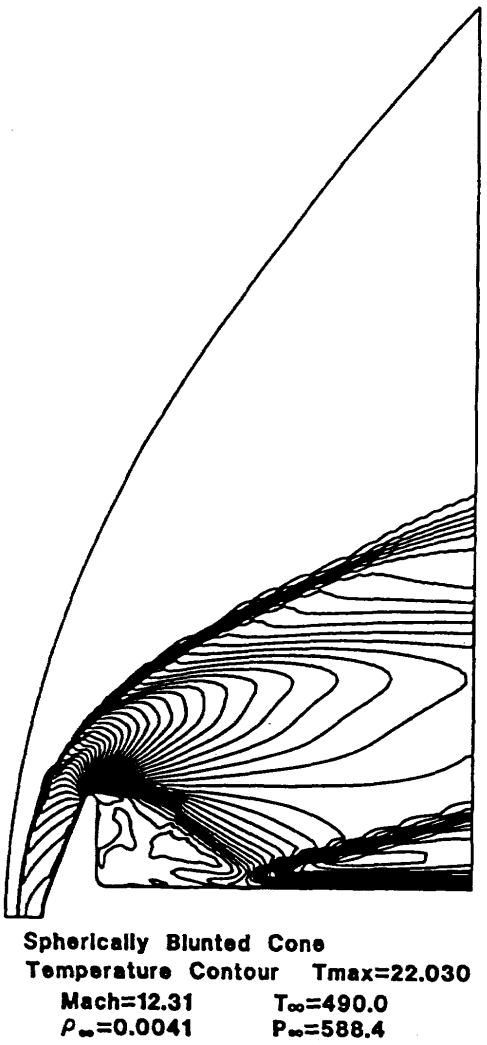

Fig.14

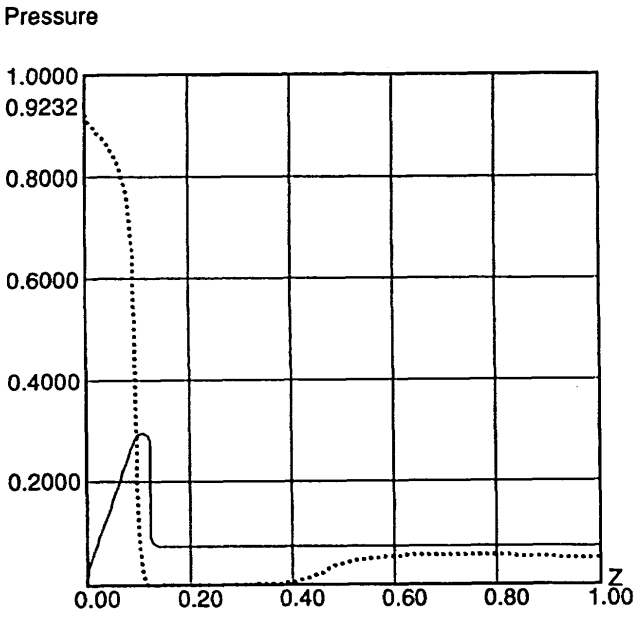

(a) Pressure Distribution

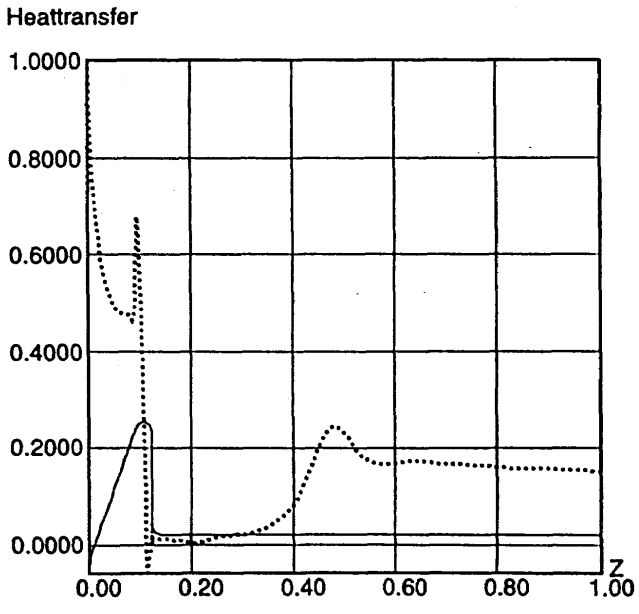

(b) Heat Transfer Distribution

Fig.15

2-9

各種鈍頭物体周りにおける高エンタルピー流れの数値計算

長友 英夫†、鹿野 信太郎†、山本 悟‡、大宮司 久明‡
† 東北大学大学院、‡ 東北大学

Numerical Simulation of Reactive and Non-reactive Hypersonic Flow Problems for High Enthalpy Flow Workshop

Hideo Nagatomo*, Shintaro Kano*,
Satoru Yamamoto** and Hisaaki Daiguji**
* Graduate School of Tohoku University
** Tohoku University

Abstract

Numerical simulations of hypersonic flow assuming no reaction and thermochemical nonequilibrium are performed. Three different methods, Implicit-Explicit Flux Vector Splitting(IEFVS), AUSM and AUSM_DV scheme are used. All of these schemes are coupled with Fourth-order MUSCL TVD scheme in space which enable us to capture vortices more clearly. AUSM scheme is applied for non-reactive flow problems, the flow around OREX (Test case problem II-5), and hyperboloid flare (III-1). On the other hand, for the thermochemical nonequilibrium flow problems, such as the flow around OREX (II-2) are calculated by the IEFVS and AUSM_DV scheme. The spherically blunted cone (IV-1) is done by the IEFVS.

1. Introduction

For the numerical simulation of hypersonic viscous flows, the computational method should be very robust for shocks and numerically non-dissipative in the boundary layer. To satisfy them, some methods have been already proposed. The authors also have developed a method based on Implicit-Explicit Flux Vector Splitting (IEFVS) for the simulation of thermochemical nonequilibrium hypersonic viscous flow[1]. This scheme is very robust for obtaining the bow shock because of the characteristic of the FVS scheme, accurate in the boundary layer by using the Roe's averaging and quite simple for the almost same formation of both implicit and explicit terms. We also know robust schemes, AUSM and AUSM_DV scheme, therefore, these schemes are also used to check reliability for the present flow problems.

On the other hand, fourth-order compact MUSCL TVD[2] is used to obtain higher-resolution results, with each IEFVS, AUSM, AUSM_DV scheme.

In this paper, the numerical procedure of discretization is firstly explained briefly and flow problems given as the present workshop subject, the flow around OREX (II-2, II-5), the hyperboloid flare (III-1) and the spherically blunted cone (IV-1) are considered. The problem II-5 and III-1 are calculated by the AUSM, the problems II-2 is calculated by the IEFVS and the AUSM_DV, and the problems IV-1 is calculated by the IEFVS.

2. Numerical Method

2.1 Fundamental Equations The two-dimensional conservation equations for the thermochemical nonequilibrium flow are expressed as follows.

$$\frac{\partial Q}{\partial t}+\frac{\partial F_i}{\partial \xi_i}+S+H=0 \qquad (1)$$

Q is the vector of unknown variables, $Q = J(\rho_s,\ \rho u_1,\ \rho u_2,\ E,\ E_v)$, where ρ is the total density and ρ_s is each density of species s. F_i, S and H are the flux, the diffusion term and the source term respectively, and they are described as follows.

$$F_i = J\begin{bmatrix} \rho_s U_i \\ \rho u_1 U_i + \partial\xi_i/\partial x_1 p \\ \rho u_2 U_i + \partial\xi_i/\partial x_2 p \\ (E+p)U_i \\ E_v U_i \end{bmatrix}$$

$$S = -J\frac{\partial \xi_i}{\partial x_j}\frac{\partial}{\partial \xi_i}\begin{bmatrix} -\rho_s v_{sj} \\ \tau_{1j} \\ \tau_{2j} \\ \tau_{\ell j}u_\ell - q_j - \sum_{s\neq e}^{n}\rho_s v_{sj}h_s \\ -q_{vj} - \sum_{s\neq e}^{m}\rho_s e_{vs}v_{sj} \end{bmatrix}$$

$$H = -J\begin{bmatrix} w_s \\ 0 \\ 0 \\ 0 \\ W_v \end{bmatrix}, \quad (s=1,\cdots,n,\ i=1,2)$$

For reacting flow, 7 chemical species (N_2, O_2, NO, NO^+, N, O, e^-) are considered so that the system includes 11 equations here. Models for chemical reactions and the vibrational relaxation time in the source term H are quoted from Park[5] and Candlar[6] mainly. The total energy E, the pressure p, and the gas constant are given below.

$$E = \sum_{s\neq e}^{n} \rho_s C_{vs} T + \frac{1}{2}\rho u_j u_j + E_v + \sum_{s\neq e}^{n} \rho_s h_s^0 + \sum_{s\neq e}^{n} \rho_s e_{els}$$

$$p = \sum_{s\neq e}^{n} \rho_s \frac{R}{M_s} T + p_e\,,\quad \bar{R} = \sum_{s\neq e}^{n} \frac{\rho_s R}{\rho M_s}$$

C_{vs}, T, h_s^0, e_{els}, R, M_s, p_e means the translational specific heat, translational-rotational temperature, heat of formation of species s, universal gas constant, atomic weight of species s and the electron pressure respectively.

2.2 Discretization

The numerical flux of F_i in eq.(1) are defined as the linearlized flux vector forms.

$$(F_i)^n_{\ell+1/2} = (A_i^+)_{\ell+1/2} Q^L_{\ell+1/2} + (A_i^-)_{\ell+1/2} Q^R_{\ell+1/2} \quad (2)$$

The superscripts L and R in the vector of unknown variables, $Q^L_{\ell+1/2}$ and $Q^R_{\ell+1/2}$ mean the weighted extrapolation from the right and left by the MUSCL approach, and they are calculated by the following equations.

$$Q^L_{\ell+1/2} = Q_\ell + \frac{1}{6}\Delta^+ \bar{Q}_{\ell-1/2} + \frac{1}{3}\Delta^- \bar{Q}_{\ell+1/2}$$
$$Q^R_{\ell+1/2} = Q_{\ell+1} - \frac{1}{6}\Delta^- \bar{Q}_{\ell+3/2} - \frac{1}{3}\Delta^+ \bar{Q}_{\ell+1/2} \quad (3)$$

where $\Delta^\pm \bar{Q}$ are the numerical functions composed of ordinary third-order term and fourth-order compact term.

On the other hand, if the LU-SGS scheme by Yoon et.al.[7] and point-implicit method by Eberhardt[8] are used, eq.(1) can be written in the implicit form as

$$[I + \Delta t\{\beta\sigma(A_i) + \mathrm{diag}(\frac{1}{\tau}) + \mathrm{diag}(\alpha_j)\}]\delta Q = RHS$$
$$-\Delta t\{(A_j^-)_{\ell+1/2}\delta Q_{\ell+1} - (A_j^+)_{\ell-1/2}\delta Q_{\ell-1}\} \quad (4)$$

where

$$RHS = -\Delta t(\Delta F_i^n + S^n + H^n)$$

In eq.(4), $\sigma(A_i)$ is an identity matrix with the spectral radius of A_i. In this paper, the maximum of absolute eigenvalues for A_i is taken. $1/\tau \equiv 1/\tau_s$ ($s = 1,\ldots,n$ and E_v) is quoted from Ref.[8] and α_j is set to $2\mu g_{jj}/(Re\rho\Delta\xi_j)$.

Next, the Implicit-Explicit Flux Vector Splitting (IEFVS) is explained. The distinctive feature is that it is applicable to both explicit and implicit calculations. It means that not only the flux $A_i^\pm Q$, but the flux $A_i^\pm \delta Q$ can be calculated from a same flux-vector splitting form. This form can be written in the vector form composed of sub-vectors as

$$A_i^\pm \tilde{Q} = J \begin{bmatrix} \tilde{q}_s \\ \tilde{q}_{u_1} \\ \tilde{q}_{u_2} \\ \tilde{q}_e \\ \tilde{q}_{e_v} \end{bmatrix} \lambda_{i1}^\pm + \frac{J}{c\sqrt{g_{ii}}} \begin{bmatrix} 0 & + & \bar{q}_s/\bar{q}_0 \cdot \Delta\bar{U}_i \\ \xi_{i,1}\bar{p} & + & \bar{q}_{u_1}/\bar{q}_0 \cdot \Delta\bar{U}_i \\ \xi_{i,2}\bar{p} & + & \bar{q}_{u_2}/\bar{q}_0 \cdot \Delta\bar{U}_i \\ \bar{U}_i\bar{p} & + & (\bar{\chi}^2 + c^2)/\tilde{\gamma} \cdot \Delta\bar{U}_i \\ 0 & + & \bar{q}_{e_v}/\bar{q}_0 \cdot \Delta\bar{U}_i \end{bmatrix} \lambda_{ia}^\pm + \frac{J}{c^2} \begin{bmatrix} \bar{q}_s/\bar{q}_0 \cdot \bar{p} & + & 0 \\ \bar{q}_{u_1}/\bar{q}_0 \cdot \bar{p} & + & \xi_{i,1}c^2/g_{ii} \cdot \Delta\bar{U}_i \\ \bar{q}_{u_2}/\bar{q}_0 \cdot \bar{p} & + & \xi_{i,2}c^2/g_{ii} \cdot \Delta\bar{U}_i \\ (\bar{\chi}^2 + c^2)/\tilde{\gamma} \cdot \bar{p} & + & \bar{U}_i c^2/g_{ii} \cdot \Delta\bar{U}_i \\ \bar{q}_{e_v}/\bar{q}_0 \cdot \bar{p} & + & 0 \end{bmatrix} \lambda_{ib}^\pm \quad (5)$$

where

$$\bar{p} = \tilde{q}_0\bar{\phi}^2 - \tilde{\gamma}(\bar{q}_{u_i}\tilde{q}_{u_i} - \bar{q}_0\tilde{q}_e - \bar{q}_0\tilde{q}_{e_v})/\bar{q}_0$$
$$\bar{\phi}^2 = \tilde{\gamma}(\bar{q}_{u_i}\bar{q}_{u_i}/2\bar{q}_0^2 - \sum_{s\neq e}^{n} \bar{q}_s h_s^0/\bar{q}_0 - \sum_{s\neq e}^{n} \bar{q}_s e_{els}/\bar{q}_0)$$
$$\bar{\chi}^2 = \tilde{\gamma}(\bar{q}_{u_i}\bar{q}_{u_i}/2\bar{q}_0^2 + \bar{q}_{e_v}/\bar{q}_0 + \sum_{s\neq e}^{n} \bar{q}_s h_s^0/\bar{q}_0 + \sum_{s\neq e}^{n} \bar{q}_s e_{els}/\bar{q}_0)$$
$$\Delta\bar{U}_i = \xi_{i,j}\tilde{q}_{u_j} - \tilde{q}_0\xi_{i,j}\bar{q}_{u_j}/\bar{q}_0$$
$$\lambda_{ij}^\pm = (\lambda_{ij} \pm |\lambda_{ij}|)/2 \qquad (j = 1,3,4)$$
$$\lambda_{ia}^\pm = (\lambda_{i3}^\pm - \lambda_{i4}^\pm)/2$$
$$\lambda_{ib}^\pm = (\lambda_{i3}^\pm + \lambda_{i4}^\pm)/2 - \lambda_{i1}^\pm$$

If we use eq.(5) in the explicit calculation, then $\tilde{Q} = (\tilde{q}_s\ \ \tilde{q}_{u_1}\ \ \tilde{q}_{u_2}\ \ \tilde{q}_e\ \ \tilde{q}_{e_v})$ is specified to Q. On the other hand, $\tilde{Q}$ is set to δQ if it is for the implicit calculation. We need no additional calculations such as matrices for eigenvectors. The values with upper bar are estimated by the Roe's averaging to overcome the excessive dissipation in the boundary layer.

AUSM scheme by Liou et.al.[3] and AUSM_DV scheme by Wada et.al.[4] are also applied here with fourth-order compact MUSCL TVD scheme.

3. Results

3.1 Non-reactive flows

Problem II-5. The axisymmetric non-reactive laminar flows around OREX is simulated. Outer boundary conditions are set to $u_\infty = 5562$ [m/sec], $p_\infty = 23.60$ [Pa], $T_\infty = 248.1$ [K] and the wall temperature is $T_{wall} = 1519$ [K].

The computational mesh has 95 × 95 grid points.(Fig.1) In this calculation, the AUSM scheme with the fourth-order compact MUSCL TVD is used to verify the capability of its application. Fig.2 to 5 show the temperature contours, pressure contours, pressure distribution and the heat flux distribution on the body surface. The shock distance from the nose is about 0.19m.

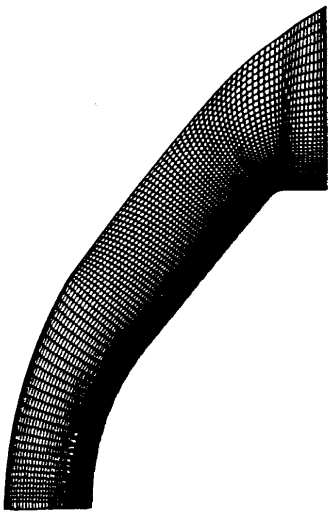

Fig.1 Computational mesh(95 × 95 grid points)

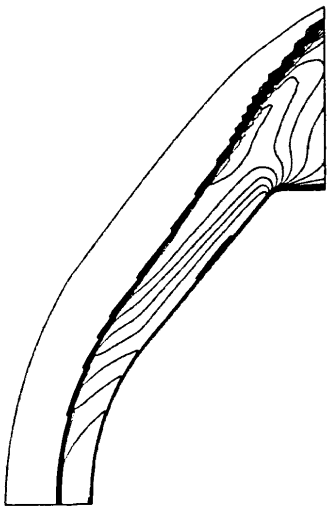

Fig.2 Temperature Contours

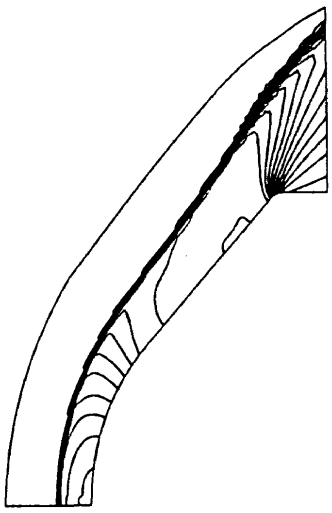

Fig.3 Pressure Contours

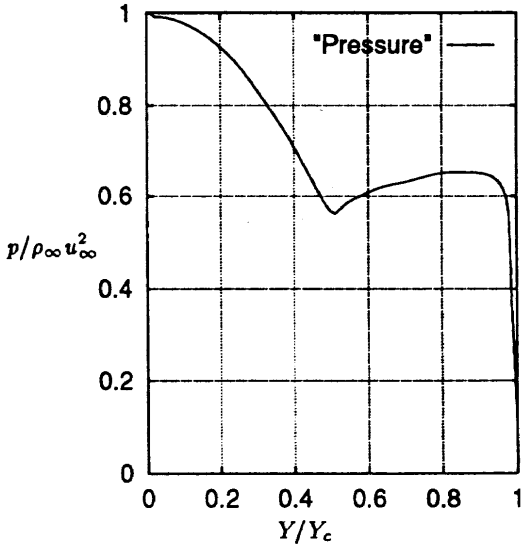

Fig.4 Pressure distribution on the surface

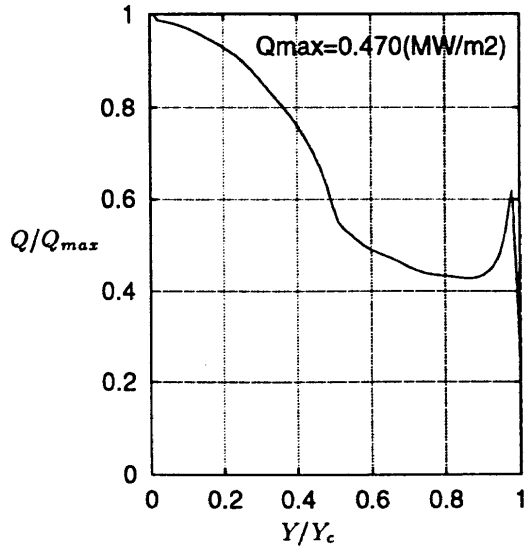

Fig.5 Heat flux distribution on the surface

Problem III. The axisymmetric non-reactive laminar flow around hyperboloid flare is simulated also by the same scheme of II-5. The computational mesh has 521 × 101 grid points which was provided by the workshop organizer.(Fig.6) The experimental data of the Geottingen Ludwig Tube (Cold Case) was used for the condition of this calculation. Outer boundary conditions are set to $M_\infty = 6.83$, $Re_\infty/m = 7.0 \times 10^6$, $T_\infty = 67.765$ [K] and the wall temperature is $T_{wall} = 310$ [K]. Calculations both by fourth-order and first-order accuracy in space were executed.

Figs.7 and 8 show the calculated results of pressure contours and temperature contours by by first-order scheme respectively and Figs. 9 and 10 show the same results by fourth-order one.

In the latter results, a large separation area near the compression corner and shock interactions are captured clearly, though small oscillations are visible. The separation point of fourth-order case estimated from pressure distributions (Fig.11) is about $X_{separate}/X_{ref} = 0.62$. The reason of the oscillations is unconsiderable here, but this should be deleted.

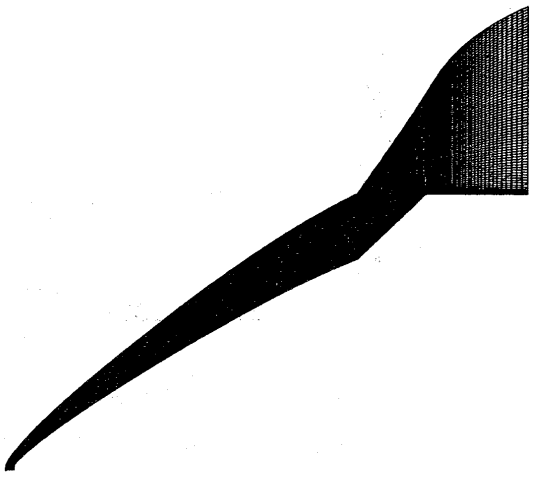

Fig.6 Computational mesh(521 × 101 grid points)

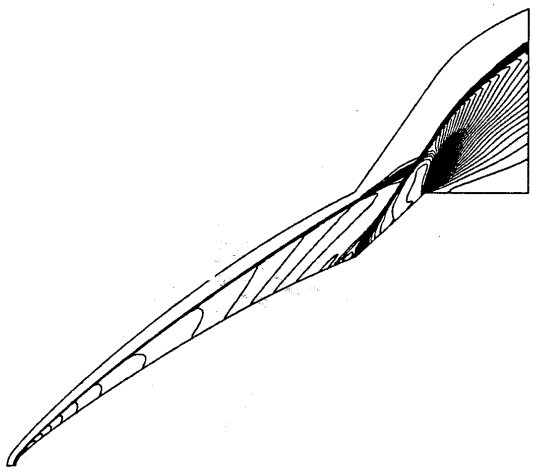

Fig.7 Pressure Contours (First-order)

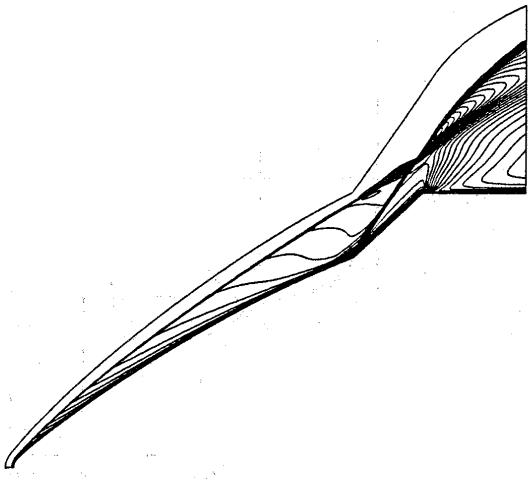

Fig.8 Temperature Contours (First-order)

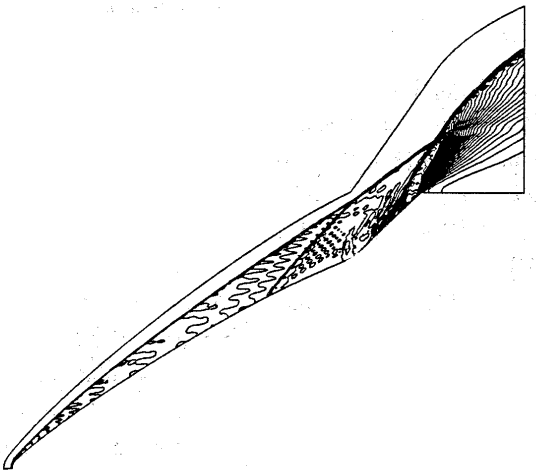

Fig.9 Pressure Contours (Fourth-order)

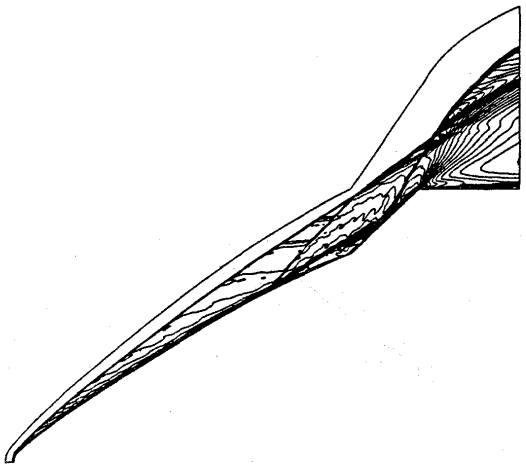

Fig.10 Temperature Contours (Fourth-order)

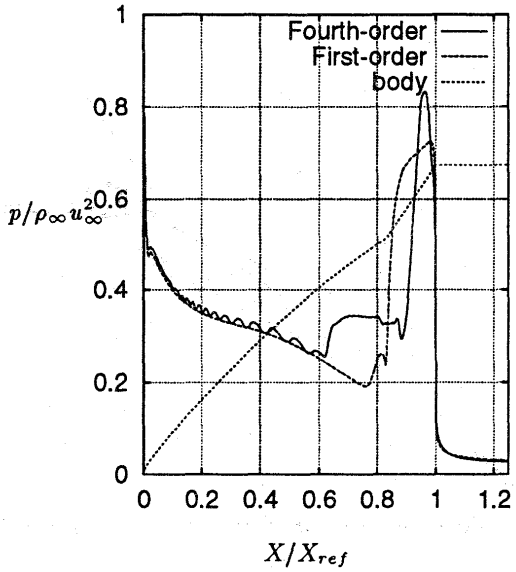

Fig.11 Pressure distributions

3.2 Reactive flows

Problem II-2. The computational mesh has 75×75 grid points.(Fig.12) Outer boundary conditions are set to $u_\infty = 5562$ [m/sec], $p_\infty = 23.60$ [Pa], $T_\infty = 248.1$ [K] and the wall temperature is $T_{wall} = 1519$ [K].

In this calculation, IEFVS and AUSM_DV schemes with fourth-order compact MUSCL TVD are used. Figs. 13 and 14 show the calculated results of pressure contours and translational-rotational temperature contours respectively by IEFVS scheme and Figs.15 and 16 show those results by AUSM_DV scheme. Fig.17 shows the temperature distributions on the stagnation streamlines. These results are similar and the shock distance from the nose by FVS is 10.9cm. On the other hand, that by AUSM_DV is slightly less than that of FVS. However the difference is only a length between a grid point and next one.

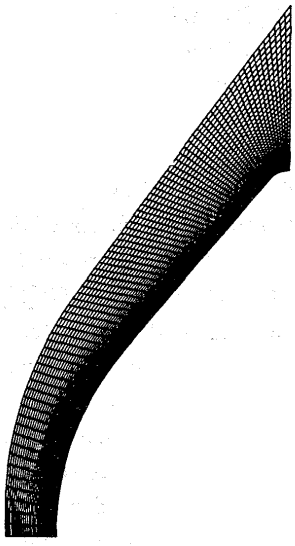

Fig.12 Computational mesh(75 × 75 grid points)

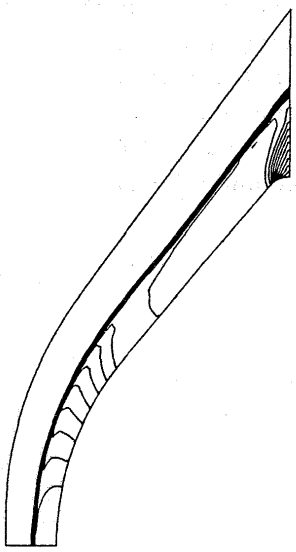

Fig.13 Pressure contours (IEFVS)

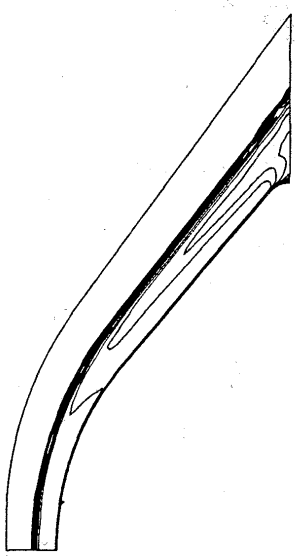

Fig.14 Translational-rotational temperature contours (IEFVS)

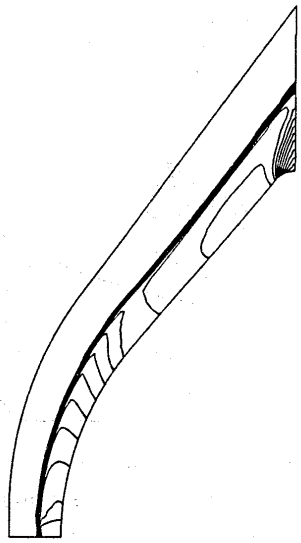

Fig.15 Pressure contours (AUSM_DV)

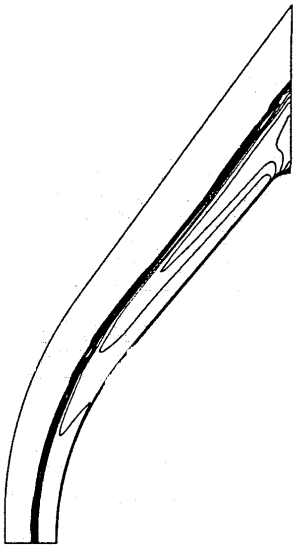

Fig.16 Translational-rotational temperature contours (AUSM_DV)

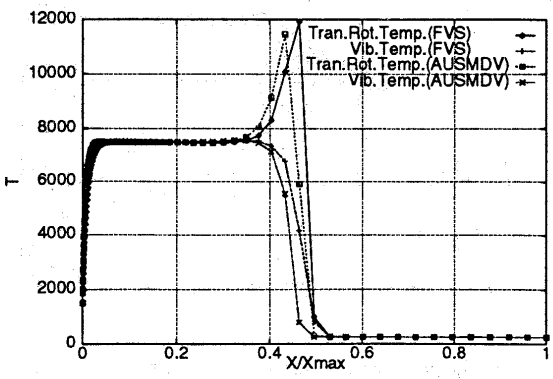

Fig.17 Temperature distributions on stagnation streamline

Problem IV-1. The axisymmetric laminar flow with chemical reacting around the spherically blunted cone is simulated. The computational mesh used here is shown in Fig.18 which was provided by the workshop organizer. Outer boundary conditions are set to $u_\infty = 4539.5$ [m/sec], $p_\infty = 588.42$ [Pa], $T_\infty = 489.89$ [K] and the wall temperature is $T_{wall} = 295$ [K].

The calculation was performed by IEFVS with fourth-order and first-order accuracy in space. Figures 19 to 21 show the calculated results of pressure contours, translational-rotational temperature contours and vibrational temperature contours respectively by the fourth-order scheme and Figs. 22 to 24 show those results by the first-order. From the comparison of these figures, the further rear stagnation point from the base is obtained by the fourth-order case than by first-order. This reason may be due to the capability of capturing separation points and vortices. Figure 25 shows the heat flux distributions of the calculated results and that of experimental data[9], where S means the distance along the body surface from the front stagnation point. The fourth-order result has a peak at the almost same position as that of experimental one whereas the value at the point is smaller. However, it seems to be at least necessary to apply higher-order scheme to simulate base region in hypersonic flow.

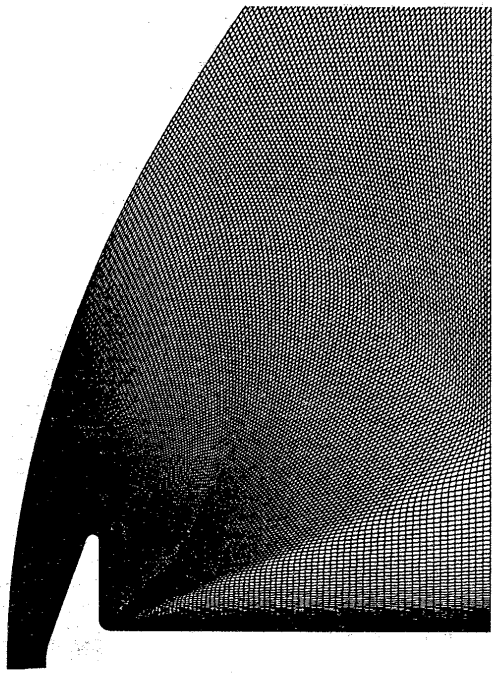

Fig.18 Computational mesh(161 × 241 grid points)

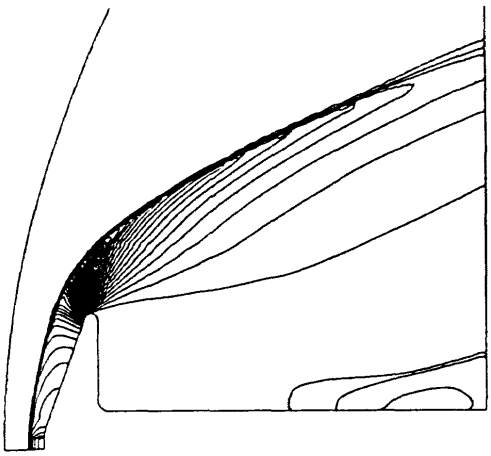

Fig.19 Pressure contours
(Fourth-order)

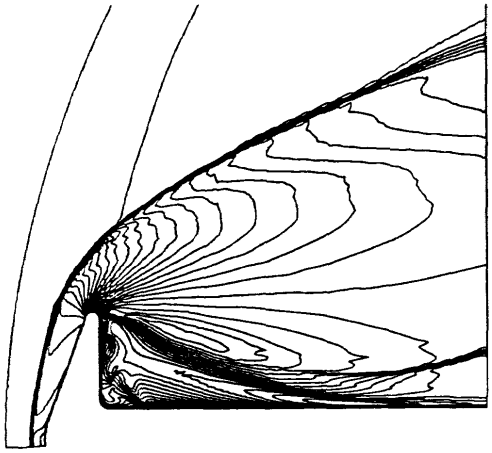

Fig.20 Translational-rotational temperature contours (Fourth-order)

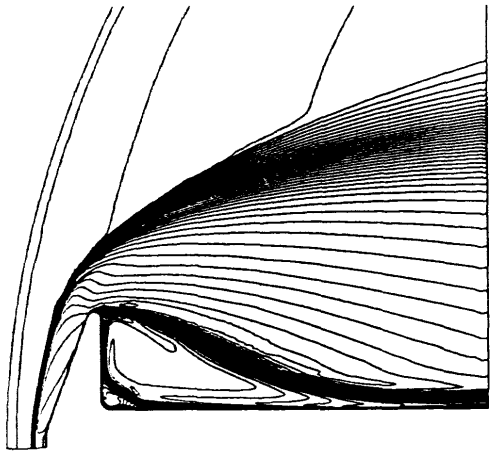

Fig.21 Vibrational temperature contours
(Fourth-order)

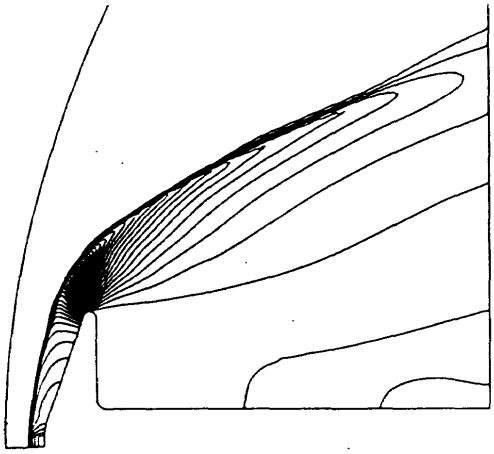

Fig.22 Pressure contours
(First-order)

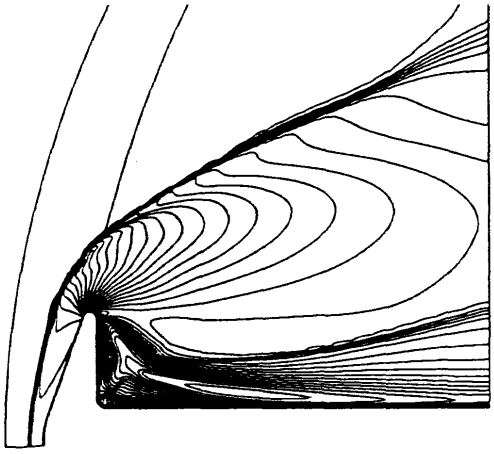

Fig.23 Translational-rotational temperature contours (First-order)

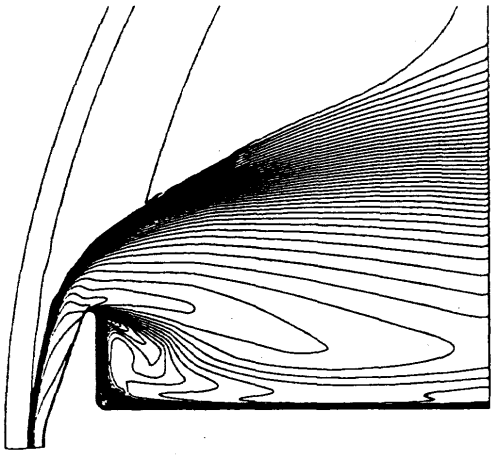

Fig.24 Vibrational temperature contours
(First-order)

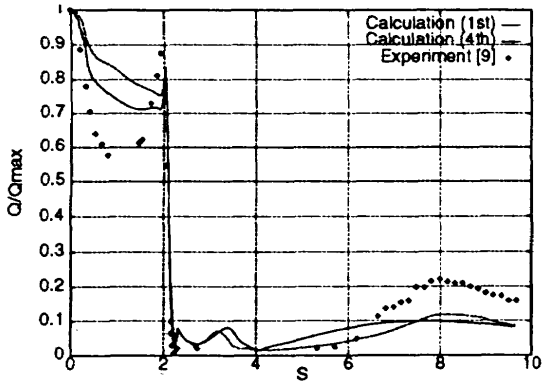

Fig.25 Heat flux distribution

4. Conclusion

Numerical simulations are performed for High Enthalpy Flow Workshop problems. The AUSM scheme was very effective for non-reactive problem. However, the oscillation in higher-order case of II-5 should be overcomed in future. The AUSM_DV and IEFVS with the higher-order accuracy were equivalently effective for the reacting flow problem II-2. The last case IV-1 indicates the necessity of higher-order accuracy at the wake region after the body. By the way, the result by the AUSM_DV for the last case is not shown because of still having a problem in the result. It must be also resolved.

References

[1] Yamamoto, S., Nagatomo, H. and Daiguji, H., *Proc. of the 14th International Conf. on Numerical Methods in Fluid Dynamics, Lecture Notes in Phys.*, Springer-Verlag (1995), pp.314-319.

[2] Yamamoto, S. and Daiguji, H., *J. Compu. & Fluids*, Vol.22, No.2/3, (1993), pp.259-270.

[3] Liou, M.-S. and Steffen, C.J., *J. Comput. Phys*, Vol.107, (1993), pp.23-39.

[4] Wada, Y. and Liou, M.-S., AIAA Paper 94-0083, (1994).

[5] Park, C. and Yoon, S., *J. Spacecraft and Rockets*, Vol.1 (1991), pp.31-39.

[6] Candler, G., Ph.D Thesis, Stanford University, (1988).

[7] Imlay, S.T. and Eberhardt, S., AIAA Paper 91-0468, (1991).

[8] Park, C. and Yoon, S., *J. Spacecraft and Rockets*, Vol.28, No.1, (1991), pp.31-39.

[9] Kastell, D., Horvath T. J. and Eitelberg, G., Proc. of the Second European Symp. on Aerothermodynamics for Space Vehicles, (1994), pp.383-389.

2−10

Numerical Simulations of High Enthalpy Flow

by
Nobuhiro SEKINO, Toru SHIMADA and Naoki TAMURA
Aerospace Division , Nissan Motor Co., LTD.

ABSTRACT

Eleven results of ours to the problems of the 13th NAL Symposium on Aircraft Computation Aerodynamics - High Enthalpy Flow Workshop are presented. The problems are the simulation of flow around a sphere (problem I) and the simulation of flow around the re-entry vehicle, OREX (problem II). To perform these simulations, three kinds of numerical codes for different gas properties are used; for thermo-chemically non-equilibrium gas, for equilibrium gas, and for frozen (ideal) gas. In these codes, Navier-Stokes equations are discretized in the finite volume form using Harten-Yee type TVD flux estimation and LU-SGS implicit method. For the thermo-chemically non-equilibrium flow, eleven chemical species are considered and Park's two temperature model is adopted. The computed heat fluxes for the sphere case agree well with the experimental data provided by the workshop organizer. As for the OREX case, although the computed heat fluxes are somewhat larger than the flight data, the computational results agree with the flight data in the same order. For the particular flow conditions in the case of sphere, our results show that the heat fluxes to the non-catalytic walls are larger than those to the fully-catalytic walls. It is shown that one of the causes for this phenomenon is rapid recombination rate of chemical spices.

1. Introduction

Re-entry vehicles experience severe thermal circumstances during their atmospheric re-entry. Owing to recent progress of computer power, it is realized to simulate such hypersonic flowfields and to evaluate physical values by CFD. In the high enthalpy flow workshop, the CFD performance for this problem is compared by applicants. We use several in-house numerical codes to solve given hypersonic flow problems.

In the following sections, after the discussion of the flow models and numerical methods , some of our results are presented.

2. Numerical Models

2.1 Flow models

The flows around re-entry vehicles vary depending on the flight altitude and velocity. Because of the strong shock waves formed in front of vehicles, the dissociation and the ionization of air may occur. The chemical reaction process may change the flow features such as the shock standoff distance.

Non-equilibrium processes occur in a flow when the time scale required for a process to accommodate itself to local conditions is of the same order as the transit time scale across the considered region. If the accommodation time scale is very short compared with the transit time scale, the process is considered as equilibrium. On the other hand, if the accommodation time scale is very long compared with the transit time scale, the process is frozen.

Three kinds of numerical codes have been developed in our group. They are codes for the thermo-chemically non-equilibrium flow, for the equilibrium flow, and for the frozen flow. Usually one of them is used to simulate a hypersonic flow depending on a problem.

2.2 Thermo-chemically non-equilibrium flow

The approach employed in our code to the thermo-chemically non-equilibrium flow is a two-temperature thermal model proposed by Park. As the chemical species, following 11 species, namely N, O, N_2, O_2, NO, N^+, O^+, N_2^+, O_2^+, NO^+ and e^-, are considered. Therefore the modeled system includes 11 species continuity equations, 3 momentum equations, and 2 energy equations describing the conservation of vibrational-electronic and total energies.

The mass rate of production of each species is expressed by Park's chemical kinetic model. This model includes totally 43 reactions of 21 kinds.

A Landau-Teller model is used to determine the vibrational-translational relaxation process, in which the relaxation rate is proportional to the deviation from the equilibrium state. Millikan and White [1] presented semiempirical formula for estimation of vibrational relaxation time. For

temperatures above 8000 K, Park [2] proposed correction for the vibrational relaxation time, so called collision limiting. We use above two models (Millikan & White's model + Park's collision limiting) to estimate vibrational relaxation time.

As the chemical-vibrational coupling model, the preferential dissociation and recombination model is used. In this model, the dissociation of molecular species is assumed to occur preferentially when the molecules are vibrationally excited. To put it in the concrete, the rate-controlling temperature of dissociation is evaluated by the geometrical average of the local translational-rotational temperature (T_{tr}) and the vibrational-electronic temperature (T_v). If one assumes preferential dissociation and recombination of molecules in the higher vibrational states, the vibrational energy of diatomic molecules, which are created or destroyed, should be larger than the average vibrational energy. This effect is also included in the code.

The transport coefficients are estimated by an extension of Yos's formula to the multi-temperature gas mixture.

Most part of the mathematical model is based on the paper by Gnoffo et. al. [3]

2.3 Wall catalytic effect

For the chemically non-equilibrium flow, results vary according to wall catalytic effects. Generally, we assume the wall catalycity to be fully catalytic or non-catalytic. For the fully catalytic wall, we assume the composition of air at the wall to be equilibrium one that is characterized by the local wall pressure and temperature. For the non-catalytic wall , we set the normal derivative of concentration of each species to the wall to be zero.

2.4 Equilibrium and frozen flow

The procedures to simulate the equilibrium flow and the frozen flow are almost the same. The difference between them is the treatments of the thermodynamic relations. For the frozen air model, the thermodynamic relations are expressed by the ideal gas equation of state. On the other hand, for the equilibrium air model the thermodynamic relations can not be expressed by simple formula. We use curve-fit for the thermodynamic and transport properties [4,5] in simulations of equilibrium flows.

3. Numerical methods

3.1 Discretization in space

The governing equations are expressed in a generalized curvilinear coordinate system and discretized in a finite volume form. We use a structured grid system.

3.2 Flux estimation

To estimate the convective flux term, the Harten-Yee's method [4] extended to the real gas is used. This method is consists of the central difference term and the additional correctional term, with which 2nd-order numerical flux preserving the TVD characteristics is obtained. As the limiter function, we use conventional minmod function.

As for the viscous, thermal conduction, and diffusion terms, the central difference method is used.

3.3 Time integration

To obtain a steady state solution as a time asymptotic one, we use the LU-SGS method [7]. In this method, using the lower-upper symmetric Gauss-Seidel (LU-SGS) factorization, the scalar calculations in forward/backward sweeping are performed instead of the matrix inversion. It is expected that the computational cost can be much reduced with this method.

In the case of the chemically non-equilibrium flow, because of the rapid production rate of species, sometimes the governing equations become stiff. To reduce the stiffness, the point-implicit method is used. In this method, the source term is treated implicitly apart from the convective terms.

3.4 Heat flux estimation

The heat flux to the wall is evaluated by the following expression:

$$\dot{q} = \eta \frac{\partial T_{tr}}{\partial n} + \eta_v \frac{\partial T_v}{\partial n} + \rho \sum_{s=1}^{11} h_s D_s \frac{\partial y_s}{\partial n} \qquad (1)$$

where $\dot{q}$ is the heat flux to the wall, T_{tr} the translational-rotational temperature, T_v the vibrational-electronic temperature, ρ the density, η and η_v the thermal conductivity, h the enthalpy, D the diffusion coefficient, and y the mole fraction, respectively. The normal derivative to the wall is denoted by $\partial/\partial n$. The subscript s represents a species. In the case of non-catalytic wall, the third term in the right-hand side of the equation (1) is zero.

4. Applied cases

In table I, the cases that we have applied in this workshop are summarized. We have performed the computations on the 11 cases of two problems.

Table I Applied cases

Problem	Case	Non-equilibrium		Equilibrium	Frozen
		Non-cat	Full-cat		
I Sphere	1	●			
	2		●		
	3	●			
	4		●		
	5	●			
	6		●		
II OREX	1	●			
	2	●			
	3		●		
	4			●	
	5				●

5. Problem I

Problem I treats flows around a sphere of 40 mm in diameter, where axisymmetric laminar flows are assumed. Computations are performed for 6 cases which include three kinds of main flows and two kinds of wall conditions.

5.1 Computational Grid

In figure 1, the computational grid used in this problem is shown. The number of grid points is 51×81 and the minimum grid spacing near the wall is 2.0×10^{-3} mm.

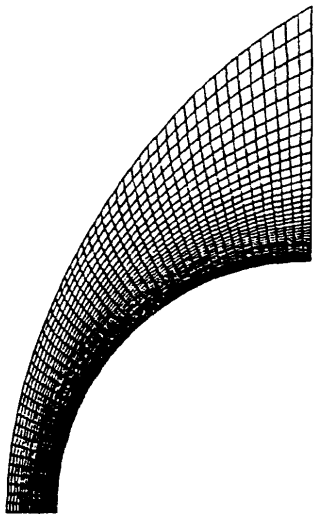

Figure 1 Computational grid for problem I

5.2 Results

Figure 2 shows the pressure contours of cases 1, 3 and 5 respectively. As for cases 2, 4, and 6, almost the same pressure contours are obtained. In these figures, sharp shock waves are captured with no unphysical oscillations.

In figure 3, the temperature distributions along the stagnation streamlines are shown. In these figures, T_{tr} and T_v denote the transrational-rotational temperature and vibrational-electronic temperature, respectively. The horizontal axes in these figures represent the non-dimensional distance from the stagnation point normalized by the maximum length of the computational domain along the axis (in our

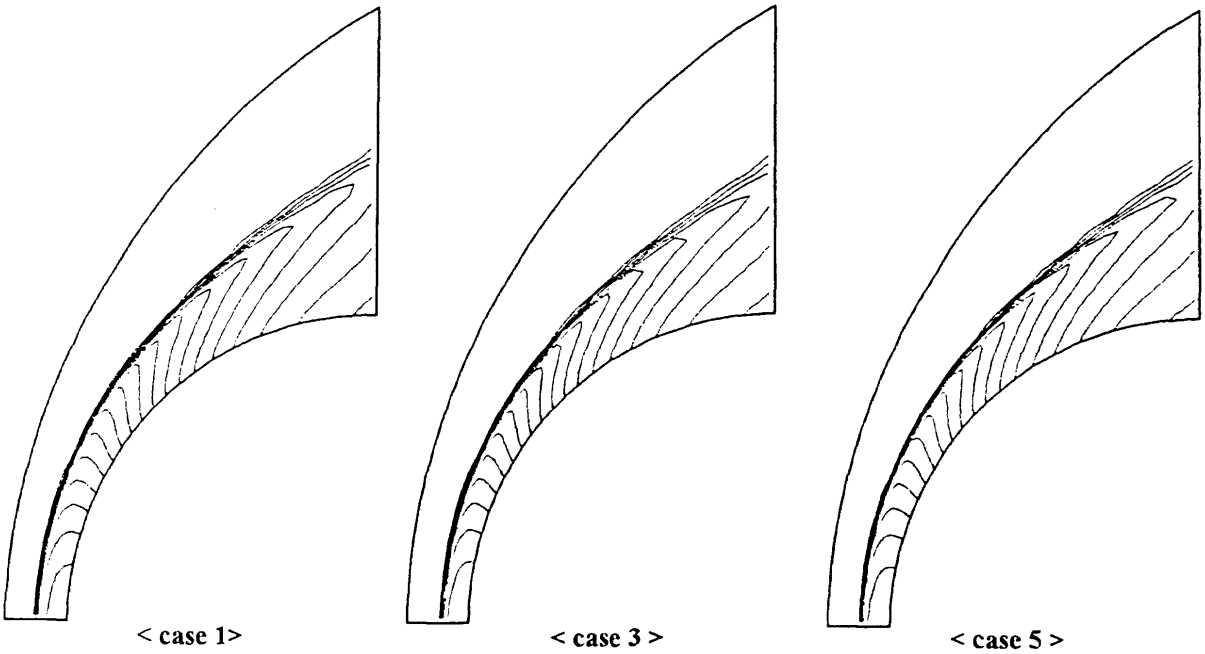

< case 1> < case 3 > < case 5 >

Figure 2 Pressure contours (problem I)

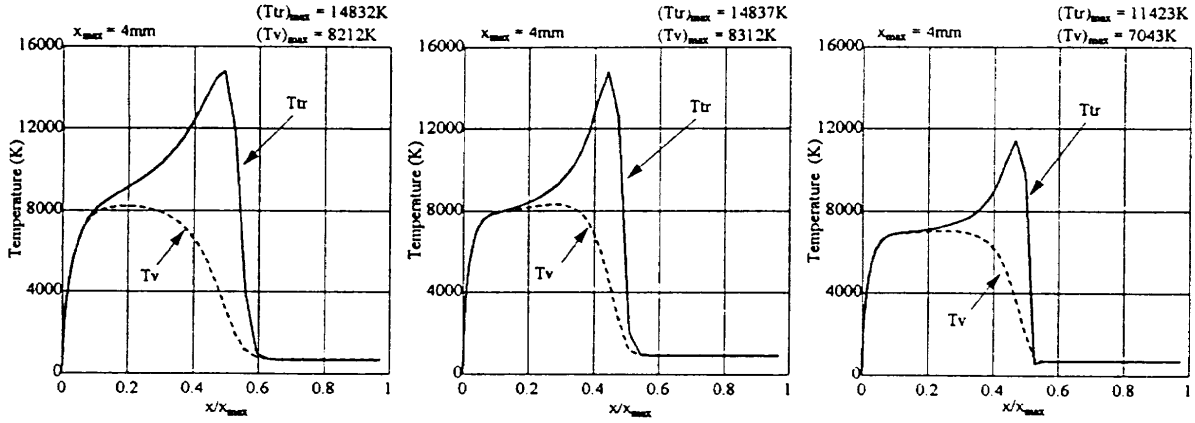

< case 1 > < case 3 > < case 5 >

Figure 3 Temperature distributions along the stagnation streamline

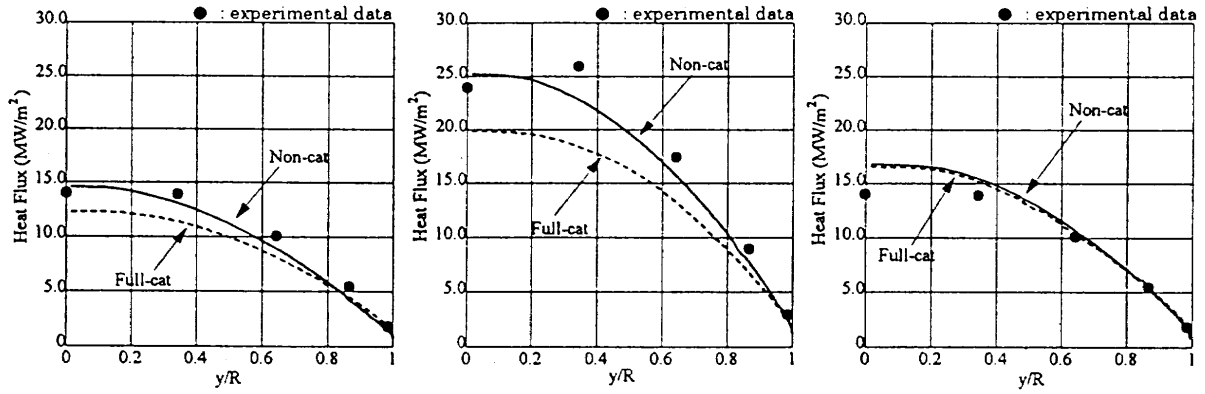

< case 1, 2 > < case 3, 4 > < case 5, 6 >

Figure 4 Heat flux distributions along the body surface

case x_{max} = 4 mm). In case 1 it can be seen that the relaxation between T_{tr} and T_v is relatively slow and the non-equilibrium effect seems to be large. On the other hand, in case 5 the relaxation between the two energies seems to be faster than those of the other cases and it is expected that the non-equilibrium effect in this case is relatively small.

Figure 4 shows the heat flux distributions along the body surface. The horizontal axes in these figures represent the non-dimensional distance from the axis line normalized by the sphere radius. In comparison with the results of cases 5 and 6, the heat flux to the non-catalytic wall and fully catalytic wall are almost the same. This fact suggests that the flows of these cases can be considered in equilibrium.

The symbols in these figures represent the experimental results of the wind tunnel tests provided by the workshop organizer. The experimental data agree well with the computed results of non-catalytic wall case. The detail of the test condition is not available, but according to the paper [8] the Teflon coated calorimeter shows non-catalytic behavior.

Usually, it is said that heat flux to a fully catalytic wall is larger than that to a non-catalytic wall under the same flow condition. But contrary to our expectations, in our computed results, heat fluxes to the non-catalytic walls are larger than those of the fully catalytic walls. We will consider this subject in detail in the following section.

5.3 Detail of the heat flux distribution

In figure 5, the calculated heat flux distributions of cases 3 and 4 are shown similarly as in figure 4. In addition to these, the conductive part of heat flux to the fully catalytic wall is shown in figure 5. Figure 6 is taken from the Fay & Riddell's paper [9] and this figure shows the heat flux variation with the recombination rate. The important points in this figure are the reduction of heat transfer to a non-catalytic wall and the fact that a conductive part of heat flux to a catalytic wall is smaller than a heat flux to a non-catalytic wall. The same tendency can be observed in figure 5.

Figure 7 shows the mole fraction along the stagnation streamline. This figure is a close view near the wall. The solid lines in this figure represent the

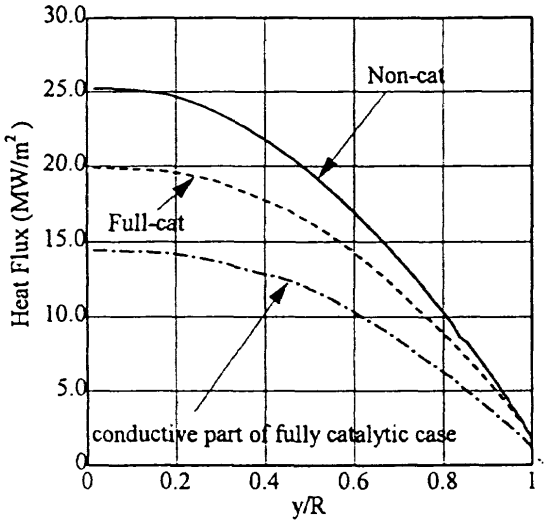

Figure 5 Detail of the heat flux (case 3, 4)

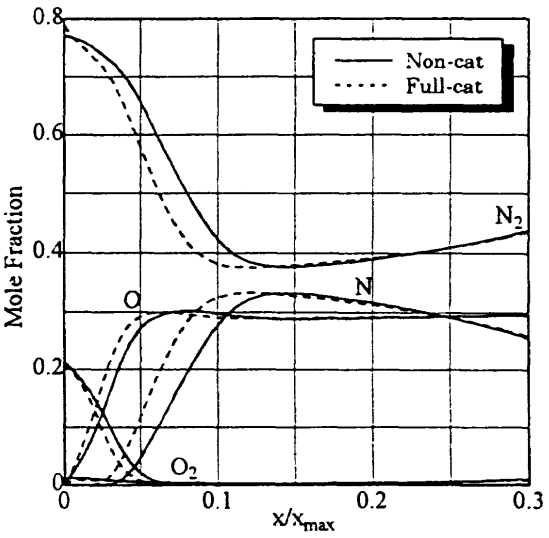

Figure 7 Mole fraction along the streamline (case 3, 4)

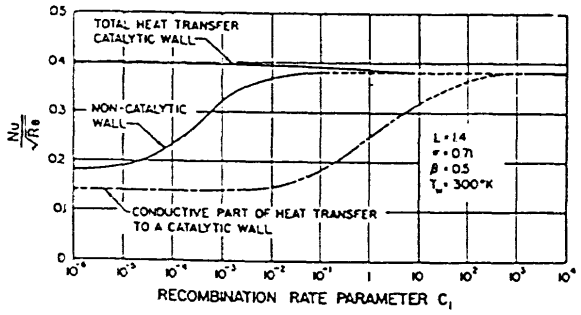

Figure 6 Heat flux variation with the recombination rate (*from Fay & Riddell, ref. 9*)

non-catalytic case and the doted lines the fully catalytic case. As pointed out in reference 9, in the non-catalytic case, the atoms are dammed up and the greater recombination occurs. As a result, the convective heat flux to the non-catalytic wall becomes larger than that to the fully catalytic wall.

Therefore one of the causes of this phenomenon in which the heat fluxes to the non-catalytic walls are larger than those to the fully catalytic walls seems to be rapid recombination rate.

6. Problem II

Problem II deals with the flows around the re-entry vehicle, OREX. In this problem, an axisymmetric laminar flow is assumed as it is in problem I. Two flow conditions are given, and four kinds of air and wall models are applied for one of them. Therefore, in all, 5 cases of computations have been carried out for this problem.

6.1 Computational grid

Figure 8 shows the computational grid used for the computations of cases 2, 3 and 4. The number of grid points is 58×61. For case 1, because the expansion region at the vehicle shoulder makes the computation difficult, the grid that is cut off at the shoulder is used. For case 5, which is the computation of ideal gas, because a shock formed farther away from a body than other cases, a wider computational region is taken.

6.2 Case 1

In figure 9, the computational results of case 1 are presented. The Knudsen number of this case is about 7×10^{-3}, and because of the rarefaction effect, a rather thick shock wave is formed. Figure 10 shows the temperature distributions along the stagnation streamline. The heat flux along the body surface is shown in figure 11. In figure 11, the flight data is plotted by the symbol. The flight data is somewhat smaller than the computational result.

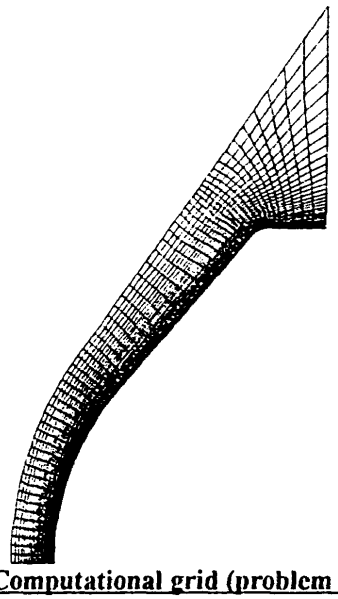

Figure 8 Computational grid (problem II, case 2, 3, 4)

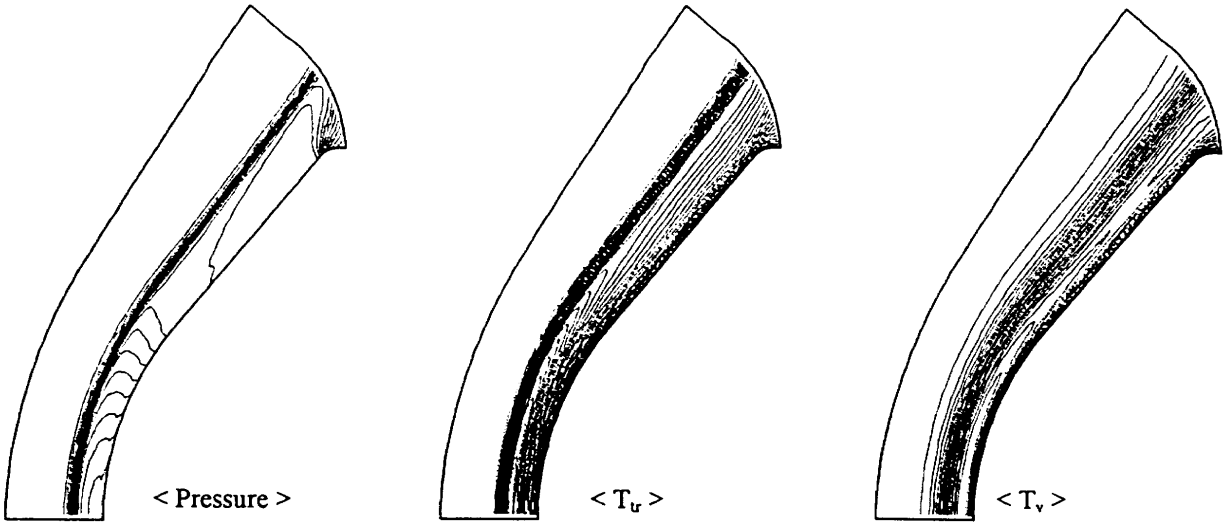

Figure 9 Computational results (Problem II, Case 1)

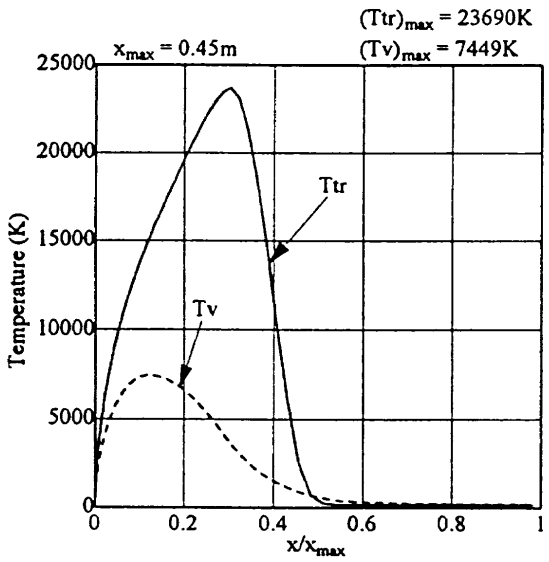

Figure 10 Temperature distributions along the stagnation streamline (problem II, case 1)

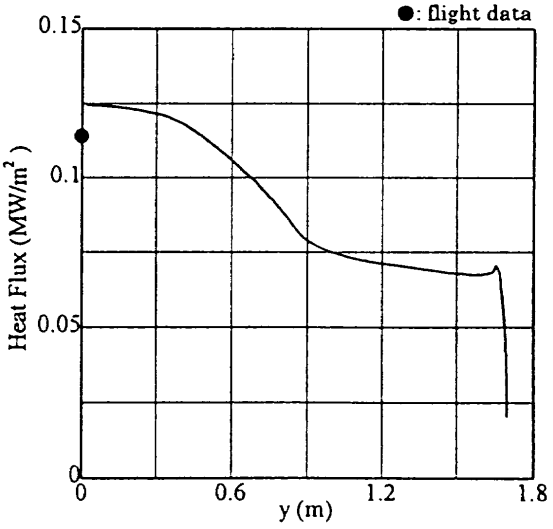

Figure 11 Heat flux distribution along the body surface (problem II, case 1)

6.3 Cases 2, 3, 4 and 5

In problem II, all cases except case 1 are computed under the same flow condition. For cases 2 and 3, the thermo-chemically non-equilibrium flows are assumed. The difference between the cases 2 and 3 is the wall catalytic effect. The non-catalytic wall and the fully-catalytic wall are assumed in cases 2 and 3, respectively. Case 4 is the equilibrium flow case and case 5 is the frozen gas (ideal gas) case. In figure 12, the pressure contours for cases 2, 4, and 5 are shown. Since, in case 5, ideal gas is assumed, the larger shock standoff distance is observed. On the other hand, in case 4 (equilibrium case), because of fast reaction rate, the shock standoff distance becomes the shortest. The heat fluxes to the wall in cases 2, 3, 4 and 5 are summarized in figure 13. For this problem, the heat flux to the fully-catalytic wall is larger than that to the non-catalytic wall. In this figure, the symbol also represents the flight data provided by the workshop organizer. Also in these cases, the computed stagnation heat fluxes are larger than the flight data in some degree.

7. Conclusion

The computations for 11 cases which are our task in "The 13th NAL Symposium on Aircraft Computation Aerodynamics - High Enthalpy Flow Workshop" are described.

In the case of problem I (sphere case), the computed results of non-catalytic wall case agree well with the experimental results. In this problem, the heat fluxes to the non-catalytic walls are larger than those to the fully-catalytic walls. One of the causes of this phenomenon seems to be a rapid recombination

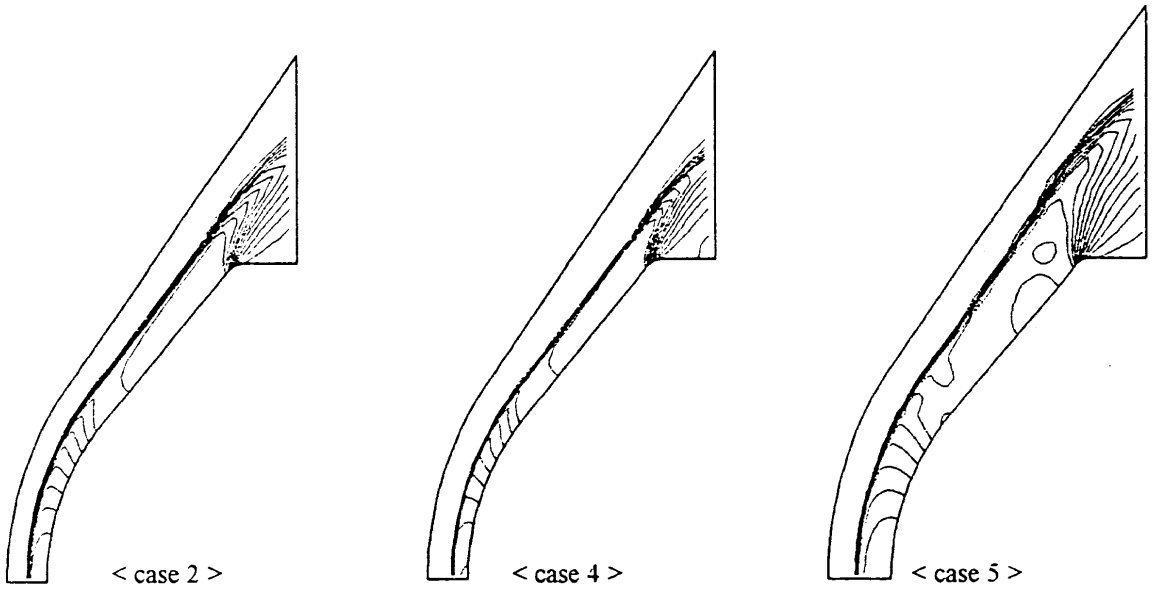

Figure 12 Computational results in the pressure contours (problem II)

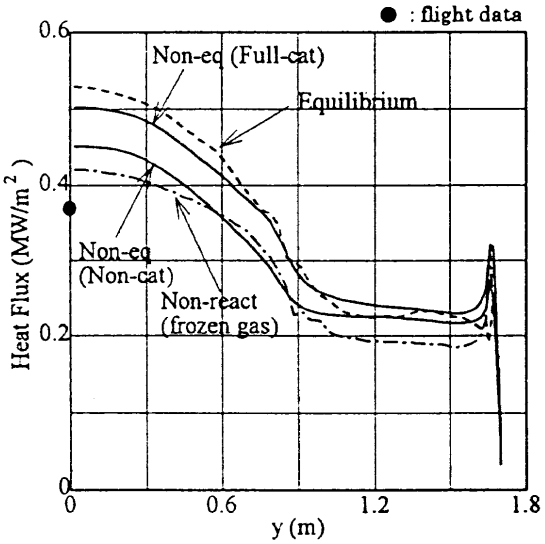

Figure 13 Heat flux distributions along the body surface (problem II, case 2, 3, 4, 5)

rate. More investigation is needed to fully understand this phenomenon.

In problem II (OREX case), the stagnation heat fluxes of two flow conditions are somewhat larger than the flight data, however the computed results agree with the flight data in the same order. In this problem, several computations are performed using different flow models under the common flow conditions. The heat flux distributions do not vary much with the flow model. For the simulation of flight at a high altitude, a thick shock wave is obtained because of rarefaction effect.

It is expected that the demand of space projects which include re-entry may increase and the importance of simulation of high enthalpy flow will be greater and greater. Hereafter we would like to try to develop more sophisticate and effective CFD tools.

References

[1] Millikan, R. C. and White, D. R.; "Systematics of Vibrational Relaxation," J. Chem. Phys., Vol. 39, No. 2, 1963.

[2] Park. C.; "Problems of Rate Chemistry in the Flight Regimes of Aeroassisted Orbital Transfer Vehicles," in *Thermal Design of Aeroassisted Orbital Transfer Vehicles*, H. F. Nelson, ed., Vol. 96 of Progress in Astronautics and Aeronautics, AIAA Inc., 1985.

[3] Gnoffo, P. A., Gupta, R. N. and Shinn, J. L.; "Conservation Equation and Physical Models for Hypersonic Air Flows in Thermal and Chemical Nonequilibrium," NASA-TP-2867, 1989.

[4] Tannehill, J. C. and Mugge, P. H.; "Improved Curve Fits for the Thermodynamic Properties of Equilibrium Air Suitable for Numerical Computation using Time-Dependent or Shock-Capturing methods," NASA-CR-2470, 1974.

[5] Srinivasan, S., Tannehill, J. C. and Weilmuenster, K. J.; "Simplified Curve fits for the Transport Properties of equilibrium Air," ISU-ERI-Ames-88405, 1987.

[6] Yee, H. C. and Harten, A.; "Implicit TVD Schemes for Hyperbolic Conservation Laws in Curvilinear Coordinates," AIAA paper 85-1513, 1985.

[7] Shuen, J. S. and Yoon, S.; "Numerical Study of Chemically reacting Flows Using an LU Scheme," AIAA paper 88-0436, 1988.

[8] Nevin, K. H. and Carroll, F. C.; "Comparative Evaluation of Ablating Materials in Arc Plasma Jets," NASA-CR-1207, 1968.

[9] Fay, J. A. and Riddell, F. R.; "Theory of Stagnation Point Heat Transfer in Dissociated Air," Journal of the Aeronautical Sciences, Vol. 25, No. 2, 1958.

2-11 Numerical Simulation of High Enthalpy Flow
— High Enthalpy Flow Workshop —

by

Ryoji Takaki and Yasuhiro Wada

Computational Sciences Division,
National Aerospace Laboratory in Tokyo, JAPAN

ABSTRACT

Numerical analysis of thermally and chemically nonequilibrium viscous flow around simple shapes is carried out as an entry of High Enthalpy Flow Workshop. We chose Problem I, flow around a sphere, and Problem IV, flow around a spherically blunted cone. Park's two-temperature model and Dunn & Kang's seven species and finite-rate eighteen chemical reaction model are used in order to take accounts of thermal and chemical nonequilibrium effects. Axis-symmetric full Navier-Stokes equations considering thermal and chemical nonequilibrium effects are solved by the Chakravarthy-Oshers' TVD scheme with generalized Roe's approximate Riemann solver. Regarding time integration, the LU-SGS implicit method with local time stepping method is used to suppress calculation time and increase code stability.

1 Introduction

There are a lot of research and development about hypersonic, re-entry or space vehicles recently. However, it is difficult to simulate the flow of typical flight conditions for the above vehicles with ground-based experimental devices. On the other hand, recent remarkable progress of computer hardware and numerical technique make it possible to analyze the flow including thermo-chemical nonequilibrium phenomena, so called 'real gas effect'. Hence the CFD analysis is indispensable for designing the high speed vehicles. It's necessary to validate CFD ability in order to use CFD as a design tool. But it is difficult to obtain plenty of high quality experimental data in the high speed flow fields. Therefore this High Enthalpy Flow Workshop is very precious opportunity to validate CFD ability. Hence we took part in the High Enthalpy Flow Workshop and attempt to Problem I and Problem IV.

2 Governing Equations

The flow field is regarded as two-dimensional axis-symmetric steady state flow. We consider mixed gas flow with thermo-chemical nonequilibrium effects [1, 2]. In order to treat the flow exactly, each energy level of chemical species must be considered respectively. However, such treatment increases the number of variables, the unreliability of relaxation models and the difficulties in solving the equations. Therefore Park's two-temperature model [3, 4]is used in these calculations, which is simple but has been reported to get good results. In this model, the translational energy mode and rotational energy mode are considered to be the equilibrium state and they are presented by one temperature, so-called '*temperature*, T'. The vibrational energy mode and electronic excitation energy mode are also considered to be the equilibrium state and they are presented by another temperature, so-called '*vibrational-temperature*, T_V'. Hence the governing equations consist of, two-dimensional unsteady full Navier-Stokes equations, the conservation equations of chemical species and the conservation equations of the vibrational energy:

$$\frac{\partial \boldsymbol{q}}{\partial t} + \frac{\partial \boldsymbol{F}_j}{\partial \boldsymbol{x}_j} + \frac{\partial \boldsymbol{F}_{Vj}}{\partial \boldsymbol{x}_j} = \boldsymbol{S} \tag{1}$$

where

$$\boldsymbol{q} = \begin{pmatrix} \rho \\ \rho u_i \\ E \\ \rho \gamma_s \\ e_V \end{pmatrix}, \boldsymbol{F}_j = \begin{pmatrix} \rho u_j \\ \rho u_i u_j + p\delta_{ij} \\ (E+p)u_j \\ \rho \gamma_s u_j \\ e_V u_j \end{pmatrix}, \boldsymbol{S} = \begin{pmatrix} 0 \\ \alpha_i \\ 0 \\ \dot{w}_s \\ \beta \end{pmatrix},$$

$$\boldsymbol{F}_{Vj} = \begin{pmatrix} 0 \\ \tau_{ij} \\ \tau_{ij} u_i - \rho \sum_s h_s D_s \dfrac{\partial y_s}{\partial x_j} - \eta \dfrac{\partial T}{\partial x_j} - (\eta_v + \eta_e) \dfrac{\partial T_V}{\partial x_j} \\ -\rho D_s \dfrac{\partial y_s}{\partial x_j} \\ -\rho \sum_s h_{V,s} D_s \dfrac{\partial y_s}{\partial x_j} - (\eta_v + \eta_e) \dfrac{\partial T_V}{\partial x_j} \end{pmatrix},$$

$$E = \epsilon + \frac{1}{2}\rho u_j^2.$$

$$\epsilon = \sum_s \rho\gamma_s(\varepsilon_{t,r,s} + \varepsilon_{v,s} + \varepsilon_{e,s})$$

$$e_V = \sum_s \rho\gamma_s(\varepsilon_{v,s} + \varepsilon_{e,s}) + \rho\gamma_e\varepsilon_{t,r,e},$$

$$p = \sum_{s\neq e} \rho\gamma_s\bar{R}T + \rho\gamma_e\bar{R}T_V,$$

$$\tau_{ij} = -\mu(\frac{\partial u_i}{\partial x_j} + \frac{\partial u_j}{\partial x_i} - \frac{2}{3}\frac{\partial u_k}{\partial x_k}\delta_{ij}),$$

$$y_s = \frac{\rho\gamma_s}{\sum_r \rho\gamma_r},$$

$$\beta = -p_e\frac{\partial u_j}{\partial x_j} + \sum_{s=mol} \rho_s\frac{(\varepsilon^*_{v,s} - \varepsilon_{v,s})}{< \tau_s >}$$
$$+2\rho_e\frac{3}{2}\bar{R}(T - T_V)\sum_s \frac{\nu_{e,s}}{M_s} + \sum_{s=mol} \dot{w}_s\hat{D}_s.$$

$\boldsymbol{F}$ and $\boldsymbol{F}_V$ are the convective and viscous flux vectors, and the vector $\boldsymbol{S}$ is a set of elements of thermo-chemical nonequilibrium source terms. e presents total internal energy and it consists of translational-rotational energy $\varepsilon_{t,r,s}$, vibrational energy $\varepsilon_{v,s}$ and electronic excitation energy $\varepsilon_{e,s}$ for each chemical species. e_V is the total of vibrational energy, electronic excitation energy and translational-rotational energy of electron and it is characterized by vibrational temperature, T_V.

These equations are transformed into generalized curvilinear coordinates (τ,ξ_1,ξ_2):

$$\frac{\partial\hat{\boldsymbol{q}}}{\partial\tau} + \frac{\partial\hat{\boldsymbol{F}}_j}{\partial\boldsymbol{\xi}_j} + \frac{\partial\hat{\boldsymbol{F}}_{Vj}}{\partial\boldsymbol{\xi}_j} = \hat{\boldsymbol{S}}, \tag{2}$$

with

$$\hat{\boldsymbol{q}} = V\boldsymbol{q}, \hat{\boldsymbol{S}} = V\boldsymbol{S},$$
$$\hat{\boldsymbol{F}}_j = n_{j1}\boldsymbol{F}_1 + n_{j2}\boldsymbol{F}_2,$$
$$\hat{\boldsymbol{F}}_{Vj} = n_{j1}\boldsymbol{F}_{V1} + n_{j2}\boldsymbol{F}_{V2}.$$

V is the volume of a computational cell surrounding a grid point. Vector $\boldsymbol{n}_j \equiv (n_{j1}, n_{j2})$ is cell interface normal of ξ_j-direction. The effect of axis-symmetricity is introduced by the treatment of metrics in finite volume method and additional element, α_i appeared in the source term, $\boldsymbol{S}$. Each conservation equation of chemical species, and total mass equation are calculated together in order to suppress the total numerical error.

3 Chemical Model

As a chemical reaction model, seven chemical species, O_2, N_2, N, O, NO, NO^+ and e^- and eighteen finite-rate chemical reactions are considered.

- $O_2 + M \leftrightarrow O + O + M, M = N, NO, O, O_2, N_2$
- $N_2 + M \leftrightarrow N + N + M, M = N, NO, O, O_2, N_2$
- $NO + M \leftrightarrow N + O + M, M = N, NO, O, O_2, N_2$
- $O + NO \leftrightarrow N + O_2$
- $O + N_2 \leftrightarrow N + NO$
- $O + N \leftrightarrow NO^+ + e^-$

The mass production rate of species s per unit volume, $\dot{w}_s$ is expressed as

$$\dot{w}_s = M_s\sum_{r=1}^{N_r}(\beta_{s,r} - \alpha_{s,r})(R_{f,r} - R_{b,r}), \tag{3}$$

where N_r is the number of reactions, $\alpha_{s,r}$ and $\beta_{s,r}$ are respectively the stoichiometric coefficients for reactants and products in the r reaction. $R_{f,r}$ and $R_{b,r}$ are respectively the forward and backward reaction rates for the r reaction, as expressed by

$$R_{f,r} = k_{f,r}\prod_s(\rho\gamma_s)^{\alpha_{s,r}},$$
$$R_{b,r} = k_{b,r}\prod_s(\rho\gamma_s)^{\beta_{s,r}}, \tag{4}$$

where $k_{f,r}$ and $k_{b,r}$ are respectively the forward and backward reaction rate constants. In this calculation, Dunn and Kang's chemical reaction model is applied and these reaction rate constants are determined as follows:

$$k_{f,r} = C_{f,r}T_q^{n_{f,r}}exp(\frac{-E_{f,r}}{kT_q}),$$
$$k_{b,r} = C_{b,r}T_q^{n_{b,r}}exp(\frac{-E_{b,r}}{kT_q}), \tag{5}$$

where T_q is a dummy variables for the rate-controlling temperature and defined below.

$T_q = \sqrt{TT_V}$	for dissociative reactions
$T_q = T_V$	for the reaction of electron impact ionization
$T_q = T$	for other reactions

Millikan and White's semi-empirical equation with Park's modification which limits the collision at the high temperature (above 8000K) is used as a relaxation model between vibrational and translational energy. Transport properties are calculated from the collision integrals [1].

4 Numerical Techniques

The convective flux vectors are differenced using post-processing TVD scheme [5, 6] with the generalized Roe's approximate Riemann solver [7, 8]. The viscous flux vectors are differenced with second order central differencing. Therefore the right hand side has a second order accuracy in space. The form of gasdynamic matrices is described first, and then the treatment of the generalized Roe's approximate Riemann solver is presented. Three-dimensional treatment is used for this description. Two-dimensional formulation is a subset of three-dimensional one.

4.1 Gasdynamic Matrices for Real Gas

The eigenvalues and eigenvectors of Jacobian matrices of the convective term are analytically derived for nonequilibrium flow [6]. The Jacobian matrix $\boldsymbol{A} \equiv (\frac{\partial \hat{\boldsymbol{F}}}{\partial \boldsymbol{q}})$ at an averaging state satisfying the property U, in generalized coordinates, is decomposed like this:

$$\boldsymbol{A} = \boldsymbol{T}\boldsymbol{\Lambda}\boldsymbol{T}^{-1}, \tag{6}$$

where $\boldsymbol{T}^{-1}$ and $\boldsymbol{T}$ are, respectively, the left and right eigenvector matrices. The diagonal matrices of eigenvalues $\boldsymbol{\Lambda}$ are expressed by

$$\boldsymbol{\Lambda} = diag(U, U, U, U + |n_j|c, U - |n_j|c, U, U, \cdots), \tag{7}$$

where

$$U = n_j u_j, \quad |n_j| = \sqrt{n_j{}^2},$$

$$c^2 = \frac{\partial p}{\partial \rho} + \frac{e+p}{\rho}\frac{\partial p}{\partial e} + \gamma_s \frac{\partial p}{\partial \rho \gamma_s} + \frac{e_V}{\rho}\frac{\partial p}{\partial e_V}.$$

The eigenvectors used for this study, are calculated using reciprocal vectors $\boldsymbol{l}$ and $\boldsymbol{m}$,
$(\boldsymbol{n}\cdot\boldsymbol{l} = 0, \boldsymbol{n}\cdot\boldsymbol{m} = 0, \boldsymbol{l}\cdot\boldsymbol{m} = 0, \boldsymbol{l}\cdot\boldsymbol{l} = \boldsymbol{m}\cdot\boldsymbol{m} = 1)$.

4.2 Generalized Roe's approximate Riemann solver

Recently, upwind differencing schemes are often used for flow computations. Up to now several upwind schemes have been developed and most of them are categorized as either Flux Difference Splitting (FDS) or Flux Vector Splitting(FVS). FDS scheme uses an approximate solution of the local Riemann problem, and the most popular approximate Riemann solver is Roe's approximate Riemann solver [9]. Roe's approximate Riemann solver has good efficiency and possibility of achieving high resolution of stationary discontinuities. This solver can catch the stationary discontinuities with one intermediate point. Roe has presented an averaged gasdynamic matrix for perfect gas. For nonequilibrium gas, the following averaged values are taken [6, 7]:

$$\begin{aligned}
\bar{u}_j &= \frac{u_j^L + D u_j^R}{1+D}, \\
\bar{\gamma}_s &= \frac{\gamma_j^L + D\gamma_j^R}{1+D}, \\
\bar{H} &= \frac{H^L + DH^R}{1+D}, \\
\bar{\rho} &= \rho^L D,
\end{aligned} \tag{8}$$

where

$$D \equiv \sqrt{\frac{\rho^R}{\rho^L}} \quad .$$

Then Δp is reduced to be

$$\Delta p = \frac{\bar{\partial} p}{\partial \rho}\Delta\rho + \frac{\bar{\partial} p}{\partial \epsilon}\Delta\epsilon + \frac{\bar{\partial} p}{\partial \rho\gamma_s}\Delta\rho\gamma_s + \frac{\bar{\partial} p}{\partial \epsilon_V}\Delta\epsilon_V. \tag{9}$$

The averaged pressure derivatives which satisfy Eq.(9) are determined as:

$$\begin{aligned}
\frac{\bar{\partial} p}{\partial \rho} &= \hat{D}[\frac{\hat{\partial} p}{\partial \rho}], \\
\frac{\bar{\partial} p}{\partial e} &= \hat{D}\frac{\hat{\partial} p}{\partial e}, \\
\frac{\bar{\partial} p}{\partial \rho\gamma_s} &= \hat{D}[\frac{\hat{\partial} p}{\partial \rho\gamma_s} + \frac{\delta p}{D}(\bar{R}T)^2\Delta\rho\gamma_s], \\
\frac{\bar{\partial} p}{\partial e_V} &= \hat{D}[\frac{\hat{\partial} p}{\partial e_V} + \frac{\delta p}{D}(\bar{R}T_V)^2\Delta e_V],
\end{aligned} \tag{10}$$

where

$$\hat{D} \equiv \frac{D}{D - \Delta p \delta p},$$

$$\hat{A} \equiv \frac{1}{2}[A_L + A_R],$$

$$D \equiv \Delta P^2 + (\bar{R}T\Delta\rho\gamma_s)^2 + (\bar{R}T_V e_V)^2,$$

$$\Delta p = \frac{\hat{\partial} p}{\partial \rho}\Delta\rho + \frac{\hat{\partial} p}{\partial e}\Delta e + \frac{\hat{\partial} p}{\partial \rho\gamma_s}\Delta\rho\gamma_s + \frac{\hat{\partial} p}{\partial e_V}\Delta e_V.$$

When $\boldsymbol{T}^{-1}$ is evaluated at the Roe averaging state, a simple form for the characteristic vector $\bar{\boldsymbol{T}}^{-1}\Delta\boldsymbol{q}$ is given as:

$$\begin{aligned}
\bar{\boldsymbol{T}}^{-1}\Delta\boldsymbol{q} &\equiv (a^1, a^2, a^3, a^4, a^5, a^{5+s}, a^n)^t \\
&= \begin{pmatrix}
\bar{c}^2\Delta\rho - \Delta p \\
\bar{\rho}\bar{c}(\boldsymbol{l}\cdot\Delta\boldsymbol{u}) \\
\bar{\rho}\bar{c}(\boldsymbol{m}\cdot\Delta\boldsymbol{u}) \\
\frac{1}{2}[\Delta p + \bar{\rho}\bar{c}(\boldsymbol{n}\cdot\Delta\boldsymbol{u})] \\
\frac{1}{2}[\Delta p - \bar{\rho}\bar{c}(\boldsymbol{n}\cdot\Delta\boldsymbol{u})] \\
\bar{c}^2\Delta\rho\gamma_s - \bar{\gamma}_s\Delta p \\
\bar{c}^2\Delta e_V - \frac{\bar{e_V}}{\bar{\rho}}\Delta p
\end{pmatrix}.
\end{aligned} \tag{11}$$

4.3 Time integral method

Generally, nonequilibrium viscous flows have several characteristic time scales such as a fluid scale or chemical reaction scale. Such a disparity in time scale is referred to as 'stiffness' causing numerical instability. Thus, each term in the governing equations, especially chemical sources should be treated implicitly to construct stable schemes. For this purpose, the source term is treated with the point implicit method in order to increase the rate of convergence on steady state solutions. The time integration of the left hand side is carried with the LU-SGS [10] implicit method, and the steady state is achieved by the local time step method. The implicit time integration with LU-SGS method is expressed as:

$$
\begin{aligned}
(1+\frac{1}{2}\Delta t\varrho)\Delta\hat{\boldsymbol{q}}^{***}_{i,j} - \frac{1}{2}\Delta t\hat{\boldsymbol{A}}^{+}_{i-1,j}\Delta\hat{\boldsymbol{q}}^{***}_{i-1,j} - \frac{1}{2}\Delta t\hat{\boldsymbol{B}}^{+}_{i,j-1}\Delta\hat{\boldsymbol{q}}^{***}_{i,j-1} &= -\Delta t[RHS]_{i,j}, \\
(1+\frac{1}{2}\Delta t\varrho)^{-1}\Delta\hat{\boldsymbol{q}}^{*}_{i,j} &= \Delta\hat{\boldsymbol{q}}^{***}_{i,j}, \\
(1+\frac{1}{2}\Delta t\varrho)\Delta\hat{\boldsymbol{q}}_{i,j} + \frac{1}{2}\Delta t\hat{\boldsymbol{A}}^{-}_{i+1,j}\Delta\hat{\boldsymbol{q}}_{i+1,j} + \frac{1}{2}\Delta t\hat{\boldsymbol{B}}^{-}_{i,j+1}\Delta\hat{\boldsymbol{q}}_{i,j+1} &= \Delta\hat{\boldsymbol{q}}^{*}_{i,j},
\end{aligned}
\tag{12}
$$

where,

$$\varrho = \kappa \sum_k \max_l[|\lambda^l(\hat{\boldsymbol{A}}_k)|],$$

$$\hat{\boldsymbol{A}}_k = \frac{\partial \hat{\boldsymbol{F}}_k}{\partial \hat{\boldsymbol{q}}},$$

$$\hat{\boldsymbol{A}}^{\pm}_k = \frac{1}{2}[\hat{\boldsymbol{A}} \pm \kappa \max_l[|\lambda^l(\hat{\boldsymbol{A}}_k)|]\boldsymbol{I}].$$

κ is a constant that is greater than or equal to one. The use of approximate Jacobian matrices in the LU-SGS method makes the inverse algorithm very simple. With this approximation the implicit operators can be completely vectorized on oblique planes, which are equivalent to oblique lines in two-dimensional cases and the inversion of these operators is equal to forward and backward sweep of these planes and lines.

5 Results and Discussions

5.1 Problem I Sphere

Figure 1 shows a computational grid for Problem I. This grid is composed over a semi-sphere because it is not necessary to calculate the base region in this problem. The number of grid points is 73 points normal to the surface times 56 points along the sphere surface. This grid is used for calculations from Case 1 to 6.

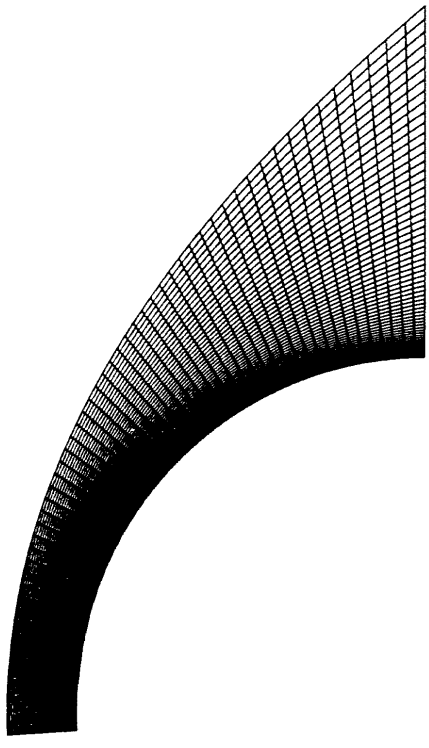

Fig. 1 : Computational grid around a Sphere

A minimum grid length is $0.0002mm$. Hence Cell Reynolds number is about 0.05, 0.1, 0.18 for Case 1(2), Case 3(4) and Case 5(6), respectively.

It is very important for designing of thermal protection system to estimate heat flux distributions precisely. The heat flux values depend on the grid length near the wall, which are evaluated by Cell Reynolds number. Therefore, we especially pay attention to the size of the Cell Reynolds number. We calculate with grids which have different size of the Cell Reynolds number and compare the heat flux values to investigate the influence of the Cell Reynolds number. The stagnation heat flux values obtained after such precalculations are 8.791, 12.03, 13.93, 18.72, 10.27 and 13.88 for Case 1 to 6, respectively. The stagnation heat flux values of Case 2,4 and 6, which are fully catalytic cases, are about 1.4 times higher than Case 1,3 and 5, which are non catalytic cases.

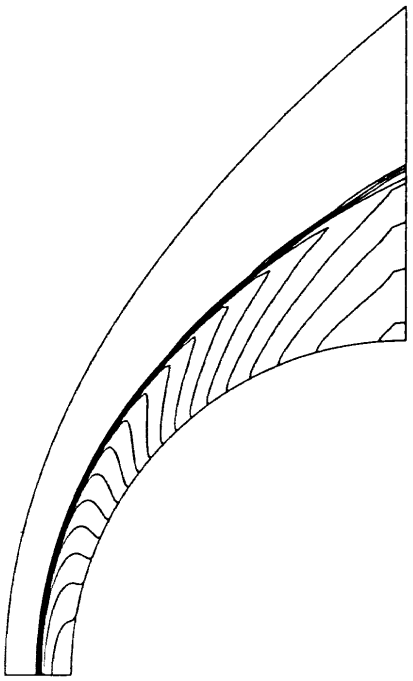

Fig. 2 : Pressure contours (Case 1)

For example, Fig. 2 shows the pressure contours in Case 1. Figure 3, 4 and 5 respectively show the heat flux distributions along the body surface (Fig. 3), temperature distributions along the stagnation line (Fig. 4) and distributions of mass fraction for chemical species along the stagnation line (Fig. 5).

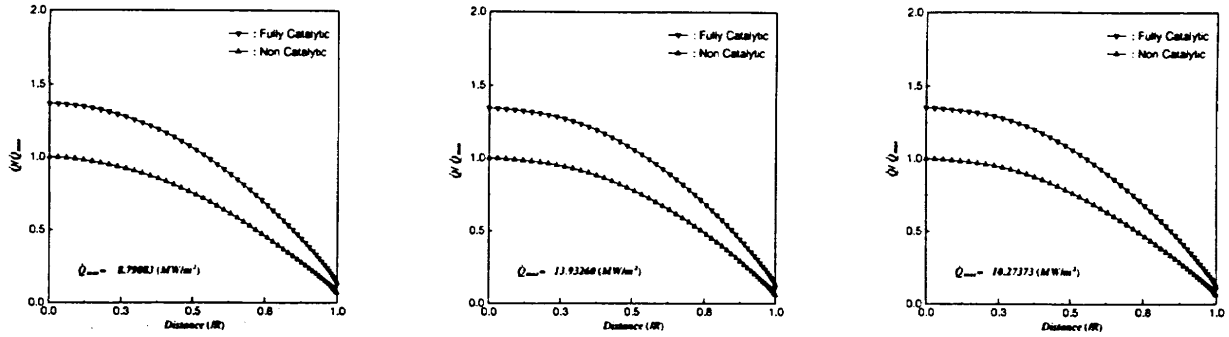

a) Case 1 and 2 b) Case 3 and 4 c) Case 5 and 6

Fig. 3 : Heat Flux Distributions along the surface

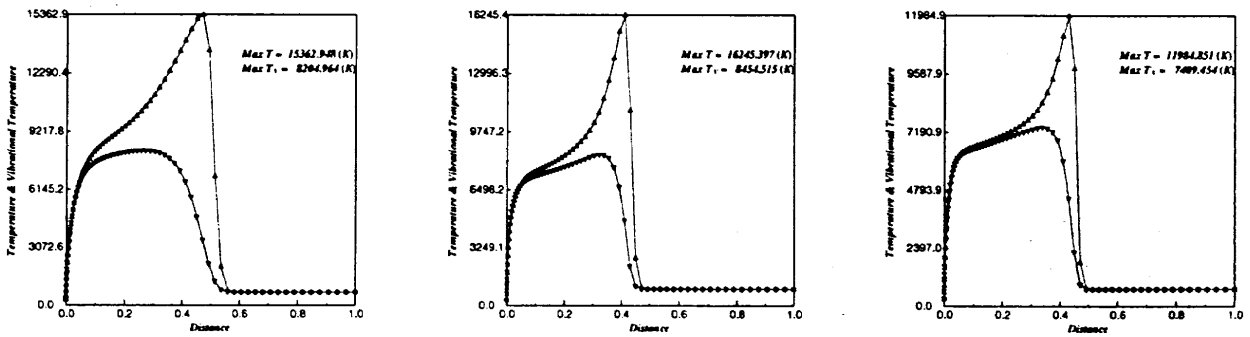

a) Case 2 b) Case 4 c) Case 6

Fig. 4 : T and T_V distributions along the stagnation line

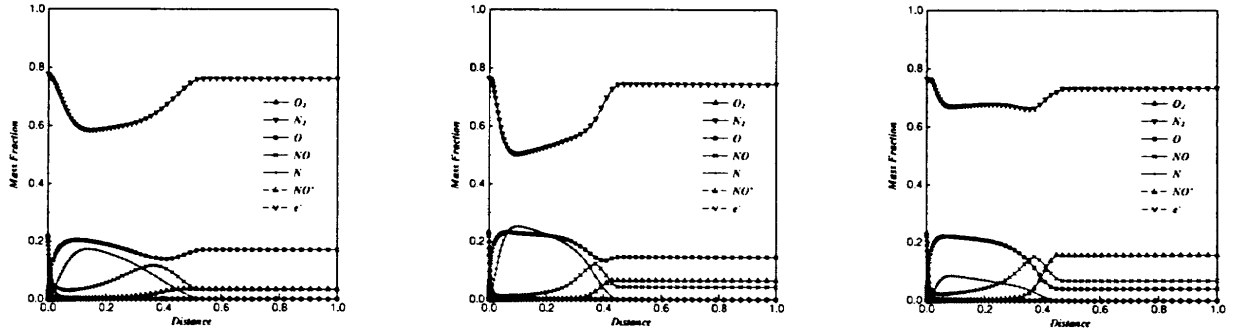

a) Case 2 b) Case 4 c) Case 6

Fig. 5 : Mass Fraction distributions along the stagnation line

We regard Case 1, 3 and 5 as Case 2, 4 and 6, respectively because the results are almost the same each other. From Fig. 4-a and 4-b, the temperature jump at the shock wave are similar in Case 2 and Case 4. Therefore the Shock wave in Case 2 and Case 4 have almost the same strength. However, the temperature distributions after the shock wave of Case 2 are different from Case 4. The energy exchange between T(translational-rotational energy) and T_V(vibrational-electron excitational energy) of Case 4 is more active than that of Case 2. Hence T_V follows T beter in Case 4 due to the difference of free stream pressure. The free stream pressure of Case 2 is relatively lower than that of Case 4. Hence the flow of Case 2 is more nonequilibrium than that of Case 4. This tendency also can be seen at the difference of the dissociation of N_2 between Fig. 5-a and 5-b.

The free stream pressure in Case 6 is heighest among these cases. Therefore, there is the smallest difference between distributions of T and distributions of T_V in Case 6. From Fig. 5-c, N_2 dissociation in Case 6 is least because of the relatively lower temperature after

the shock wave.

5.2 Problem IV Spherically Blunted Cone

Figure 6 shows a computational grid for Problem IV. The number of grid points is 90 points normal to the surface times 163 points along the surface. A minimum grid length is $0.0026mm$. Hence Cell Reynolds number is about 2.

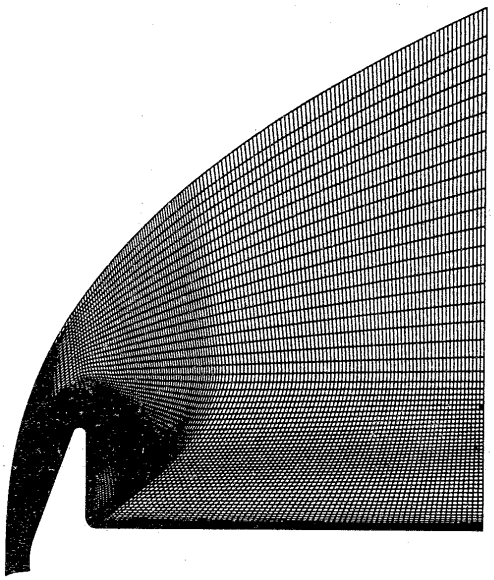

Fig. 6 : Computational grid around the Spherically Blunted Cone

Figure 7,8 and 9 respectively show the temperature contours (Fig. 7), vibrational temperature contours (Fig. 8) and pressure contours (Fig. 9) for Case 2. We can see strong bow shock at the front of the body and share layer starting from the shoulder of the cone.

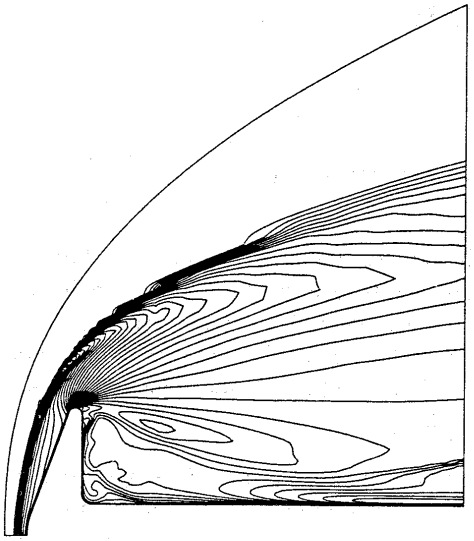

Fig. 7 : Temperature contours (Case 2)

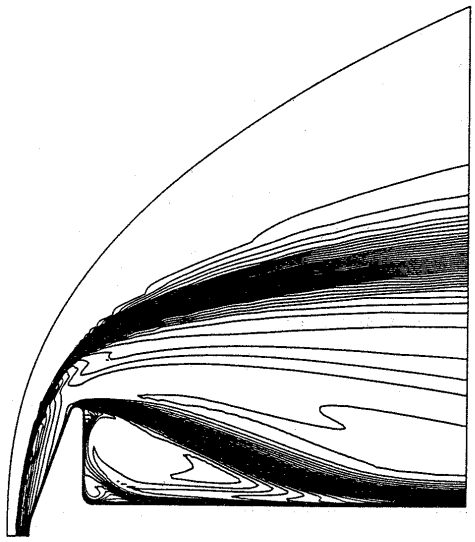

Fig. 8 : Vibrational temperature contours (Case 2)

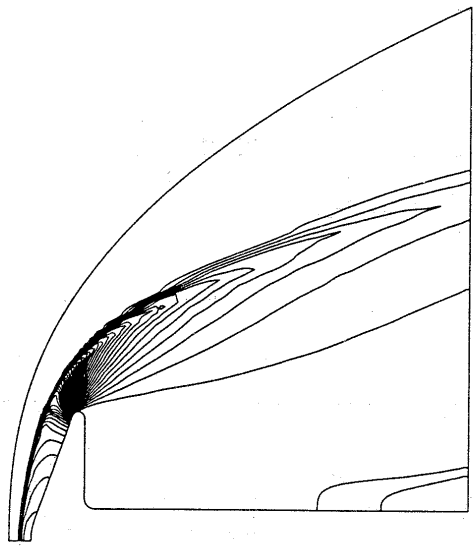

Fig. 9 : Pressure contours (Case 2)

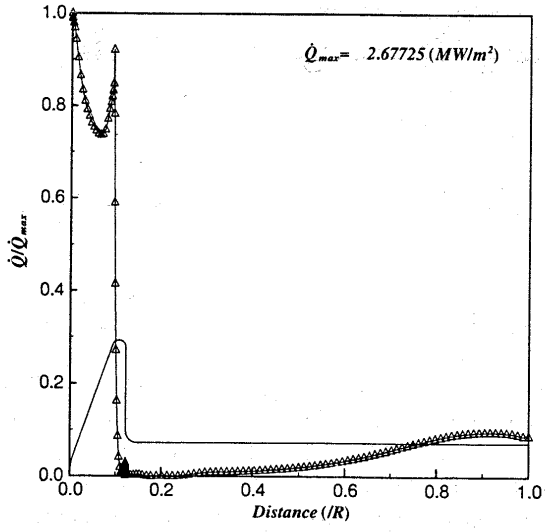

Fig. 10 : Heat flux distribution (Case 2)

Figure 10 shows the heat flux distributions along the body surface. The values of heat flux at the stagnation point are 2.23 for fully catalytic case and 2.68 for

non catalytic case, respectively. The heat flux distributions have maximum value at the stagnation point, local extreme value at the shoulder of the cone and increase at the aftbody. The re-attachment point and re-compression shock wave cannot be seen clearly in Fig. 7, 8 and 9. However, the increase of heat flux at the aftbody in Fig. 10 means a existence of re-attachment point and re-compression shock wave.

Finally, Figure 11 and 12 show stream lines at the wake region.

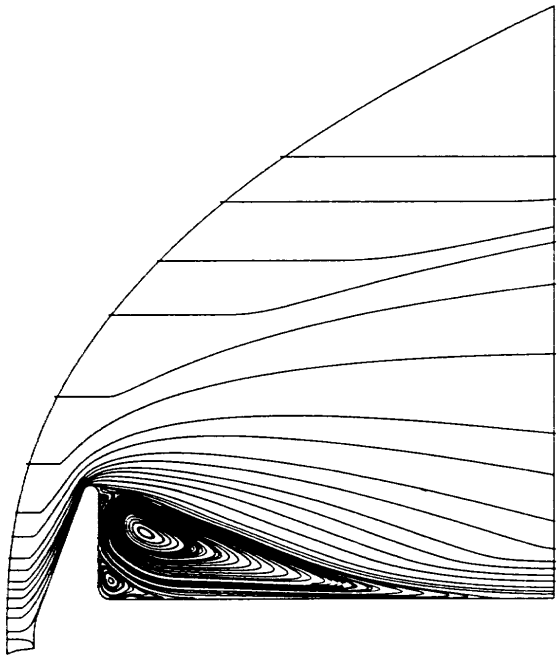

Fig. 11 : Stream lines

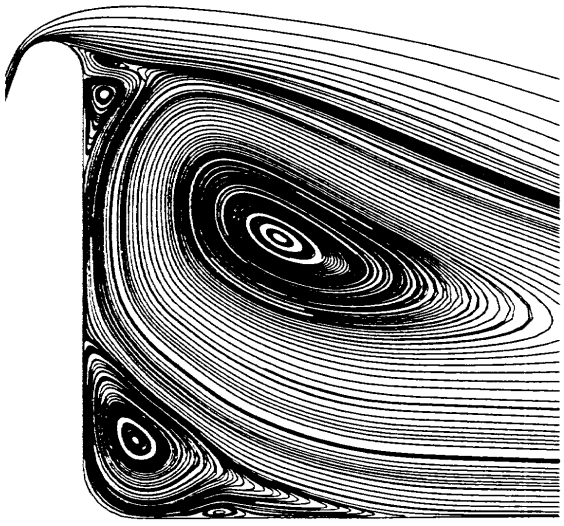

Fig. 12 : Stream lines at the wake region

From Fig. 11 and 12, there are some eddys at the wake region. One large first eddy, one middle eddy and three small eddies can be seen.

5.3 Conclusions

Numerical analysis of thermo-chemical nonequilibrium viscous flow are carried out for the problems of High Enthalpy Flow Workshop.

Dunn & Kang's seven species and eighteen reaction model is used as a chemical nonequilibrium model and Park's two temperature model is also used to take account of thermal nonequilibrium effects.

In the high speed flow analysis, it is still difficult to validate CFD code because we can not get a plenty of high quality data from the experiment. However, it is necessary to validate CFD code to make CFD be useful tool for the design of high speed or space vehicles.

Acknowledgments

We are deeply saddened to the death of Dr. Yasuhiro Wada on March 11, 1995. His sudden departure from all of us is a great loss to the CFD community of the world. He was an excellent and brilliant researcher and had a very inquistive mind. We shall always remember his kindness shown to us.

References

[1] R.N. Gupta P.A. Gnoffo and J.L. Shinn. Conservation Equations and Physical Models for Hypersonic Air Flows in Thermal and Chemical Nonequilibrium. *NASA TP-2867*, 1989.

[2] R. Takaki. Numerical Simulation of Arc Wind Tunnel Flow Using Navier-Stokes. *ISTS 94-d-38*, 1994.

[3] C. Park. Assessment of Two-temperature Kinetic Model for Dissociating and Weakly-Ionizing Nitrogen. *AIAA Paper 86-1247*, 1986.

[4] C. Park and S. Yoon. A Fully-Coupled Implicit Method for Thermo-Chemical Nonequilibrium Air at Sub-Orbital Flight Speeds. *AIAA Paper 89-1974*, 1989.

[5] S.R. Chakravarthy and S. Osher. A New Class of High Accuracy TVD Schemes for Hyperbolic Conservation Laws. *AIAA Paper 85-0363*, 1985.

[6] S. Ogawa Y. Wada, H. Kubota and T. Ishiguro. A Diagonalizing Formulation of General Real Gas-Dynamic Matrices with A New Class of TVD Schemes. *AIAA Paper 88-3596CP*, 1988.

[7] Y. Liu and M. Vinokur. Upwind Algorithms for General Thermo-Chemical Nonequilibrium Flows. *AIAA Paper 89-201*, 1989.

[8] Y. Liu and M. Vinokur. Nonequilibrium Flow Computations I. Analysis of Numerical Formulations of Conservation Laws. *J. Comput. Phys.*, 83:373-397, 1989.

[9] P.L. Roe. Approximate Rieman Solvers, Parameter Vectors, and Difference Schemes. *J. Comput. Phys.*, 43:357-372, 1981.

[10] S. Yoon and A. Jameson. An LU-SSOR Scheme for the Euler and Navier-Stokes Equations. *AIAA Paper 87-0600*, 1987.

Ⅲ－3　計算結果出力フォーマット

1. Problem I Sphere 部門 出力フォーマット

非平衡流計算結果については、課題番号別にそれぞれ別個の図を作成し、各図とも大きさはA4におさまるようにする。図番号の付け方は、たとえば非平衡流の等温度線図の場合には課題番号のProblem-I-1と図番号の②を組み合わせてProblem-I-1-②とする。

① 等圧線図 (Problem I-1, I-3, I-5, 非触媒ケースに対して)

圧力Pは一様流の密度ρ_∞、一様流の速度U_∞を用いて無次元量$P/(\rho_\infty U_\infty^2)$をプロットする。等圧線の間隔は 0.0から 1.0の間で等間隔で20分割する。なお、計算の外側境界もプロットすること。

② 等温度線図 (Problem I-1, I-3, I-5, 非触媒ケースに対して)

温度Tはケルビン単位とし、一様流の温度T_∞で無次元化したものをプロットすること。計算領域内の最高温度Tmaxは図中にその値を明記すること。
2温度モデルを用いた計算では振動温度についても同様なフォーマットでプロットを行い、Tv,maxの値を明記する。

③ 表面圧力分布 (Problem I-1, I-3, I-5, 非触媒ケースについて)

表面圧力分布は、表面圧力の最高値 Pmaxで無次元化し、物体対称軸に垂直な座標に沿ってその分布をプロットする。縦軸を圧力、横軸を座標軸とし、座標は物体の最大半径で無次元化を行う。なお、圧力の最大値を$P/(\rho_\infty U_\infty^2)$で無次元化した形で、図中にその値を明記すること。

④ 表面空力加熱分布

非触媒性のケースについては、空力加熱 'Q' は空力加熱の最高値 Qmaxで無次元化を行い、これをプロットする。表示方法は③の圧力分布の方式と同様とする。ただし、Qmaxの値を W/m^2 で図中に明記すること。
触媒性のある結果については、非触媒性の空力加熱分布図に同時にプロットする。このため、縦軸の最高値は 1.0を越えるが、その値は、任意とする。

⑤ よどみ点流線に沿う質量分率

質量分率は、用いた化学反応種のすべての成分を1枚の図にプロットすること。横軸は物体面から、物体軸に沿って計算領域の最外側の点までとり、最外側の座標軸が1.0となるように無次元化する。縦軸は質量分率で0.0から 1.0の範囲を取る。また、物体面から計算領域最外側の点までの距離を図中に明記すること。

⑥ よどみ点流線に沿う温度分布

横軸は⑤と同様とし、縦軸は、温度そのものをケルビン単位でプロットすること。また図中にTmaxの値をケルビン単位（K）で明記すること。
２温度モデルを用いた計算では振動温度の値そのものも並進、回転温度の図にプロットし、ケルビン単位で表示する。Tvmaxの値も明記する。

なおキャプション、図番号、各最大値の値は手書きでも結構です。

最後に表面熱流速の計算式、計算方法、また計算に用いた空気の物体表面温度での熱伝導係数の値を明記して下さい。

2. Problem II OREX 部門 出力フォーマット

非平衡流、平衡流及び完全気体計算結果については、それぞれの別個の図を作成し、各図とも大きさはA4におさまるようにする。図番号の付け方は、たとえば非平衡流の等温度線図の場合には課題番号のProblem-II-1と図番号の②を組み合わせてProblem-II-1-②とする。

① 等圧線図

圧力Pは一様流の密度ρ_∞、一様流の速度U_∞を用いて無次元量$P/(\rho_\infty U_\infty^2)$をプロットする。等圧線の間隔は0.0から1.0の間で等間隔で20分割する。なお、計算の外側境界もプロットすること。

② 等温度線図

温度Tはケルビン単位とし、一様流の温度T_∞で無次元化し、計算領域内の最高温度Tmaxは図中にその値を明記すること。

2温度モデルを用いた計算では振動温度についても同様なプロットを行う。

③ 表面圧力分布

表面圧力分布は、表面圧力の最高値Pmaxで無次元化し、物体対称軸に垂直な座標に沿ってその分布をプロットする。縦軸を圧力、横軸を座標軸とし、座標は物体の最大半径で無次元化を行う。なお、圧力の最大値を$P/(\rho_\infty U_\infty^2)$で無次元化した形で、図中にその値を明記すること。

④ 表面空力加熱分布

空力加熱 'Q' は表面熱流速 (W/m^2) で表し、空力加熱の最高値Qmaxで無次元化を行い、これをプロットする。表示方法は③の圧力分布の方式と同様とする。ただし、Qmaxの値を W/m^2 で図中に明記すること。

⑤ よどみ点流線に沿う質量分率（課題 Problem-II-1 ～ Problem-II-4 に対して）

質量分率は、用いた化学反応種のすべての成分を1枚の図にプロットすること。横軸は物体面から、物体軸に沿って計算領域の最外側の点までとり、最外側の座標軸が1.0となるように無次元化する。縦軸は質量分率で0.0から1.0の範囲を取る。また、物体面から計算領域最外側の点までの距離を図中に明記すること。

⑥ よどみ点流線に沿う温度分布

横軸は⑤と同様とし、縦軸は、温度そのものをケルビン単位でプロットすること。また図中にTmaxの値をケルビン単位（K）で明記すること。
2温度モデルを用いた計算では振動温度の値そのものを並進、回転温度分布図にケルビン単位で表示する。

⑦ Cone部と肩の接合点から垂直方向にのばした直線上における電子密度分布
（課題 Problem−II−1に対して）

今回は内挿のわずらわしいことも有り、Cone部と肩の接合点に最も近い、物体面に交わる方向の計算面での座標線に沿う電子密度分布に変更いたします。

電子密度の単位は電子数密度 Ne(1/cm³)とし、座標線に沿う電子数密度の最高値で無次元化し、縦軸へのプロットは $\log_{10}(Ne)/\log_{10}(Ne\ max)$ を用います。横軸は座標線に沿った物体面からの距離とし、実スケールで物体面から10 cm前後までの座標線に沿った分布をプロットします。

なおキャプション、図番号、各最大値の値は手書きでも結構です。

最後に表面熱流速の計算式、計算方法、また計算に用いた空気の物体表面温度での熱伝導係数の値を明記して下さい。

３．　Ｐｒｏｂｌｅｍ Ⅲ
Ｈｙｐｅｒｂｏｌｏｉｄ Ｆｌａｒｅ 部門
出力フォーマット

非平衡流、完全気体計算結果については、それぞれの別個の図を作成し、各図とも大きさはA4におさまるようにする。図番号の付け方は、たとえば非平衡流の等温度線図の場合には課題番号のProblem-III-1と図番号の②を組み合わせてProblem-III-1-②とする。

① 等圧線図

圧力Ｐは一様流の密度ρ_∞、一様流の速度U_∞を用いて無次元量$P/(\rho_\infty U_\infty^2)$をプロットする。等圧線の間隔は 0.0 から 1.0 の間で等間隔で 50 分割する。

② 等温度線図

温度Ｔはケルビン単位とし、T_∞で無次元化したものをプロットすること。計算領域内の最高温度Tmaxは図中にその値を明記すること。
２温度モデルを用いた計算では振動温度についてもT_∞で無次元化し、Tvmaxの値を明記し同様なプロットを行う。

③ 表面圧力分布

表面圧力分布は、表面圧力の最高値 $\rho_\infty U_\infty^2$ で無次元化し、物体長さ方向に沿ってその分布をプロットする。縦軸を圧力、横軸を座標軸とし、座標は頭部からフレアー部分までの長さＬを1.0としたプロットを行う。なお、圧力の最大値を$P/(\rho_\infty U_\infty^2)$で無次元化した形で、図中にその値を明記すること。なお、同図に形状の輪郭を示せれば示すこと。

④ 表面空力加熱分布

空力加熱　'Q' は表面熱流速 (W/m²) で表し、Qmaxの値で無次元化し、これをプロットする。表示方法は③の圧力分布の方式と同様とする。ただし、Qmaxの値を W/m² で図中に明記すること。特にフレアー再圧縮部の空力加熱部分についてはその拡大図を別紙にて表示すること。寸法は任意。なお、同図に形状の輪郭を示せれば示すこと。

⑤ よどみ点流線に沿う質量分率（課題 Problem-III-2 ～ Problem-III-3 に対して）

質量分率は、用いた化学反応種のすべての成分を１枚の図にプロットすること。横軸は物体面から、物体軸に沿って計算領域の最外側の点までとり、最外側の座標軸が1.0となるように無次元化する。縦軸は質量分率で0.0から 1.0 の範囲を取る。また、物体面から計算領域最外側の点までの距離を図中に明記すること。

⑥ よどみ点流線に沿う温度分布

横軸は⑤と同様とし、縦軸は、温度そのものをケルビン単位でプロットすること。また図中にTmaxの値をケルビン単位（K）で明記すること。
2温度モデルを用いた計算では振動温度の値そのものをケルビン単位で表示する。

なおキャプション、図番号、各最大値の値は手書きでも結構です。

最後に表面熱流速の計算式、計算方法、また計算に用いた空気の物体表面温度での熱伝導係数の値を明記して下さい。

4. Problem Ⅳ Blunted Cone 部門 出力フォーマット

非触媒、触媒ケースの計算結果については、それぞれの別個の図を作成し、各図とも大きさはA4におさまるようにする。図番号の付け方は、たとえば非平衡流の等温度線図の場合には課題番号のProblem-IV-1と図番号の②を組み合わせてProblem-IV-1-②とする。

① 等圧線図

圧力Pは一様流の密度ρ_∞、一様流の速度U_∞を用いて無次元量$P/(\rho_\infty U_\infty^2)$をプロットする。等圧線の間隔は0.0から1.0の間で等間隔で50分割する。ただし、触媒、非触媒の両ケースを計算している場合には非触媒の結果のみのプロットでよい。

② 等温度線図

温度Tはケルビン単位とし、T_∞で無次元化したものをプロットすること。計算領域内の最高温度Tmaxは図中にその値を明記すること。

2温度モデルを用いた計算では振動温度についてもT_∞で無次元化し、Tvmaxの値を明記し同様なプロットを行う。

ただし、触媒、非触媒の両ケースを計算している場合には非触媒の結果のみのプロットでよい。

③ 表面圧力分布

表面圧力分布は、表面圧力の最高値$\rho_\infty U_\infty^2$で無次元化し、物体長さ方向に沿ってその分布をプロットする。縦軸を圧力、横軸を座標軸とし、座標は全長Lを1.0としたプロットを行う。なお、圧力の最大値を$P/(\rho_\infty U_\infty^2)$で無次元化した形で、図中にその値を明記すること。なお、同図に形状の輪郭を示せれば示すこと。

④ 表面空力加熱分布

空力加熱 'Q' は表面熱流速 (W/m^2) で表し、Qmaxの値で無次元化し、これをプロットする。表示方法は③の圧力分布の方式と同様とする。ただし、Qmaxの値を W/m^2 で図中に明記すること。なお、同図に形状の輪郭を示せれば示すこと。

⑤ よどみ点流線に沿う質量分率

質量分率は、用いた化学反応種のすべての成分を1枚の図にプロットすること。横軸は物体面から、物体軸に沿って計算領域の最外側の点までとり、最外側の座標軸が1.0となるように無次元化する。縦軸は質量分率で0.0から1.0の範囲を取る。また、物体面から計算領域最外側の点までの距離を図中に明記すること。

⑥ よどみ点流線に沿う温度分布

横軸は⑤と同様とし、縦軸は、温度そのものをケルビン単位でプロットすること。また図中にTmaxの値をケルビン単位（K）で明記すること。
2温度モデルを用いた計算では振動温度の値そのものをケルビン単位で表示する。

なおキャプション、図番号、各最大値の値は手書きでも結構です。

最後に表面熱流速の計算式、計算方法、また計算に用いた空気の物体表面温度での熱伝導係数の値を明記して下さい。

Ⅲ－4　ワークショップ
まとめ

4-1 高エンタルピー流れのワークショップ まとめ

航空宇宙技術研究所 山本 行光

Summary of High Enthalpy Flow Workshop

National Aerospace Laboratory Yukimitsu YAMAMOTO

Abstract

In the perspective of Japanese space projects, the knowledge of high enthalpy and high Mach number flow, occuring during the atmospheric reentry of space vehicles, has regained recently considerable interest. The need to support aerodynamic design of space vehicles under the enviroments where experiments is very difficult and costly, has driven the use of High Enthalpy Flow. Hence, high enthalpy flow workshop was held at NAL in June, 1995 for axisymmetric flow problems. Four problems are proposed to the participants; flow around shere in DLR HEG high enthalpy shock tunnel comdition, OREX at flight comdition, hyperbolid flare in Geottingen Ludwig Tube and ONERA F4 hot shot tunnel condition and 70deg blunt cone in flow conditionHEG. This paper summarizes the computational results and discusses future improvement in the analysis of high enthalpy flow by High Enthalpy Flow.

1．はじめに

我が国におけるOREX,HYFLEX,HOPE等の宇宙往還輸送システムのための実験、開発が進展するとともに、これらの機体の再突入飛行時の極超音速空気力学の問題が、熱防御システムの構築を中心として、重要な研究課題として位置づけられるようになってきた。とりわけ再突入時の衝撃波直後の再圧縮加熱による、高温環境下での空気中の分子の解離、電離を伴う実在気体効果は機体表面の空力加熱特性のみならず、空力特性にも大きな影響を与えるため、この評価は超高速飛行体の設計、開発にとって、必須の条件となっている。この分野では、実飛行条件に対応可能な完全な風洞試験設備が存在しないため、CFDによる評価・検討が主要な手段になると考えられる。

このため平成６年度６月に、第１２回航空機計算空気力学シンポジウムの特別企画として、極超音速流のワークショップ[1)]を開催し、OREX形状、及びアーク風洞較正モジュールまわりの極超音速流のＣＦＤ解析結果の比較、検討を行った。今回の高エンタルピー流れのワークショップは、第１３回航空機計算空気力の特別企画として、前年度に引き続き平成7年度6月に開催されたもので、前回のワークショップでの不足と思われる部分を補完し、新たに高エンタルピーの衝撃風洞試験を課題の一部に設定した。また、ヨーロッパ宇宙機構構(ESA)のESTEC研究所から、J.Muylaert氏を招待し、ESA側からハイパーボロイドフレアー及び70° ブラントコーンの課題及び試験データの提供を受け、内容も剥離、再付着流を含む解析の困難なものになっている。本まとめでは、これらの結果についてその概要を紹介する。なお、球及びOREXの課題については、NAL-NASDA共同研究の一環として、宇宙開発事業団よりデータの提供を受けた。

2．課題設定背景

課題は4つに大別される。最初の課題はドイツのDLR研究所HEG高エンタルピー衝撃風洞による球のまわりの流れである。高温衝撃風風洞は、米国のT-5,NALのHEK及び現在NALに整備中のHIESTなどにみられるように、高温、、高エンタルピー流れの試験設備として最も注目されているものの一つである。今回の課題設定は、最も簡単な球の形状を例にとり、高エンタルピー衝撃風洞の特性及び、実在気体効果による空力熱環境の基本特性を知るために、三つの流れの条件を設定した。PloblemI-1,2は高エンタルピー、低密度Ploblem I-3, 4は、高エンタルピー、高密度、Ploblem I-5, 6は低エンタルピー、高密度の条件で、それぞれの流れの条件につき表面触媒性の空力加熱に与える影響を調べるため、非触媒及び、完全触媒壁条件の計算ケースを課している。実験模型は金属製であることから触媒壁と考えられ、熱流束は、同軸熱電対により計測された[2)]。

2番目の課題はOREXである[3)]。OREXは前年度の極超音速流のCFDワークショップにも取り上げたが、今回はOREXの実飛行推定軌道に基ずき、一様流条件を修正した。また、電子密度計測に対応させ、かつ非平衡性の大きくあらわれる高度90km条件のPloblemII-1を新たに設定した。PloblemII-2以降は、前年度と同様に、空力加熱が最大になる高度

60kmでの一様流条件を設定した。ただし、前回とは異なり、新たに完全触媒壁の条件であるProblemII -3を追加した。これは、実飛行環境下でのOREXの空力加熱が、必ずしも非触媒ではないという点を考慮して設定したものである。したがって、フライトデータによる空力加熱の同定値は非触媒壁の仮定のもとでの値と異なることが予想され、その値は、非触媒及び完全触媒の中間にあると推定される[4]。

3番目及び、4番目の課題は、ESA側から提案された課題である。3番目の課題のハイパーボロイドフレアー形状は、フレアー部をボディーフラップに見たてたもので、剥離、再付着による空力加熱への影響を調べることを目的としている。実験は、ドイツ、DLR、ゲッチンゲンのルートヴィックチューブ及び、フランスONERAのF4アーク加熱型衝撃風洞で行なわれた。なお、本課題に対しては、1994年11月に、ESA,ESTEC研究所で開かれた『宇宙機の熱空気力学に関する第2回ヨーロッパシンポジウム及び、第4回ヨーロッパ高速流のデータベースワークショップ』会議[5]でのワークショップ課題の一つとして取り上げられており、ヨーロッパ側からは多くの応募計算結果があり、実験データもESA側から提供された。

4番めの課題は、半頂角70°の鈍頭物体まわりの高エンタルピ流れの課題である。本課題では、解析の極めて困難とされるベースフローの問題が含まれ、ウェーク領域での再圧縮衝撃波の発生及び、その後の空力加熱の上昇をとらえることが目的の一つである。実験はDLR,HEG,高温衝撃風洞及び、カルスバンLENS衝撃風洞試験結果がある。

後者の２つの課題は、剥離、再付着という複雑な現象を含んでおり、軸対称流といえども解析が困難で、今回のワークショップでレベルの高くなったテーマとしてとらえられよう。なお、この２つの課題に対しては、ワークショップオーガナイザーからあらかじめ決められた格子が提供されている、課題３では流れ方向５２１点、物体面に垂直方向１０１点、課題４では、流れ方向１６１点、垂直方向２４１点である。詳細な格子図は、III-1節課題募集要項の最後の部分に示す。

3 形状と出力形式

課題1は球形状で、直径40ｍｍである。課題2のOREX形状は、最大直径3.4mの実機サイズ、課題3のハイパーボロイドフレアー形状は、全長1.0として、頭部半径が、0.017の曲率半径を持つ双曲線形状の前部に半頂角43.6°の直線のフレアー部が接続する。頭部からフレアー後部までの長さが、低温完全気体ケースでは、0.05924m、の高温実在気体ケースでは、0.1114mである。課題4の鈍頭物体形状は、半頂角70°の鈍頭円錐部に後から、円柱状のステイングに相当するものが接続し、肩及び、接続部分には、丸みが与えられている。最大半径は、76.2ｍｍである。出力結果は、（１）等圧線図　（２）等温度線図　（３）表面圧力分布　（４）表面空力加熱分布　（５）よどみ点流線に沿う質量率分布　（６）よどみ点流線に沿う温度分布で、III-3節で述べられているフォーマットの課題出力として、設定された。OREXの課題ProblemII-1については、さらに電子密度分布の出力が追加されている。

4. 比較検討

応募者ID及び実施課題一覧をIII-5-1節に、解析概要をIII-5-2節に示す。今回、全ての応募者はナビエ・ストークス方程式を使用した数値解析を実施している。以下にその比較結果の概要を説明する。個々の詳細についてはIII-2節応募論文、及びIII-5-4節応募者提出図を参考にしていただきたい。

4-1 球

本課題に関してははH-1,H-3,H-8,H-10,H-11の５件の応募があり、それぞれ触媒、非触媒を含め、全てのケースが各応募者によって計算されている。このうちH-8のみが一温度モデルによる計算で、他は温度非平衡も考慮した二温度モデルによる解析を行っている。

(1) Problem I-1,2 高エンタルピー、低密度ケース

最初に非触媒ケースの結果を中心に概観する。等圧力線図では全ての応募結果は類似したパターンを示す。並進、回転の等温度線図も同様である。等温度線図では衝撃波前後で温度の急激なピークが生じるため、その近傍で等温度線が密になり、また物体表面近傍でも壁温度が低く設定されているため、表面近傍で密となる傾向を示す。

振動温度の分布線図では、H-3の結果が、他の計算結果と比較して衝撃波層内の中央部で、振動温度の変化が小さい。表面圧力分布はどの結果も相似であるが、よどみ点上の最高値がH-3のみ0.9315とやや低い値を示す。他の結果は0.944～0.943と、ほぼそろった値を示している。

空力加熱分布結果については偏差が大きい。Qmaxの計算結果はH-8の17.34MW/m^{2}からH-1の6.38 MW/m^{2}に至るまで大きく変動している。実験結果はよどみ点空力加熱14.0MW/m^{2}で表面が完全触媒によるデータであると想定されているが、H-11の触媒計算ケースのQmaxがおよそ14.1MW/m^2 及びH-10 の非触媒性を仮定した計算結果が14.6MW/m^{2}と近い値をとっ

ている。しかしながら、H-11の計算ではIII-5-3節の数値比較表で見られるように、表面の空気の熱伝導係数の見積もりが、他の応募者のそれに比較して2倍程高い値を示し、H-10では非触媒の計算結果であることから、数値自体の吟味には、なお考慮を必要としよう。また触媒性がある場合には、一般に空力加熱は、非触媒ケースに比較して高くなることが予想されるが、触媒性を付加したことによる表面空力加熱の上昇倍率がH-1では1.22倍、H-3では1.55倍、H-8では2.0倍、H-11では1.4倍、さらにH-10では上記傾向と逆に、触媒ケースの値が非触媒の計算よりも小さくなる結果が示されている。触媒性ある計算では、境界条件等の変更による触媒性のとり入れ方法等、十分検討していかなければならないように考えられる。

次に、よどみ点流線に沿う質量分率の図では、ほぼ同様な傾向を示すが、細かく観察すると、それぞれ違いが認められる。H-1の図は対数プロットなので、比較は困難である。窒素分子N_2の分布はH-3,H-4で最低値0.55Wをとるのに対してH-10, H-11 では、ほぼ0.6である。また物体表面近傍でも酸素原子がH-8,H-10で0.1程に低下するが、H-3,H-11では0.2のままである。さらに窒素原子NについてはH-3, H-10でほぼゼロになるのに比較してH-11は0.07の値を示す。NOについてはH-11が他の計算結果に比べて高い分布を示し、最高値で0.1程度の値をとっている。このように質量分率については有意差が生じている。。

一方、よどみ点流線に沿う温度分布であるが、並進、回転温度では、物体表面に近づく手前の温度が7000～9000Kの間で、そこから表面に近づくにつれて急激に温度が下降していく。各計算結果で最高温度に違いは認められるものの、分布形状は相似である。振動温度もそれぞれ最高値は異なるが同様な傾向を示す。但し、H-1では振動温度が並進、回転温度を上回っており、H-3では振動温度の分布がやや平たんになっている。なお、H-8は一温度モデルによる結果で、振動温度は提出されていない。

Problem I-2の完全触媒ケースでは、触媒性の影響が表面近傍のみに限定され、等温度線図及び圧力分布には表れにくいことから、これらの図を省略し、よどみ点流線に沿う分布結果のみを掲載する。温度分布は、非触媒ケース及び触媒ケースとも各計算結果で、ほぼ同一となるが、質量分率の分布は、物体表面近傍で、触媒性がある場合には、酸素分子O_2の割合が再結合により急激に上昇していくことから、非触媒を仮定した計算結果との違いが判別される。H-3,H-11の結果ではこのような違いが最も大きく、H-8がこれに続き、H-10では、触媒性を仮定した結果が非触媒性を課した計算に比較して、酸素分子の割合が表面で、若干上昇している程度である。触媒性による質量分率の変化は空力加熱にも大きく影響してくるため、今後、各応募計算結果の詳細な検討が必要になると考えられる。

(2) Problem I-3,4 高エンタルピー、高密度ケース

この課題においても、それぞれの計算結果の傾向は前課題と同様である。実験値のよどみ点加熱率はこのケースが最も大きく、およそ24MW/m^{2}である。これに対してH-3 がが22.0, H-8が24.0, H-10が20.0, H-11が18.0MW/m^{2}と、それぞれ前課題の計算よりも高くなっている。非触媒に対する触媒性の空力加熱への影響の度合いも、それぞれ異なるものとなっていることは前述した点と同様である。また、H-8では、よどみ点からずれた領域で空力加熱が局所的に最高となるが、これは実験結果と同一の傾向を示す。実験結果の加熱率の最大値が、よどみ点からずれることは、乱流遷移の影響とみる観点もあるが、本実験ケースは極めて低いレイノルズ数の条件であることから、検討は今後の課題となろう。このような現象は同様な型式の高エンタルピー衝撃風洞T-5の実験においても観察されている。

よどみ点流線に沿う質量分率では、高エンタルピー条件のため、衝撃波層内の窒素分子の減少が前ケースよりも顕著に現れる。よどみ点流線に沿う温度分布では、一温度モデルによるH-8の温度が他の計算結果に比べて、かなり低い。完全触媒ケースの質量分率及び温度分布の特徴は、Problem I-1, 2のケースと同様である。

(3) Problem I-5, 6 低エンタルピー、高密度ケース

本ケースは低エンタルピー、高密度ケースのためか、空力加熱分布ではH-1及びH-10Nの結果に見られるように非触媒壁及び完全触媒壁でほぼ値が一致する傾向が得られている。H-8,H-11では、完全触媒壁を仮定した加熱率の増加はほぼ前課題と同様な比をとるが、H-3ではその比が減少する傾向を示している。よどみ点流線に沿う質量分率分布では、低エンタルピー条件のため、窒素分子N_2の減少が抑制されている。

対応する温度分布では、2温度モデルを使用したH-1, H-3, H-10, H-11で、衝撃波前後を除き振動温度と並進・回転温度が一致するようになり、温度平衡の状態となっていることがわかる。ただし、平衡になる温度がH-1,H-3で6000K, H-8, H-10, H-11で7000K 前後となり、各計算結果で差が認められる.

完全触媒壁条件でのよどみ点流線に沿う質量分率では、H-3,H-10, H-11のケースで窒素分子N_2が、表面近傍で局所的なピークをもつ分布になることが特色である。

4-2 OREX

(1) Problem II-1 OREX 高々度ケース

本課題にはH-2,H-3,H-5,H-8の4件の応募があり、H-8を除き、解析には温度非平衡を考慮した2温度モデルがとり入れられている。本条件は高々度でかつ飛行速度も大きいことから、非平衡性も高く、2温度モデルによる解析が適切と考えられる領域である。

等圧力線図では、この後の課題番号の高度60km付近での非平衡流の結果に比べ、本課題が高度90km付近の希薄領域であることから、衝撃波層も厚くなり、衝撃波も若干緩やかな立ち上がりのカーブとしてあらわれるようになる。

圧力線図、等温度線図については各計算結果とも相似な傾向を示す。表面圧力分布に関しては、よどみ点での値に若干のバラツキがみられる。コーン部での圧力分布は、H-5が平坦な分布を示し、他はやや右上がりの傾向を示す。

空力加熱分布に関してはH-2,H-3,H-8が相似であるが、H-5ではOREXの肩の部分の局所的な加熱のピークが大きくあらわれている。よどみ点の熱流束の値はH-3,H-8が実飛行実験結果に近く、H-2,H-5はやや小さい。

よどみ点流線に沿う質量分率では、表面近傍で、H-2の結果では窒素分子の解離反応が進み、逆にH-3 では窒素分子の減少がそれほど進んでいない。H-5, H-8はH-2とH-3の中間の傾向を示す。よどみ点を流線に沿う温度分布では並進、回転の最高温度が、H-2とH-3で25000K前後、H-5とH-8がそれぞれ19000及び21000K程になっている。振動温度についてはH-2とH-3が10000Kを越えて、並進、回転温度に近づき、熱的平衡状態になっていることを示している。これに対してH-3のK結果では、衝撃波層全般に渡って、非平衡となっていることが特色である。

（2）Problem II-2 OREX 高度60km, 非触媒ケース

本課題にはH-3, H-5, H-8, H-9, H-10の５件の応募があった。本課題の目的は、空力加熱最大となるＯＲＥＸ再突入飛行高度での熱空力環境の解析にある。高度は低いため、平衡流に近い状態になることが予想されるケースである。従って、本計算条件では後に述べるように、完全触媒、平衡流、完全気体等のケースも課題として含まれている。

圧力線図、振動温度を含めた等温度線図からは、読みとれる項目は少ないが、H-5の結果で圧力及び温度線図のよどみ点近傍での振る舞いが、他とは少し異なる。表面圧力及び熱流束分布で見ると、H-5の分布はよどみ点領域で、局所的なピークを表している。H-9でも若干この傾向が認められる。圧力分布については上述した点を除き、定量的にも良好な一致が得られるものの、空力加熱分布では、よどみ点熱流束の値に大きな違いが見られる。OREX飛行実験解析及び前年度の同様なケースの解析結果から、0.30～0.35 MW/m^{2}の値が非触媒ケースでは妥当な加熱量と推定される。

よどみ点流線に沿う質量分率では、低高度のため、窒素分子の解離は比較的小さく、各計算結果では、衝撃波層内で0.6から0.7の間にある。但し、物体表面では窒素原子の再結合がH-8のみ小さく、他の計算では急激に再結合が進み、窒素分子の質量分率が一様流の値にほぼ近づいている。

よどみ点流線に沿う温度分布では、衝撃波近傍の温度の最高値が10000～13000k前後の値をとり、振動温度も並進、回転温度に追随し、流れは平衡流に近いことを示している。但し、平衡と考えられる領域では、温度は5500Kから7500K までの幅を持っている。

（3）Problem III-3 OREX 高度60km 完全触媒ケース

本課題の応募はH-3,H-5,H-10である。本ケースでは空力加熱分布、及びよどみ点流線に沿う質量分率の結果を除いて、基本的には（2）の非触媒壁のケースと同様な流れ場となっている。よどみ点での空力加熱量はH-3で0.53MW/m^2,H-10で0.50MW/m^{2}で、H-5はこれに比べてやや低く0.38MW/m^{2}の値を提出している。よどみ点流線に沿う質量分率分布を見ると、表面近くでH-3、及びH-10が窒素分子Ｎ２の分布において局所的なピークを表す結果となっている。これに対してH-5のケースでは表面の質量分率が一様流の値そのものに復帰しているように見られる。完全触媒性の壁面での計算法について、さらに、詳細な検討を行う余地があるように思われる。OREXの実飛行結果の高度60kmでのよどみ点空力加熱の同定値が0.41MW/m^{2}程度であること、及びFay-Riddelleらによる平衡流仮定の理論値が0.48 MW/m^{2}であることから、完全触媒壁を仮定した計算値は、後者の値に近づくと考えられる。OREXのよどみ点空力加熱の同定推算値0.4MW/m2は、非触媒壁と、完全触媒壁の空力加熱の中間に位置すると考えられる。

（4）Problem II-4 OREX 高度60km 平衡流

この課題ではH-4,H-6,H-10の３件の応募があり、本応募者は前年度のワークショップにも参加している。表面圧力については、前年度と同様にH-6の計算結果がコーン部で振動を起こしている。よどみ点圧力もそれぞれの結果で開きが大きい。空力加熱分布に関してはH-6及びH-10がほぼ同じ0.53MW/m2のよどみ点熱流速値を出している。H-4はこれに対して低い値を示している。H-4の空力加熱の分布に関しては、前年度よりも分布形が改善されていることがわかる。

よどみ点流線に沿う質量分率ではH-4がモル分率の単位で結果を示していることから、直接的な比較はできな

いが、分布形態は相似である。よどみ点流線に沿う温度分布では衝撃波層内での温度が3ケースともほぼ一定の、５５００K程になっており、良好な一致を示す。

(5) Problem II-5 OREX 高度60km 完全気体

この課題ではH-4,H-5,H-6,H-8,H-9,H-10の６件の応募があり、化学反応モデル等が入ってこないことから圧力線図、等温度線図、表面圧力分布とも各計算で良好な一致を示し、よどみ点圧力値も各計算結果で0.92前後に集中している。表面空力加熱分布ではH-6,H-8,H-9,H-10が肩の局所的なピーク値の違いを除き、相似な分布を示す。よどみ点加熱量についてはH-10の0.42MW/m^2から、H-9の0.47 MW/m^2までの差はあるものの、対応するFay-Riddelleらの理論値は0.46MW/m^2でありこれに対してはH-8,H-9,及びH-6の結果が近い値を提出している。よどみ点流線に沿う温度分布では、各計算ケースとも16000Kをやや下まわる値を示しており、定量的な一致は良好である。

4-3 Hyperboloid Flare

(1) LTB条件、完全気体ケース

本課題にはH-6, H-7, H-9の３件の応募があった。この課題の目的の一つは、フレアー部前方の剥離領域を如何に正確にとらえるかということにある。従って、本課題では剥離領域を正確にとらえられるように、流れ方向に521点の計算格子をあらかじめ各応募者に配布している。配布格子はIII-1節付録に示す。各応募者の使用した流れ方向の格子数はH-6とH-9が521点、H-7が177点である。

実験結果の圧力分布は、本章4-2節、付録4-2-DのD-1図に示されるように、フレアー部手前で非常に大きな剥離が起こっている。これを各応募者の等圧力線図で見るとH-6及びH-9がこの流れの形態を模擬していると考えられる。なおH-9は、図が2種類提出されているが、一方が3次精度、他方が1次精度による結果で、このうち高次精度の計算が良好な結果を示す。H-7の計算結果は用いられた格子数が少ないため、フレアー部手前の大きな剥離が現れていない。

表面に沿う圧力分布では、フレアー部で各計算結果とも非常に大きな再圧縮のピーク値を示すが、H-6ではフレアー部での圧力の変動が大きく、H-9の高精度計算ではフレアー部前方ハイパーボロイド部での圧力分布に変動が見られる。H-9の一次精度の計算結果では、H-7と同様に剥離域が正確に捉えられておらず、圧力のピークも平坦で低い値となっている。

空力加熱分布はH-6及びH-9の高次精度の結果がフレアー部で、非常に大きな加熱のピークを示している。また、よどみ点に沿う温度分布は各計算とも良好な一致を示す。

4-4 Blunted Cone

本課題にはH-3,H-9及びH-11の３件の応募があった。このうちH-11のみが、IV-1,IV-2の非触媒及び完全触媒の２つのケースの計算結果を提出している。また、H-8は完全気体計算を実施しており、参考のために応募者提出図に付け加えた。本課題の特色はベース・フローの解析にあり、前課題と同様に剥離・再付着を含むが、肩付近の急激な膨張により、流れが凍結状態になり、強いシアーレイヤーが形成される等、現象の解明においては今回の課題群の中では最も難しいケースともなっている。

圧力線図は、どの計算も相似な結果を示す。並進・回転の等温度線図ではH-9の結果がシアーレイヤー及び再圧縮衝撃波をよくとらえている。振動の温度分布ではベース部とスティングとが接続するコーナー部でそれぞれ違いがみられる。また、H-11の触媒ケースでは、離脱衝撃波の後方ベース領域で線図にうねりがみられる。圧力分布を見るとスティング部の再付着による圧力上昇が、H-9の計算で最もベースよりに起こっている。表面空力加熱分布を観察すると、HEGの実験結果では肩の部分の加熱のピークがよどみ点の値に比べて、0.9程の割合になっているが、計算結果は各応募者とも低い値をとっている。一方、スティングの再付着による加熱率は実験で0.22程のピークを得ているが、各計算結果は実験に比較して0.1前後の低いピーク値を示す。また各計算で特色のある点は、ベースとスティングの接合するコーナー部で、値は低いものの加熱のピークが現れていることである。これに関しては、超音速逆流の現象が関与していると推測される。よどみ点流線に沿う質量分率分布は各計算で相似な傾向を示し、対応する温度分布はH-9が衝撃波層中央で比較的大きな平衡温度を示す他は、分布が相似となっている。

5. まとめ

高エンタルピー流れのワークショップを通じて、基本的な軸対称物体まわりの流れの検証、計算結果の比較、検討を行ない、多くの有意義な示唆を得ることができた。

課題1の球の問題に関しては、形状は簡単であるもの

の流れの解析はきわめて困難であると結論づけられる。HEG等の高エンタルピー衝撃風洞では、まず一様流条件の同定が難しく、一般に測定された球のよどみ点空力加熱率から、平衡条件を仮定して、逆に一様流条件を決定する手法がとられている。これによれば、加熱率分布に関しては平衡流条件を仮定した計算が最も加熱率を再現することになる[6]。また、よどみ点加熱率を測定する球の形状等の違いによっても一様流条件は変更される。また、実飛行条件とは異なり、加熱率が数10MW/m^{2}になり、さらにレイノルズ数が極端に低くなる等、極めて特異な流れの現象を呈する。加熱率分布に関してもよどみ点以外の部分で最高値をとる等、実験例にも多くの課題をかかえている。

一方、計算例においても、圧力分布等は良好な一致を示すものの、よどみ点流線に沿う温度分布、質量分率分布等、細かく観察すると明らかな違いが生じている。特に、空力加熱分布に関しては、各計算ケースで差が大きく、重要な検討課題の一つである。壁の触媒性の問題についても、各計算ケースでそのあらわれ方に多きな差が生じている。各計算に使用された熱伝動率、温度勾配、成分分布、格子密度等の個々のより詳細な値を比較検討し、議論していくことが必要と考えられる。

課題2のOREXについては、主流が一様性で成分比も単純で、よどみ点加熱率も0.5MW/m^{2}以内で、レイノルズ数は低すぎることもなく、素直な流れを呈することから、高エンタルピー流れの課題としては、最も対処しやすい課題であると考えられる。また、よどみ点加熱率もFay-Riddelleらの理論値を使用して、ある程度は推定が可能なことから、計算コードの適否を見分けるには適切な課題であろう。今回の応募者CFDコードの中には、なお未完のものも含まれているように感じられるが、完全気体ケースの課題では、結果の一致が良好になり、非平衡流の課題についても、より具体的な検討、討議を行うことにより空力加熱については、かなり統一された結果の得られる見通しがついてきたように思われる。極超音速飛行実験についてはOREXの後もHYFLEX,HOPE-Xへと連続して続けられる予定であり、CFDコードのより洗練された、統一的な整備、及び経験の積み重ねを通して、今後も続けられるCFD解析結果の検討をしていくことが重要となろう。今後は、電子密度計測等、より困難な現象の解明が興味の対象になっていくと考えられ、実験飛行では、より正確な一様流の同定法の確立が重要である。

課題3のHyperboloid Flareについては、前2者の課題とは異なり、剥離・再付着を含むより複雑な課題設定になっている。最初のケースのLTB条件、完全気体流れでは、剥離を正確にとらえるためには、流れ方向の格子を密にとらなければならないことがわかる。

流れ方向に格子を密にとった結果では、剥離領域をほぼ正確にとらえているが、なお、表面圧力分布等に変動が見られる。本課題が、軸対称流といえども、正確な解を得るためには、綿密な現象の理解と、CFD計算の経験を積むことが大事であることを示唆しているように思われる。なお、本ケースの圧力分布の実験については、2種類の結果が示されている。最初の実験結果では、ヨーロッパ側のいくつかのCFD計算結果と実験による圧力分布間で、ハイパーボロイド部表面の圧力分布に大きな不一致が生じたことから、再度実験の見直しが行われ、データが新しく修正されたものである。ワークショップを開くことの意義の一つが見いだされた例と言えよう。

なお、今回提案した課題の中では、Problem IIIのハイパーボロイドフレアー形状の課題が、実験、計算結果とも詳細な部分において、ヨーロッパ側でかなり統一された成果が得られており、正確な計算結果を得るためには相当な努力を必要とするが、今後、これらの課題にも取り組まれることを推奨したい。

課題4のBlunted Coneのケースでは、ベース・フローの領域で難問が山積する。格子数や格子密度の影響も詳細に検討していかなければならないが、現状では解が得られたという段階であるように思われる。特に化学反応が含まれる非平衡流では、まだまだ課題として、実験的にも理論的にも詰めていかなければならない領域が多い。本課題に着手する前に同一形状で完全気体ケースの実験及び計算を詳細に実施する必要があるとも考えられる。

全体的なまとめとして、今回は前回の極超音速流のCFDワークショップに比較して、課題内容や実験データの提供についてもかなり充実してきたと考えられる。さらに今後ワークショップでの実績と経験を積み重ねることにより、本格的に宇宙往還機の設計や高エンタルピー流れの現象解明に役立つコードの構築に向けて、各応募者間で横断的な討議及び検討を加え、物理モデル、計算スキームの改良発展を行っていくことが重要であろう。そのためには、将来、広く公開可能なデータ・ベースの整備も必要になると考えられる。

現在、各応募者の計算データは、3.5インチフロッピーディスクの形で送付していただいており、次回の航空機計算空力シンポジウムにおいて、より細かな検討を加えてゆきたいと考えている。本まとめは、今年度6月の時点で得られた資料に基づいている。応募論文の中にはその後、改定された計算結果が載せられているものも含まれていると思われるが、この点について今回のまとめでふれられなかった。御容赦いただきたい。

最後に、今回のワークショップ応募のため、貴重な時間を割いていただいた応募者各位には本誌面を借りて、深く感謝の意を表する。

参考文献

1) 第12回航空機計算空気力学シンポジウム論文集特別企画/極超音速流のワークショップ,航技研特別別資料 SP-26, 1994年12月
2) 往還技術試験予備空力特性試験(そのイ)
06HOPE極超音速風洞熱試験
06HOPE高エンタルピ衝撃風洞試験(その1)成果報告書
平成7年6月川崎重工株式会社
3) NAL/NASDA共同研究成果報告書
HOPEの研究(その15)軌道再突入実験(OREX)
平成7年3月
4) 大山、秋元「OREXまわりの非平衡流解析」
第39回宇宙科学技術連合講演会講演集
平成7年10,11月、pp615～～616
5) Proceeding of Second European Symposium on Aerothermodynamics for Space Vehicles, ESTEC, Noordwijk, The Netherlands 21-25 November 1994
esa SP-367, Feburuasy 1995, ISBN92-9092-310-5
6) 岸本、花光、尾藤「簡易形状まわりの高エンタルピ流れについて～HEG風洞試験とCFD解析～」
第27回流体力学講演会講演集
平成7年9月、pp13～16

4-2 実験結果解説及び資料

航空宇宙技術研究所 山本行光

本節では、各課題における実験結果資料をまとめ、その概略を説明する。

Problem I 球

DLR,HEG高温衝撃風洞条件の球のまわりの加熱率分布、及び一様流条件を付録4－2－Aに示す。空力加熱は同軸熱電対による計測結果である。詳細は、参考文献1）の報告書に報告されている。また本報告書、第1章企画セッションI-2の論文も参照されたい。HEGの一様流条件については、課題設定時とは、若干異なった値が示されている。

Ploblem II OREX

高度92kmでの静電プローブによる電子密度計測位置、電子密度導出に用いられたCFD解析法とその結果、及び各計測点での電子密度の時間履歴を付録4－2－Bに示す。詳細は参考文献2）を参照されたい。

よどみ点空力加熱の飛行軌道に沿う同定値と、非触媒壁を仮定したCFDと有限要素法カップリング空力加熱解析による推算値を付録4－2－Cに示す。飛行同定値は表面触媒性の影響が入っていると推定され、CFD-FEMカップリング解析による結果が、非触媒ケースの飛行実験解析値として妥当であると考えられる。なお、後者の解析はC－C材の内側の輻射率を0.0と仮定した時の結果である。詳細なよどみ点空力加熱推算法については、本報告書第1章企画セッションの論文I-3及び、I-4を参照されたい。

Ploblem III ハイパーボロイド・フレアー

LTB(ColdCase)及び、F4(HotCase)条件での実験資料を付録4－2－Dに示す。LTBは圧力分布、F4は、圧力及びスタントン数であらわされた熱流束分布が示されている。両ケースとも、実験データの他に、対応するヨーロッパ側CFD計算結果もプロットされている。これらの実験結果は今回のシンポジウムの特別講演者であるESA,ESTEC研究所のJ. Muyleart氏から提供された。

Ploblem IV 70° 鈍頭円錐

DLR,HEG条件での空力加熱分布に関する実験資料を付録4-2-E に示す。課題に対応する実験データはRun No.132 のデータである。詳細は、参考文献3）の論文を参照されたい。なお、よどみ点の加熱量の値は論文には明記されていない。

参考文献

1) 往還技術試験予備空力特性試験(そのイ)
06HOPE極超音速風洞熱試験
06HOPE高エンタルピ衝撃風洞試験(その1)成果報告書
平成7年6月川崎重工株式会社

2) NAL/NASDA共同研究成果報告書
HOPEの研究(その15)軌道再突入実験(OREX)
平成7年3月

3) D. Kastell, T. J. Harvath, G. Eitelberg
"Non equilibrium Flow Expansion
Experiment around a Blunted Cone."
Procedding of Second European Symposium on
Aerothermodynamics for Space Vehicles, ESTEC,
Noordwijk, The Netherlands 21-25 November 1994
esa SP-367, pp 383～389 Feb. 1995, ISBN92-9092-310-5

付録４－２－Ａ

課題Ｉ

球

DLR HEG 実験資料

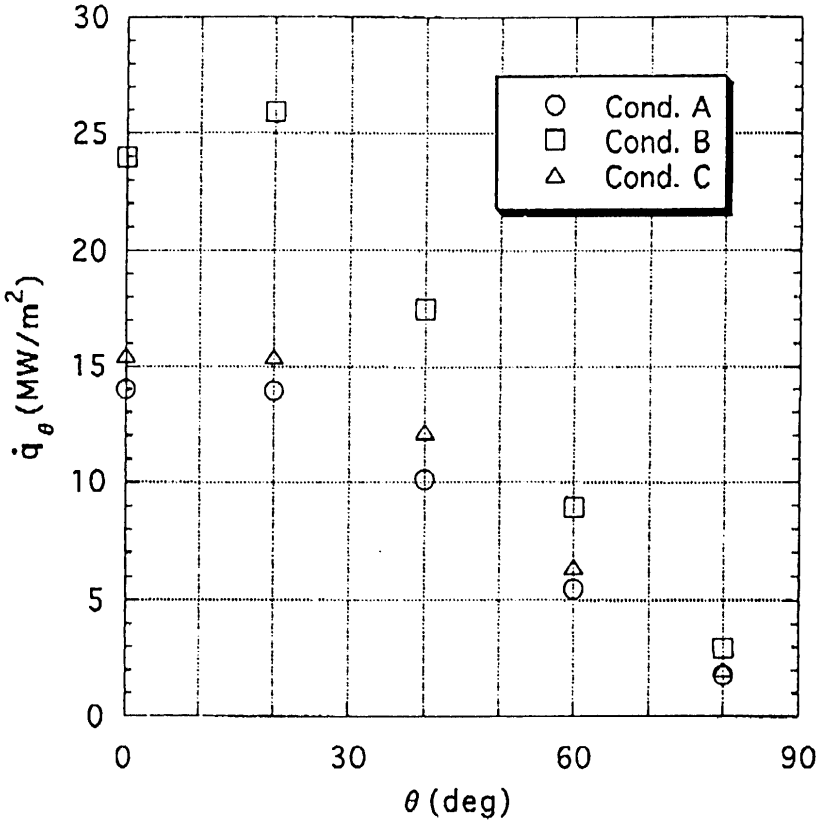

図　A–1 球加熱率分布

表　A–1 試験条件

条件(Run No.)	A (005)	B (002)	C (007)
V_∞ (m/s)	5957.7	6297.4	5185.3
T_∞ (K)	782.9	1328.8	839.0
ρ_∞ (kg/m^3)	0.00190	0.00317	0.00544

表 A–2 球の加熱率分布 (MW/m^2)

条件 / θ (deg)	A	B	C
0	14.007	23.960	15.500
2 0	13.935	25.907	15.418
4 0	10.116	17.475	12.148
6 0	5.4679	8.9465	6.4038
8 0	1.8026	2.9684	2.0355

表　A–3 一次元非平衡計算より求めた気流条件

条件(Run No.)	A (005)	B (002)	C (007)
V_∞ (m/s)	6106.0	6152.6	5063.5
T_∞ (K)	858.89	941.34	705.83
ρ_∞ (kg/m^3)	0.00160698	0.00303320	0.00563064
p_∞ (bar)	4.65450E-3	9.35101E-3	1.18144E-2
M (平衡)	9.5494	9.3904	9.4189
N_2 (mol/g)	2.64702E-2	2.62701E-2	2.57859E-2
O_2 (mol/g)	7.51650E-4	1.72179E-3	4.87294E-3
N (mol/g)	7.77437E-8	1.06374E-8	9.45994E-9
O (mol/g)	1.20867E-2	9.74609E-3	2.47536E-3
NO (mol/g)	9.07599E-4	1.30788E-3	2.27633E-3
NO^+ (mol/g)	1.34802E-8	8.53453E-9	1.83538E-9
e^- (mol/g)	1.34802E-8	8.53453E-9	1.83538E-9
Ar (mol/g)	3.45180E-4	3.45180E-4	3.45180E-4
MW (g/mol)	24.654	25.386	27.968

付録４－２－Ｂ

課題Ⅱ－１

ＯＲＥＸ

電子密度計測実験資料

Measuremnet Locations of Electron Static Probe

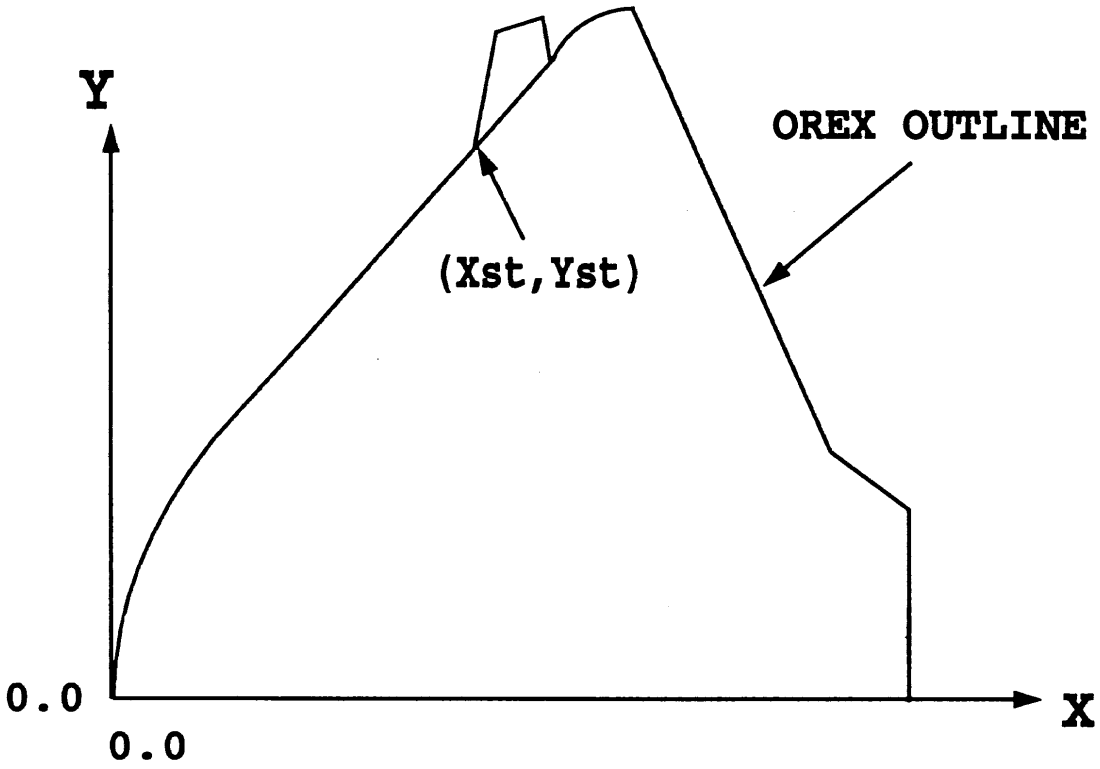

Xst = 875.07 mm
Yst = 1534.22 mm

Details of Electron Static Probe

Measurement locations

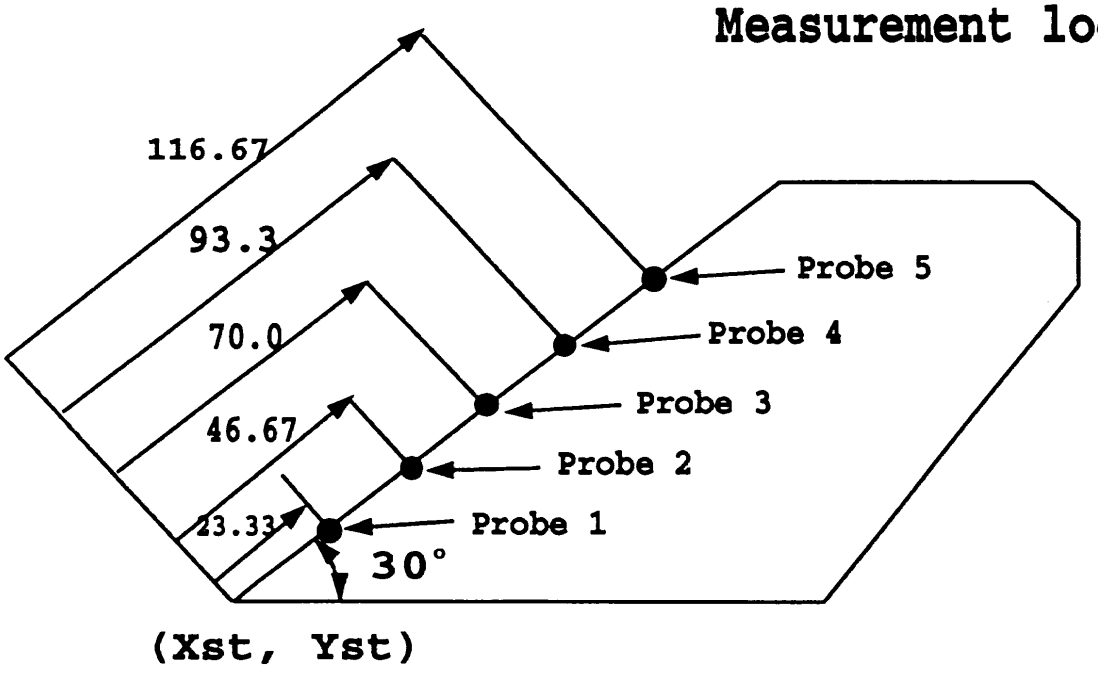

図 B-1

Flow Simulation by CFD

• Numerical method

- Axis-symmetric calculation by the use of control-volume metric
- Chakravarthy-Osher non-MUSCL second-order TVD scheme based on the generalized Roe's approximate Riemann solver

• Physical model

- Park's two-temperature model
  - * T-V relaxation
    - · Collision limiting
    - · Diffusive relaxation model/ alternative relaxation model
  - * Preferential Dissociation model
  - * Park's reaction rate model $T_d = \sqrt{TT_v}$
- Blottner's 7-species chemical reaction model

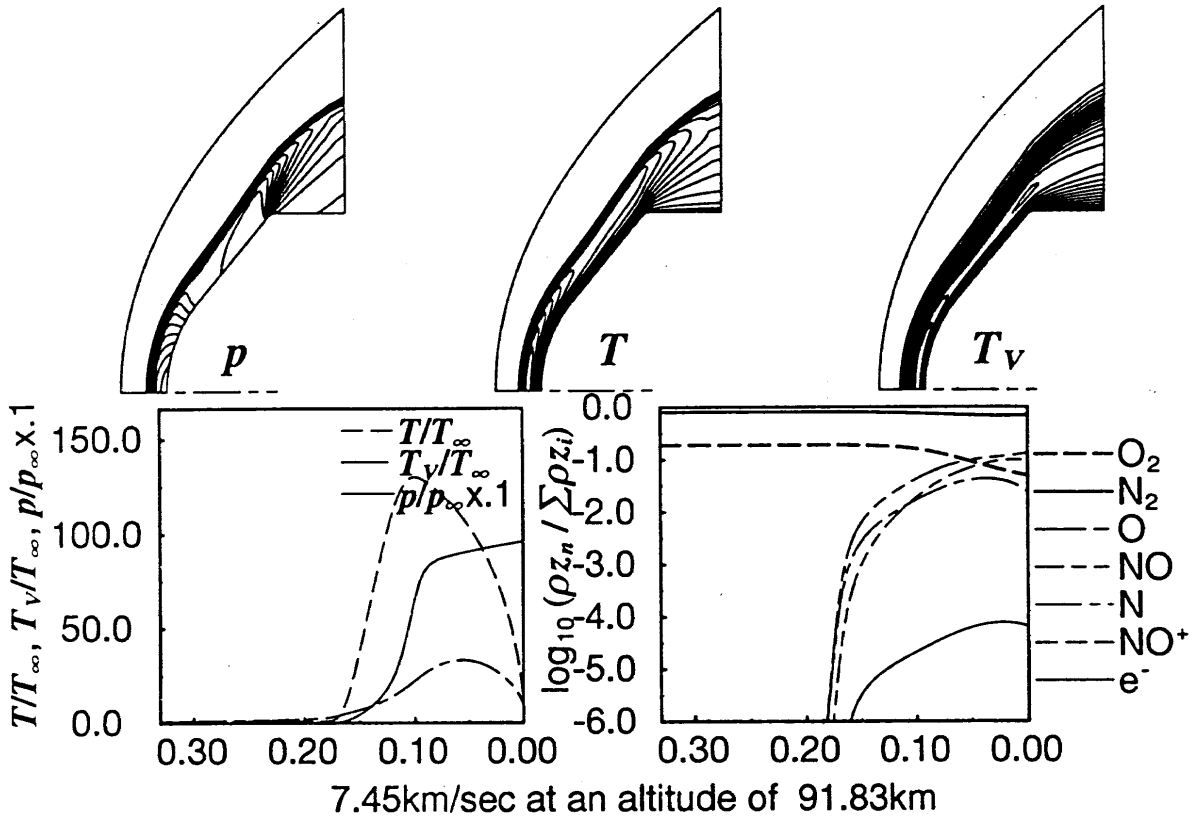

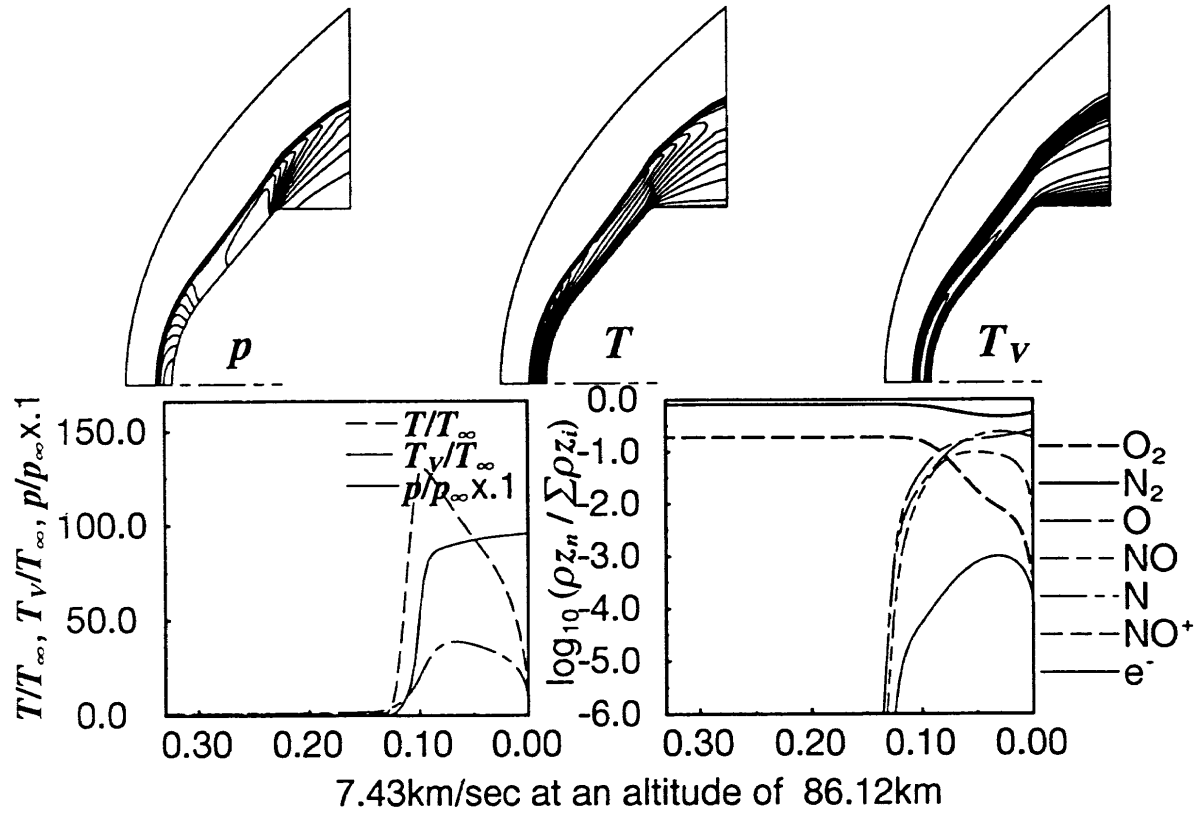

図 B-2

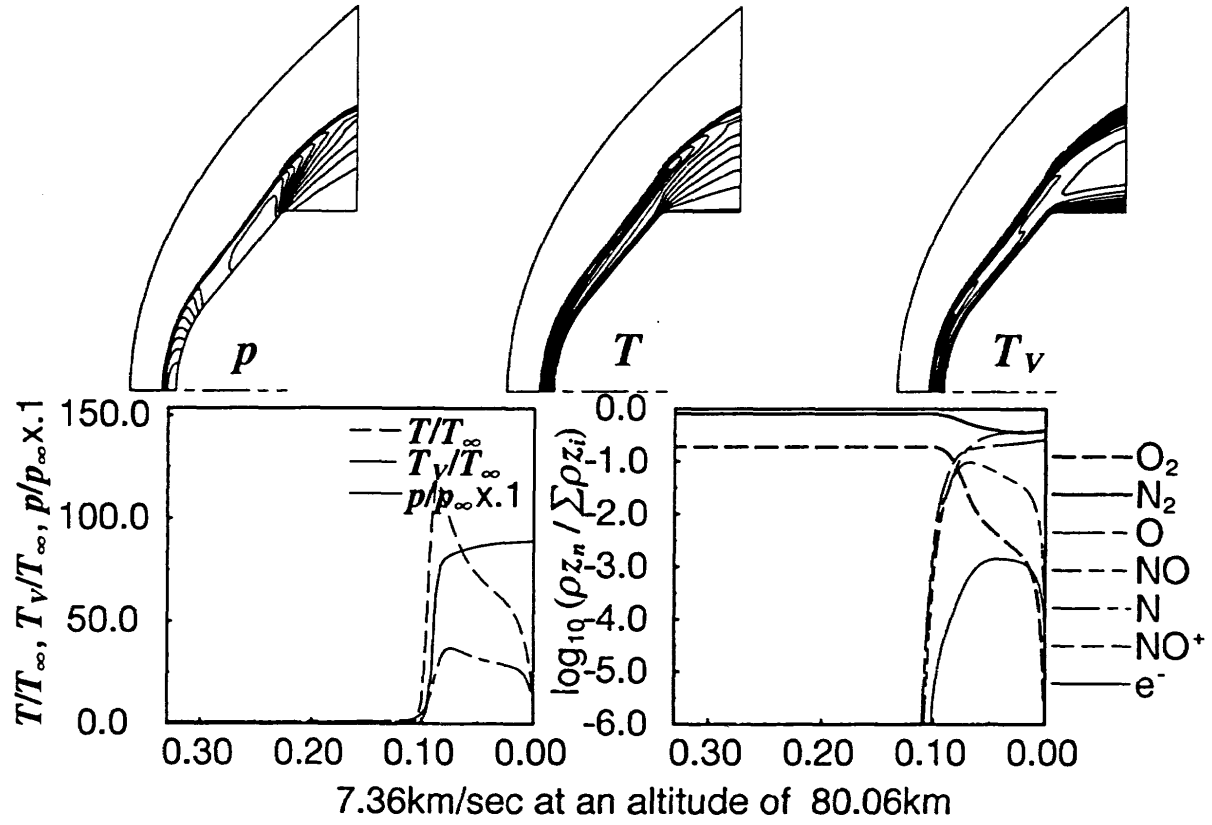

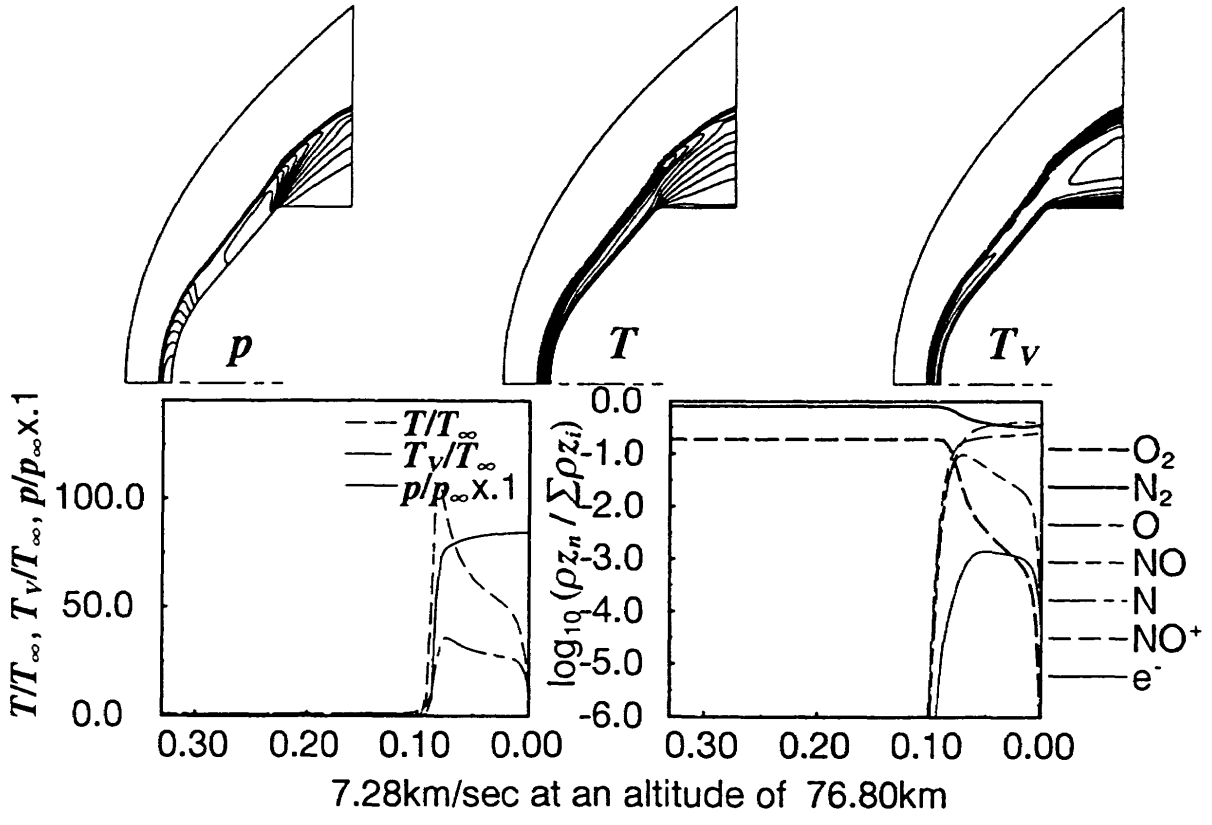

図 B-2

Flight Trajectory and Probe Temperature History

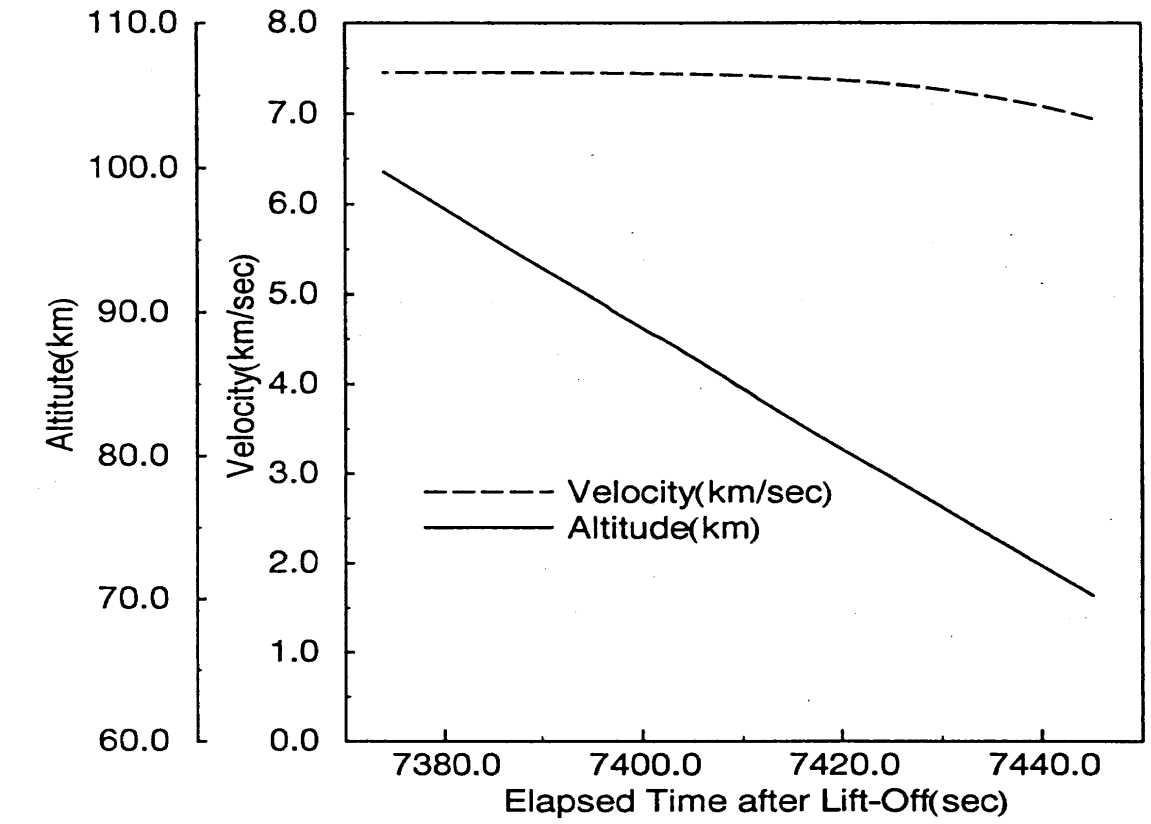

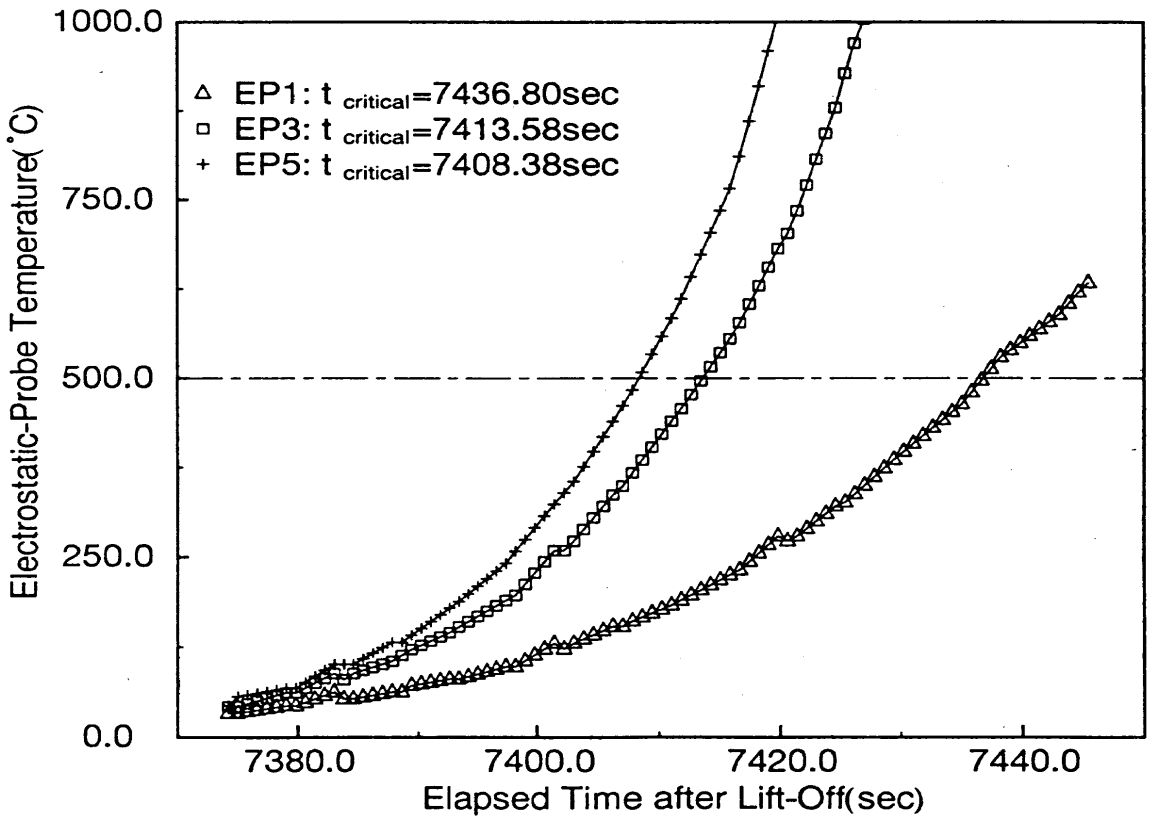

図 B-3

Data supplement by CFD — temperature

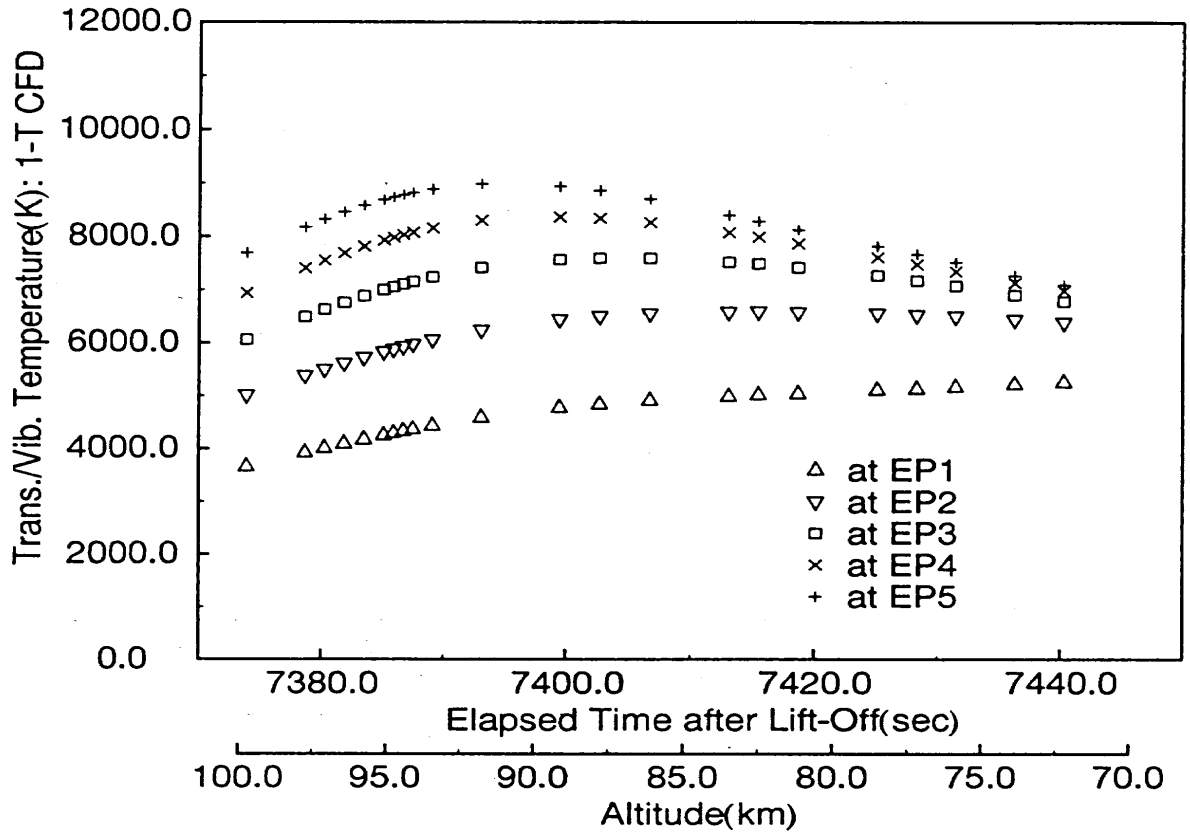

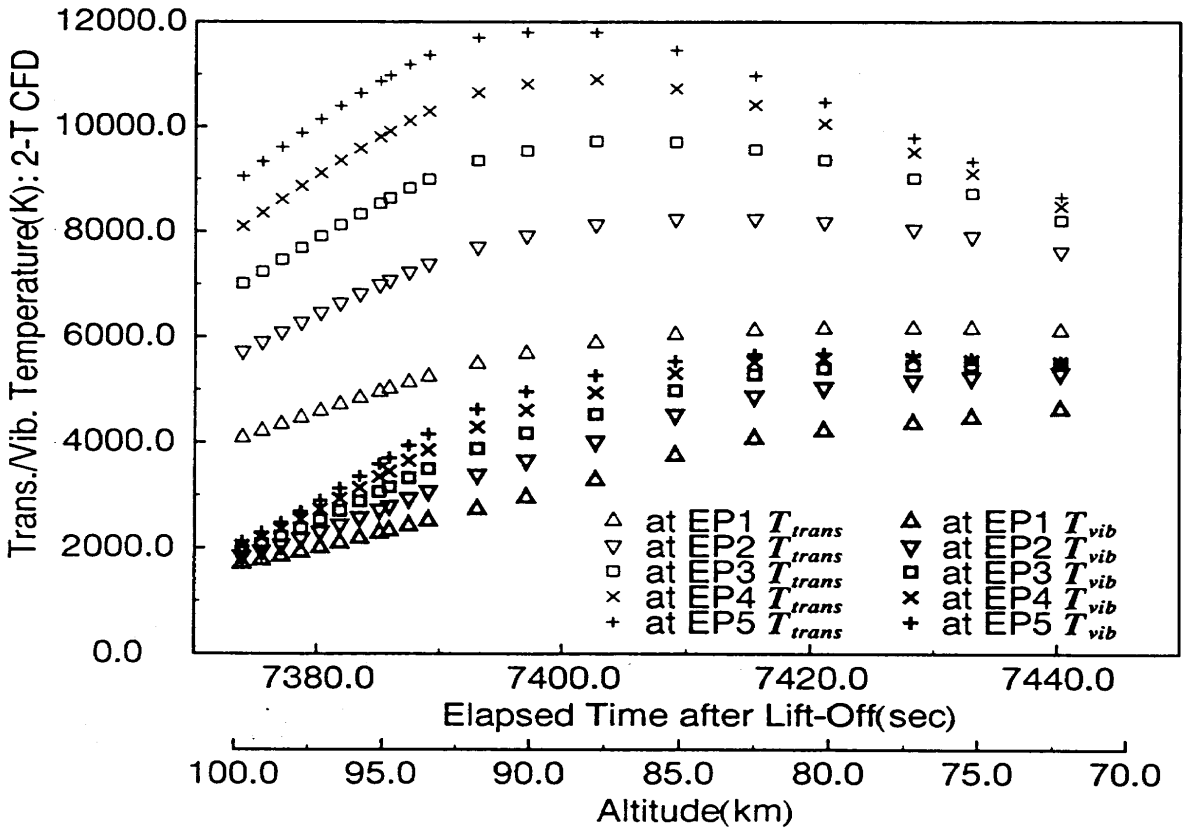

図 B-4

Data supplement by CFD — velocity

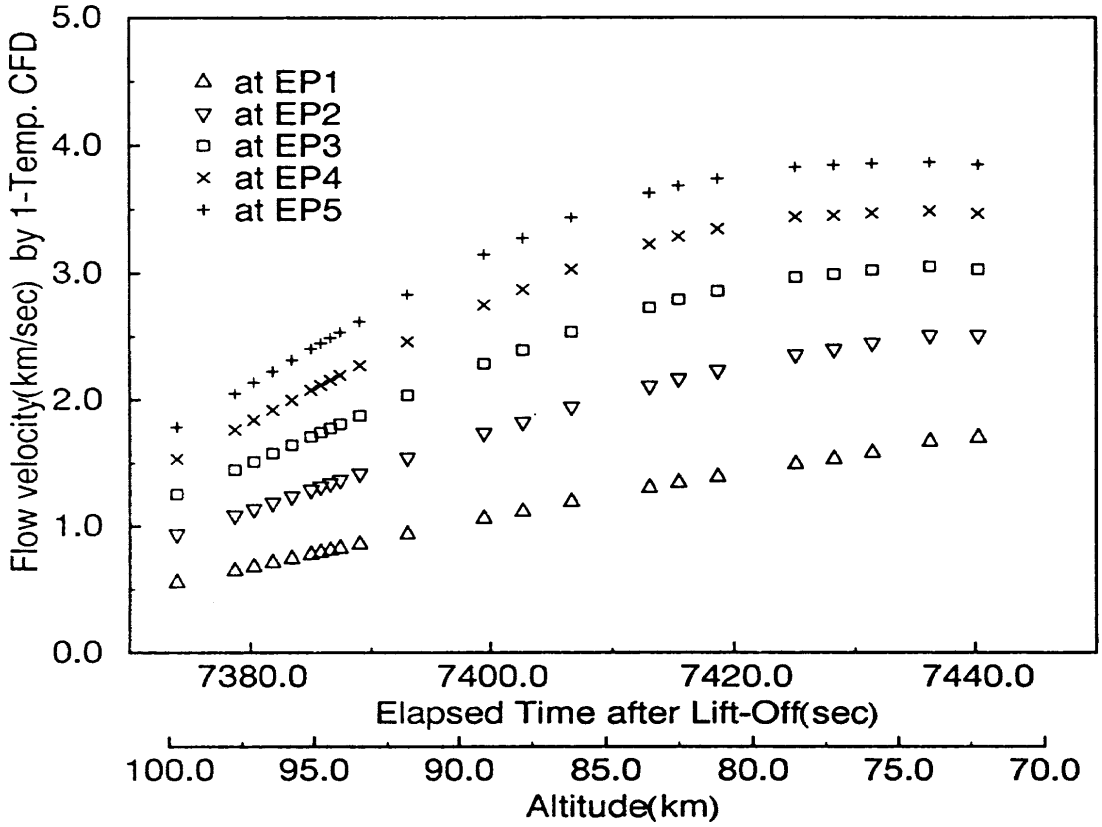

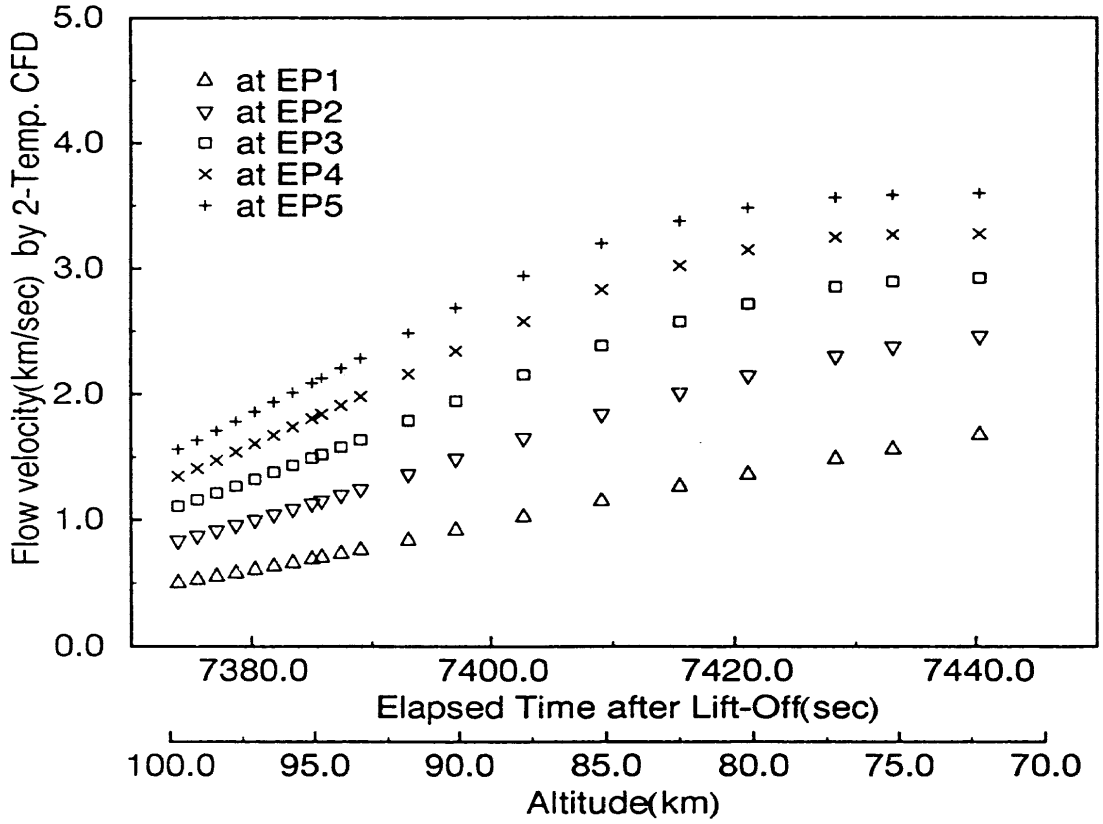

図 B-5

Electron Density Calculation

Calculation procedure

Probe theory:

$$n = n(I, U_{flow}, Te)$$

Flight data: I: Ion-saturation current

CFD: U_{flow}, Te

Results

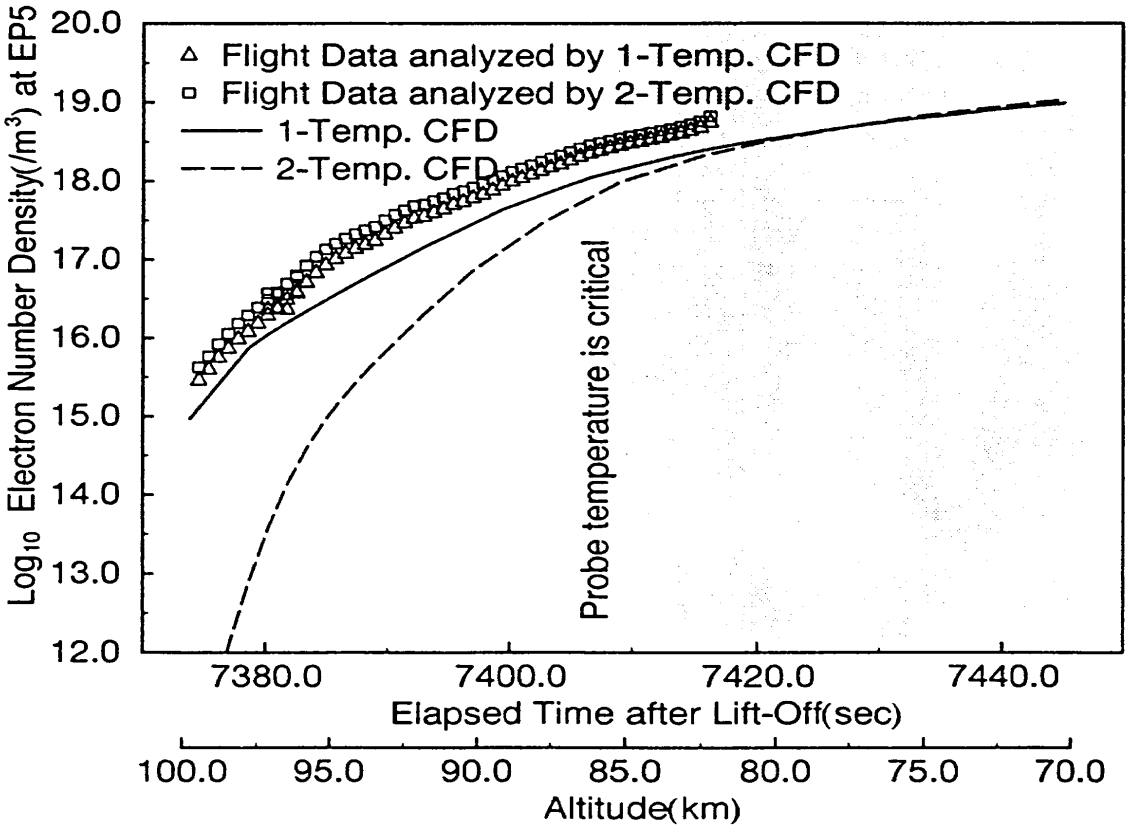

Electron Density at Probe 5

Δz = 58.3 mm

図 B-6

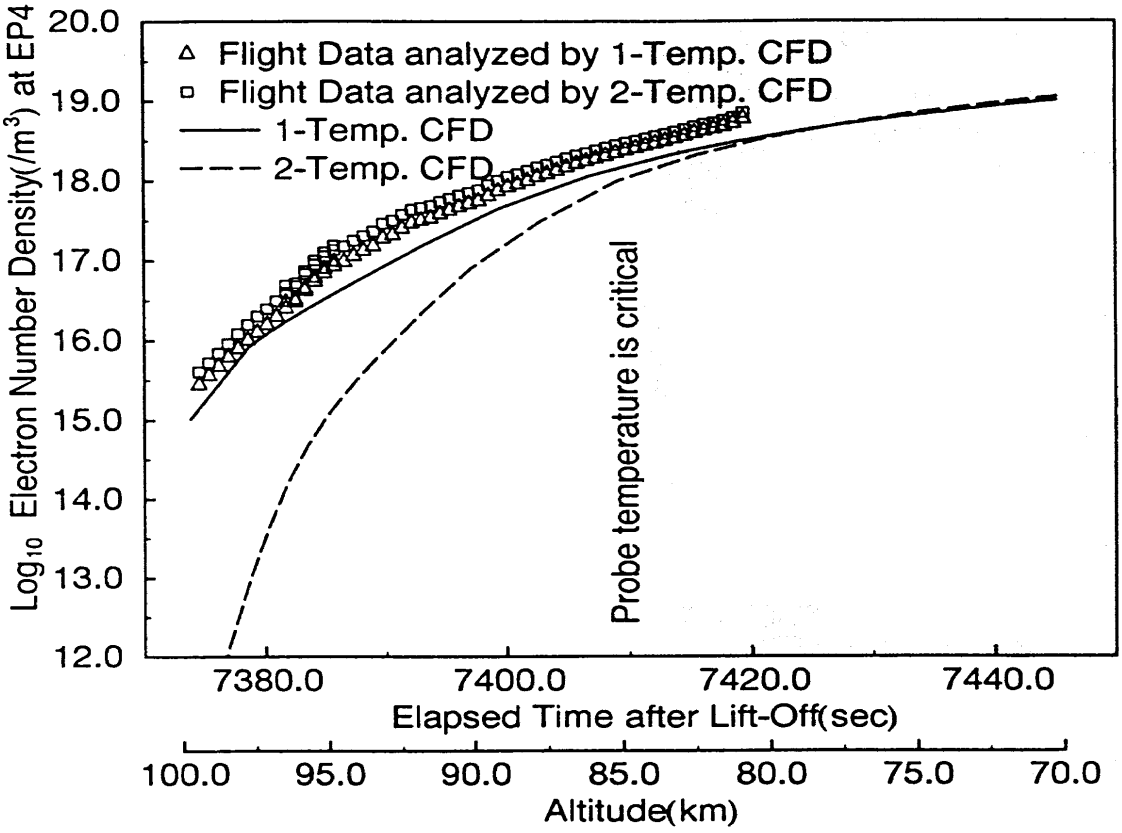

図 B-7 Electron Density at Probe 4

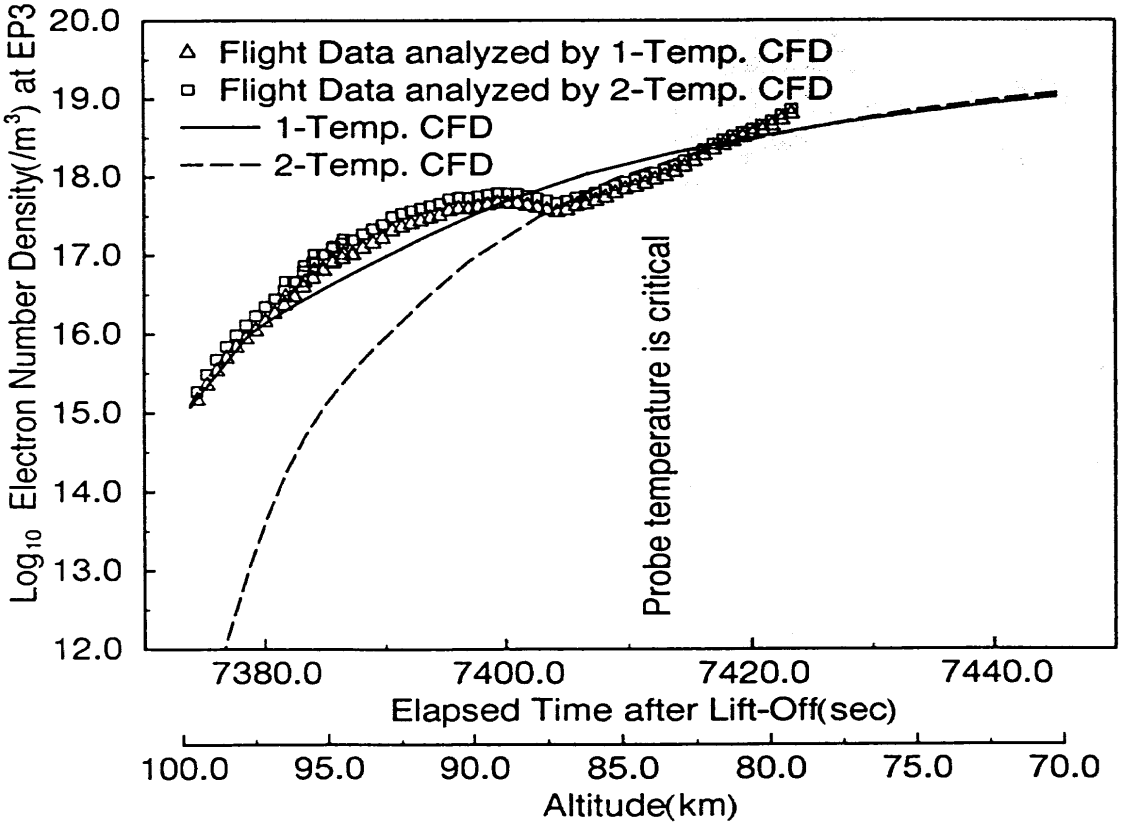

図 B-8 Electron Density at Probe 3

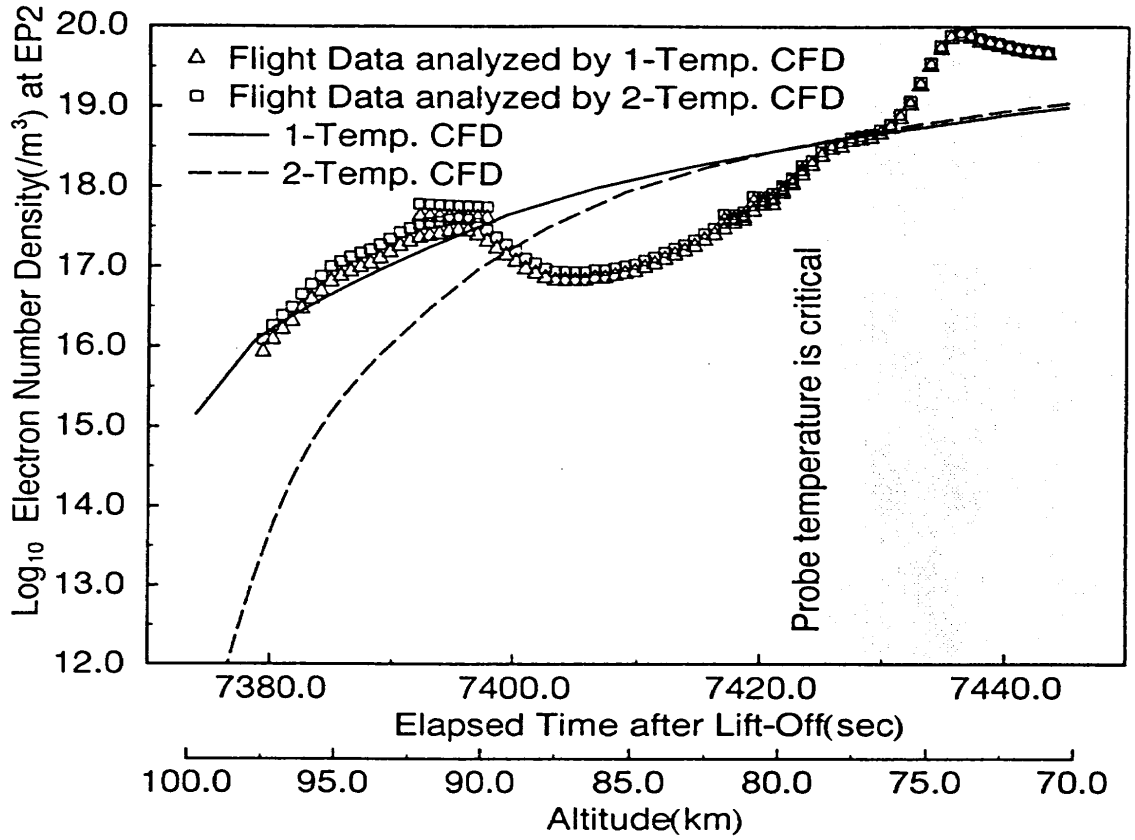

図 B-9 Electron Density at Probe 2

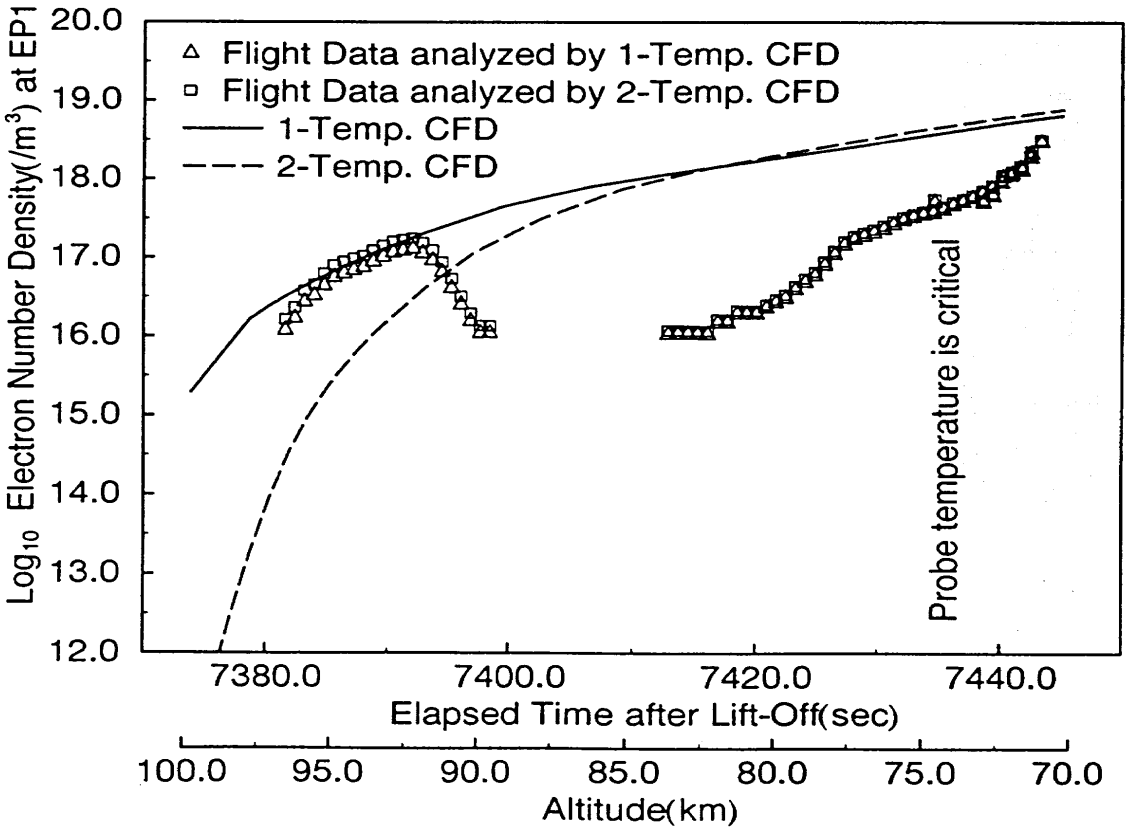

図 B-10 Electron Density at Probe 1

付録４－２－Ｃ

課題Ⅱ－２～５

ＯＲＥＸ

空力加熱解析データ

OREX Flight Trajectory

Time t	Flight Time t (sec)	Altitude H (km)	Velocity U - (m/sec)	Temperature T - (K)	Pressure P - (N/m ^{2})	C/C Stag Temp (Flight Data) Ts (K)	M -
0	7361.0	105.0	7451.0	217.5	0.0196	332	25.11
10	7370.6	101.1	7454.65	195.1	0.032	365	26.53
20	7381.0	96.77	7456.3	192.3	0.0726	422	26.72
30	7396.0	92.816	7454.1	188.7	0.163	492	26.97
40	7401.0	88.45	7444.3	186.87	0.231	587	27.07
50	7411.5	84.01	7415.9	188.9	0.594	690	26.82
60	7421.5	79.90	7360.2	198.64	1.0524	808	25.96
70	7431.5	75.81	7245.7	206.82	2.1717	928	25.04
80	7441.5	71.73	7049.2	214.98	4.023	1078	23.89
90	7451.5	67.66	6720.3	225.99	7.892	1251	22.22
100	7461.5	63.60	6223.4	237.14	14.02	1413	20.09
110	7471.5	59.60	5561.6	248.12	23.60	1519	17.55
120	7481.5	55.74	4759.1	258.74	39.48	1571	14.71
130	7491.5	51.99	3873.4	268.2	63.48	1557	11.8
140	7501.5	48.40	3000.0	270.65	98.5	1501.0	9.06

表 C-1

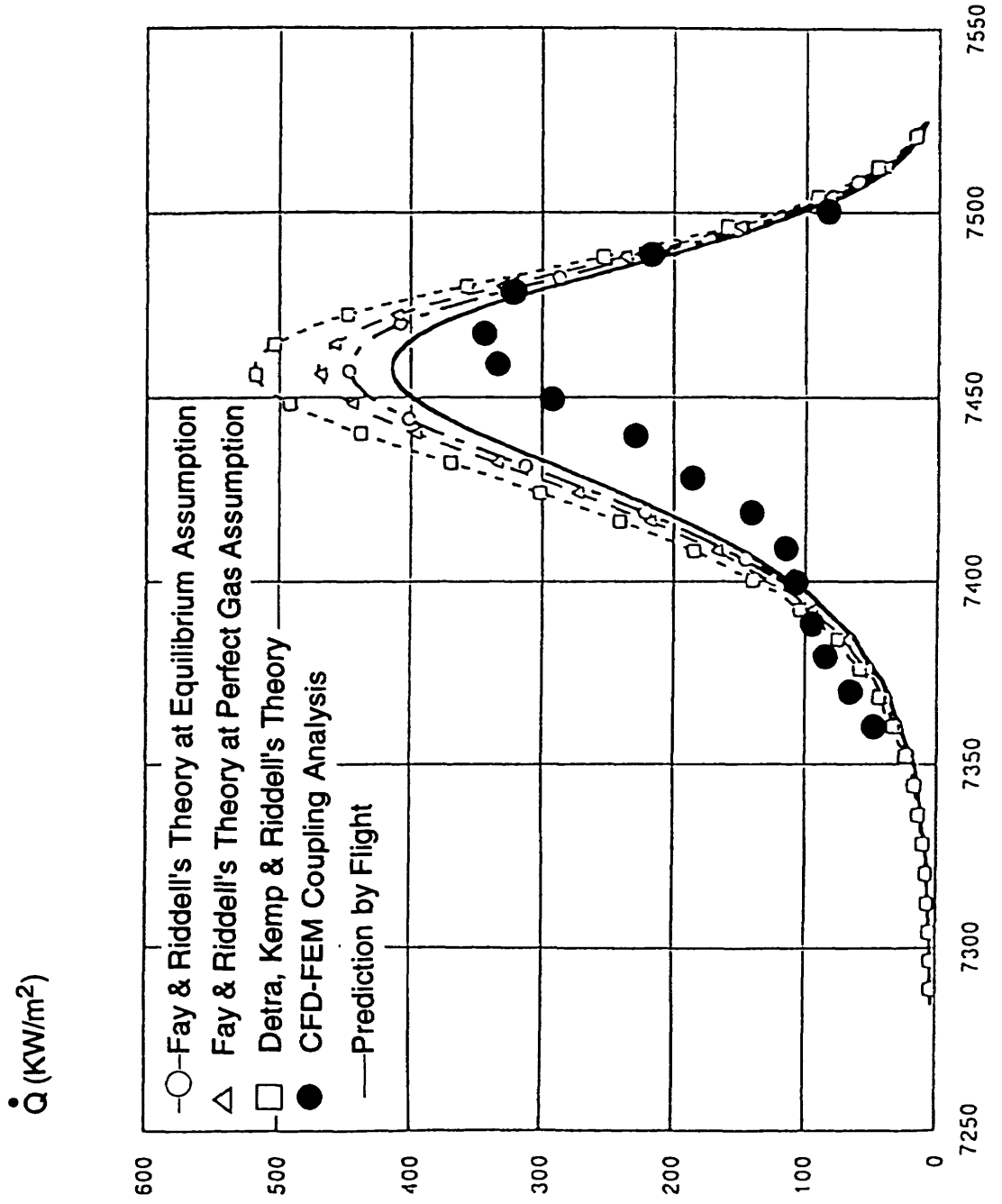

Comparison of Stagnation Point Heat Transfer

図 C-2 OREX 飛行時刻に沿った、よどみ点空力加熱の同定値
及び表面非触媒仮定 CFD 解析推算値

付録４－２－Ｄ

課題Ⅲ

ハイパーボロイド・フレア

LTB、F4　実験資料

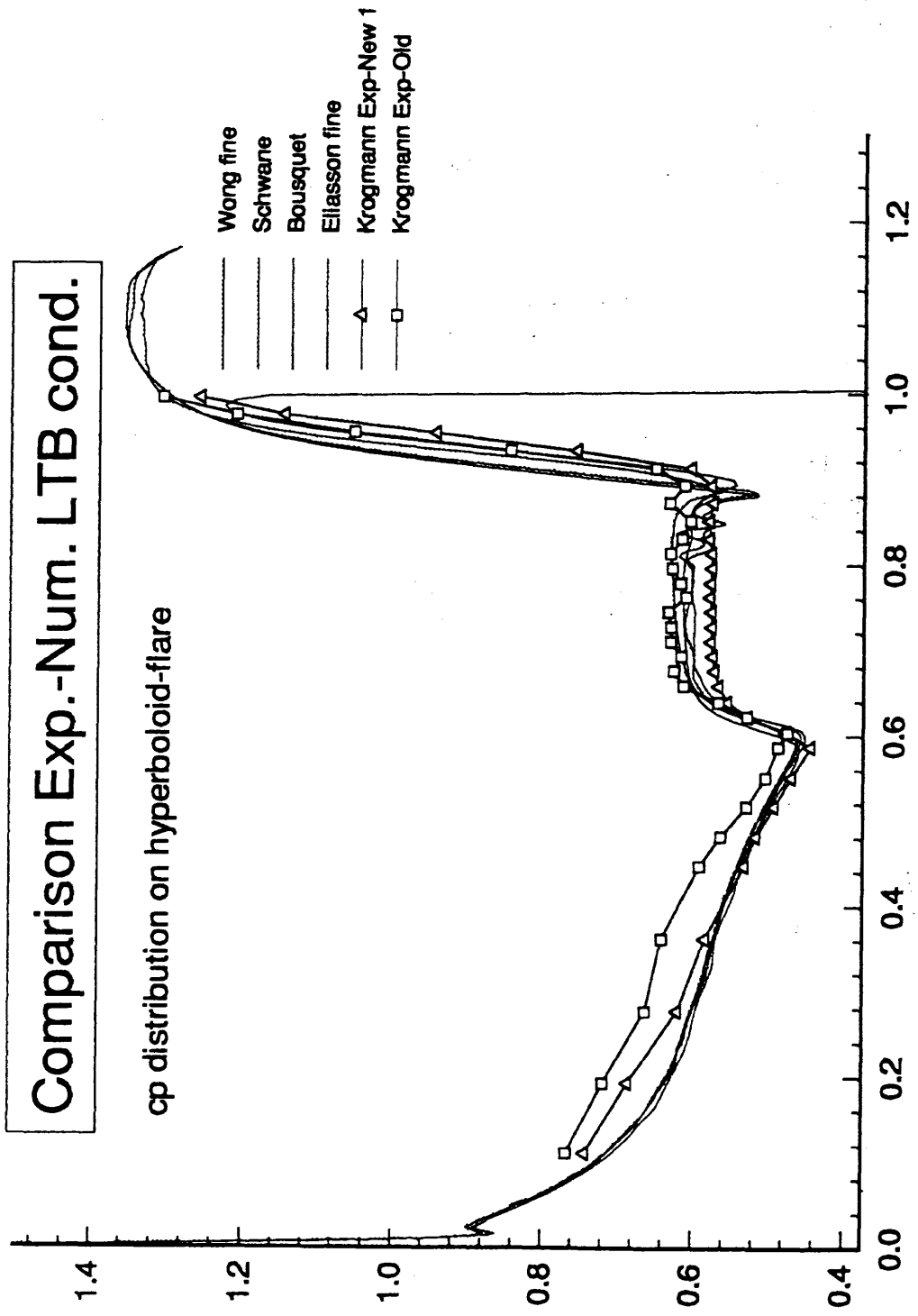

図 D-1 LTB(Cold Case), 表面圧力分布

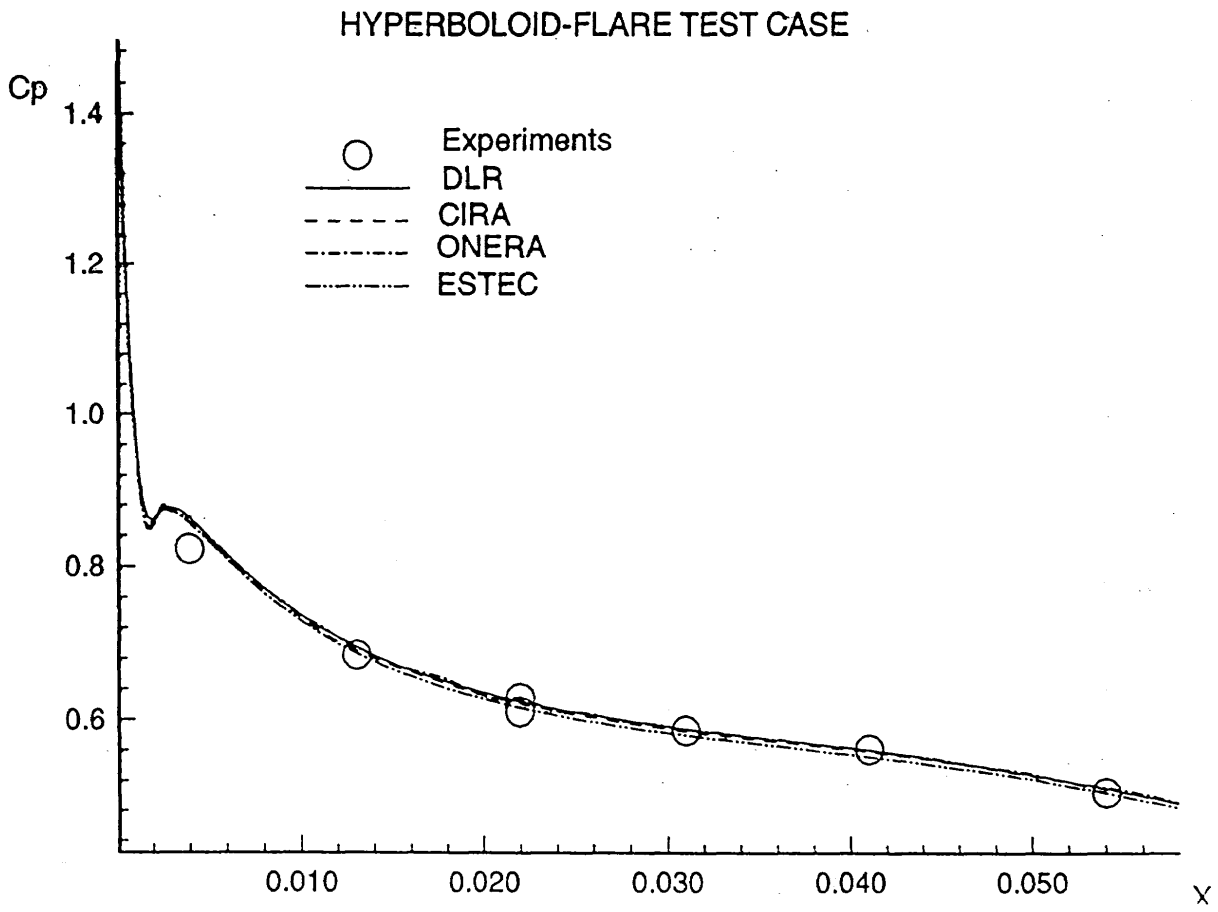

(a) 前方拡大図

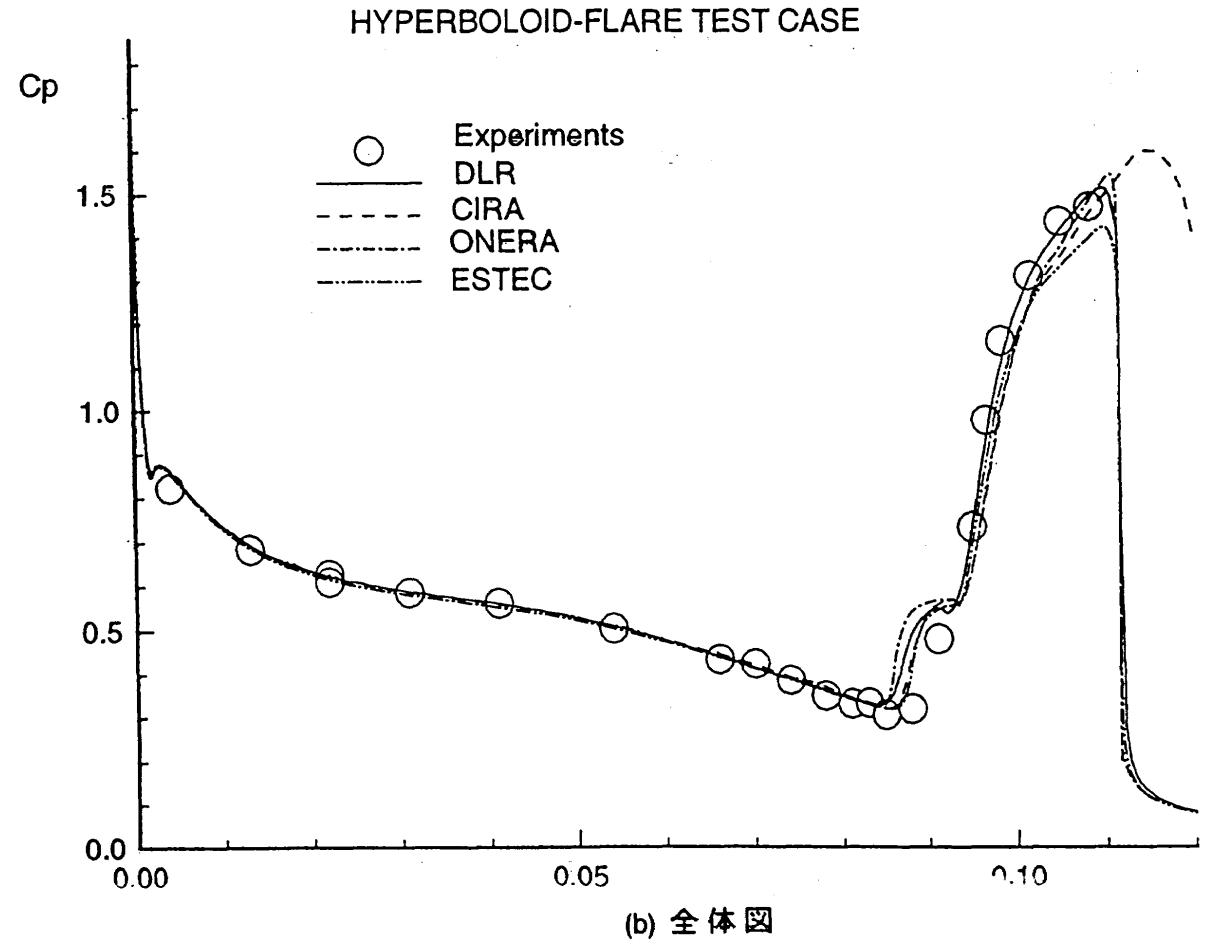

(b) 全体図

図 D-2 F4 (Hot Case) 条件、表面圧力分布

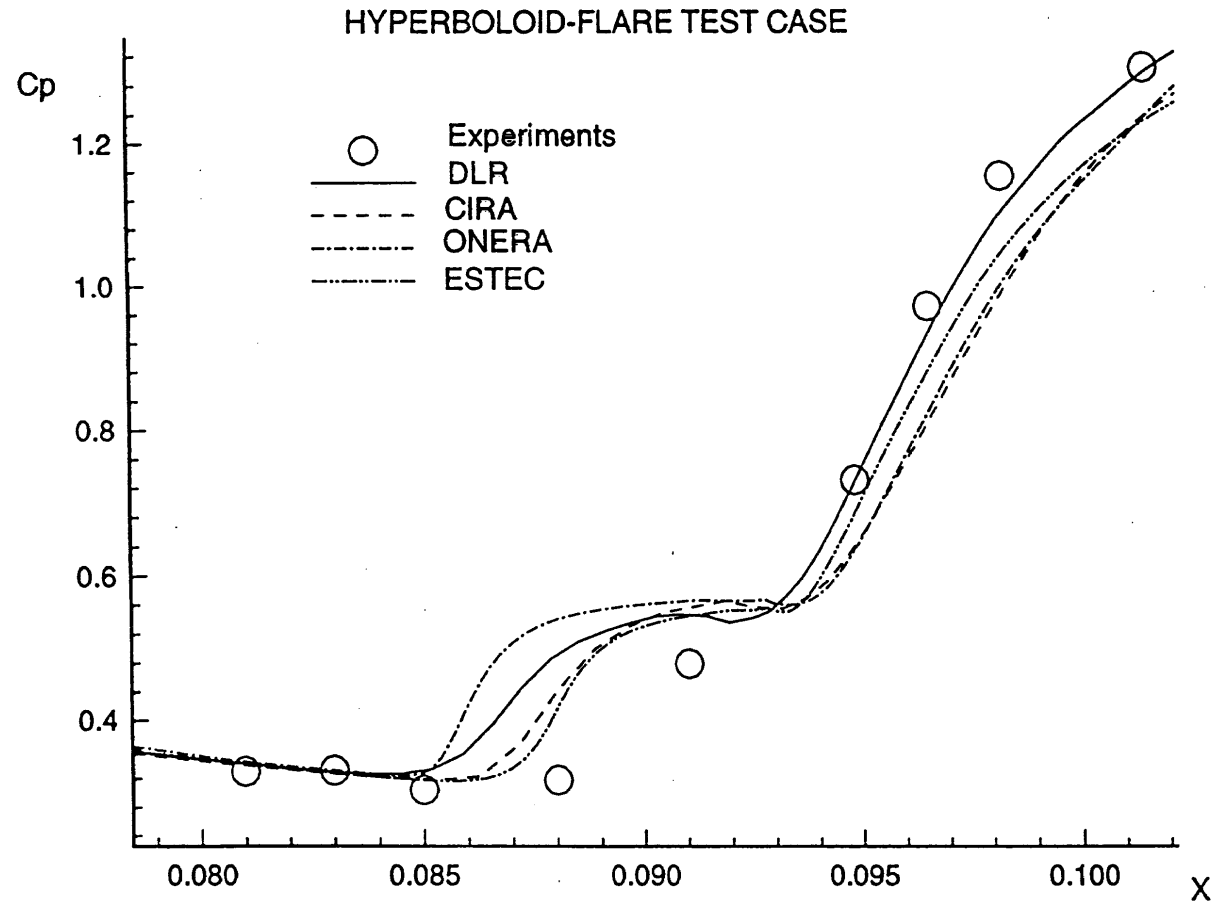

図 D-2 F4 (Hot Case) 条件、表面圧力分布 (c) 剥離領域拡大図

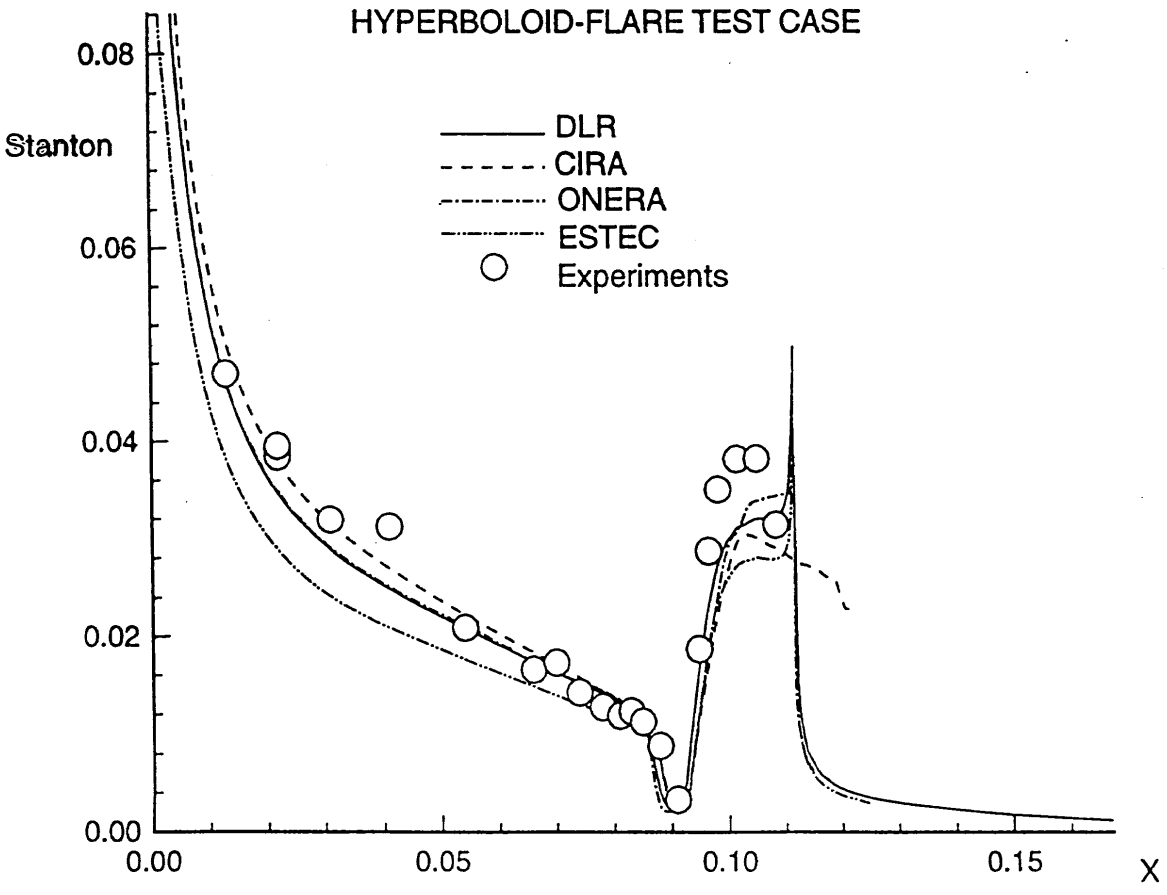

図 D-3 F4(Hot Case) 条件 熱流束分布

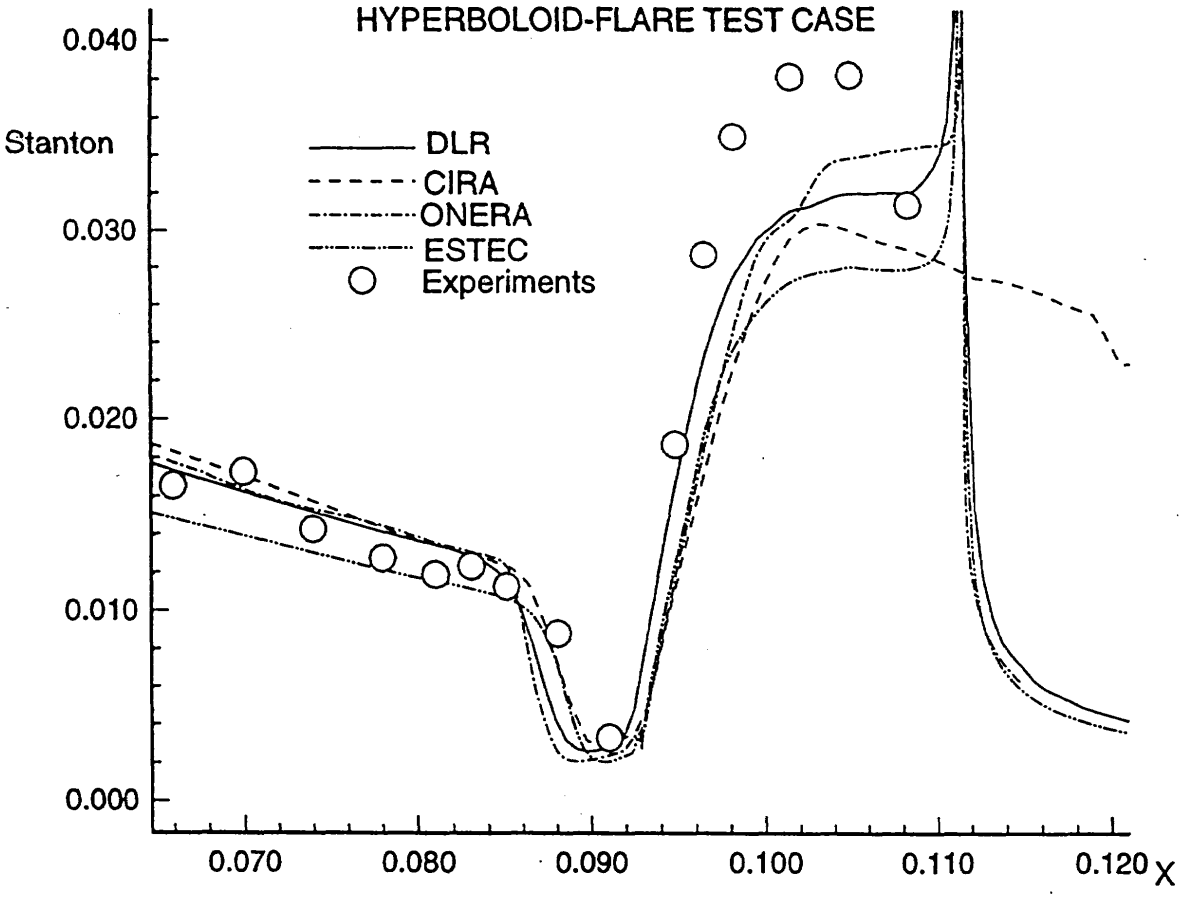

(c) 剥離領域拡大図

図 D-3 F4(Hot Case) 条件 熱流束分布

付録４－２－Ｅ

課題Ⅳ

７０° 鈍頭円錐

DLR HEG 実験資料

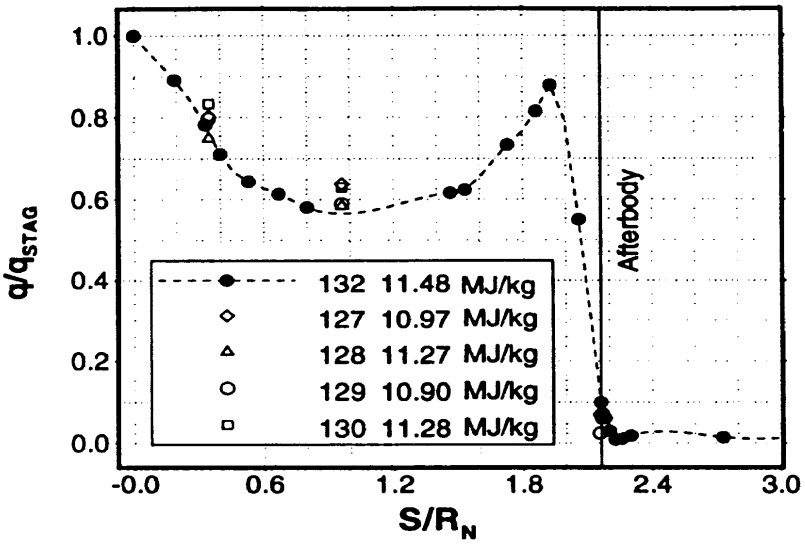

図 E-1 鈍頭円錐 HEG条件 頭部熱流束分布

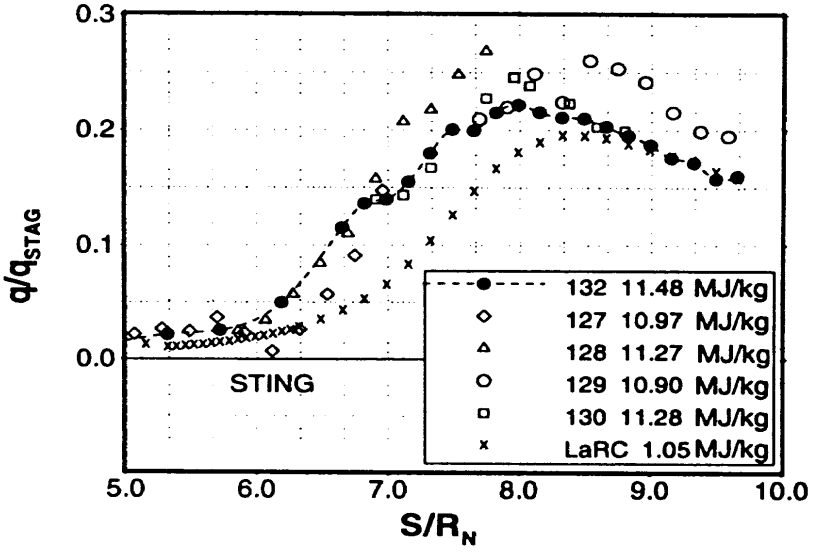

図 E-2 鈍頭円錐 HEG条件 スティング部熱流束分布

Ⅲ－5　資料編

Ⅲ－５－１　応募者ID，実施課題一覧

Applicant ID and Computation Case

ID	Applicant Name	Organization	Problem I Sphere						Problem II OREX					Problem III Hyperboloid Flare			Problem IV Spherically Blunted Cone	
			I-1	I-2	I-3	I-4	I-5	I-6	II-1	II-2	II-3	II-4	II-5	III-1	III-2	III-3	IV-1	IV-2
H-1	Igor Men'shov and Y. Nakamura	Nagoya Univ.	●	●	●	●	●	●										
H-2	I. Nakamori and Y. Nakamura	Nagoya Univ.							●									
H-3	T. Kurotaki	Mitsubishi Electoric Cor.	●	●	●	●	●	●	●	●	●						●	
H-4	M. Nakao	M. H. I										●	●					
H-5	K. Murakami, T. Fujiwara and S. Nakano	Nagoya Univ.							●	●	●		●					
H-6	T. Kishimoto and S. Kaneko	K. H. I										●	●	●				
H-7	H. Ohtsu, K. Suzuki and T. Abe	ISAS												●				
H-8	Y. Yamamoto	NAL	●	●	●	●	●	●	●	●			●		●		○	
H-9	H. Nagatomo, S. Kano, S. Yamamoto and H. Daiguji	Tohoku Univ.								●			●	●			●	
H-10	T. Shimada, N. Tamura and N. Sekino	Nissan Motor	●	●	●	●	●	●		●	●	●	●					
H-11	R. Takaki and Y. Wada	NAL	●	●	●	●	●	●									●	●

Ⅲ－5－2　解析概要一覧

Description of Numerical Methods

Applicant ID / First Author	Method	Numericalr Algorithm	No. of Grids Streamwise x normal	Reaction Model	Transport Property	Temperature and Vibrational Relaxation Model
H-1 Igor. Men'shov	AUSM	LU-SGS	30x60(Prob. I-1 ~ 4) 60x60(Prob. I-5, 6) 160x65(Prob. IV)	5 Species Park's Model	Yos's formula	Park's Two Tem. Model
H-2 I. Nakamori	AUSM and Steger-Warming FVS	LU-SGS	32x64	5 Species Park's Model	Yos's formula	Park's Two Temp. Model
H-3 T. Krotaki	AUSMDV	LU-SGS Diagonal Approximation of Source Terms	81x81 (Prob. I and II) 161x131 (Prob. IV)	7 Species Park's Model	Kinetic Theory	Two Temp. Model SSH Theory
H-4 M. Nakao	FDS based on Roe's Riemann Solver	Modified LU-ADI	40x50 (Prob. II-4, 5)	-	Curve Fitting by Srinivasan	Equilibrium Flow
H-5 K. Murakami	Harte-Yee and Roe's average by Liu and Vinokur	Explicit	51x150 (Prob. II-1,2,3 and 5)	11Species	Yos's formula	Park's Two Temp. Model

H-6 T. Kishimoto	AUSMDV	Planar Gauss- Seidel Relaxation	71x81(Prob. II-5) 66x41(Prob. II-4) 521x101(Prob.III-1)	-	Curve Fitting by Srinivasan	Equilibrium(OREX) and Perfect Gas Flow (Hyperboloid Flare)
H-7 H. Ohtsu	Haten-Yee Type TVD	Explicit	34x177 (Prob. III-1)	-	Sutherland's law	Perfect Gas Flow
H-8 Y. Yamamoto		ADI	41x60 (Prob. I and Prob. II-1, 2, 5)	7 Species Park's Model	Blottner's Formulation	One Temp. Model
H-9 H. Nagatomo	AUSM(Prob. II-5 and Prob. III) AUSM=DV(Prob.II-2) IEFVSrob. II-2 and Prob. IV)	LU-SGS for AUSM and AUSM=DV Explicit for IEFVS	75x75(Prob. II-2) 95x95(Prob. II-5) 521x101(Prob.III-1) 161x241(Prob.IV-1)	7 Species Park's Model		Park's Two Temp. Model
H-10 N. Sekino	Harten-Yee Type TVD	LU-SGS	51x81 (Prob. I) 58x61 (Prob. II- 2, 3, 4 and 5)	11 Species Park's Model	Yos's formula	Equilibrium, Frogen and Park's Two Temp. Model
H-11 R. Takaki	ChaKravarthy-Osher TVD	LU-SGS	56x73(Prob. I) 163x90 (Prob. IV)	7 Species Dunn and Kang	Yos's formula	Park's Two Temp. Model

Ⅲ－５－３　数値比較表

The values of themal Conductivities (w/mk) ($x10^{-2}$)

ID	Applicant Name	Organization	Problem I Sphere						Problem II OREX					Problem III Hyperboloid Flare			Problem IV Spherically Blunted Cone	
			I-1	I-2	I-3	I-4	I-5	I-6	II-1	II-2	II-3	II-4	II-5	III-1	III-2	III-3	IV-1	IV-2
H-1	Igor Men'shov and Y. Nakamura	Nagoya Univ.	●	●	●	●	●	●										
H-2	I. Nakamori and Y. Nakamura	Nagoya Univ.							●									
H-3	T. Kurotaki	Mitsubishi Electoric Cor.	2.53	2.66	2.54	2.66	2.55	2.66	4.00	8.73	7.83						2.533	
H-4	M. Nakao	M. H. I										2.47	2.17					
H-5	K. Murakami, T. Fujiwara and S. Nakano	Nagoya Univ.							●	●	●		●					
H-6	T. Kishimoto and S. Kaneko	K. H. I										7.24	●	0.73				
H-7	H. Ohtsu, K. Suzuki and T. Abe	ISAS												●				
H-8	Y. Yamamoto	NAL	2.78	●	2.71	●	2.69	●	4.84	9.69			7.46		●		○	
H-9	H. Nagatomo, S. Kano, S. Yamamoto and H. Daiguji	Tohoku Univ.								●			●	●			●	
H-10	T. Shimada, N. Tamura and N. Sekino	Nissan Motor	2.49	2.44	2.46	2.44	2.48	2.44		8.70	7.88	7.12	7.58					
H-11	R. Takaki and Y. Wada	NAL	5.21	4.41	4.36	3.91	4.92	4.40									5.802	5.124

Problem I Sphere

ID	HEAT FLUX(MW/m^2)						Tmax (K)						Pmax ($P/\rho_\infty V_\infty$)					
	I-1	I-2	I-3	I-4	I-5	I-6	I-1	I-2	I-3	I-4	I-5	I-6	I-1	I-2	I-3	I-4	I-5	I-6
H-1	5.21	6.38	8.57	8.03	6.07	5.78	15,207		14,578		10,716		0.9444		0.956		0.953	
H-3	8.32	12.89	14.35	21.76	11.24	15.99	15,645		16,895		11,986		0.943		0.953		0.954	
H-8	9.57	17.34	11.46	23.65	9.85	20.84	13,479		9,820		9,926		0.944		0.957		0.95	
H-10	14.58	12.4	25.23	19.68	16.81	16.47	14,832		14,837		11,423		0.932		0.937		0.939	
H-11	10.1	14.13	12.87	18.02	13.49	19.3	14,813		15,494		11,306		0.943		0.948		0.951	

Problem II OREX

I D	HEAT FLUX(MW/m^2)					Tmax (K)					Pmax ($P/\rho_\infty V_\infty$)				
	I-1	I-2	I-3	I-4	I-5	I-1	I-2	I-3	I-4	I-5	I-1	I-2	I-3	I-4	I-5
H-2	0.0416					25,500					0.9575				
H-3	0.109	0.2898	0.5302			24,268	13,224	13,267			0.934	0.9595	0.9597		
H-4				0.305	0.361				5,504	15,594				0.985	0.918
H-5	0.0263	0.1819	0.3829		0.2462	17,713	9,719	9,774		15,541	0.9395	1.009	1.0319		0.9455
H-6				0.5307	0.4476				5,486	15,635				0.9351	0.9147
H-8	0.1242	0.344			0.4583	20,895	9,065			16,997	0.953	0.9535			0.927
H-9		0.412			0.47		12,275					0.952			0.922
H-11		0.452	0.5024	0.5295	0.421		9,836	9,829	5,496	15,593		0.9423	0.942	0.9571	0.9197

Ⅲ－５－４　応募者提出図

Problem I－1, 2

HEG条件

球まわりの流れ

非触媒及び完全触媒ケース

計算条件

V_∞ =5939m/s

T_∞ =705K

ρ_∞ =0.00156kg/m^3

Twall=300K

W_N = 0.0

W_O = 0.1708

W_{N2}= 0.762

W_{O2}= 0.0348

W_{NO}= 0.0317

PROBLEM I-1

Pressure contours

$P/(\rho_\infty U_\infty^2)$, 20 izo-lines on the interval [0,1]

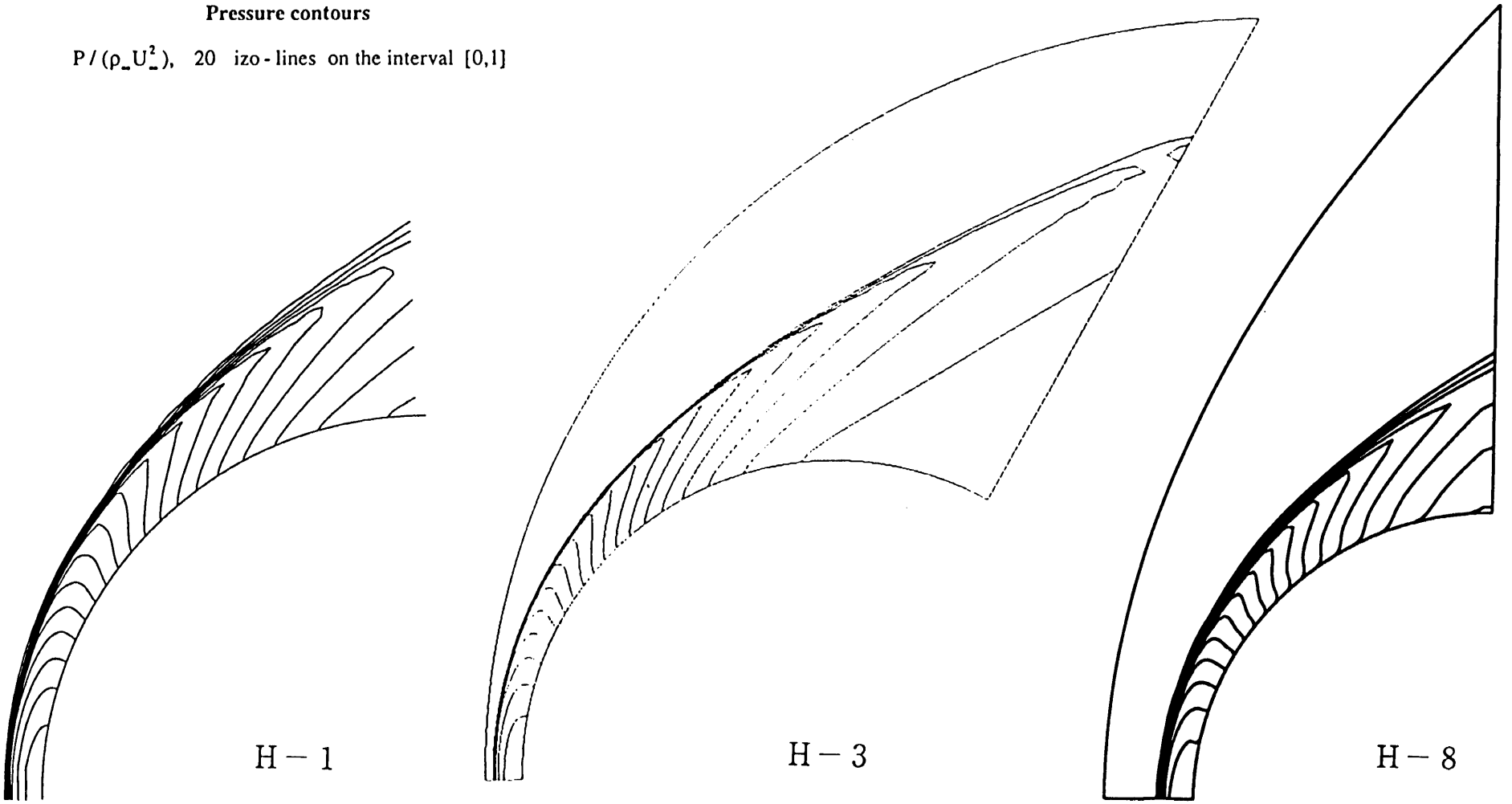

Problem I-1 圧力線図

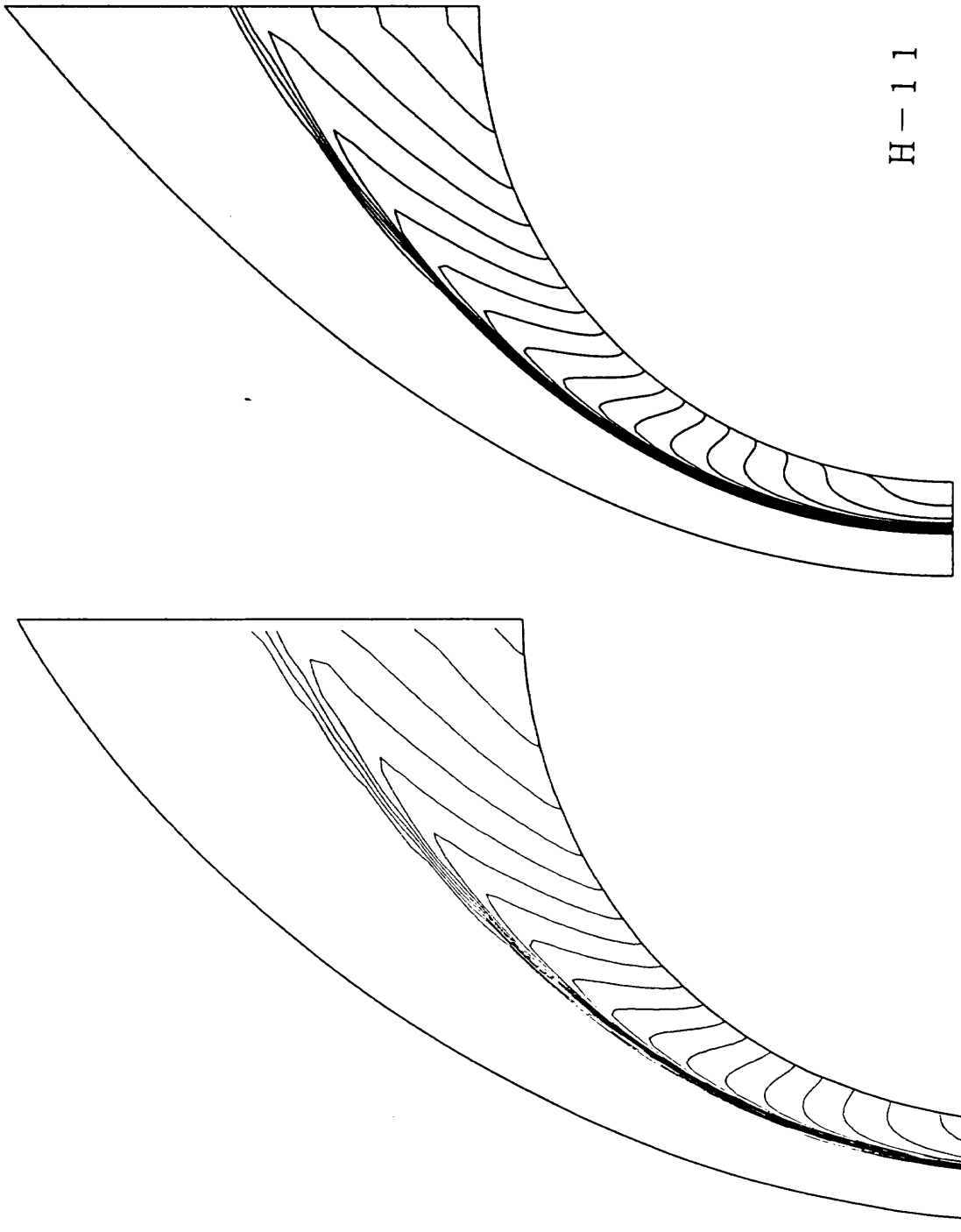

Problem I-1 圧力線図

PROBLEM I-1

Translational/rotational temperature contours

T / T_{∞}, 20 izo-lines on the interval $[1, \frac{T_{max}}{T_{\infty}}]$, T_{max} = 15207.2 °K

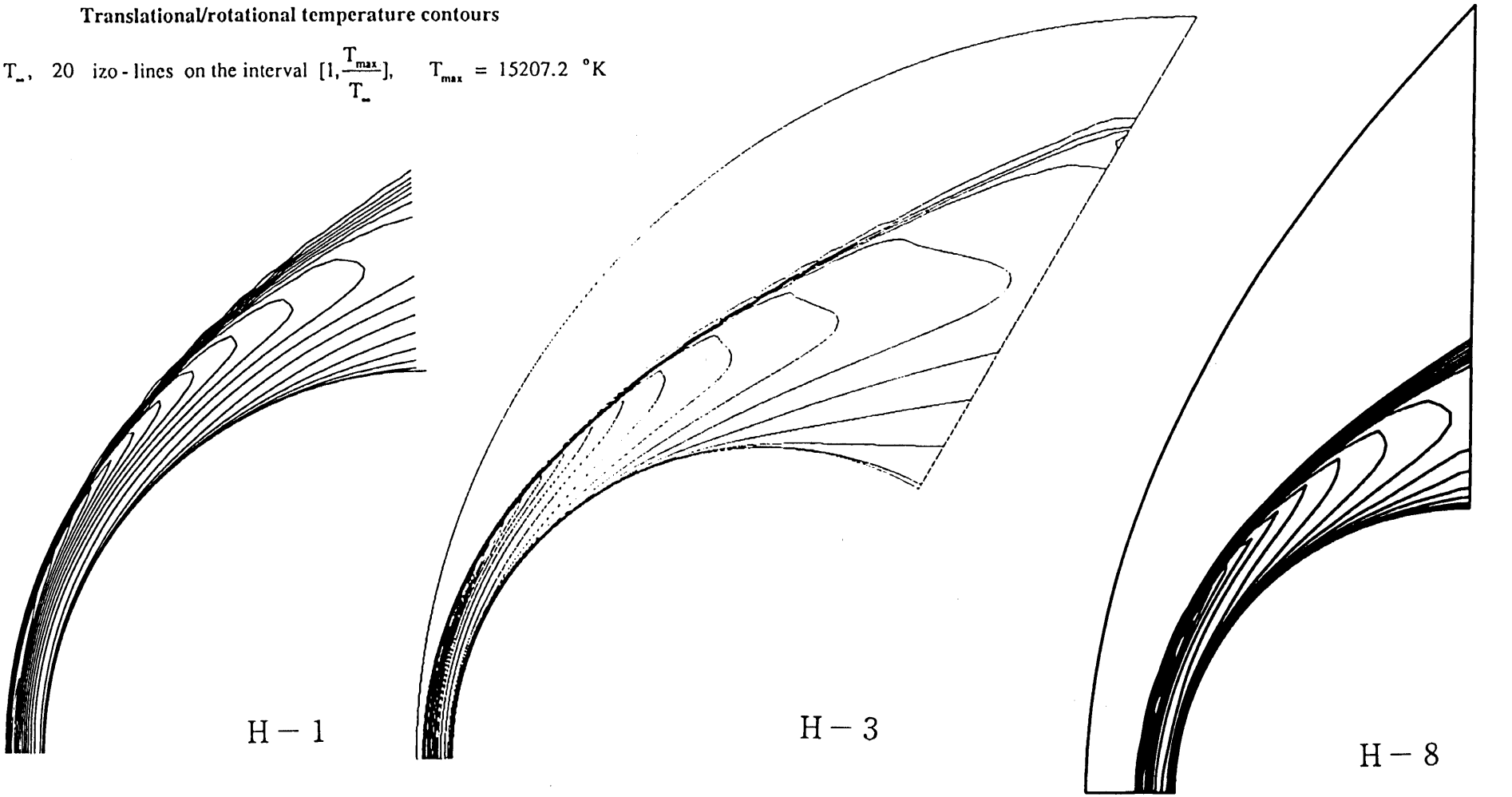

Problem I-1 Sphere Tmax=19.370
Temperature Contour Non catalytic
V_{∞}=5939m/s T_{∞}=705K
ρ_{∞}=0.00156 T_{wall}=300K

ProblemI-1-2 (Tmax = 1.5645e4 K)

Problem I-1 等温度線図（並進、回転）

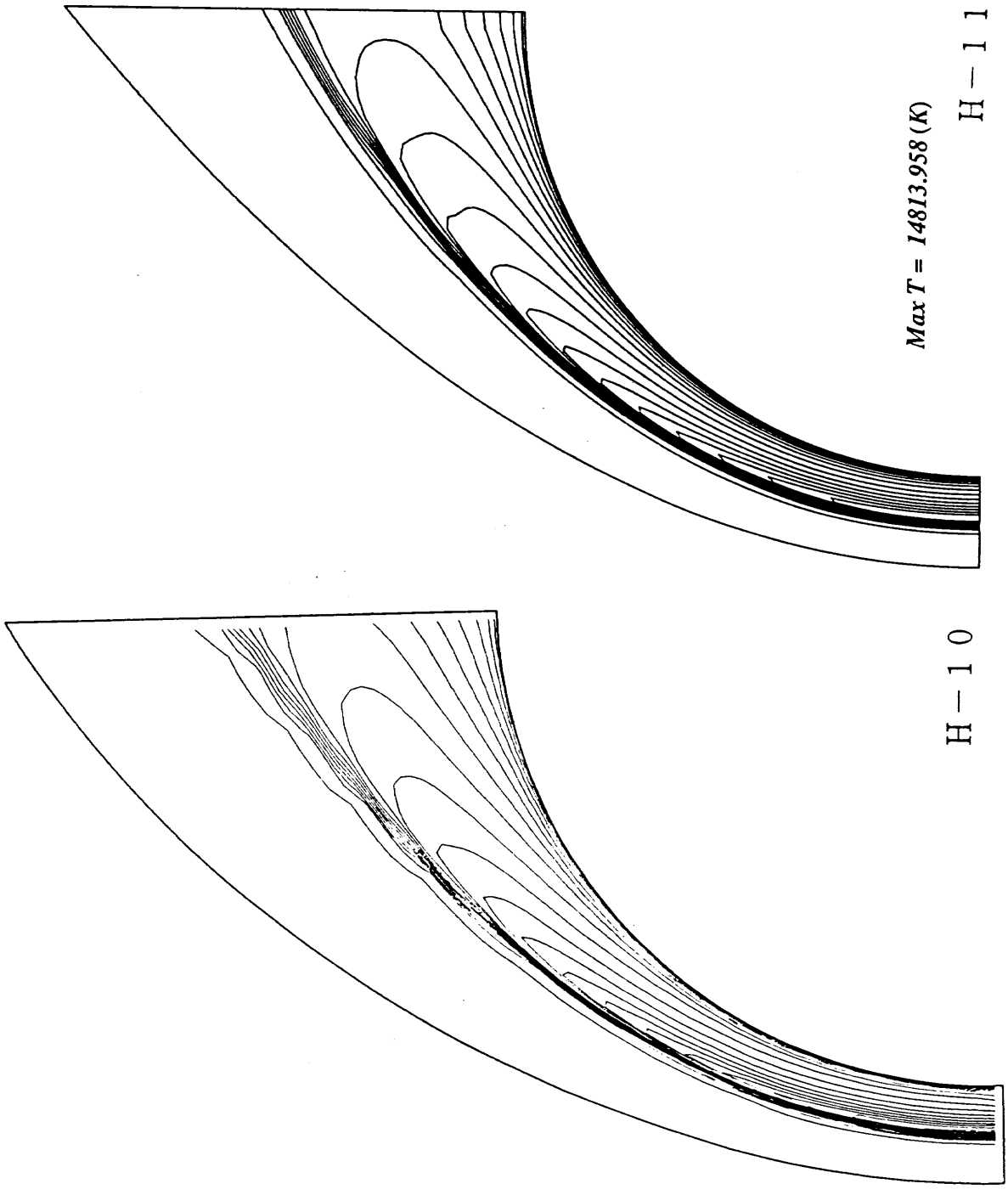

Problem I-1 等温度線図（並進、回転）

PROBLEM I-1

Vibrational temperature contours

T_v / T_∞, 20 izo-lines on the interval $[1, \frac{T_{v,max}}{T_\infty}]$, $T_{v,max}$ = 9302.3 °K

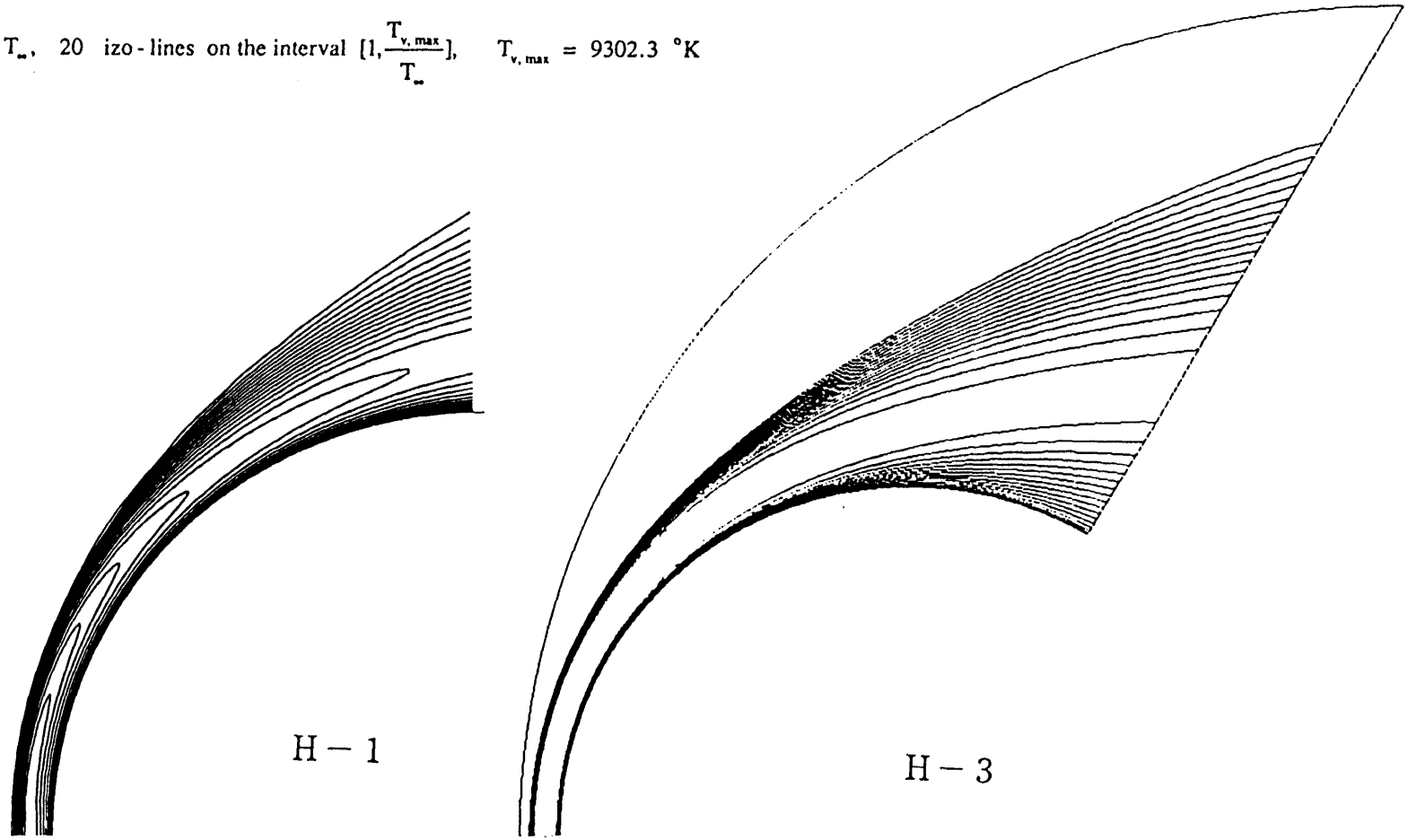

Problem I-1 等温度線図（振動）

ProblemI-1-2 (Tvmax = 6.5419e3 K)

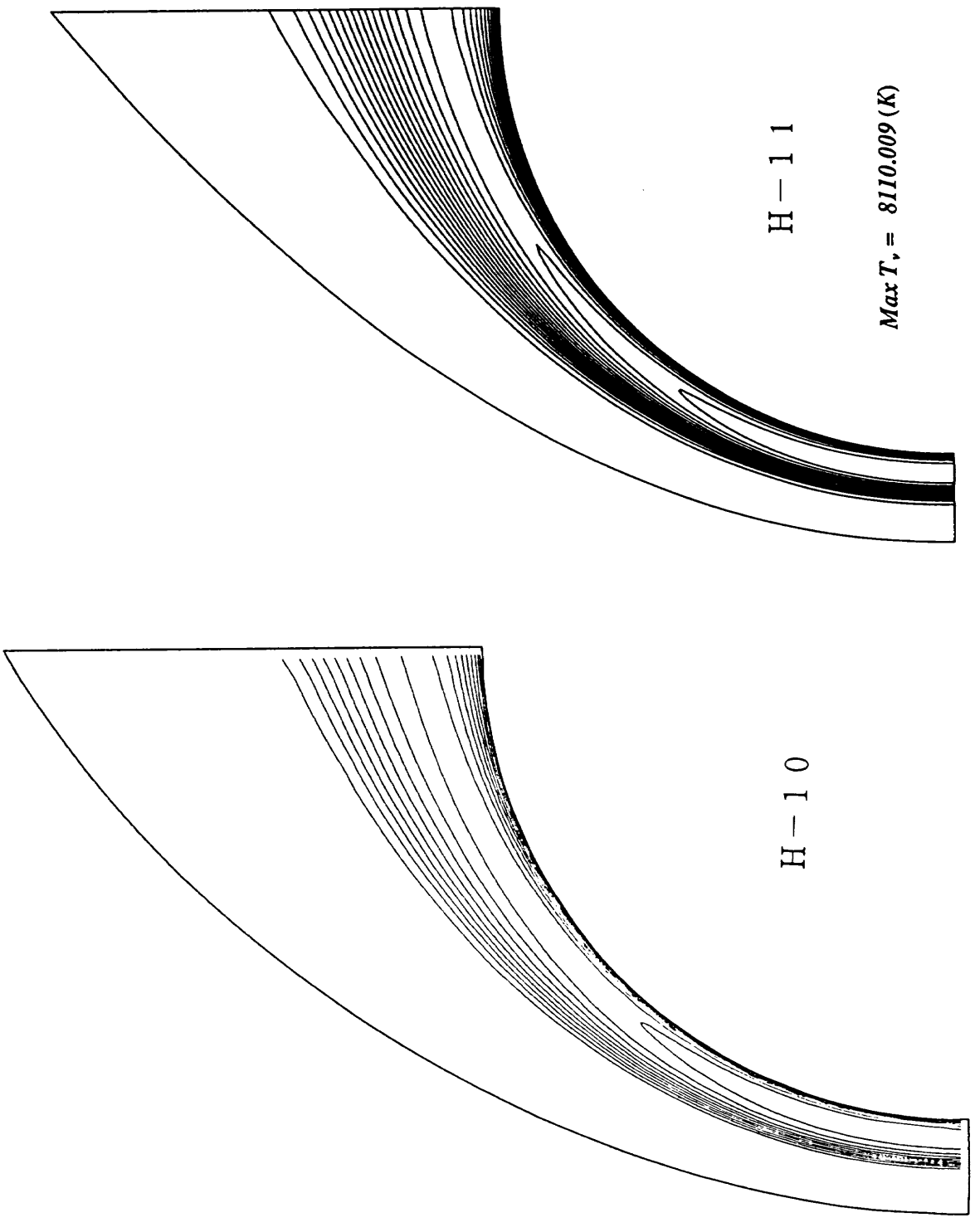

Problem I-1 等温度線図（振動）

PROBLEM I-1

Pressure distribution along the sphere surface

$P_{max} / (\rho_\infty U_\infty^2) = 0.9444$

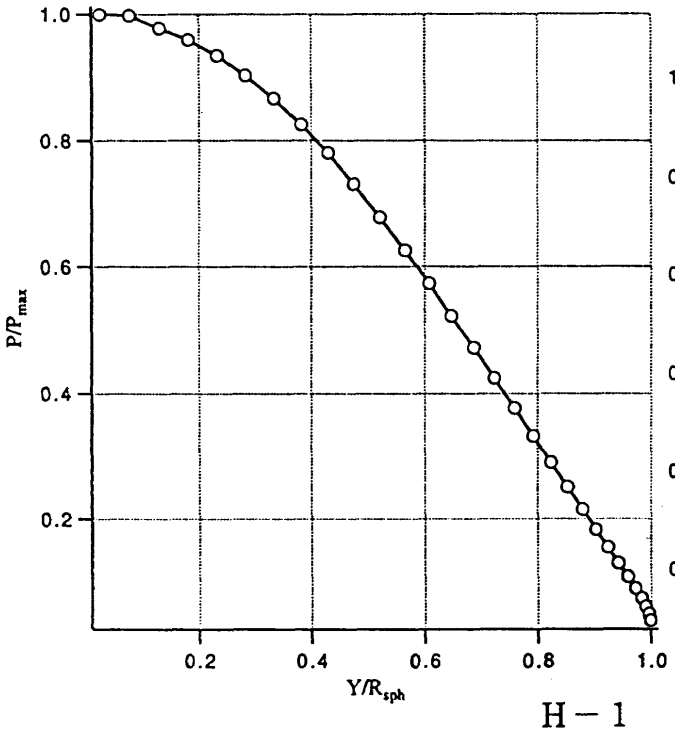

H－1

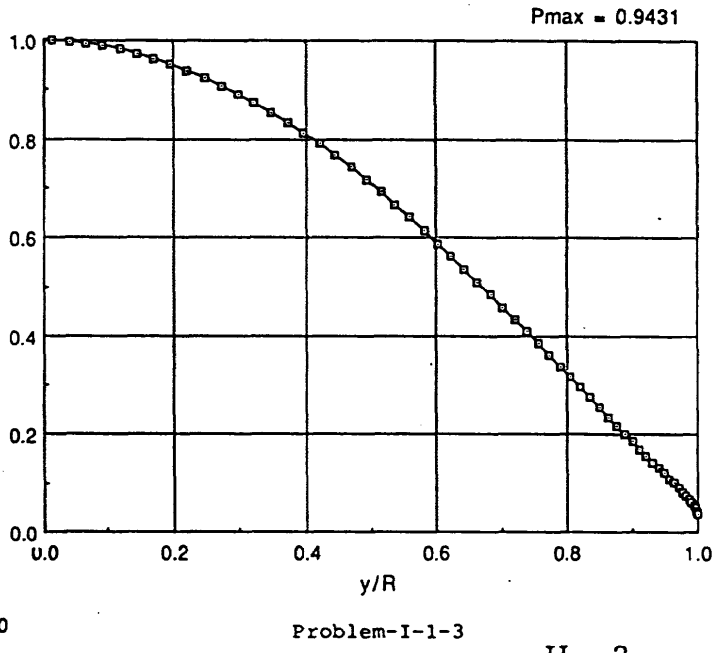

H－3

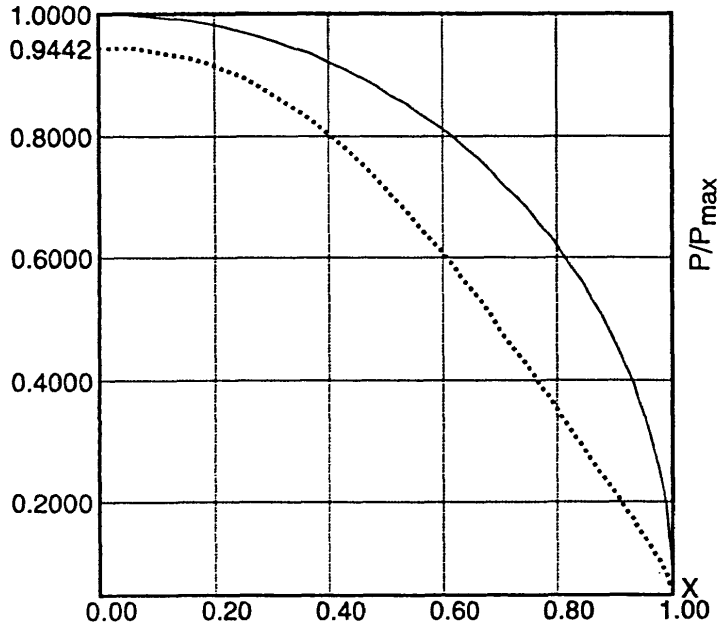

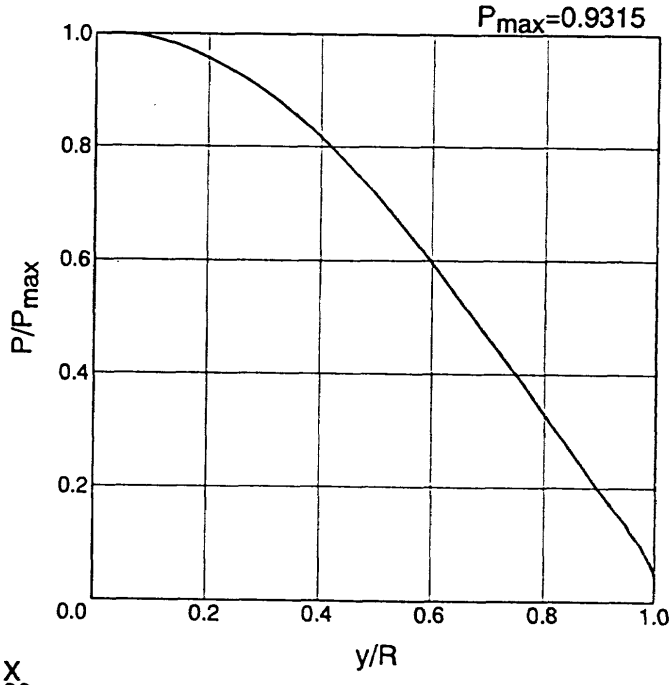

H－10

Problem I-1 Sphere H－8
Non Catalytic Case
Pressure Distribution

Problem I-1 表面圧力分布

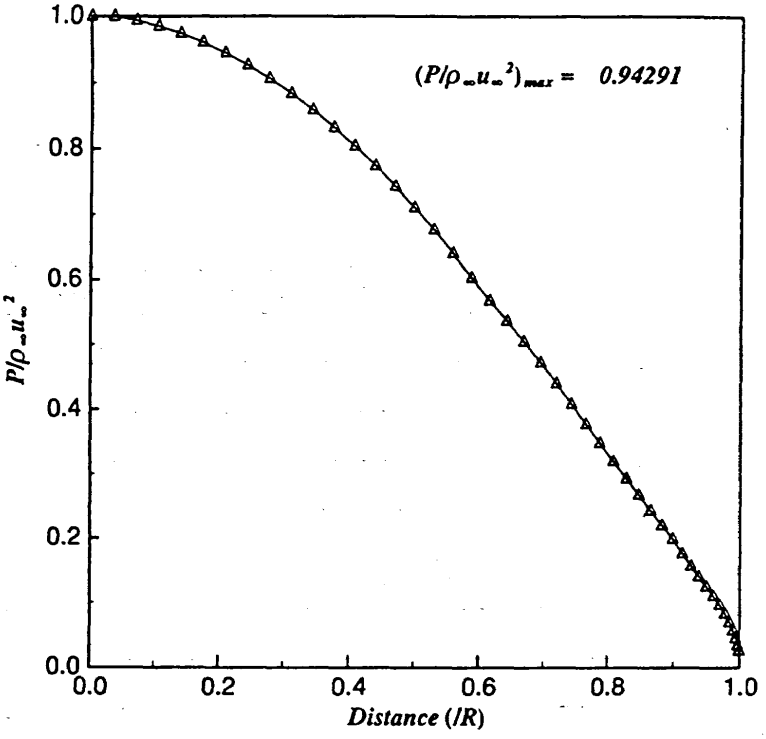

Fig. Problem-I-1-3 : Pressure Distribution along the Surface

H－１１

Problem I-1 表面圧力分布

PROBLEM I-1,2

Heat flux distribution along the sphere

$Q_{max}^{non-cat} = 0.521 \times 10^7$ w / m^2, $Q_{max}^{full-cat} = 0.638 \times 10^7$ w / m^2

$Q_{max} = 0.638 \times 10^7$ w / m^2

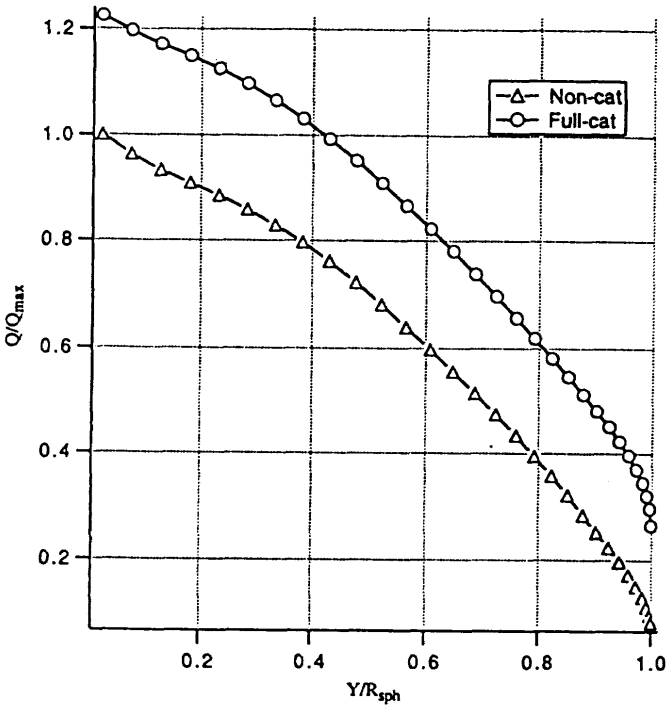

H－1

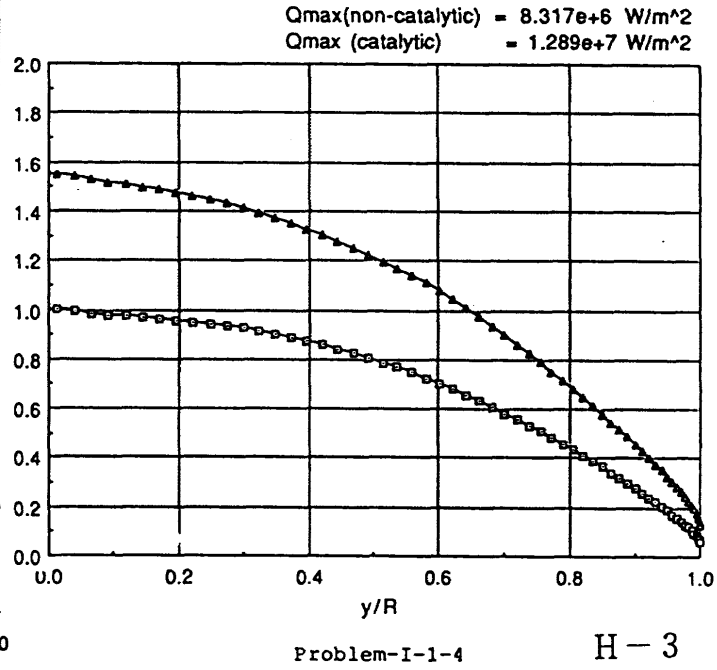

H－3

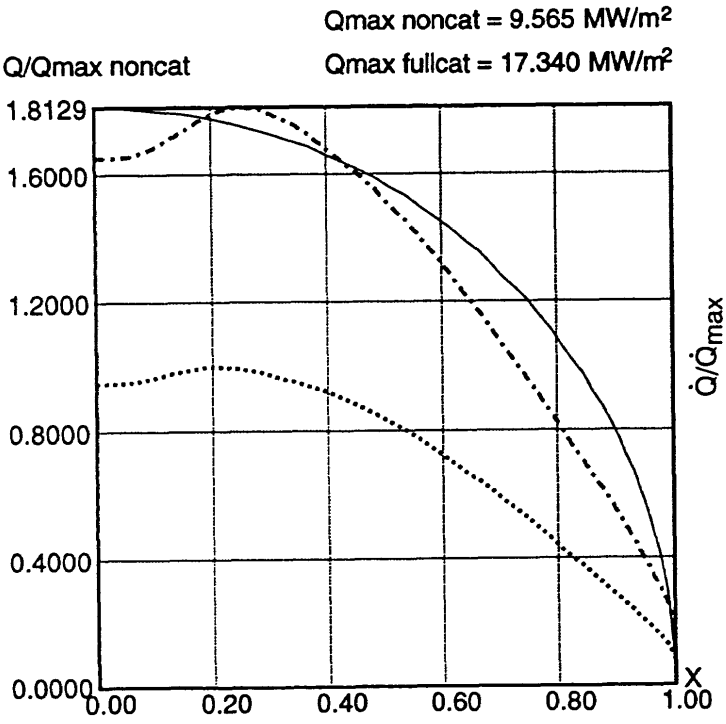

H－8

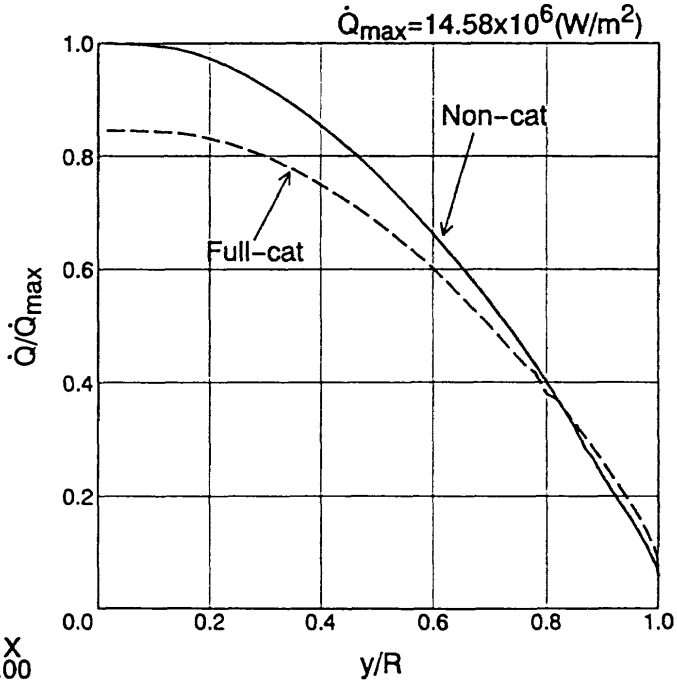

H－10

H－8 Problem I-1,2 Sphere Heat Transfer Distribution

Problem I-1,2 表面熱流束分布

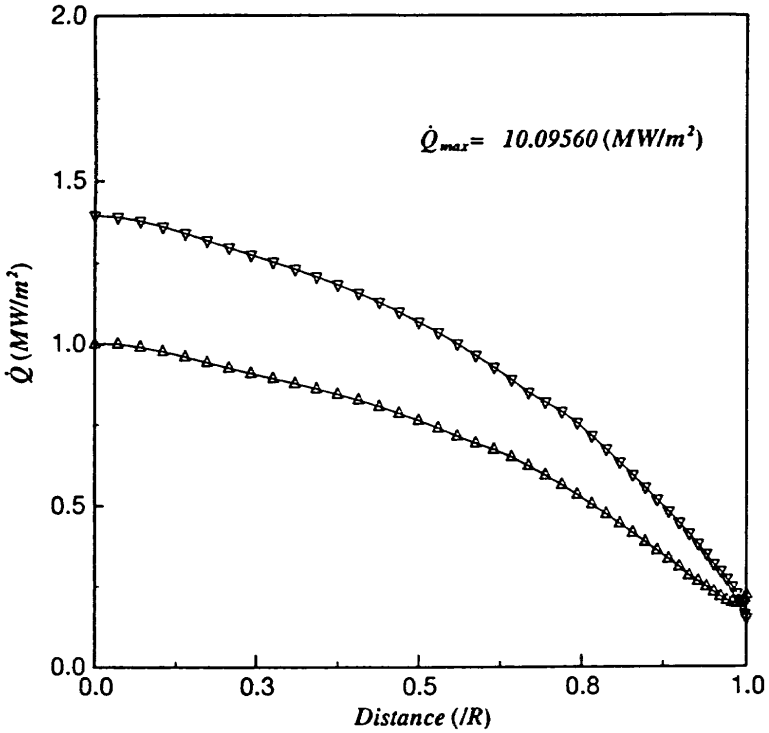

Fig. Problem-I-1-4 : Heat Flux Distribution along the Surface

H－11

Problem I-1,2 表面熱流束分布

PROBLEM I-1

Species mass fraction distribution along the stagnation streamline

X / L = 0 – the sphere surface, L = 10 mm

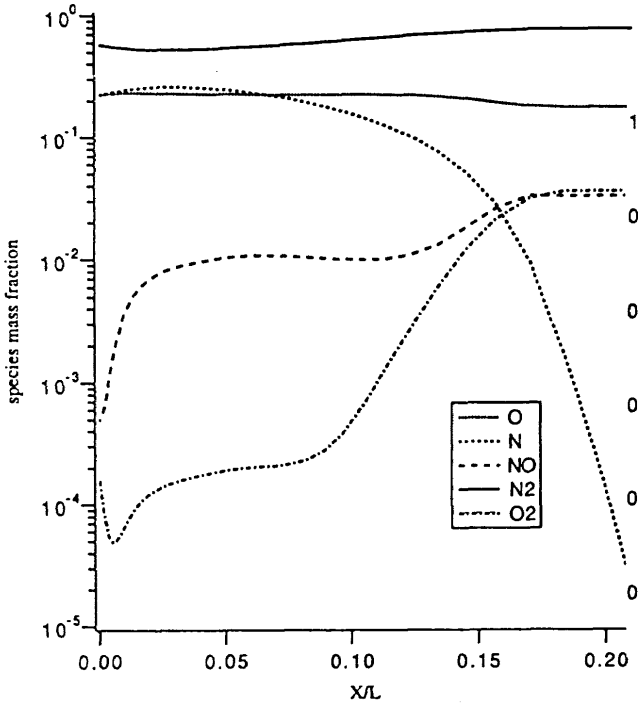

H－1

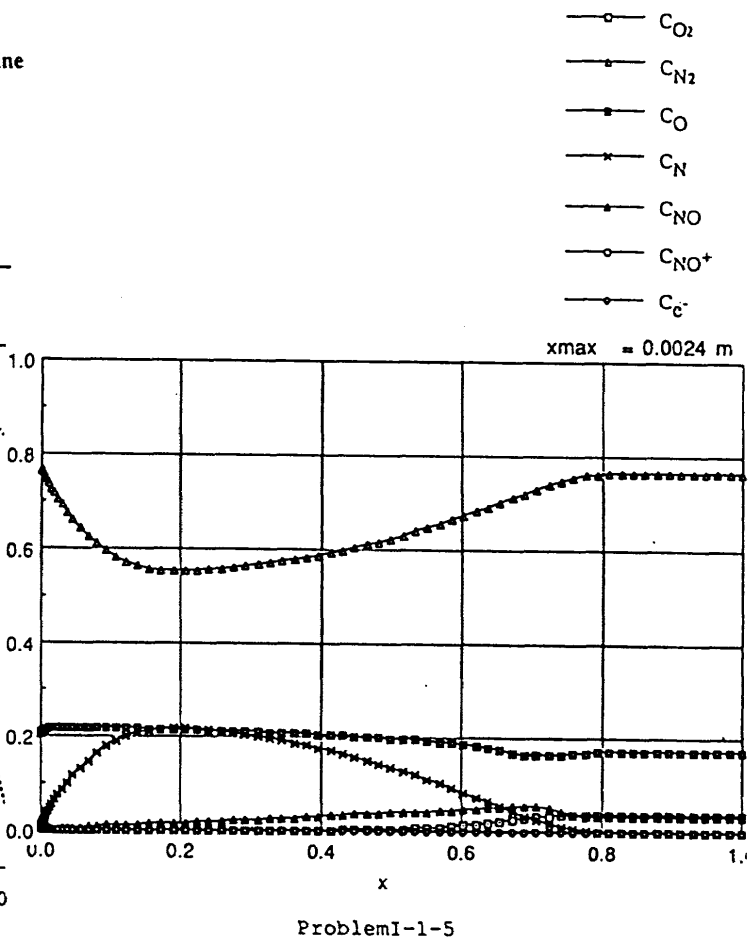

H－3

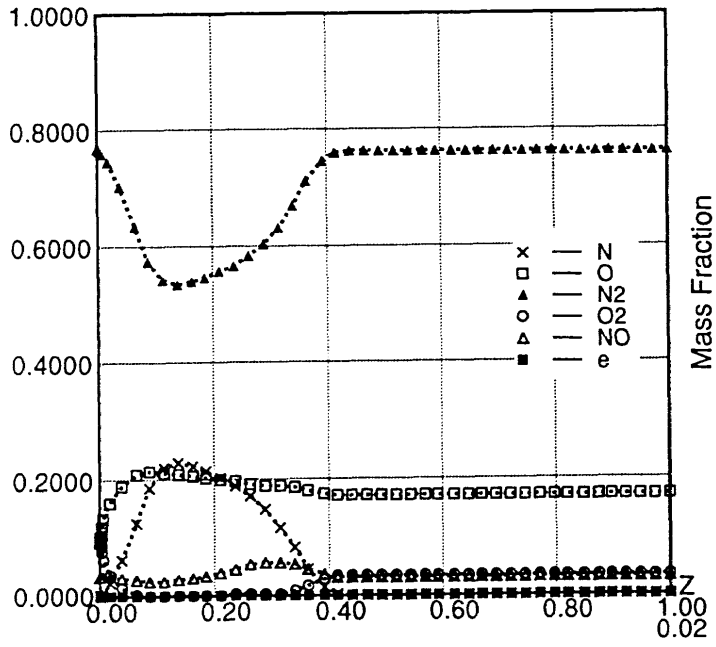

Problem I - 1 Sphere Non Catalytic

H－8

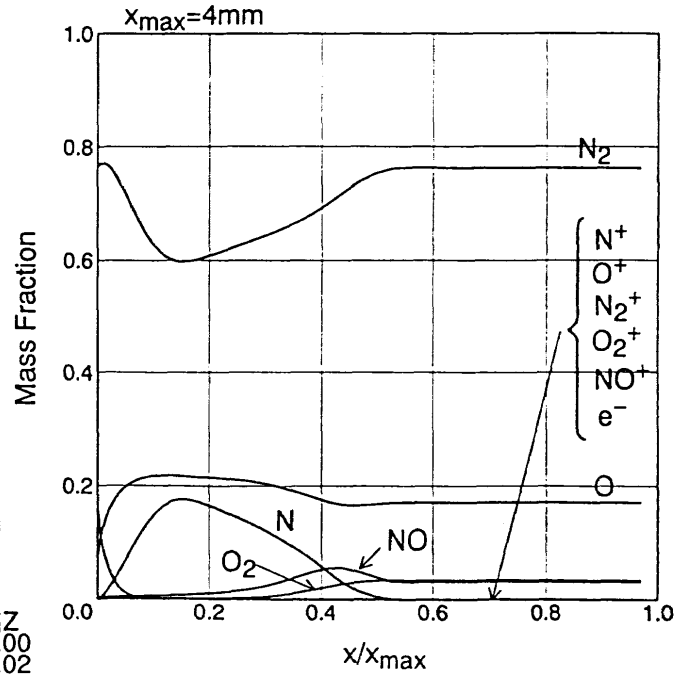

H－10

Mass Fraction along the Stagnation Stream Line

Problem I-1 よどみ点流線質量分率分布（非触媒ケース）

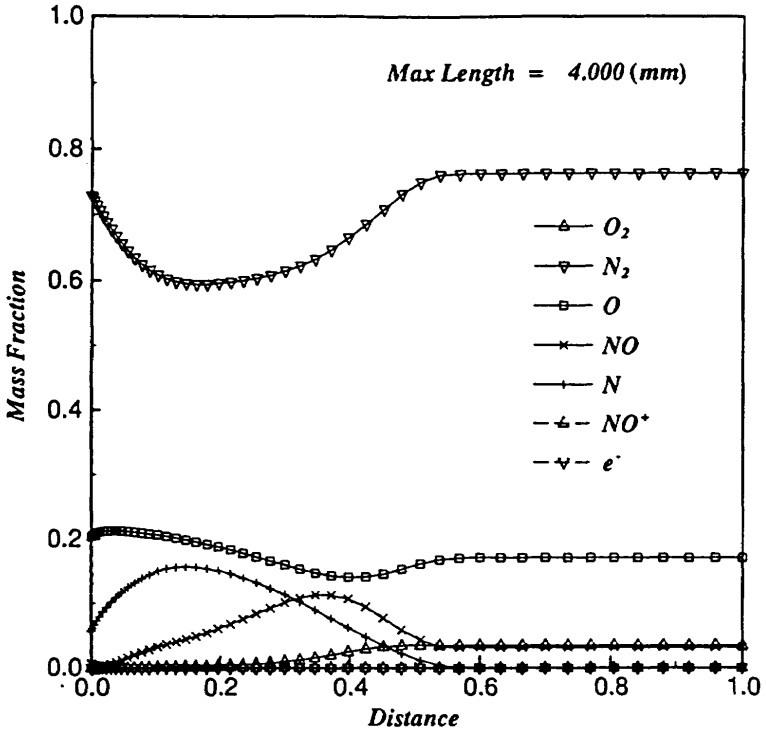

Fig. Problem-I-1-5 : Mass Fraction along the Stagnation Line

H－１１

Problem I-1 よどみ点流線質量分率分布（非触媒ケース）

PROBLEM I-1

Temperature distribution along the stagnation streamline

X / L = 0 – the sphere surface, L = 10 mm

T- translational/rotational temperature, T_{max} = 15207.17 °K
T_v - vibrational/electronic temperature, $T_{v,max}$ = 9302.34 °K

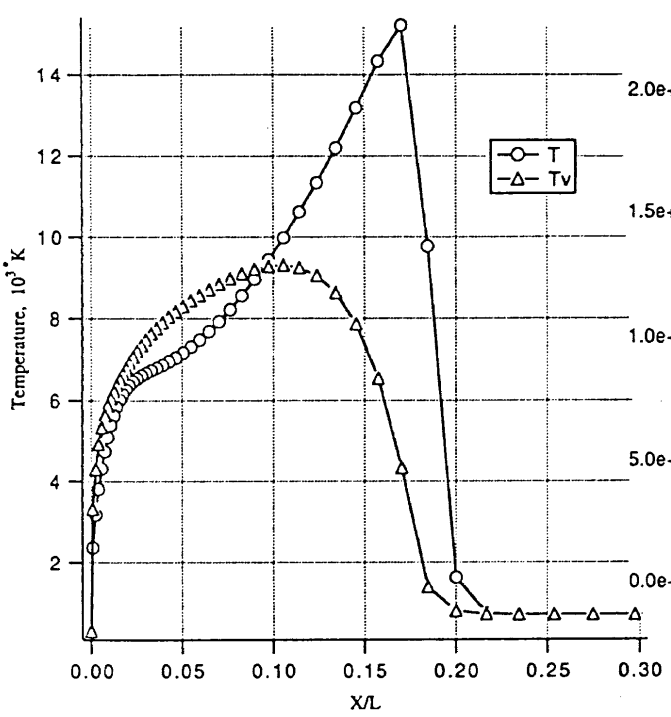

H－1

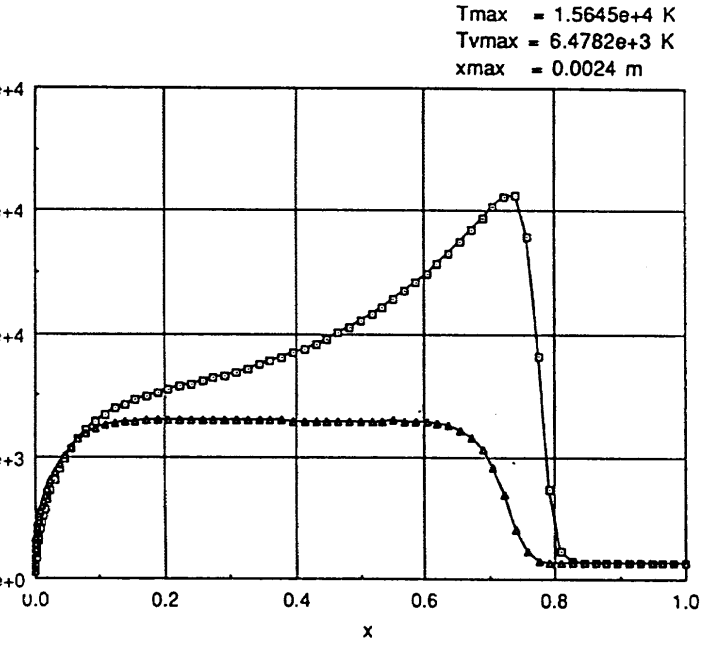

H－3

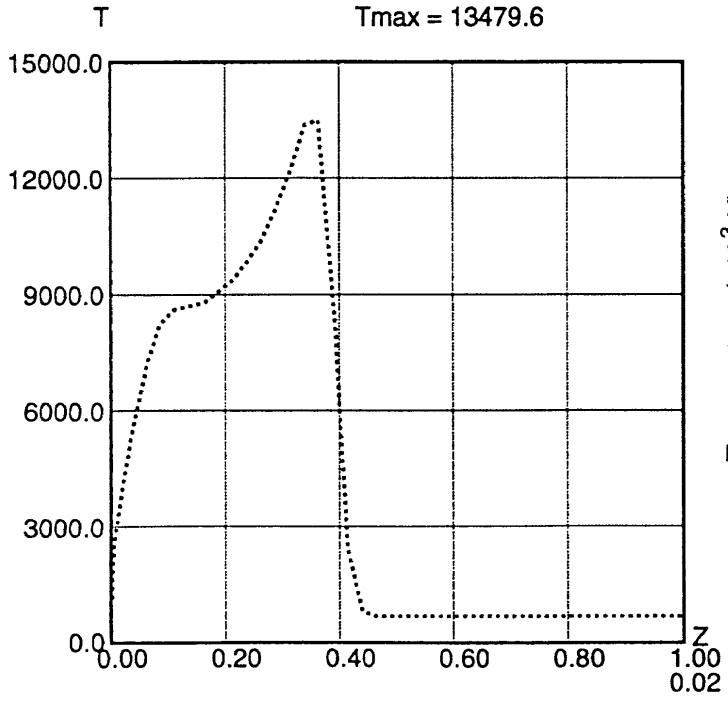

Problem I-1-⑥ Sphere H－8
Non Catalytic Case

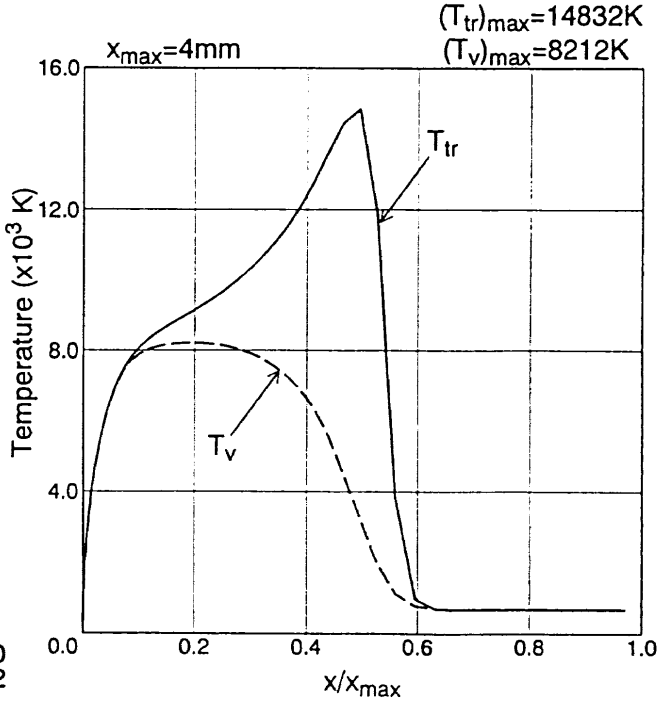

H－10

Problem I-1 よどみ点流線温度分布（非触媒ケース）

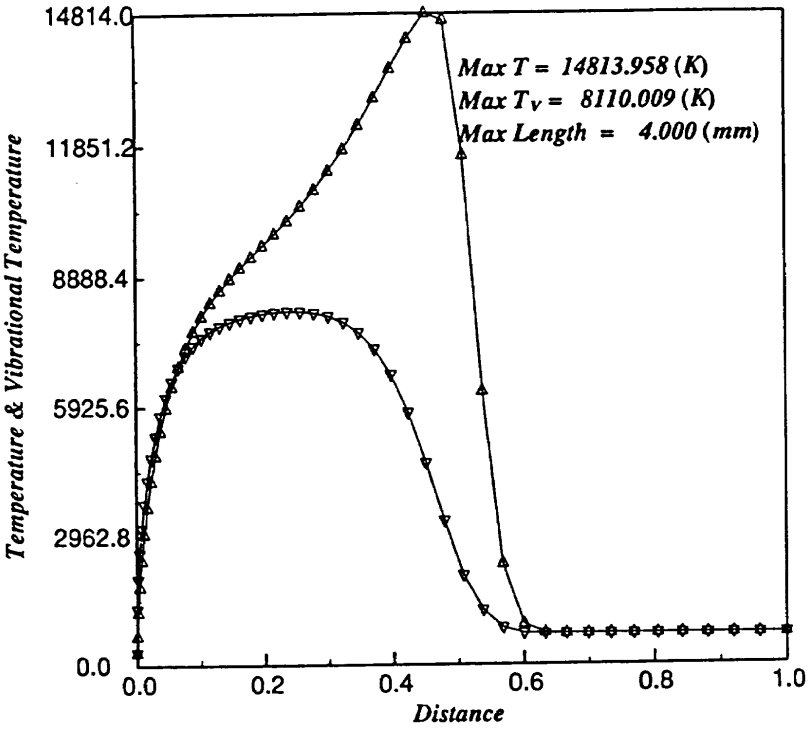

Fig. Problem-I-1-6 : Temperature Distribution along the Stagnation Line

H－11

Problem I-1 よどみ点流線温度分布（非触媒ケース）

PROBLEM I-2

Species mass fraction distribution along the stagnation streamline

X/L=0 – the sphere surface, L=10 mm

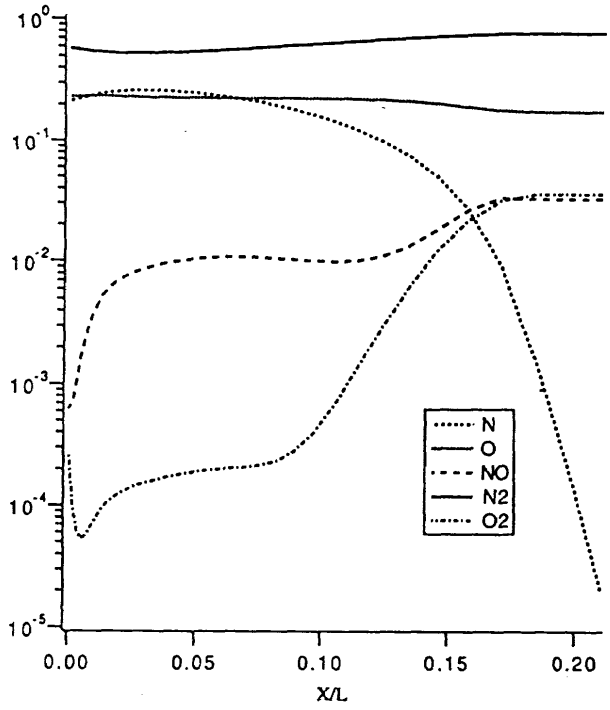

H－1

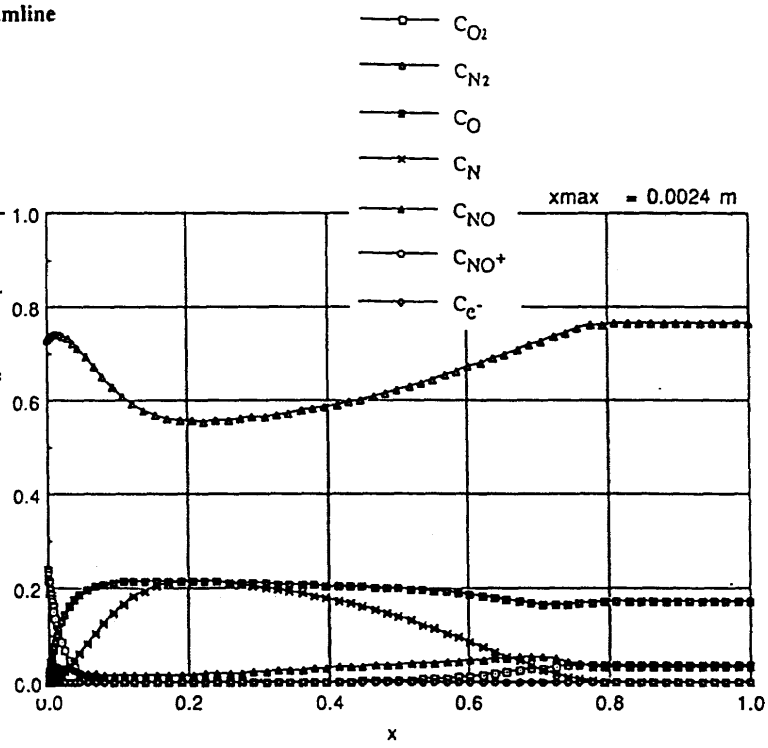

ProblemI-2-5 H－3

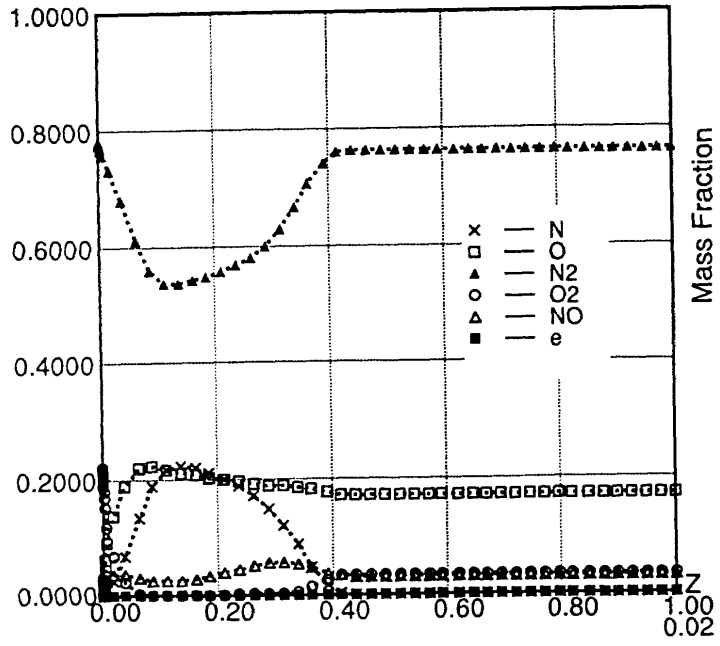

Problem I-2 Sphere Full Catalytic H－8

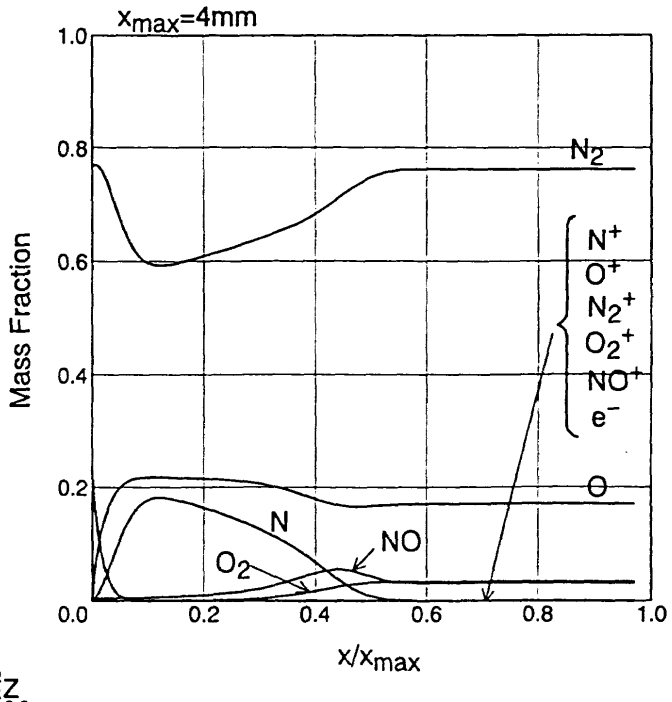

H－10

Mass Fraction along the Stagnation Stream Line

Problem I-2 よどみ点流線質量分率分布（完全触媒ケース）

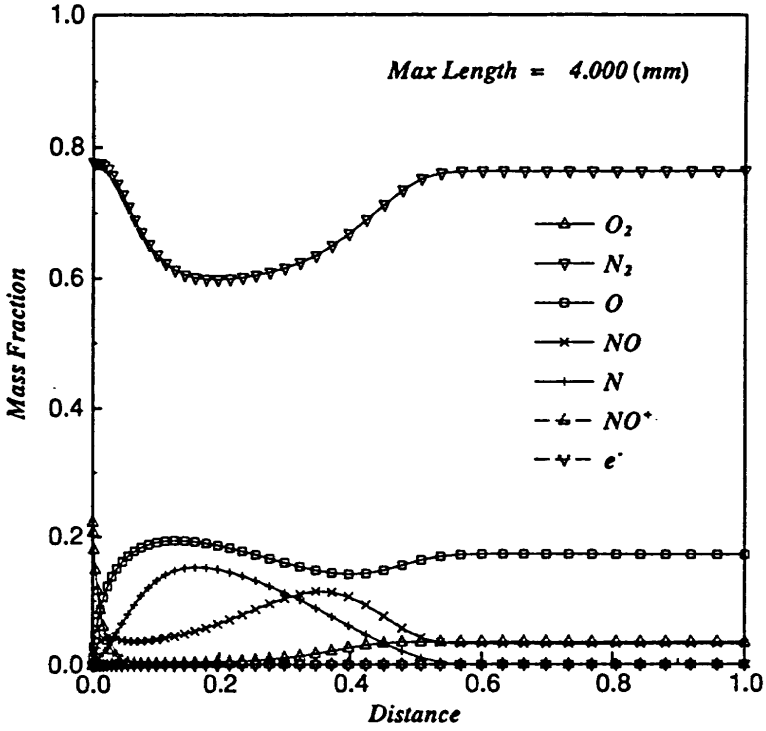

Fig. Problem-I-2-5 : Mass Fraction along the Stagnation Line

H－11

Problem I-2　よどみ点流線質量分率分布（完全触媒ケース）

PROBLEM I-2

Temperature distribution along the stagnation streamline

X / L = 0 – the sphere surface, L = 10 mm

T- translational/rotational temperature, T_{max} = 15754.63 °K
T_v - vibrational/electronic temperature, $T_{v,max}$ = 9303.02 °K

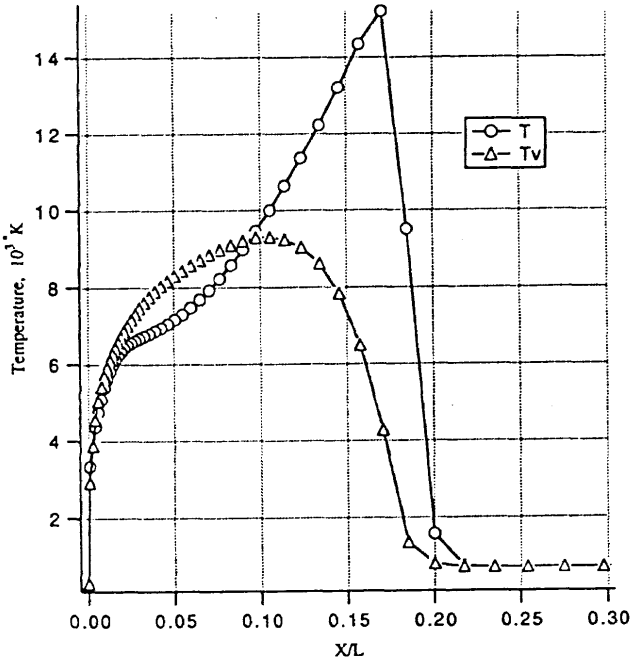

H－1

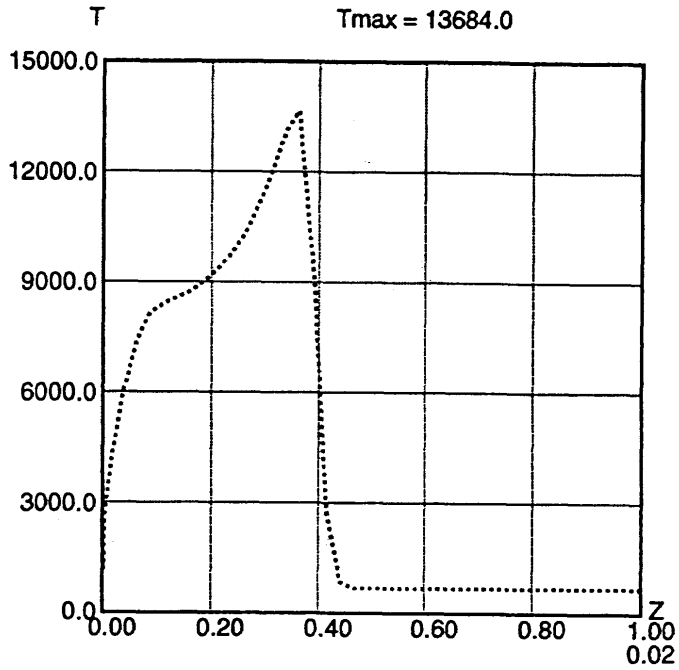

H－8 Problem I-2-⑥ Sphere
Full Catalytic Case
Stagnation Line Temperature Distribution

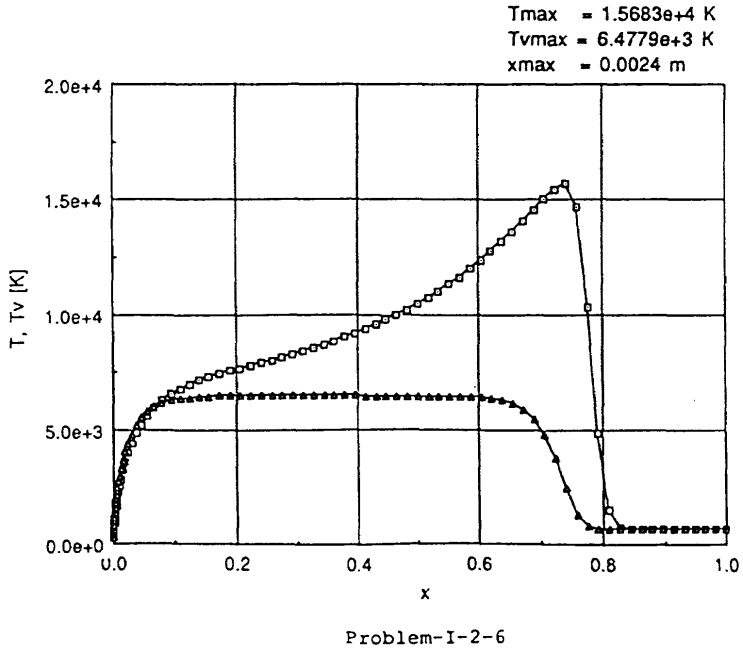

H－3

Problem I-2 よどみ点流線温度分布（完全触媒ケース）

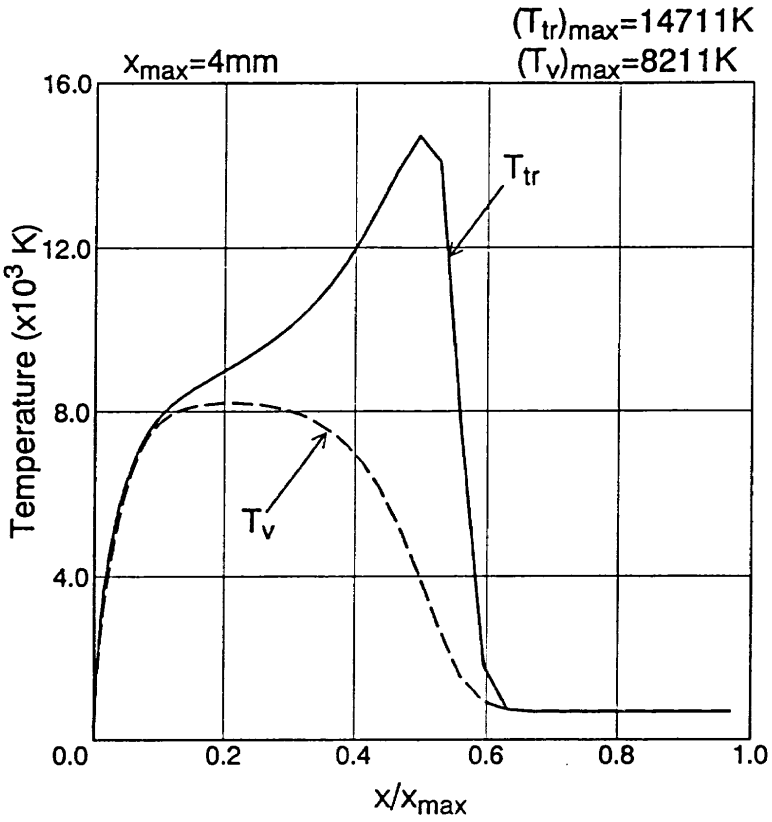

H－10

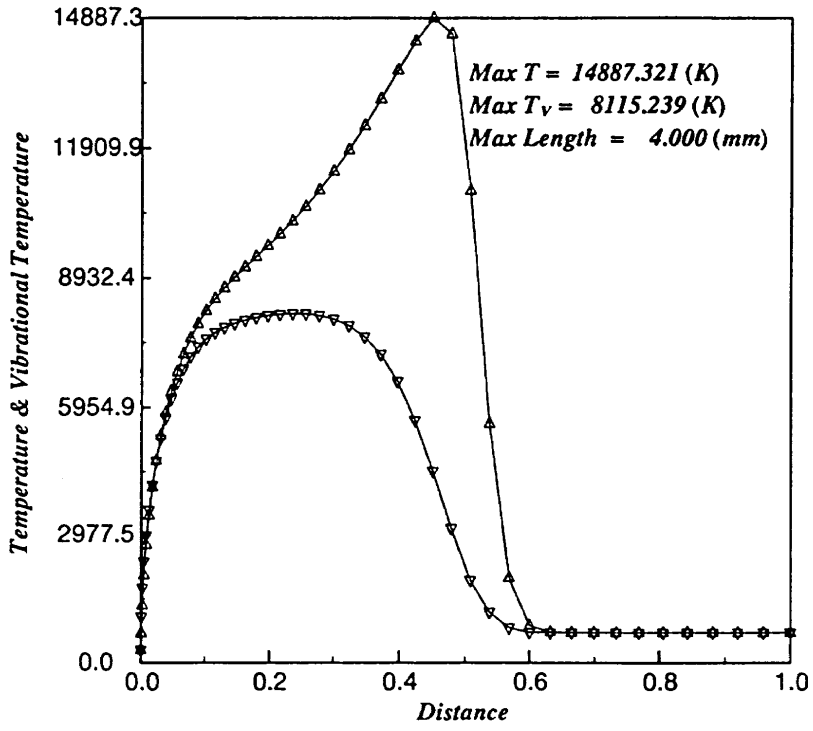

Fig. Problem-I-2-6 : Temperature Distribution along the Stagnation Line

H－11

Problem I-2 よどみ点流線温度分布（完全触媒ケース）

Problem I－3, 4

HEG条件

球まわりの流れ

非触媒及び完全触媒ケース

計算条件

V_∞ =6180m/s

T_∞ =934K

ρ_∞ =0.0034kg/m^3

Twall=300K

W_N = 0.0

W_O = 0.1468

W_{N2}= 0.744

W_{O2}= 0.0659

W_{NO}= 0.0429

PROBLEM I-3

Pressure contours

$P/(\rho_\infty U_\infty^2)$, 20 izo-lines on the interval [0,1]

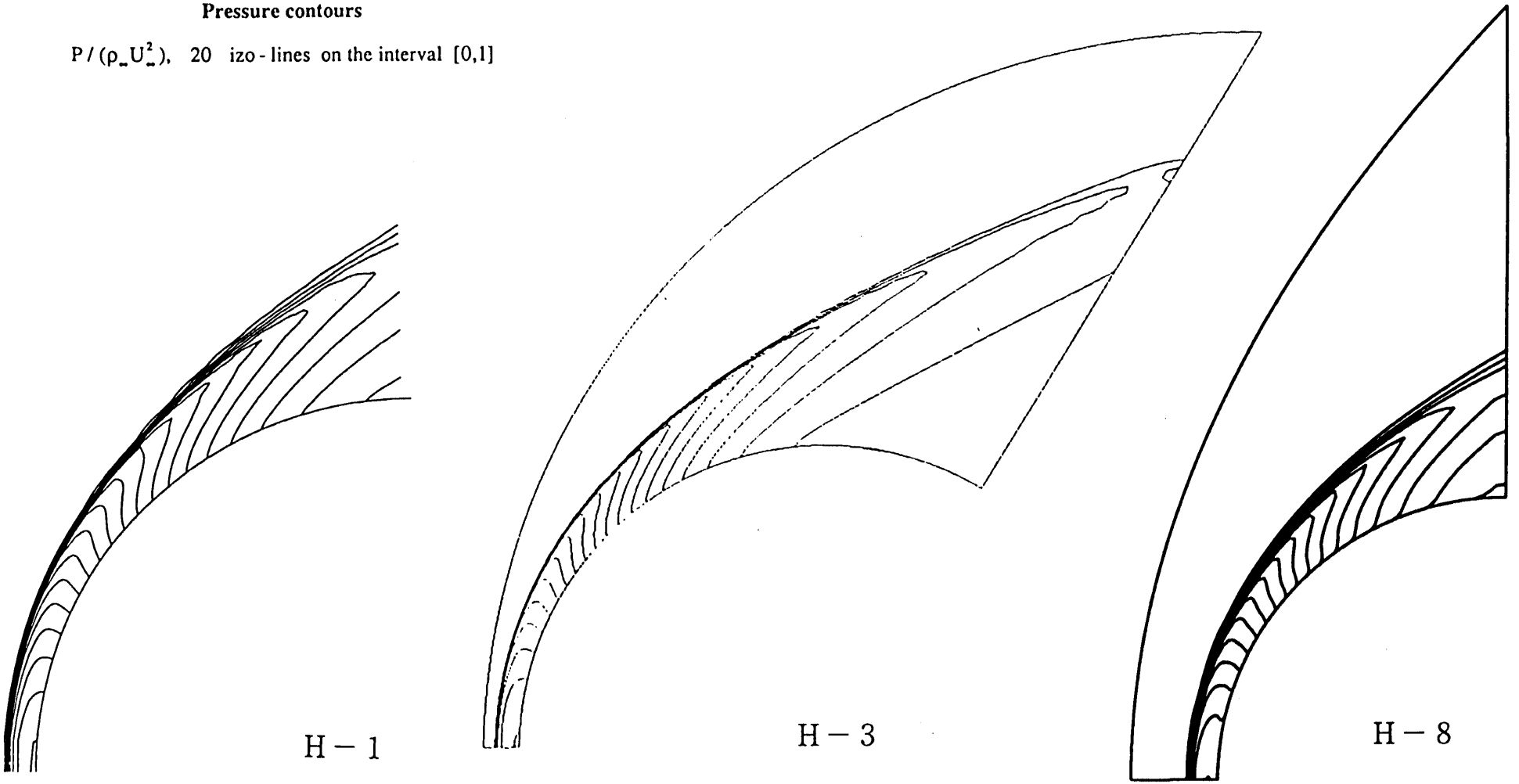

Problem I-3 圧力線図

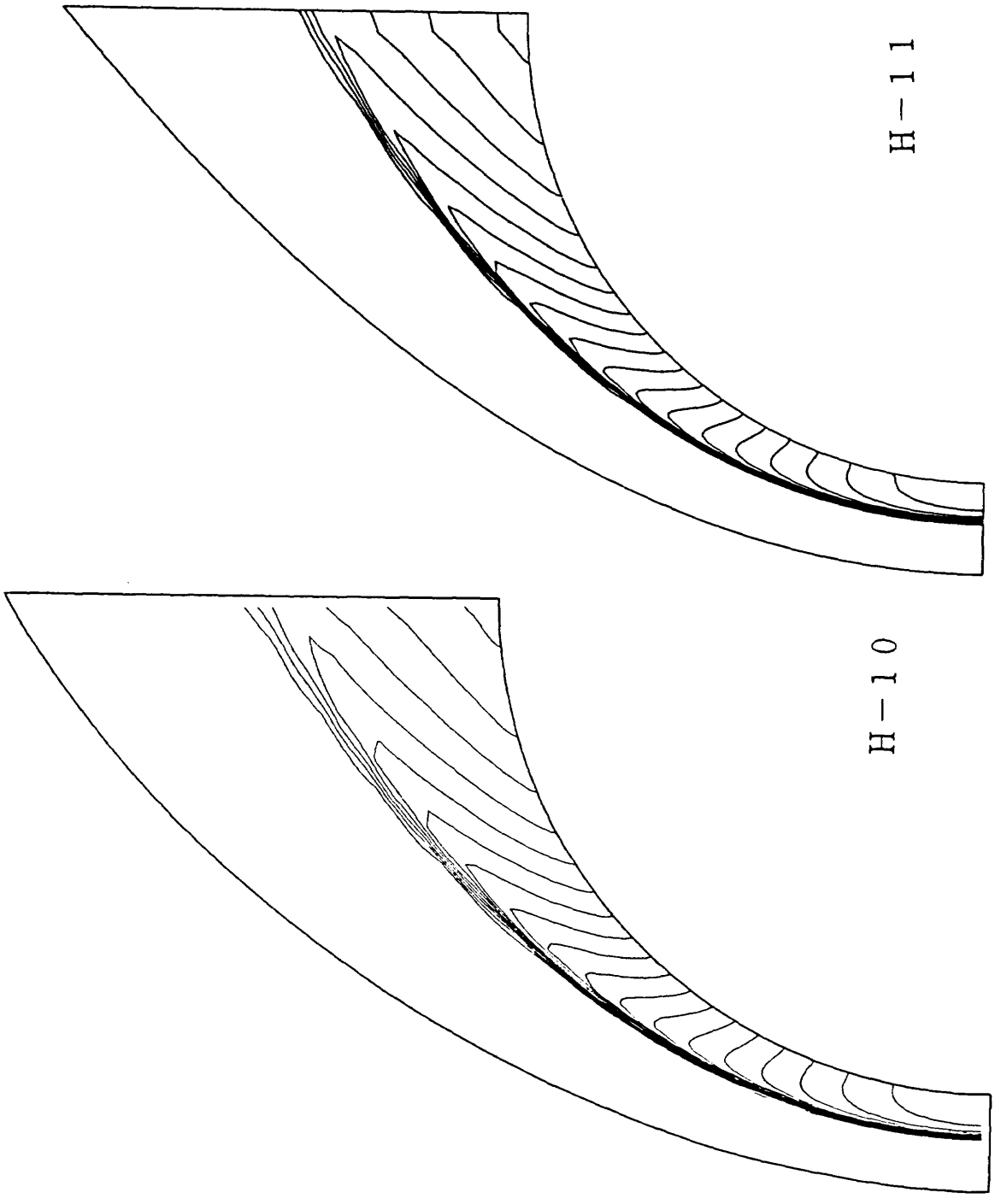

Problem I-3 圧力線図

PROBLEM I-3

Translational/rotational temperature contours

T/T_∞, 20 izo-lines on the interval $[1, \frac{T_{max}}{T_\infty}]$, T_{max} = 15351.45 °K

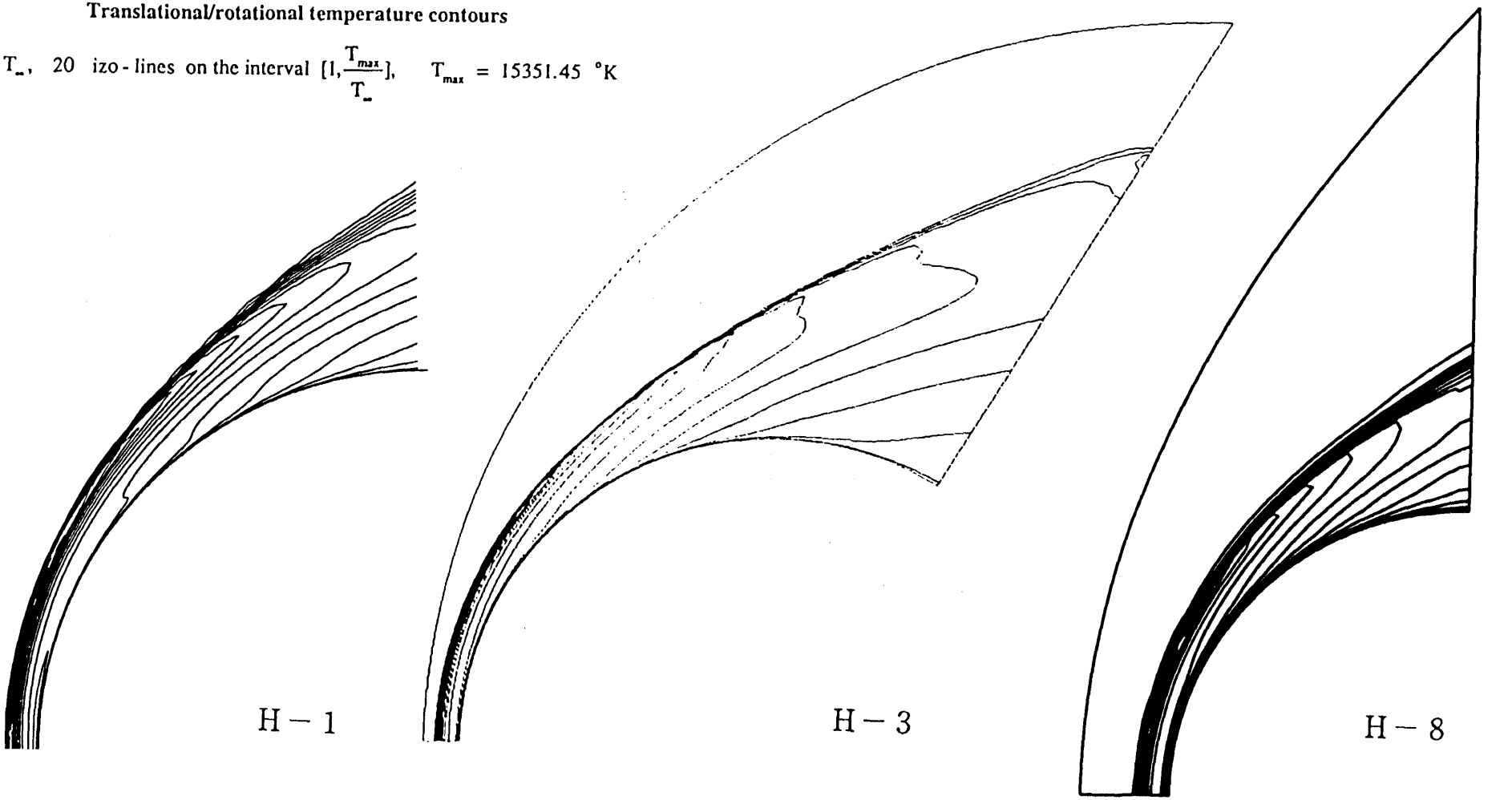

Problem I-3 Sphere Tmax=14.340
Temperature Contour Non catalytic
V_∞=6180m/s T_∞=934K
ρ_∞=0.0034 T_{wall}=300K

Problem I-3 等温度線図（並進、回転）

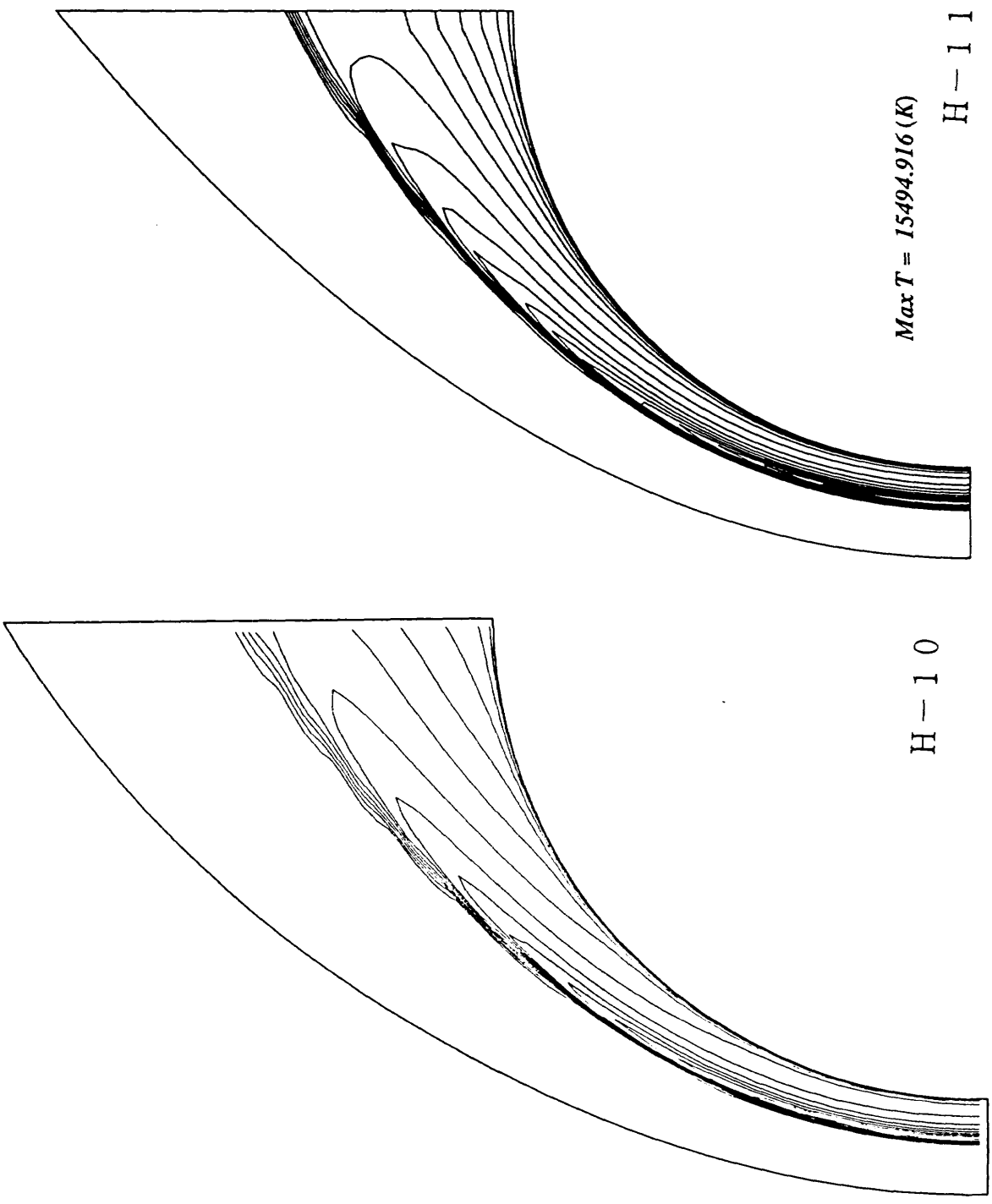

Problem I-3 等温度線図（並進、回転）

PROBLEM I-3

Vibrational temperature contours

T_v / T_∞, 20 izo-lines on the interval $[1, \frac{T_{v,max}}{T_\infty}]$, $T_{v,max} = 9229.2$ °K

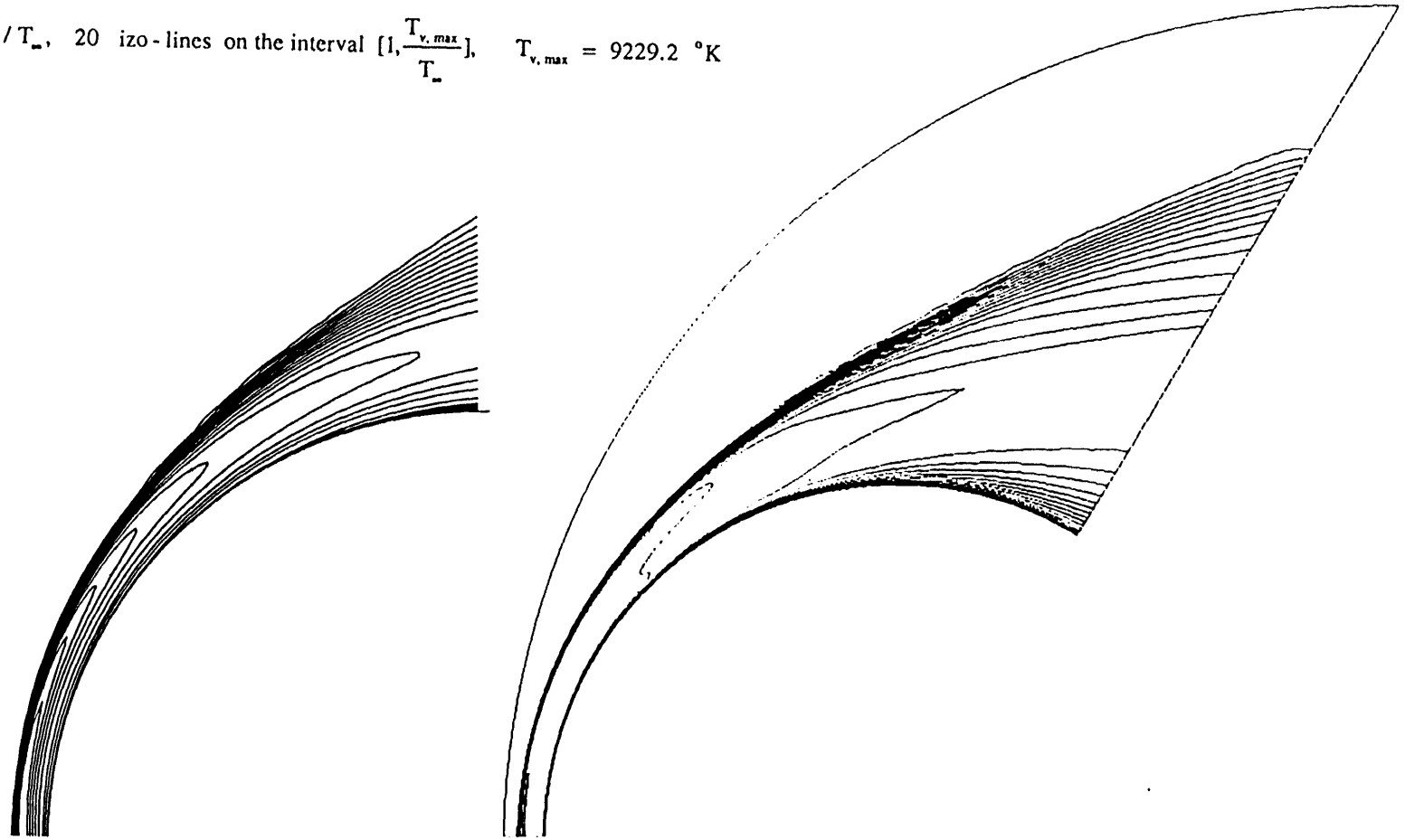

H－1　　H－3

Problem I-3　　等温度線図（振動）

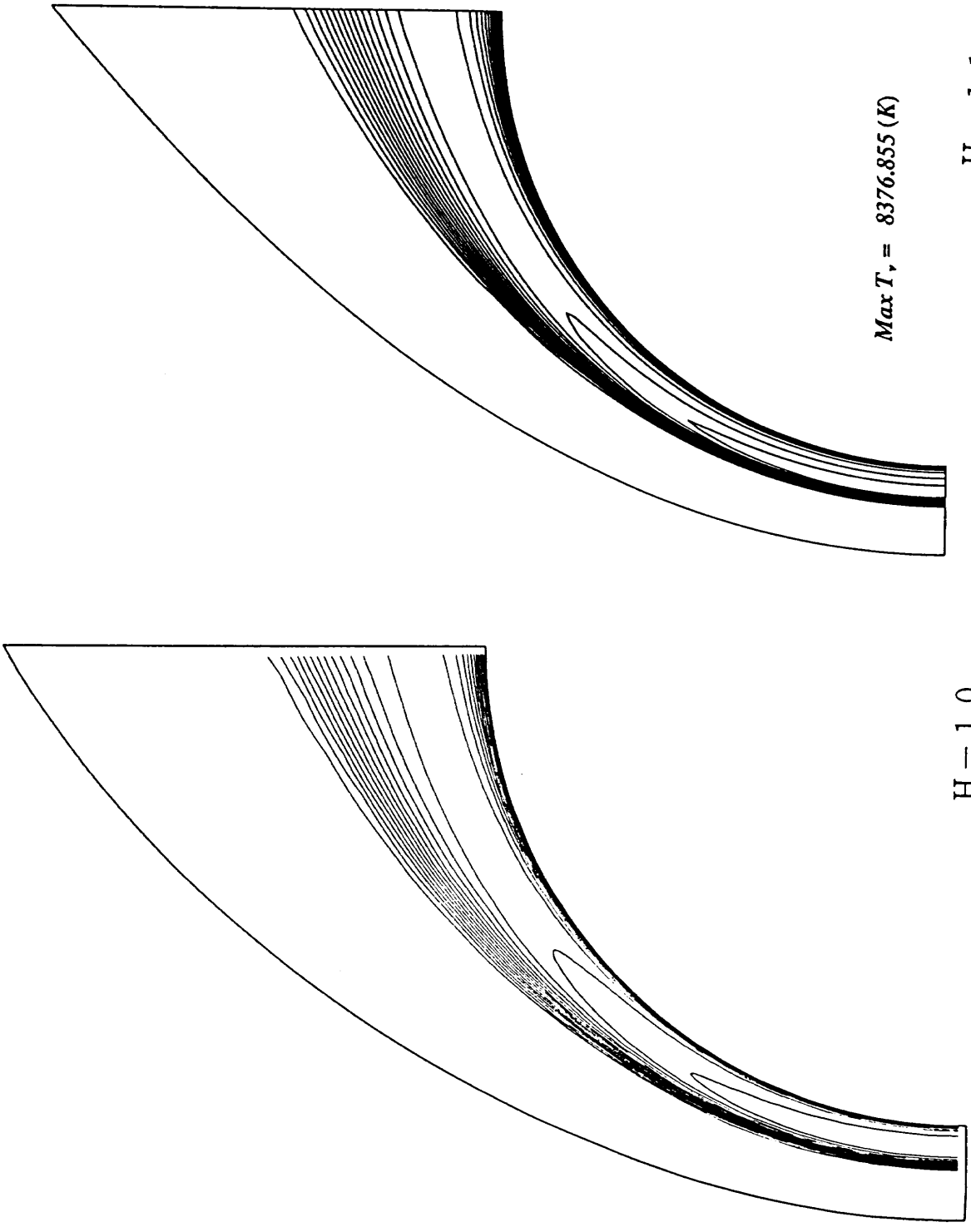

Problem I-3 等温度線図（振動）

PROBLEM I-3

Pressure distribution along the sphere surface

$P_{max} / (\rho_\infty U_\infty^2) = 0.9559$

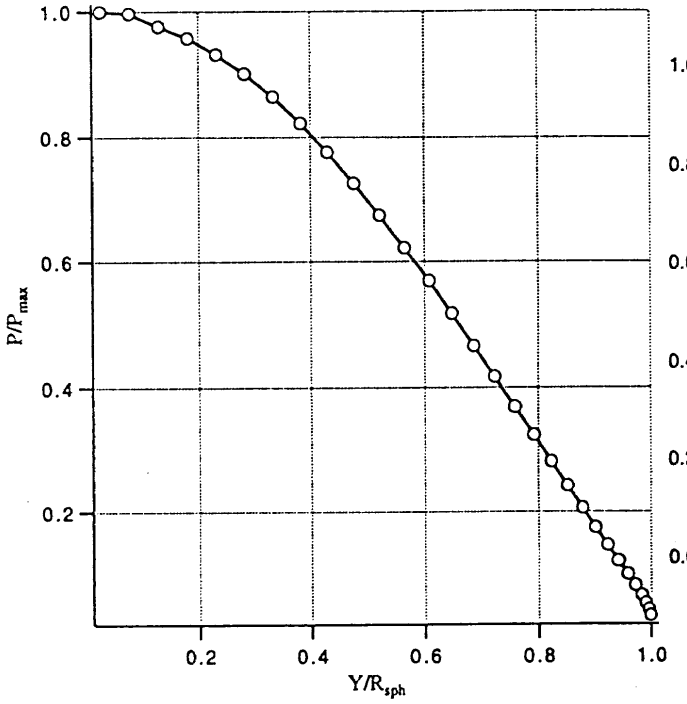

H－1

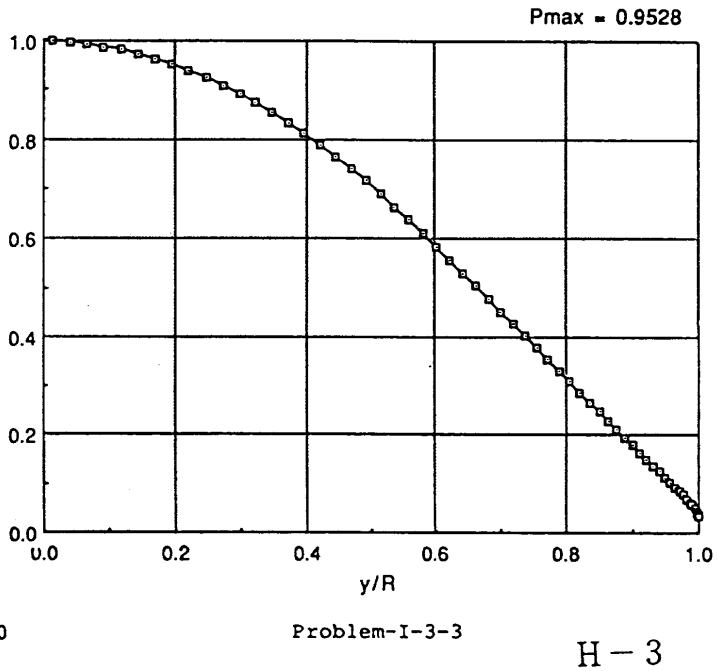

H－3

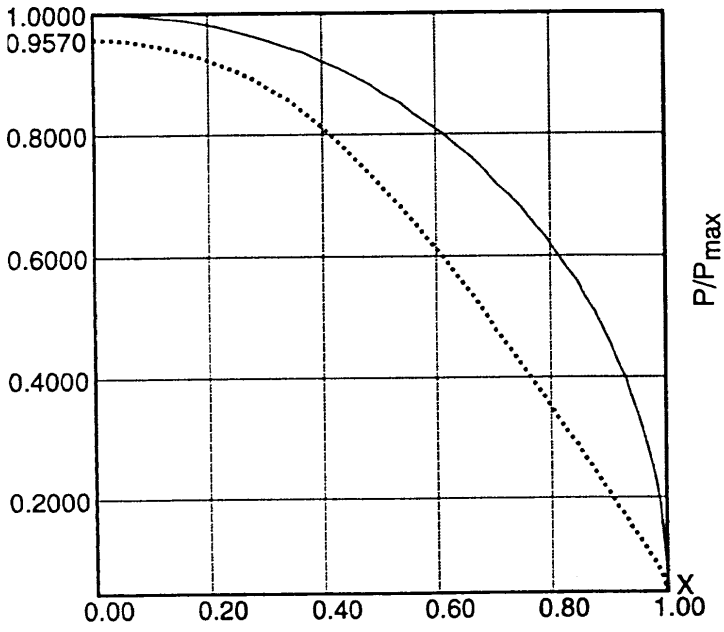

H－8

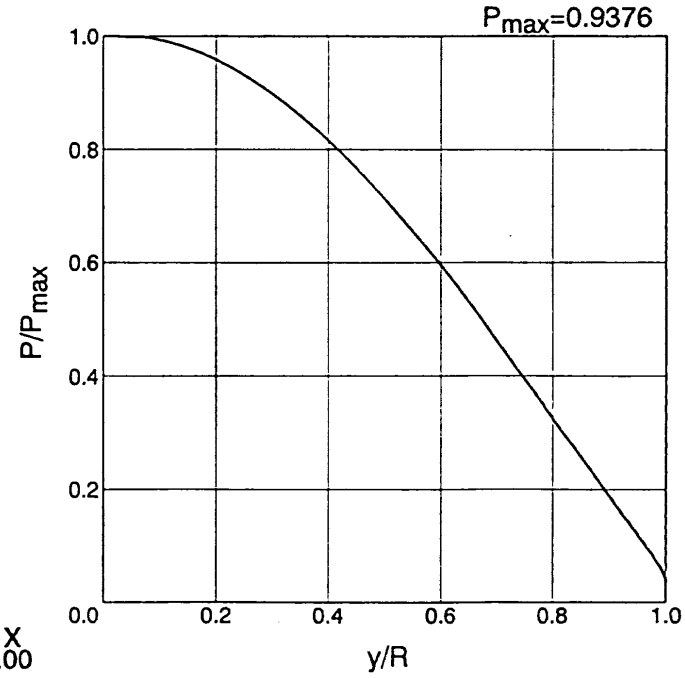

H－10

Problem I-3 Sphere
Non Catalytic Case
Pressure Distribution

Problem I-3 表面圧力分布

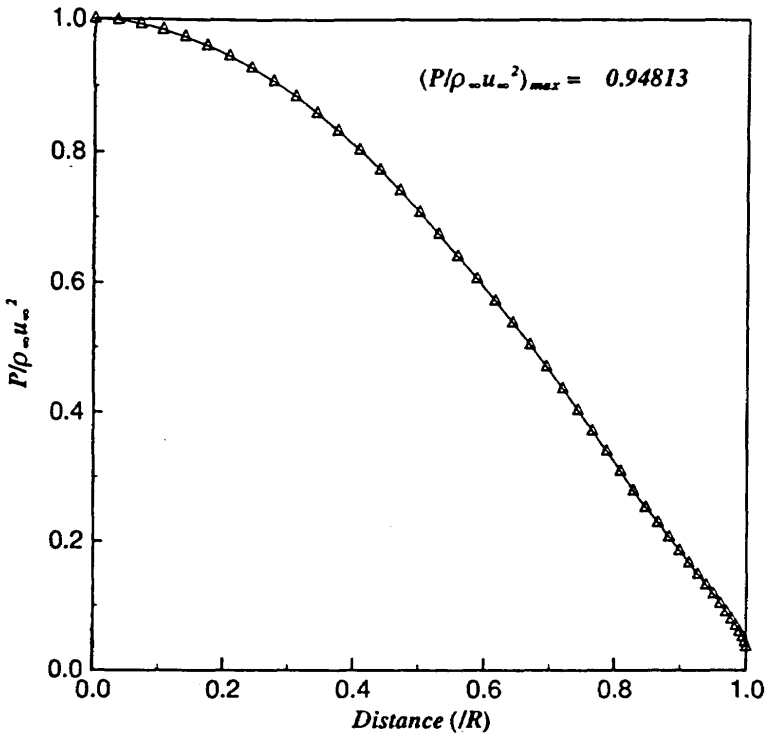

Fig. Problem-I-3-3 : Pressure Distribution along the Surface

H－11

Problem I-3 表面圧力分布

PROBLEM I-3,4

Heat flux distribution along the sphere

$Q_{max}^{non-cat} = 0.857 \times 10^7$ w / m^2 , $Q_{max}^{full-cat} = 0.803 \times 10^7$ w / m^2

$Q_{max} = 0.857 \times 10^7$ w / m^2

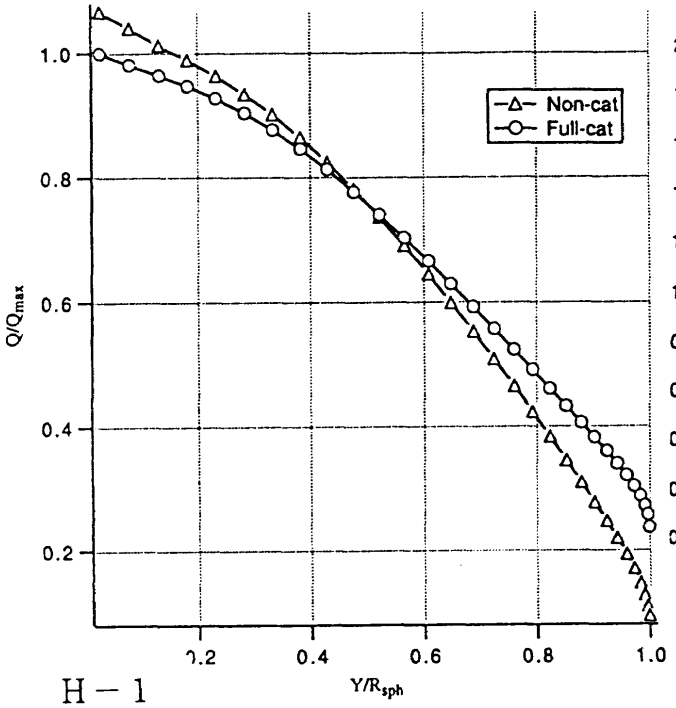

H－1

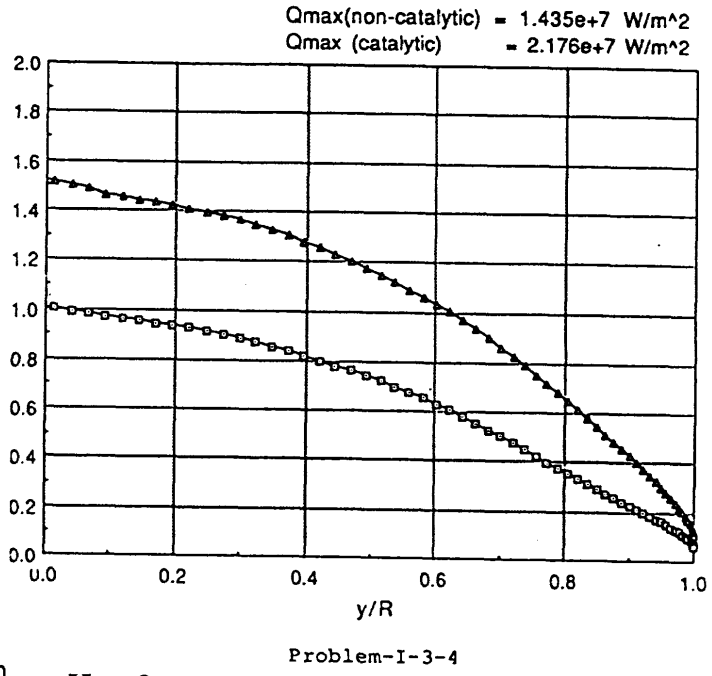

H－3

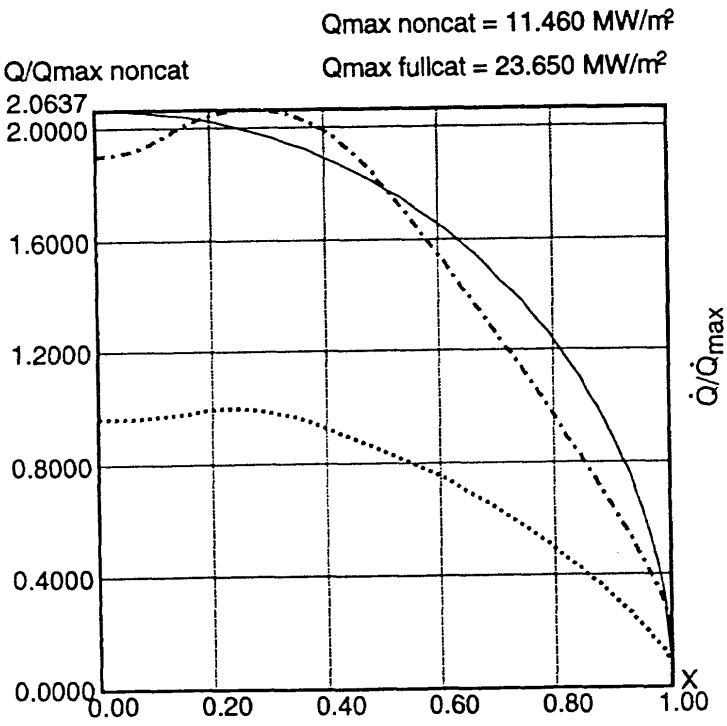

H－8

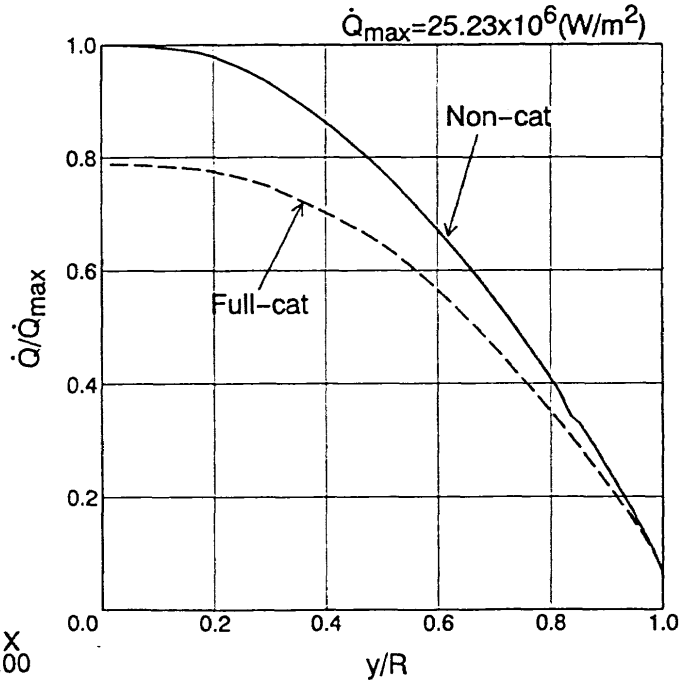

H－10

Problem I-3,4 Sphere Heat Transfer Distribution

Problem I-3,4 表面熱流束分布

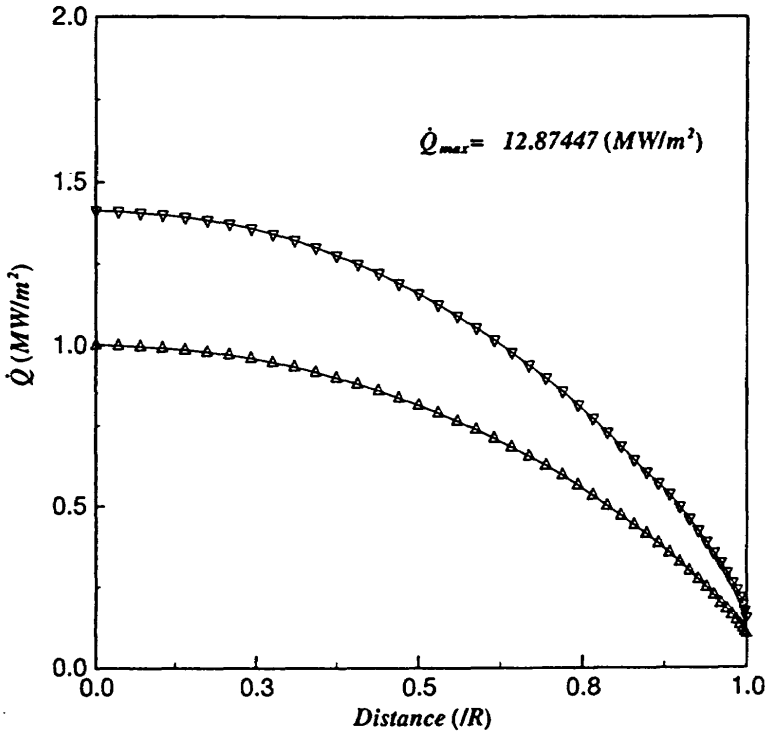

Fig. Problem-I-3-4 : Heat Flux Distribution along the Surface

H－11

Problem I-3,4 表面熱流束分布

PROBLEM I-3

Species mass fraction distribution along the stagnation streamline

X / L = 0 – the sphere surface, L = 10 mm

H－1

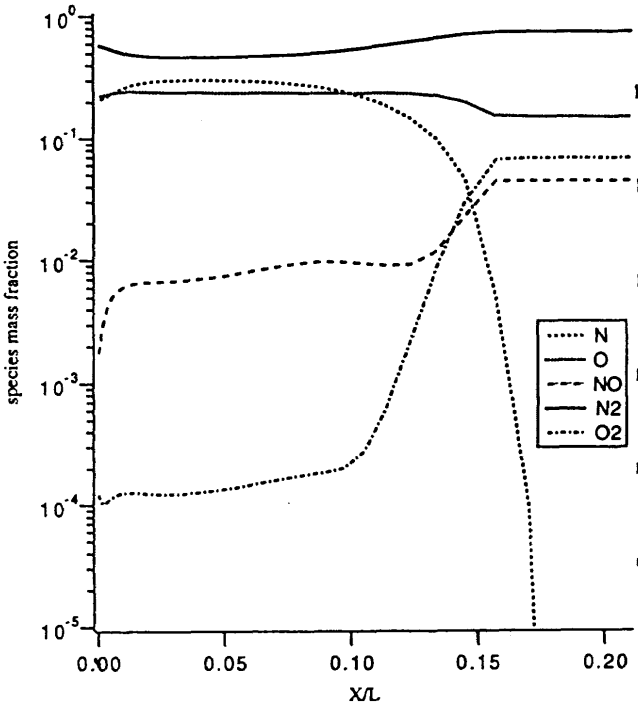

H－3

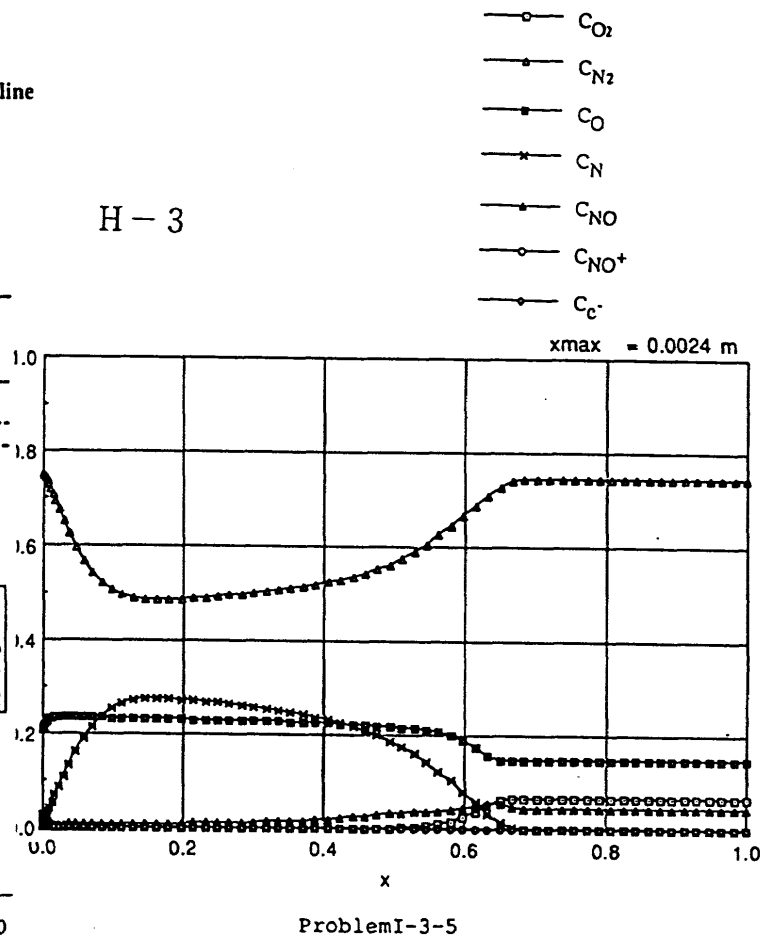

H－8

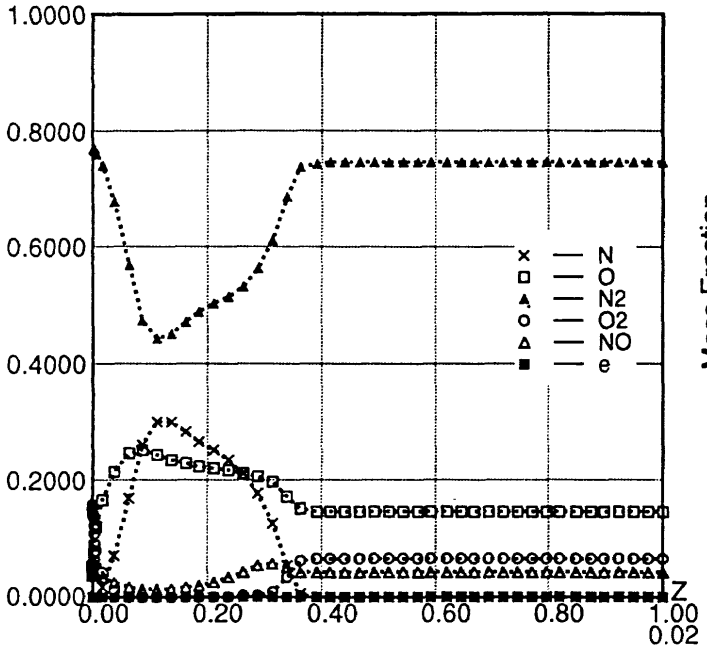

H－10

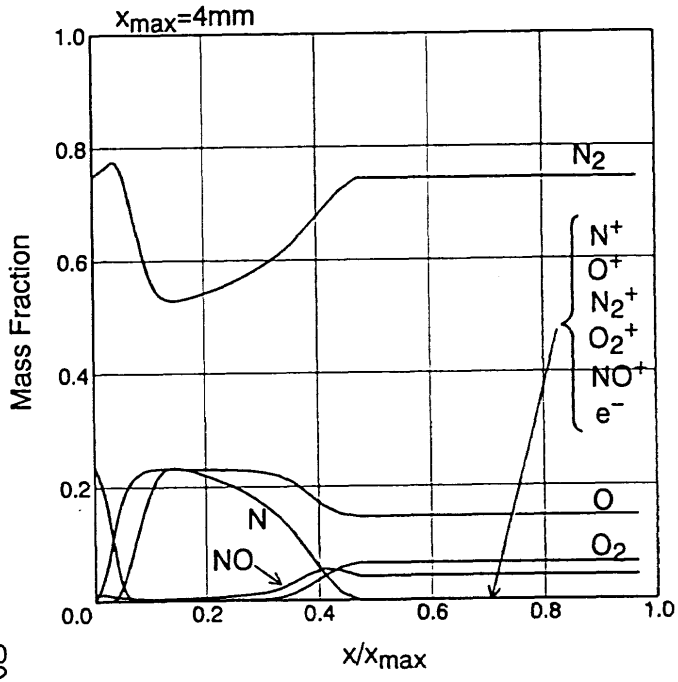

Problem I - 3 Sphere Non Catalytic

Mass Fraction along the Stagnation Stream Line

Problem I-3 よどみ点流線質量分率分布（非触媒ケース）

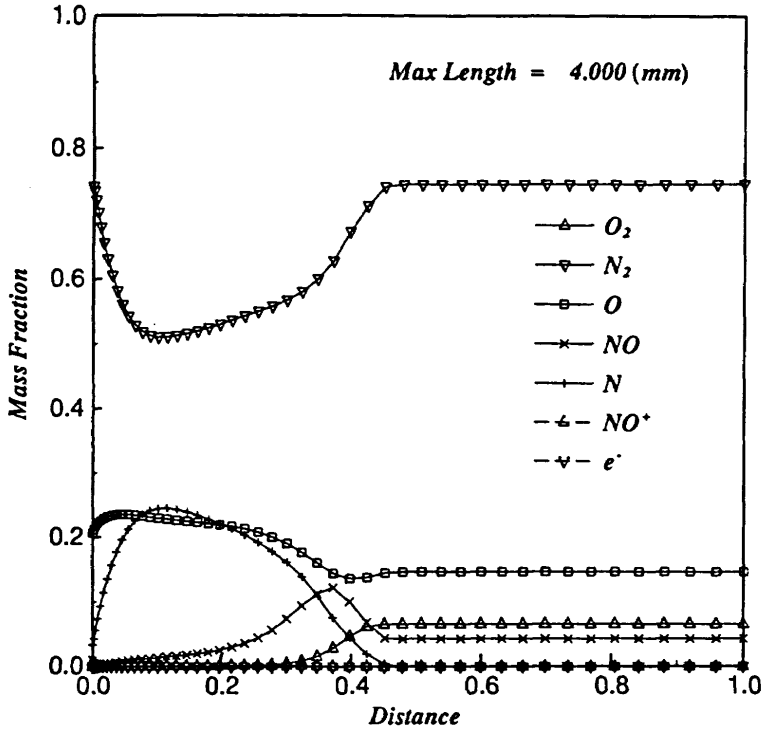

Fig. Problem-I-3-5 : Mass Fraction along the Stagnation Line

H－11

Problem I-3 よどみ点流線質量分率分布（非触媒ケース）

PROBLEM I-3

Temperature distribution along the stagnation streamline

X / L = 0 – the sphere surface, L = 10 mm

T- translational/rotational temperature, T_{max} = 14578.06 °K
T_v - vibrational/electronic temperature, $T_{v,max}$ = 9073.00 °K

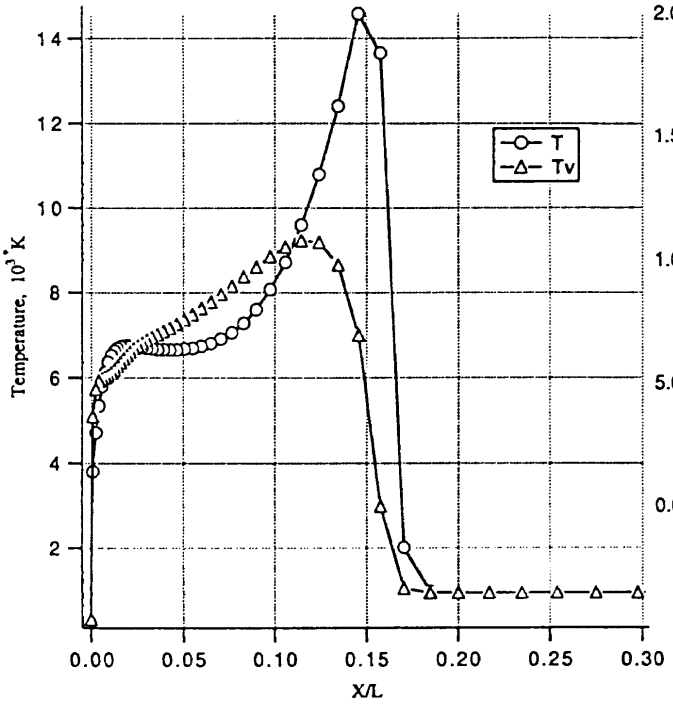

H－1

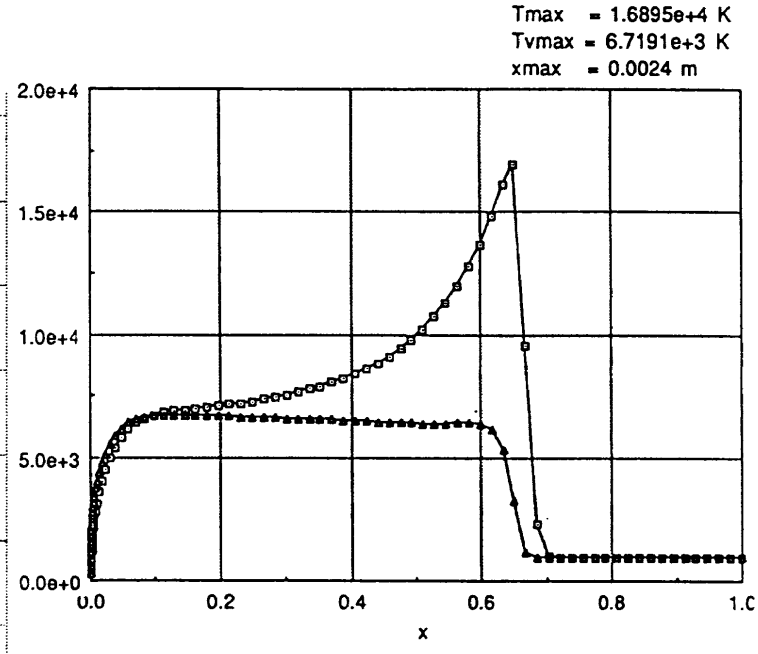

Problem-I-3-6

H－3

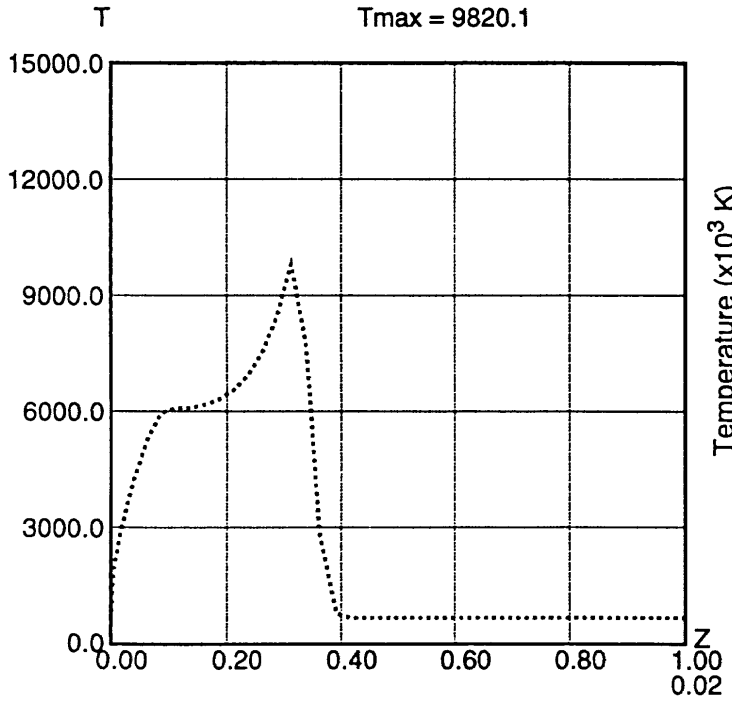

H－8

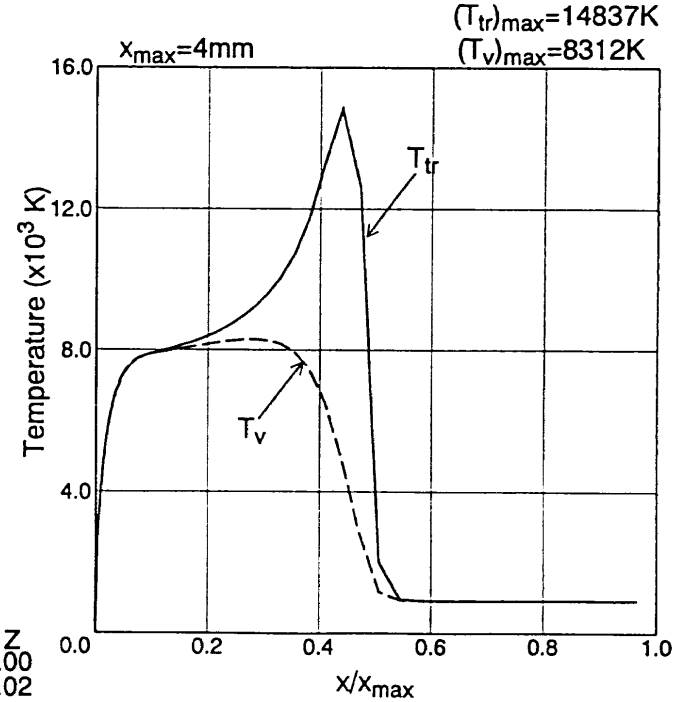

H－10

Problem I-3-⑥ Sphere
Non Catalytic Case
Stagnation Line Temperature Distribution

Problem I-3 よどみ点流線温度分布（非触媒ケース）

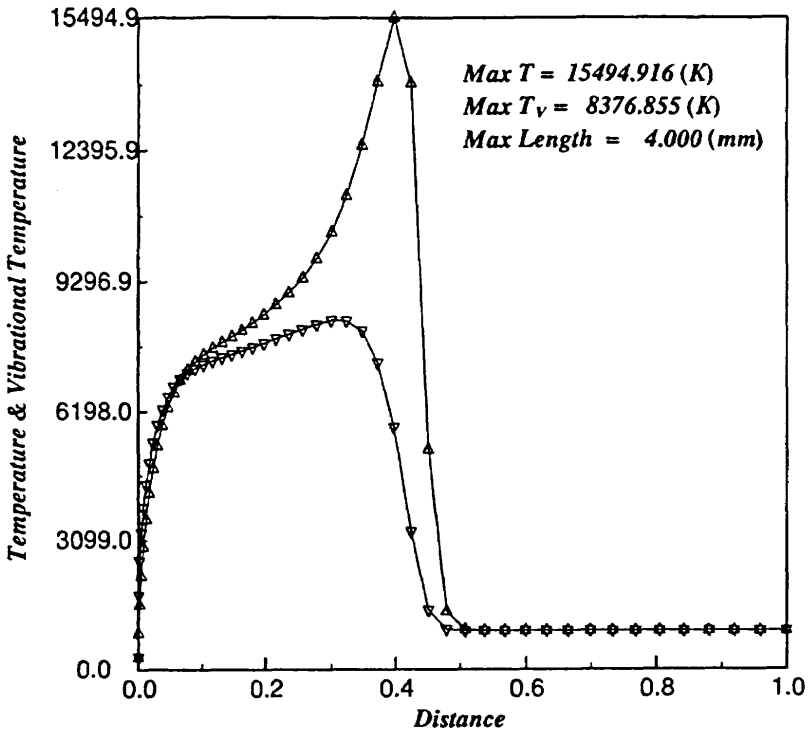

Fig. Problem-I-3-6 : Temperature Distribution along the Stagnation Line

H－１１

Problem I-3 よどみ点流線温度分布（非触媒ケース）

PROBLEM I-4

Species mass fraction distribution along the stagnation streamline

X/L=0 – the sphere surface, L=10 mm

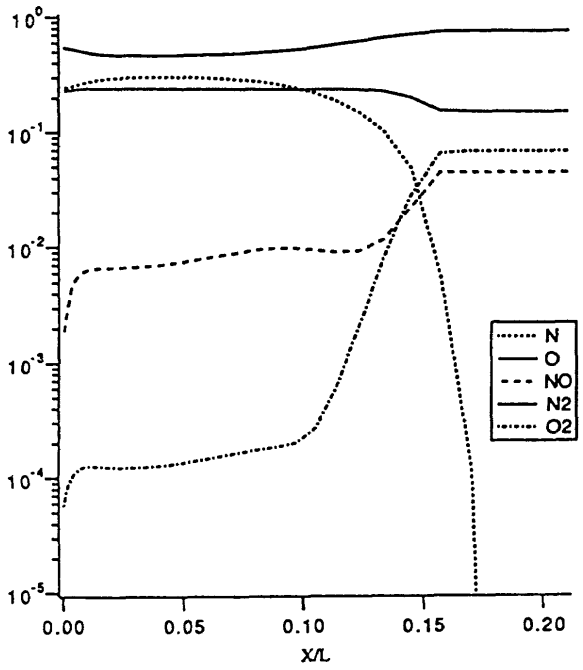

H－1

H－8

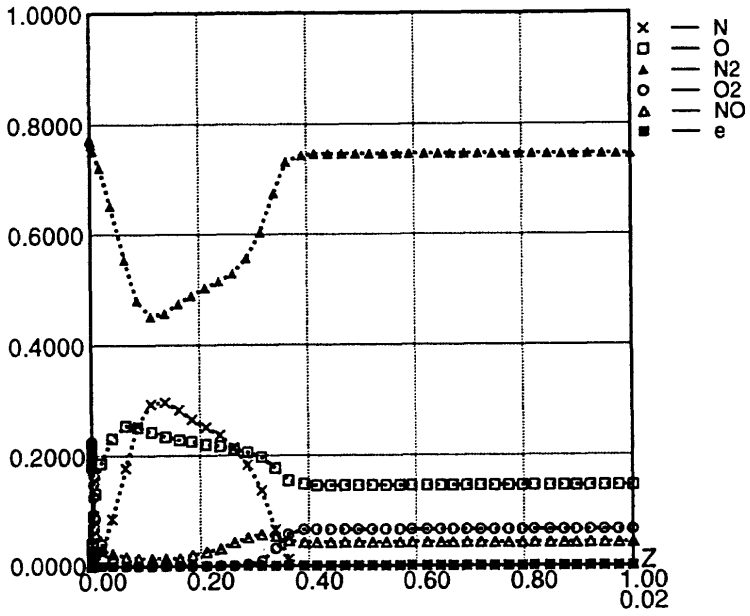

Problem I-4 Sphere Full Catalytic

Mass Fraction along the Stagnation Stream Line

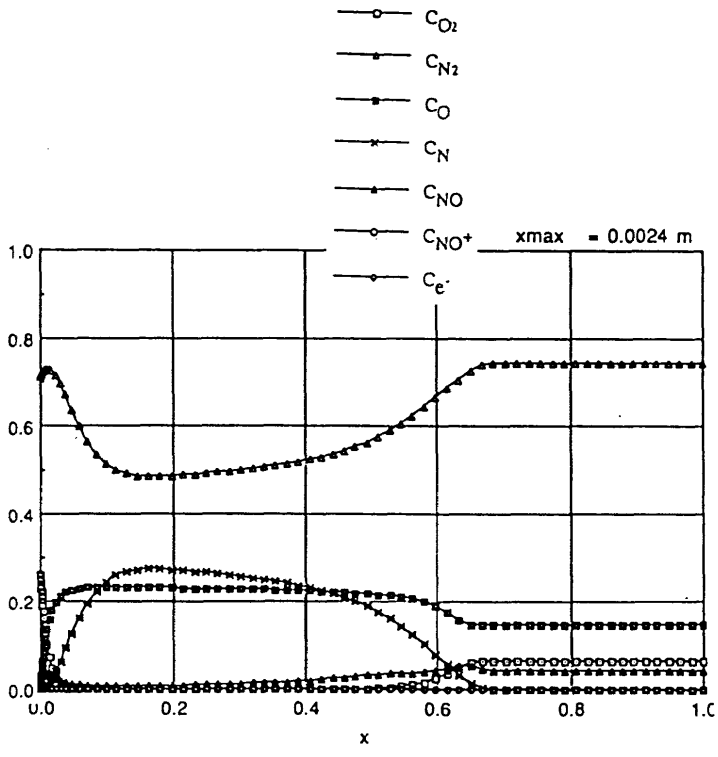

H－3

Problem I-4 よどみ点流線質量分率分布（完全触媒ケース）

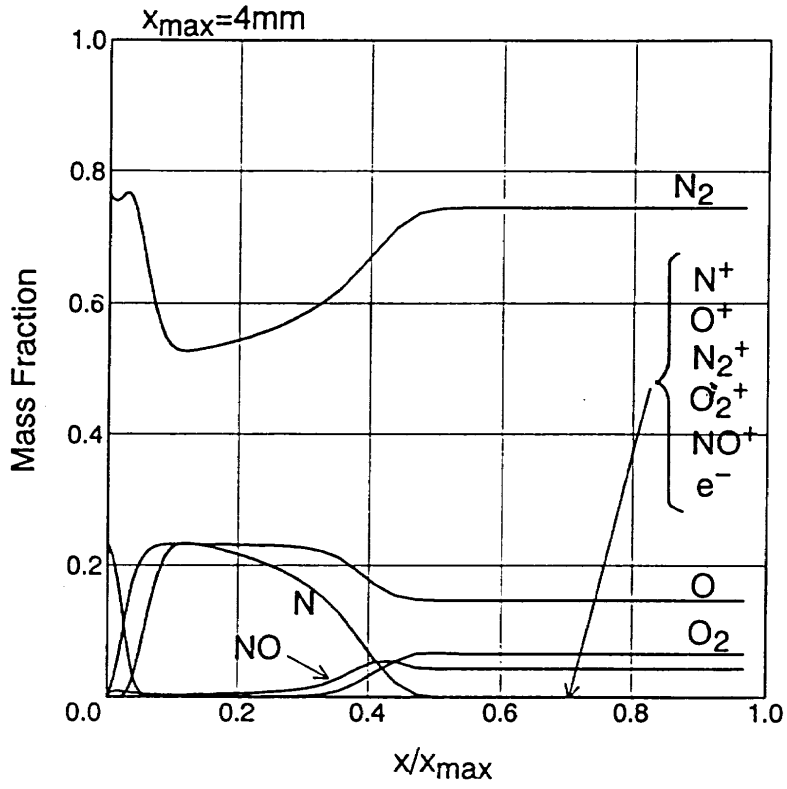

H－１０

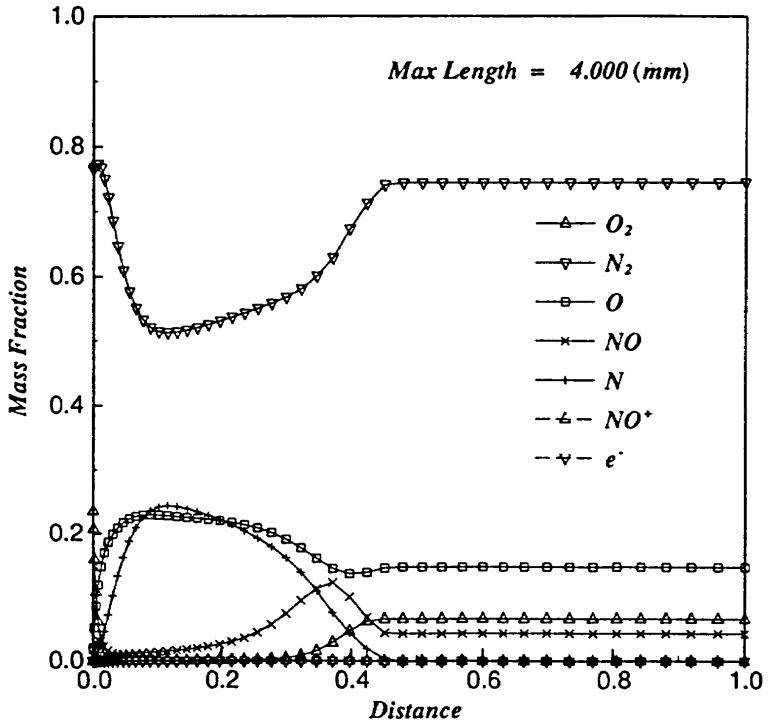

Fig. Problem-I-4-5 : Mass Fraction along the Stagnation Line

H－１１

Problem I-4　よどみ点流線質量分率分布（完全触媒ケース）

PROBLEM I-4

Temperature distribution along the stagnation streamline

X / L = 0 – the sphere surface, L = 10 mm

T- translational/rotational temperature, T_{max} = 14479.48 °K
T_v - vibrational/electronic temperature, $T_{v,max}$ = 9225.59 °K

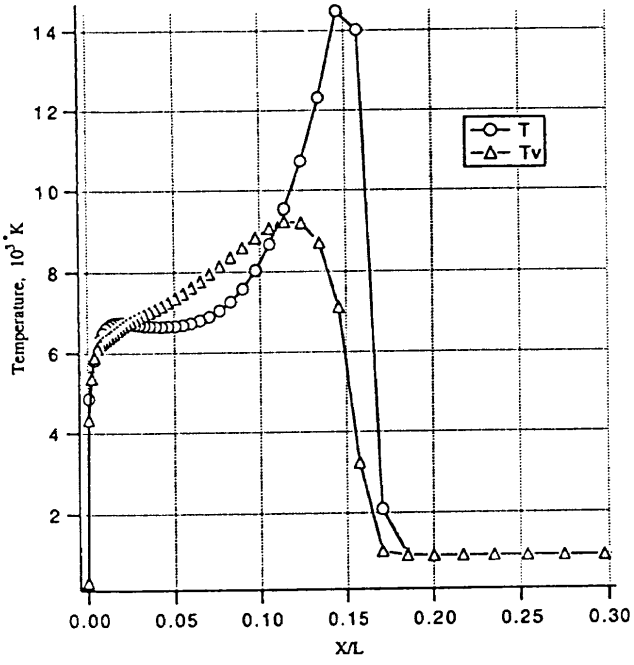

H－1

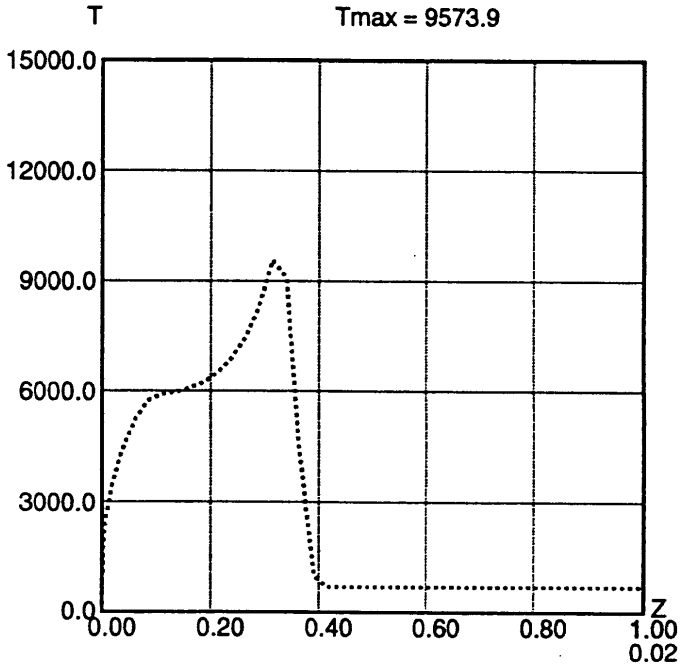

Problem I - 4 -⑥ Sphere
Full Catalytic Case
Stagnation Line Temperature Distribution

H－8

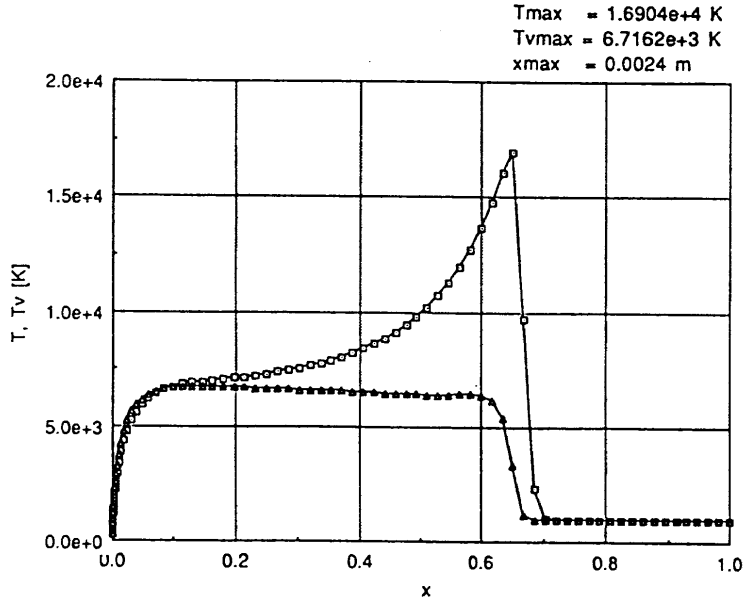

H－3

Problem I-4 よどみ点流線温度分布（完全触媒ケース）

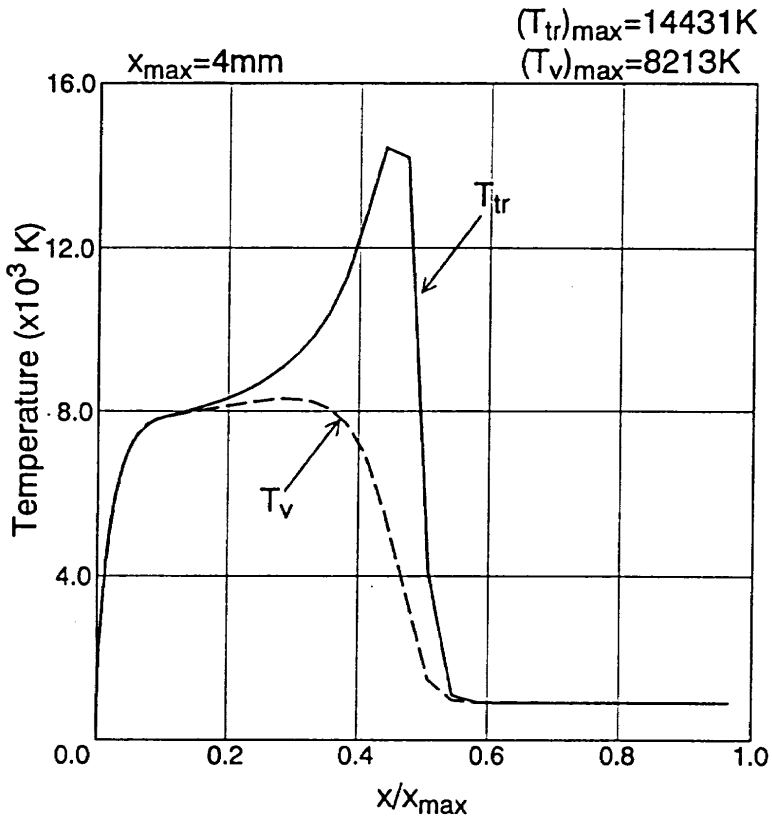

H－１０

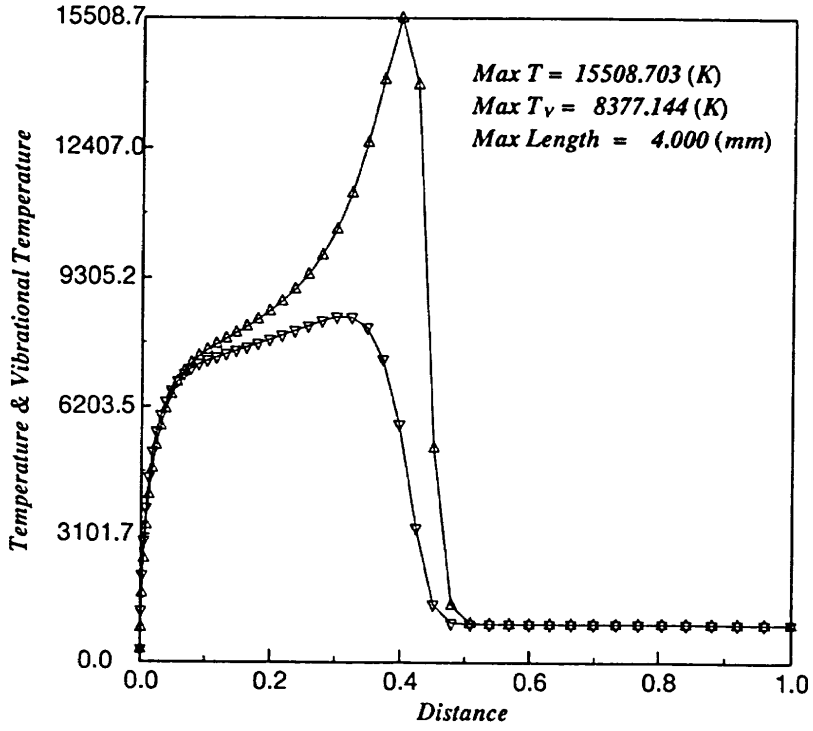

Fig. Problem-I-4-6 : Temperature Distribution along the Stagnation Line

H－１１

Problem I-4　　よどみ点流線温度分布（完全触媒ケース）

Problem I－5, 6

HEG条件

球まわりの流れ

非触媒及び完全触媒ケース

計算条件

V_∞ =5151m/s

T_∞ =708K

ρ_∞ =0.0058kg/m^3

Twall=300K

W_N = 0.0

W_O = 0.0406

W_{N2}= 0.733

W_{O2}= 0.1578

W_{NO}= 0.0688

PROBLEM I-5

Pressure contours

$P/(\rho_\infty U_\infty^2)$, 20 izo-lines on the interval [0,1]

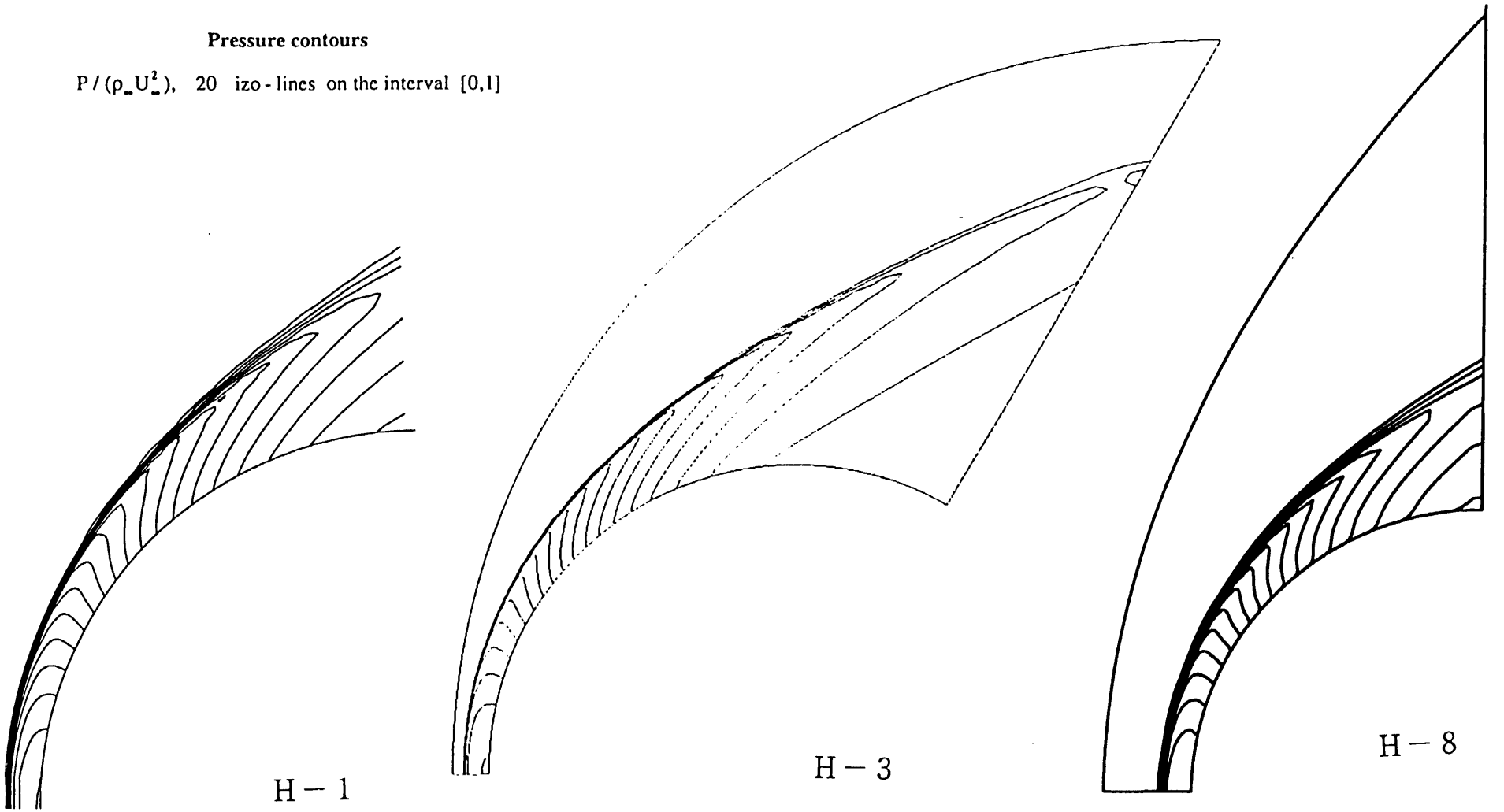

Problem I-5 Sphere Pmax=0.950
Pressure Contour Non catalytic
V_∞=5151m/s T_∞=708K
ρ_∞=0.0058 T_{wall}=300K

Problem I-5 圧力線図

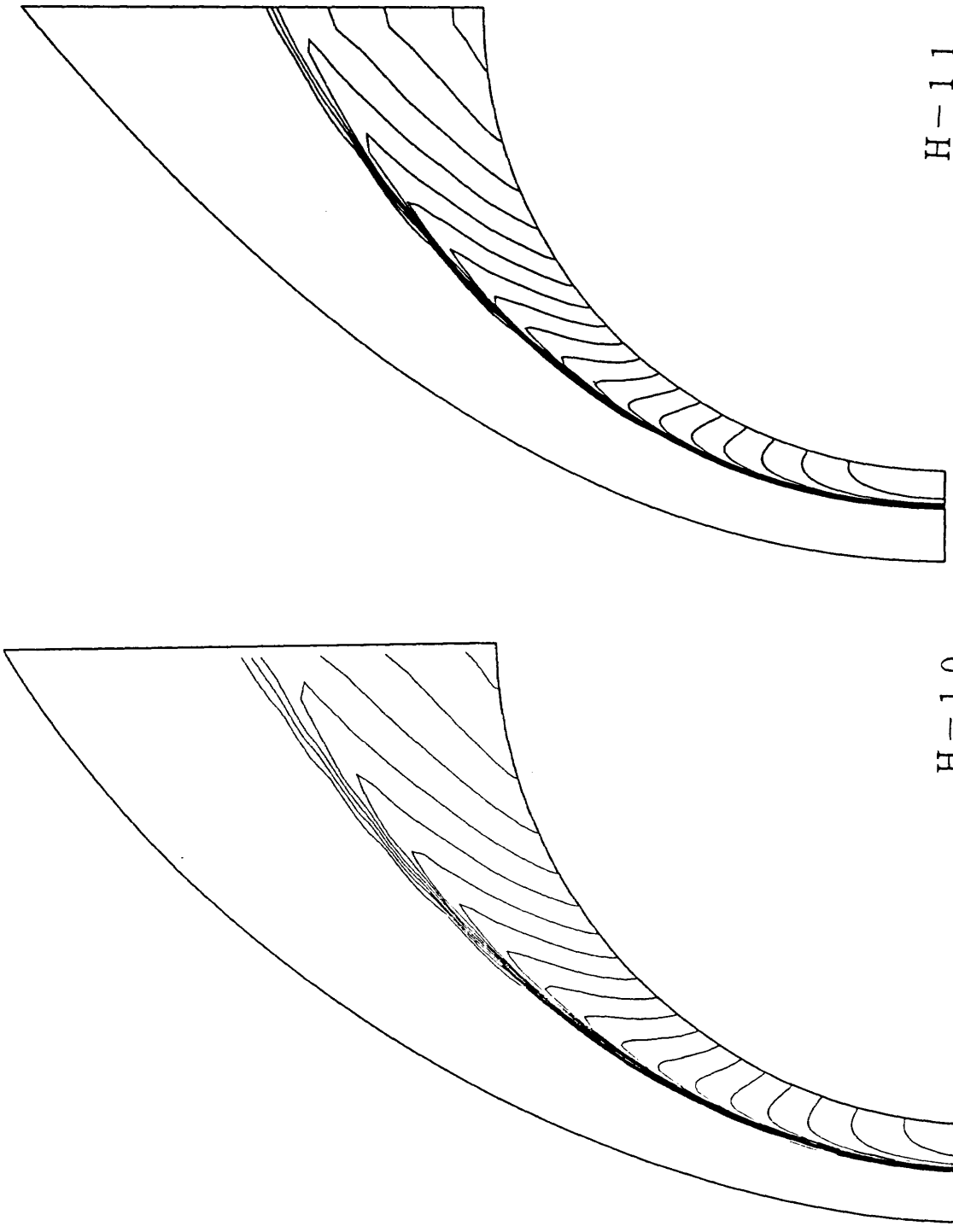

Problem I-5 圧力線図

PROBLEM I-5

Translational/rotational temperature contours

T/T_∞, 20 izo-lines on the interval $[1, \frac{T_{max}}{T_\infty}]$, T_{max} = 11336.3 °K

H－1

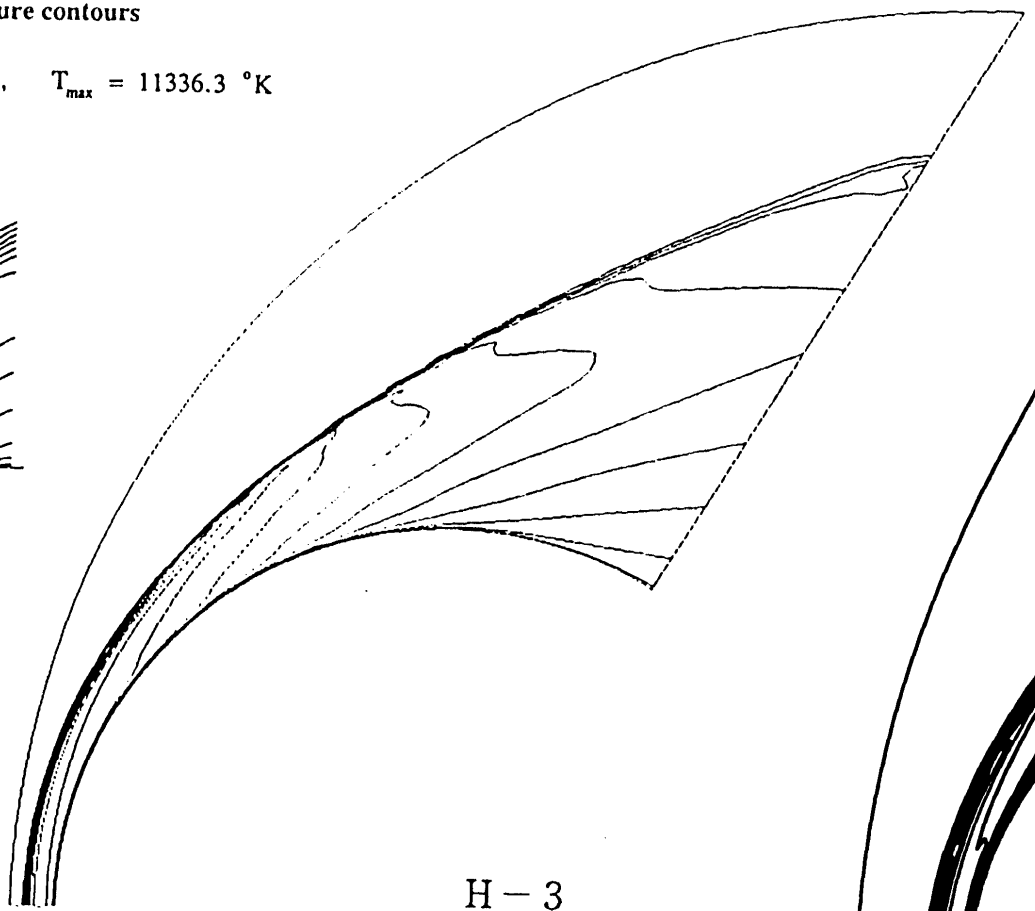

H－3

H－8

Problem I-5 Sphere Tmax=14.080
Temperature Contour Non catalytic
V_∞=5151m/s T_∞=708K
ρ_∞=0.0058 T_{wall}=300K

Problem I-5 等温度線図（並進、回転）

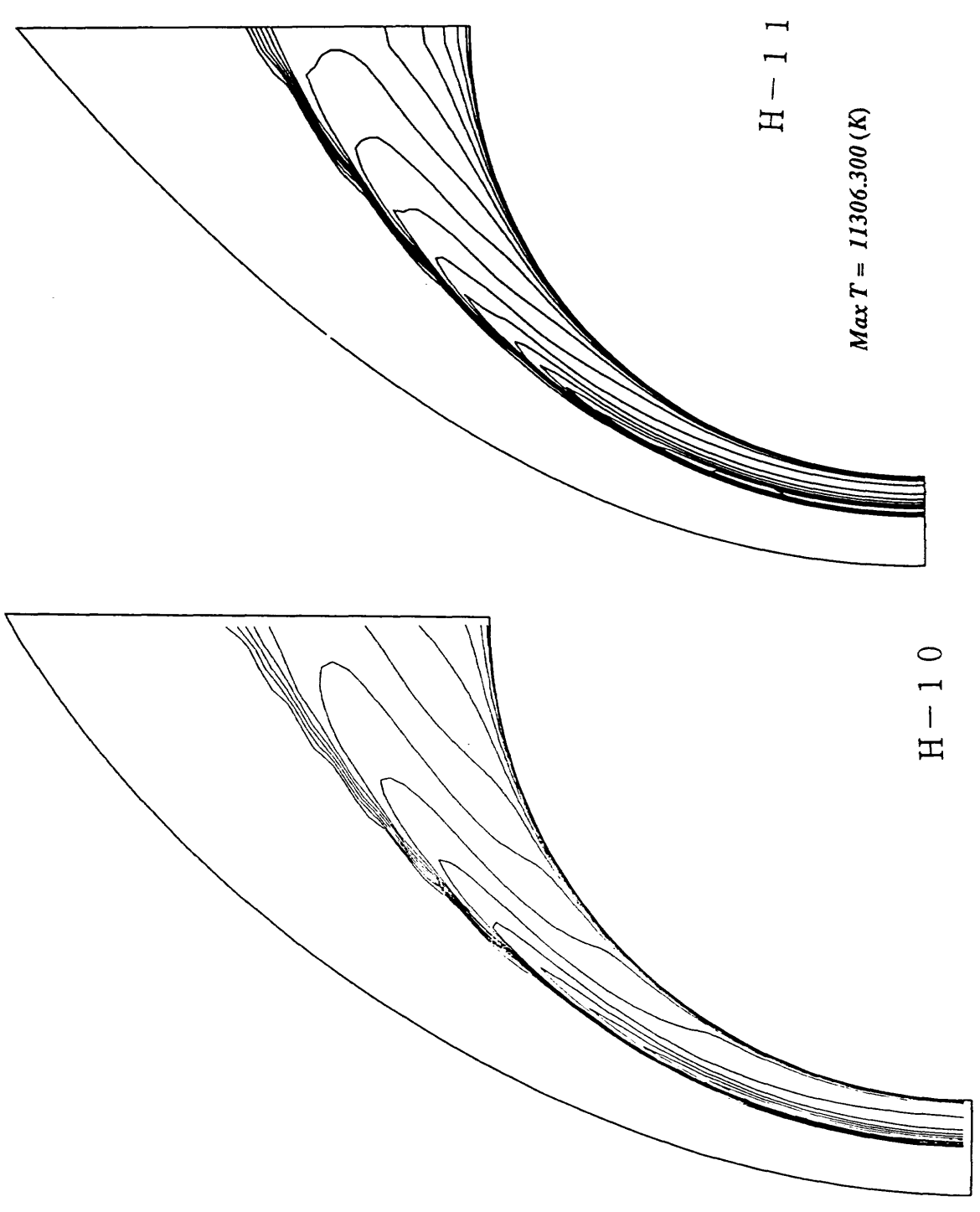

Problem I-5 等温度線図（並進、回転）

PROBLEM I-5

Vibrational temperature contours

T_v / T_∞, 20 izo-lines on the interval $[1, \frac{T_{v,max}}{T_\infty}]$, $T_{v,max} = 6925.3$ °K

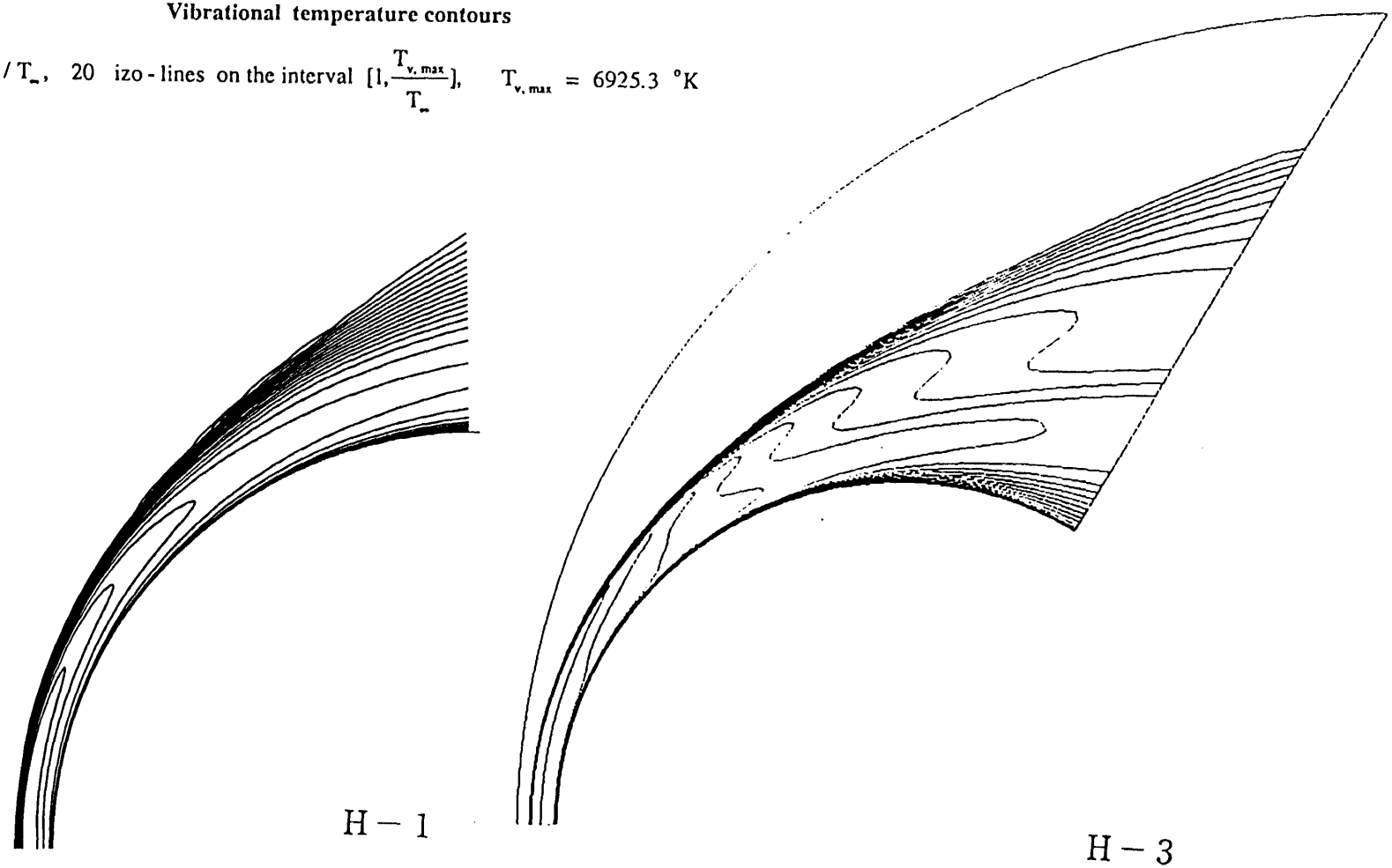

Problem I-5　等温度線図（振動）

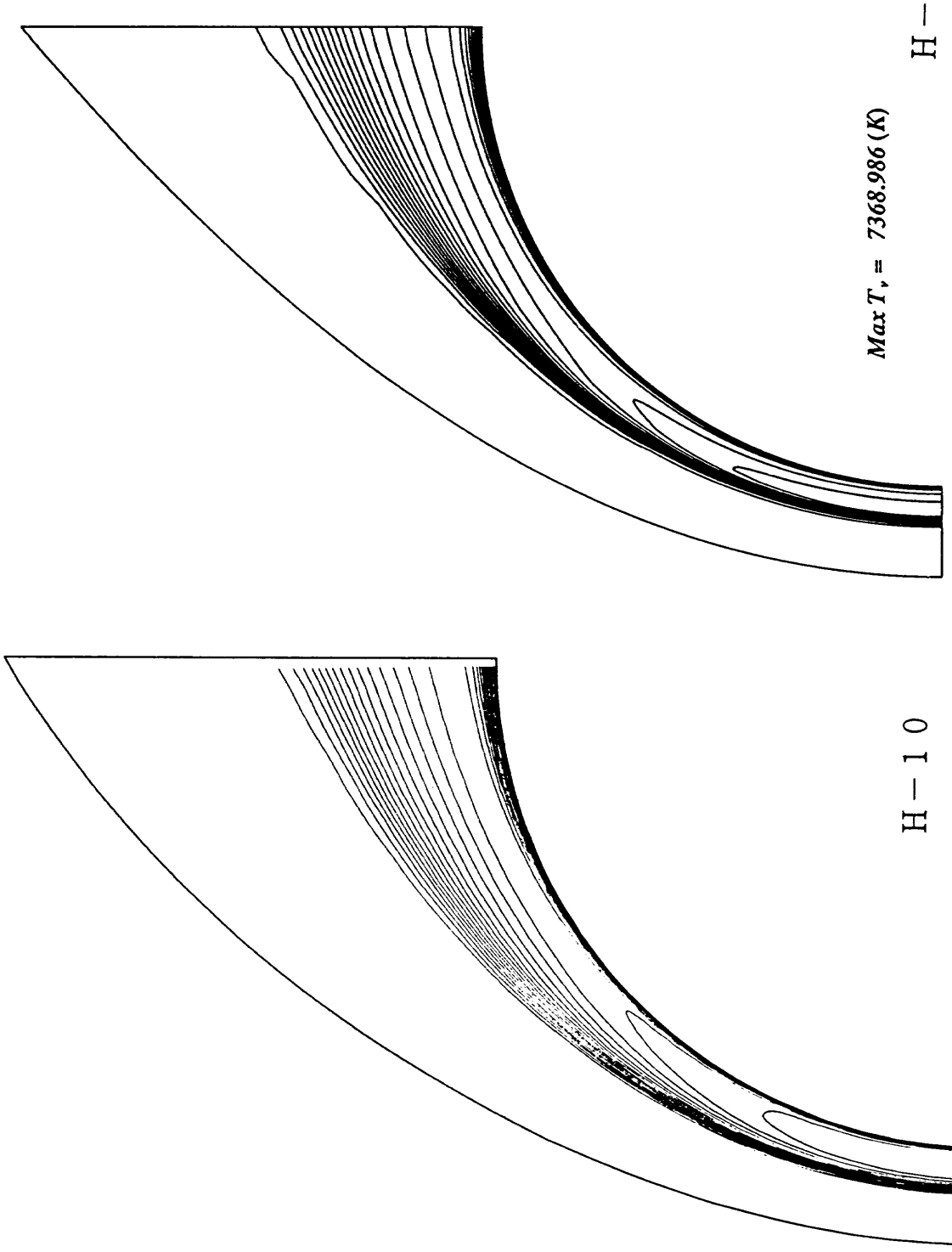

Problem I-5 等温度線図（振動）

PROBLEM I-5

Pressure distribution along the sphere surface

$P_{max} / (\rho_\infty U_\infty^2) = 0.9533$

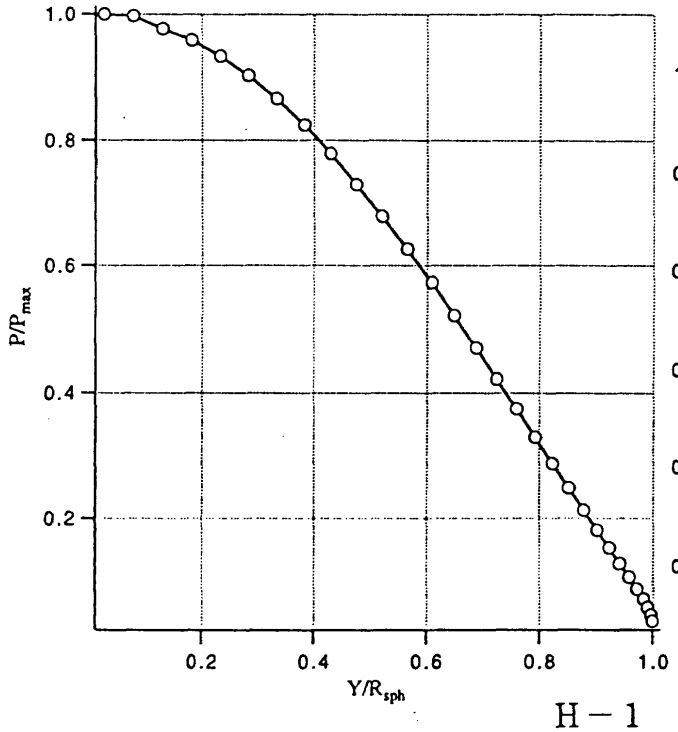

H－1

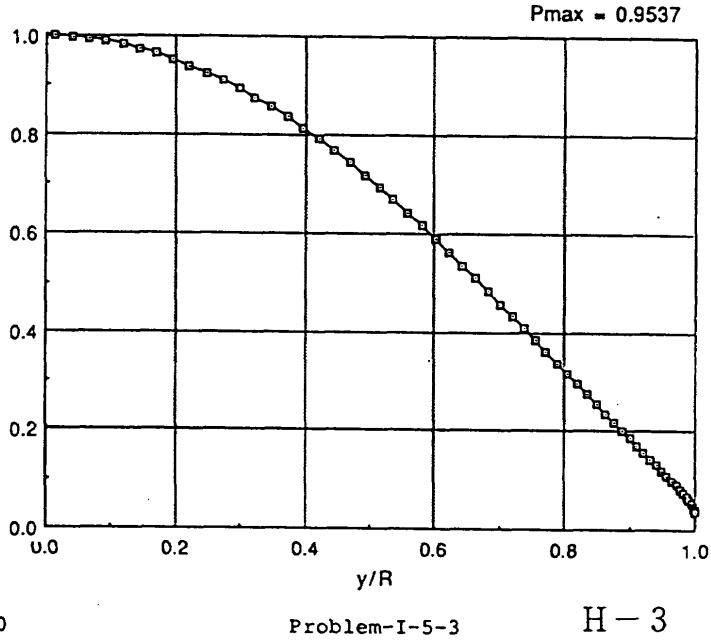

H－3

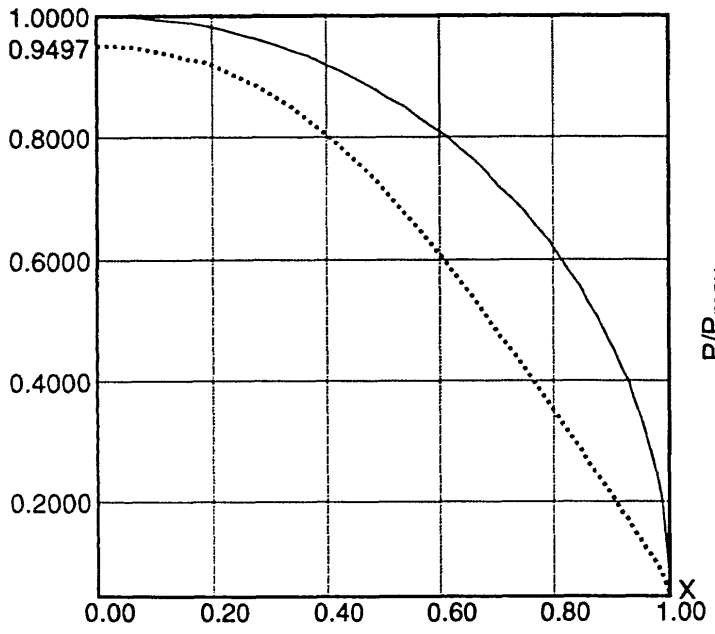

Problem I-5 Sphere H－8
Non Catalytic Case
Pressure Distribution

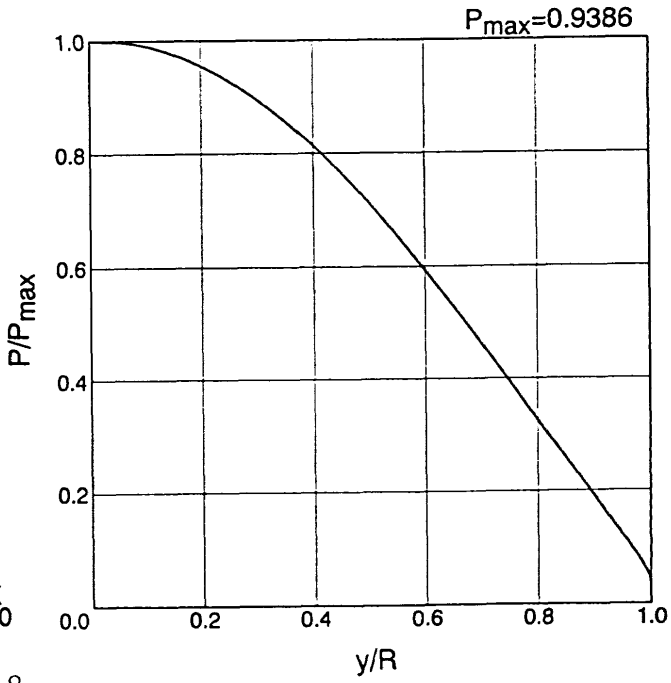

H－10

Problem I-5 表面圧力分布

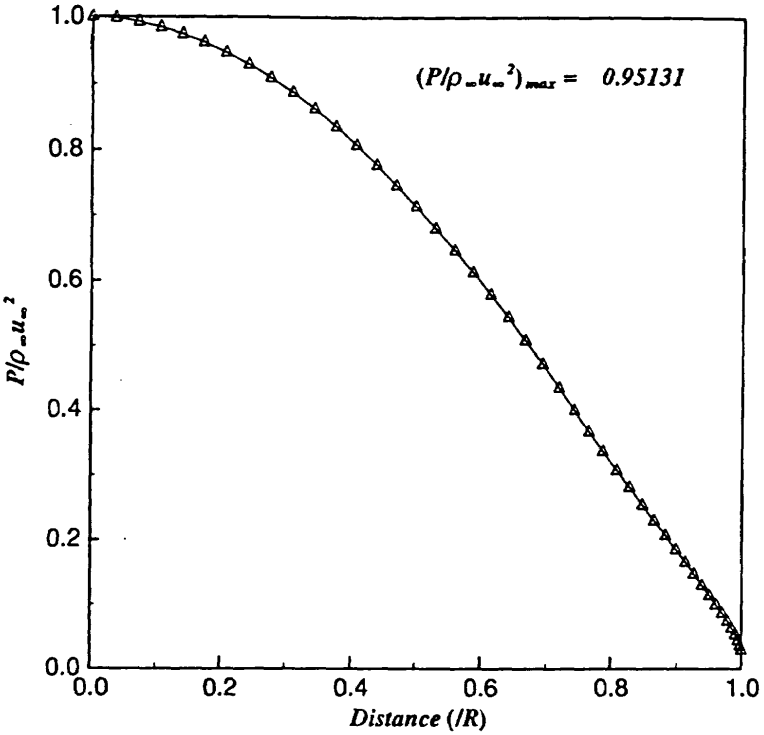

Fig. Problem-I-5-3 : Pressure Distribution along the Surface

H－11

Problem I-5 表面圧力分布

PROBLEM I-5,6

Heat flux distribution along the sphere

$Q_{max}^{non-cat} = 0.607 \times 10^7$ w / m^2, $Q_{max}^{full-cat} = 0.578 \times 10^7$ w / m^2

$Q_{max} = 0.607 \times 10^7$ w / m^2

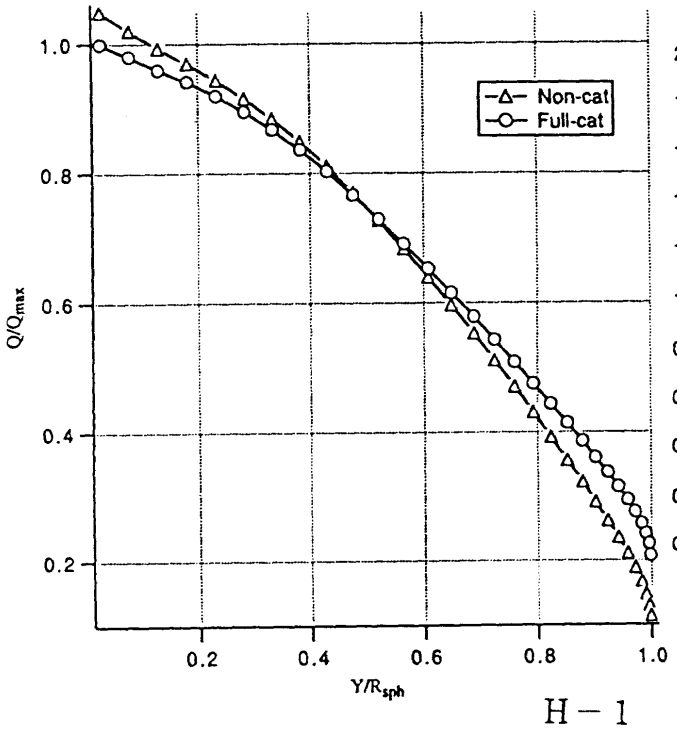

H－1

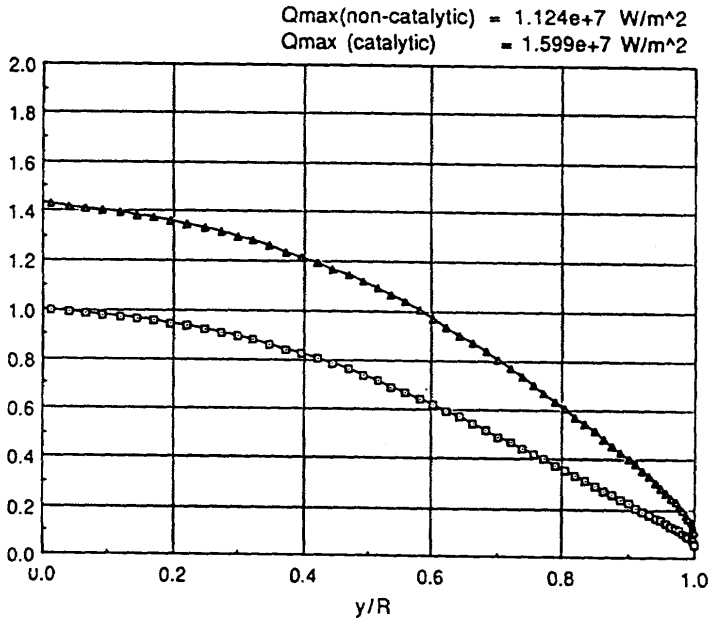

Problem-I-5-4 H－3

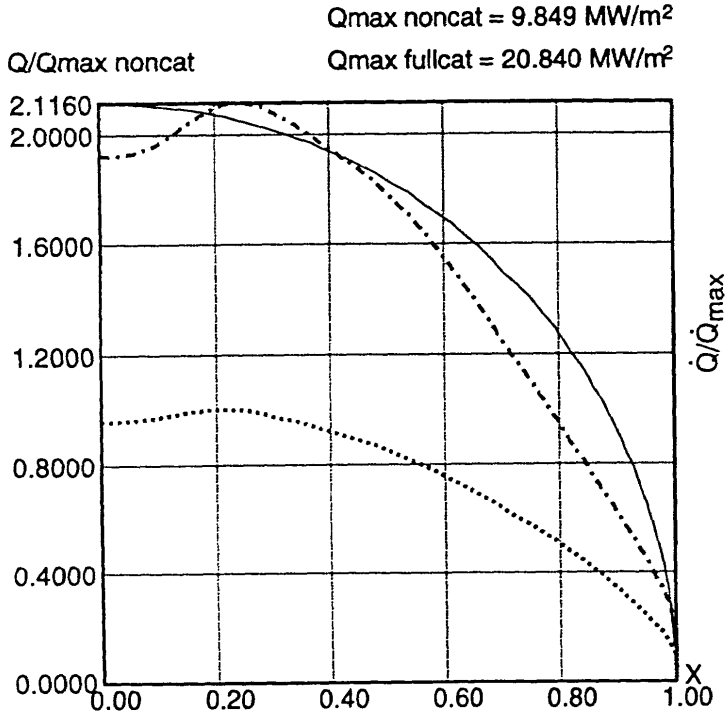

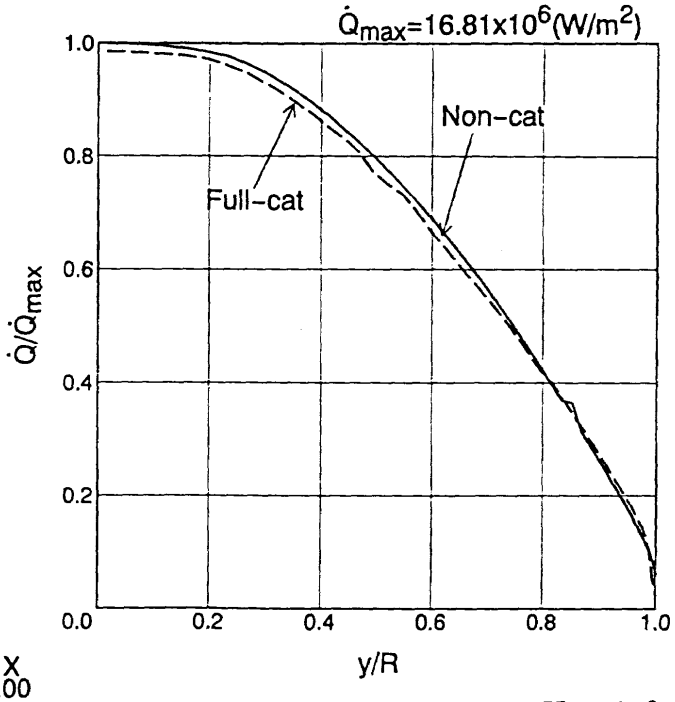

H－10

H－8 Problem I-4,5 Sphere Heat Transfer Distribution

Problem I-5,6 表面熱流束分布

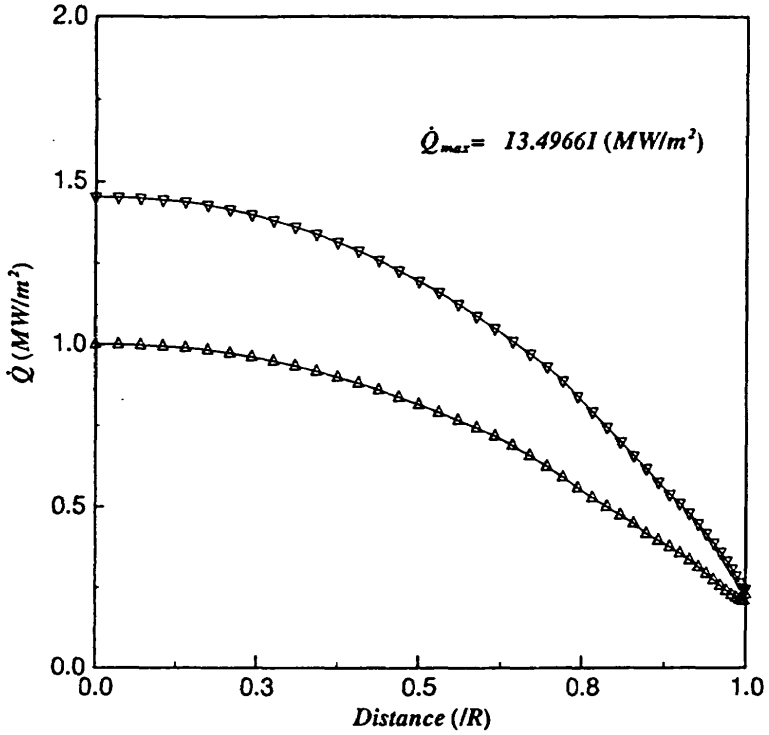

Fig. Problem-I-5-4 : Heat Flux Distribution along the Surface

H－11

Problem I-5,6 表面熱流束分布

PROBLEM I-5

Species mass fraction distribution along the stagnation streamline

X / L = 0 – the sphere surface, L = 10 mm

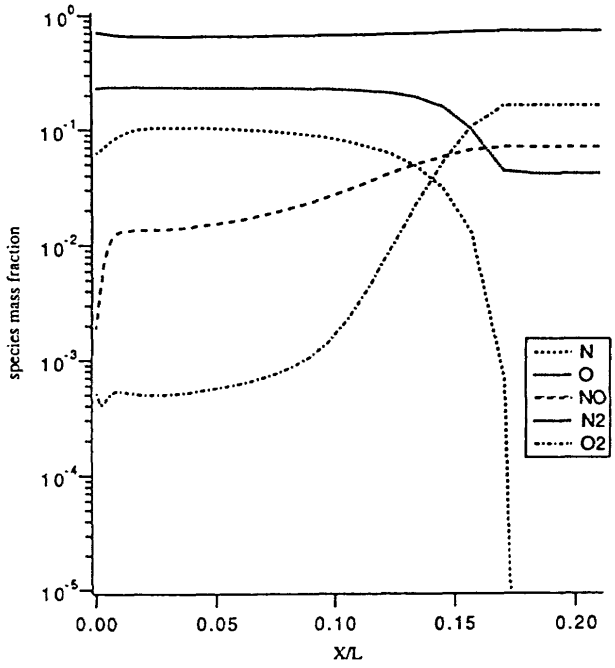

H－1

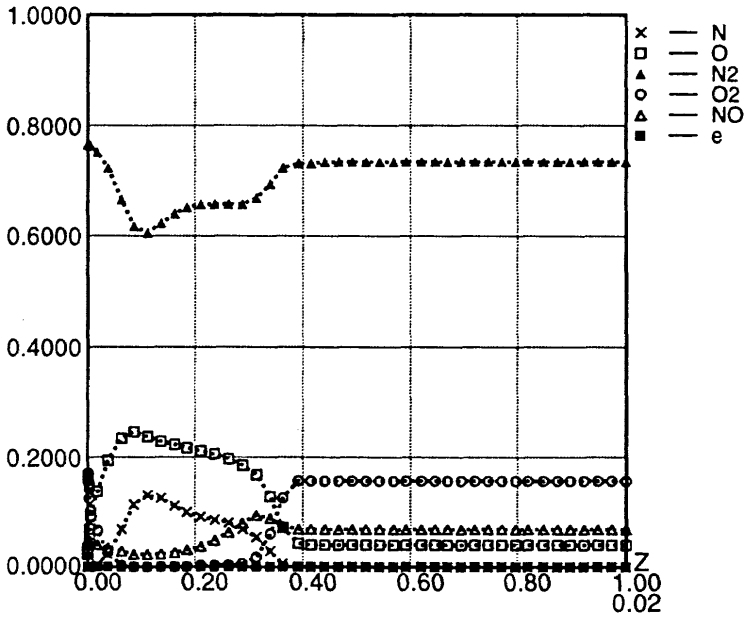

Problem I - 5 Sphere Non Catalytic

Mass Fraction along the Stagnation Stream Line

H－8

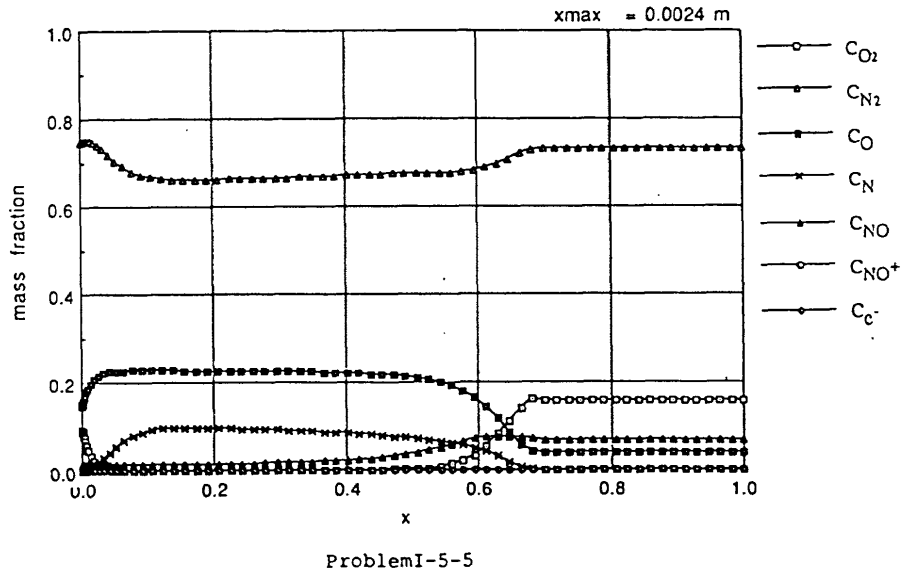

H－3

Problem I-5 よどみ点流線質量分率分布（非触媒ケース）

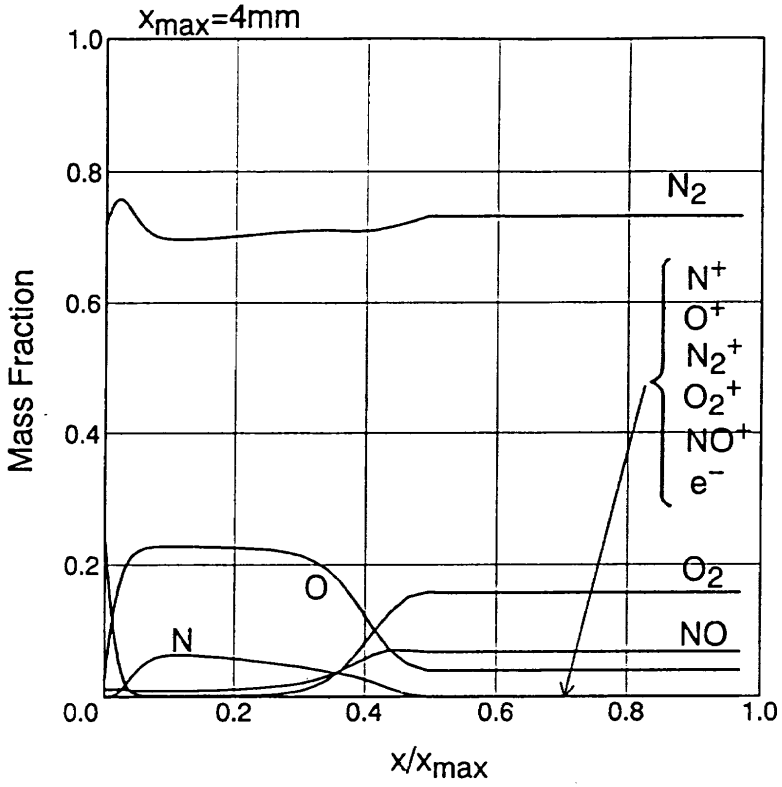

H－10

Problem I-5 よどみ点流線質量分率分布（非触媒ケース）

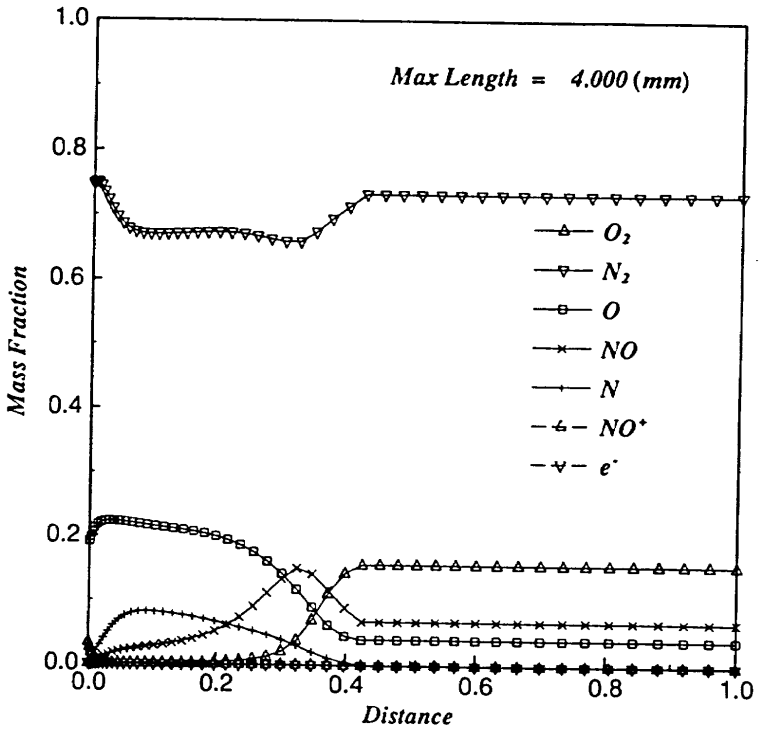

Fig. Problem-I-5-5 : Mass Fraction along the Stagnation Line

H－11

PROBLEM I-5

Temperature distribution along the stagnation streamline

X / L = 0 – the sphere surface, L = 10 mm

T- translational/rotational temperature, T_{max} = 10716.32 °K
T_v - vibrational/electronic temperature, $T_{v,max}$ = 6925.33 °K

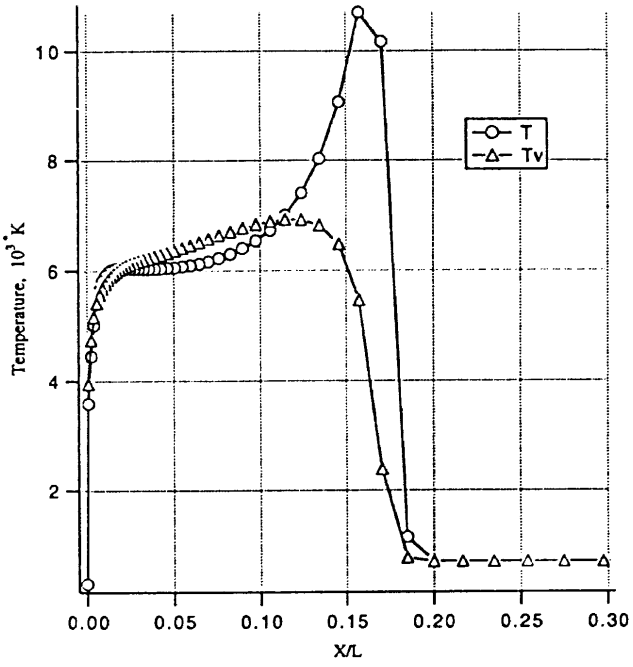

H－1

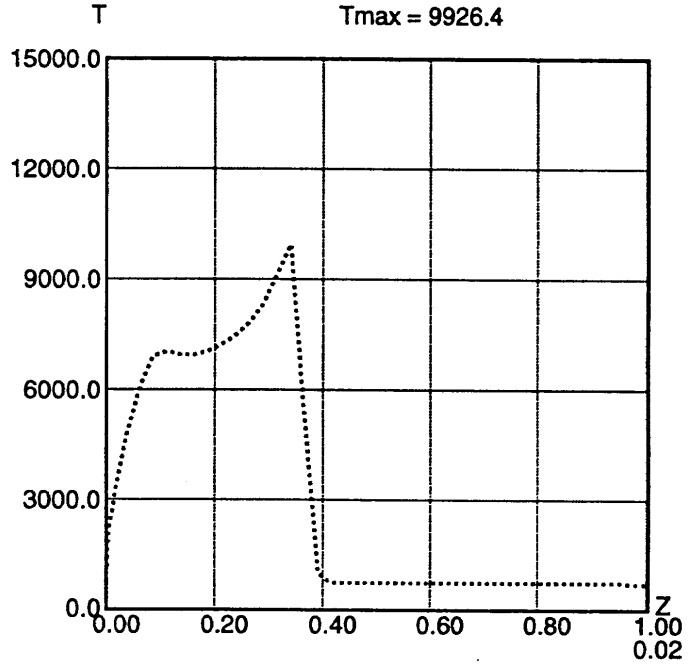

H－8 Problem I - 5 -⑥ Sphere
Non Catalytic Case
Stagnation Line Temperature Distribution

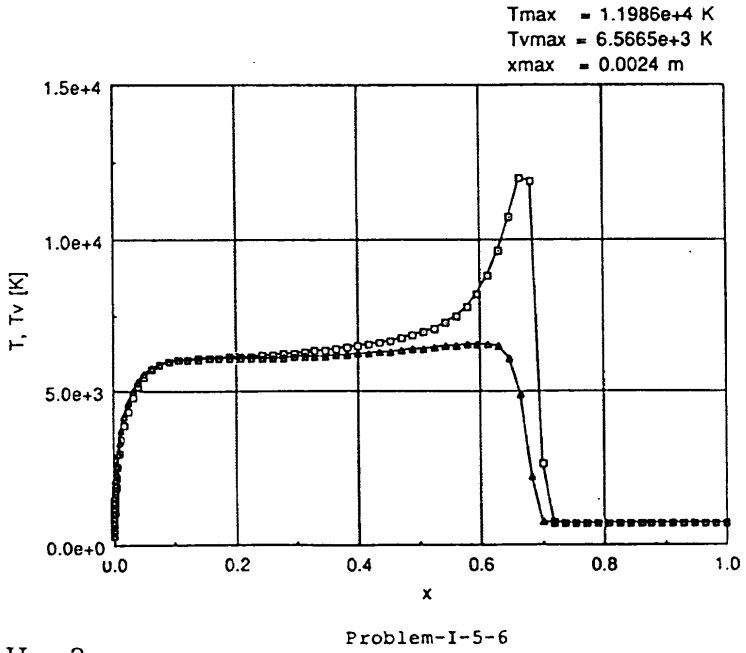

H－3

Problem I-5 よどみ点流線温度分布（非触媒ケース）

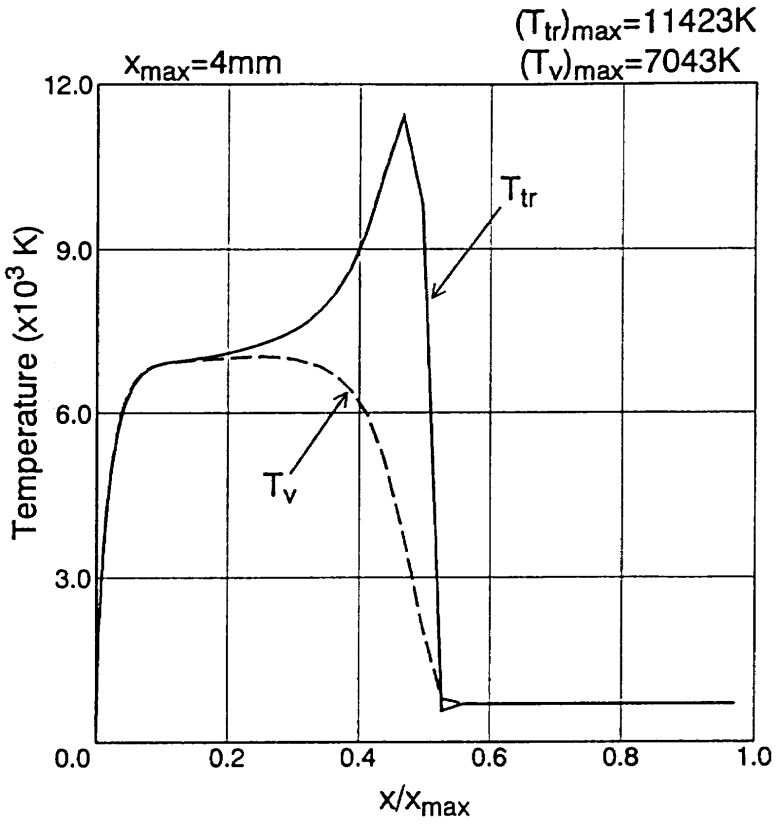

H－１０

Problem I-5　よどみ点流線温度分布（非触媒ケース）

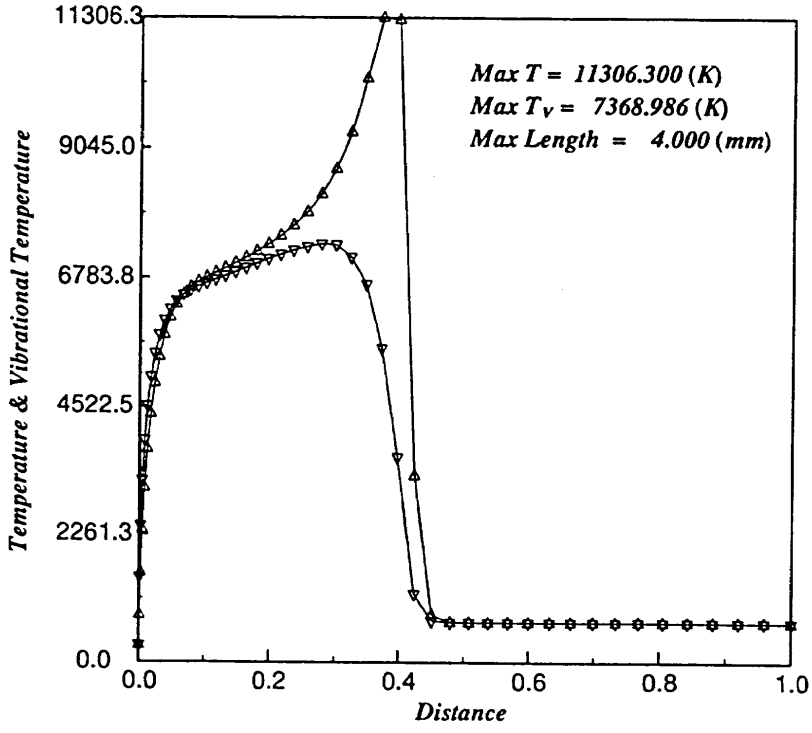

Fig. Problem-I-5-6 : Temperature Distribution along the Stagnation Line

H－１１

PROBLEM I-6

Species mass fraction distribution along the stagnation streamline

X/L=0 – the sphere surface, L=10 mm

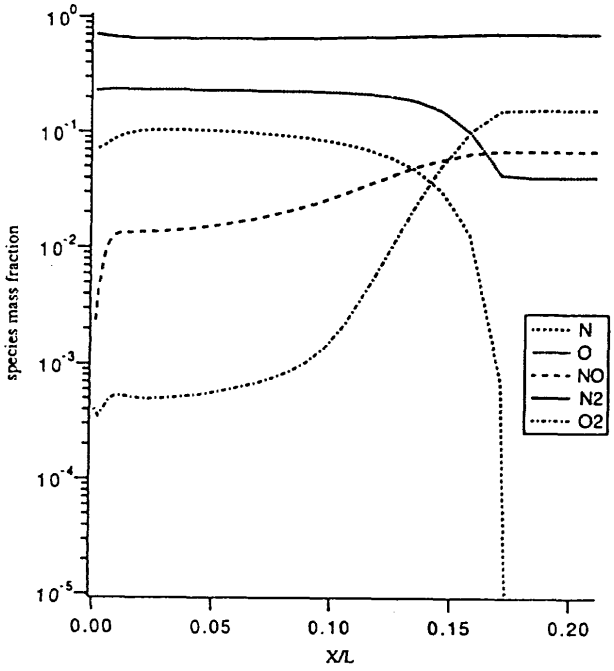

H－1

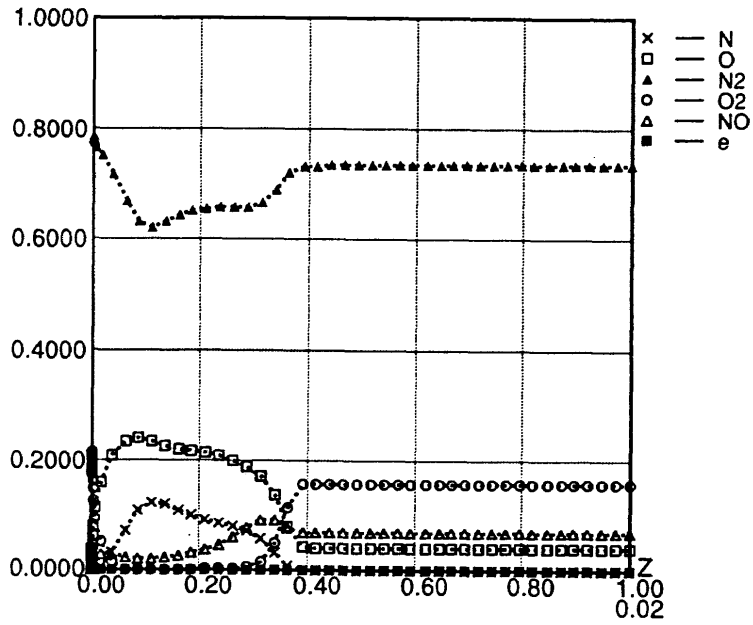

Problem I - 6 Sphere Full Catalytic H－8

Mass Fraction along the Stagnation Stream Line

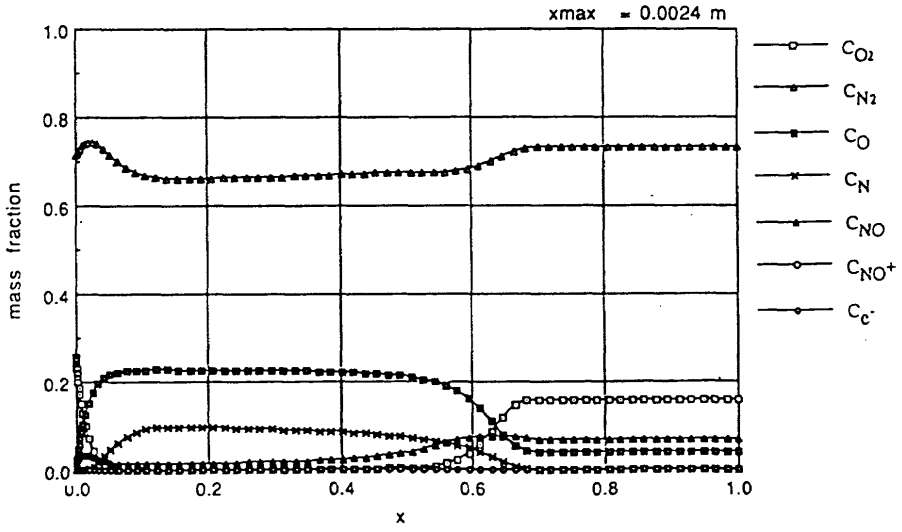

ProblemI-6-5

H－3

Problem I-6 よどみ点流線質量分率分布（完全触媒ケース）

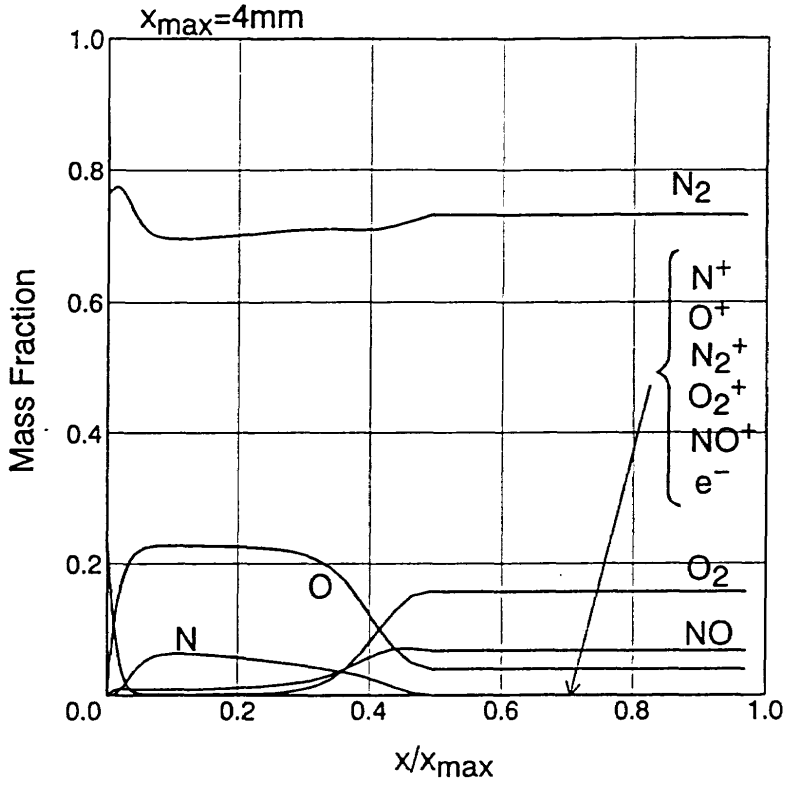

H－１０

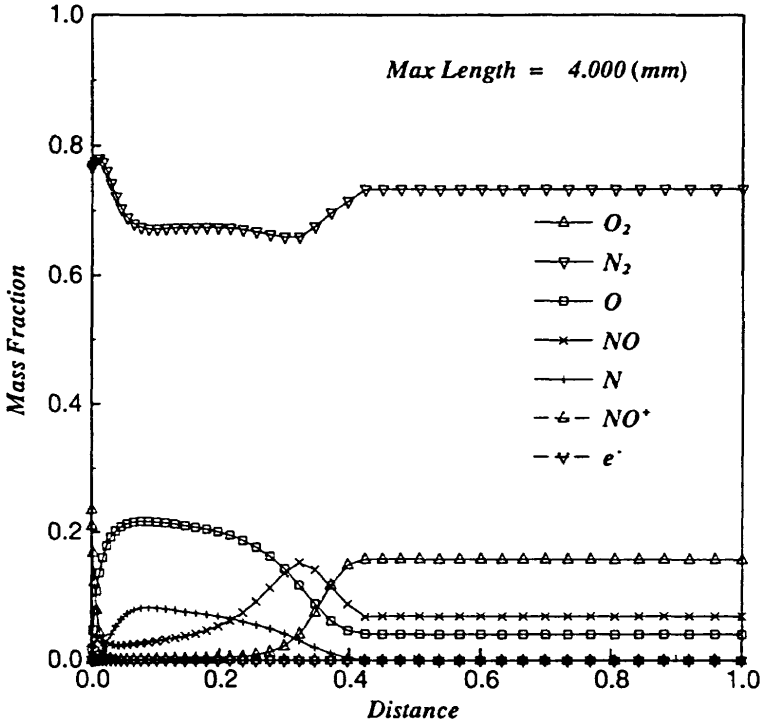

Fig. Problem-I-6-5 : Mass Fraction along the Stagnation Line

H－１１

Problem I-6　よどみ点流線質量分率分布（完全触媒ケース）

PROBLEM I-6

Temperature distribution along the stagnation streamline

X/L=0 - the sphere surface, L=10 mm

T- translational/rotational temperature, T_{max} = 10677.58 °K
T_v - vibrational/electronic temperature, $T_{v,max}$ = 6925.37 °K

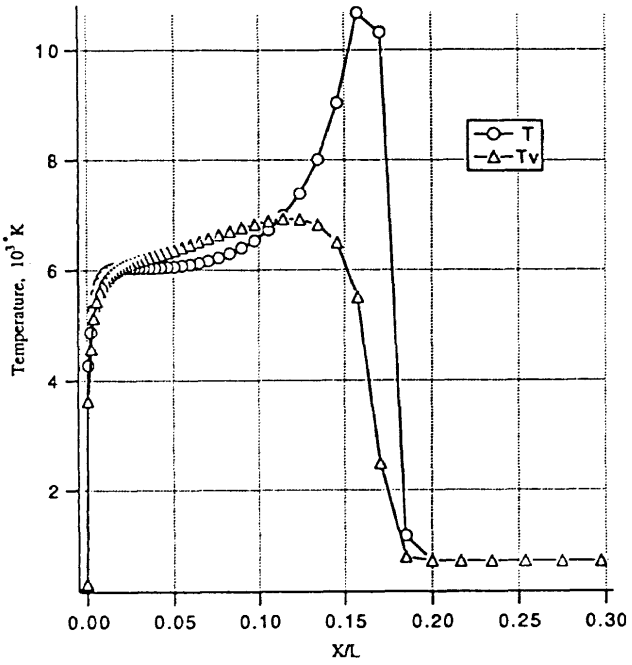

H－1

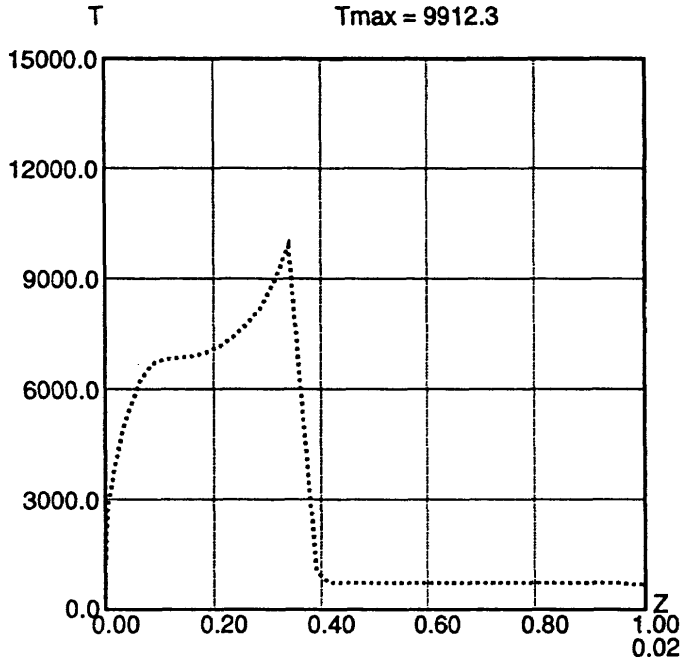

Problem I - 6 -⑥ Sphere
Full Catalytic Case
Stagnation Line Temperature Distribution

H－8

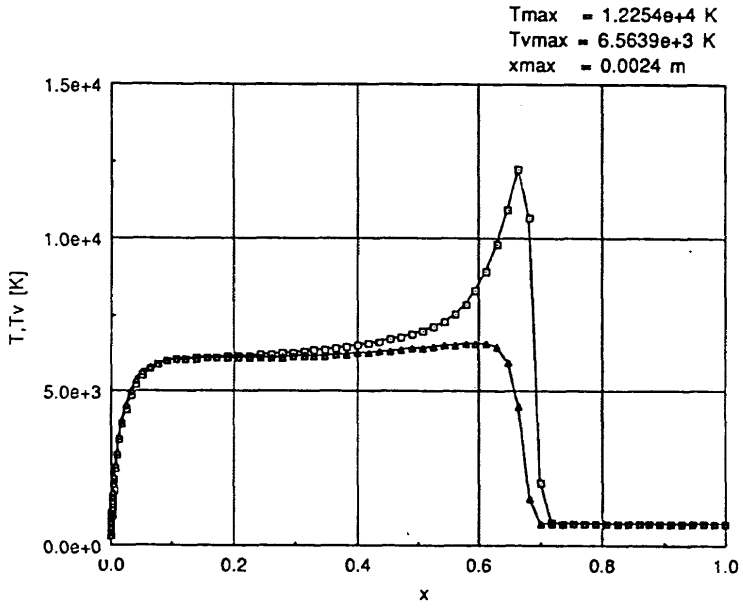

H－3

Problem I-6 よどみ点流線温度分布（完全触媒ケース）

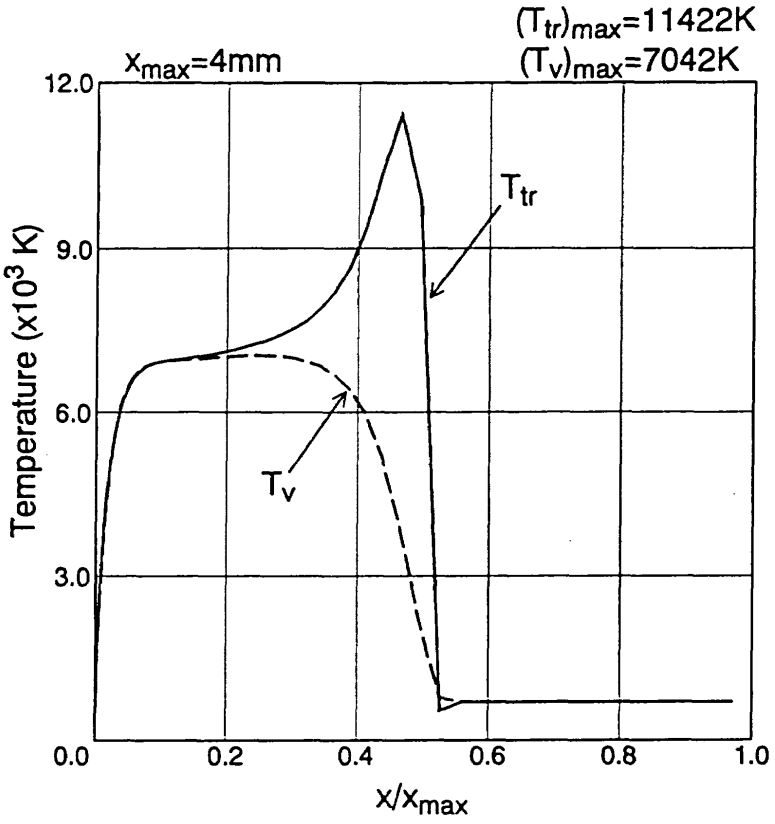

H－１０

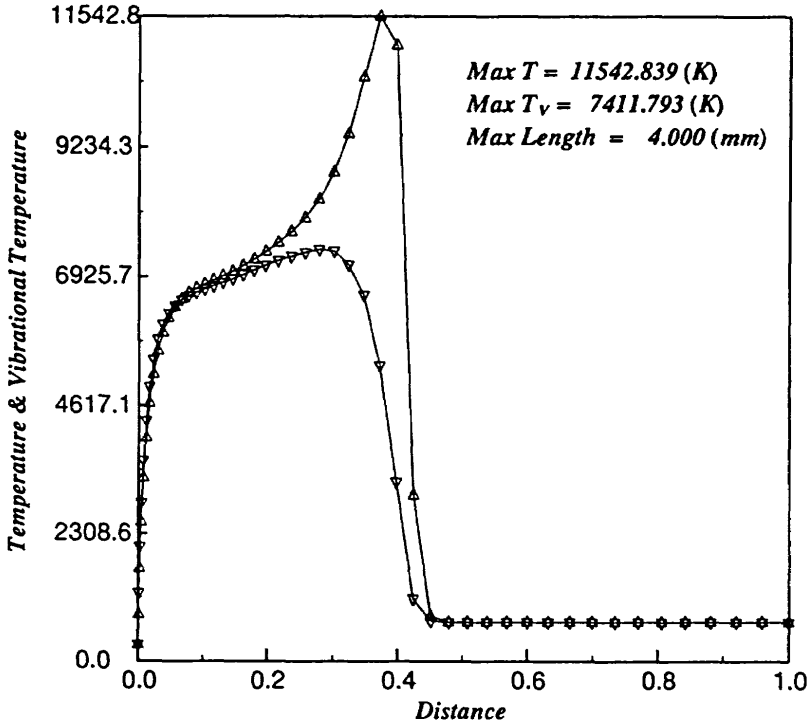

Fig. Problem-I-6-6 : Temperature Distribution along the Stagnation Line

H－１１

Problem I-6　よどみ点流線温度分布（完全触媒ケース）

Problem Ⅱ－1

OREX

高度　90km

非触媒ケース

計算条件

V_∞ =7450m/s　　W_{N2}= 0.79

T_∞ =186.9K　　W_{O2}= 0.21

P_∞ =0.169N/m^2

Twall=540K

Problem II-1 OREX 圧力等高図

Problem II-1 OREX 圧力線図

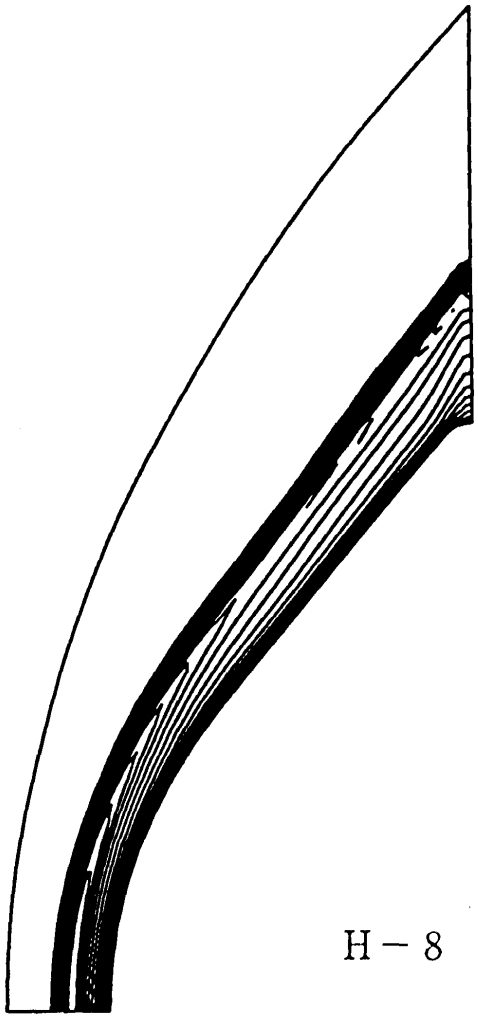

Problem II-1 OREX Tmax=111.812
Temperature Contour Non catalytic
U_∞=7450m/s T_∞=186.9K
P_∞=0.169N/m^2 T_{wall}=540K

Problem II-1 OREX 等温度線図（並進、回転）

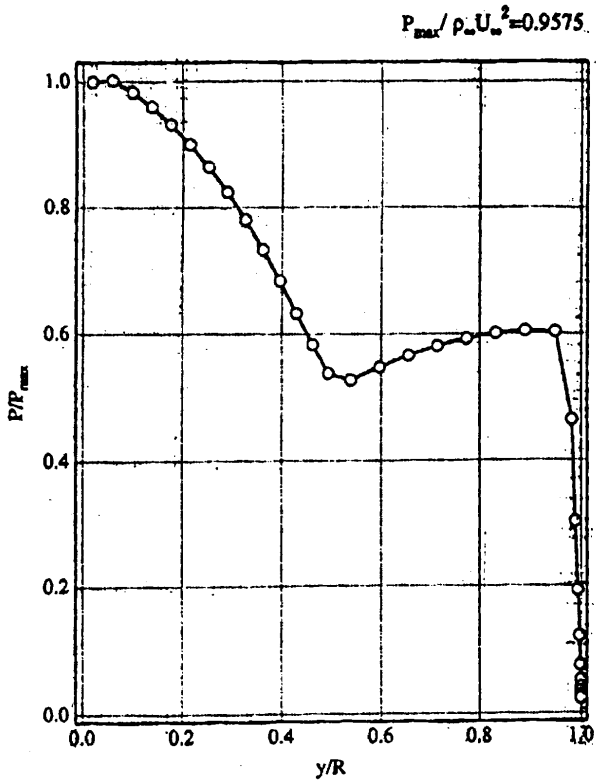

H－2

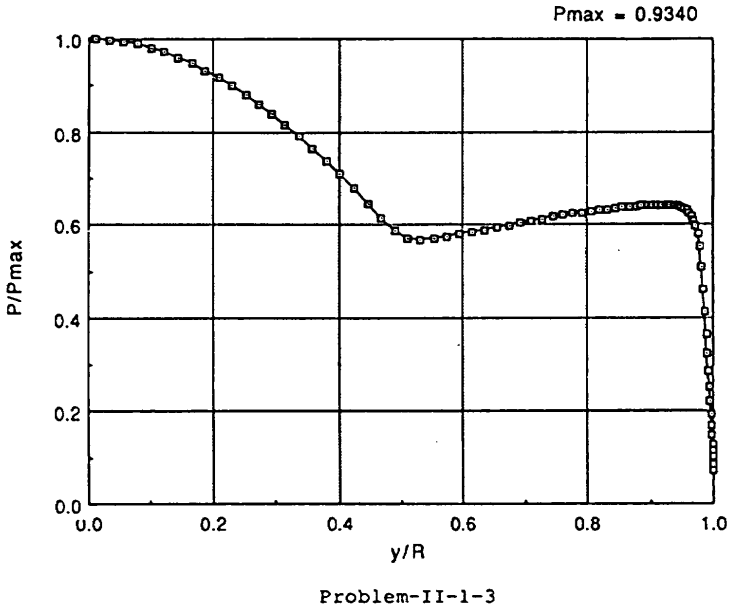

H－3

PROBLEM II-1-3

Pressure distribution

$P_{max}/(\rho_\infty U_\infty^2)$ = 0.9395

Length = 2.400 [m]

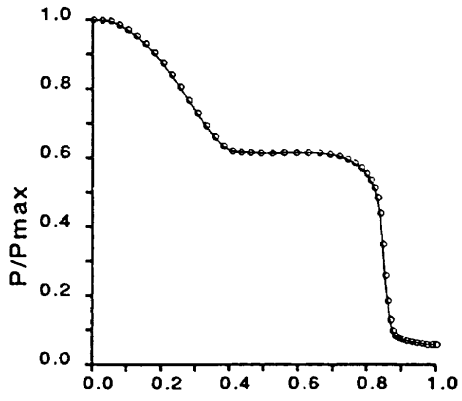

Problem-II-1-③

Pressure Distribution along the Body Surface

H－5

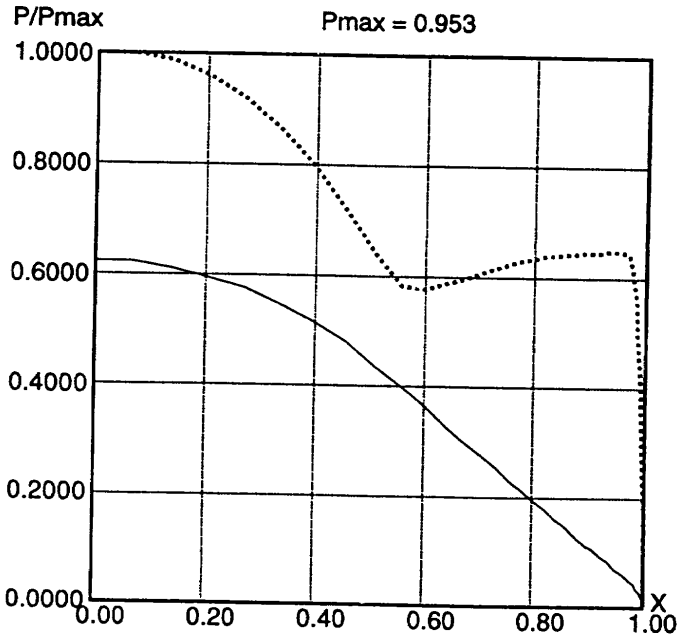

Problem II - 1 OREX
Pressure Distribution

H－8

Problem II-1 OREX 表面圧力分布

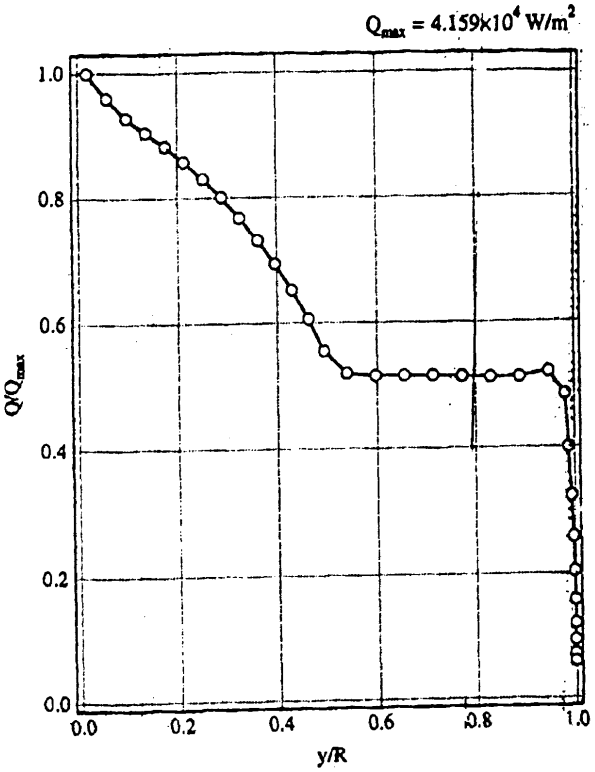

H－2

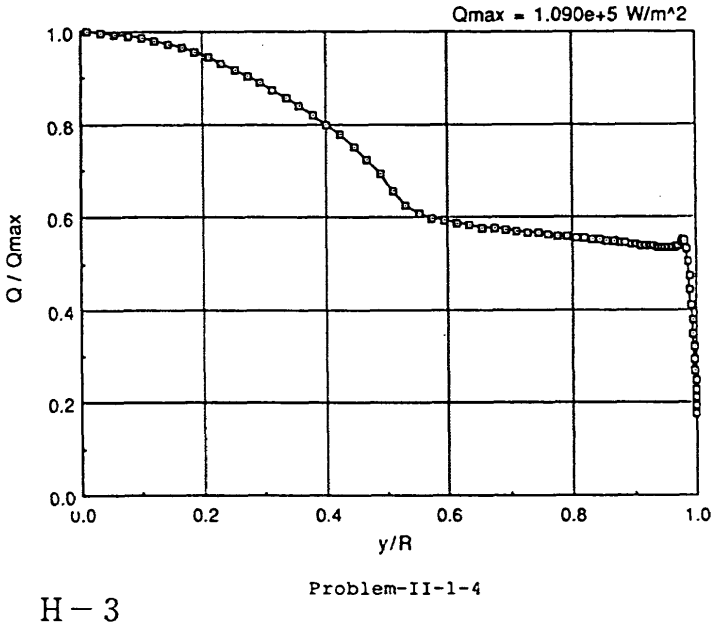

H－3

PROBLEM II-1-4

Heat flux distribution

Problem II-1 OREX 表面熱流束分布

Q_{max} = 26284 [W/m^2]
Length = 2.400 [m]

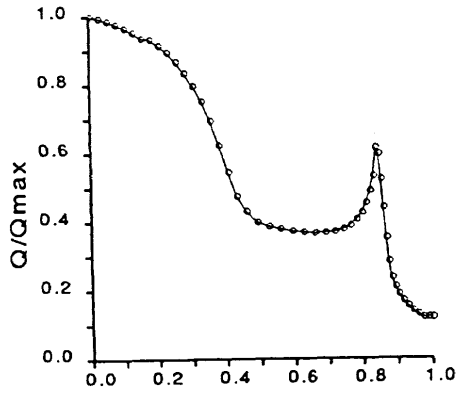

Problem-II-1-④

Heat Transfer Distribution along the Body Surface

H－5

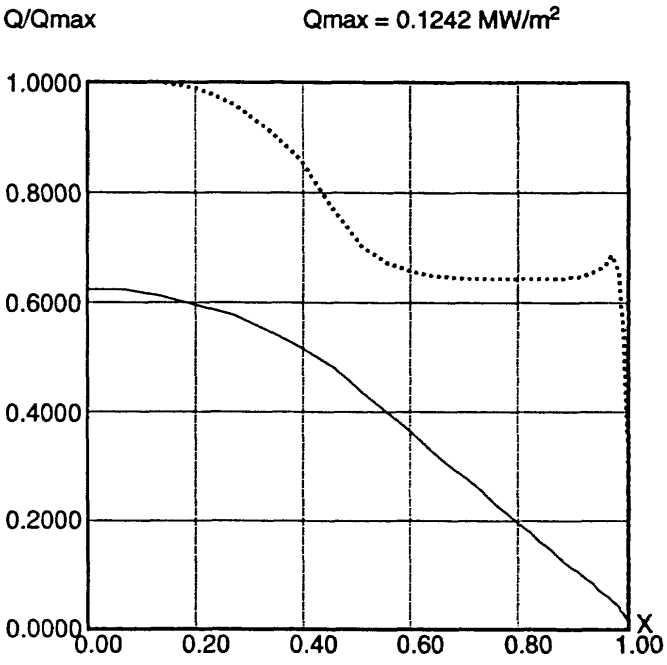

H－8

Problem II - 1 OREX

Heat Transfer Distribution

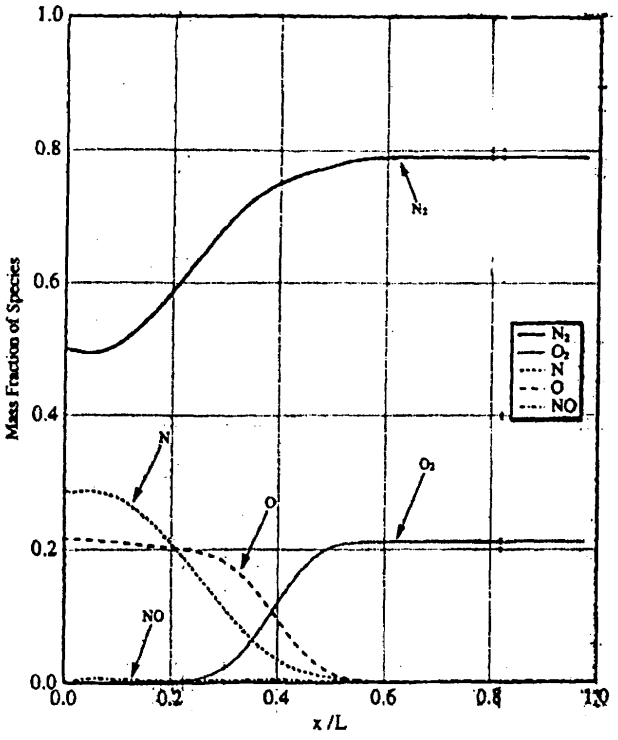

H－2

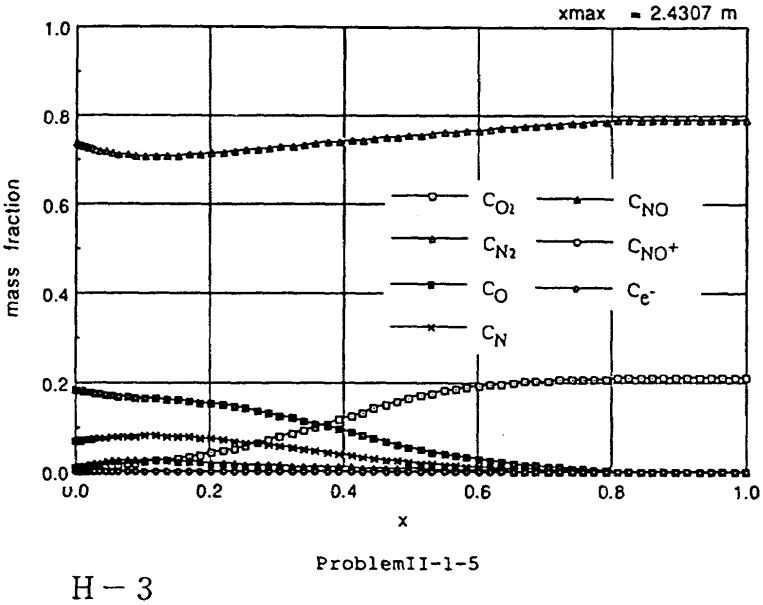

H－3

PROBLEM II-1-5

Mass fraction distributions.

Problem II-1 OREX よどみ点流線質量分率分布

Distance = 0.2186 [m]

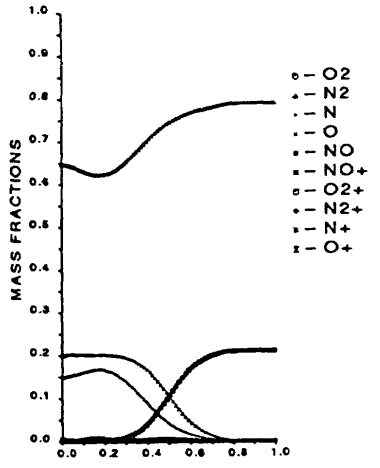

H－5

Problem-II-1-⑤

Mass Fractions along the Stagnation Stream Line

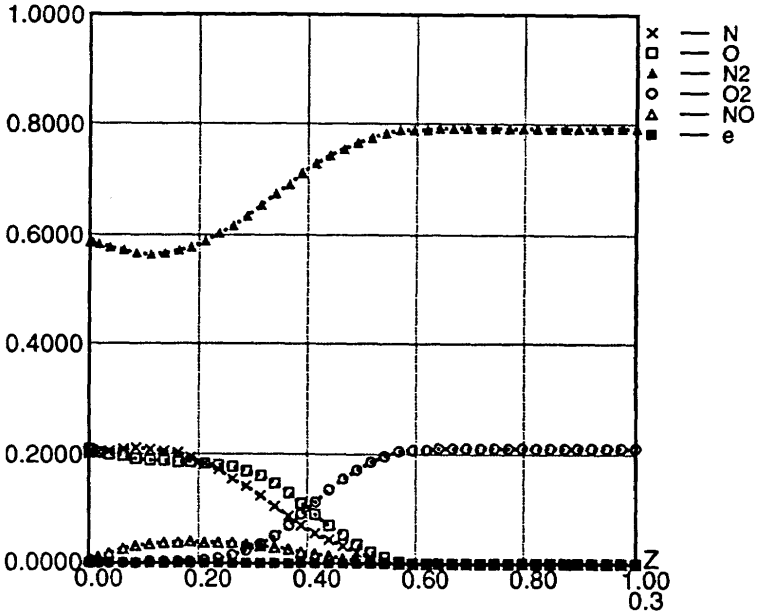

H－8 Problem II - 1 OREX Non Catalytic

Mass Fraction along the Stagnation Stream Line

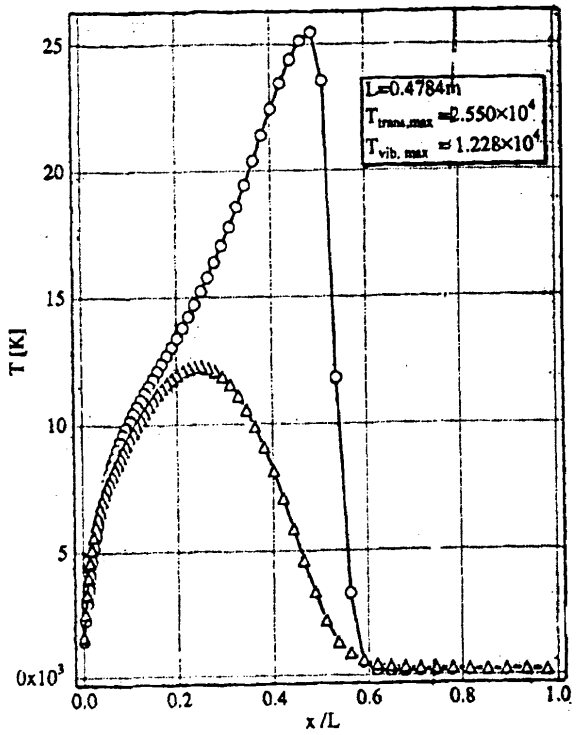

PROBLEM II-1-6

Translational and vibrational temperature distributions

H－2

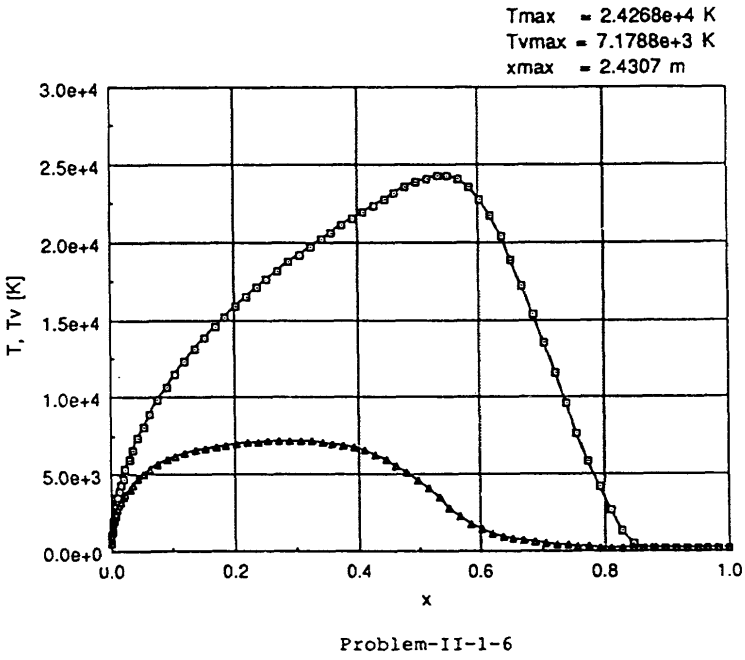

H－3

Problem II-1 OREX よどみ点流線温度分布

T_{max} = 17713 [K]

Distance = 0.2186 [m]

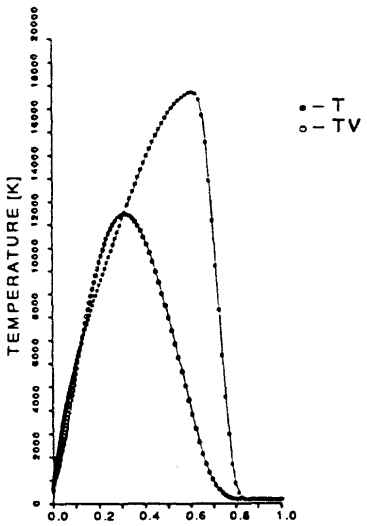

Problem-II-1-⑥

Temperature Distribution along the Stagnation Stream Line

H－5

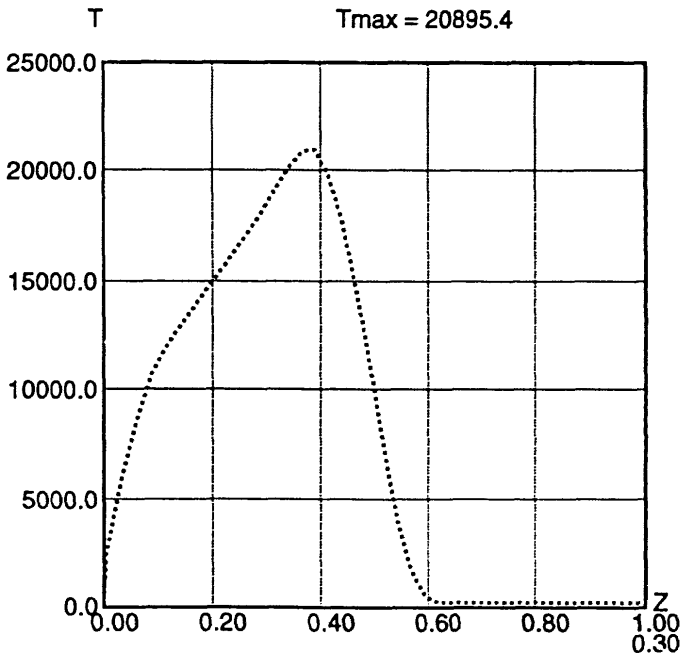

Problem II - 1 -⑥ OREX

Non Catalytic Case

Stagnation Line Temperature Distribution

H－8

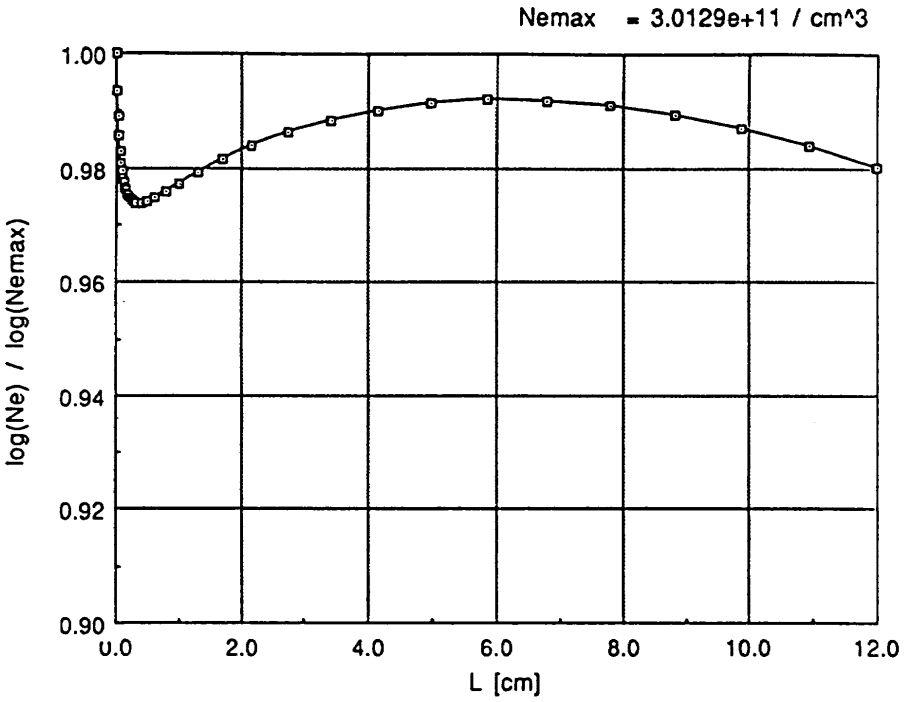

Problem-II-1-7

H－3

Ne_{max} = **3.1917× 10^{11} [1/cm^3]**

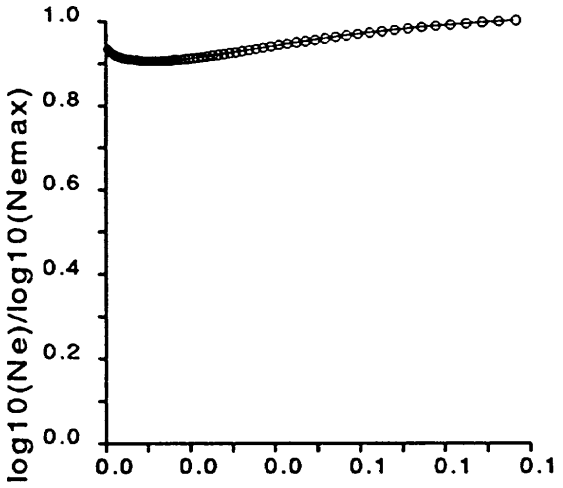

H－5

Problem-II-1-⑦

Temperature Distribution along the Stagnation Stream Line

Problem II-1 OREX 電子密度分布

Problem Ⅱ－2

OREX

高度　60km

非触媒ケース

計算条件

V_∞ =5562m/s　　W_{N2}= 0.79

T_∞ =248.1K　　W_{O2}= 0.21

P_∞ =23.60N/m^2

Twall=1519K

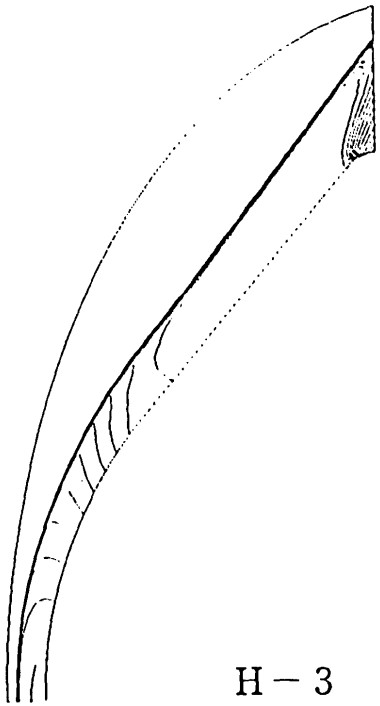

ProblemII-2-1

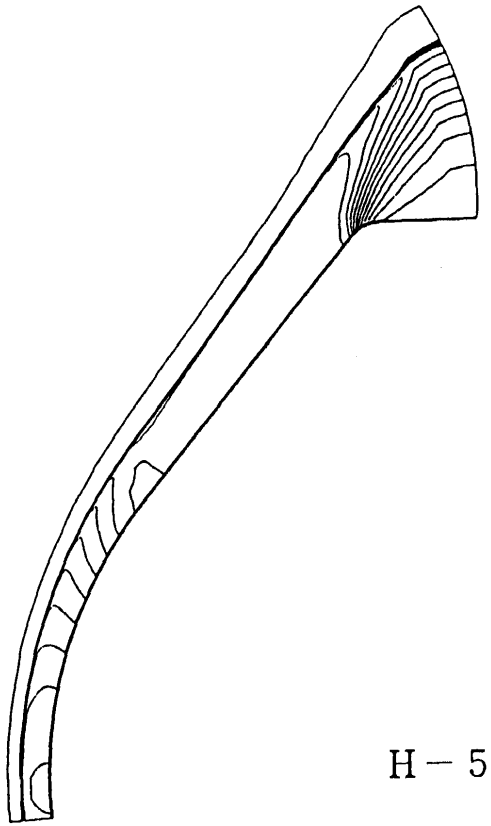

Problem-II-2-①

Pressure Contour $P/(\rho_\infty U_\infty^2)$

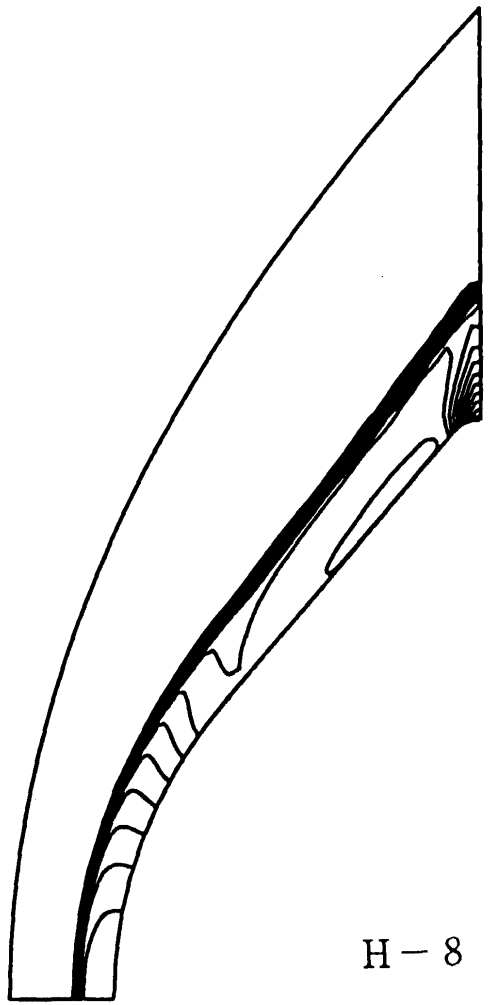

Problem II-2 OREX Pmax=0.962
Pressure Contour Non catalytic
U_∞=5562m/s T_∞=248.1K
P_∞=23.60N/m^2 T_{wall}=1519K

Problem II-2 OREX 圧力線図

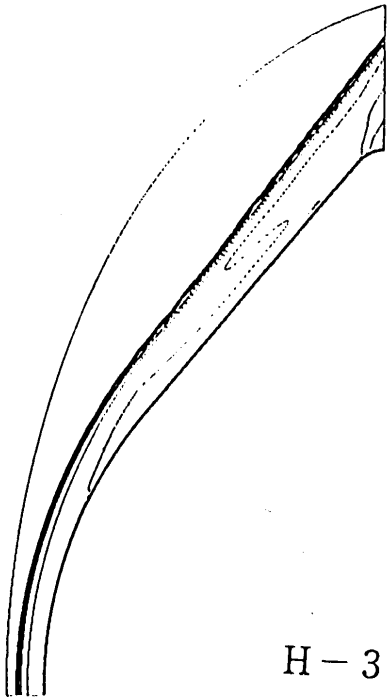

H－3

ProblemII-2-2 (Tmax = 1.3224e4 K)

Tmax = 9719 [K]

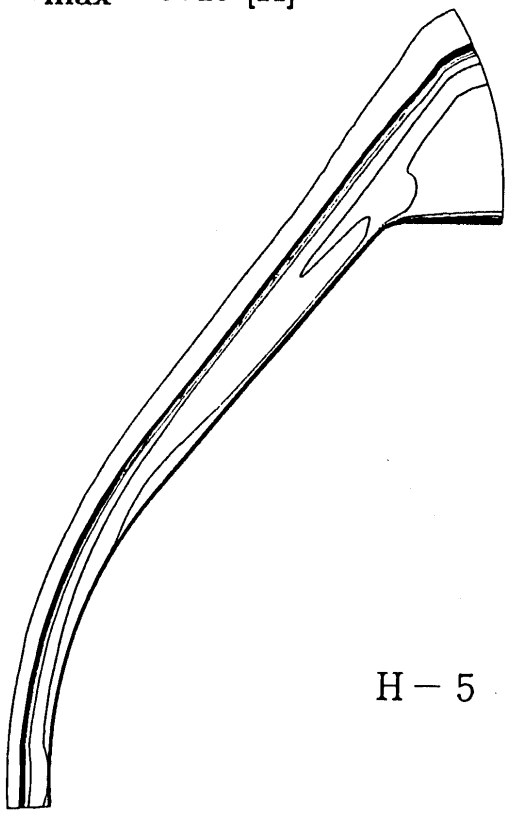

H－5

Problem-II-2-②

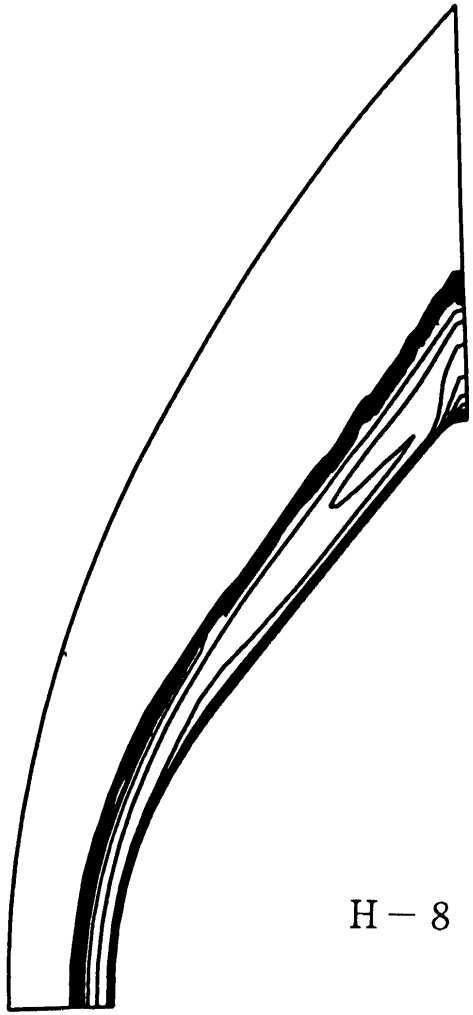

H－8

Problem II-2 OREX Tmax=36.457
Temperature Contour Non catalytic
U_∞=5562m/s T_∞=248.1K
P_∞=23.60N/m^2 T_{wall}=1519K

Transrational Temperature Contour T/T_∞

Problem II-2 OREX 等温度線図（並進、回転）

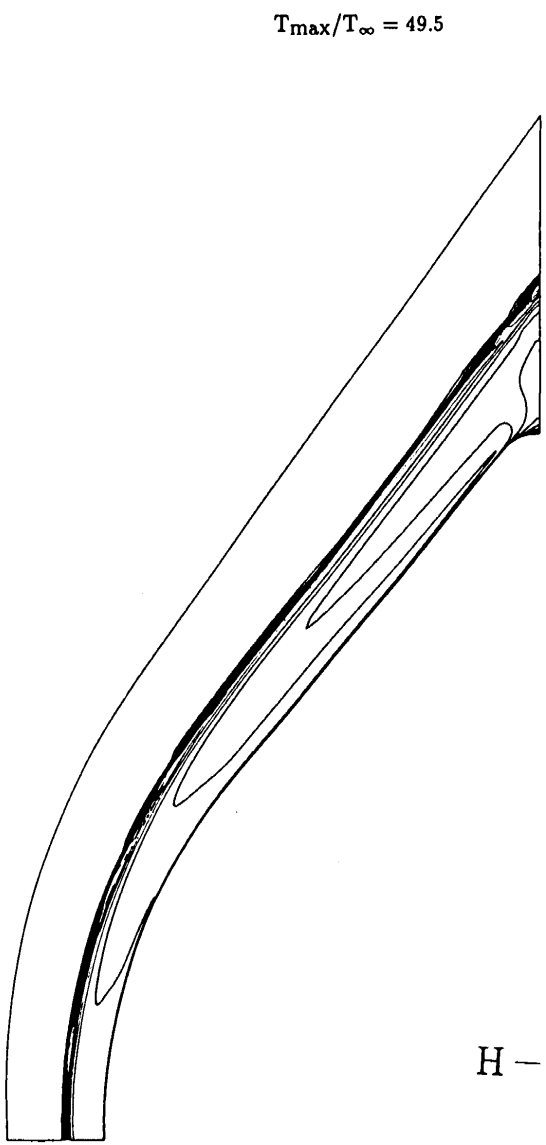

Problem-II-2-(2) Trans. Rot. Temp.

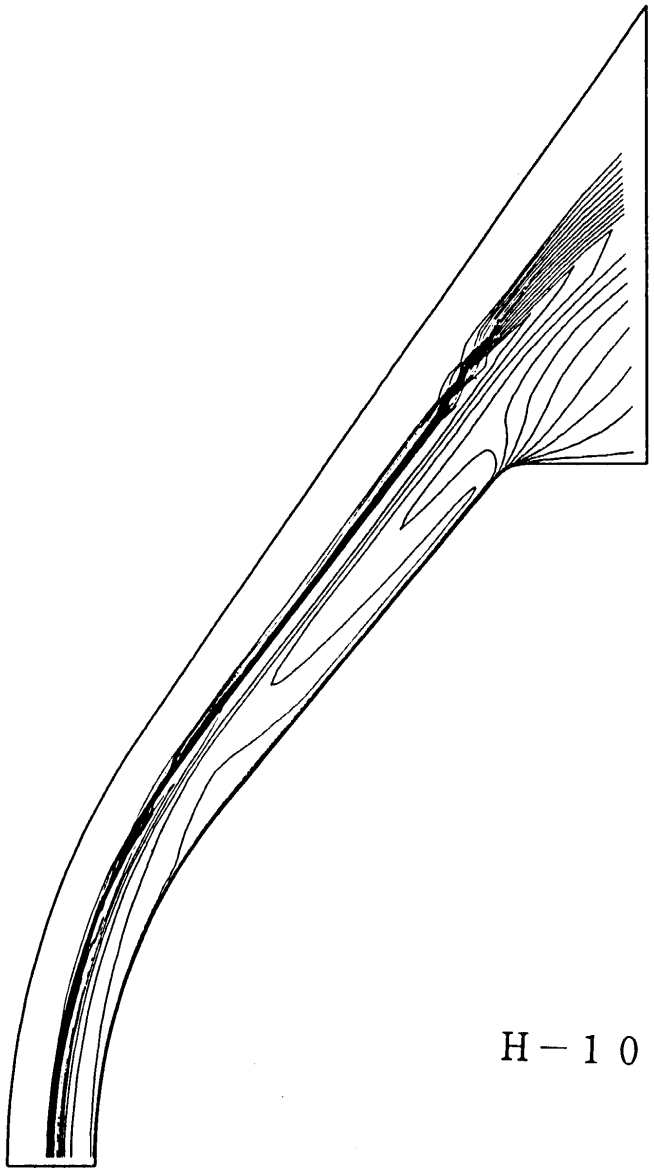

Problem II-2 OREX 等温度線図（並進、回転）

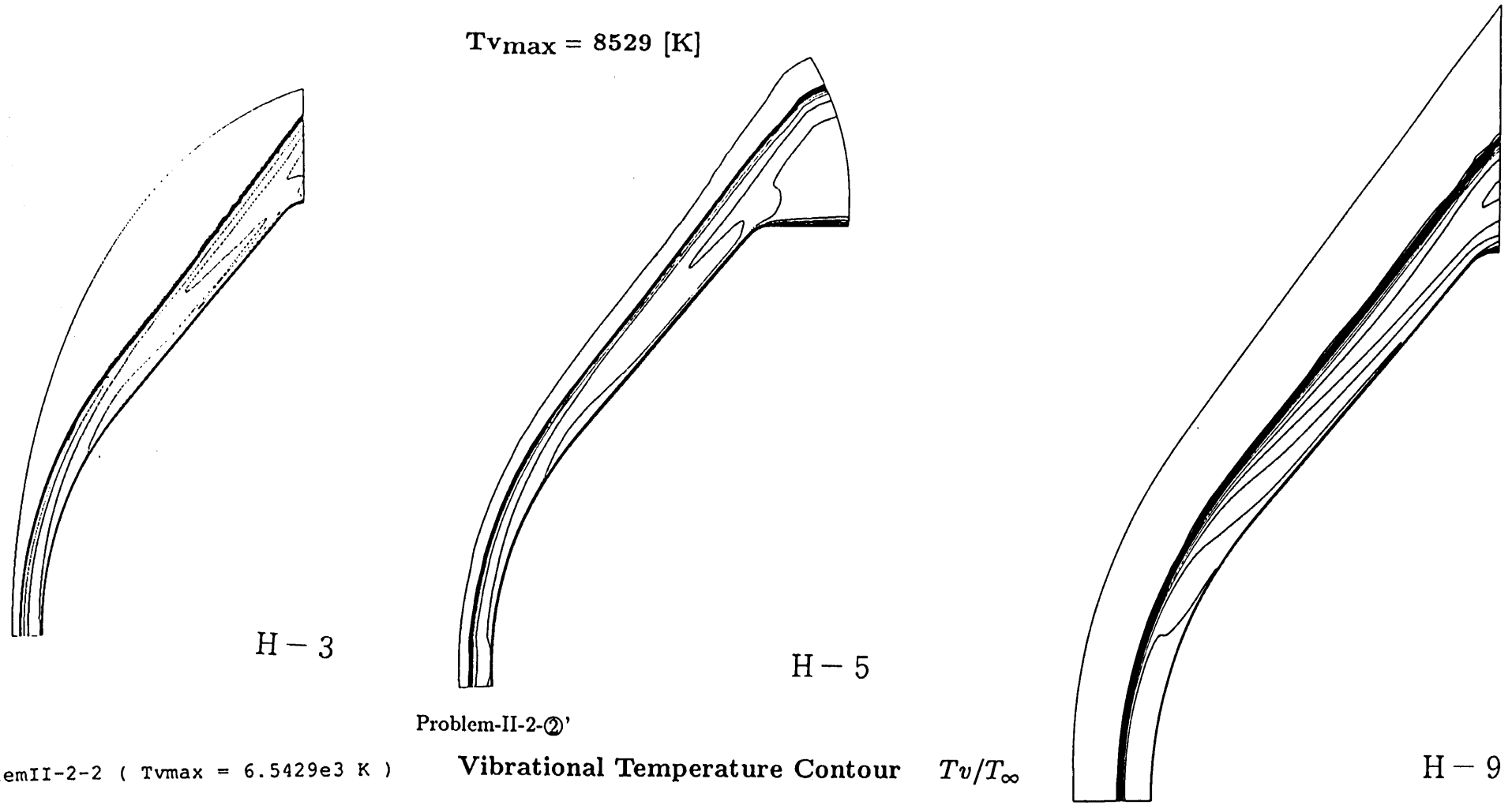

Problem II-2 OREX 等温度線図（振動）

Problem II-2 OREX 等温度線図（振動）

H－10

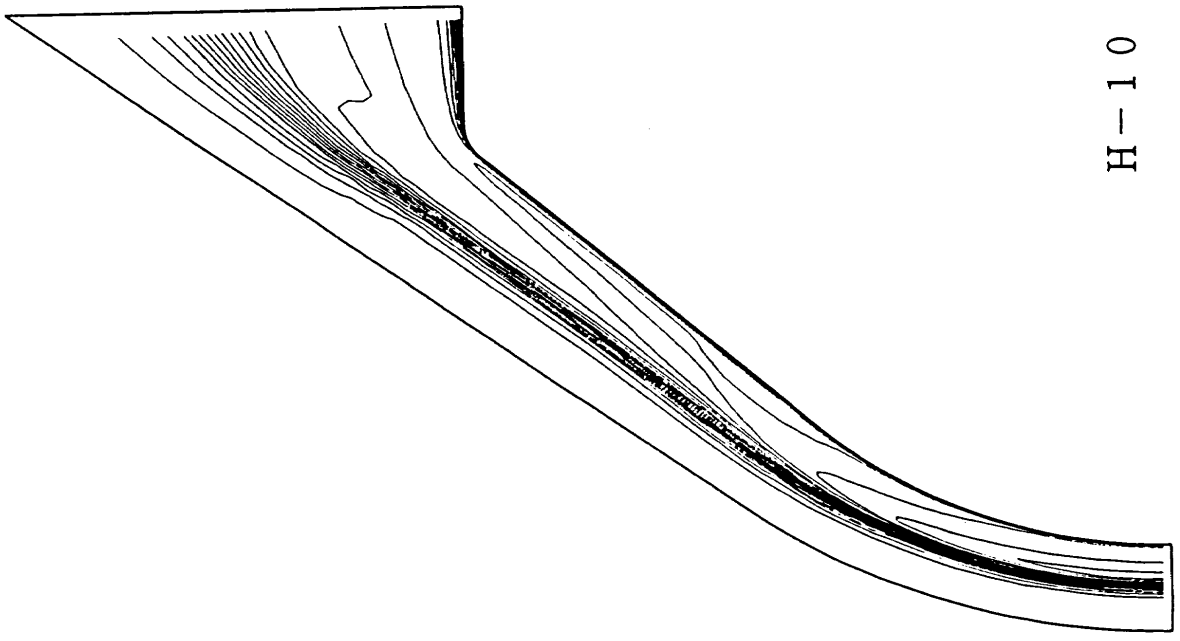

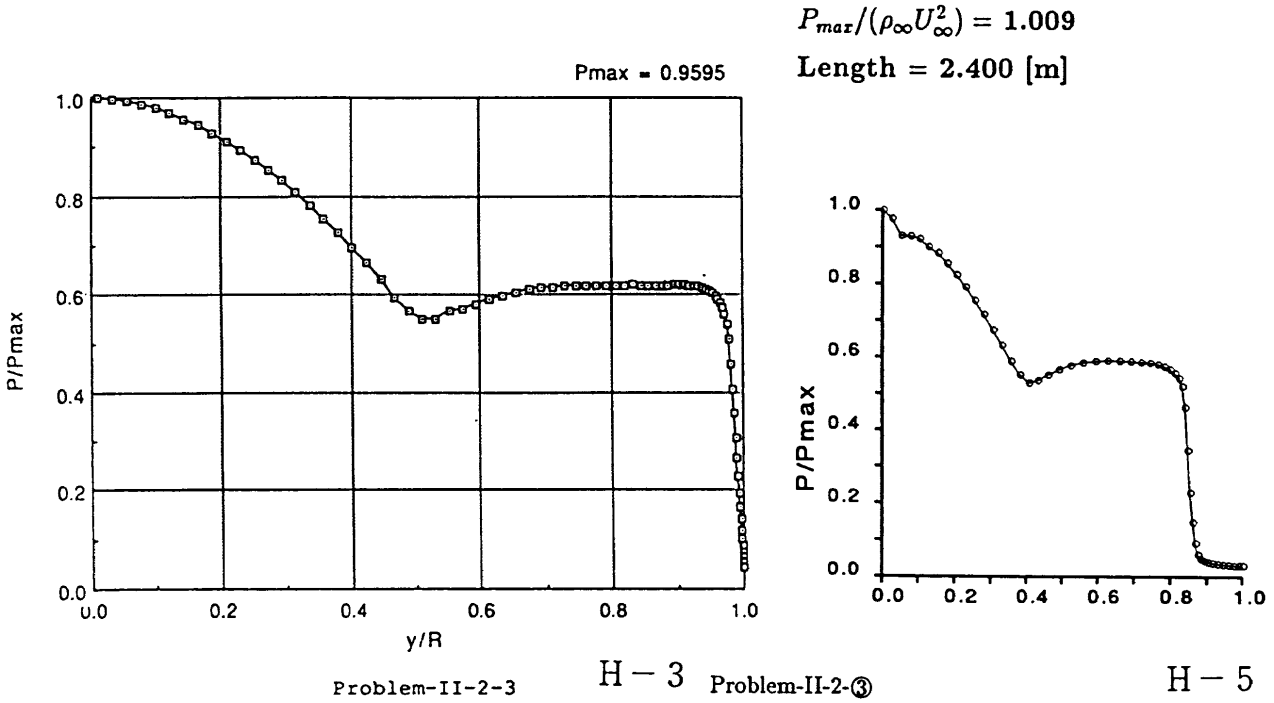

$P_{max}/(\rho_\infty U_\infty^2) = 1.009$

Length = 2.400 [m]

Problem-II-2-3 H－3 Problem-II-2-③ H－5

Pressure Distribution along the Body Surface

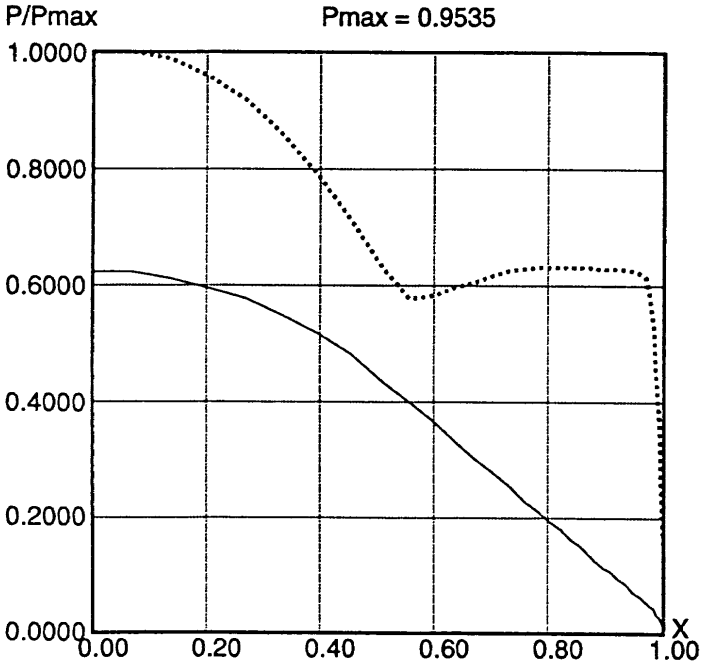

H－8 Problem II - 2 OREX
Pressure Distribution

Problem II-2 OREX 表面圧力分布

P_{max} = 0.952

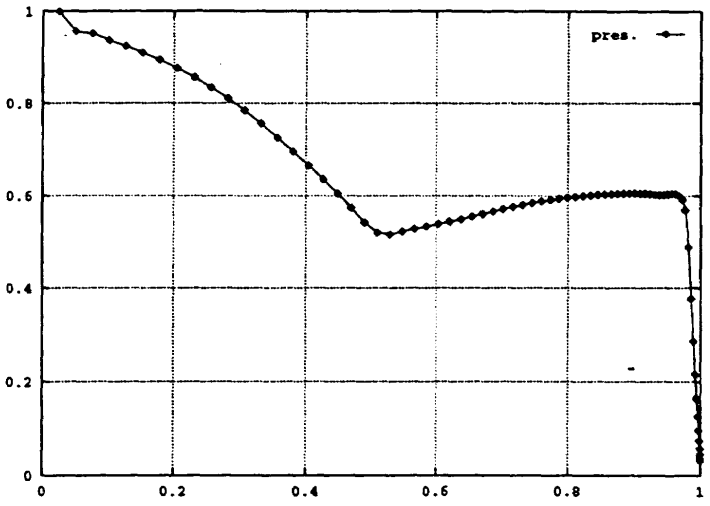

Problem-II-2-(3) Pressure H－9

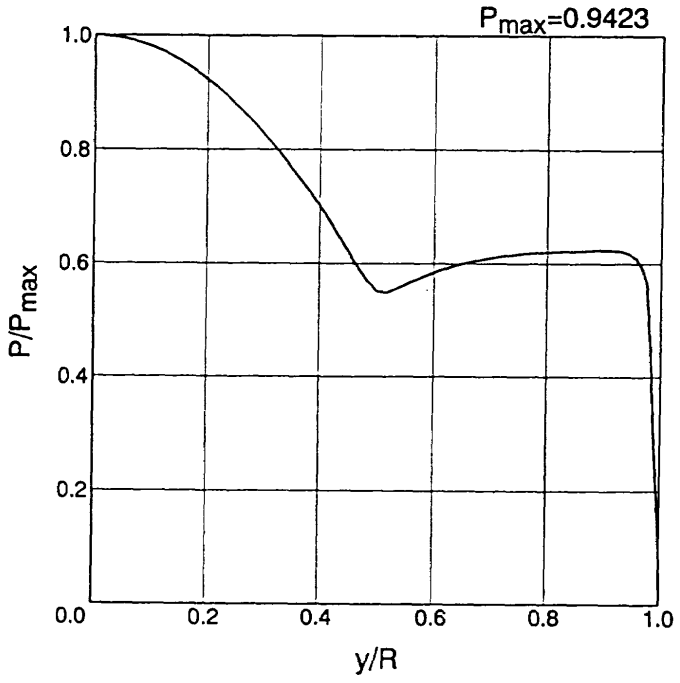

H－10

Problem II-2 OREX 表面圧力分布

H－3

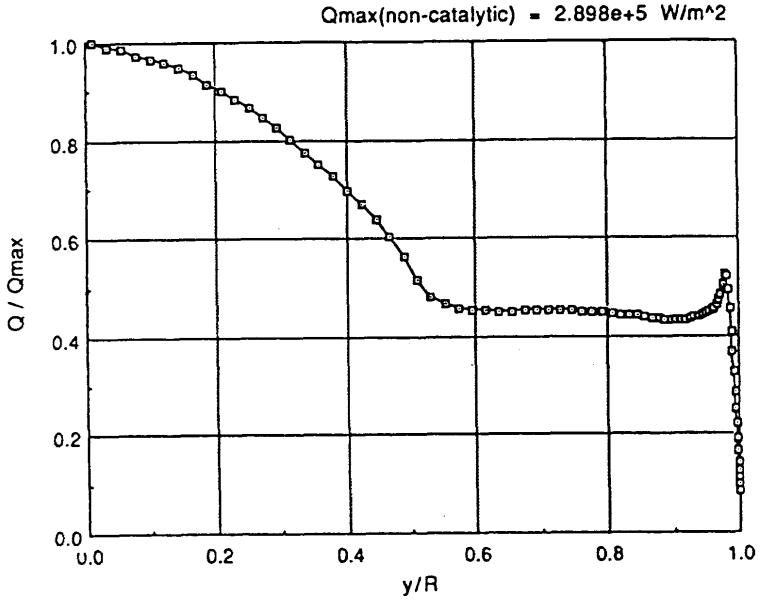

Problem-II-2-④

Q_{max} = 181908 [W/m²]

Length = 2.400 [m]

H－5

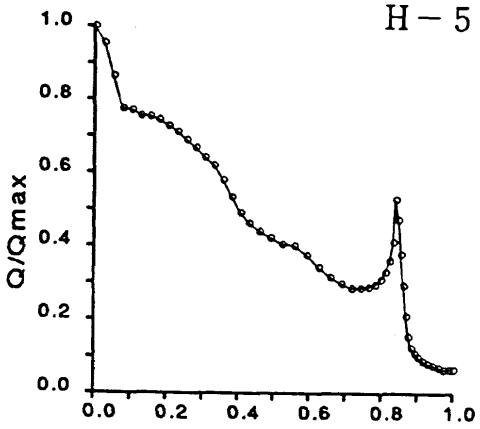

Heat Transfer Distribution along the Body Surface

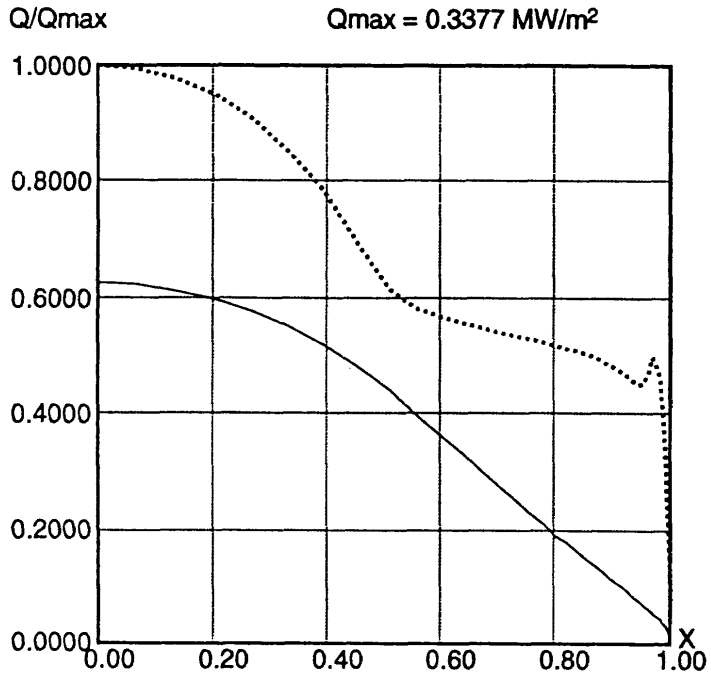

H－8 Problem II - 2 OREX

Heat Transfer Distribution

Problem II-2 OREX 表面熱流束分布

X_{max} = 0.237[mm] Q_{max} = 0.412[MW/m^2]

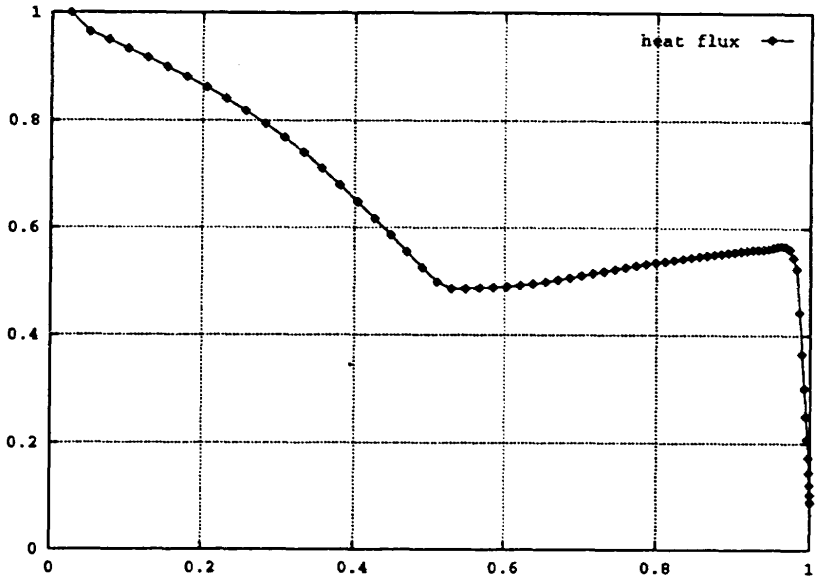

Problem-II-2-(4) Heatflux

H－9

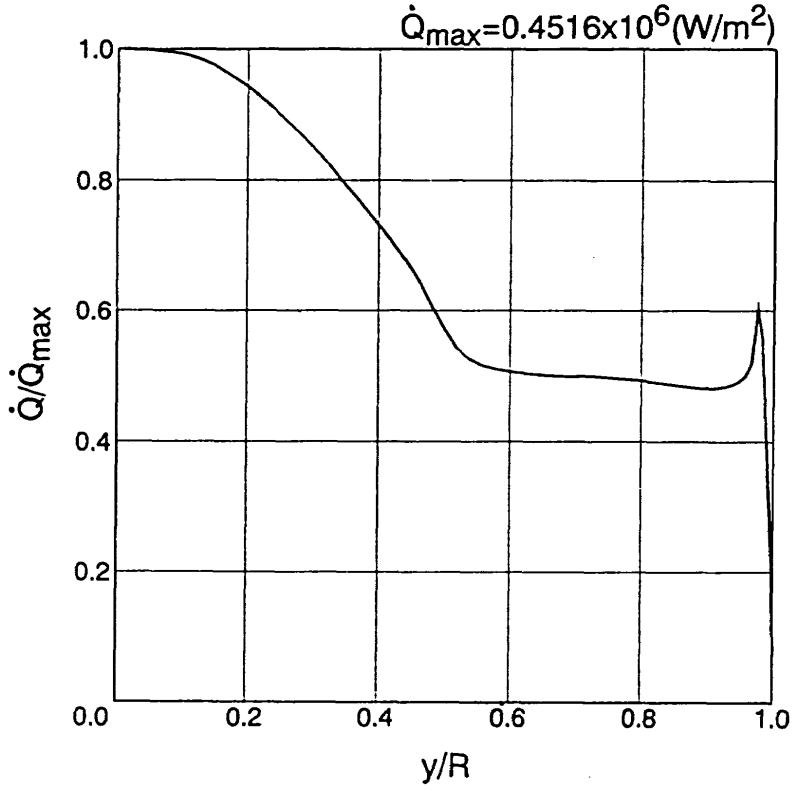

H－10

Problem II-2 OREX 表面熱流束分布

Distance = 0.128 [m]

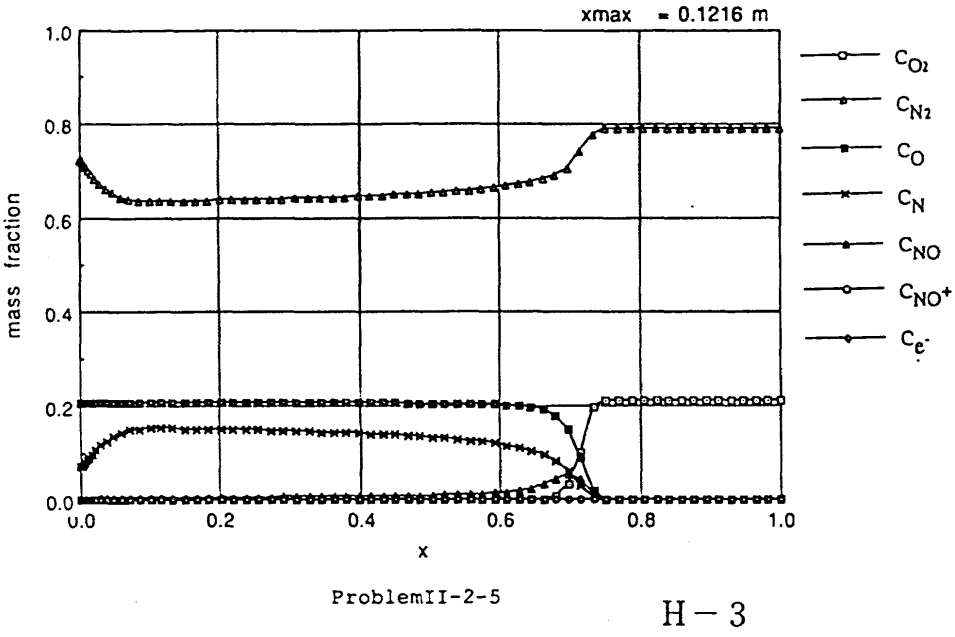

ProblemII-2-5

H－3

H－5

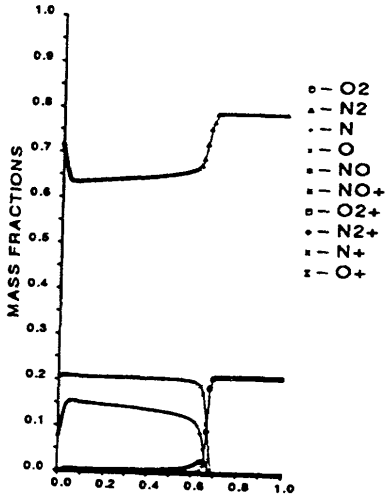

Problem-II-2-⑤

Mass Fractions along the Stagnation Stream Line

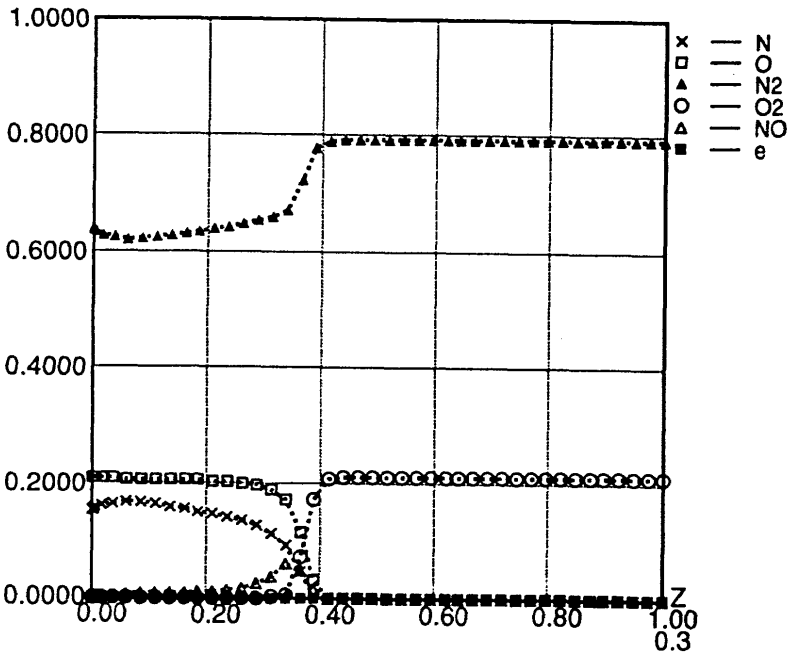

Problem II - 2 OREX Non Catalytic

H－8

Mass Fraction along the Stagnation Streem Line

Problem II-2 OREX よどみ点流線質量分率分布

X_{max} = 0.237[m]

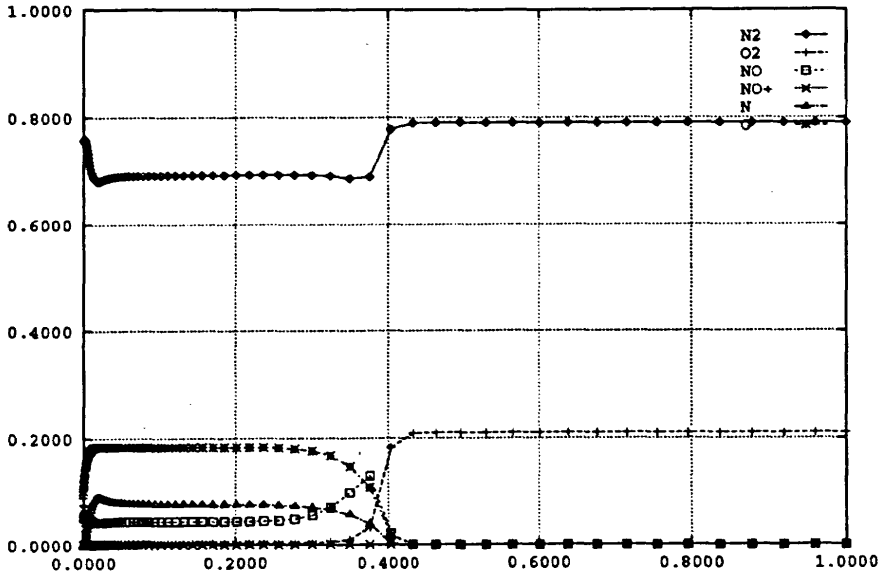

Problem-II-2-(5)

H－9

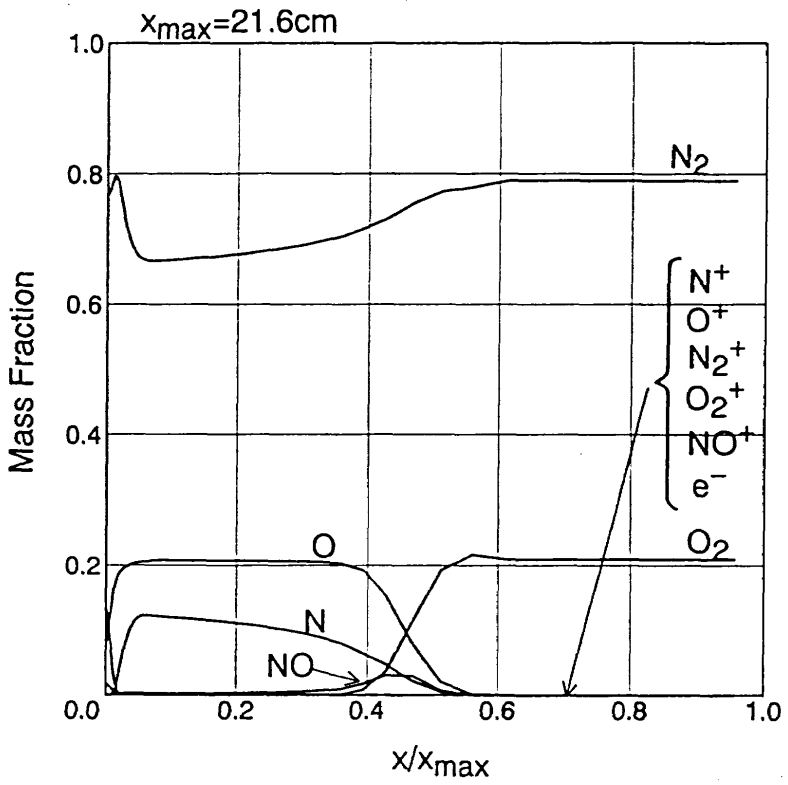

H－10

Problem II-2 OREX よどみ点流線質量分率分布

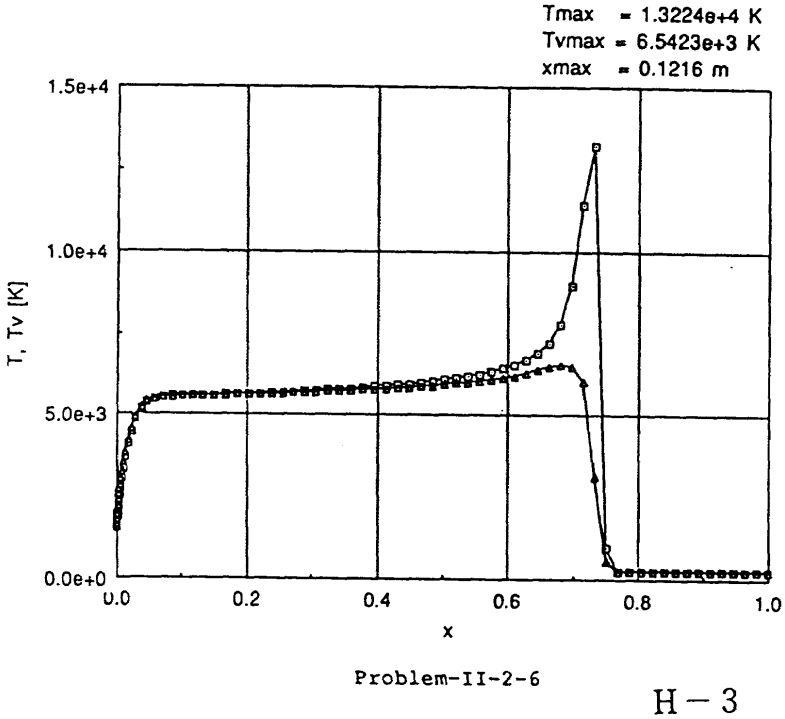

Problem-II-2-6

H－3

T_{max} = 9719 [K]

Distance = 0.128 [m]

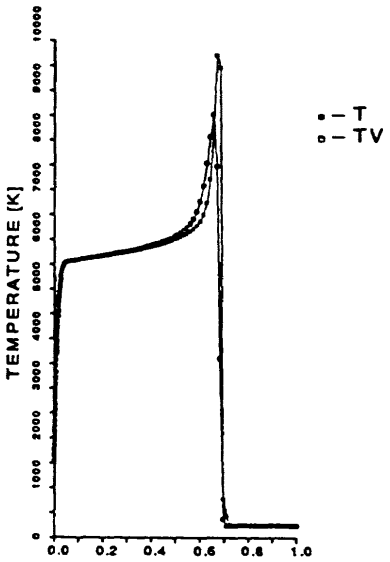

Problem-II-2-⑥

H－5

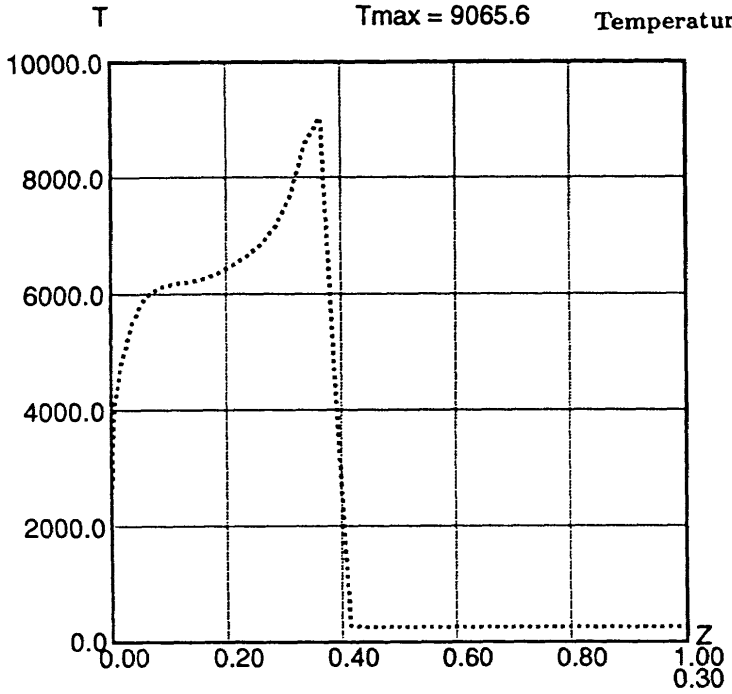

Temperature Distribution along the Stagnation Stream Line

H－8

Problem II - 2 -⑥ OREX

Non Catalytic Case

Stagnation Line Temperature Distribution

Problem II-2 OREX よどみ点流線温度分布

X_{max} = 0.237[m]　T_{max} = 12275[K]　Tv_{max} = 7482[K]

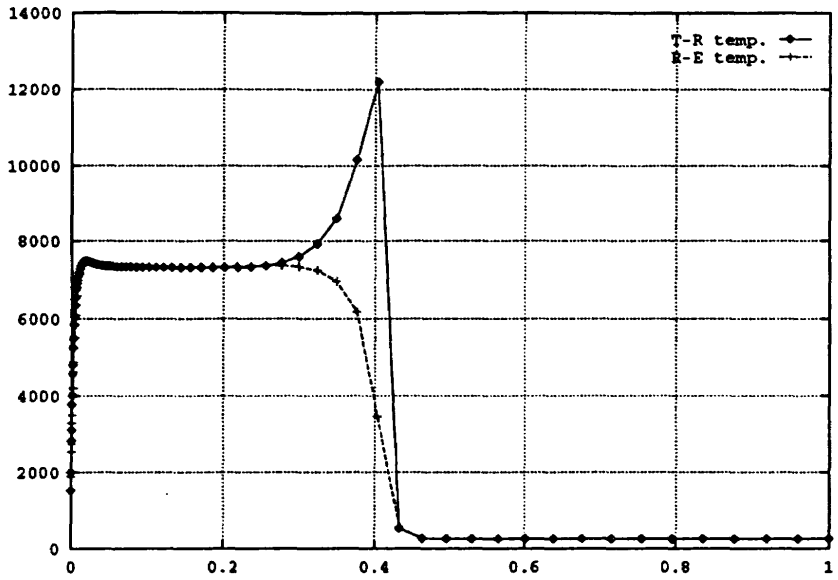

Problem-II-2-(6)　　H－9

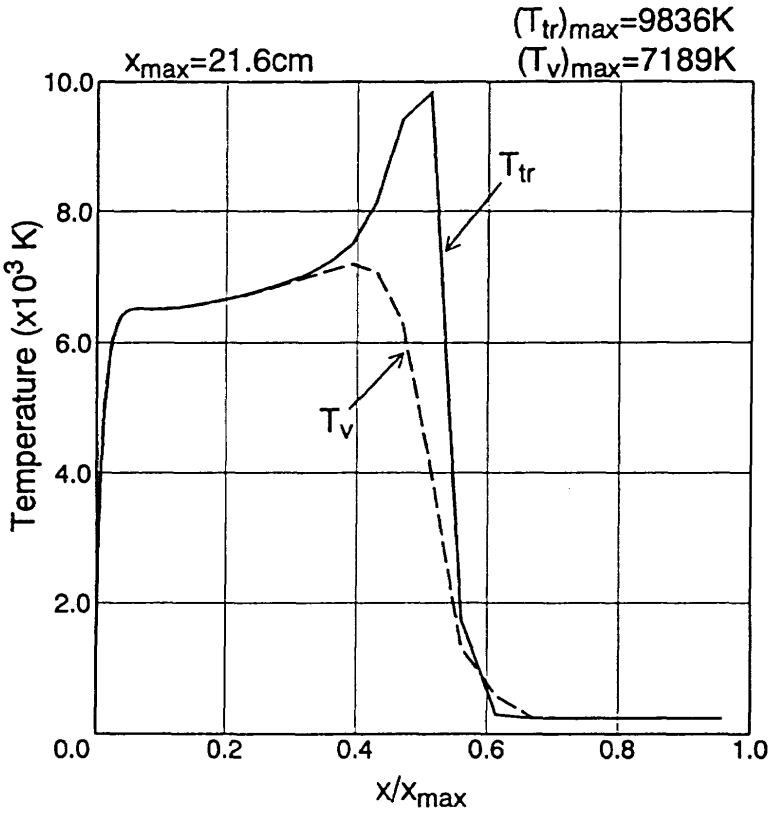

H－10

Problem　II-2　　OREX よどみ点流線温度分布

Problem Ⅱ－3

OREX

高度　60km

完全触媒ケース

計算条件

V_∞ =5562m/s　　W_{N2}= 0.79

T_∞ =248.1K　　W_{O2}= 0.21

P_∞ =23.60N/m^2

Twall=1519K

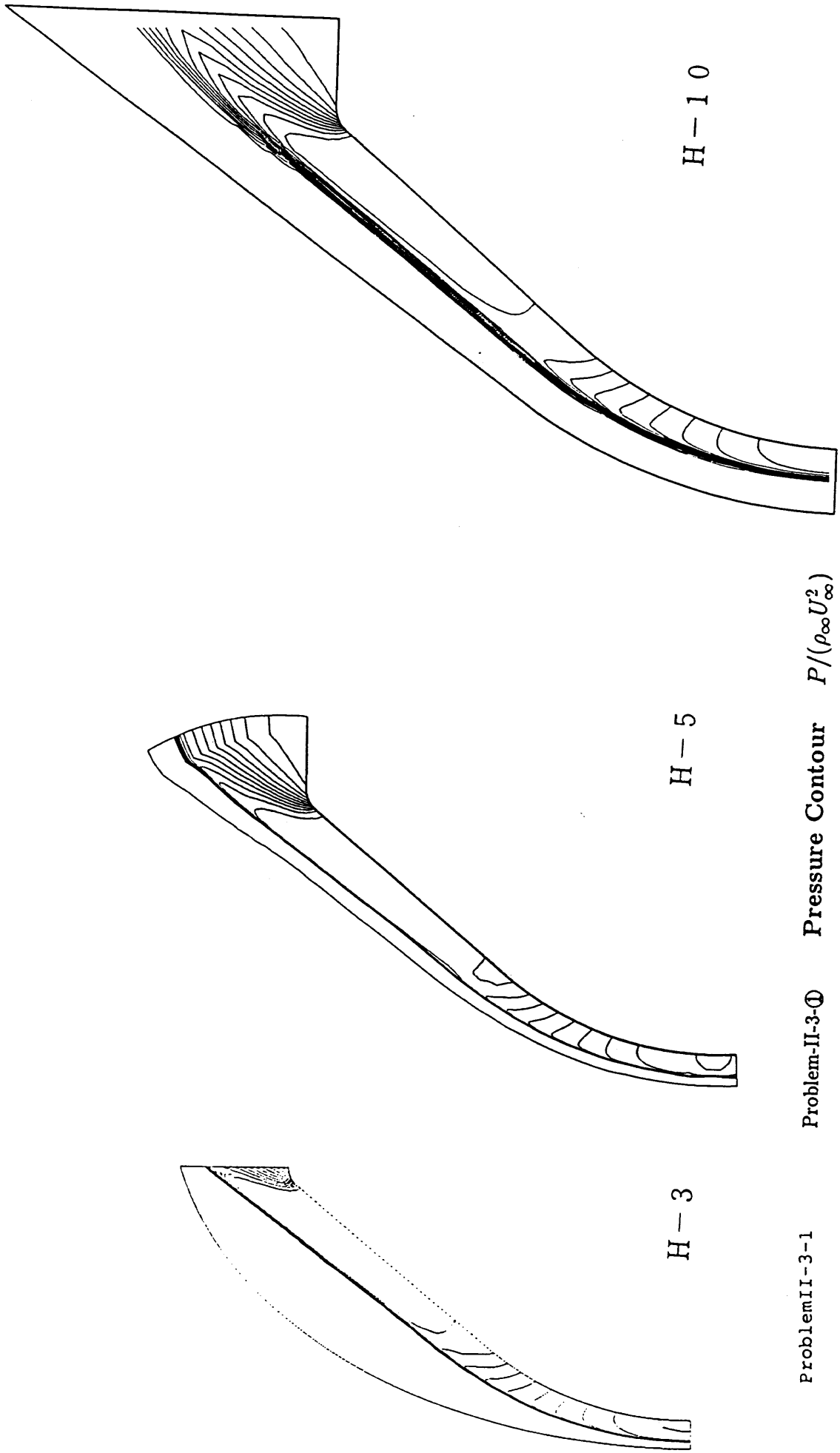

Problem II-3 OREX 完全触媒 ケース 圧力線図

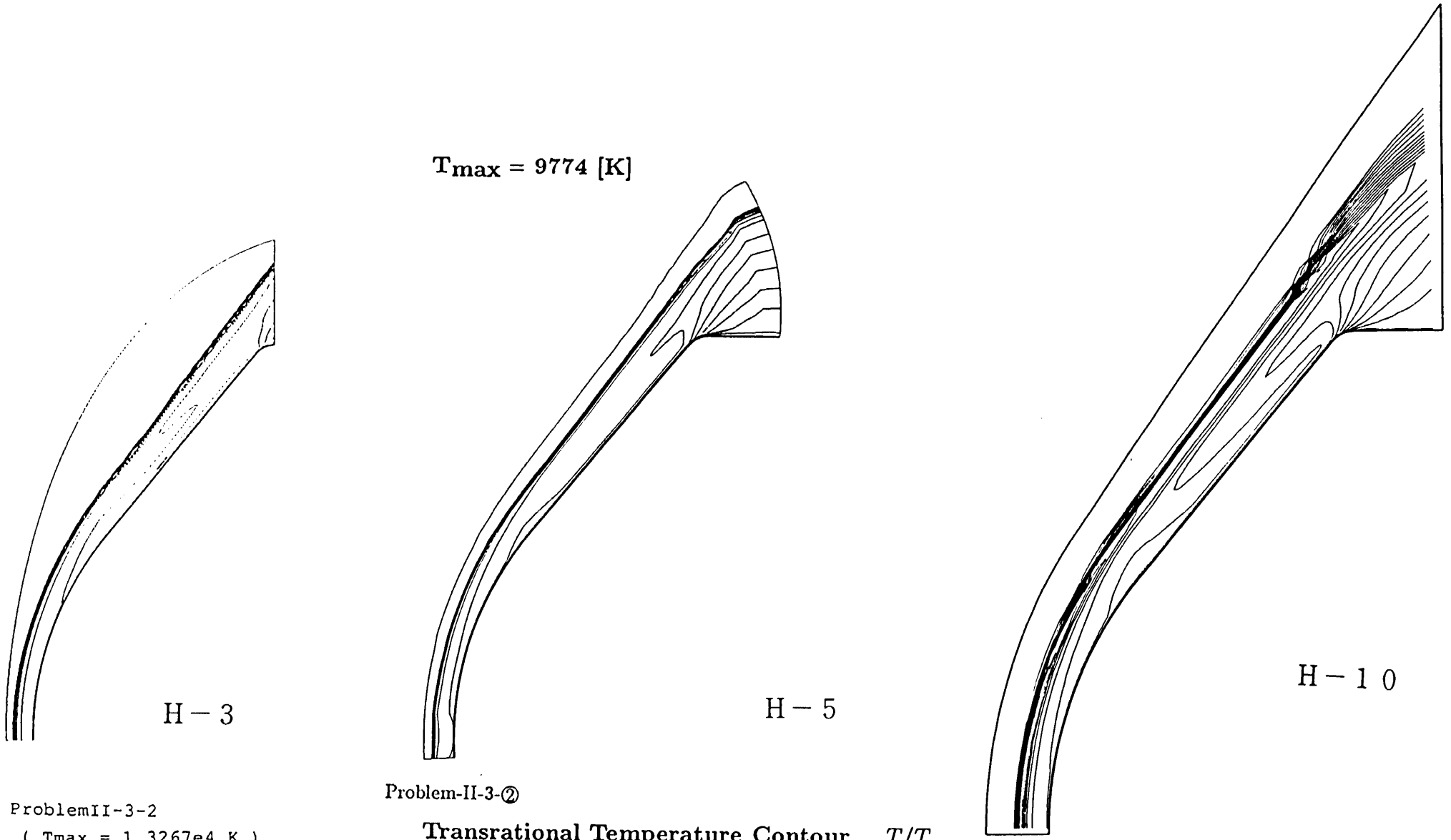

Problem II-3 OREX 完全触媒 ケース 等温度線図（並進、回転）

Problem II-3 OREX 完全触媒 ケース 等温度線図（振動）

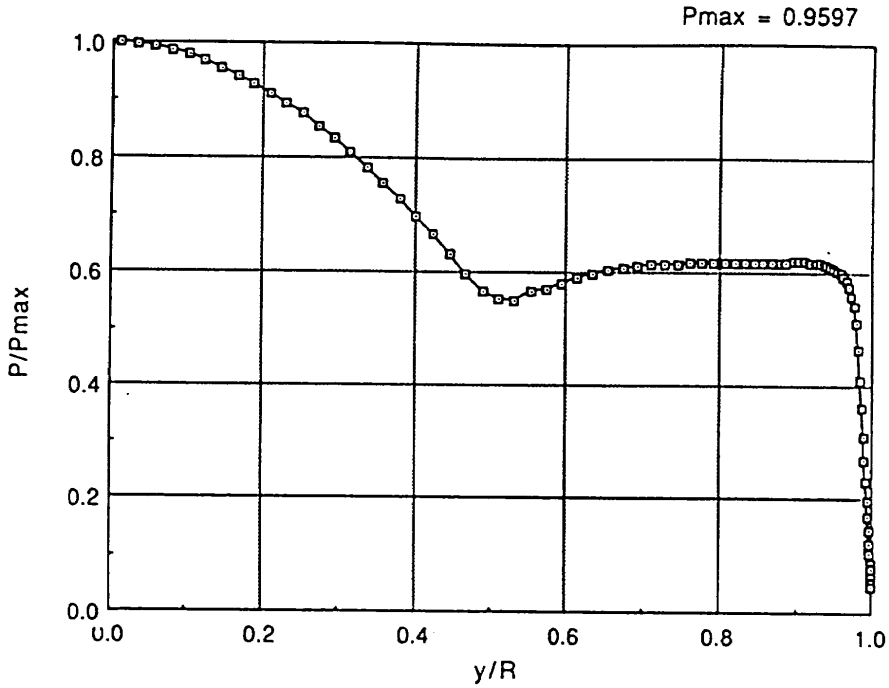

Problem-II-3-3

H－3

$P_{max}/(\rho_\infty U_\infty^2) = 1.0319$

Length = 2.400 [m]

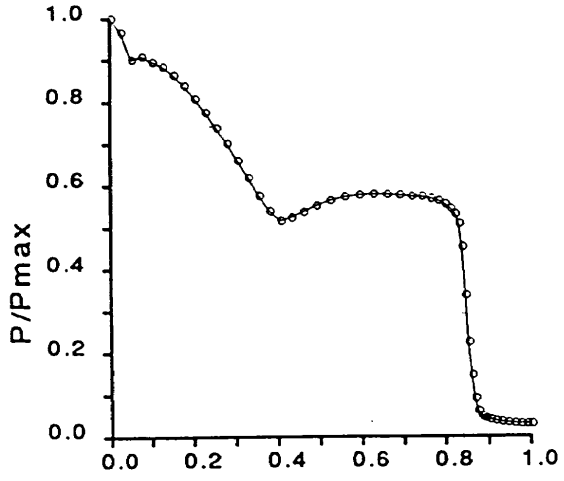

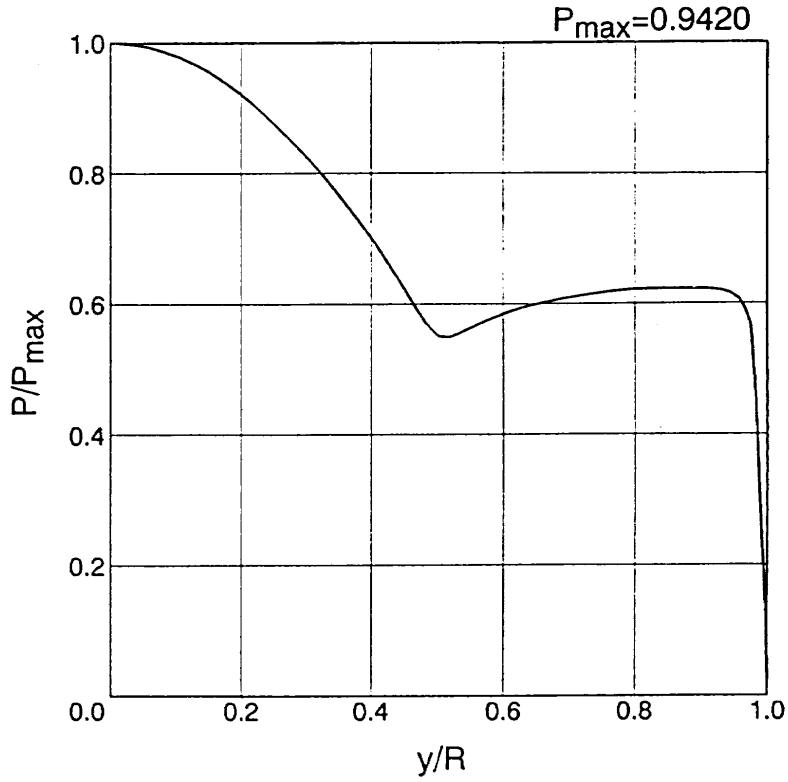

Problem-II-3-③

H－5

H－10

Pressure Distribution along the Body Surface

Problem II-3 OREX 完全触媒 ケース 表面圧力分布

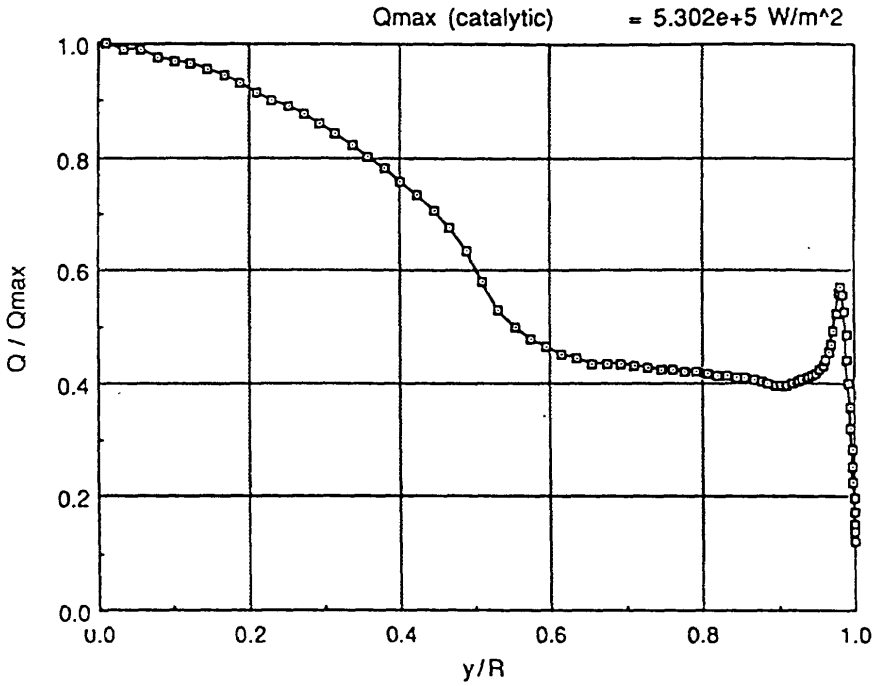

Problem-II-3-4

H－3

Q_{max} = 382906 [W/m^2]

Length = 2.400 [m]

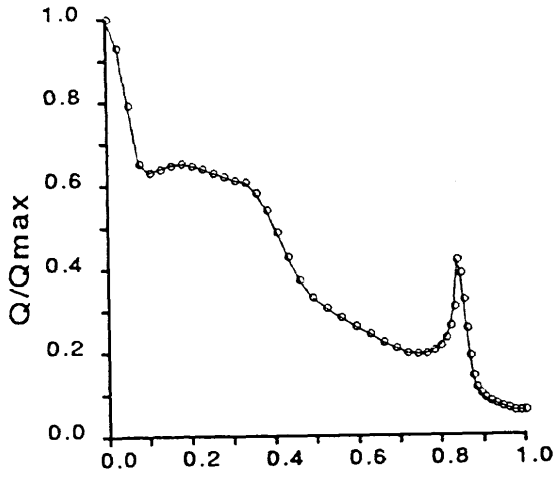

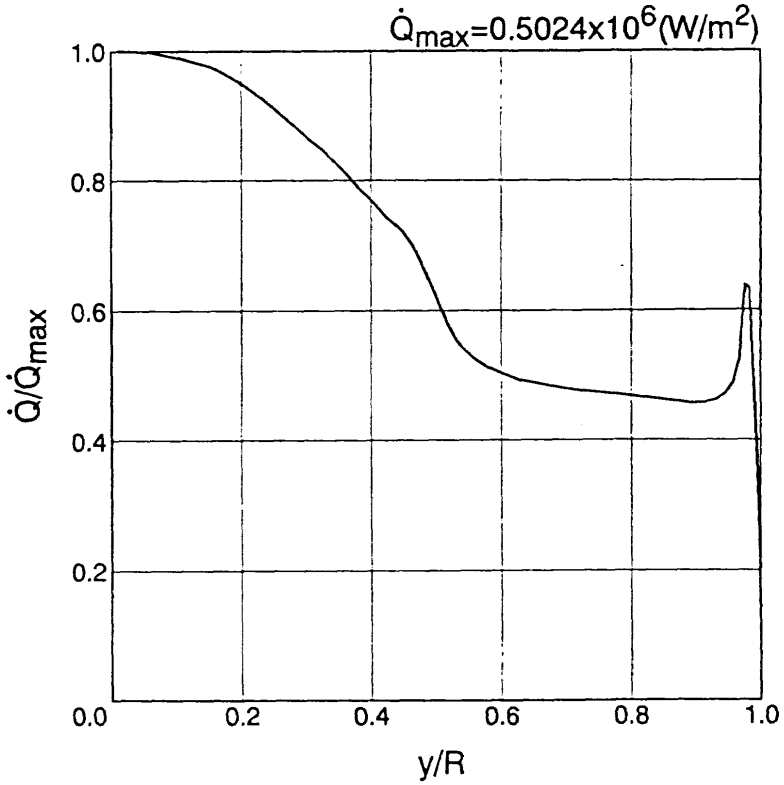

Problem-II-3-④

H－5

H－10

Heat Transfer Distribution along the Body Surface

Problem II-3 OREX 完全触媒 ケース 表面熱流束分布

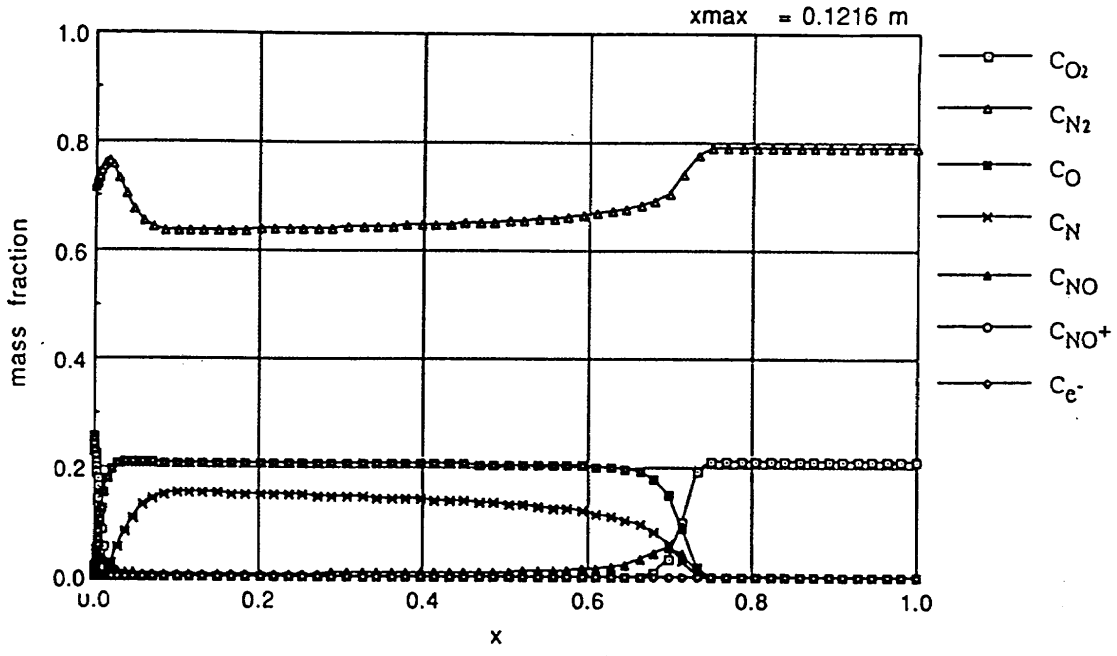

ProblemII-3-5

H－3

Distance = 0.1285 [m]

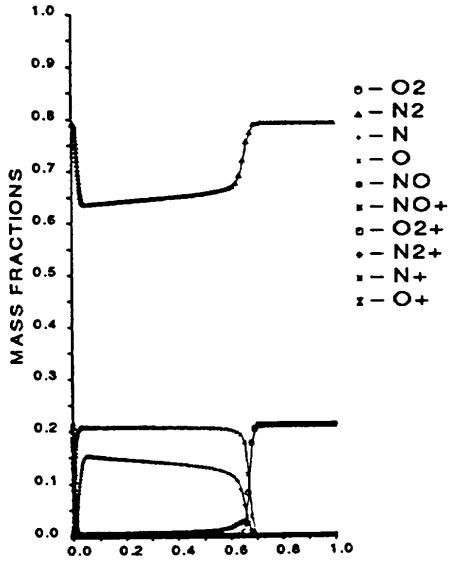

H－5

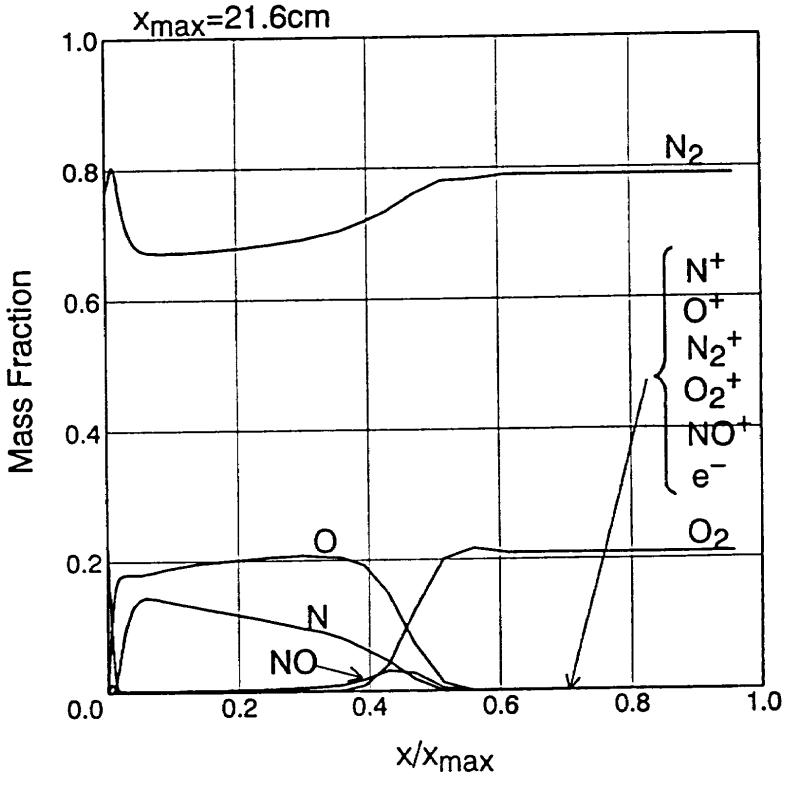

H－10

Problem-II-3-⑤

Mass Fractions along the Stagnation Stream Line

Problem II-3 OREX 完全触媒 ケース よどみ点流線質量分率分布

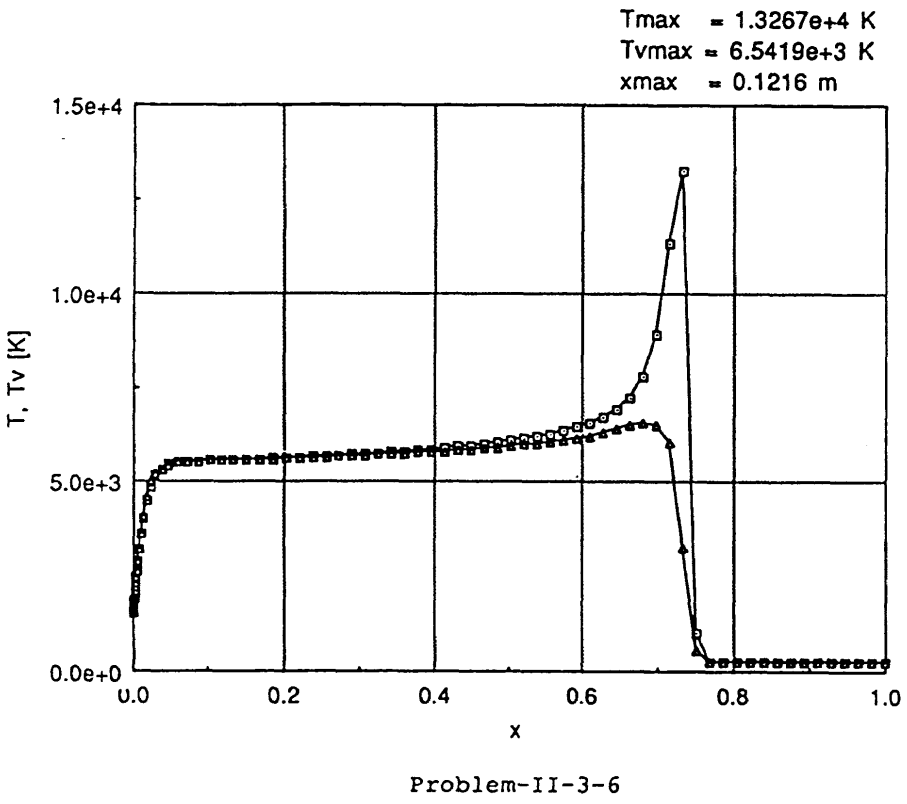

Problem-II-3-6

H－3

T_{max} = 9774 [K]

Distance = 0.1285 [m]

H－5

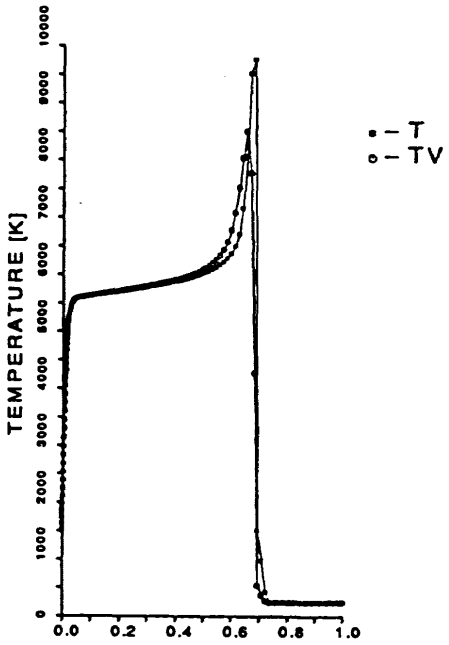

Problem-II-3-⑥

Temperature Distribution along the Stagnation Stream Line

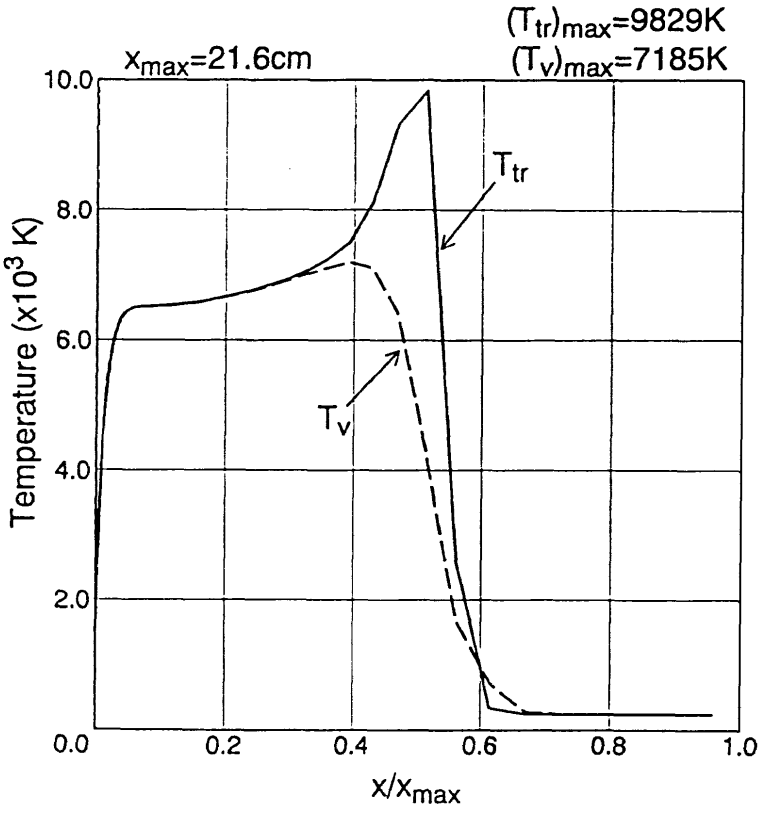

H－10 Problem II-3 OREX 完全触媒 ケース よどみ点流線温度分布

Problem Ⅱ－4

OREX

高度　60km

平衡流

計算条件

V_∞ =5562m/s　　W_{N2}= 0.79

T_∞ =248.1K　　W_{O2}= 0.21

P_∞ =23.60N/m^2

Twall=1519K

Problem-II-4-① Pressure Contour

Problem II-4 OREX 平衡流 圧力線図

図 Problem-II-4-①

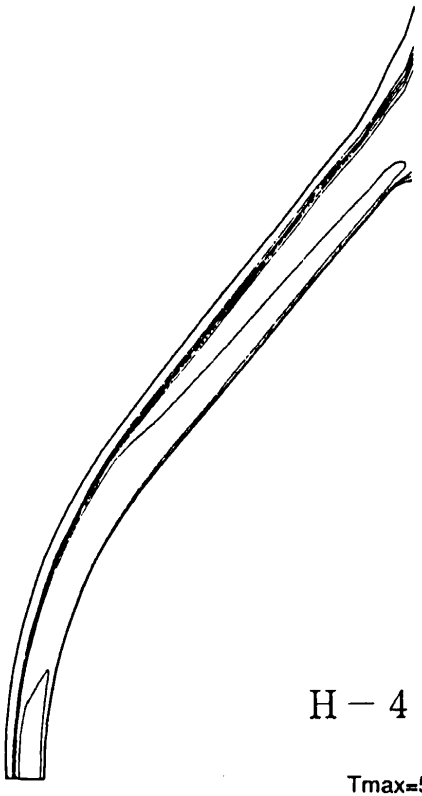

図　Problem-II-4-②

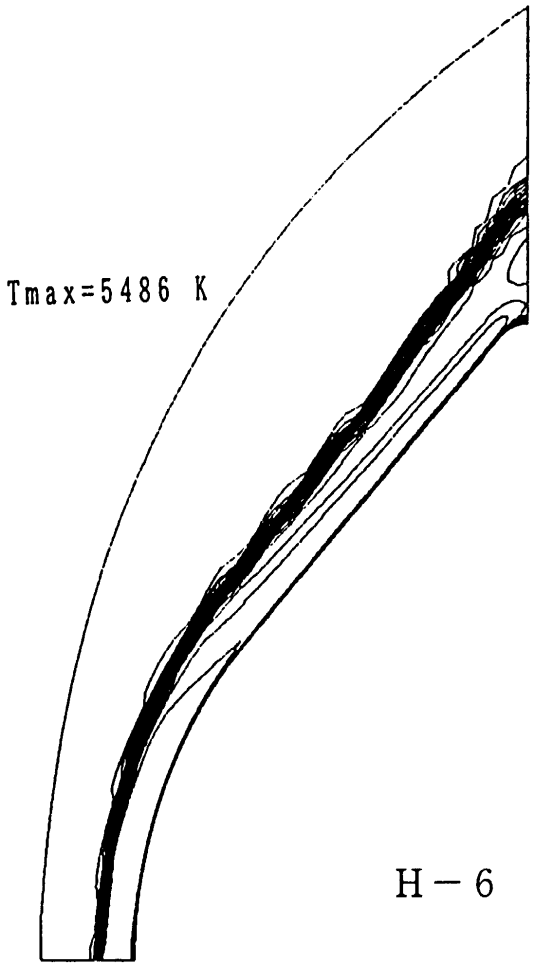

Problem-Ⅱ-4-②　Temperature Contour

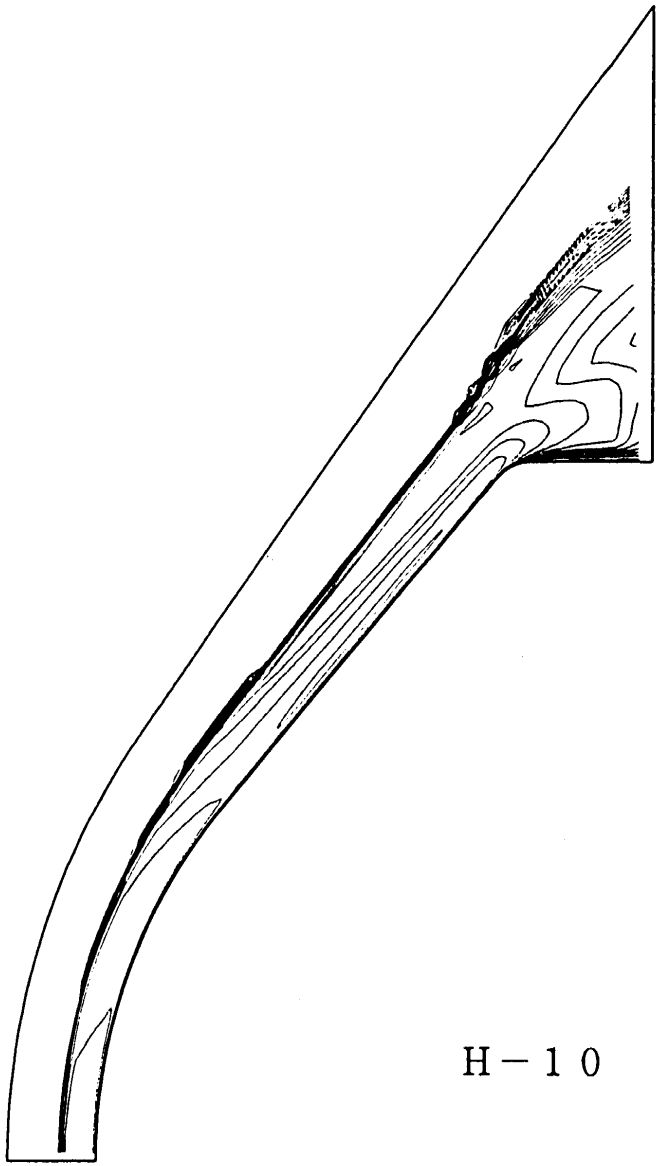

Problem　II-4　　OREX 平衡流 等温度線図

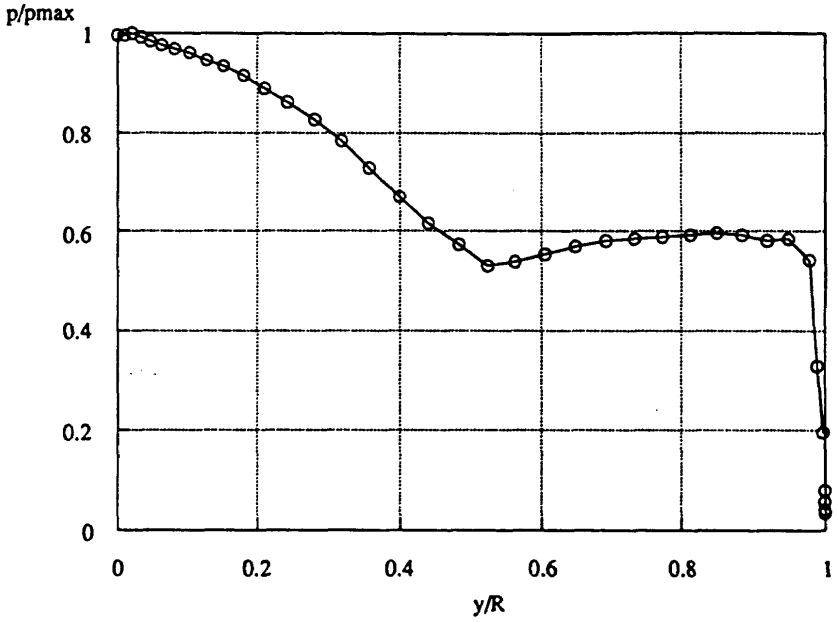

Pmax= 0.985

図 Problem-II-4-③

H－4

Problem II-4 OREX 平衡流 表面圧力分布

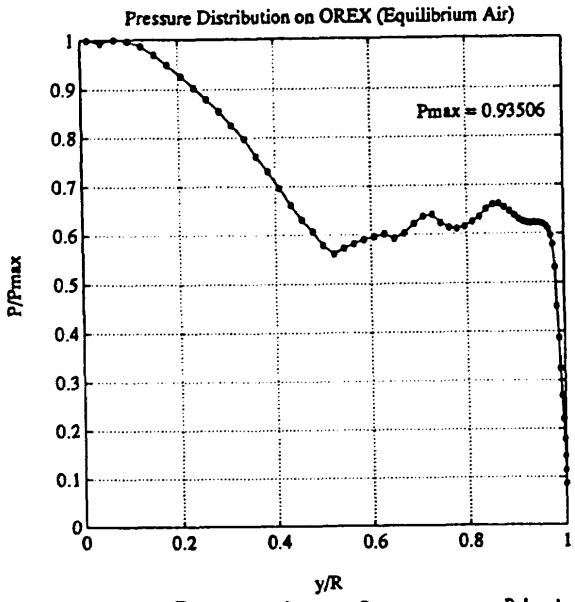

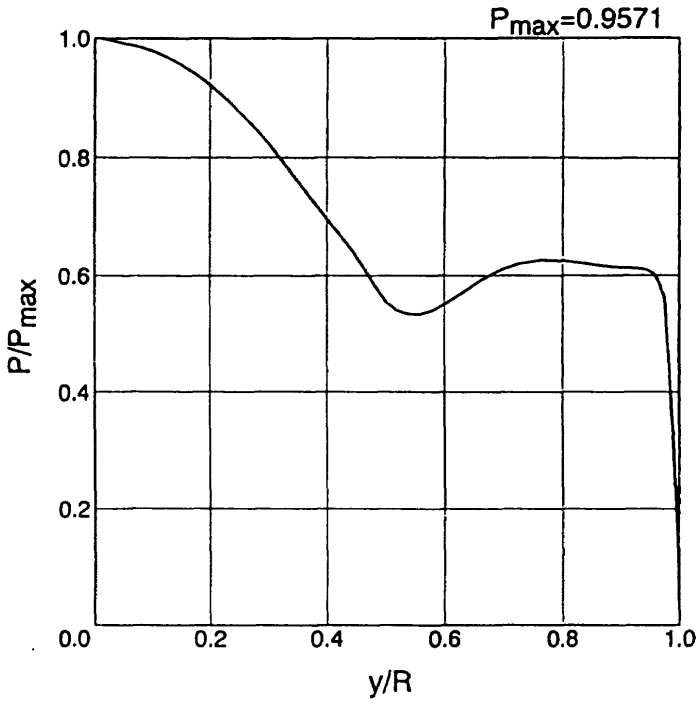

Problem-Ⅱ-4-③ Surface Pressure Distribution

H－6 H－10

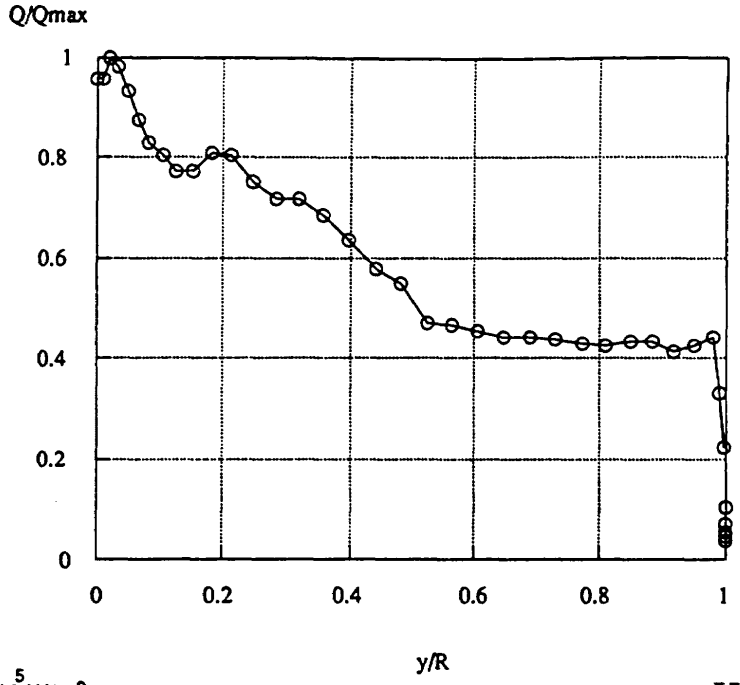

Qmax=3.05×10^{5} W/m^{2}

H－4

図 Problem-II-4-④

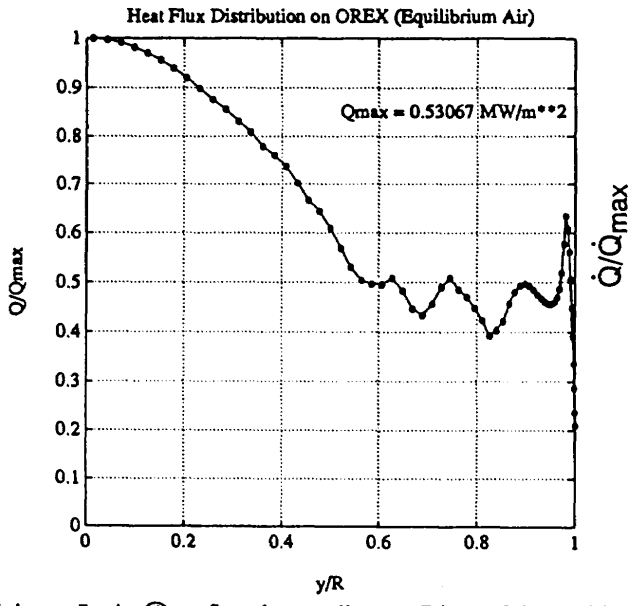

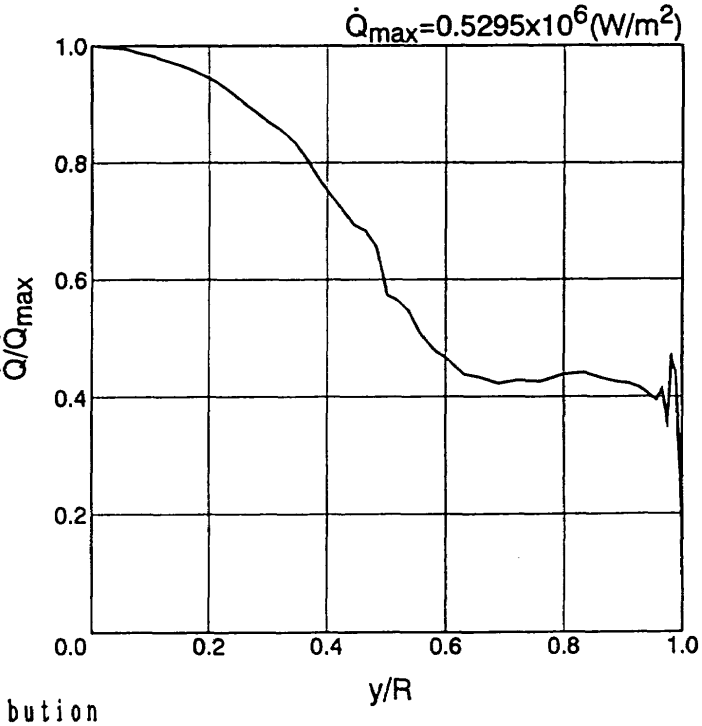

Problem-II-4-④ Surface Heat Flux Distribution

H－6

H－10

Problem II-4 OREX 平衡流 表面熱流束分布

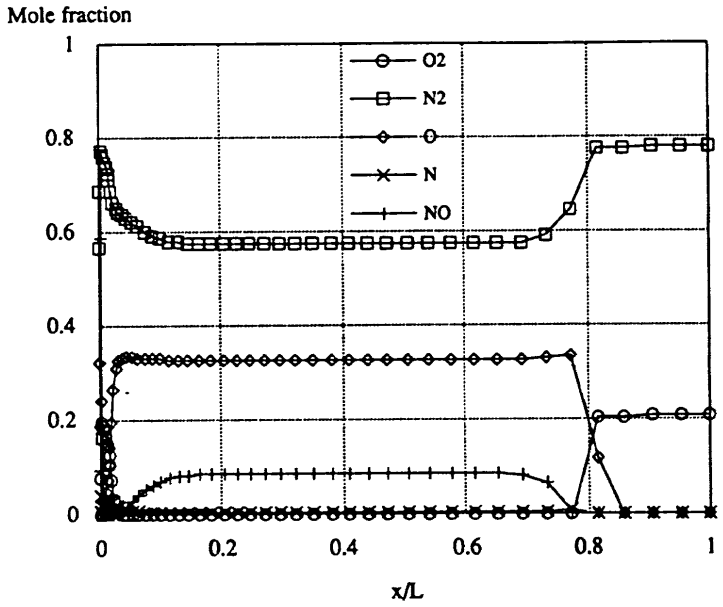

H－4

物体面から計算領域外側までの距離＝0.11m

図　Problem-II-5-⑤

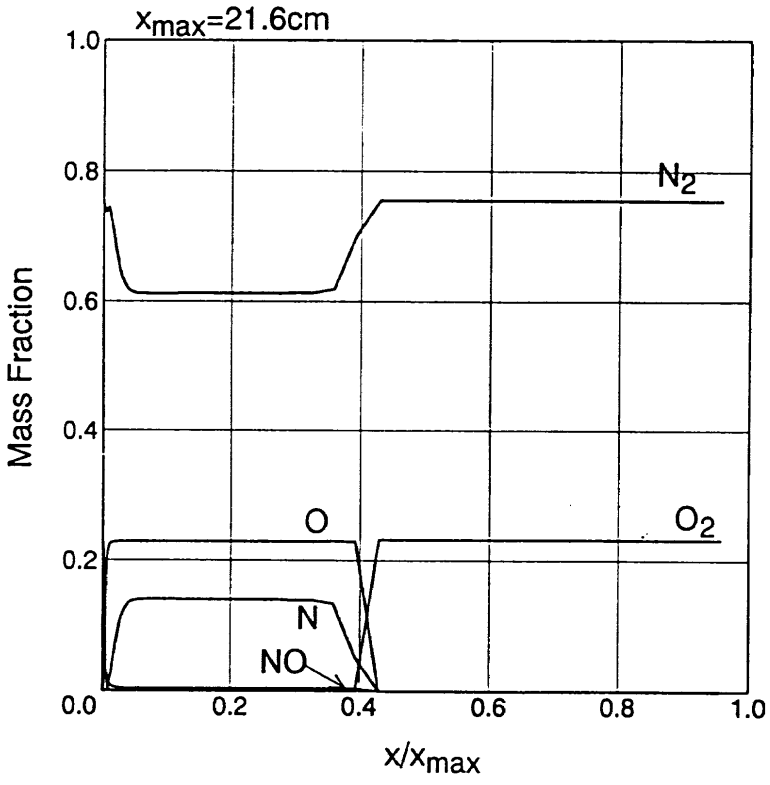

H－10

Problem　II-4　　OREX 平衡流 よどみ点流線質量分率分布

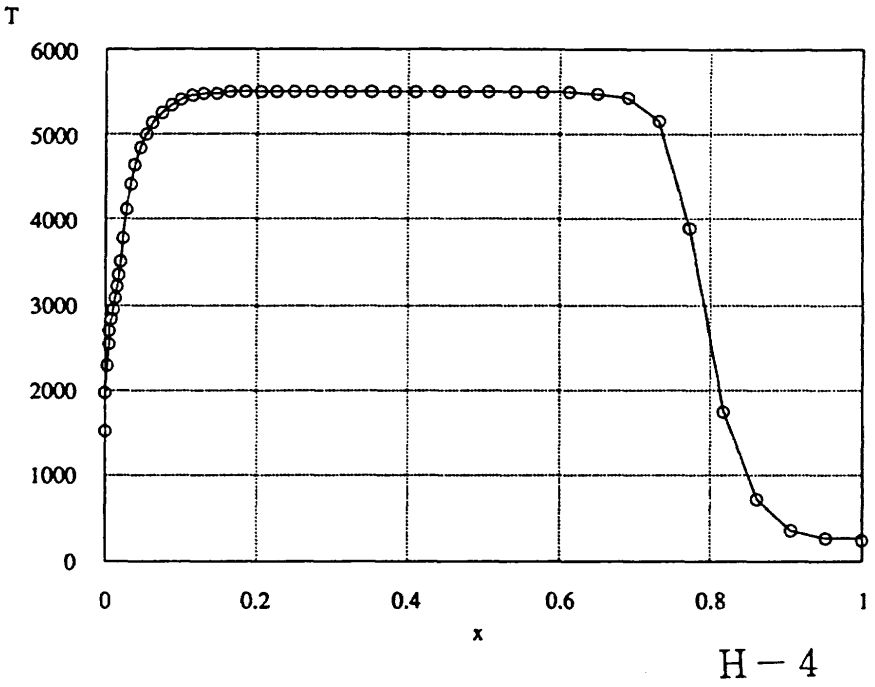

Tmax=5,504 K

図 Problem-II-4-⑥

Problem II-4 OREX 平衡流 よどみ点流線温度分布

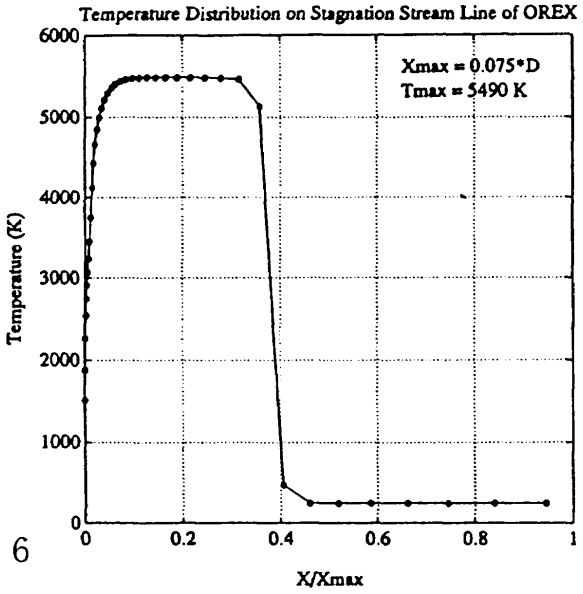

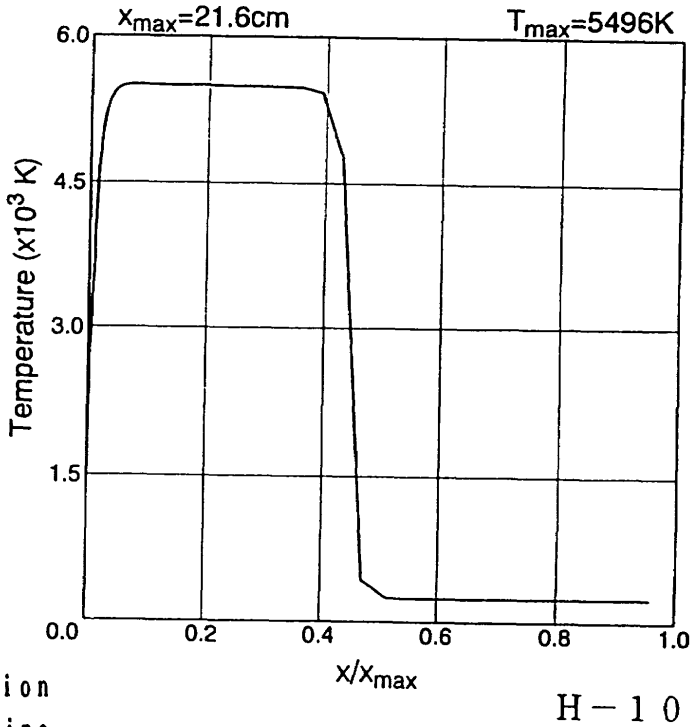

Problem-II-4-⑥ Temperature Distribution on Stagnation Stream Line

Problem Ⅱ－5

OREX

高度　60km

完全気体

計算条件

V_∞ =5562m/s　　W_{N2}= 0.79

T_∞ =248.1K　　W_{O2}= 0.21

P_∞ =23.60N/m^2

Twall=1519K

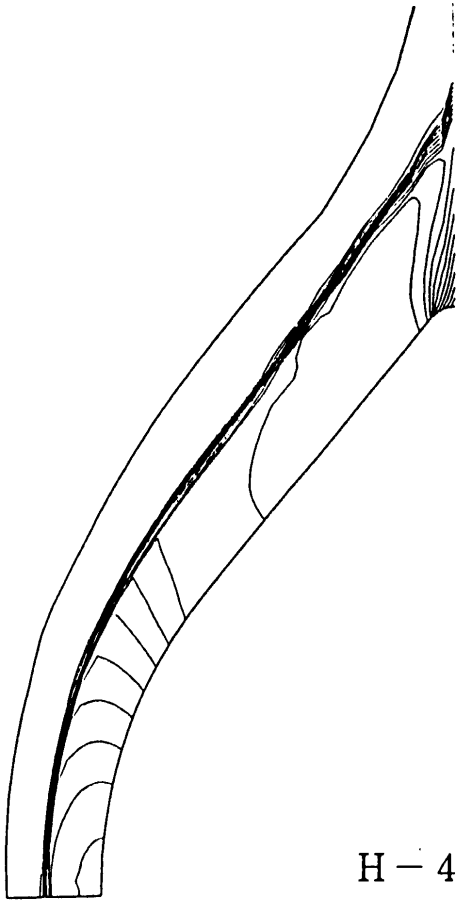

図 Problem-II-5-①

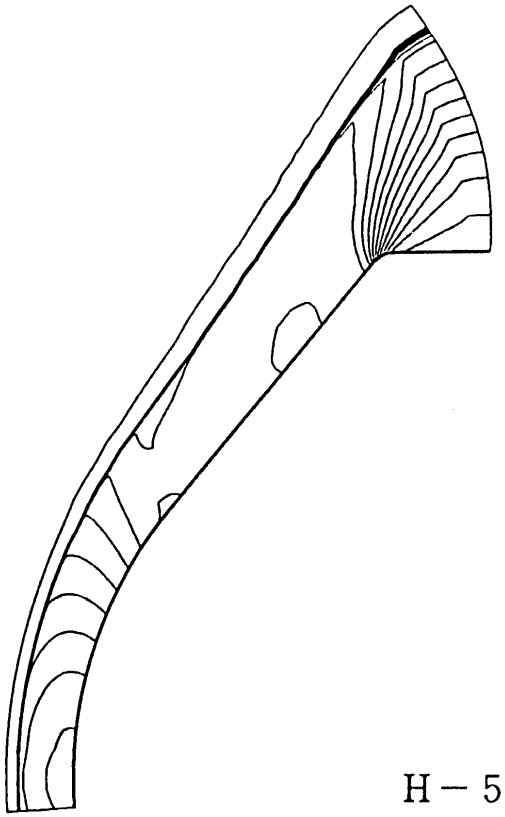

Problem-II-5-① **Pressure Contour** $P/(\rho_\infty U_\infty^2)$

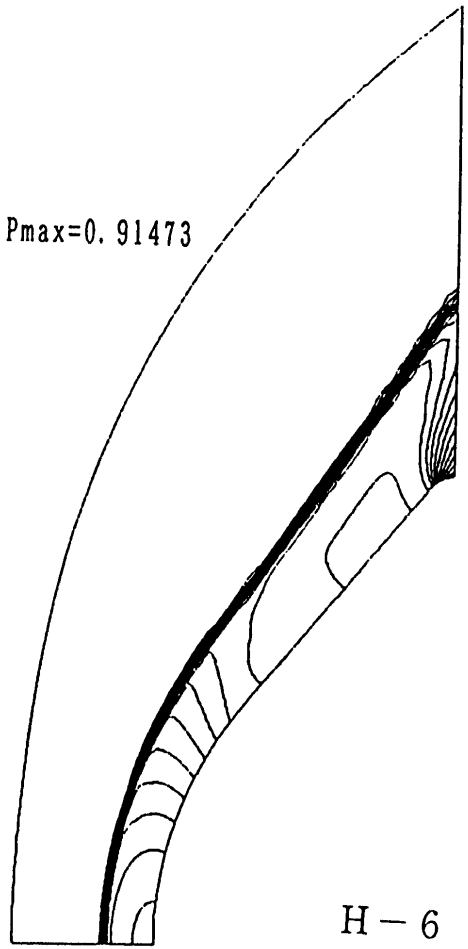

Problem-Ⅱ-5-① Pressure Contour

Problem II-5 OREX 完全気体 圧力線図

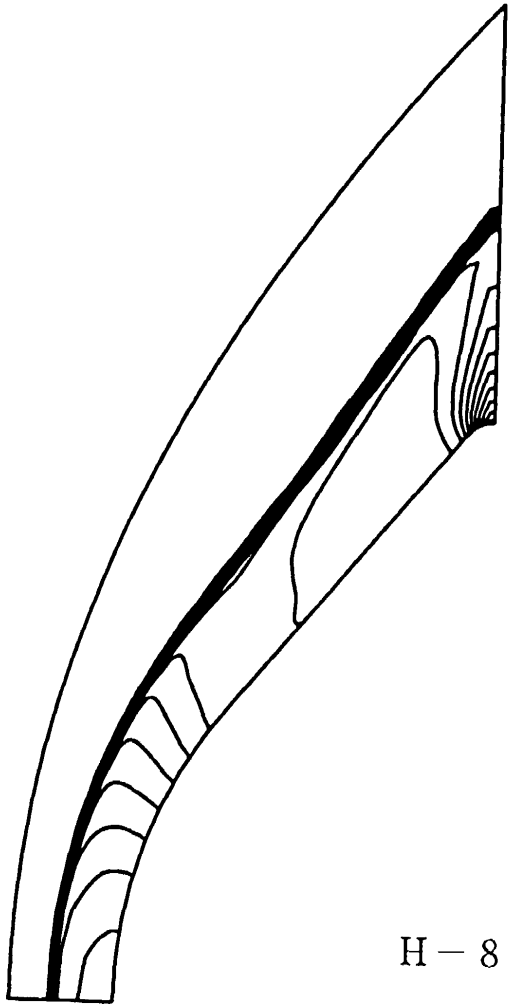

H－8

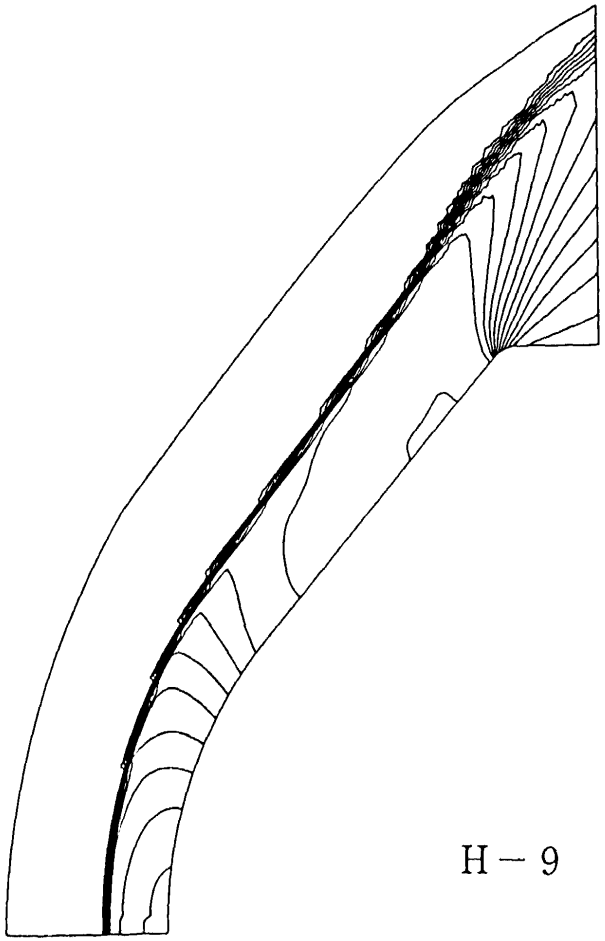

H－9

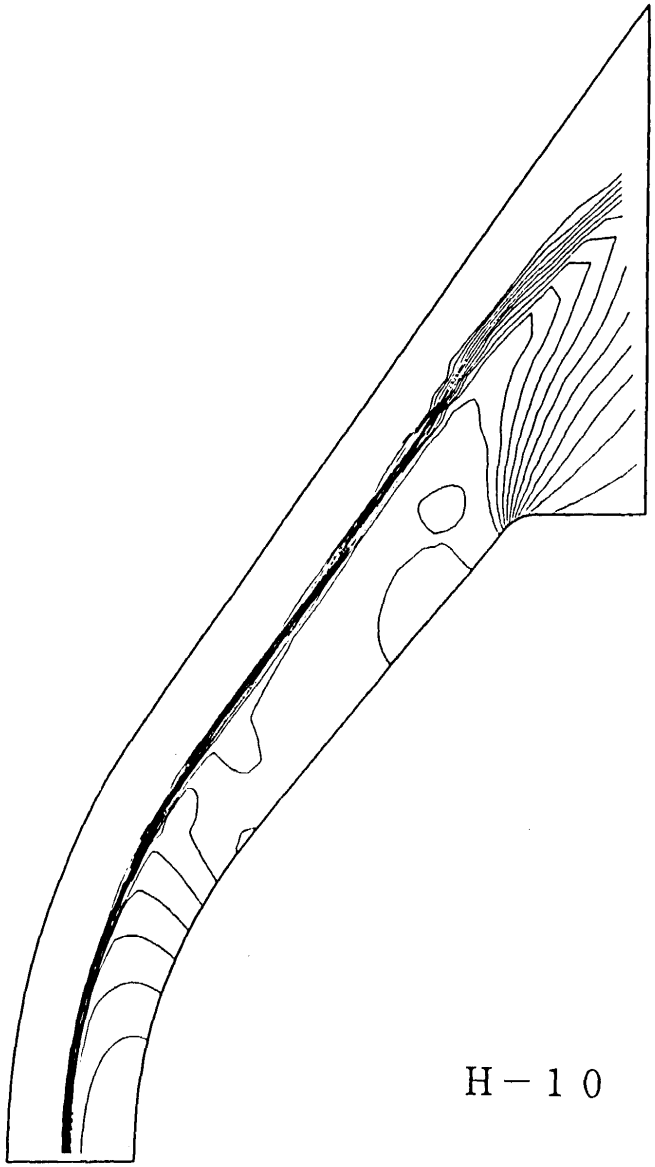

H－10

Problem II-5 OREX Pmax=0.921
Pressure Contour Non React
U_∞=5562m/s T_∞=248.1K
P_∞=23.60N/m^2 T_{wall}=1519K

Problem-II-5-(1)

Problem II-5 OREX 完全気体 圧力線図

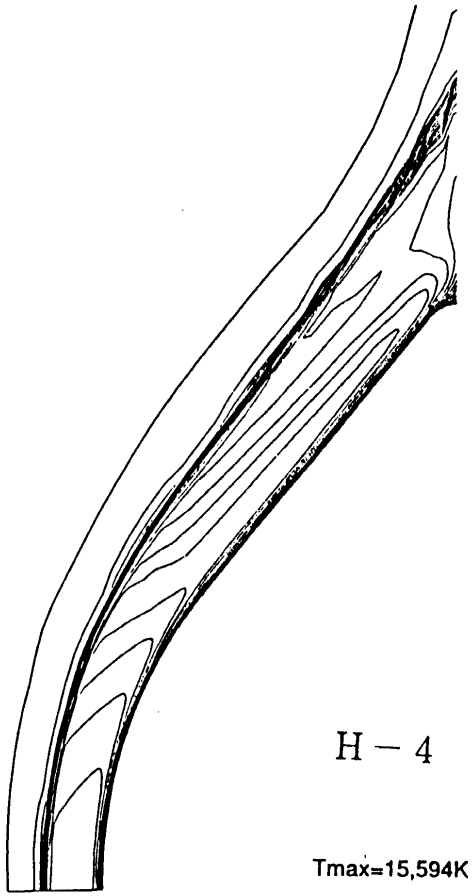

図 Problem-II-5-②

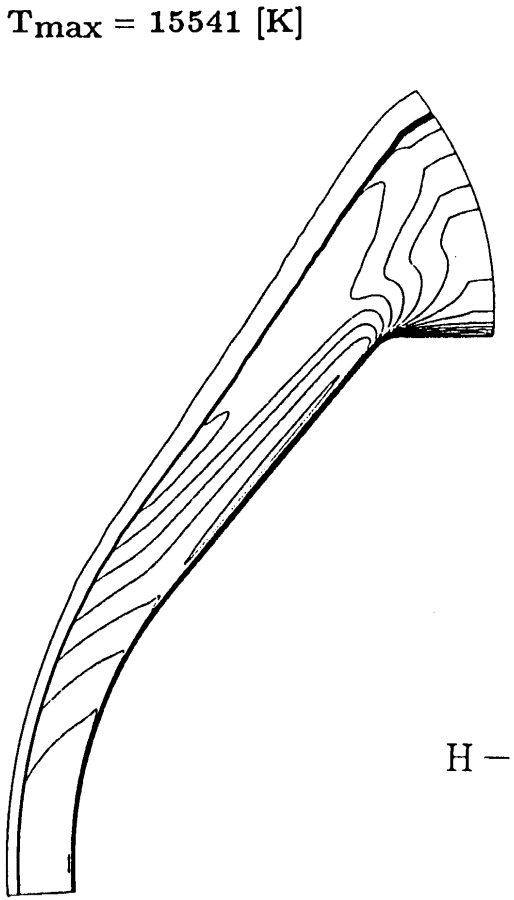

Problem-II-5-② Temperature Contour T/T_∞

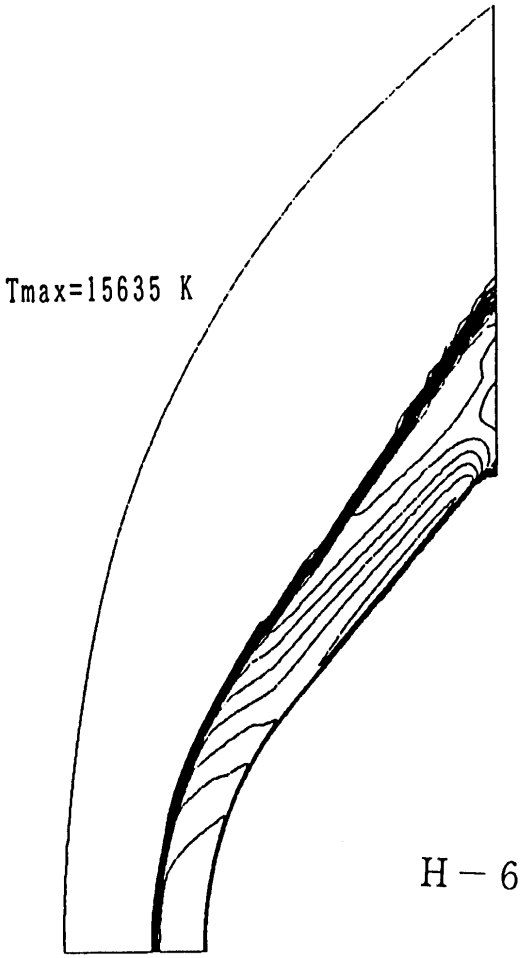

Problem-Ⅱ-5-② Temperature Contour

Problem II-5 OREX 完全気体 等温度線図

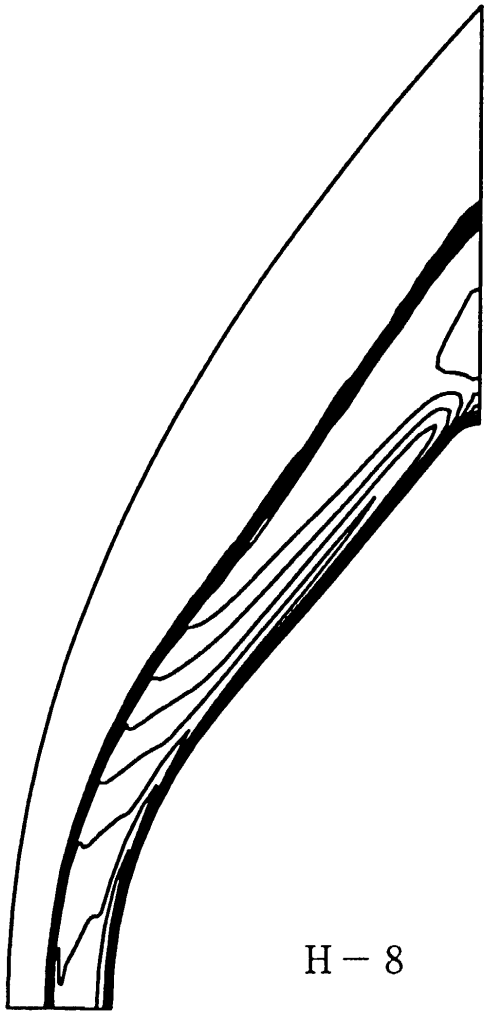

H－8

Problem II-5 OREX Tmax=68.510
Temperature Contour Non React
U_∞=5562m/s T_∞=248.1K
P_∞=23.60N/m^2 T_{wall}=1519K

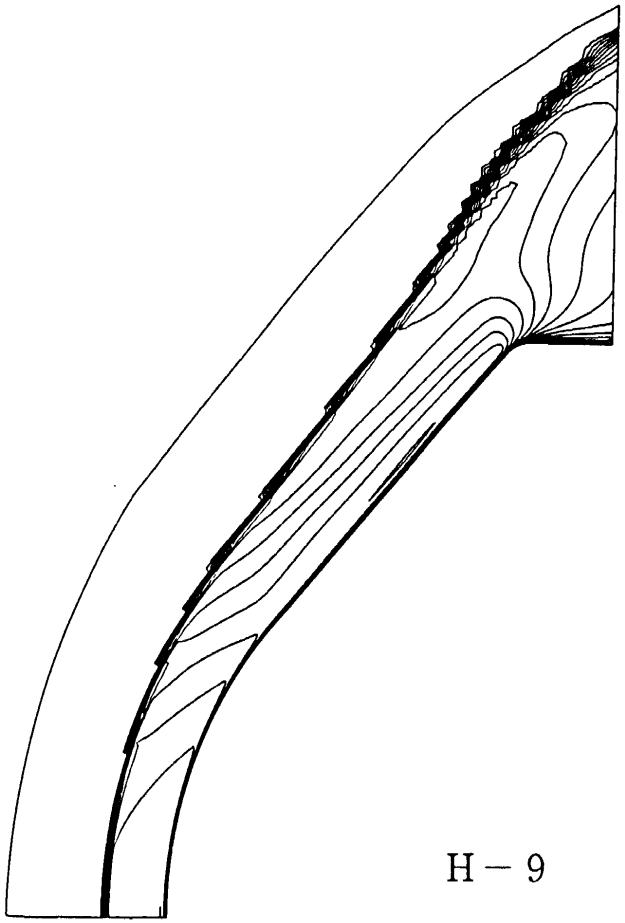

H－9

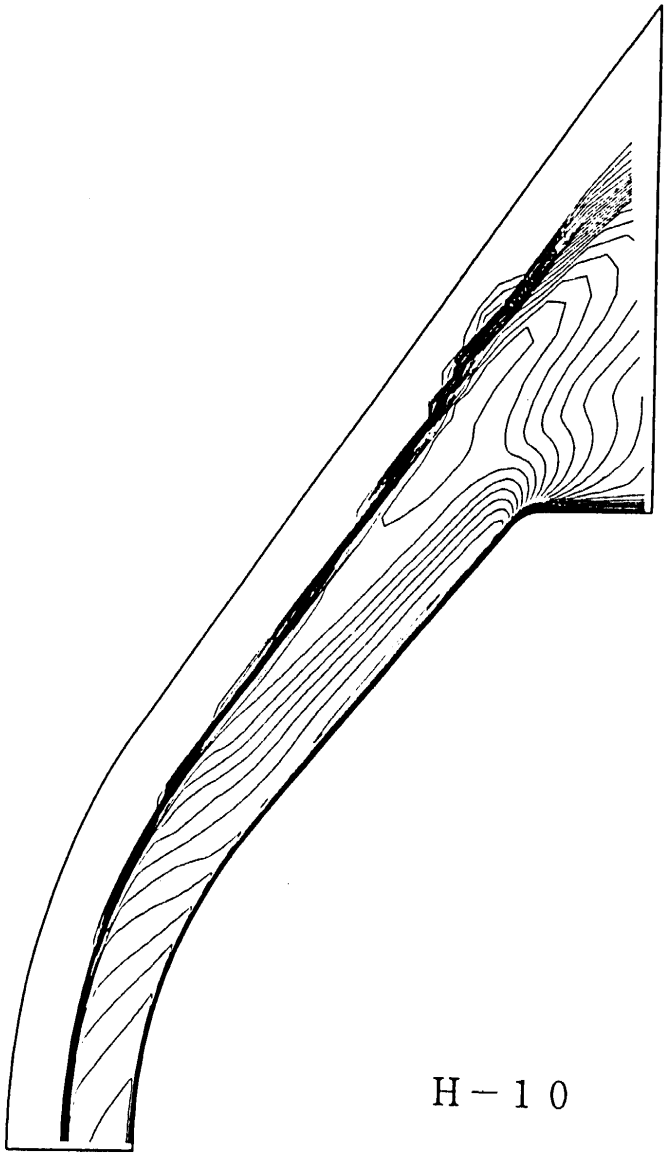

H－10

Problem-II-5-(2)

Problem II-5 OREX 完全気体 等温度線図

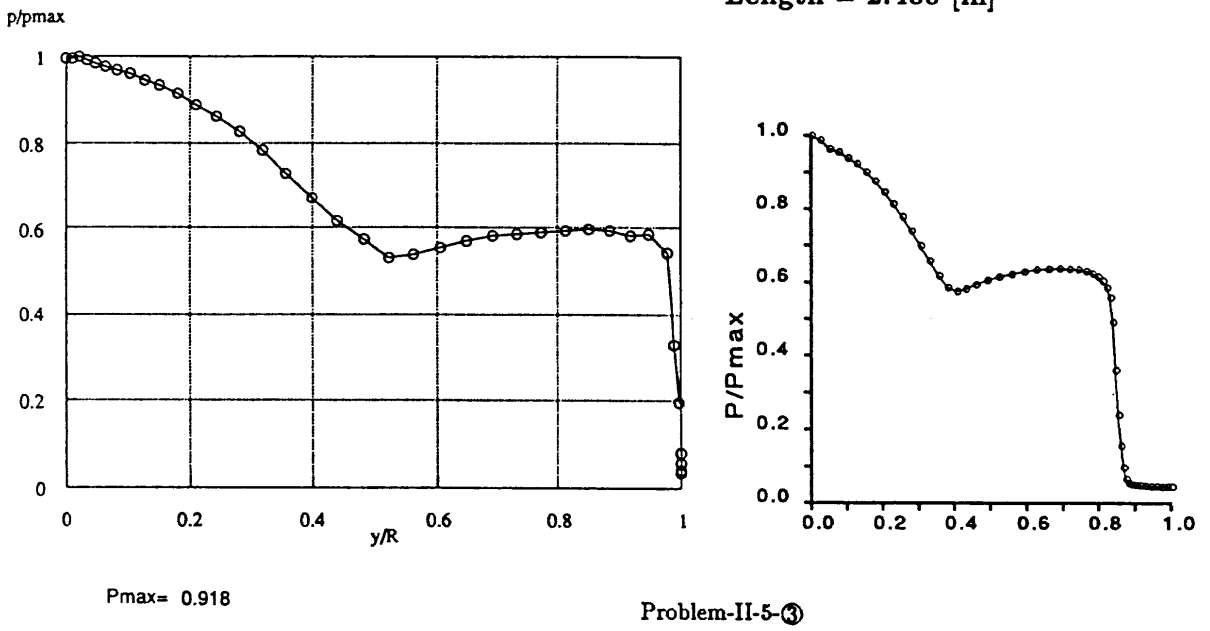

図 Problem-II-5-③

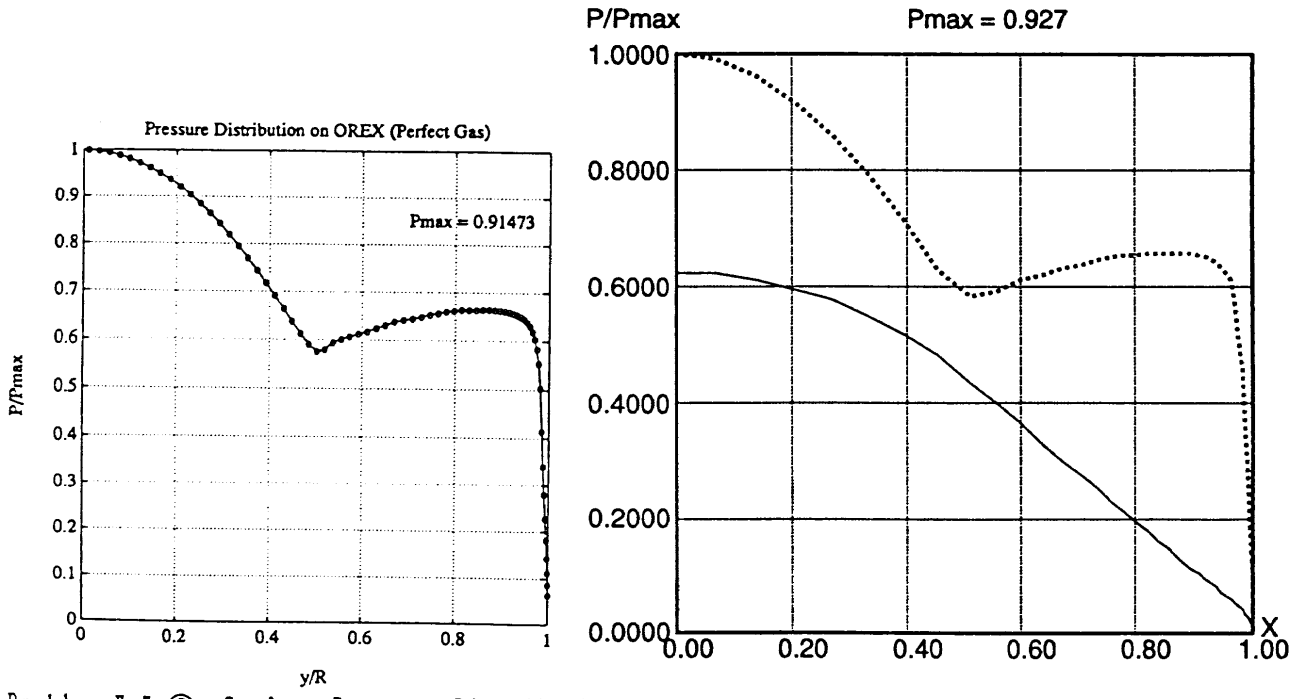

H－6

H－8

Problem II-5 OREX 完全気体 表面圧力分布

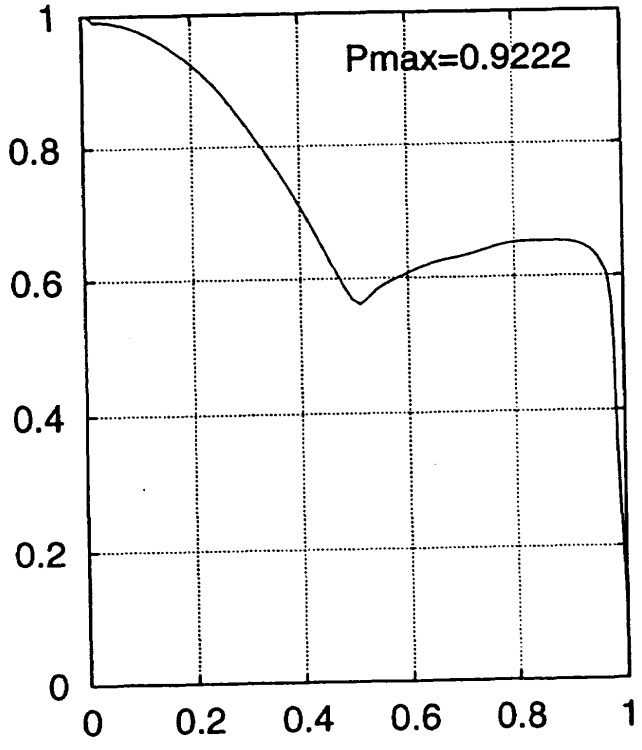

Problem-II-5-(3) H－9

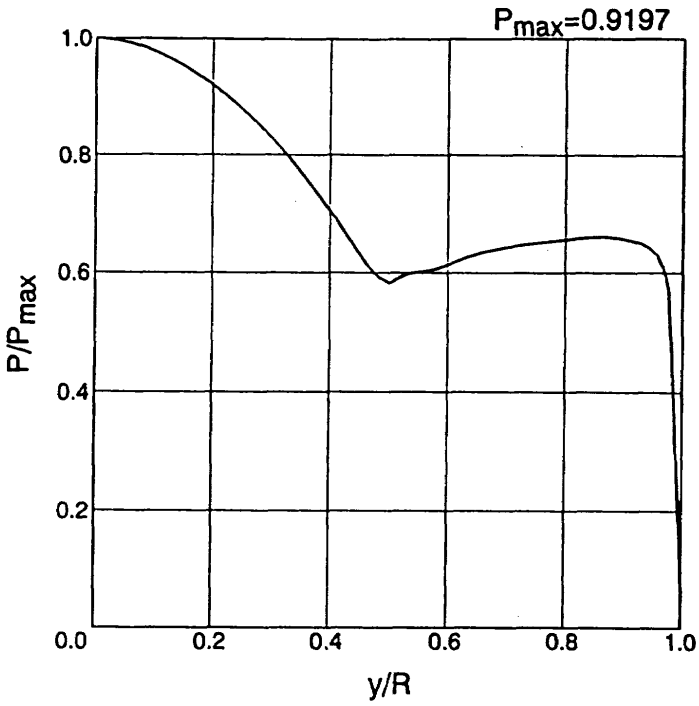

H－10

Problem II-5 OREX 完全気体 表面圧力分布

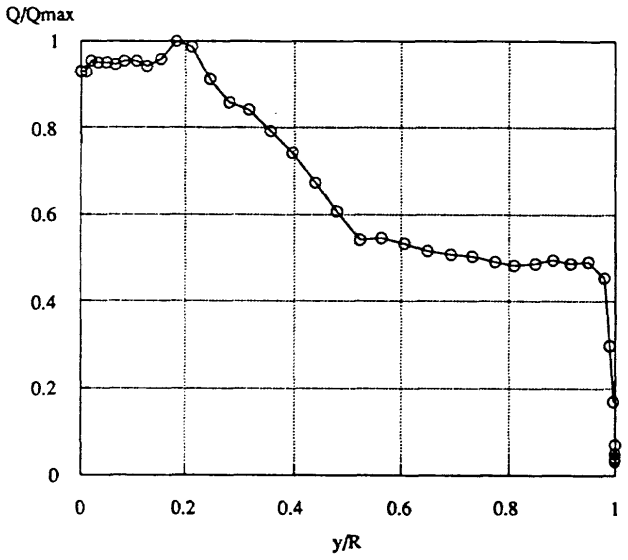

Qmax=3.61×10^5 W/m^2 H－4

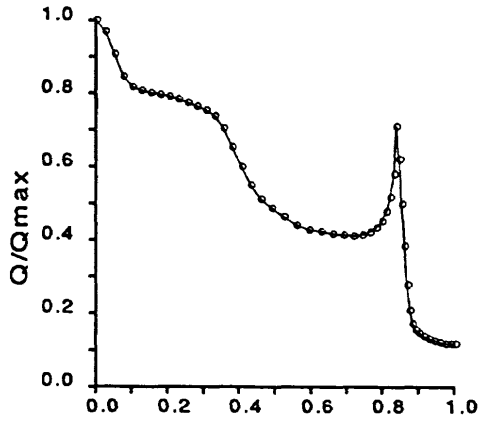

Q_{max} = 246245 [W/m^2]
Length = 2.400 [m]

Problem-II-5-④ H－5

Heat Transfer Distribution along the Body Surface

図 Problem-II-5-④

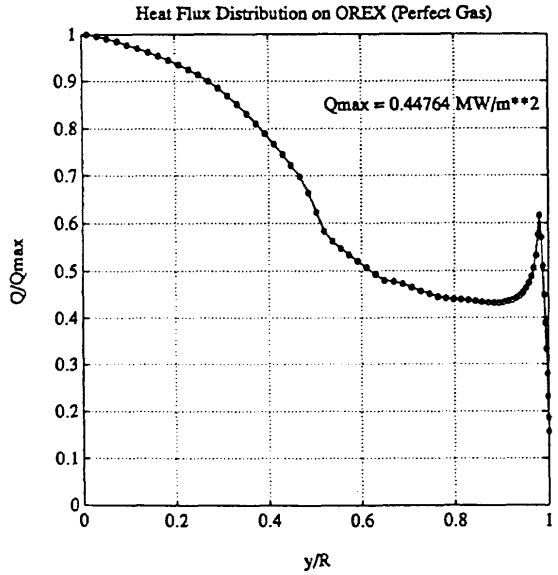

Problem-Ⅱ-5-④ Surface Heat Flux Distribution

H－6

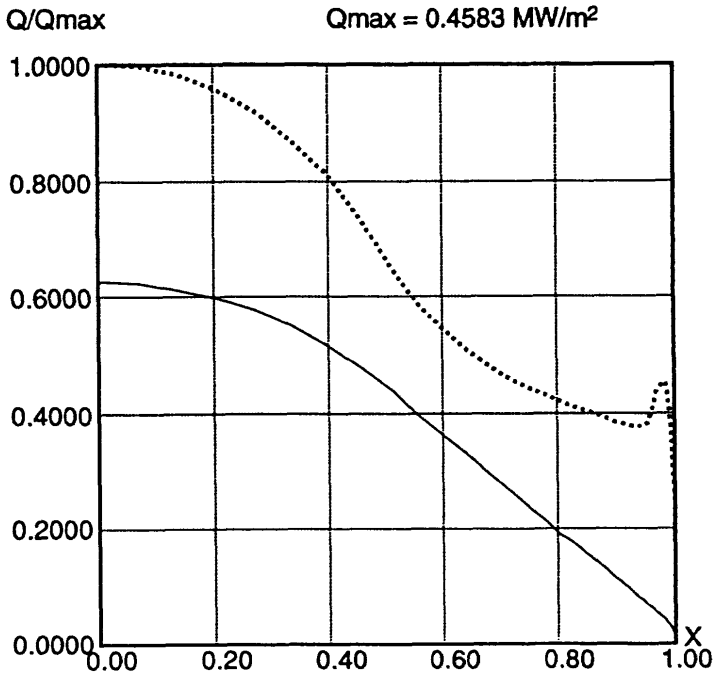

Problem II - 5 OREX

Heat Transfer Distribution

H－8

Problem II-5 OREX 完全気体 表面熱流束分布

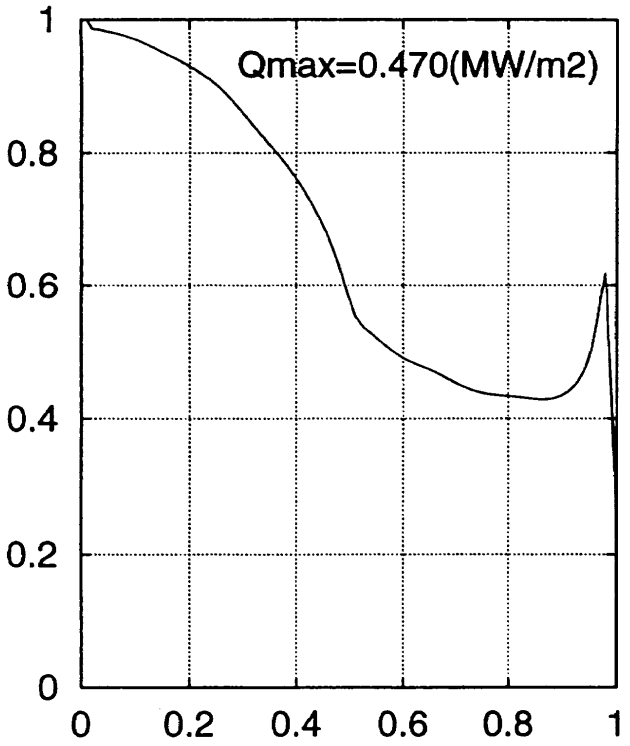

Problem-II-5-(4) H－9

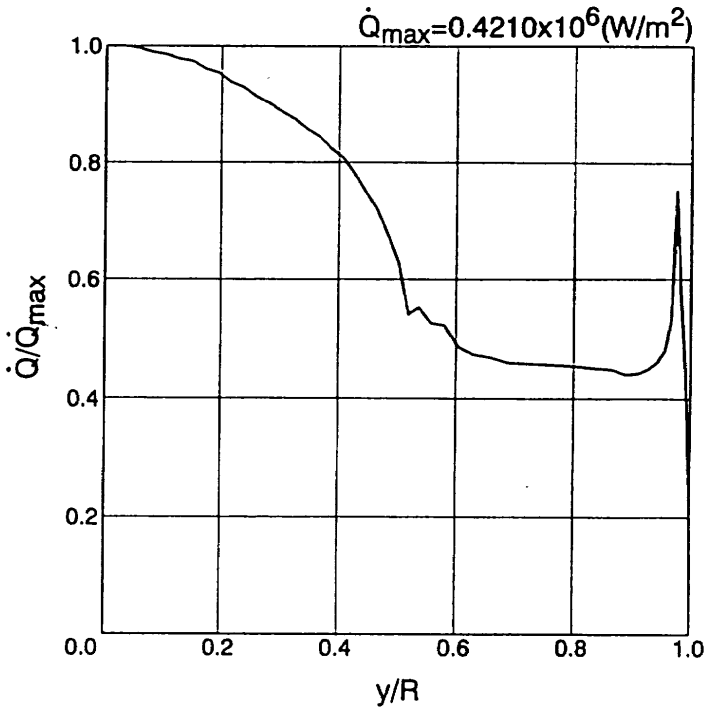

H－10

Problem II-5 OREX 完全気体 表面熱流束分布

T_{max} = 15541 [K]
Distance = 0.218 [m]

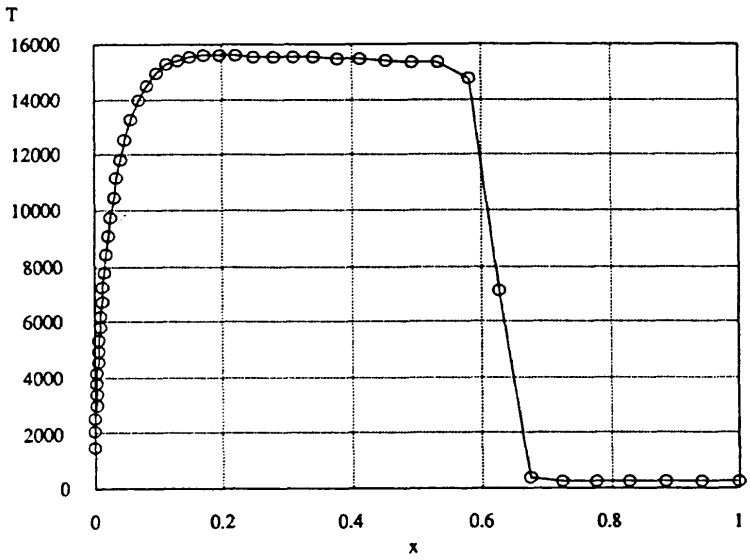

Tmax=15,594 K

図 Problem-II-5-⑥

H－4

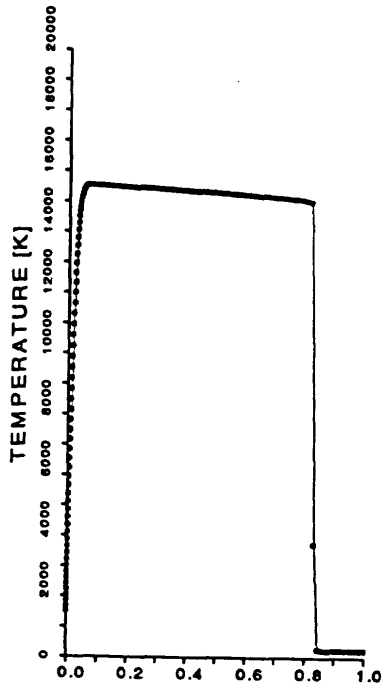

Problem-II-5-⑥

H－5

Temperature Distribution along the Stagnation Stream Line

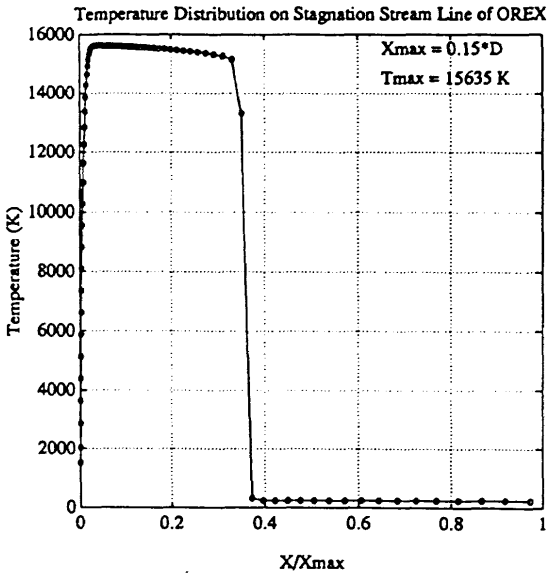

H－6

Problem-II-5-⑥ Temperature Distribution on Stagnation Stream Line

Problem II-5 OREX 完全気体 よどみ点流線温度分布

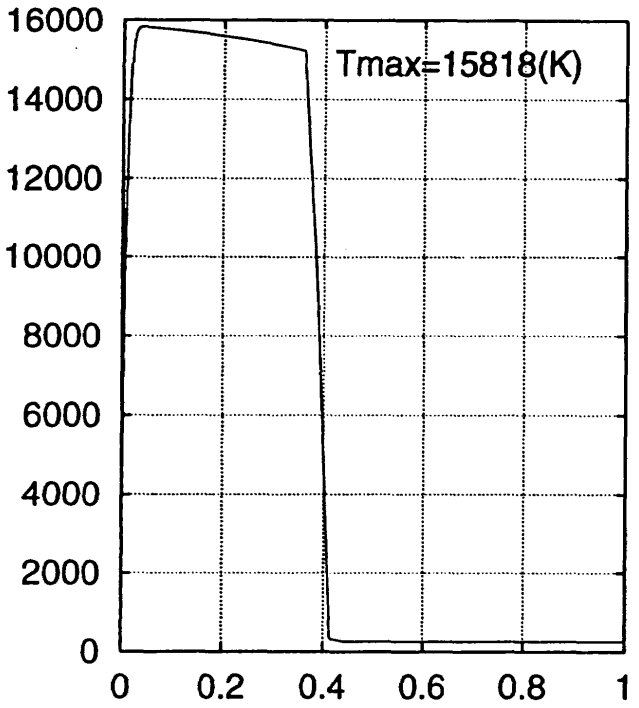

Problem-II-5-(6) H－9

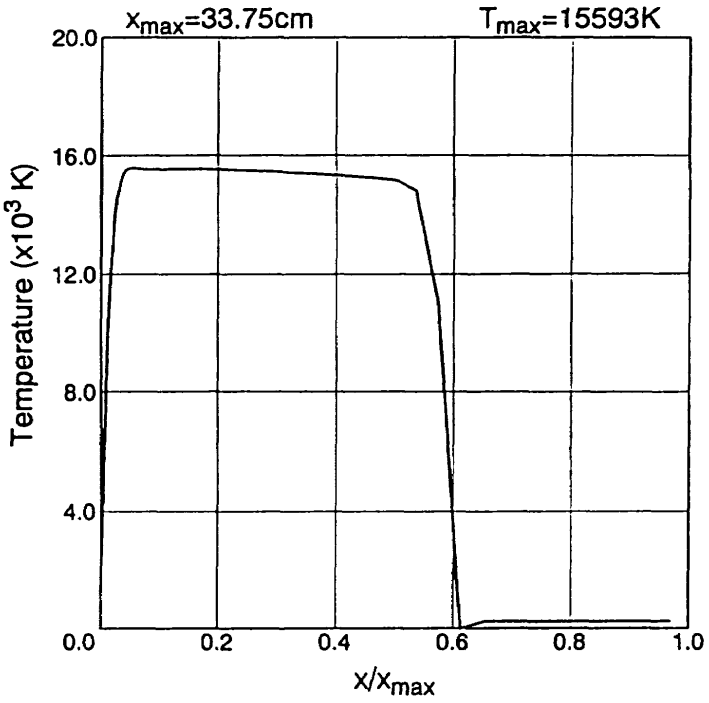

H－10

Problem II-5 OREX 完全気体 よどみ点流線温度分布

Problem Ⅲ－1

Hyperboloid Flare

LTB 条件

Cold Case

計算条件

$M_\infty = 6.83 m/s$

$T_\infty = 67.765 K$

$Re_\infty /m = 0.004085 kg/m^3$

$T_{wall} = 310 K$

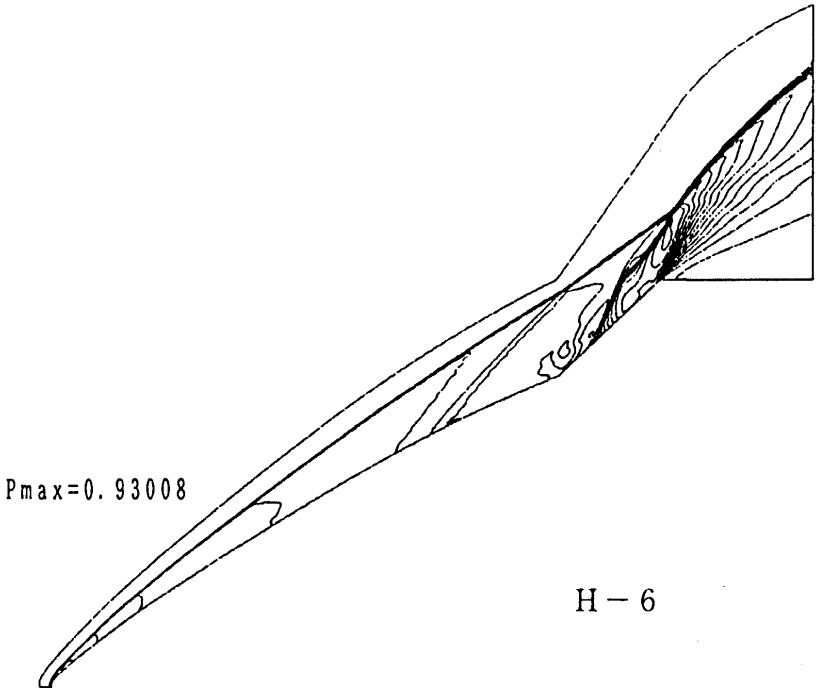

H－6

Problem-Ⅲ-1-① Pressure Contour

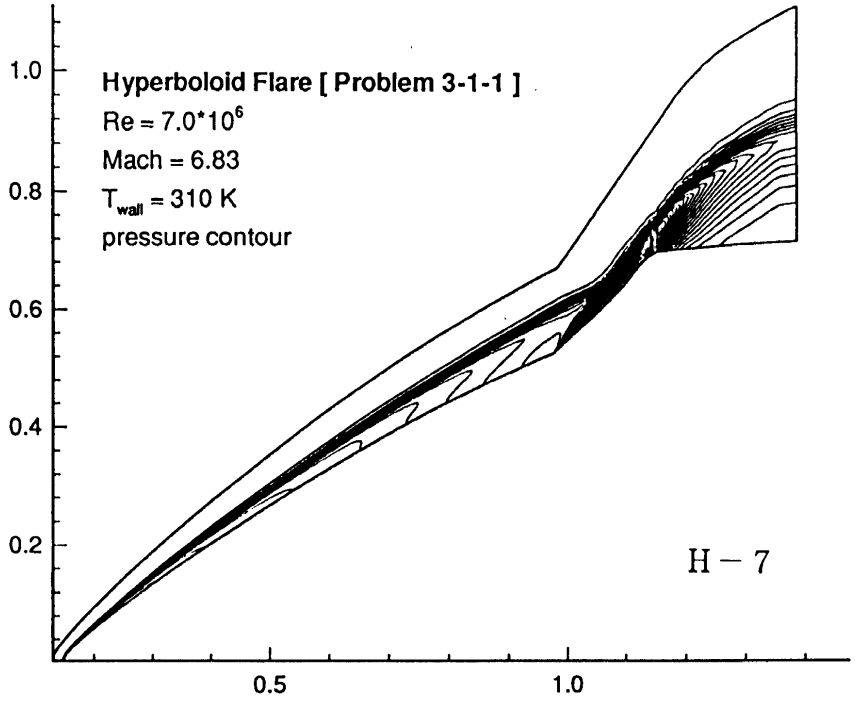

H－7

Problem III Hyperboloid Flare

等圧線図

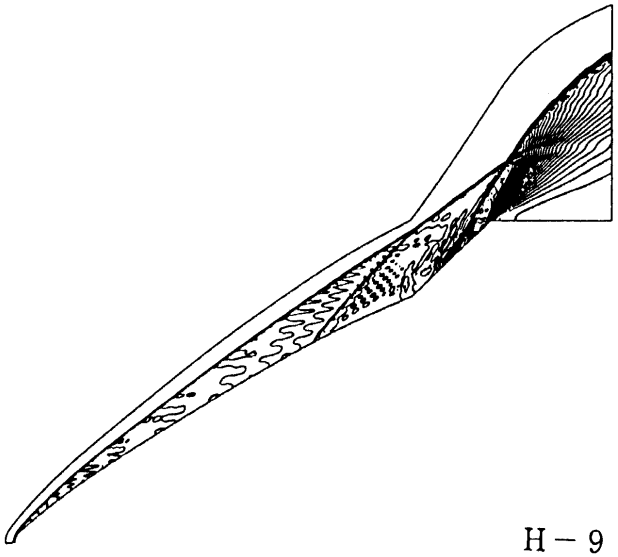

H－9

Problem-III-1-(1)

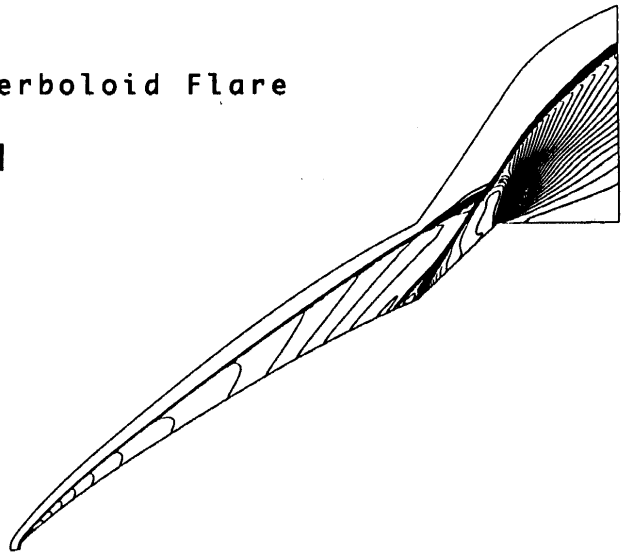

H－9

Problem-III-1-(1)

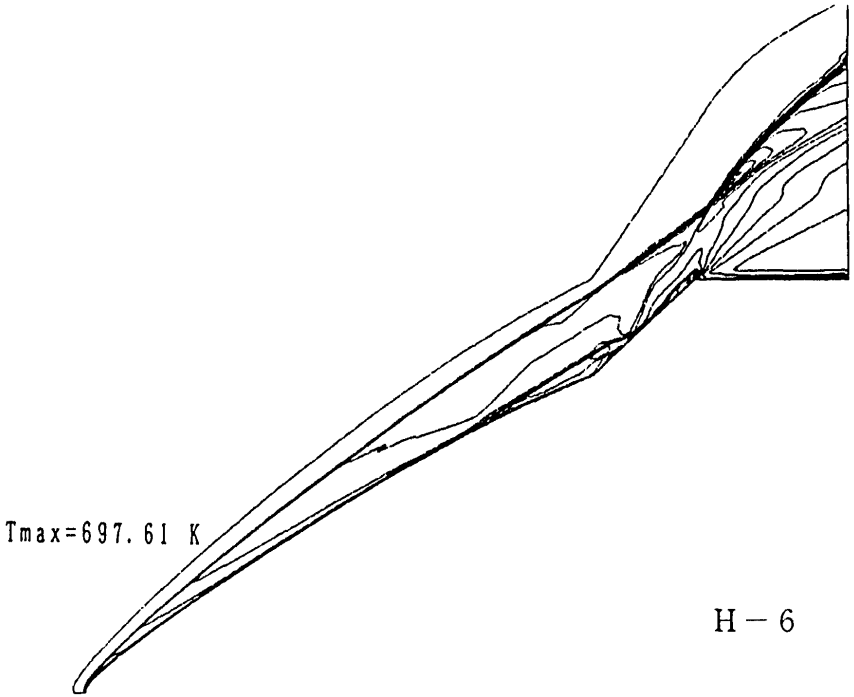

H－6

Problem-Ⅲ-1-② Temperature Contour

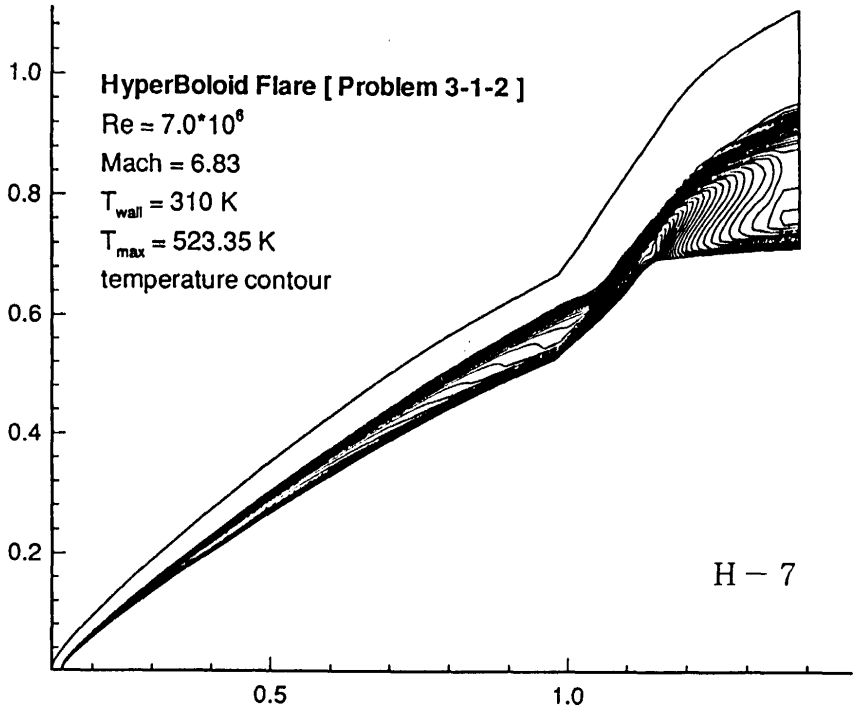

H－7

Problem III Hyperboloid Flare

等温度線図

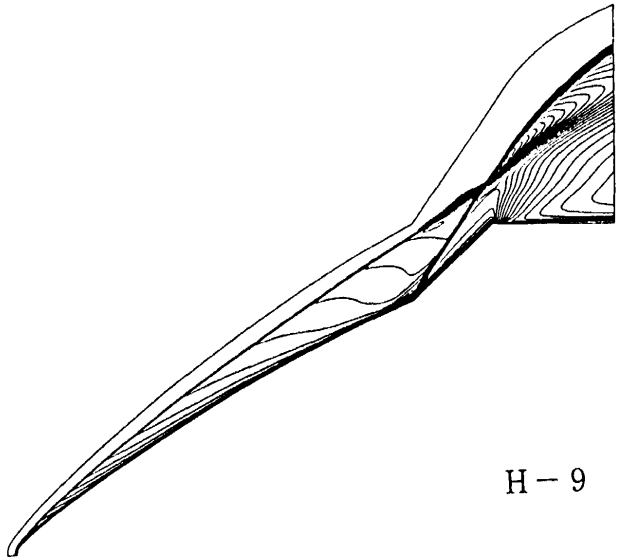

H－9

Problem-III-1-(2)

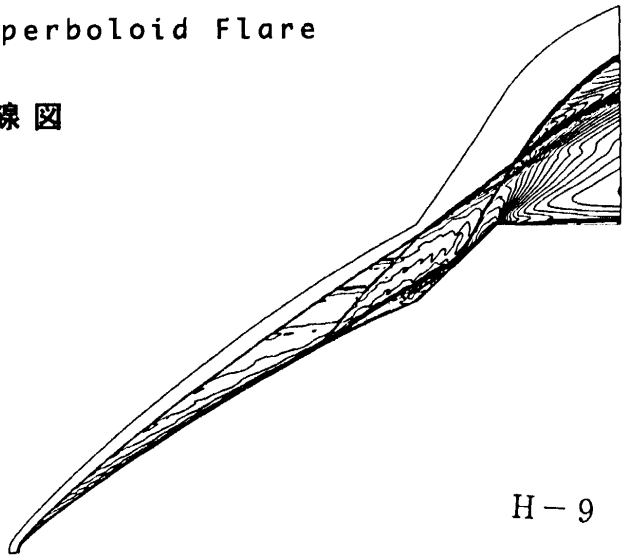

H－9

Problem-III-1-(2)

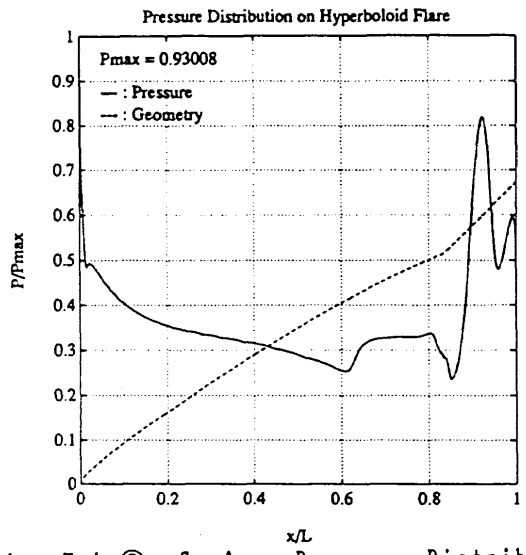

Problem-Ⅲ-1-③ Surface Pressure Distribution

H－6

Problem 3-1-3

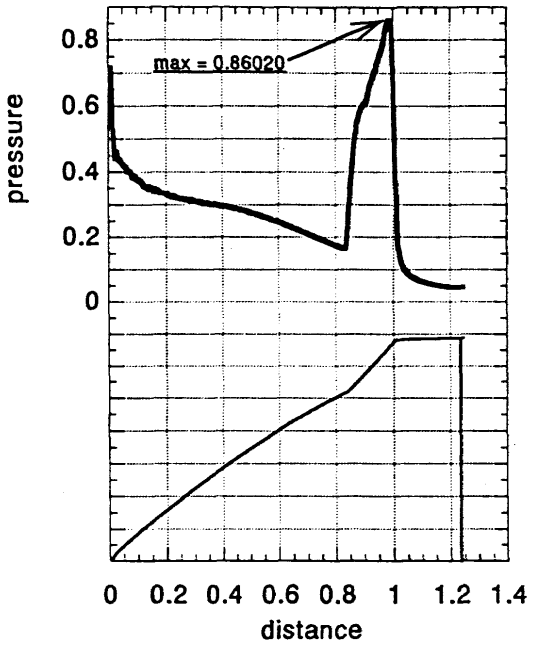

H－7

pressure distribution on body surface

body surface
pressure

Re = $7.0*10^6$

Mach = 6.83

Problem III Hyperboloid Flare

表面圧力分布

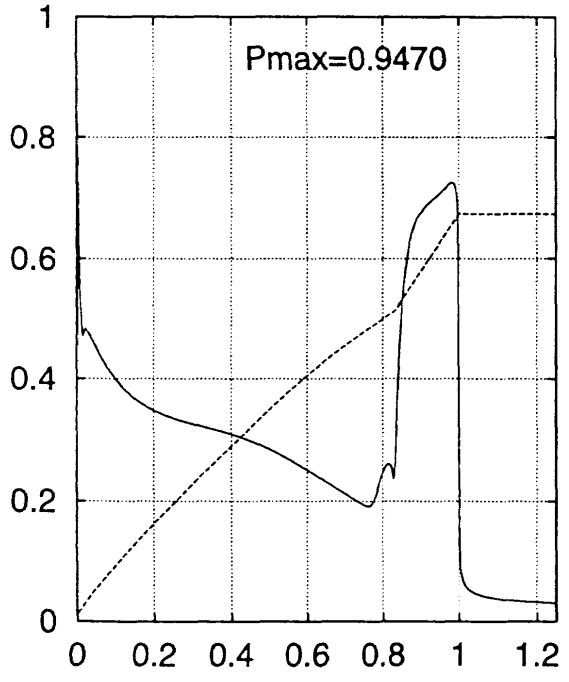

Problem-III-1-(3) H－9

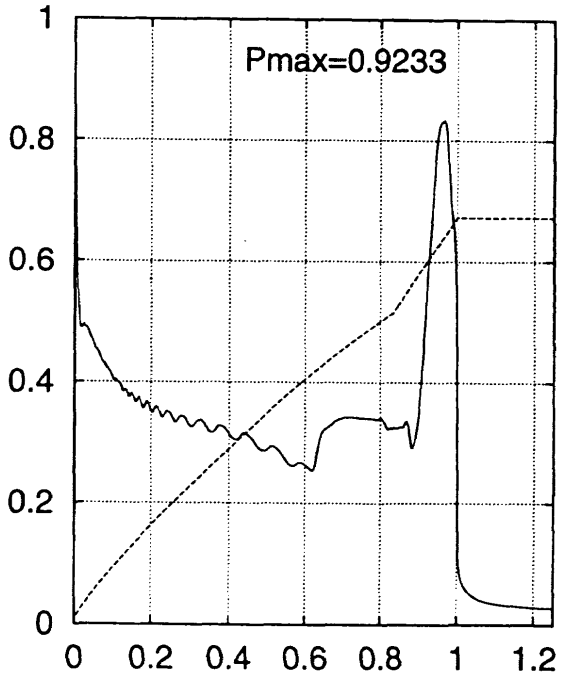

Problem-III-1-(3) H－9

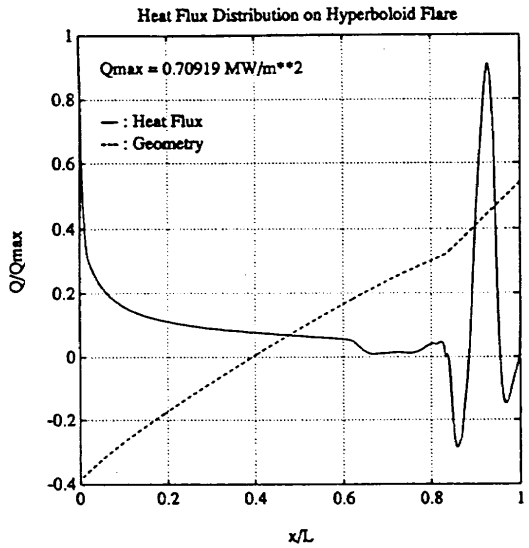

Problem-Ⅲ-1-④ Surface Heat Flux Distribution

Heat Flux Calculation is same as Problem- Ⅱ-5.

$\mu_w = 1.8267\times10^{-5}$ [kg/m/s]

$\kappa_w = \frac{\mu_w C_p}{Pr} = 7.2831\times10^{-3}$ [J/K/m/s]

H－6

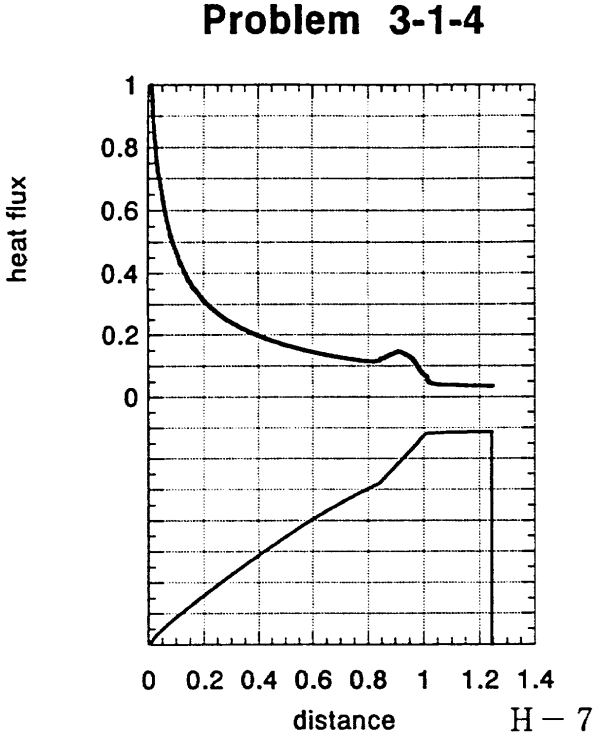

H－7

Problem III Hyperboloid Flare

表面空力加熱分布

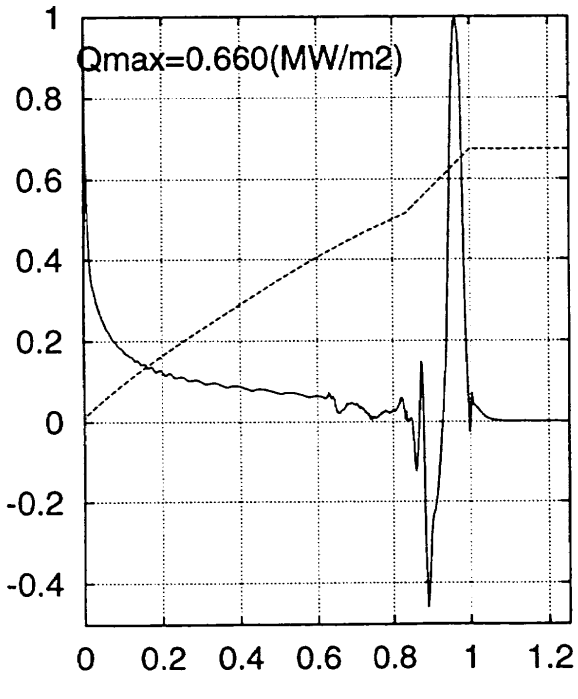

Problem-III-1-(4) H－9

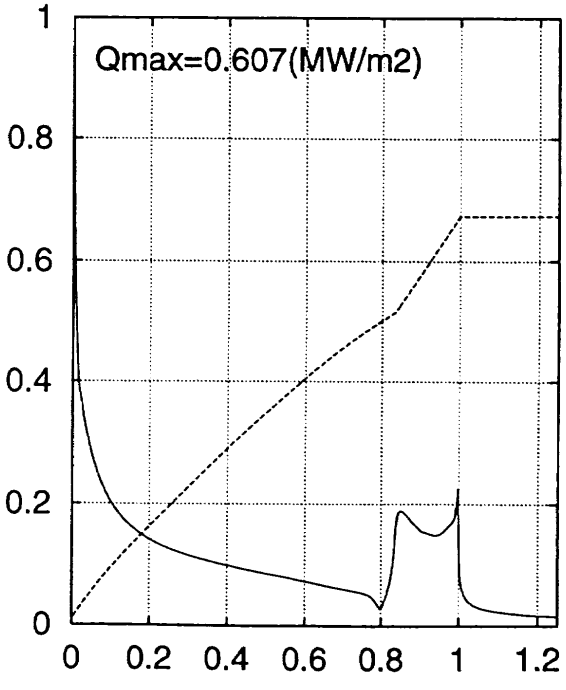

Problem-III-1-(4) H－9

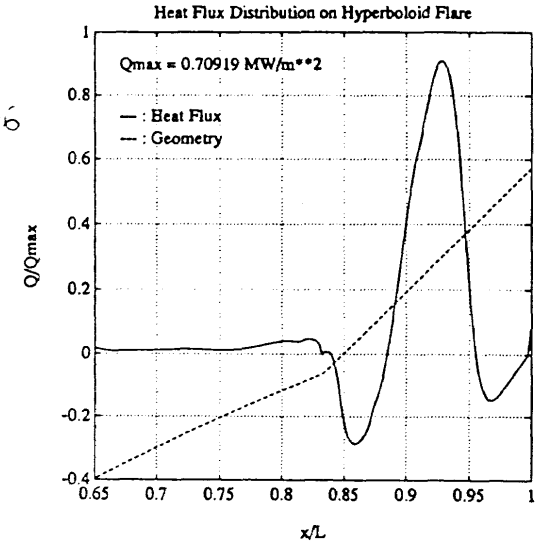

H-6

Problem-Ⅲ-1-④ Surface Heat Flux Distribution
(Focused on Recompression Region)

H－6

Problem 3-1-4

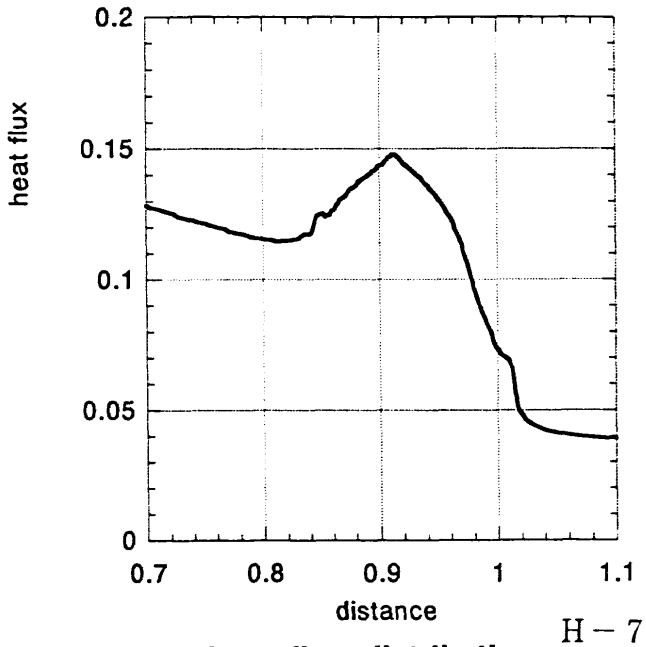

H－7

heat flux distribution on body surface (detail)

heat flux
body surface

Problem III Hyperboloid Flare

表面空力加熱分布

・再付着領域拡大図

Re = $7.0*10^6$

Mach = 6.83

Qmax = $2.017*10^4$ (W/m^2)

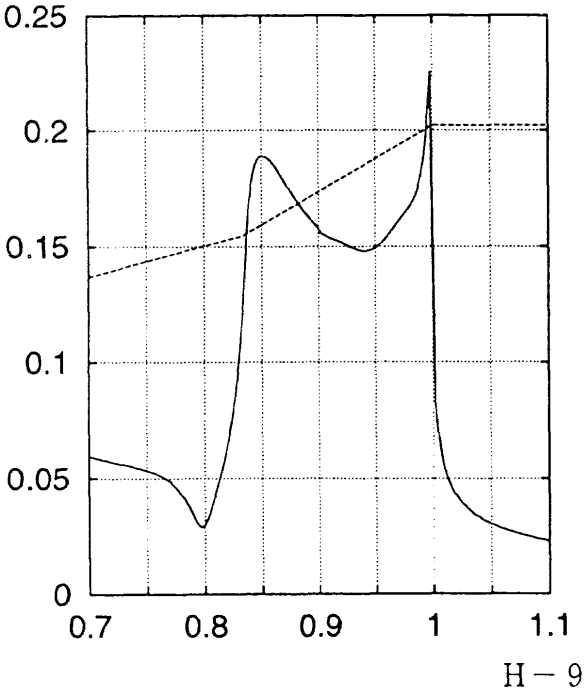

H－9

Problem-III-1-(4) EXTENSION

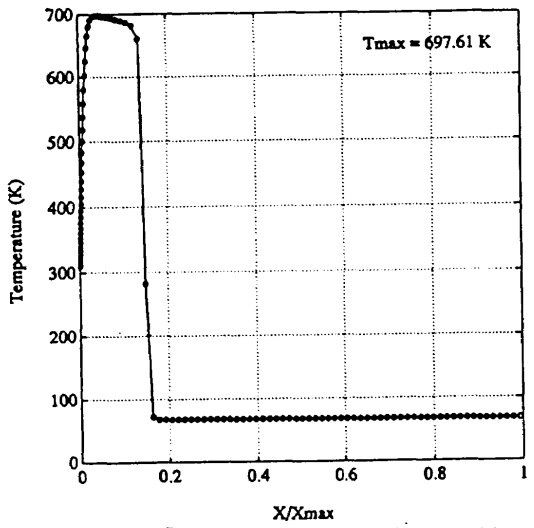

Problem-Ⅲ-1-⑥ Temperature Distribution on Stagnation Stream Line

H－6

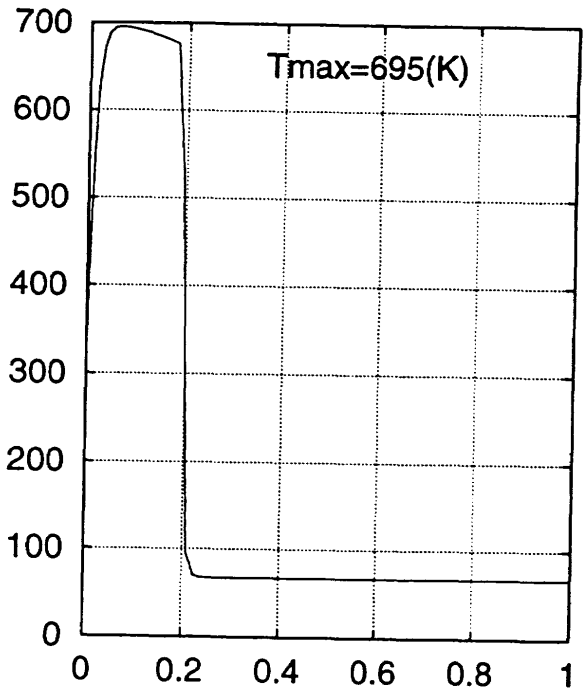

H－9 Problem-III-1-(6)

Problem III Hyperboloid Flare よどみ点流線温度分布

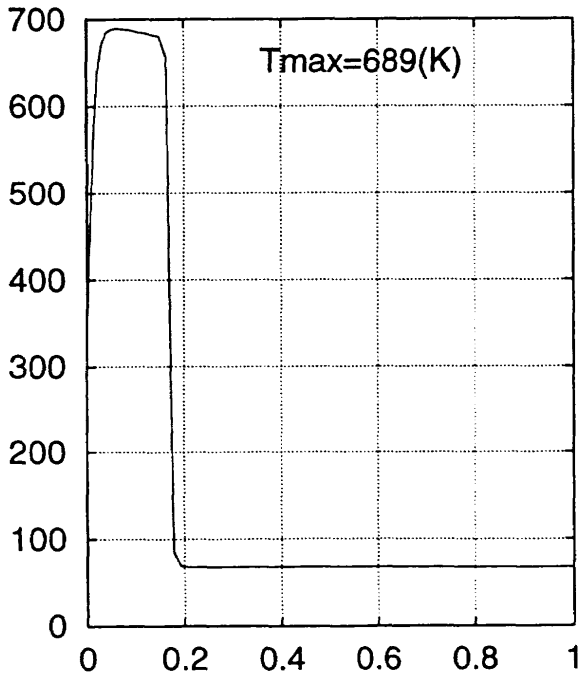

H－9 Problem-III-1-(6)

Problem Ⅲ－2, 3

Hyperboloid Flare

ONERA F4 条件

非触媒及び完全触媒ケース

計算条件

V_∞ =3934m/s

T_∞ =188.3K

ρ_∞ =0.00157kg/m^3

Twall=300K

W_N = 0.0

W_O = 0.0497

W_{N2}= 0.7254

W_{O2}= 0.1354

W_{NO}= 0.0895

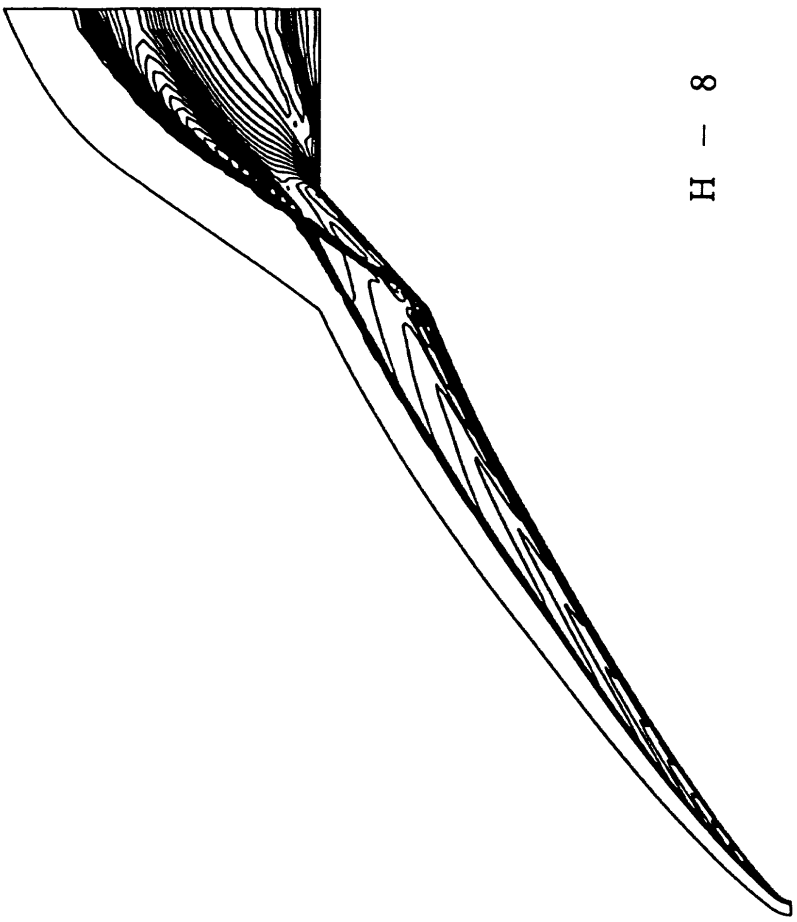

等温度線図

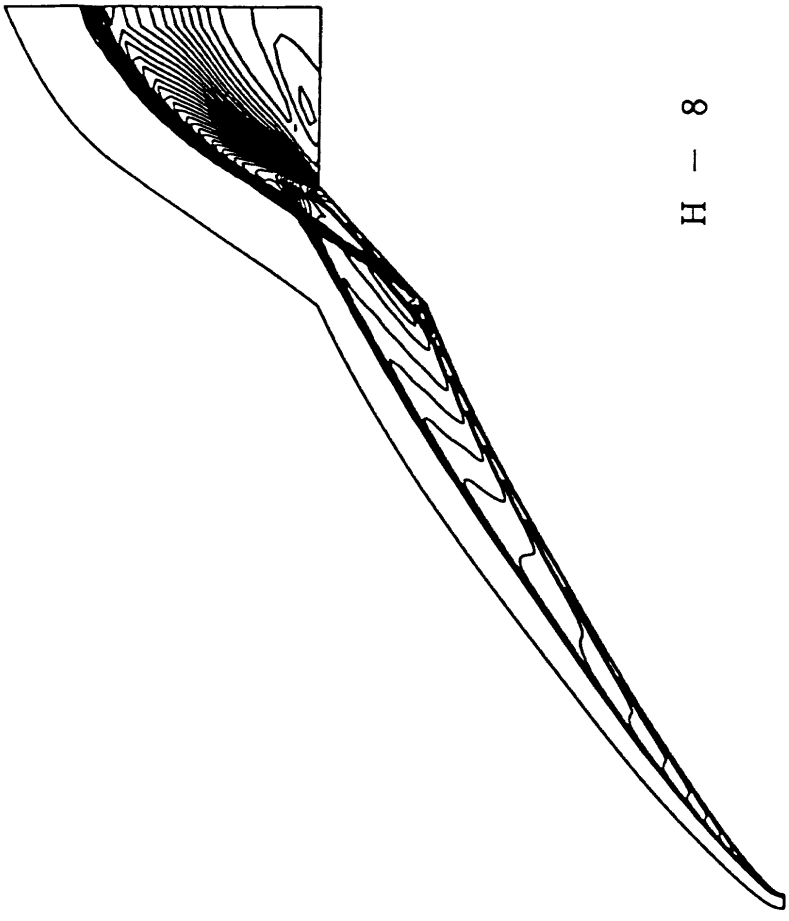

等圧線図

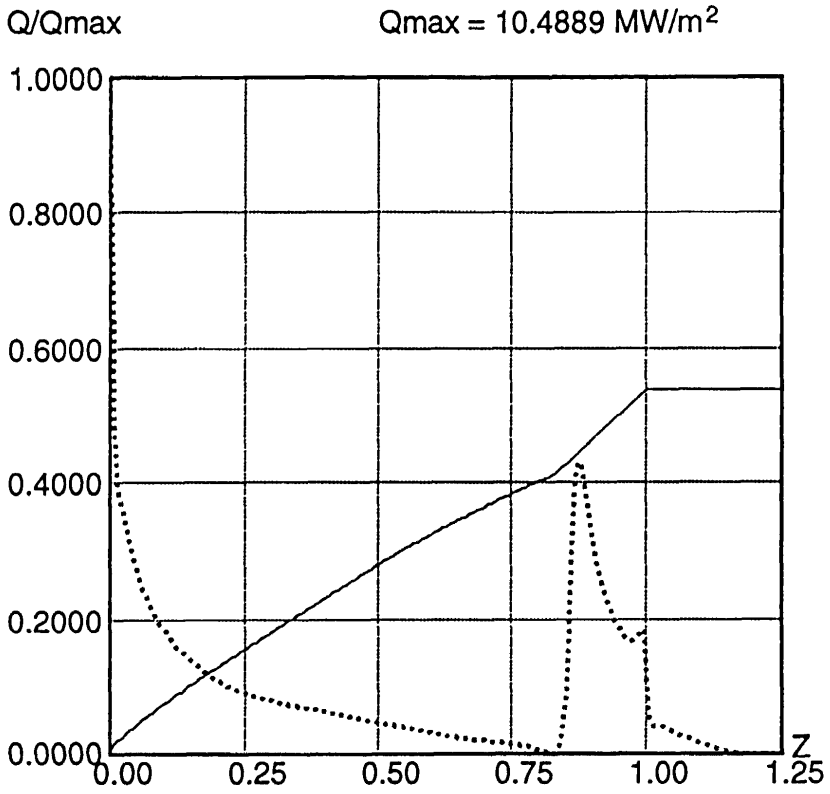

Problem III - 2 Hyperboloid Flare

Heat Transfer Distribution

H － 8　　表 面 圧 力 分 布

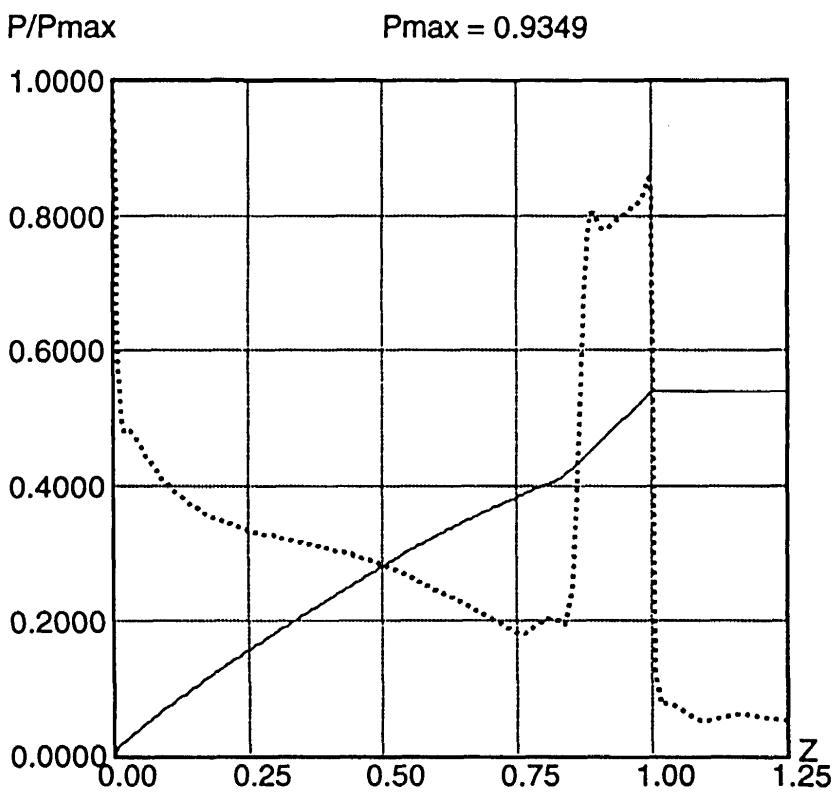

Problem III - 2 Hyperboloid Flare

Pressure Distribution

H － 8　　表 面 空 力 加 熱 分 布

Problem Ⅳ－1, 2

Spherically 70° Blunted Cone

HEG条件

非触媒及び完全触媒ケース

計算条件

V_∞ =10.31m/s

T_∞ =489.9K

ρ_∞ =0.004085kg/m^3

Twall=295K

W_N = 0.0

W_O = 0.0483

W_{N2}= 0.7350

W_{O2}= 0.1490

W_{NO}= 0.0677

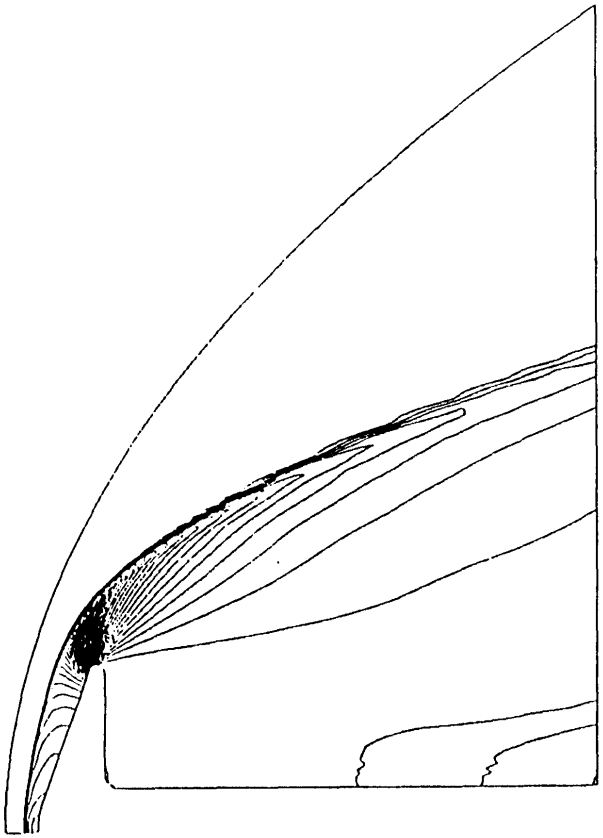

H－3

Problem IV-1-1

H－8

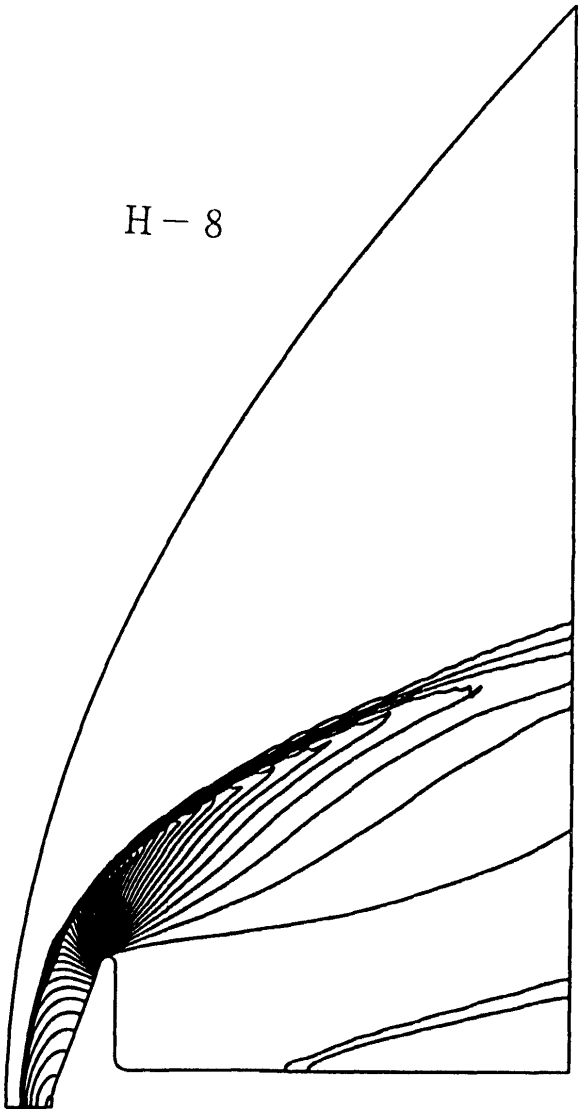

Spherically Blunted Cone
Pressure Contour Pmax=0.923
Mach=12.31 T_∞=490.0
ρ_∞=0.0041 P_∞=588.4

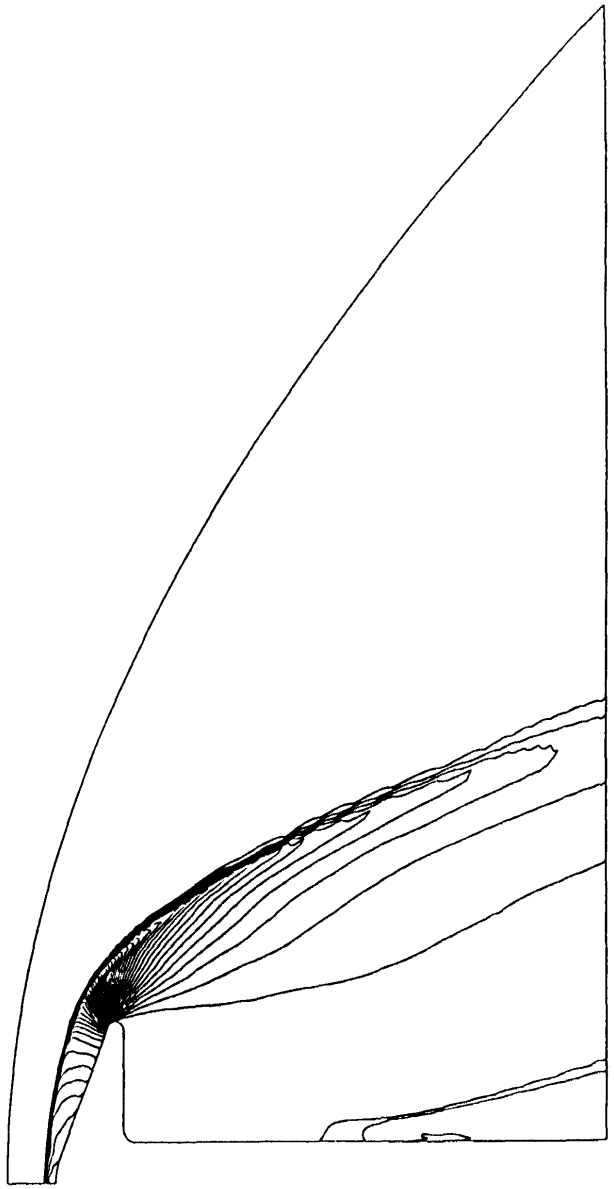

H－9

Problem-IV-1-(1)

Problem IV Blunt Cone 等圧線図

Problem IV Blunt Cone 等圧線図

Fig. Problem-IV-2-1 : Pressure Contours

Fig. Problem-IV-1-1 : Pressure Contours

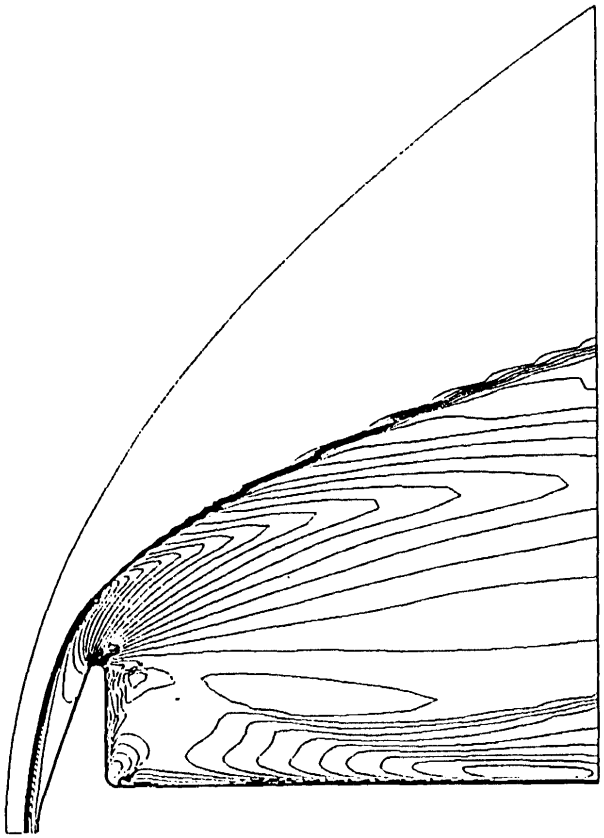

H－3

Problem IV-1-2 (Tmax = 9.2032e3 K)

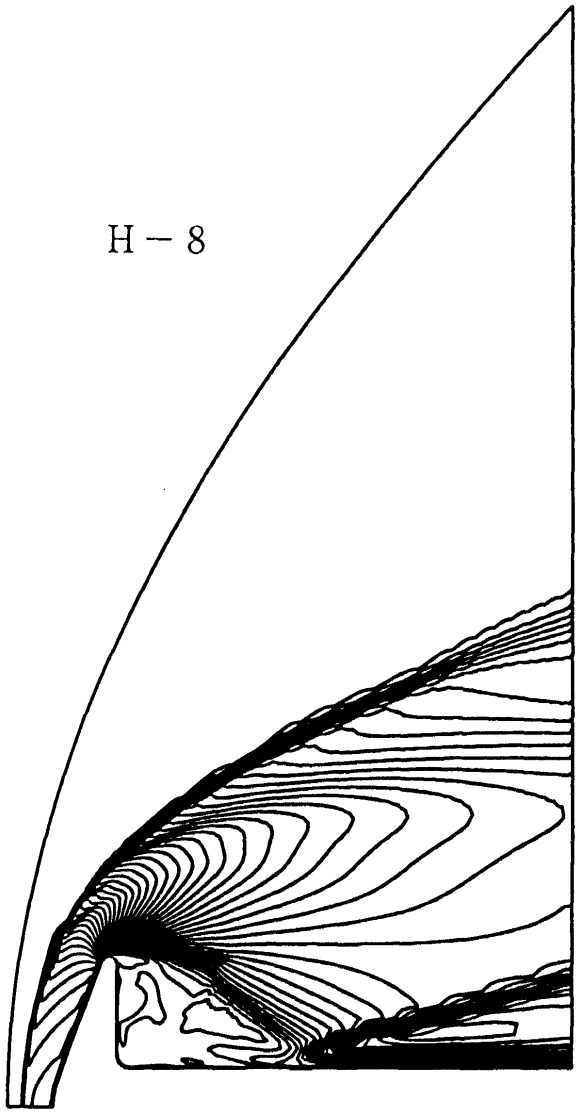

H－8

Spherically Blunted Cone
Temperature Contour Tmax=22.030
Mach=12.31 T_∞=490.0
ρ_∞=0.0041 P_∞=588.4

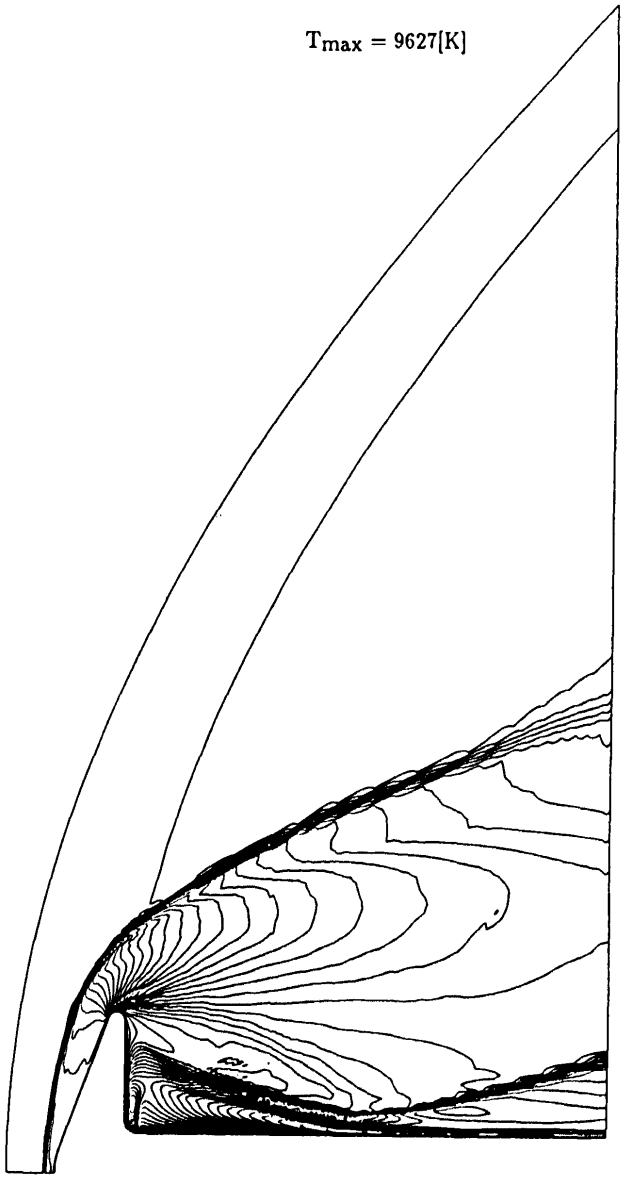

H－9

Problem-IV-1-(2) Trans. Rot. Temp.

Problem IV Blunt Cone 等温度線図（並進、回転）

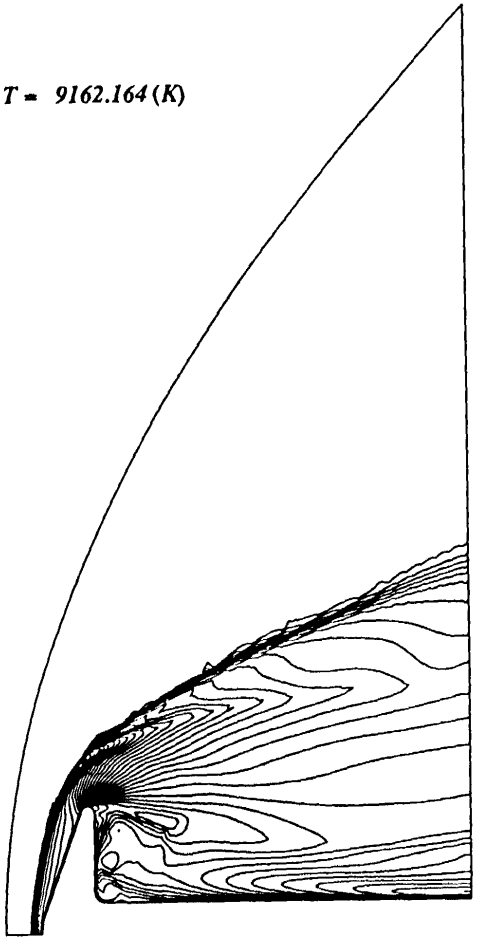

Fig. Problem-IV-1-2 : Temperature Contours

Fig. Problem-IV-2-2 : Temperature Contours

Problem IV Blunt Cone

等温度線図（並進、回転）

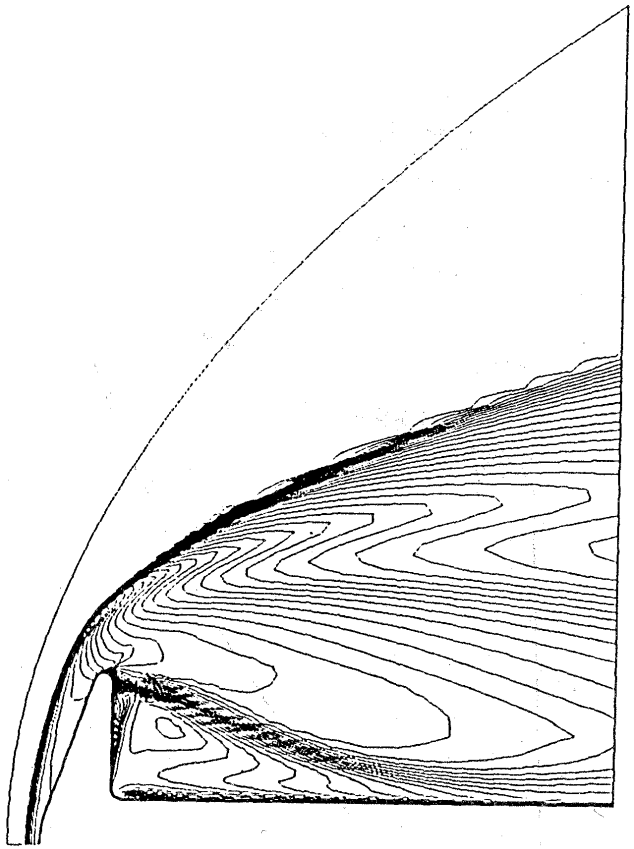

H－3

Problem IV-1-2 (Tvmax = 6.2608e3 K)

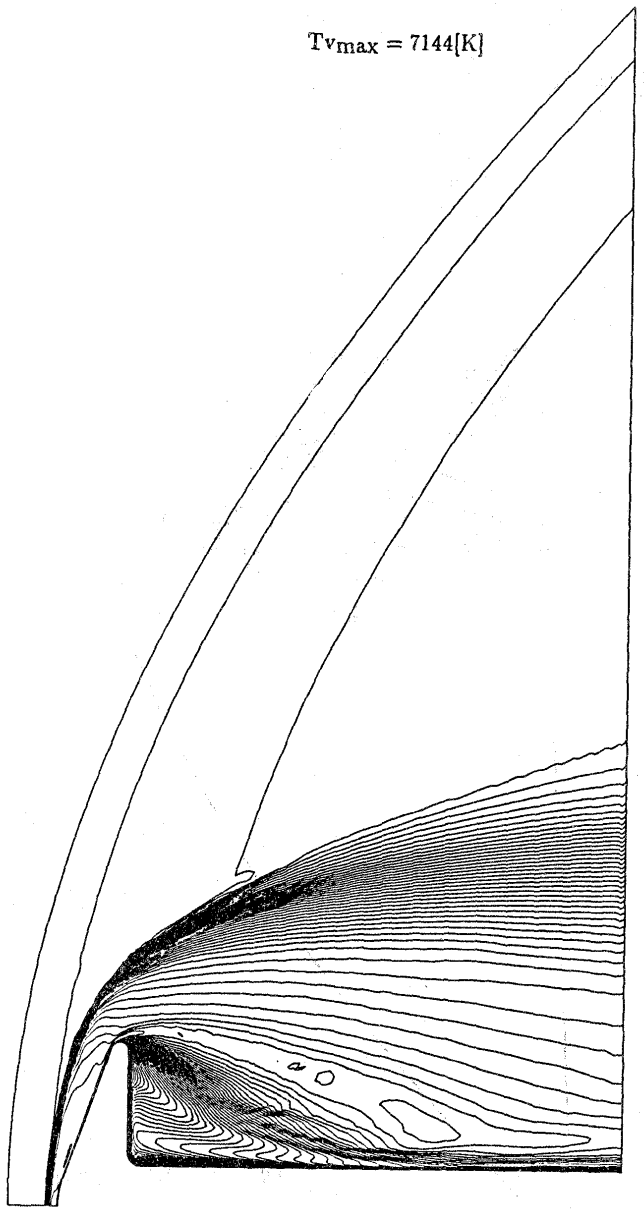

H－9

Problem-IV-1-(2) Vib. Elc. Temp.

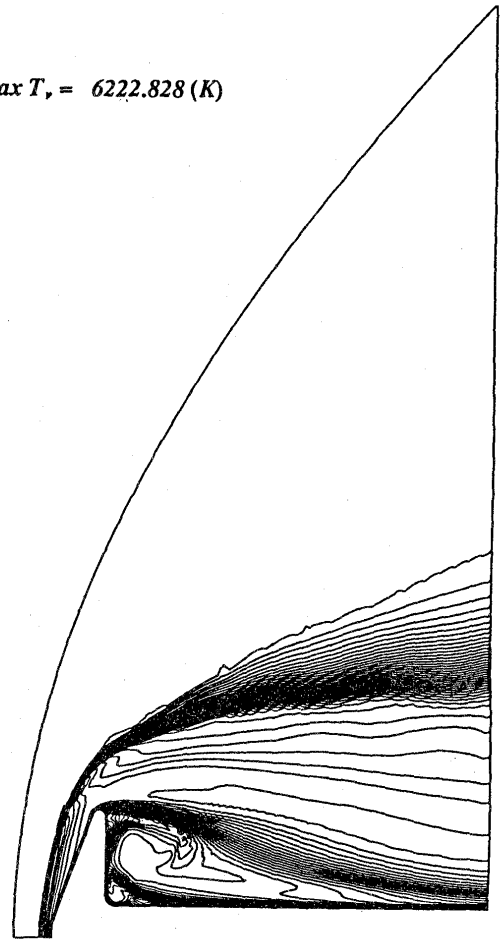

H－11

Fig. Problem-IV-1-2 : Vibrational Temperature Contours

Problem IV Blunt Cone 等温度線図（振動）

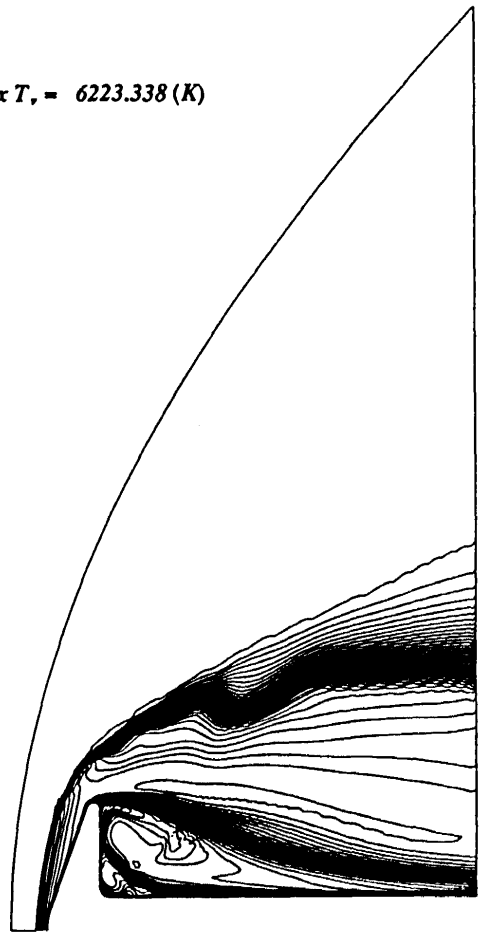

H − 11

Fig. Problem-IV-2-2 : Vibrational Temperature Contours

Problem IV Blunt Cone 等温度線図（振動）

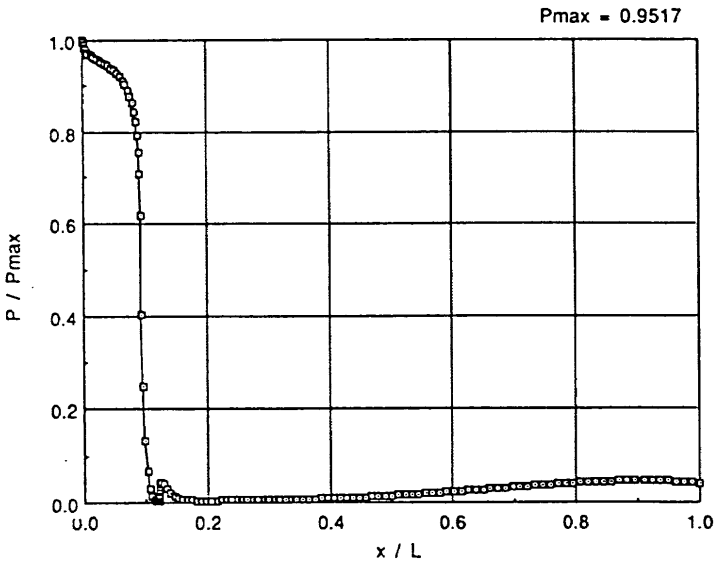

Problem-IV-1-3 H－3

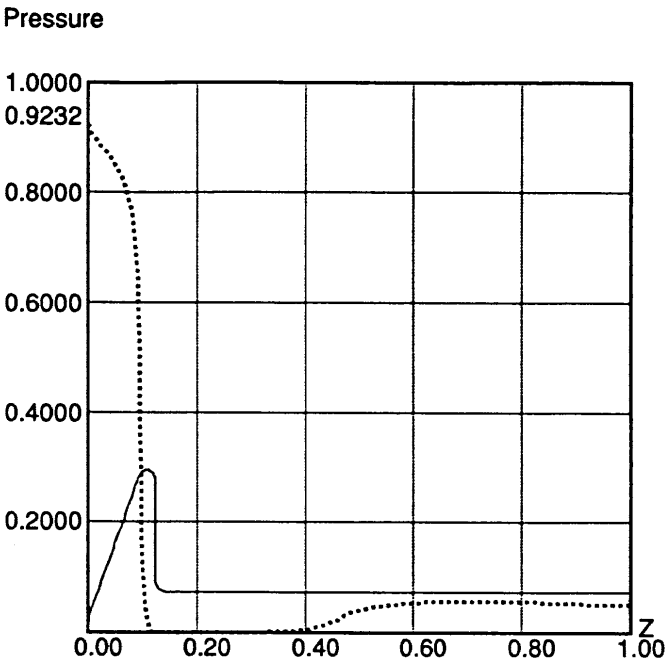

blcopq.data H－8

Problem IV Blunt Cone 表面圧力分布

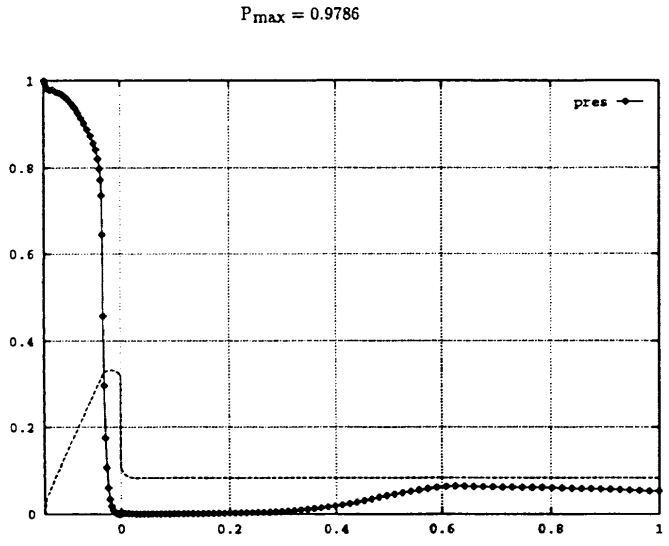

Problem-IV-1-(3) Pressure H－9

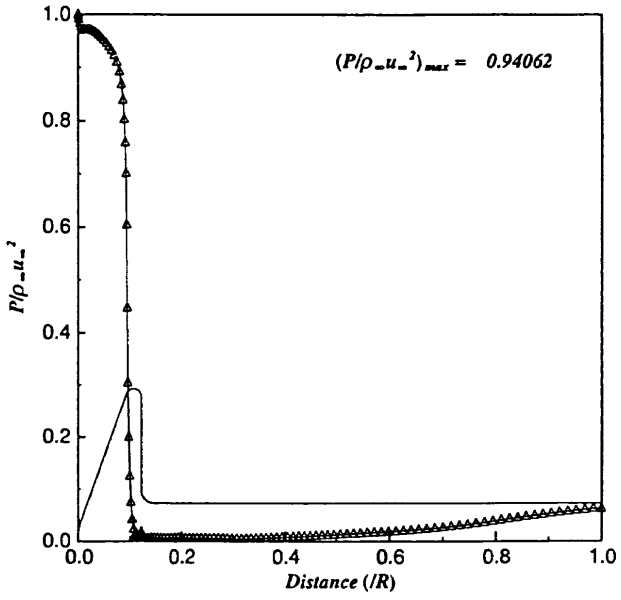

Fig. Problem-IV-1-3 : Pressure Distribution along the Surface

H－11

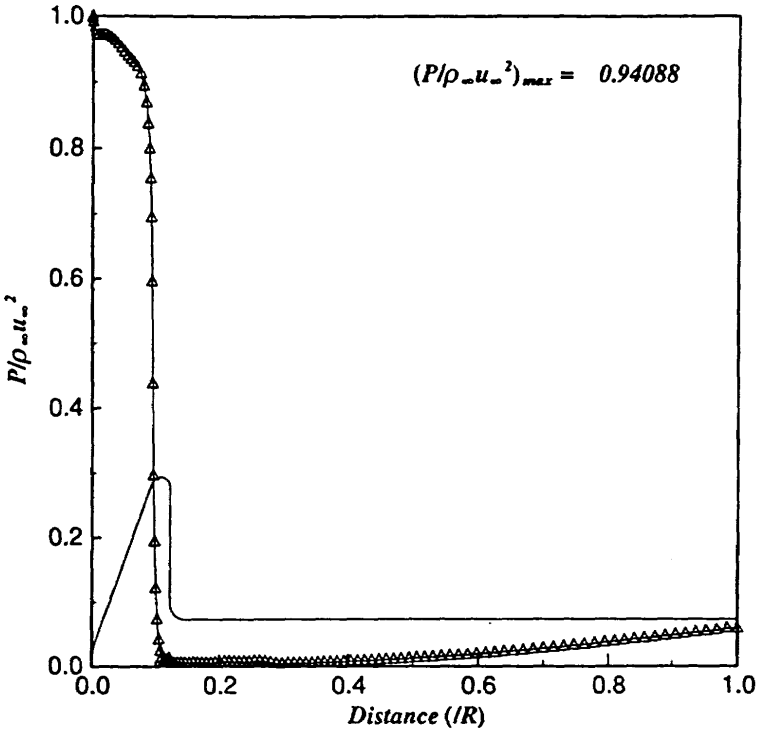

Fig. Problem-IV-2-3 : Pressure Distribution along the Surface

H－11

Problem IV Blunt Cone 表面圧力分布

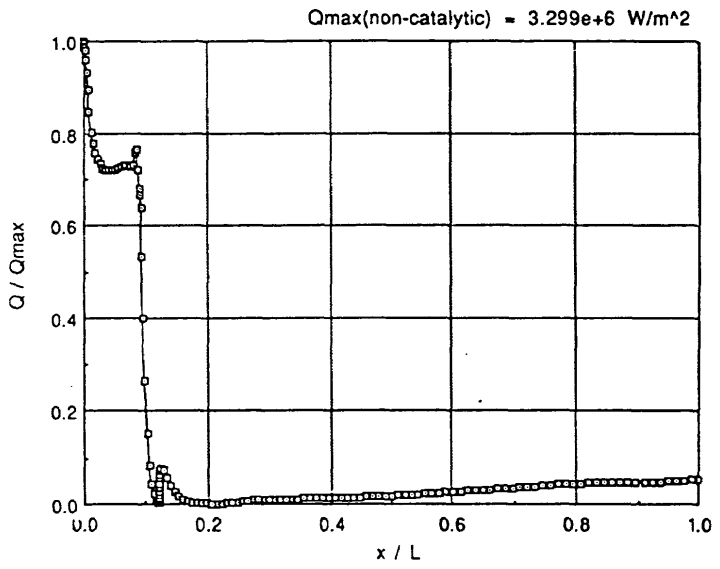

H－3

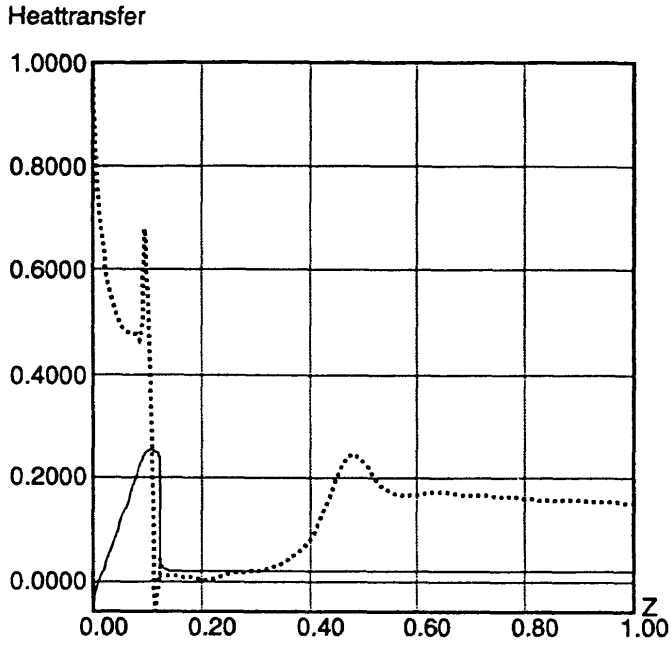

H－8

Problem IV Blunt Cone 表面空力加熱分布

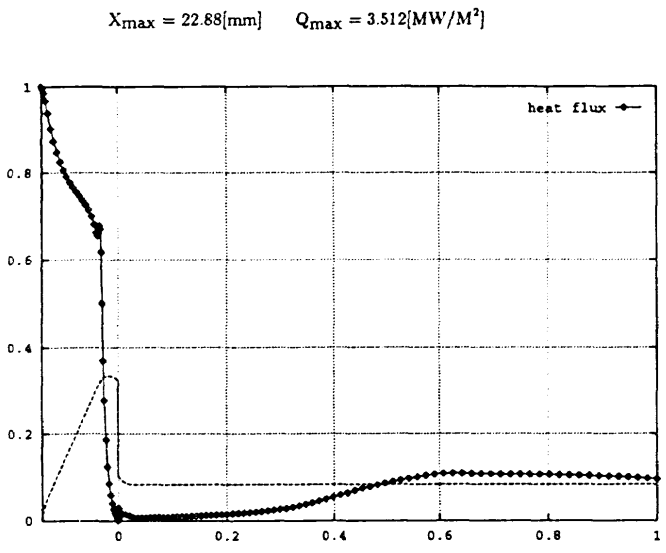

Problem-IV-1-(4) Heatflux

H－9

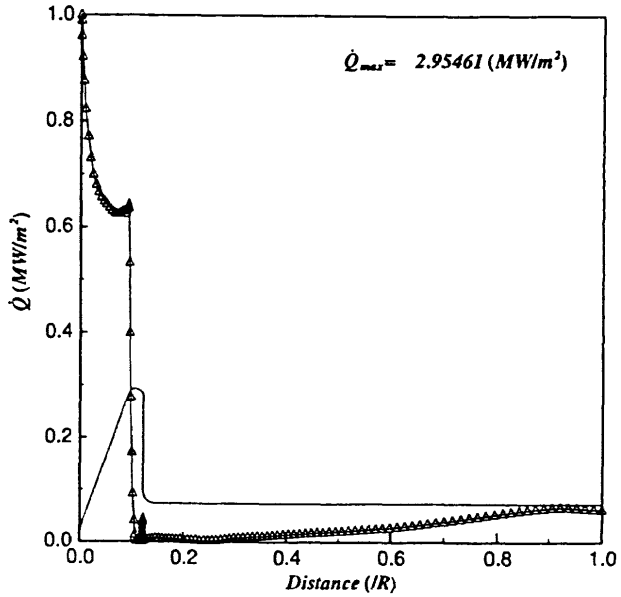

Fig. Problem-IV-1-4 : Heat Flux Distribution along the Surface

H－11

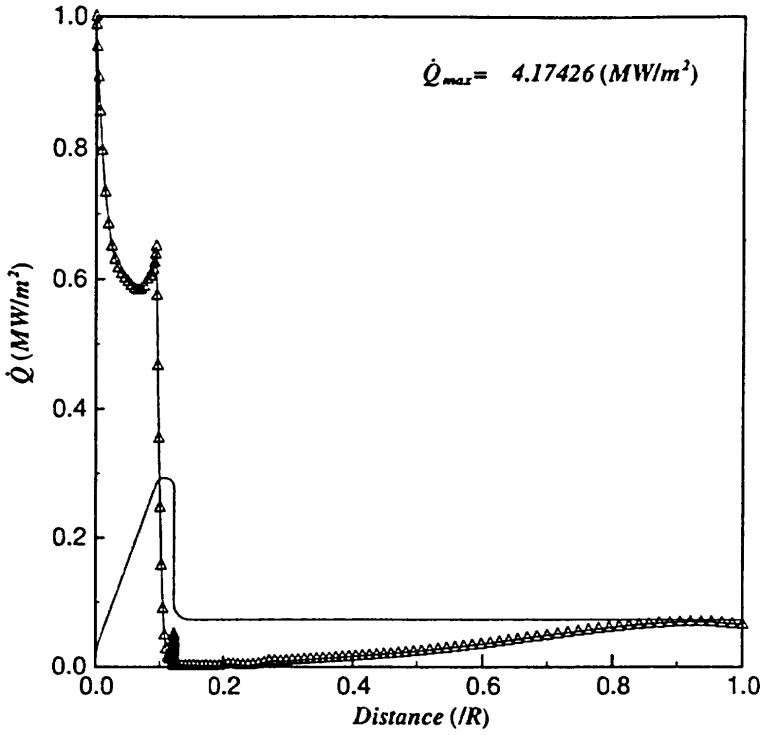

Fig. Problem-IV-2-4 : Heat Flux Distribution along the Surface

H－11

Problem IV Blunt Cone 表面空力加熱分布

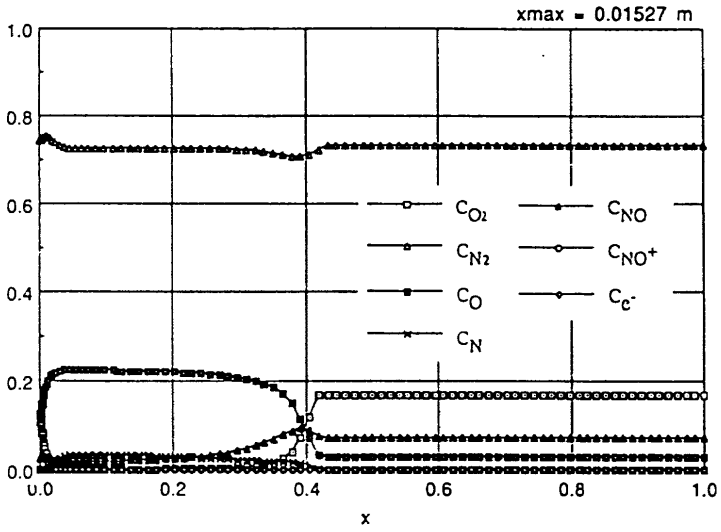

ProblemIV-1-5

H－3

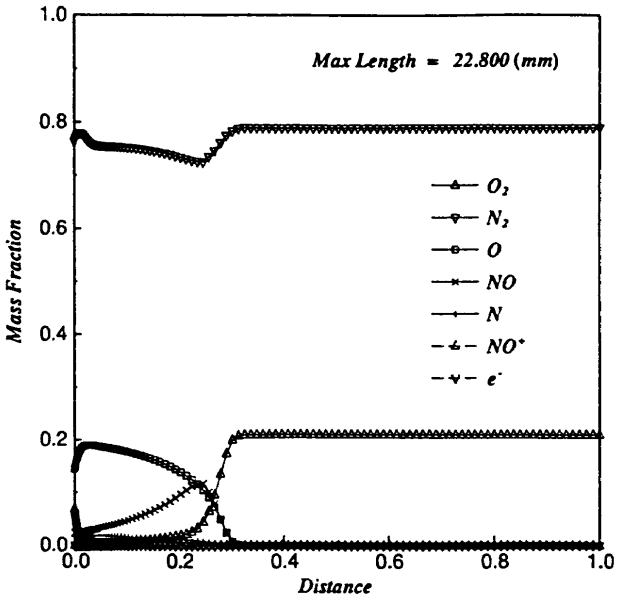

Fig. Problem-IV-1-5 : Mass Fraction along the Stagnation Line

H－11

Problem IV Blunt Cone

よどみ点流線質量分率分布

X_{max} = 22.88[mm]

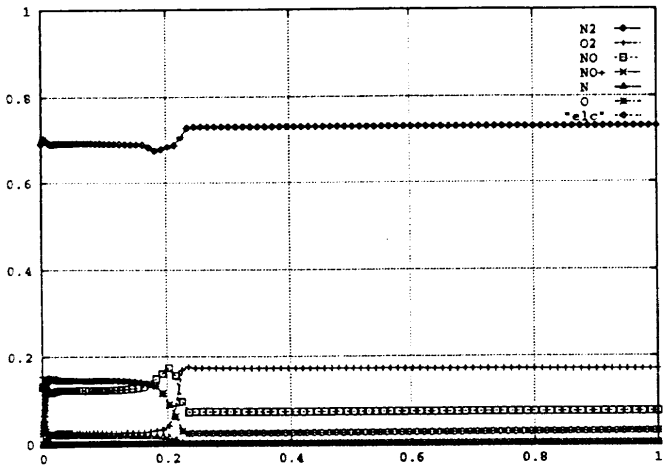

Problem-IV-1-(5)

H－9

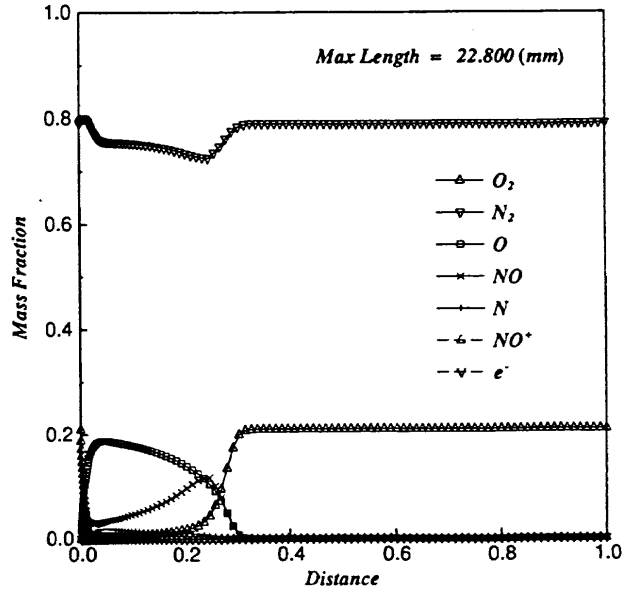

Fig. Problem-IV-2-5 : Mass Fraction along the Stagnation Line

H－11

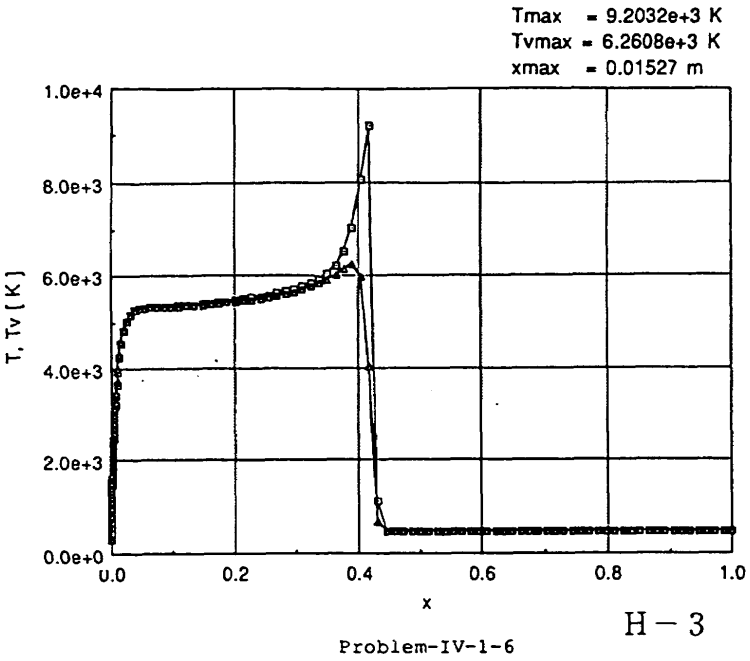

Problem-IV-1-6

H－3

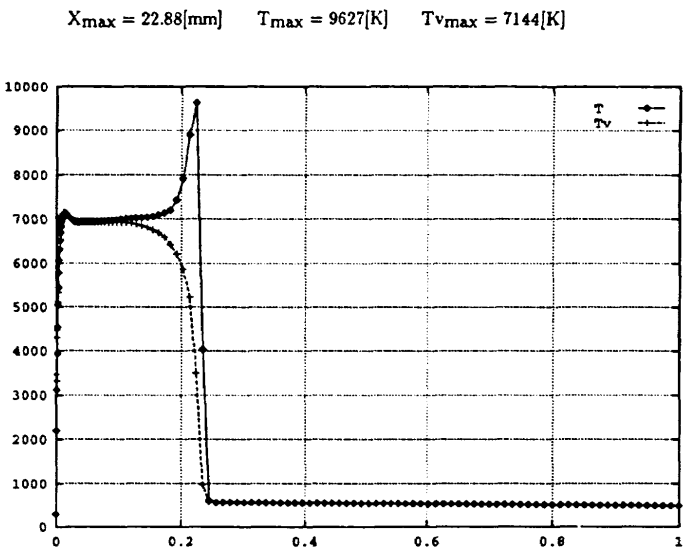

Problem-IV-1-(6)

H－9

Problem IV Blunt Cone

よどみ点流線温度分布

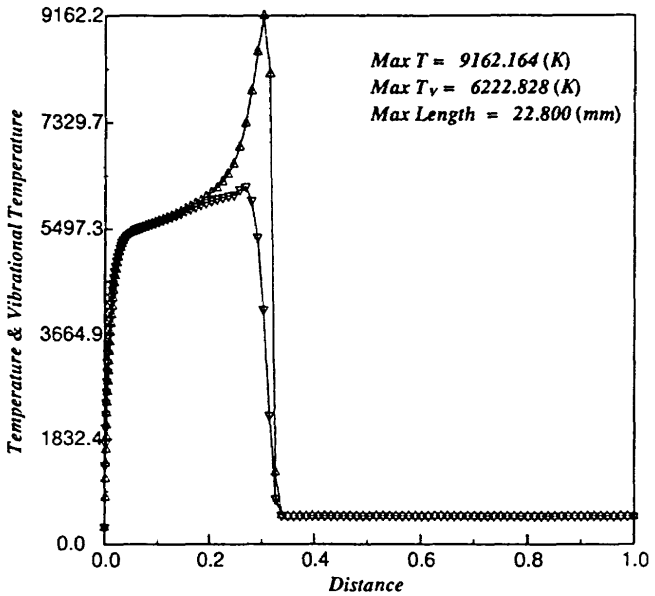

Fig. Problem-IV-1-6 : Temperature Distribution along the Stagnation Line

H－11

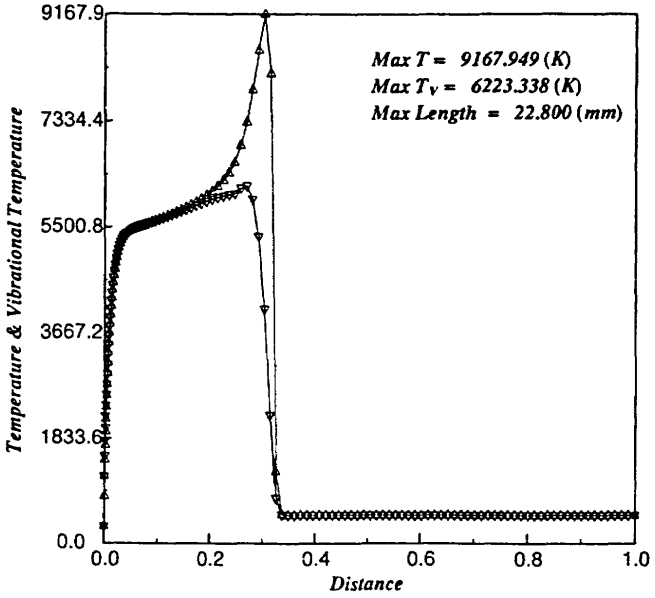

Fig. Problem-IV-2-6 : Temperature Distribution along the Stagnation Line

H－11

航空宇宙技術研究所特別資料29号

平成8年1月発行

発行所 航空宇宙技術研究所
東京都調布市深大寺東町7丁目44番地1
電話三鷹(0422)47-5911(大代表)〒182

印刷所 株式会社三興印刷
東京都新宿区西早稲田2-1-18

Printed in Japan